



**Defense Special Weapons Agency
Alexandria, VA 22310-3398**



DNA-TR-96-10

Laboratory Rock Testing and Hydrologic Calculations to Support the Underground Technology Program

**Daniel E. Chitty
Scott E. Blouin
Applied Research Associates, Inc.
New England Division
RFD#1 Box 120A
Waterman Road
South Royalton, VT 05068**

19980421 163

April 1998

DEFENSE QUALITY INSPECTED 2

Technical Report

CONTRACT No. DNA 001-93-C-0045

**Approved for public release;
distribution is unlimited.**

DESTRUCTION NOTICE:

Destroy this report when it is no longer needed.
Do not return to sender.

PLEASE NOTIFY THE DEFENSE SPECIAL WEAPONS
AGENCY, ATTN: CSTI, 6801 TELEGRAPH ROAD,
ALEXANDRIA, VA 22310-3398, IF YOUR ADDRESS IS
INCORRECT, IF YOU WISH IT DELETED FROM THE
DISTRIBUTION LIST, OR IF THE ADDRESSEE IS NO
LONGER EMPLOYED BY YOUR ORGANIZATION.



DISTRIBUTION LIST UPDATE

This mailer is provided to enable DSWA to maintain current distribution lists for reports. (We would appreciate your providing the requested information.)

- ☐ Add the individual listed to your distribution list.
- ☐ Delete the cited organization/individual.
- ☐ Change of address.

NOTE:

Please return the mailing label from the document so that any additions, changes, corrections or deletions can be made easily. For distribution cancellation or more information call DSWA/IMAS (703) 325-1036.

NAME: _____

ORGANIZATION: _____

OLD ADDRESS

CURRENT ADDRESS

TELEPHONE NUMBER: () _____

DSWA PUBLICATION NUMBER/TITLE

CHANGES/DELETIONS/ADDITIONS, etc.)

(Attach Sheet if more Space is Required)

DSWA OR OTHER GOVERNMENT CONTRACT NUMBER: _____

CERTIFICATION OF NEED-TO-KNOW BY GOVERNMENT SPONSOR (if other than DSWA):

SPONSORING ORGANIZATION: _____

CONTRACTING OFFICER OR REPRESENTATIVE: _____

SIGNATURE: _____

CUT HERE AND RETURN



DEFENSE SPECIAL WEAPONS AGENCY
ATTN: IMAS
6801 TELEGRAPH ROAD
ALEXANDRIA, VA 22310-3398

DEFENSE SPECIAL WEAPONS AGENCY
ATTN: IMAS
6801 TELEGRAPH ROAD
ALEXANDRIA, VA 22310-3398

REPORT DOCUMENTATION PAGE			Form Approved OMB No. 0704-0188	
Public reporting burden for this collection of information is estimated to average 1 hour per response including the time for reviewing instructions, searching existing data sources, gathering and maintaining the data needed, and completing and reviewing the collection of information. Send comments regarding this burden estimate or any other aspect of this collection of information, including suggestions for reducing this burden, to Washington Headquarters Services, Directorate for Information Operations and Reports, 1215 Jefferson Davis Highway, Suite 1204, Arlington, VA 22202-4302, and to the Office of Management and Budget, Paperwork Reduction Project (0704-0188), Washington, DC 20503.				
1. AGENCY USE ONLY (Leave blank)	2. REPORT DATE 980401	3. REPORT TYPE AND DATES COVERED Technical 930303 - 951031		
4. TITLE AND SUBTITLE Laboratory Rock Testing and Hydrologic Calculations to Support the Underground Technology Program		5. FUNDING NUMBERS C - DNA 001-93-C-0045 PE - 62715H PR - AC TA - AB WU - DH330460		
6. AUTHOR(S) Daniel E. Chitty and Scott E. Blouin (ARA), and L. Stephen Melzer (U of T)				
7. PERFORMING ORGANIZATION NAME(S) AND ADDRESS(ES) Applied Research Associates, Inc. New England Division RFD#1 Box 120A Waterman Road South Royalton, VT 05068		8. PERFORMING ORGANIZATION REPORT NUMBER 5796		
9. SPONSORING/MONITORING AGENCY NAME(S) AND ADDRESS(ES) Defense Special Weapons Agency 6801 Telegraph Road Alexandria, VA 22310-3398 PMT/Senseny		10. SPONSORING/MONITORING AGENCY REPORT NUMBER DNA-TR-96-10		
11. SUPPLEMENTARY NOTES This work was sponsored by the Defense Special Weapons Agency under RDT&E RMC Code B4662D AC AB 0022 4300A 25904D.				
12a. DISTRIBUTION/AVAILABILITY STATEMENT Approved for public release; distribution is unlimited.			12b. DISTRIBUTION CODE	
13. ABSTRACT (Maximum 200 words) This report presents the results of laboratory testing and analysis conducted to support the Defense Nuclear Agency Underground Technology Program (UTP). The primary emphasis is on the UTP test site in the Rodgers Hollow area at Fort Knox, Kentucky. An extensive series of laboratory tests was performed on carbonate rock specimens prepared from cores retrieved from two deep drilled holes at the Fort Knox test site, including density/porosity characterization, ultrasonic wavespeeds, unconfined and triaxial compression, hydrostatic compression, and uniaxial strain loading. The testing and data analysis will support definition of the mechanical properties of the rock as functions of porosity, as well as assignment of porosity values for the various <i>in situ</i> layers, from which the layer properties can be assigned. Laboratory tests were also performed on rock from two shallow core holes in the U16a tunnel at Nevada Test Site, the site of the Dipole Hale test. The objective of these tests was to evaluate the air content in this porous tuff, which was partially saturated with water. This was done using both undrained uniaxial strain tests and standard mass/volume determinations. This report also presents the results of a detailed hydrologic study of the moderate to high permeability aquifer in the Louisville formation at the Fort Knox test site. The study integrated all hydrologic data from the site and included both analytical and two-dimensional numerical simulations.				
14. SUBJECT TERMS Rock Mechanics Laboratory Testing Underground Technology Program Hydrology			15. NUMBER OF PAGES 260	
			16. PRICE CODE	
17. SECURITY CLASSIFICATION OF REPORT UNCLASSIFIED	18. SECURITY CLASSIFICATION OF THIS PAGE UNCLASSIFIED	19. SECURITY CLASSIFICATION OF ABSTRACT UNCLASSIFIED	20. LIMITATION OF ABSTRACT SAR	

UNCLASSIFIED

SECURITY CLASSIFICATION OF THIS PAGE

CLASSIFIED BY:

N/A since Unclassified.

DECLASSIFY ON:

N/A since Unclassified.

7. PERFORMING ORGANIZATION NAME(S) AND ADDRESS(ES) (Continued)

Center for Energy and Economic Diversification
The University of Texas of the Permian Basin
4901 East University
Odessa, TX 79762

SUMMARY

This report presents the results of laboratory testing and analysis conducted to support the Defense Nuclear Agency Underground Technology Program (UTP). It describes three distinct efforts, each conducted to support a different aspect of the UTP. Sections 2 and 3 present the results of laboratory testing on rocks from UTP test site in the Rodgers Hollow area at Fort Knox, Kentucky, and analysis of the test results. Section 4 describes testing performed on specimens of tuff from Tunnel U16a at Nevada test site. Section 5 presents hydrologic analyses of the Fort Knox site.

An extensive series of laboratory tests was performed on carbonate rock specimens prepared from cores retrieved from two deep drilled holes at the Fort Knox test site, including density/porosity characterization, ultrasonic wavespeeds, unconfined and triaxial compression, hydrostatic compression, and uniaxial strain loading. The testing was confined to the Louisville formation, which is approximately 30 m thick at the location of interest. Over that 30-m range, there are significant variations in the properties of the rock. Thus, the test program was designed to characterize, as well as possible, the variation in properties of the material over the extent of the formation. Previous investigators had defined a layered model for the site with seven layers in the Louisville formation. In this work, specimens were selected for testing in such a way that each type of test was performed on at least one specimen from each layer, and also on specimens spanning the range of porosities encountered in the formation. Thus, the testing and data analysis will support definition of the mechanical properties of the rock as functions of porosity, as well as assignment of porosity values for the various *in situ* layers, from which the layer properties can be assigned.

Analysis of the data was conducted to characterize the variation in mechanical properties with rock porosity. Models are proposed for strength as a function of porosity at confining pressures of 0, 50, 100, and 400 MPa. Those relationships can then use to derive a complete strength envelope for any porosity value of interest, and strength envelopes are presented for .03, .06, .09, .12, and .15. It is also shown that the test data are reasonably well represented by a previously defined expression for the relationship between porosity and constrained modulus, although a site specific model would yield a better fit.

Laboratory tests were performed on rock from two shallow core holes in the U16a tunnel at Nevada Test Site, the site of the Dipole Hole test. The objective of these tests was to evaluate the air content in this porous tuff which was partially saturated with water. This was done using both undrained uniaxial strain tests and standard mass/volume determinations. In the undrained uniaxial strain test, there is a distinct change in response when the unsaturated void space is crushed out and the specimen becomes fully saturated. At that point, the apparent stiffness of the specimen increases and the pore pressure begins to build up. The volumetric strain at which this occurs is a very good approximation of the air content in the unstressed material. Excellent agreement was found between air contents determined in this manner and determinations based on simple mass and volume measurements.

This report also presents the results of a detailed hydrologic study of the moderate to high permeability aquifer in the Louisville formation at the Fort Knox test site. The study integrated

all hydrologic data from the site and included both analytical and two-dimensional numerical simulations. This study leads to the following conclusions:

For the UTP conditions, the water influx into the adit has been estimated to peak at 170-180 gpm assuming no reinjection (or efficient recharge).

- The UTP pump test was only conducted for a period of 25 hours. From that test, a relatively firm minimum of nine billion gallons of reservoir capacity was calculated, and a possible size of as much as 317 billion gallons was indicated. An aquifer thickness of 74 feet based on well-log data was used in the volumetric calculations. With these parameters for the aquifer, it would require over 100 years to completely deplete the minimum size aquifer.
- Without reinjection or sealing of the underground opening (adit) walls, the water level in the test area will decline below the top of the Louisville formation, resulting in an unsaturated condition in the shape of an inverted cone in the materials above and lateral to the opening. This unsaturated zone is estimated to extend a lateral distance of 650 feet from the opening within five years.
- Without efficient recharge capacity of an aquifer like that surrounding the UTP adit, reinjection of produced water or sealing of the adit walls would be required to maintain a saturated condition in the vicinity of the adit. Only sealing can maintain a saturation condition very near an adit.
- The profile of the desaturated zone results in unsaturated material above the underground opening. For hardness calculations, the shock wave attenuation from bursts above the opening will be affected by the change in material properties as a result of the desaturated zone.
- Analysis of the pump test data at the UTP site indicates skin or wellbore damage in the pumping well at the site. Data from the injectivity tests at the site indicated possible, but not conclusive, damage in those wells also. This induced skin complicates conclusions related to water influx and formation of the desaturated zone. Depending on the type of excavation, the walls of an underground opening may be damaged in a fashion similar to the UTP pumping well, or, alternatively, they may be stimulated because of procedures such as blasting during excavation. Stimulation would lead to enhanced water flow and resulting in an enlargement of the desaturated zone above and lateral to the opening.
- With other conditions being equal, the inverted cone of desaturation above an underground opening will be larger for materials of high permeability than for materials of low porosity/permeability such as shales and siltstones. The range of permeabilities of the UTP carbonates falls within the expected range of fine to medium grained sandstones, below that of coarse grained sandstones and most soils, and above that of siltstones and shales.

- Even rocks of low permeability are often fractured and saturated with water. The same hydrological effects observed around the UTP adit can be postulated to occur in igneous or metamorphic materials of low intact porosity and permeability.
- Linings in shallow underground openings are often designed to mitigate required pumping. In those cases where sealing is effective and pumping requirements are minimal, the above concerns about the zone of desaturation are overstated. However, it is reasonable to expect that a cone of water table depression will exist above the opening. Depending on the level of aquifer recharge, the desaturation zone may be permanent in spite of the sealing effectiveness. Even in the case of minimal pumping, calculations should be performed to assess whether the water table has been permanently lowered by the pumping during construction.

CONVERSION TABLE

MULTIPLY TO GET \longleftrightarrow BY BY \longleftrightarrow TO GET DIVIDE

angstrom	1.000 000 X E -10	meters (m)
atmosphere (normal)	1.013 25 X E +2	kilo pascal (kPa)
bar	1.000 000 X E +2	kilo pascal (kPa)
barn	1.000 000 X E -28	meter ² (m ²)
British thermal unit (thermochemical)	1.054 350 X E +3	joule (J)
calorie (thermochemical)	4.184 000	joule (J)
cal (thermochemical)/cm ²	4.184 000 X E -2	mega joule/m ² (MJ/m ²)
curie	3.700 000 X E +1	*giga becquerel (GBq)
degree (angle)	1.745 329 X E -2	radian (rad)
degree Fahrenheit	$t_k = t_{\text{bf}} + 459.67/1.8$	degree kelvin (K)
electron volt	1.602 19 X E -19	joule (J)
erg	1.000 000 X E -7	joule (J)
erg/second	1.000 000 X E -7	watt (W)
foot	3.048 000 X E -1	meter (m)
foot-pound-force	1.355 818	joule (J)
gallon (U.S. liquid)	3.785 412 X E -3	meter ³ (m ³)
inch	2.540 000 X E -2	meter (m)
jerk	1.000 000 X E +9	joule (J)
joule/kilogram (J/kg) radiation dose absorbed	1.000 000	Gray (Gy)
kilotons	4.183	terajoules
kip (1000 lbf)	4.448 222 X E +3	newton (N)
kip/inch ² (ksi)	6.894 757 X E +3	kilo pascal (kPa)
ktap	1.000 000 X E +2	newton-second/m ² (N-s/m ²)
micron	1.000 000 X E -6	meter (m)
mil	2.540 000 X E -5	meter (m)
mile (international)	1.609 344 X E +3	meter (m)
ounce	2.834 952 X E -2	kilogram (kg)
pound-force (lbs avoirdupois)	4.448 222	newton (N)
pound-force inch	1.129 848 X E -1	newton-meter (N-m)
pound-force/inch	1.751 268 X E +2	newton-meter (N/m)
pound-force/foot ²	4.788 026 X E -2	kilo pascal (kPa)
pound-force/inch ² (psi)	6.894 757	kilo pascal (kPa)
pound-mass (lbm avoirdupois)	4.535 924 X E -1	kilogram (kg)
pound-mass-foot ² (moment of inertia)	4.214 011 X E -2	kilogram-meter ² (kgm ²)
pound-mass/foot ³	1.601 846 X E +1	kilogram/meter ³ (kg/m ³)
rad (radiation dose absorbed)	1.000 000 X E -2	**Gray (Gy)
roentgen	2.579 760 X E -4	coulomb/kilogram (C/kg)
shake	1.000 000 X E -8	second (s)
slug	1.459 390 X E +1	kilogram (kg)
torr (mm Hg O°C)	1.333 22 X E -1	kilo pascal (kPa)

* The becquerel (Bq) is the SI unit of radioactivity; 1 Bq = 1 event/s.

**The Gray (Gy) is the SI unit of absorbed radiation.

TABLE OF CONTENTS

Section	Page
SUMMARY.....	iii
CONVERSION TABLE.....	vi
FIGURES.....	x
TABLES.....	xv
1 INTRODUCTION.....	1
1.1 BACKGROUND.....	1
1.2 OBJECTIVES.....	1
1.3 SCOPE.....	2
2 LABORATORY TESTING OF FORT KNOX LIMESTONE.....	3
2.1 MATERIAL ORIGIN.....	3
2.2 PHYSICAL PROPERTIES.....	4
2.2.1 Grain Density.....	4
2.2.2 Bulk Density.....	5
2.2.3 Ultrasonic Compressional Wavespeeds.....	5
2.3 SPECIMEN SELECTION.....	6
2.4 SPECIMEN FABRICATION.....	7
2.5 SPECIMEN PREPARATION.....	8
2.6 LOADING.....	9
2.6.1 Hydrostatic Compression.....	9
2.6.2 Triaxial Compression.....	10
2.6.3 Uniaxial Strain.....	10
2.7 INSTRUMENTATION.....	10
2.8 DATA RECORDING AND REDUCTION.....	11
2.9 TEST RESULTS.....	12
2.9.1 Hydrostatic Compression Test Results.....	12
2.9.2 Triaxial Compression Test Results.....	13
2.9.3 Uniaxial Strain Tests.....	14
3 ANALYSIS OF LIMESTONE TEST DATA.....	48
3.1 MODULUS MODELING.....	48
3.2 STRENGTH MODELING.....	49
3.3 DISCUSSION.....	51
4 LABORATORY TESTING OF TUFF FROM NEVADA TEST SITE.....	63
4.1 MATERIAL ORIGIN.....	63
4.2 SPECIMEN PREPARATION.....	63

TABLE OF CONTENTS (Continued)

Section	Page
4.3 INSTRUMENTATION.....	64
4.4 PHYSICAL PROPERTIES.....	65
4.4.1 Grain Density.....	65
4.4.2 Bulk Densities and Water Content.....	65
4.5 MECHANICAL PROPERTY TESTS.....	66
4.5.1 Compressibility Tests.....	67
4.5.2 Strength Tests.....	70
4.5.3 Table Summary.....	72
5 ISSUES RELATED TO THE HYDROLOGIC PUMPING OF UNDERGROUND OPENINGS	84
5.1 INTRODUCTION.....	84
5.2 HYDROLOGICAL SUMMARY AND ANALYTICAL MODELING.....	85
5.2.1 Test Site Materials.....	85
5.2.2 Analytical Ground Water Modeling.....	86
5.3 TWO-DIMENSIONAL MODELING.....	88
5.3.1 ASM Groundwater Flow Modeling Software.....	89
5.3.2 Description of the MODFLOW Groundwater Modeling Software.....	92
5.3.3 Description of MODFLOW Test Site Grid Idealizations.....	92
5.4 HARDNESS ISSUES.....	94
5.5 CONCLUSIONS AND RECOMMENDATIONS.....	95
5.5.1 Conclusions.....	95
5.5.2 Recommendations.....	97
6 REFERENCES	121
 Appendix	
A HYDROSTATIC COMPRESSION TESTS ON CARBONATE ROCKS FROM FORT KNOX.....	A-1
B UNCONFINED COMPRESSION TESTS ON CARBONATE ROCKS FROM FORT KNOX.....	B-1
C TRIAXIAL COMPRESSION TESTS ON CARBONATE ROCKS FROM FORT KNOX.....	C-1

TABLE OF CONTENTS (Continued)

Section

Page

D UNIAxIAL STRAIN TESTS ON CARBONATE ROCKS FROM FORT KNOX.....D-1

E TEST DATA FOR TUFF FROM NEVADA TEST SITEE-1

FIGURES

Figure	Page
2-1 Plan of the test area at Fort Knox showing the locations of the core borings.....	26
2-2 Ultrasonic compressional wavespeeds of the CS-4 core as a function of depth.....	27
2-3 Ultrasonic compressional wavespeeds of the CS-5 core as a function of depth.....	28
2-4 Illustration of a jacketed test specimen showing the positions of the lubricating materials.....	29
2-5 Illustration of the instrumentation used to measure deformations and pore pressure of a test specimen.....	30
2-6 Relationships between confining pressure and volumetric strain for specimens of carbonate rocks from core hole CS-4 at Fort Knox tested in hydrostatic compression	31
2-7 Relationships between axial and radial strain for specimens of carbonate rocks from core hole CS-4 at Fort Knox tested in hydrostatic compression	32
2-8 Axial and radial strains plotted against stress difference for specimens of high-porosity carbonate rocks from core hole CS-4 at Fort Knox tested in unconfined compression	33
2-9 Axial and radial strains plotted against stress difference for specimens of low-porosity carbonate rocks from core hole CS-4 at Fort Knox tested in unconfined compression	34
2-10 Axial and radial strains plotted against stress difference for specimens of high-porosity carbonate rocks from core hole CS-5 at Fort Knox tested in unconfined compression	35
2-11 Axial and radial strains plotted against stress difference for specimens of low-porosity carbonate rocks from core hole CS-5 at Fort Knox tested in unconfined compression	36
2-12 Axial and radial strains plotted against stress difference for specimens high-porosity carbonate rocks from core hole CS-4 at Fort Knox tested in triaxial compression with 50 MPa confining pressure	37
2-13 Axial and radial strains plotted against stress difference for specimens low-porosity carbonate rocks from core hole CS-4 at Fort Knox tested in triaxial compression with 50 MPa confining pressure	38

FIGURES (Continued)

Figure	Page
2-14 Axial and radial strains plotted against stress difference for specimens high-porosity carbonate rocks from core hole CS-4 at Fort Knox tested in triaxial compression with 100 MPa confining pressure	39
2-15 Axial and radial strains plotted against stress difference for specimens low-porosity carbonate rocks from core hole CS-4 at Fort Knox tested in triaxial compression with 100 MPa confining pressure	40
2-16 Axial and radial strains plotted against stress difference for specimens carbonate rocks from core hole CS-4 at Fort Knox tested in triaxial compression with 400 MPa confining pressure	41
2-17 Relationships between axial stress and axial strain for specimens of high-porosity carbonate rocks from core hole CS-4 at Fort Knox tested in uniaxial strain	42
2-18 Relationships between axial stress and axial strain for specimens of low-porosity carbonate rocks from core hole CS-4 at Fort Knox tested in uniaxial strain	43
2-19 Relationships between stress difference and mean stress for specimens of high-porosity carbonate rocks from core hole CS-4 at Fort Knox tested in uniaxial strain	44
2-20 Relationships between stress difference and mean stress for specimens of low-porosity carbonate rocks from core hole CS-4 at Fort Knox tested in uniaxial strain	45
2-21 Relationships between axial stress and confining pressure for specimens of high-porosity carbonate rocks from core hole CS-4 at Fort Knox tested in uniaxial strain	46
2-22 Relationships between axial stress and confining pressure for specimens of low-porosity carbonate rocks from core hole CS-4 at Fort Knox tested in uniaxial strain	47
3-1 The constrained moduli determined from uniaxial strain tests on carbonate rocks from Fort Knox plotted against their unstressed normalized specific volumes. Also shown is a line representing a model that was previously derived for a wide range of carbonate rocks	52
3-2 Values of peak stress difference determined from unconfined compression tests on specimens of carbonate rocks from Fort Knox plotted against their initial porosity, and a straight line fit to the data points	53

FIGURES (Continued)

Figure	Page
3-3 Values of peak stress difference determined from 50-MPa triaxial compression tests on specimens of carbonate rocks from Fort Knox plotted against their initial porosity, and a straight line fit to the data points	54
3-4 Values of peak stress difference determined from 100-MPa triaxial compression tests on specimens of carbonate rocks from Fort Knox plotted against their initial porosity, and a straight line fit to the data points	55
3-5 Values of peak stress difference determined from 400-MPa triaxial compression tests on specimens of carbonate rocks from Fort Knox plotted against their initial porosity, and a straight line fit to the data points	56
3-6 Strength envelopes synthesized from the fits shown in Figures 3-2 through 3-5 for carbonate rocks with porosities ranging from 0.03 to 0.15.....	57
3-7 Synthesized strength envelope for 0.03 porosity shown along with the strength points from the Fort Knox data set that most closely match that porosity.....	58
3-8 Synthesized strength envelope for 0.06 porosity shown along with the strength points from the Fort Knox data set that most closely match that porosity.....	59
3-9 Synthesized strength envelope for 0.09 porosity shown along with the strength points from the Fort Knox data set that most closely match that porosity.....	60
3-10 Synthesized strength envelope for 0.12 porosity shown along with the strength points from the Fort Knox data set that most closely match that porosity.....	61
3-11 Synthesized strength envelope for 0.15 porosity shown along with the strength points from the Fort Knox data set that most closely match that porosity.....	62
4-1 Total axial stress, effective axial stress, and pore pressure plotted against axial strain for an undrained uniaxial strain test (M24A5) on a specimen of tuff from Nevada Test Site	75
4-2 Total mean stress, mean effective stress, and pore pressure plotted against volumetric strain for an undrained uniaxial strain test (M24A5) on a specimen of tuff from Nevada Test Site.....	76
4-3 Total axial stress, effective axial stress, and pore pressure plotted against axial strain for an undrained uniaxial strain test (M28A5) on a specimen of tuff from Nevada Test Site	77

FIGURES (Continued)

Figure	Page
4-4 Total mean stress, mean effective stress, and pore pressure plotted against volumetric strain for an undrained uniaxial strain test (M28A5) on a specimen of tuff from Nevada Test Site.....	78
4-5 Total mean stress, mean effective stress, and pore pressure plotted against volumetric strain for an undrained hydrostatic compression test (M29A5) on a specimen of tuff from Nevada Test Site	79
4-6 Axial and radial strains plotted against stress difference for specimens of tuff from Nevada Test Site tested in unconfined compression.....	80
4-7 Axial and radial strains plotted against stress difference for a specimen of tuff from Nevada Test Site, tested in undrained triaxial compression with 400 MPa confining pressure	81
4-8 Axial and radial strains plotted against stress difference for a specimen of tuff from Nevada Test Site, tested in drained triaxial compression with 200 MPa confining pressure	82
4-9 Summary of strength data for tuff from Nevada Test Site.....	83
5-1 Geologic profile along adit centerline.....	100
5-2 Estimated water influx as a function of adit length computed using an analytical model of a horizontal well assuming two different values of aquifer permeability.....	101
5-3 Schematic of the adit model used to estimate the desaturation zone	102
5-4 Computed variation with time in the water level 100 ft from the terminal end of the access adit	103
5-5 Computed water level as a function of distance from the adit with reinjection.....	104
5-6 Adit production over two years computed by the ASM model.....	106
5-7 Variation in the water level with time 100 ft from the terminal end of the adit computed by the ASM model without reinjection	107
5-8 Distance to the unsaturated zone for time periods from 60 days to five years.....	108
5-9 Variation in water level with distance at two years as predicted by the ASM model without reinjection	110

FIGURES (Continued)

Figure	Page
5-10 Water level above the adit floor at two years as predicted by the ASM model without reinjection	111
5-11 Comparison of adit production over time with and without reinjection as predicted by the ASM model	112
5-12 Comparison of the variations in the water level with time 100 ft from the terminal end of the adit computed by the ASM model with and without reinjection	113
5-13 Close-in water table position one day after beginning the excavation.....	114
5-14 Close-in water table position at the end of a 60-day simulation in which the tunnel was completed in 50 days	116
5-15 Head distribution in the test area after 360 days of reinjection commencing 10 days after completion of the adit.....	118
5-16 Variation in head with distance from the adit at three different locations after 360 days of reinjection commencing 10 days after completion of the adit.....	119
5-17 Volumetric data from Models 30 and 31 for 50 days of excavation without reinjection and then 360 days of reinjection	120

TABLES

Table	Page
2-1 Layering in borings CS-4 and CS-5.....	16
2-2 Grain density results.....	17
2-3 Summary statistics for ultrasonic wavespeeds (Km/s) of core from each layer in boreholes CS-4 and CS-5.....	18
2-4 Properties of test specimens prepared from CS-4 core.....	19
2-5 Properties of test specimens prepared from CS-5 core.....	20
2-6 Summary of hydrostatic compression tests on carbonate rock from Fort Knox.....	22
2-7 Summary of unconfined compression tests on carbonate rock from Fort Knox.....	23
2-8 Summary of triaxial compression tests on carbonate rock from Fort Knox.....	24
2-9 Summary of uniaxial strain tests on carbonate rock from Fort Knox.....	25
3-1 Engineering model for constrained modulus of carbonate rocks as a function of porosity.....	49
4-1 Summary of mechanical property tests performed on NTS tuff.....	73
4-2 Summary of NTS tuff properties.....	74
5-1 Volumetric information from 2-D areal MODFLOW calculation of access adit excavation without reinjection.....	98
5-2 Volumetric information from 2-D areal MODFLOW calculation of access adit excavation with reinjection.....	99

SECTION 1

INTRODUCTION

This report presents the results of laboratory testing and analysis performed to support an experimental investigation of the resistance of tunnels in rock to explosive shock loading. The work was performed by Applied Research Associates, Inc. (ARA) under Contract No. DNA001-93-C-0045 with the Defense Nuclear Agency (DNA). Laboratory tests to determine the physical and mechanical properties of various rocks of interest as well as analysis of those test results were performed by the Materials Testing Laboratory of ARA's New England Division in South Royalton, Vermont. The hydrogeologic analysis was conducted by The University of Texas at the Permian Basin, Center for Energy and Economic Diversification. The work was performed during the period March 1993 through September 1995.

1.1 BACKGROUND.

The research reported herein was performed as part of DNA's Underground Technology Program (UTP), a comprehensive program designed to further their theoretical and practical understanding of the vulnerability of underground openings in rock to explosive shock loading. At the time this contract was awarded, DNA planned to perform a series of tests with large explosive charges on test specimens constructed in the limestone formations beneath the Rodgers Hollow area of Fort Knox, Kentucky. Thus the initial phases of the investigation, comprising the bulk of the effort, focused on those materials. Prior to the conclusion of this research effort, the focus of the DNA UTP shifted to existing tunnels at the Nevada Test Site (NTS). The final phase of the effort involved laboratory testing of tuff from the tunnel test facilities at NTS.

1.2 OBJECTIVES.

The overall objective of the effort was to support the field experiment of the DNA UTP with necessary laboratory testing and analysis tasks. The specific objectives of the program were to:

- perform laboratory physical and mechanical property testing on specimens of rock from the test sites of interest to support development of constitutive relationships for use in first principles and empirical models;

- perform numerical simulations of proposed explosive test events to provide estimates of peak ground shock parameters for use in selection of test instrumentation; and
- analyze hydrologic consequences of various test construction and execution options and recommend alternatives that best support test objectives.

1.3 SCOPE.

A total of 69 mechanical property tests were performed in a triaxial compression apparatus at confining pressures up to 400 MPa on specimens of limestone from the Louisville formation at Fort Knox. The procedures employed and the results of those tests are described in Section 2 of this report. Section 3 presents analysis of the limestone test data, with emphasis on the variations in strength and deformation properties with rock porosity; and presents an empirical model describing those variations. Tests on the tuff from NTS are described and analyzed in Section 4. Section 5 describes the hydrologic analysis performed under this effort. Relevant references are listed in Section 6.

SECTION 2

LABORATORY TESTING OF FORT KNOX LIMESTONE

This section describes the laboratory testing performed on specimens of limestone from Fort Knox. It presents the origin and physical properties of the rock and describes the mechanical property tests performed and the test results.

2.1 MATERIAL ORIGIN.

In the course of site investigation for the planned underground structures tests, at least five core borings were made from the ground surface in the Rodgers Hollow area of Fort Knox. The coring was performed by the U.S. Army Engineer, Waterways Experiment Station (WES). Figure 2-1 is a plan view of the site showing the locations of the various coreholes along with the horizontal alignment of the access tunnel. The planned experiments were to be conducted in the carbonate rock layer existing at a depth range of approximately 155-195m. The carbonate layer of interest, consisting of the Jefferson limestone and the Louisville dolomite, is overlain by the New Providence and New Albany shales and underlain by the Waldron Shale. The exploratory borings were made by first drilling to a depth of approximately 150 m using rotary percussion that pulverizes the rock removed from the hole. From the 150-m depth, the borings were advanced to a depth of approximately 195 m using a diamond coring bit, and all of the rock core from those intervals was recovered and placed in core boxes.

The core boxes containing all of the core from holes CS-4 and CS-5 were transported to ARA for testing. All of the laboratory tests reported herein were performed on specimens prepared from cores that originated in those two boreholes. The material from hole CS-4 arrived at the ARA laboratory in March 1993. That core, along with those from holes CS-1, 2, and 3 had very irregular surfaces due to problems in the coring process. In an effort to obtain better quality cores, four additional borings (CS-5, 6, 7, and 8) were made in the same area of Fort Knox. The material from hole CS-5 arrived at ARA in August 1993.

2.2 PHYSICAL PROPERTIES.

Prior to the beginning of this effort, an idealization of the stratigraphy of the carbonate layer was developed (Blouin and Chitty, 1991). This idealization, which was based on the results of well logs, laboratory ultrasonic wavespeed measurements, and visual examination of the early cores, considered the carbonate portion of the geology to be composed of seven approximately horizontal layers. Table 2-1 presents the layer model for the core from borehole CS-4, which was determined by Green (1993). The corresponding layer breakpoints for CS-5 were selected by ARA based on the same criteria, and are also presented in Table 2-1. This layering scheme was used as the basis for the selection of samples for testing. Within each layer, an effort was made to select materials with properties representative of the median properties of the particular layer. Thus, the test results can be used to characterize the site based on the seven-layer idealization.

An alternative approach to characterization of the site is based on porosity. The porosity of each test specimen was determined in the course of laboratory testing.. By considering the lab test data set for the entire carbonate structure, it is possible to derive correlations between porosity and the mechanical properties of interest. These correlations can be used with a description of the three-dimensional variation of rock porosity, as might be determined from well logs, to develop a mechanical property characterization of the site for tunnel vulnerability calculations.

2.2.1 Grain Density.

The grain densities of multiple rock specimens from each layer were determined using a water pycnometer and a variation of the test method specified by ASTM D854. The rock was crushed until it would all pass a U.S. Standard No. 70 sieve. The resulting powder was oven dried and weighed. The mass was measured of the pycnometer filled with deaired distilled water and of the same container with the crushed rock and filled with water to the same point. From those measurements and the known density of water, the volume, and hence density, of the rock specimen were computed. Appropriate corrections were made for the temperature of the water. At least two grain density determinations were performed on materials from each layer from core CS-4. One additional measurement was made for each layer on the rock from core CS-5. The

results are summarized in Table 2-2. In layers 4 through 7, the grain density results are very consistent between cores CS-4 and CS-5, with variations of the order of 0.1%. In upper layers, there are significantly larger differences between holes. Layer 1 exhibits the greatest variability between core holes (5%), and there is about 2% difference between the two measurements made on material from layer 1 of core CS-5.

2.2.2 Bulk Density.

Measurements for bulk density determination of each specimen were performed after completion of machining, but before jacketing. The mass was determined by a laboratory electronic scale, and the length and diameter were measured with a precision digital caliper. These measurements were performed with the test specimens in the air dry condition. Since no cooling water was used in the specimen fabrication process, and several weeks had elapsed since the cores were removed from the ground, the water content of the test specimens was in equilibrium with the air in the laboratory. Based on previous experience with similar specimens, the estimated water content of the test specimens at the time of density determination was less than 0.05%. For practical purposes, they were considered to be dry. The porosity, n , of each specimen was determined using the equation :

$$n = 1 - \frac{\rho_d}{\rho_g} \quad (2.1)$$

where: ρ_g = grain density
 ρ_d = dry bulk density

Since there are significant spacial variations in grain density, specimen porosity was computed based on the average grain density, as shown in Table 2-2, for the core hole and layer of the individual specimen.

2.2.3 Ultrasonic Compressional Wavespeeds.

Ultrasonic logging was performed over the full length of both cores before specimens were prepared for mechanical property testing. Logging of CS-4 was performed by WES before the rock was shipped to the ARA, and the core from CS-5 was logged at the ARA laboratory. Since

the ultrasonic logging was performed before the rock core was cut to length for specimen preparation, the wavespeed measurements were made across the diameter of the core. The tests were performed with a pair of 670-kHz ultrasonic compressional wave transducers held tightly against diametrically opposite sides of the core with a water-based couplant. One transducer was excited by a step function generator and the other was used to detect the arriving pulse. A 20-Mhz digital oscilloscope was used to measure the transit time.

The measurements made by WES on CS-4, which were performed at equal 60-mm (0.2 ft) intervals, are presented graphically in Figure 2-2. Also shown in Figure 2-2 are the layer boundaries. Core CS-5 was logged at approximately 150-mm (0.5 ft) intervals, with a effort made to log all visually apparent changes in the rock properties. Those data are presented in Figure 2-3, along with the layering for CS-5.

After preparation of test specimens with flat ground ends, additional wavespeed measurements were performed on individual specimens. Essentially the same procedures were used. However, in the case of the finished specimens, the ultrasonic transducers were placed on the ground ends of the cores, resulting in a wavespeed measurement in the direction that would have been vertical *in situ*.

2.3 SPECIMEN SELECTION.

The ultrasonic logs were used as the basis for selection of test specimens which were representative of the materials in their respective layers. From each layer of each rock core, groups of 6-8 representative specimens were prepared for triaxial compression testing. To support this process, summary statistics were computed for each layer of each core. The statistics for both cores are summarized in Table 2-3. No attempt was made to fit specific distributions to the data sets. The means and standard deviations were computed in the usual manner. The 40, 50 (median), and 60 percentile points were determine by sorting the data for each layer into numerical order and selecting the wavespeed values corresponding to their respective fractions of the number of measurements in the layer.

Using the ultrasonic log data, an attempt was made to select specimens in the middle 20% of the range, i.e. between the 40th and 60th percentiles. However, it was not always possible to prepare

specimens from entirely within that range. Breaks in the core limited the possibilities for test specimens of the required length (2x diameter), and any visible cavities in the core were avoided because they tend to cause failure of the jacketing membrane during testing. Therefore, when it was not possible to obtain all specimen from the middle 20% based on wavespeed logs, the acceptable region was expanded to encompass the 30th through 70th percentiles.

Layer 4 was treated somewhat differently than the others because it is the thickest layer and because it was planned that the test structures would be constructed there. Thus, in addition to the specimens prepared from the materials in the mid-range of ultrasonic wavespeed properties, a group of specimens from each of the two cores was also prepared from the highest and lowest 30% of wavespeeds.

Table 2-4 lists the mechanical property test specimens prepared from the CS-4 core. The Specimen ID is a unique identifier assigned for tracking the specimen in the ARA laboratory. Relevant physical properties of the specimens are included in the table. The corresponding information for specimens prepared from the CS-5 core is presented in Table 2-5.

2.4 SPECIMEN FABRICATION.

As discussed in Section 2.1, the first material to arrive at the ARA laboratory was the core from hole CS-4. According to the field coring logs, the work was performed with NQ-wireline size equipment. This ordinarily produces a core of about 48 mm diameter, which can be cut to length and tested without further machining of the cylindrical surfaces. However, the core obtained from CS-4 had a very irregular surface with diameters ranging from about 48 to 52 mm. It was believed that the roughness of the core would have caused problems in testing and yielded questionable results if it had been tested as delivered. To remedy this situation, the material used for test specimens was machined down to a uniform 48-mm diameter in the ARA laboratory. This was accomplished by chucking an overlength segment of core in a machine lathe and turning it down with a carbide tool. To make the actual loading on the ends of the specimen as close to the ideal normal stress, with no shear, it is highly desirable to minimize the friction between the ends of the specimen and the steel endcaps. This was accomplished through the use of lubricating materials as shown in Figure 2-4. Very light cuts were taken to assure that the test

specimen was not damaged by the machining process, and no coolant was used. Once the core was machined to a uniform cylinder, individual specimens were cut to a length of approximately 100 mm with a diamond saw. To finish each specimen, its ends were ground flat and parallel using a precision surface grinder with a diamond grinding wheel. This operation was performed using a precision fixture that allowed both ends of the specimen to be ground without removing it from the fixture, thereby assuring a high degree of parallelism between the ends, typically within 0.03 mm over the diameter of the specimen.

The coring in borehole CS-5 was performed with NX size core bits, resulting in rock core with nominal diameter of 54 mm. The core received at the ARA laboratory from CS-5 was much more uniform in cross section than the CS-4 core, and test specimens were prepared from the CS-5 material without further machining of the cylindrical surfaces. It was cut to lengths of nominally 108 mm, and the ends were ground as described in the previous paragraph.

2.5 SPECIMEN PREPARATION.

In all except the unconfined compression tests, the specimen was sealed inside a membrane, or jacket, to separate it from the confining fluid. The jacket was made of heat-shrinkable polyolefin tubing, and sealed to hardened steel endcaps at both ends using epoxy adhesive and wire clamps, as shown in The endcap lubrication system consists of a 0.013-mm layer of copper against the specimen and two 0.05-mm layers of Teflon lubricated with a drop of kerosene. Evaluation made under simulated test conditions have shown that the coefficient of friction across the specimen-endcap interface is less than 0.05.

Previous research (Chitty, et al., 1994) has shown differences of approximately 20% in unconfined compressive strength between dry limestone and the same material in a moist, but not saturated, condition. Since the project was being performed to support calculations of explosive loading of underground structures which would be moist, it was considered desirable to perform the laboratory mechanical property tests in the moist condition. The requirement for performing tests at a realistic water content must be balanced against the possibility of obtaining erroneous results due to saturation of the rock during testing. For the unconfined compression tests, where saturation was not a possibility, water was added to the specimens before testing. Based on the

porosity determination described in Section 2.2.2, enough water was added to each specimen to approximately half fill its void space. For the other types of loading where the presence of confining pressure makes saturation a realistic possibility, the specimens were tested in the air dry condition, i.e. without the addition of any water.

2.6 LOADING.

The triaxial test apparatus can apply two independently controllable components of load. In preparation for testing, the specimen is placed inside a pressure vessel. When confining fluid is pumped into the vessel, the resulting pressure acts uniformly over the entire surface of the test specimen, inducing an isotropic state of normal stress with no shear. There is also a loading piston that penetrates the pressure vessel through a seal and bears on the top cap of the prepared specimen. The loading piston imposes an axial deformation, resulting in an incremental axial stress in the test specimen.

In this test program three different loading schemes were employed. Hydrostatic compression tests were conducted to determine the compressibility of the materials under the action of pure isotropic normal loading. To determine the strength of the rock, triaxial compression tests were performed at a range of confining pressures, including zero (unconfined compression). Uniaxial strain loading tests were also performed. These tests provide an alternate strain path along which to validate constitutive models derived from the hydrostatic and triaxial compression test data, and they approximate the strain field at early time in the material around an explosive detonation. More detailed descriptions of the various loading schemes are presented in the following.

2.6.1 Hydrostatic Compression.

In the hydrostatic compression test, fluid pumped into the pressure vessel of the triaxial apparatus is used to compress the test specimen isotropically. Under hydrostatic loading, the cementation in the test specimen may be crushed, resulting in a nonlinear relationship between pressure and volume strain. However, a hydrostatically loaded specimen is not subjected to any shear stresses. Consequently, it will not fail, and the test need only be terminated when the capacity of the pressure vessel or pumping system is reached. The confining pressure capacity of the ARA triaxial device is 400 MPa.

2.6.2 Triaxial Compression.

A triaxial compression test begins with hydrostatic compression loading to a predetermined pressure level. Once that confining pressure is reached, it is held constant while an additional compressive axial deformation is imposed on the specimen. Many modes of response are possible in a triaxial compression test, depending on the material and the confining pressure level. In this test series, the goal was to continue loading until an equilibrium state was reached in which additional increments of axial deformation would not cause any significant change in axial stress. In most cases this was possible. However, in a few instances, tests were cut short by failure of the jacket separating the specimen from the confining fluid.

An unconfined compression test is a special case of the triaxial compression test in which the pressure vessel is not filled with fluid or pressurized. The axial component of load is induced as the result of the axial deformation imposed by the piston. This type of loading can be continued to failure, at which point the test specimen fractures, i.e., its load resistance decreases suddenly, and further piston displacement no longer results in increased axial stress.

2.6.3 Uniaxial Strain.

In the uniaxial strain test, the loading is controlled based on real-time feedback from the deformation instruments to achieve a strain path in which the specimen is compressed axially without allowing any radial deformation. The resulting stress path typically runs roughly parallel to the strength envelope, but does not reach it. Thus, the specimen does not fail, and the test need only be terminated when the capacity of the loader is reached. In practice, this occurs when the confining pressure reaches the capacity of the vessel. In the ARA laboratory, this is 400 MPa.

2.7 INSTRUMENTATION.

Electronic instruments were used to measure the confining stress and axial load applied to the specimen, and the resulting specimen deformations.

Confining pressure measurements were made with a commercial pressure transducer having a sensing element consisting of a strain gaged diaphragm. A load cell inside the pressure vessel,

located between the top cap of the specimen and the loading piston was used to measure the axial load. Since it was inside the pressure vessel, it was not subject to errors due to seal friction. It was, however, subjected to the confining pressure. Its design, consisting of a full strain gage bridge, makes the internal load cell, in the ideal case, insensitive to the confining pressure. Since it is not ideal, there is a slight sensitivity that has been quantified and a correction was applied during data reduction.

Specimen deformations were measured with Linear Variable Differential Transformers (LVDTs). Each specimen was instrumented with three LVDTs as shown in Figure 2-5. Two LVDTs were attached to the end caps on diametrically opposite sides of the specimen to measure axial deformation. Since the axial LVDTs were mounted to the endcaps, the resulting displacement measurement included the deformation of the endcaps in addition to the intended axial deformation of the rock specimen. A correction was applied during data reduction to eliminate the effect of endcap deformation from the measurements.

The third LVDT, used to monitor radial deformation of the test specimen, was mounted in a reference ring at the specimen's mid-height. In the conventional triaxial compression tests, all of loading and measurements take place at a constant confining pressure. Thus, there should be negligible change in the thickness of the jacket as the test progresses, and the radial deformation measurements are made on the outside of the jacket. In contrast, the hydrostatic compression and uniaxial strain tests require that the confining pressure change throughout the test, resulting in variations in jacket compression during the test. In those tests, the radial deformation measurements were made using studs glued to the specimen through holes in the jacket and sealed to the jacket with o-rings. In this manner, error due to jacket compression was eliminated.

In some tests, additional strain measurements were made with foil strain gages bonded directly to the rock surface. These were used primarily in uniaxial strain tests, and only on limestone specimens with no visible voids.

2.8 DATA RECORDING AND REDUCTION.

All channels of instrumentation were digitally recorded using a 16-bit analog-to-digital converter. The sampling rates were adjusted to provide the necessary resolution in each test. The digitized

data were then multiplied by the appropriate calibration factors to convert to engineering units and, where necessary, corrected for pressure effects.

The axial stress, σ_a , was computed by dividing the measured axial load by the original cross sectional area of the test specimen. The radial stress, σ_r , is equal to the measured confining pressure. Additional stress quantities that are presented in selected data plots are the stress difference, σ_Δ , and mean stress, σ_m , which are defined as follows:

$$\begin{aligned}\sigma_\Delta &= \sigma_a - \sigma_r \\ \sigma_m &= \frac{\sigma_a + 2\sigma_r}{3}\end{aligned}\tag{2.2}$$

The deformations of the intact specimens are reported in terms of the axial and radial strains, ϵ_a and ϵ_r , respectively. The engineering axial strain is computed from the average of the two axial deformation measurements, which are first corrected to remove the influence of endcap deformation. The average of the corrected axial deformations is divided by the initial (undeformed) specimen length to obtain axial strain. Similarly, the radial deformation is divided by initial specimen diameter to yield engineering radial strain.

2.9 TEST RESULTS.

The following subsections present the results of the tests on the carbonate rocks from Fort Knox subjected to the three loading schemes described in Section 2.6.

2.9.1 Hydrostatic Compression Test Results.

Summary information for all of the hydrostatic compression tests is presented in Table 2-6. All of these tests were performed on specimens prepared from the CS-4 core. The bulk density of each specimen was determined before testing, and the corresponding grain density was assumed to be the average for Layer 4 of Core CS-4 from Table 2-3. Based on those values, the porosity of each specimen was determined. Each was loaded monotonically to 400 MPa, and then unloaded.

Figure 2-6 presents a summary plot of the relationships between confining pressure and volumetric strain for the seven tests. That figure shows that all of the curves are nonlinear and

concave upward. Such behavior in rock test results can be a result of some initial slack in the deformation/strain measurement system. However, due to the fact that bonded strain gages were used to measure the rock strain, the curvature in the stress-strain curves presented in Figure 2-6 does correctly represent the rock response. Thus, the materials are not well characterized by a single bulk modulus. In order to provide some basis for comparison among the various tests, two slopes were determined for each test. The quantity labeled low pressure bulk modulus in Table 2-6 is the slope of the initial loading portion of the pressure-volumetric strain curve. These values are representative of loading over the initial approximately 0.1% volumetric strain. The high pressure bulk modulus is the slope of the same curve over the range of approximately 200-400 MPa confining pressure. The relationship between axial and radial strain from a typical test, presented in Figure 2-7, shows that the material is reasonably isotropic.

Individual plots of the results of each hydrostatic compression test are included in Appendix A. Further analysis of these test results is presented in Section 3.

2.9.2 Triaxial Compression Test Results.

Unconfined compression tests (zero confining pressure triaxial compression tests) were performed on rock specimens prepared from the cores from both CS-4 and CS-5. All of the unconfined compression tests are summarized in Table 2-7. The results, plotted in terms of axial and radial strain against axial stress, are presented in Figures 2-8 through 2-11. They are divided into four figures for clarity. Figures 2-8 and 2-9 show data from tests on high-porosity and low-porosity specimens, respectively, from hole CS-4. The corresponding data for the CS-5 specimens are presented in Figures 2-10 and 2-11. Values of maximum stress supported by each specimen are tabulated in Table 2-7, along with elastic constants. The elastic modulus was determined by a least squares fit to the portion of the axial stress-axial strain curve between 40 and 60% of the peak stress. Similarly, Poisson's ratio was derived by fitting the axial strain-radial strain curve over the same range. Individual data plots for all of the unconfined compression tests are presented in Appendix B, and these results are included in the strength analysis in Section 3

Triaxial compression tests at non-zero confining pressures ranging from 50 to 400 MPa were performed on core from hole CS-4. No non-zero confining pressure tests were done on the material from CS-5 because the emphasis of the program shifted away from Fort Knox before the more advanced tests could be completed on that rock. The triaxial compression tests are summarized in Table 2-8. Figures 2-12 through 2-16 present the triaxial compression test results in terms of the relationships between stress difference and axial and radial strains. The plots are arranged to facilitate comparison between various materials tested at a single confining pressure. The 50- and 100-MPa tests are each divided into two plots for clarity. The tests at 50 and 100 MPa confining pressure generally exhibit brittle behavior, i.e. a peak strength is reached, after which the stress difference decreases with increasing axial strain. For the brittle materials, the strength is defined by the maximum stress difference. The specimens tested under 400 MPa confining pressure are more ductile. The stress-strain curves either do not peak in the range of the test, or they peak and decrease very gradually. For those tests in which a maximum stress difference can be defined, that value represents the strength of the specimen. Otherwise, the strength is assumed to be the stress difference at the point the specimen reaches 15% axial strain.

An analysis of the variation in strength with porosity is presented in Section 3, and Appendix C contains a complete set of data plots for all of the triaxial compression tests at non-zero confining pressure.

2.9.3 Uniaxial Strain Tests.

A total of nine uniaxial strain tests were performed, on specimens prepared from each of the seven layers from Core CS-4. The specimen characteristics and test results are summarized in Table 2-9. Because of the number of tests, comparison data plots of relevant quantities are presented in pairs. In each case, the first of the pair presents data from the higher porosity specimens and the results of the tests on lower porosity specimens are shown in the second plot of the pair. Figures 2-17 and 2-18 summarize the relationships between axial stress and axial strain. In the tests with the higher porosities, shown in Figure 2-17, the curves exhibit substantial crush-up and hysteresis. In contrast, the data for the lower porosity specimens, in Figure 2-18, are much more nearly elastic.

Stress paths are shown in two different combinations, mean stress versus stress difference and axial stress versus confining stress, in Figures 2-19 through 2-22.

Plots of all of the uniaxial strain test data for Fort Knox rocks are presented in Appendix D.

Table 2-1. Layering in borings CS-4 and CS-5.

Material	Layer No.	Description	Boring: CS-4			Boring: CS-5		
			Depth (m)	Elevation (m)	Thickness (m)	Depth (m)	Elevation (m)	Thickness (m)
New Albany Shale								
Jefferson Limestone	1	Nonporous	158.50	58.98	2.38	156.67	57.03	2.29
Louisville Dolomite	2	Nonporous	160.88	56.60	5.85	158.96	54.74	5.58
	3	Porous	166.73	50.75	3.11	164.53	49.16	5.94
	4	Nonporous	169.84	47.64	8.93	170.48	43.22	7.28
	5	Nonporous	178.77	38.71	4.97	177.76	35.94	4.42
	6	Porous	183.74	33.74	4.39	182.18	31.52	2.99
	7	Nonporous	188.12	29.35	4.25	185.17	28.53	5.94
Waldron Shale			192.38	25.10		191.11	22.59	
			Thickness =		33.88	Thickness =		34.44

Table 2-2. Grain density results.

Core	Layer	Depth (m)	Grain Density (Mg/m ³)	
			Specimen	Average
CS-4	1	159.9	2.794	2.794
CS-4	1	159.9	2.795	
CS-4	2	162.2	2.824	2.825
CS-4	2	162.1	2.826	
CS-4	3	169.7	2.862	2.862
CS-4	3	169.7	2.862	
CS-4	4	171.1	2.837	
CS-4	4	175.6	2.841	
CS-4	4	175.6	2.832	
CS-4	4	177.6	2.838	
CS-4	4	177.6	2.845	
CS-4	5	178.9	2.858	2.852
CS-4	5	178.9	2.847	
CS-4	6	186.9	2.865	2.864
CS-4	6	186.9	2.863	
CS-4	7	191.9	2.849	2.852
CS-4	7	191.9	2.854	
CS-5	1	157.1	2.876	2.848
CS-5	1	157.9	2.820	
CS-5	2	162.4	2.807	2.807
CS-5	3	167.7	2.838	2.838
CS-5	4	174.0	2.838	2.838
CS-5	5	179.4	2.849	2.849
CS-5	6	183.9	2.863	2.863
CS-5	7	186.2	2.856	2.856

Table 2-3. Summary statistics for ultrasonic wavespeeds (Km/s) of core from each layer in boreholes CS-4 and CS-5.

Layer No.	CS-4					CS-5				
	Standard Deviation		40 th Percentile		60th Percentile	Standard Deviation		40 th Percentile		60th Percentile
	Mean					Mean				
1	5.27	0.39	5.16	5.17	5.28	5.52	0.81	5.69	5.74	5.78
2	4.89	0.17	4.86	4.91	4.96	5.34	0.16	5.29	5.35	5.40
3	4.52	0.55	4.44	4.61	4.71	4.87	0.80	4.75	4.93	5.11
4	4.61	0.41	4.52	4.68	4.76	5.06	0.56	5.00	5.11	5.25
5	5.17	0.33	5.12	5.22	5.28	5.89	0.42	5.81	5.94	6.08
6	4.33	0.47	4.33	4.40	4.48	5.13	1.00	4.67	5.38	5.81
7	4.94	0.49	4.82	5.00	5.10	5.24	0.64	5.12	5.19	5.49

Table 2-4. Properties of test specimens prepared from CS-4 core.

Sample ID	Layer No.	Depth (m)	Bulk Density (Mg/m ³)	Grain Density (Mg/m ³)	Porosity	Ultrasonic Compressional Wavespeed (km/s)	Comments
FK10 - 1 - 02	1	159.9	2.735	2.794	0.021	5.477	
FK10 - 1 - 03	1	160.0	2.730	2.794	0.023	5.677	
FK10 - 1 - 05	1	160.3	2.702	2.794	0.033	5.770	
FK10 - 1 - 04	1	160.2	2.695	2.794	0.035	5.614	
FK10 - 1 - 01	1	159.1	2.579	2.794	0.077	5.882	Vugular
FK10 - 2 - 04	2	164.8	2.689	2.825	0.048	4.716	
FK10 - 2 - 03	2	164.7	2.669	2.825	0.055	4.760	
FK10 - 2 - 06	2	165.1	2.661	2.825	0.058	4.775	
FK10 - 2 - 05	2	165.0	2.660	2.825	0.058	4.808	
FK10 - 2 - 01	2	161.5	2.594	2.825	0.082	5.005	
FK10 - 2 - 02	2	161.6	2.565	2.825	0.092	4.818	
FK10 - 3 - 05	3	168.6	2.664	2.862	0.069	5.805	Cavities
FK10 - 3 - 04	3	168.3	2.645	2.862	0.076	5.939	Vugular
FK10 - 3 - 01	3	166.8	2.622	2.862	0.084	5.418	
FK10 - 3 - 02	3	167.0	2.579	2.862	0.099	5.228	
FK10 - 3 - 06	3	169.1	2.445	2.862	0.146	5.261	
FK10 - 4 - 01H	4	169.9	2.693	2.838	0.051	5.966	Cavities
FK10 - 4 - 06H	4	178.5	2.672	2.838	0.059	6.126	
FK10 - 4 - 04H	4	173.4	2.654	2.838	0.065	5.333	
FK10 - 4 - 05H	4	178.4	2.651	2.838	0.066	6.050	
FK10 - 4 - 02H	4	170.4	2.637	2.838	0.071	5.225	
FK10 - 4 - 07	4	174.8	2.630	2.838	0.073	5.391	
FK10 - 4 - 03	4	170.9	2.622	2.838	0.076	5.009	
FK10 - 4 - 01	4	170.1	2.611	2.838	0.080	5.573	
FK10 - 4 - 04	4	171.0	2.610	2.838	0.080	4.974	
FK10 - 4 - 03H	4	170.5	2.603	2.838	0.083	5.117	
FK10 - 4 - 04L	4	175.9	2.562	2.838	0.097	4.640	
FK10 - 4 - 02	4	170.6	2.590	2.838	0.088	4.998	Small Cavity
FK10 - 4 - 01L	4	171.9	2.537	2.838	0.106	5.210	Large Cavity
FK10 - 4 - 05L	4	176.1	2.529	2.838	0.109	4.447	
FK10 - 4 - 06L	4	176.6	2.528	2.838	0.109	4.547	
FK10 - 4 - 06	4	174.2	2.550	2.838	0.102	5.661	
FK10 - 4 - 02L	4	172.2	2.511	2.838	0.115	4.477	
FK10 - 4 - 03L	4	172.6	2.478	2.838	0.127	5.092	Vugular
FK10 - 4 - 07L	4	176.7	2.433	2.838	0.143	4.365	
FK10 - 5 - 04	5	181.2	2.726	2.852	0.044	5.989	
FK10 - 5 - 03	5	180.8	2.722	2.852	0.046	5.769	
FK10 - 5 - 05	5	182.4	2.707	2.852	0.051	5.640	
FK10 - 5 - 02	5	179.4	2.690	2.852	0.057	5.711	
FK10 - 5 - 01	5	178.9	2.676	2.852	0.062	5.693	
FK10 - 6 - 06	6	188.0	2.582	2.864	0.098	5.130	
FK10 - 6 - 03	6	186.6	2.564	2.864	0.105	4.683	Large Cavity
FK10 - 6 - 02	6	185.2	2.550	2.864	0.109	5.250	Vugular
FK10 - 6 - 01	6	185.0	2.519	2.864	0.120	5.685	Vugular
FK10 - 6 - 04	6	187.1	2.477	2.864	0.135	4.809	Vugular
FK10 - 6 - 05	6	187.9	2.407	2.864	0.159	4.684	
FK10 - 7 - 03	7	188.8	2.706	2.852	0.051	5.145	
FK10 - 7 - 06	7	190.2	2.706	2.852	0.051	5.254	
FK10 - 7 - 04	7	189.0	2.704	2.852	0.052	4.535	
FK10 - 7 - 02	7	188.7	2.701	2.852	0.053	5.392	
FK10 - 7 - 05	7	189.9	2.701	2.852	0.053	5.399	
FK10 - 7 - 01	7	188.5	2.692	2.852	0.056	4.724	
FK10 - 7 - 07	7	190.5	2.668	2.852	0.064	5.602	

Table 2-5. Properties of test specimens prepared from CS-5 core.

Specimen ID	Layer No.	Depth (m)	Bulk Density (Mg/m ³)	Grain Density (Mg/m ³)	Porosity	Ultrasonic Compressional Wavespeed (km/s)
FK2-01-1	1	156.80	2.715	2.848	0.047	5.88
FK2-01-2	1	156.92	2.674	2.848	0.061	5.81
FK2-01-3	1	157.03	2.608	2.848	0.084	5.55
FK2-01-4	1	157.82	2.751	2.848	0.034	5.95
FK2-01-5	1	158.30	2.699	2.848	0.052	5.75
FK2-01-6	1	158.41	2.703	2.848	0.051	5.94
FK2-01-7	1	158.92	2.718	2.848	0.046	5.82
FK2-02-1	2	161.55	2.667	2.807	0.050	5.09
FK2-02-2	2	161.67	2.663	2.807	0.051	4.89
FK2-02-3	2	162.19	2.665	2.807	0.051	4.90
FK2-02-4	2	162.30	2.672	2.807	0.048	5.06
FK2-02-5	2	163.38	2.696	2.807	0.040	5.01
FK2-02-6	2	163.57	2.710	2.807	0.035	5.04
FK2-02-7	2	163.68	2.685	2.807	0.044	5.16
FK2-03-1	3	164.75	2.469	2.838	0.130	4.96
FK2-03-2	3	165.84	2.519	2.838	0.112	5.19
FK2-03-3	3	166.97	2.454	2.838	0.135	4.19
FK2-03-4	3	167.60	2.418	2.838	0.148	4.36
FK2-03-5	3	168.50	2.375	2.838	0.163	4.39
FK2-03-6	3	169.60	2.443	2.838	0.139	5.00
FK2-03-7	3	169.91	2.481	2.838	0.126	4.43
FK2-04-1	4	171.05	2.624	2.838	0.075	4.61
FK2-04-2	4	171.61	2.531	2.838	0.108	5.04
FK2-04-3	4	173.07	2.521	2.838	0.112	4.78
FK2-04-4	4	173.43	2.645	2.838	0.068	4.81
FK2-04-5	4	173.71	2.589	2.838	0.088	4.97
FK2-04-6	4	175.11	2.490	2.838	0.123	4.52
FK2-04-7	4	175.51	2.568	2.838	0.095	5.36
FK2-04-1L	4	170.68	2.549	2.838	0.102	4.88
FK2-04-2L	4	172.32	2.601	2.838	0.083	5.23
FK2-04-3L	4	172.69	2.504	2.838	0.118	4.54
FK2-04-4L	4	173.65	2.488	2.838	0.123	4.66
FK2-04-5L	4	174.06	2.542	2.838	0.104	4.64
FK2-04-6L	4	174.52	2.470	2.838	0.130	5.04
FK2-04-7L	4	175.93	2.500	2.838	0.119	5.05
FK2-04-1H	4	170.57	2.654	2.838	0.065	5.18
FK2-04-2H	4	170.91	2.590	2.838	0.087	5.10
FK2-04-3H	4	171.24	2.652	2.838	0.065	5.26
FK2-04-4H	4	171.36	2.639	2.838	0.070	5.55
FK2-04-5H	4	172.46	2.541	2.838	0.105	5.27
FK2-04-6H	4	174.80	2.590	2.838	0.087	5.22
FK2-04-7H	4	176.28	2.605	2.838	0.082	5.62

Table 2-5. Properties of test specimens prepared from CS-5 core (Continued).

Specimen ID	Layer No.	Depth (m)	Bulk Density (Mg/m ³)	Grain Density (Mg/m ³)	Porosity	Ultrasonic Compressional Wavespeed (km/s)
FK2-05-1	5	178.61	2.694	2.849	0.054	5.80
FK2-05-2	5	179.20	2.683	2.849	0.058	5.31
FK2-05-3	5	179.32	2.712	2.849	0.048	5.76
FK2-05-4	5	180.44	2.693	2.849	0.055	5.78
FK2-05-5	5	180.62	2.698	2.849	0.053	6.04
FK2-05-6	5	180.75	2.700	2.849	0.052	5.88
FK2-05-7	5	181.29	2.752	2.849	0.034	6.13
FK2-06-1	6	182.61	2.589	2.863	0.096	5.81
FK2-06-2	6	182.85	2.550	2.863	0.109	5.87
FK2-06-3	6	183.05	2.536	2.863	0.114	5.51
FK2-06-4	6	183.66	2.324	2.863	0.188	4.41
FK2-06-5	6	183.78	2.364	2.863	0.174	3.97
FK2-06-6	6	184.41	2.405	2.863	0.160	5.03
FK2-06-7	6	184.52	2.364	2.863	0.174	4.44
FK2-07-1	7	185.77	2.636	2.856	0.077	5.58
FK2-07-2	7	185.93	2.655	2.856	0.070	4.88
FK2-07-3	7	186.14	2.656	2.856	0.070	5.05
FK2-07-4	7	188.12	2.694	2.856	0.057	4.85
FK2-07-5	7	188.52	2.761	2.856	0.033	5.65
FK2-07-6	7	189.97	2.615	2.856	0.085	5.71
FK2-07-7	7	190.81	2.727	2.856	0.045	4.94

Table 2-6. Summary of hydrostatic compression tests on carbonate rock from Fort Knox.

Test ID	Core	Specimen ID	Bulk Density (Mg/m ³)	Grain Density (Mg/m ³)	Porosity	Peak Load (MPa)	Bulk Modulus (GPa)		Instrumentation Type
							Low Pressure	High Pressure	
Y20A3	CS-4	FK10-1-05	2.709	2.794	0.0305	400	28.6	53.8	Strain Gages
Y20B3	CS-4	FK10-2-06	2.669	2.825	0.0552	400	22.9	32.6	Strain Gages
A20B3	CS-4	FK10-3-02	2.593	2.862	0.0939	400	11.3	37.9	LVDTs
Y21A3	CS-4	FK10-4-04	2.615	2.838	0.0787	400	18.4	34.1	Strain Gages
Y21B3	CS-4	FK10-5-05	2.717	2.852	0.0475	400	36.2	45.4	Strain Gages
U7A3	CS-4	FK10-6-06	2.581	2.864	0.0987	400	16.8	54.3	Strain Gages
Y21C3	CS-4	FK10-7-04	2.710	2.852	0.0496	400	25.2	61	Strain Gages

Table 2-7. Summary of unconfined compression tests on carbonate rock from Fort Knox.

Test ID	Core	Specimen ID	Bulk Density (Mg/m ³)	Grain Density (Mg/m ³)	Porosity	Unconfined Strength (MPa)	Elastic Modulus (GPa)	Poisson's Ratio
A15E3	CS-4	FK10-1-02	2.735	2.794	0.021	87	60.7	0.2912
A15B3	CS-4	FK10-2-03	2.671	2.825	0.054	125	37.2	0.3123
A14C3	CS-4	FK10-3-01	2.618	2.862	0.085	88	51.3	0.4466
A15D3	CS-4	FK10-4-01H	2.691	2.838	0.052	79	60	0.5128
A16A3	CS-4	FK10-4-03	2.633	2.838	0.072	114	40	0.4335
A14B3	CS-4	FK10-4-06L	2.527	2.838	0.110	82	44	0.3349
A14A3	CS-4	FK10-4-07L	2.434	2.838	0.142	48	35.9	0.4202
A16B3	CS-4	FK10-5-04	2.739	2.852	0.040	162	74.9	0.4484
A15A3	CS-4	FK10-6-01	2.521	2.864	0.120	60	60.2	0.3839
A15C3	CS-4	FK10-7-02	2.706	2.852	0.051	146	64.7	0.4804
S8A3	CS-5	FK2-01-3	2.609	2.848	0.084	118.3	54.9	0.3413
S8B3	CS-5	FK2-02-1	2.667	2.807	0.050	153.5	36.3	0.3497
S9A3	CS-5	FK2-03-1	2.469	2.838	0.130	82	35.2	0.5120
S9B3	CS-5	FK2-04-2	2.532	2.838	0.108	63.2	37.7	0.2672
S9C3	CS-5	FK2-04-7L	2.500	2.838	0.119	80.4	39.6	0.2347
S9D3	CS-5	FK2-04-7H	2.606	2.838	0.082	69.4	47.1	0.2219
S9E3	CS-5	FK2-05-1	2.695	2.849	0.054	148.3	57.2	0.3379
S9F3	CS-5	FK2-06-3	2.536	2.863	0.114	117	55.1	0.3107
S9G3	CS-5	FK2-07-1	2.637	2.856	0.077	129.7	52.7	0.3612

Table 2-8. Summary of triaxial compression tests on carbonate rock from Fort Knox.

Test ID	Core	Specimen ID	Bulk Density (Mg/m ³)	Grain Density (Mg/m ³)	Porosity	Confining Pressure (MPa)	Strength (MPa)
A23B3	CS-4	FK10-1-03	2.735	2.794	0.021	50	264
A23D3	CS-4	FK10-2-01	2.595	2.825	0.081	50	314
A28F3	CS-4	FK10-3-06	2.449	2.862	0.144	50	155
A27H3	CS-4	FK10-4-05H	2.65	2.838	0.066	50	241.5
A28B3	CS-4	FK10-4-07	2.632	2.838	0.073	50	245
A28D3	CS-4	FK10-4-01L	2.536	2.838	0.107	50	199.1
A27B3	CS-4	FK10-5-03	2.724	2.852	0.045	50	422
A28H3	CS-4	FK10-6-03	2.566	2.864	0.104	50	147
A27F3	CS-4	FK10-7-03	2.712	2.852	0.049	50	331
A27D3	CS-4	FK10-7-01	2.7	2.852	0.053	50	260
A29B3	CS-4	FK10-2-04	2.689	2.825	0.048	100	404
A30H3	CS-4	FK10-3-05	2.666	2.862	0.068	100	314
A30J3	CS-4	FK10-4-03H	2.608	2.838	0.081	100	389
A30B3	CS-4	FK10-4-01	2.616	2.838	0.078	100	371
A30D3	CS-4	FK10-4-04L	2.564	2.838	0.097	100	310
A29H3	CS-4	FK10-5-01	2.679	2.852	0.061	100	465
A30F3	CS-4	FK10-6-05	2.411	2.864	0.158	100	176
A29F3	CS-4	FK10-7-06	2.705	2.852	0.051	100	339
A29D3	CS-4	FK10-7-07	2.666	2.852	0.065	100	381
U16B3	CS-4	FK10-4-07H	2.623	2.838	0.076	400	755
U15D3	CS-4	FK10-4-08	2.608	2.838	0.081	400	840
U15B3	CS-4	FK10-5-05L	2.531	2.852	0.113	400	670
L9B3	CS-4	FK10-1-05	2.709	2.794	0.030	400	710
L12A3	CS-4	FK10-6-08	2.519	2.864	0.120	400	870

Table 2-9. Summary of uniaxial strain tests on carbonate rock from Fort Knox.

Test ID	Core	Specimen ID	Bulk Density (Mg/m ³)	Grain Density (Mg/m ³)	Porosity	Peak Conf. Pressure (MPa)	Initial Constr'n'd Modulus (GPa)
Y13A3	CS-4	FK10-1-04	2.697	2.794	0.035	400	82.4
Y14A3	CS-4	FK10-2-05	2.663	2.825	0.057	400	49.1
U21B3	CS-4	FK10-3-04	2.655	2.862	0.072	400	77.5
U18A3	CS-4	FK10-4-02	2.592	2.838	0.087	400	47.2
U21A3	CS-4	FK10-4-03L	2.482	2.838	0.126	400	39.4
U18B3	CS-4	FK10-4-04H	2.652	2.838	0.066	400	65.4
Y14B3	CS-4	FK10-5-02	2.693	2.852	0.056	400	73
U22A3	CS-4	FK10-6-02	2.558	2.864	0.107	400	71.4
Y14C3	CS-4	FK10-7-05	2.707	2.852	0.051	400	66.6

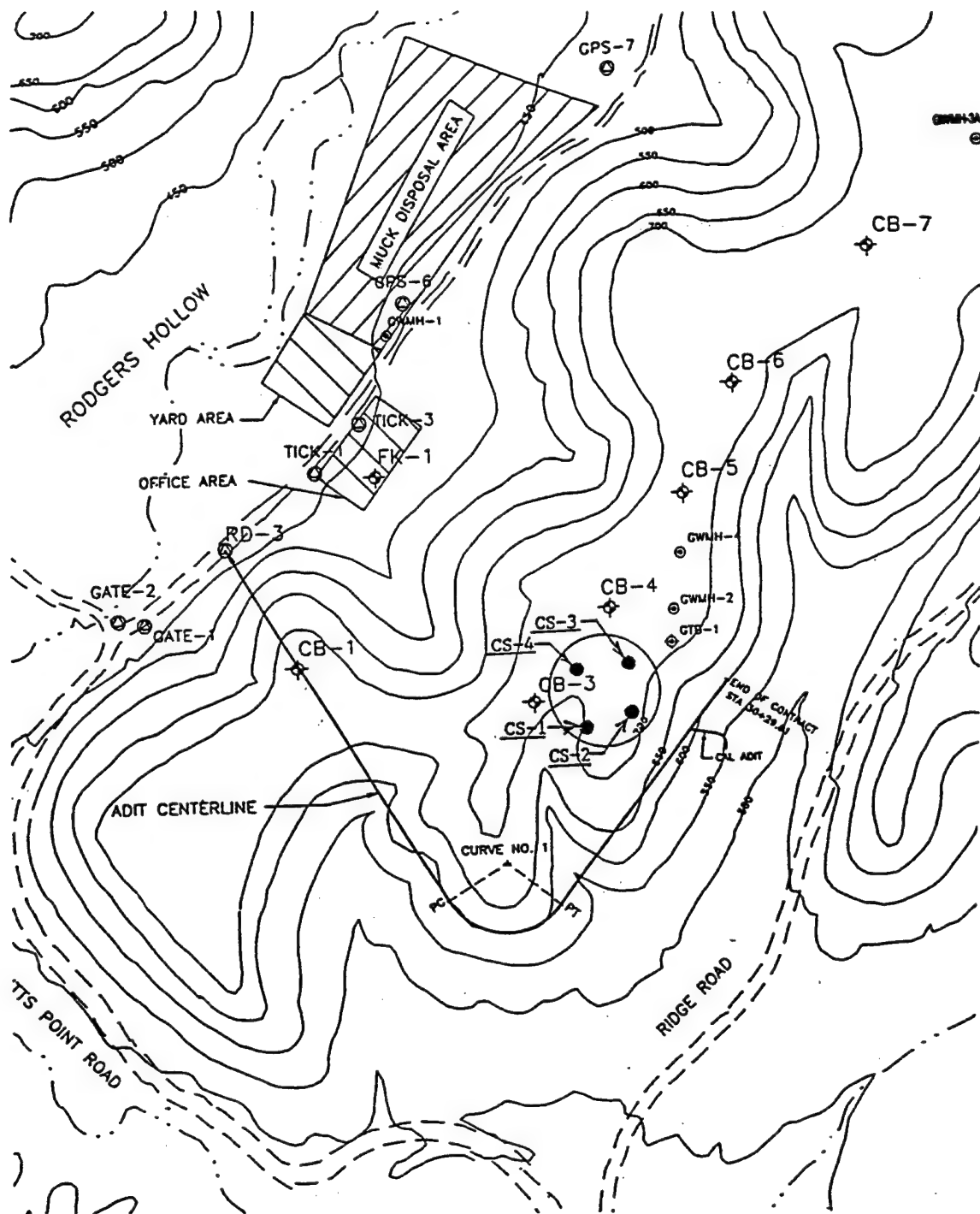


Figure 2-1. Plan of the test area at Fort Knox showing the locations of the core borings.

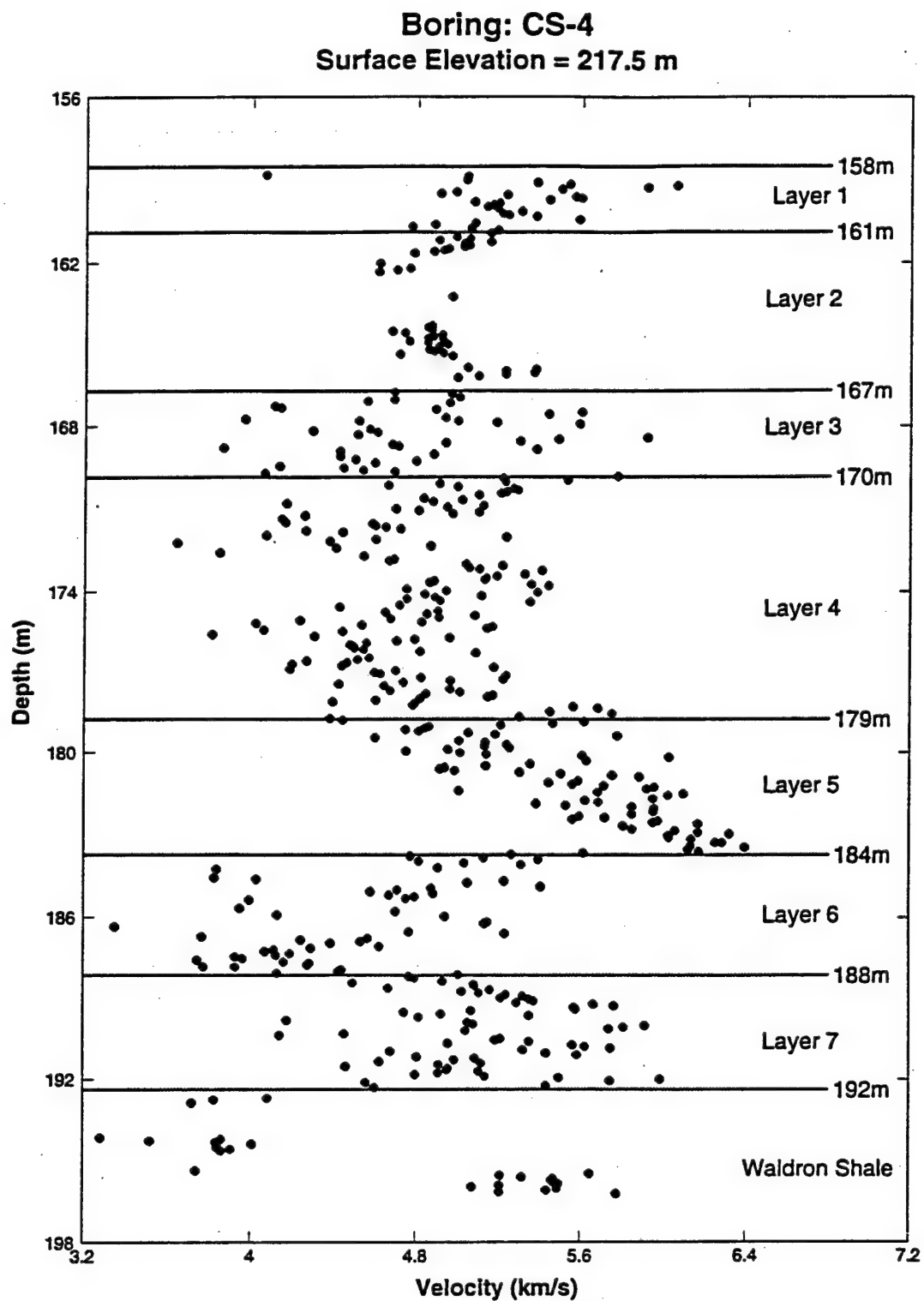


Figure 2-2. Ultrasonic compressional wavespeeds of the CS-4 core as a function of depth.

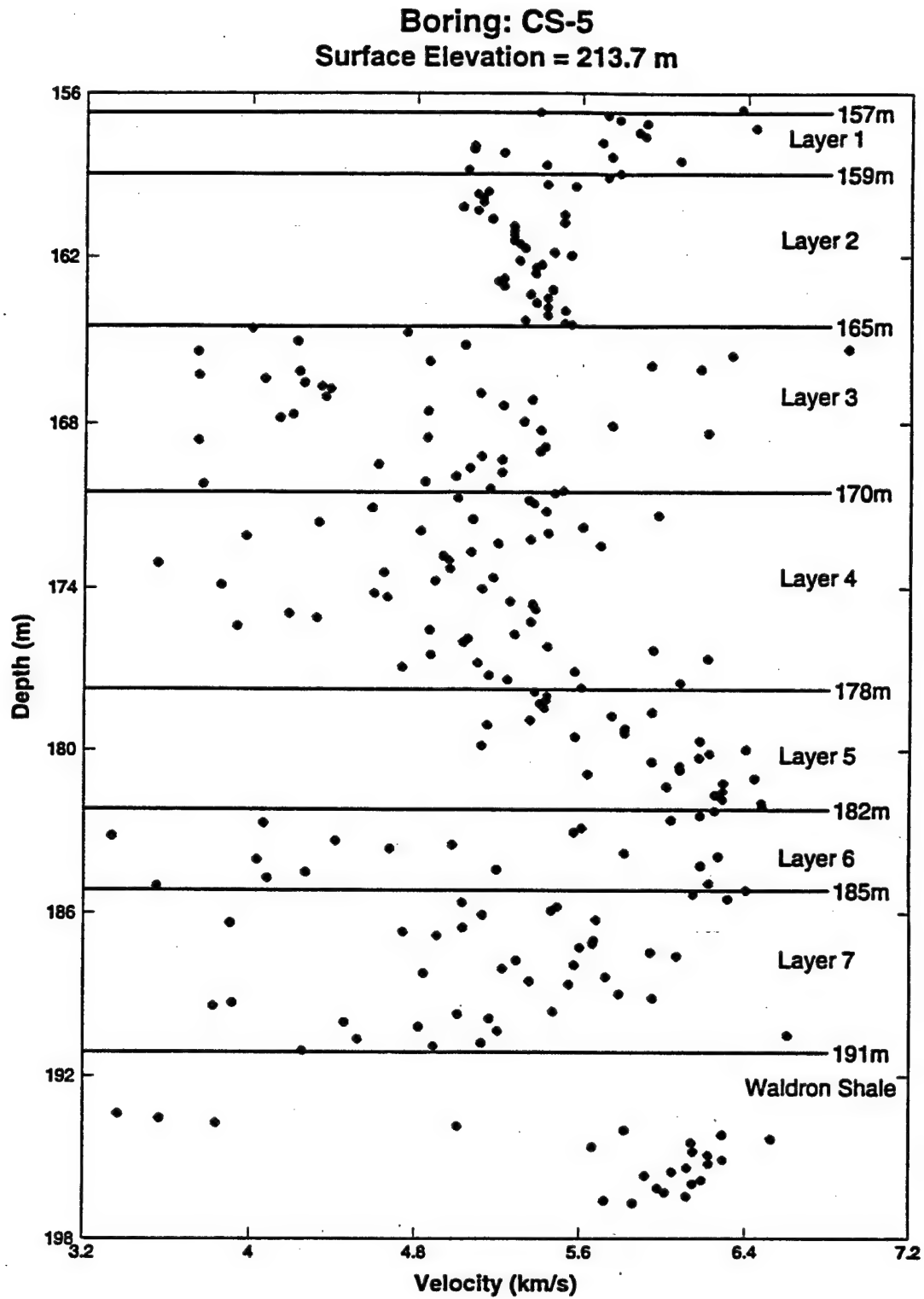


Figure 2-3. Ultrasonic compressional wavespeeds of the CS-5 core as a function of depth.

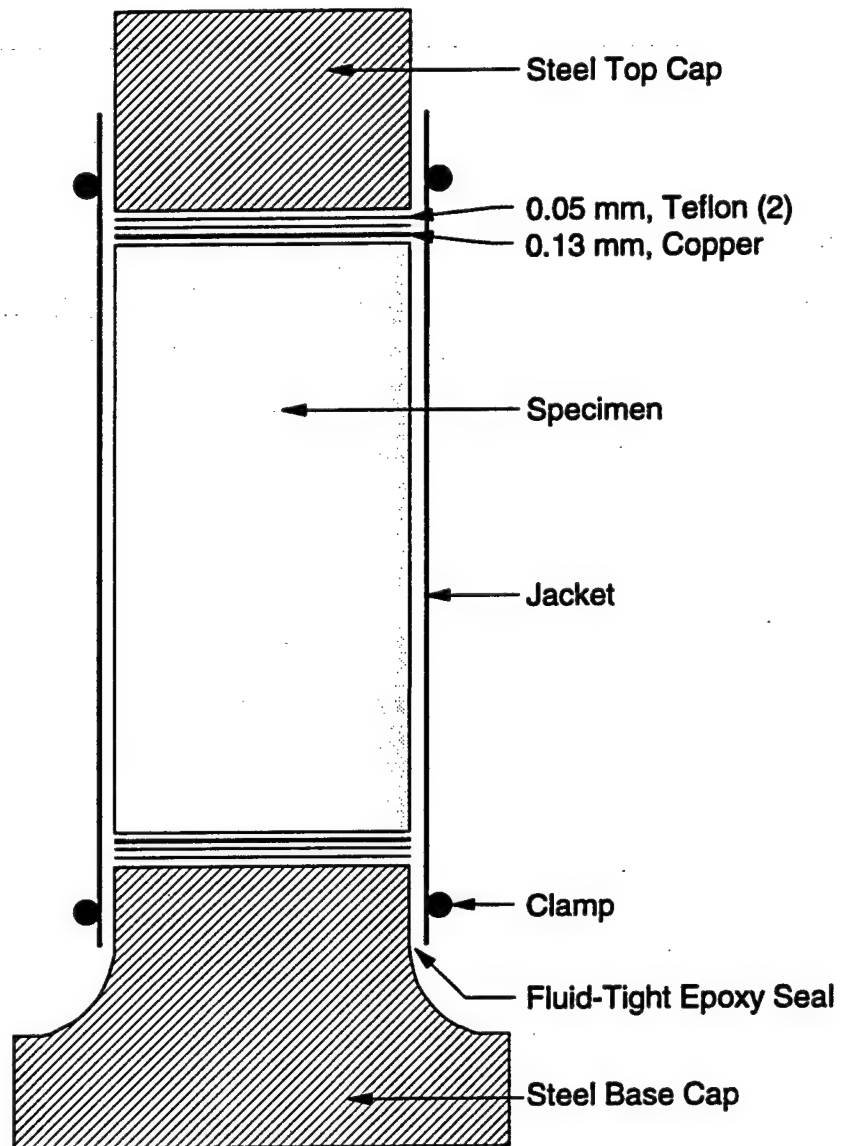


Figure 2-4. Illustration of a jacketed test specimen showing the positions of the lubricating materials.

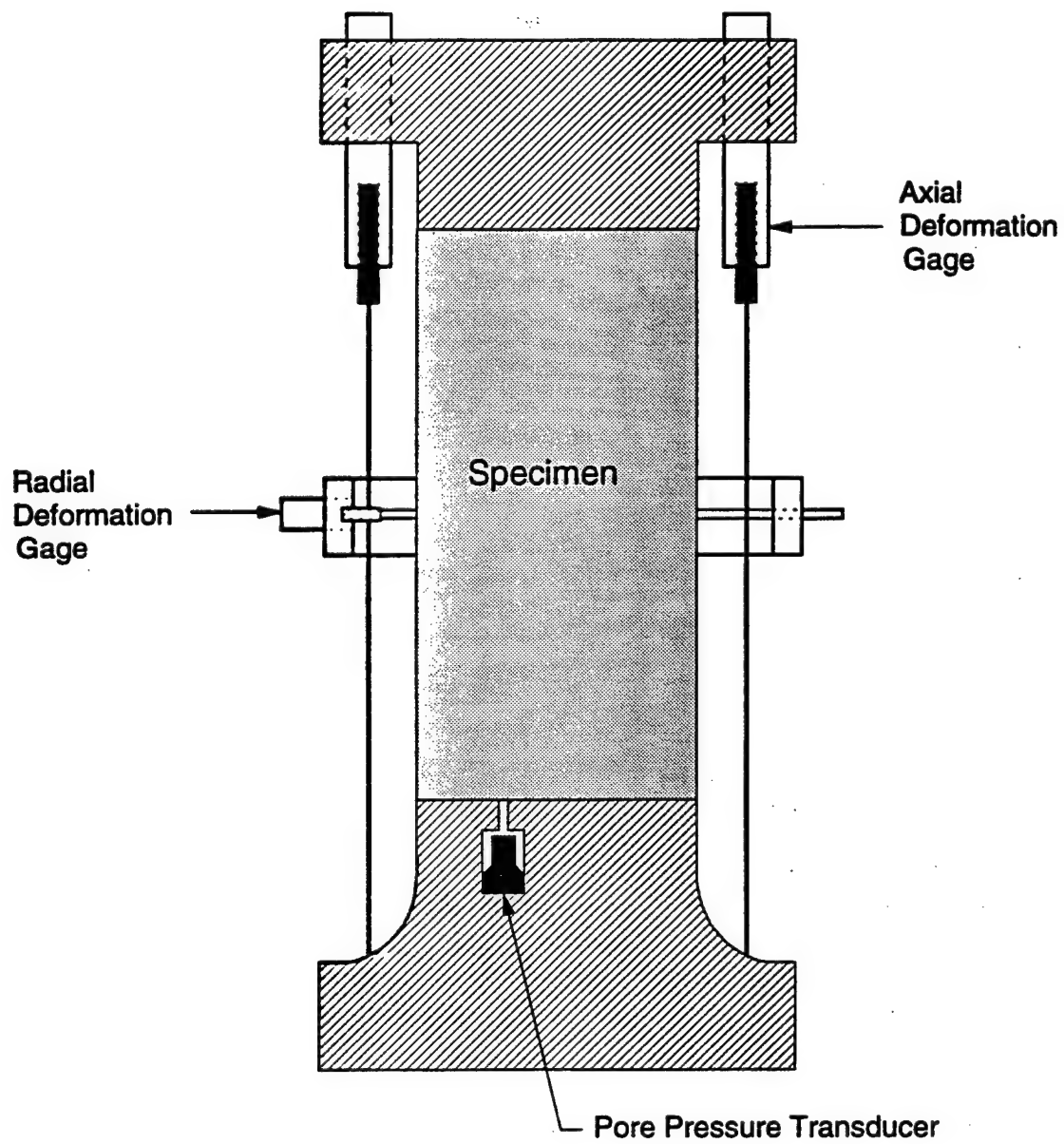


Figure 2-5. Illustration of the instrumentation used on to measure deformations and pore pressure of a test specimen.

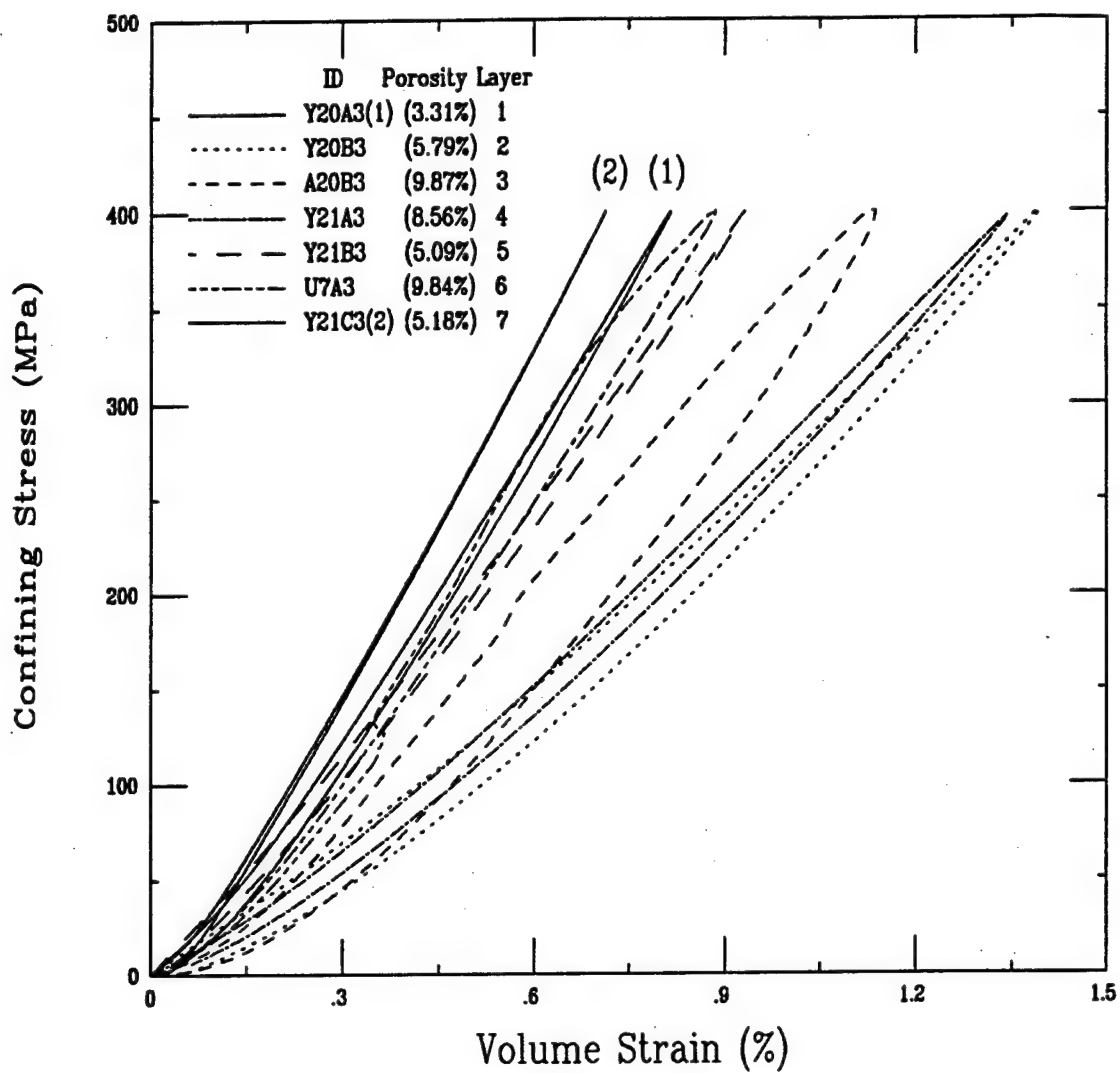


Figure 2-6. Relationships between confining pressure and volumetric strain for specimens of carbonate rocks from core hole CS-4 at Fort Knox tested in hydrostatic compression.

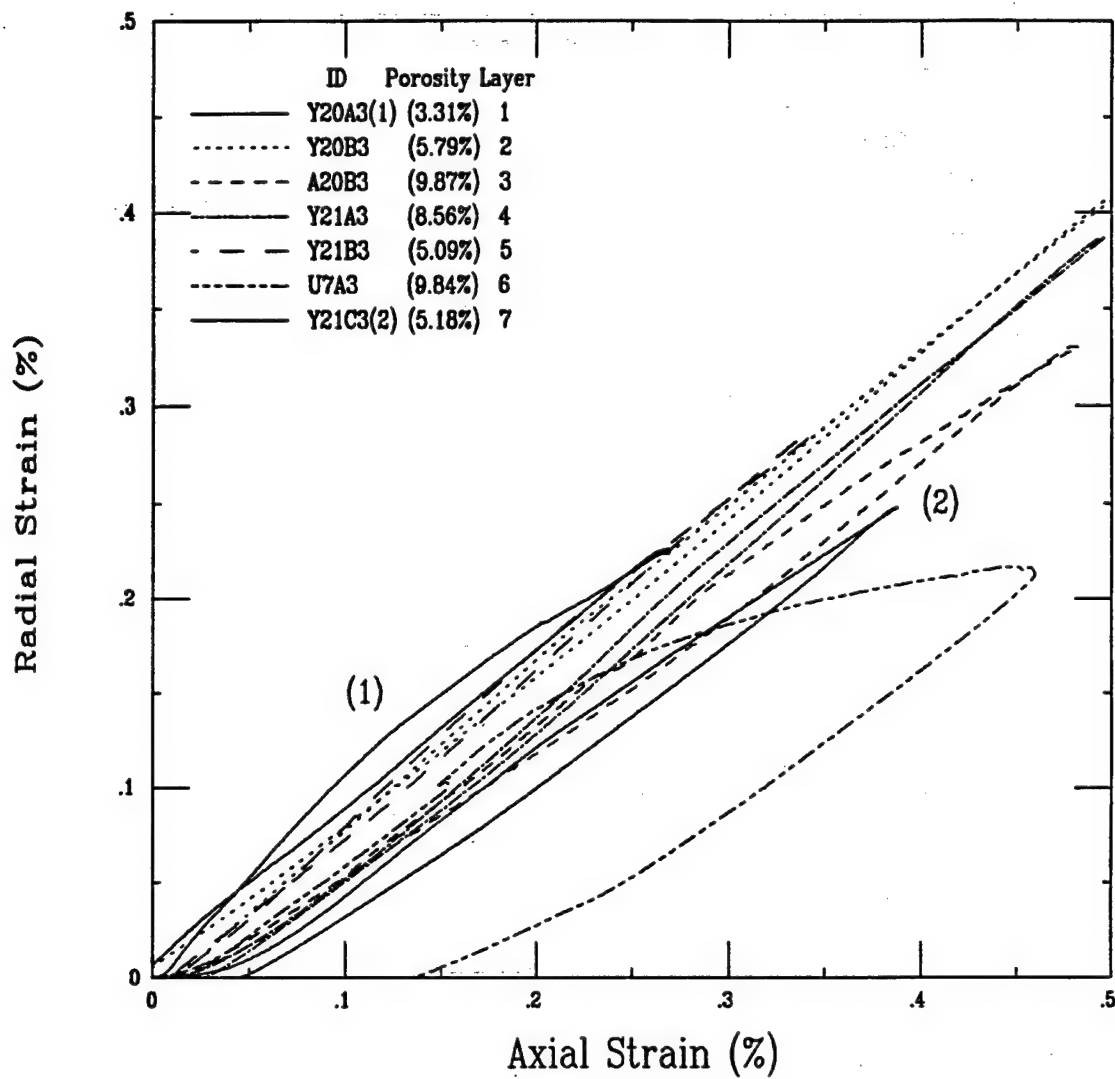


Figure 2-7. Relationships between axial and radial strain for specimens of carbonate rocks from core hole CS-4 at Fort Knox tested in hydrostatic compression.

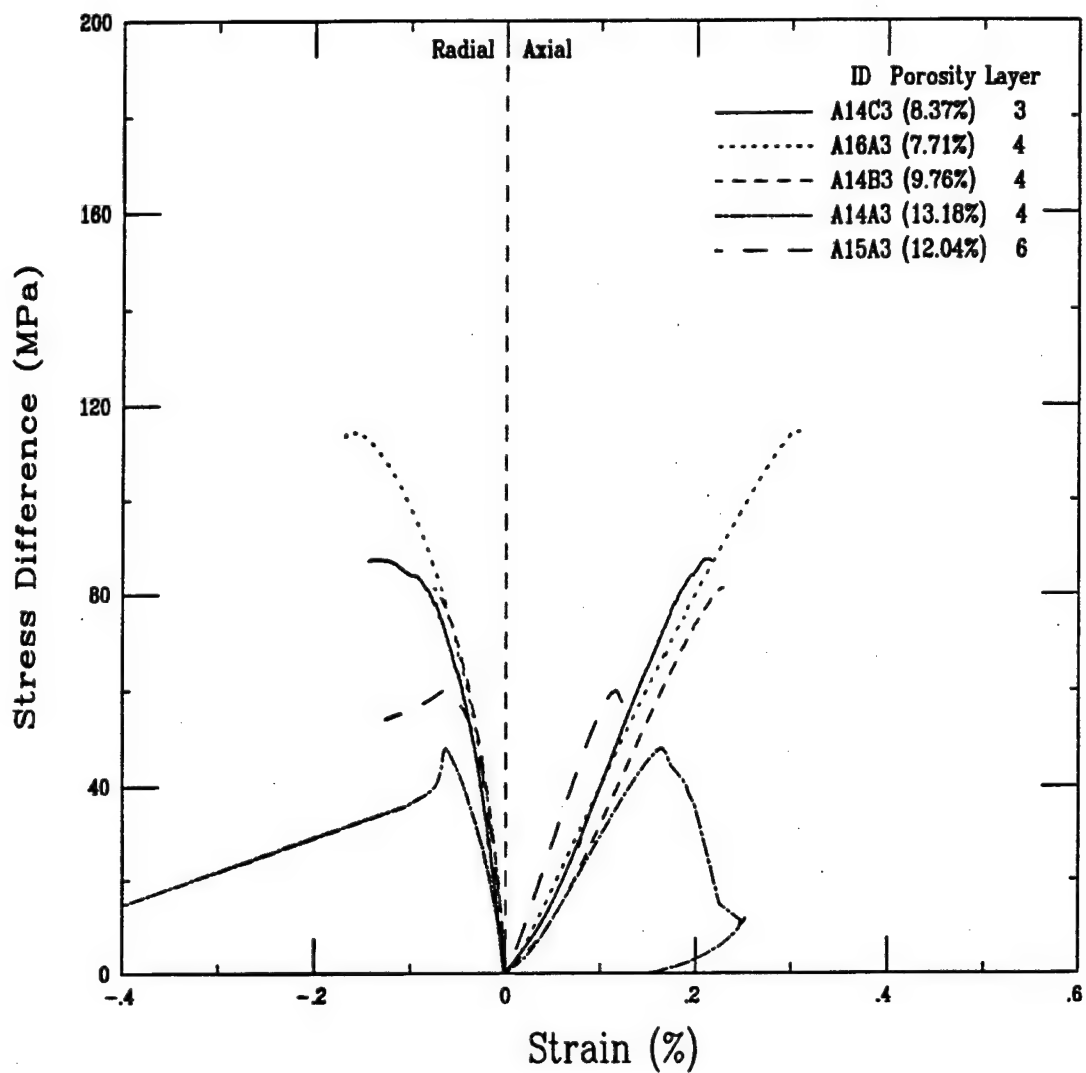


Figure 2-8. Axial and radial strains plotted against stress difference for specimens of high-porosity carbonate rocks from core hole CS-4 at Fort Knox tested in unconfined compression .

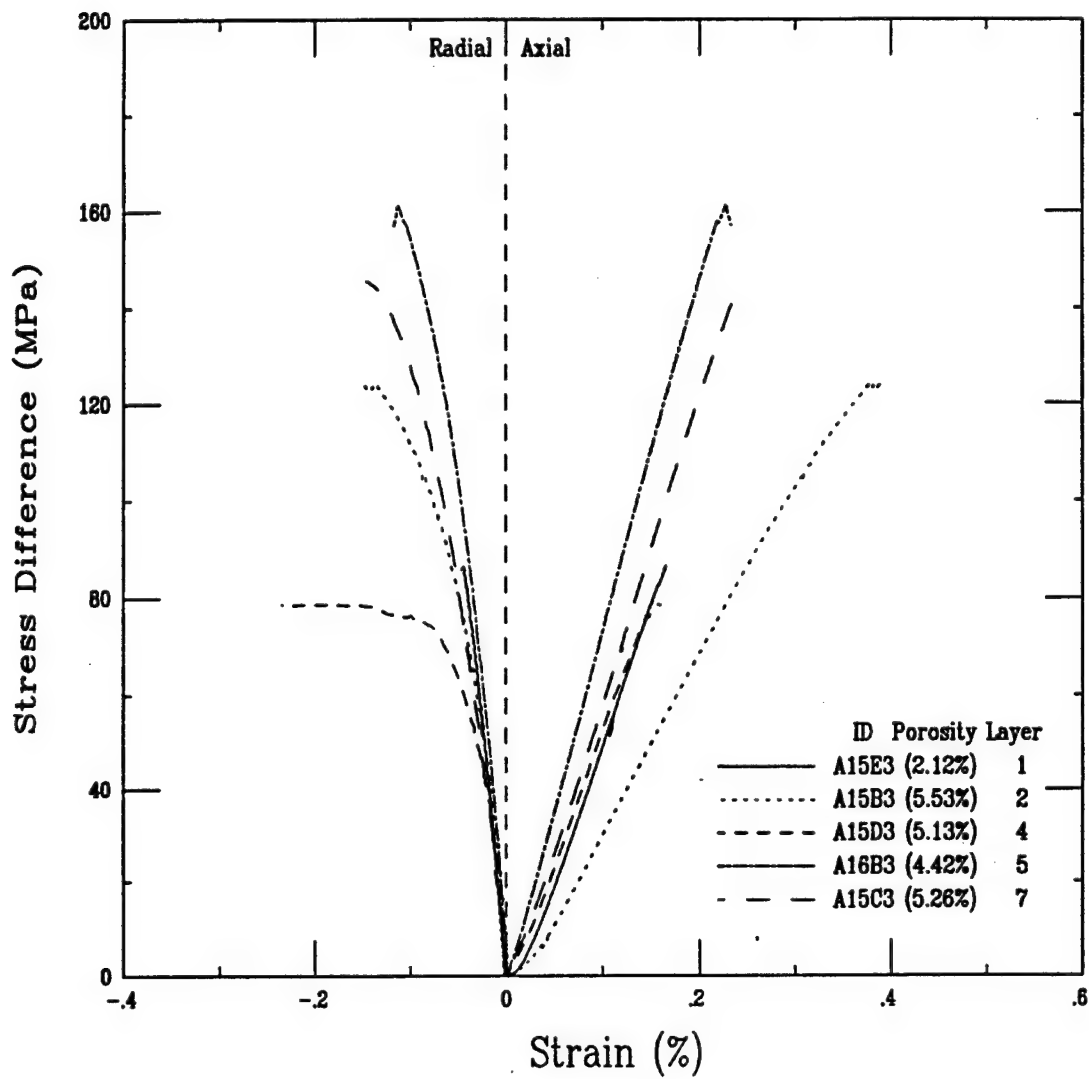


Figure 2-9. Axial and radial strains plotted against stress difference for specimens of low-porosity carbonate rocks from core hole CS-4 at Fort Knox tested in unconfined compression.

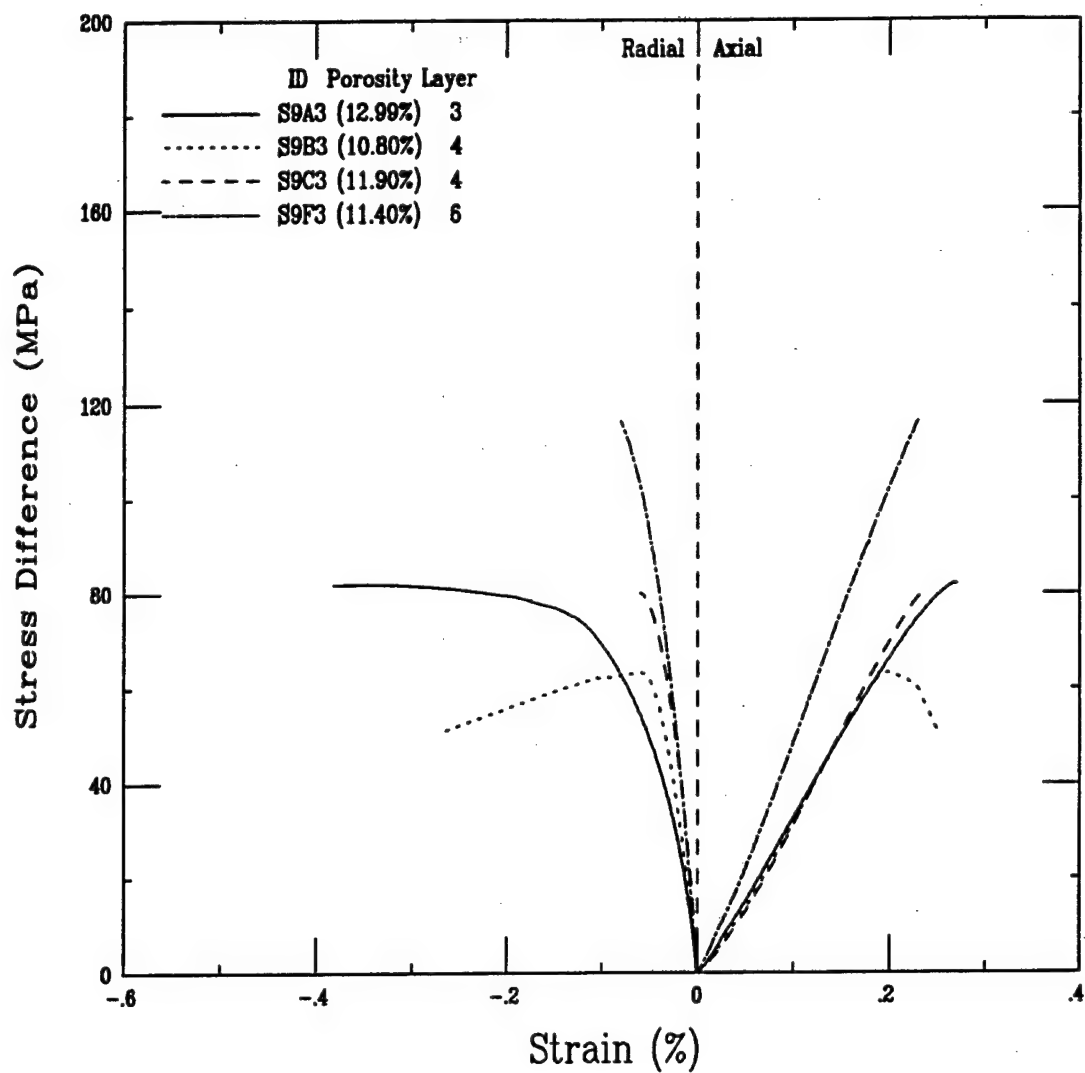


Figure 2-10. Axial and radial strains plotted against stress difference for specimens of high-porosity carbonate rocks from core hole CS-5 at Fort Knox tested in unconfined compression.

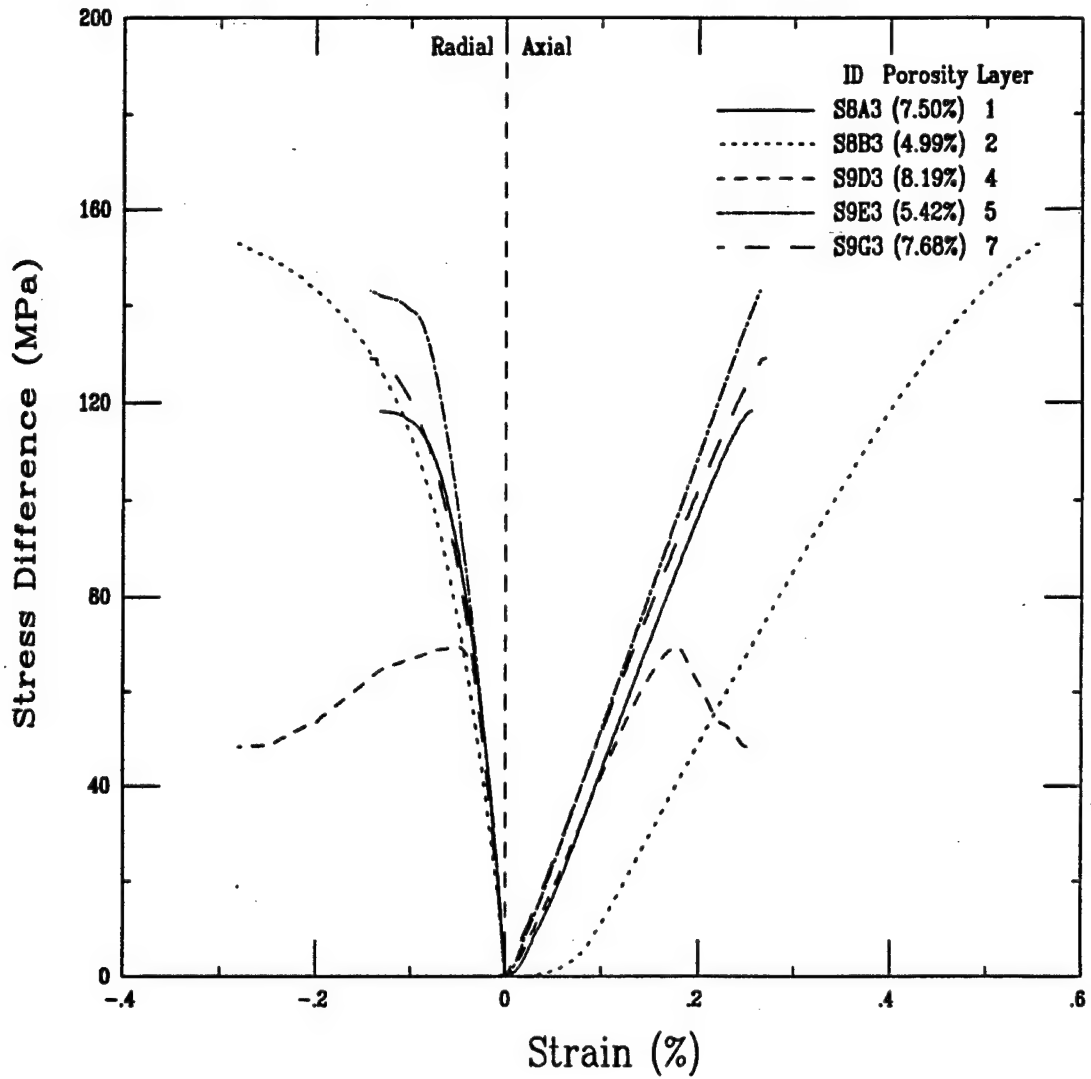


Figure 2-11. Axial and radial strains plotted against stress difference for specimens of low-porosity carbonate rocks from core hole CS-5 at Fort Knox tested in unconfined compression.

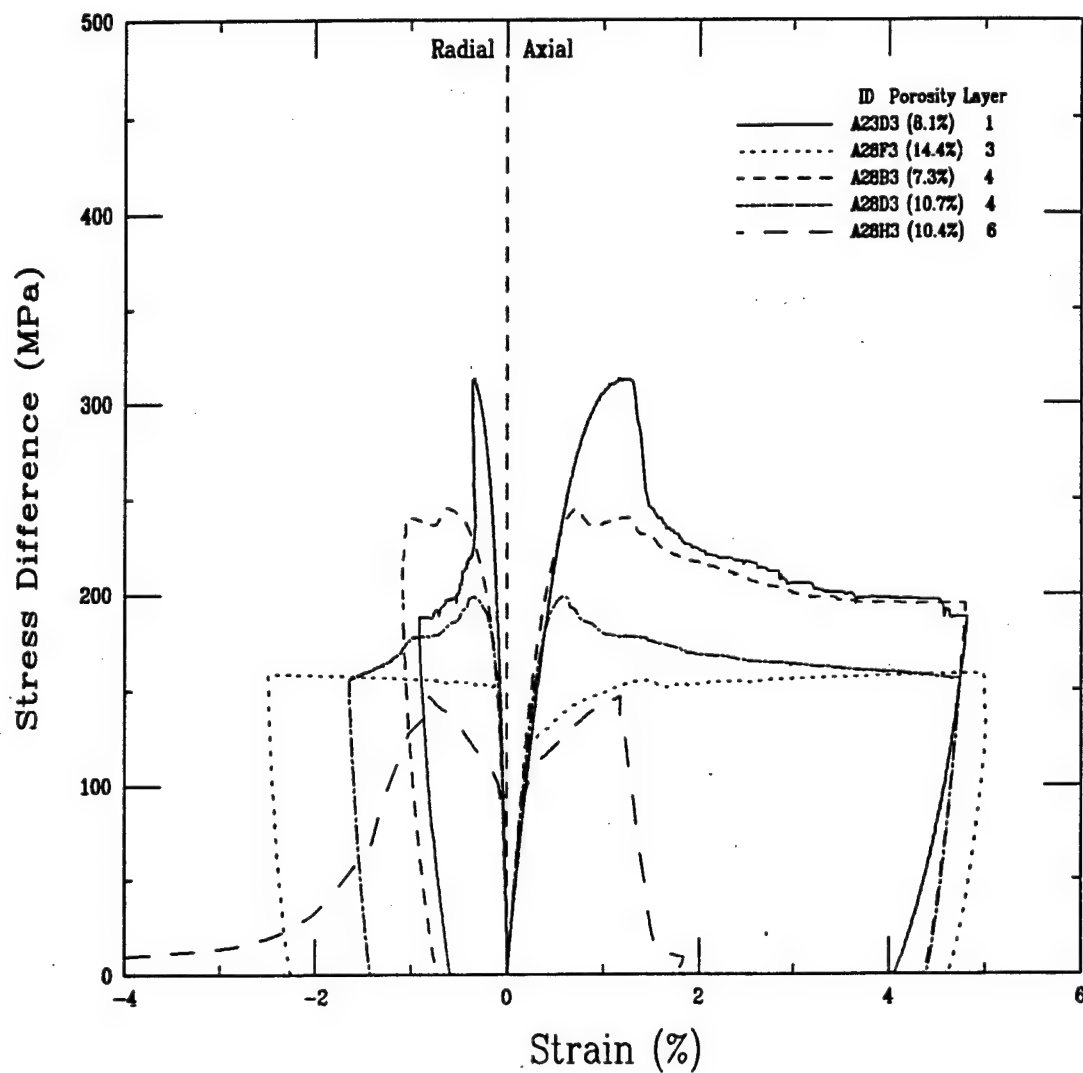


Figure 2-12. Axial and radial strains plotted against stress difference for specimens high-porosity carbonate rocks from core hole CS-4 at Fort Knox tested in triaxial compression with 50 MPa confining pressure.

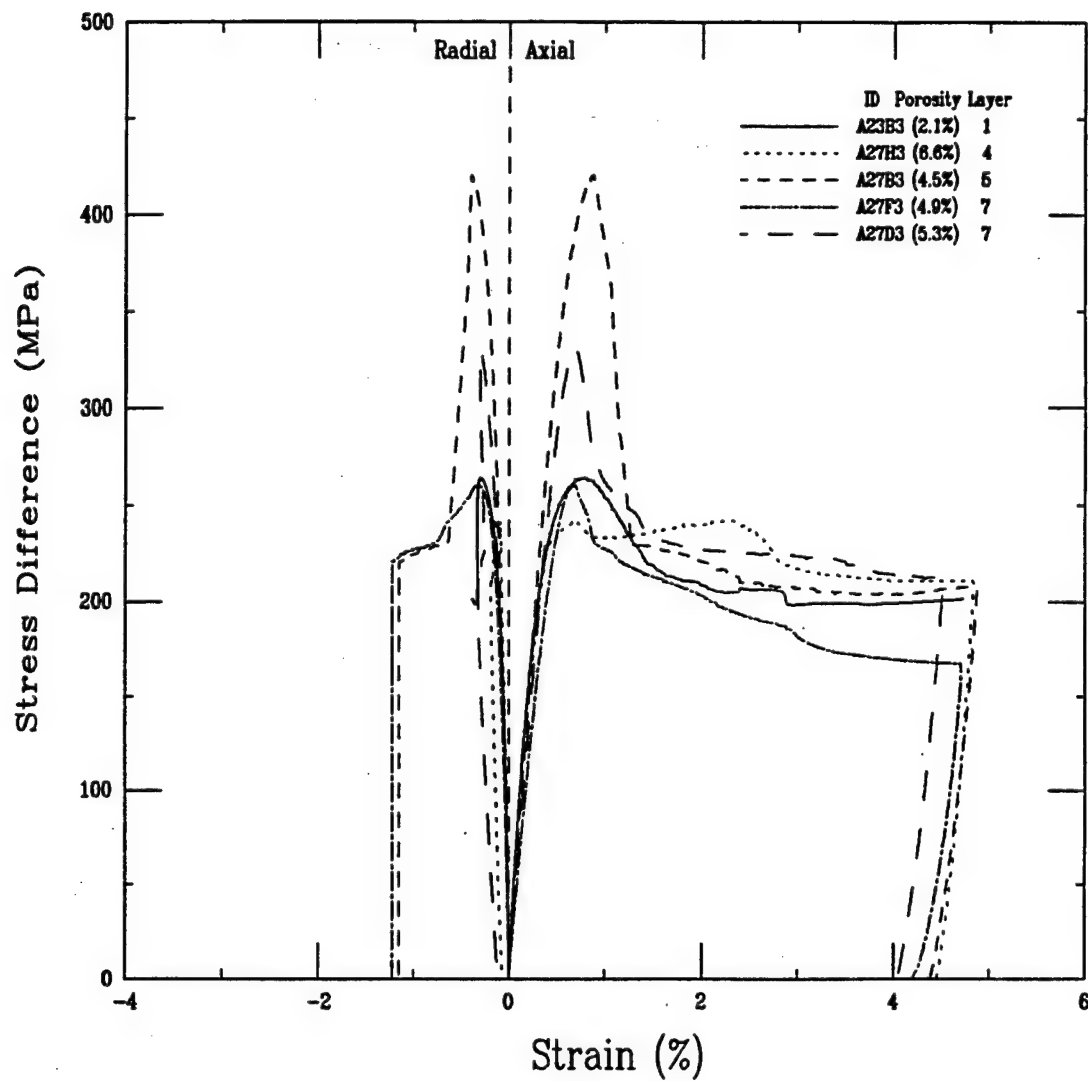


Figure 2-13. Axial and radial strains plotted against stress difference for specimens low-porosity carbonate rocks from core hole CS-4 at Fort Knox tested in triaxial compression with 50 MPa confining pressure.

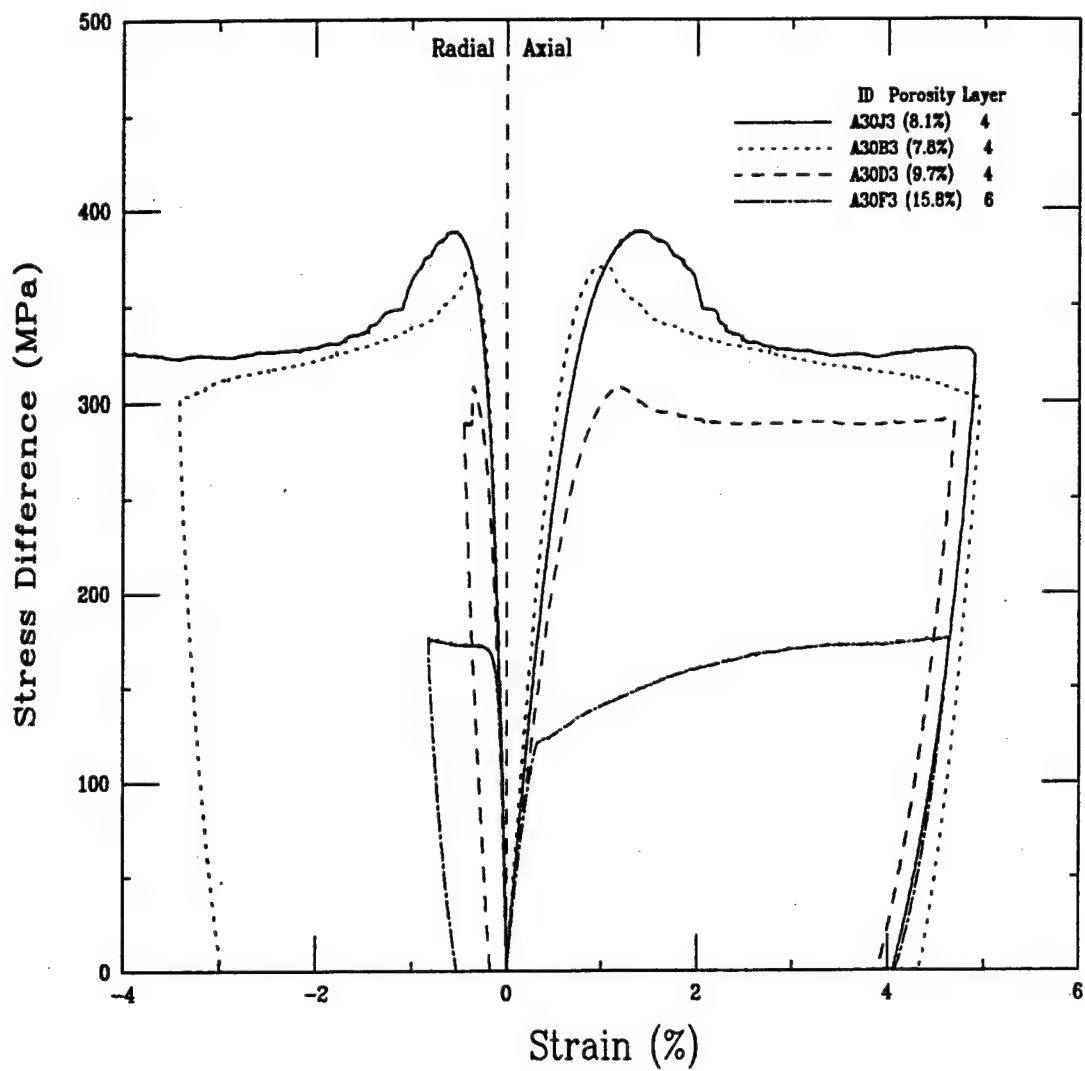


Figure 2-14. Axial and radial strains plotted against stress difference for specimens high-porosity carbonate rocks from core hole CS-4 at Fort Knox tested in triaxial compression with 100 MPa confining pressure.

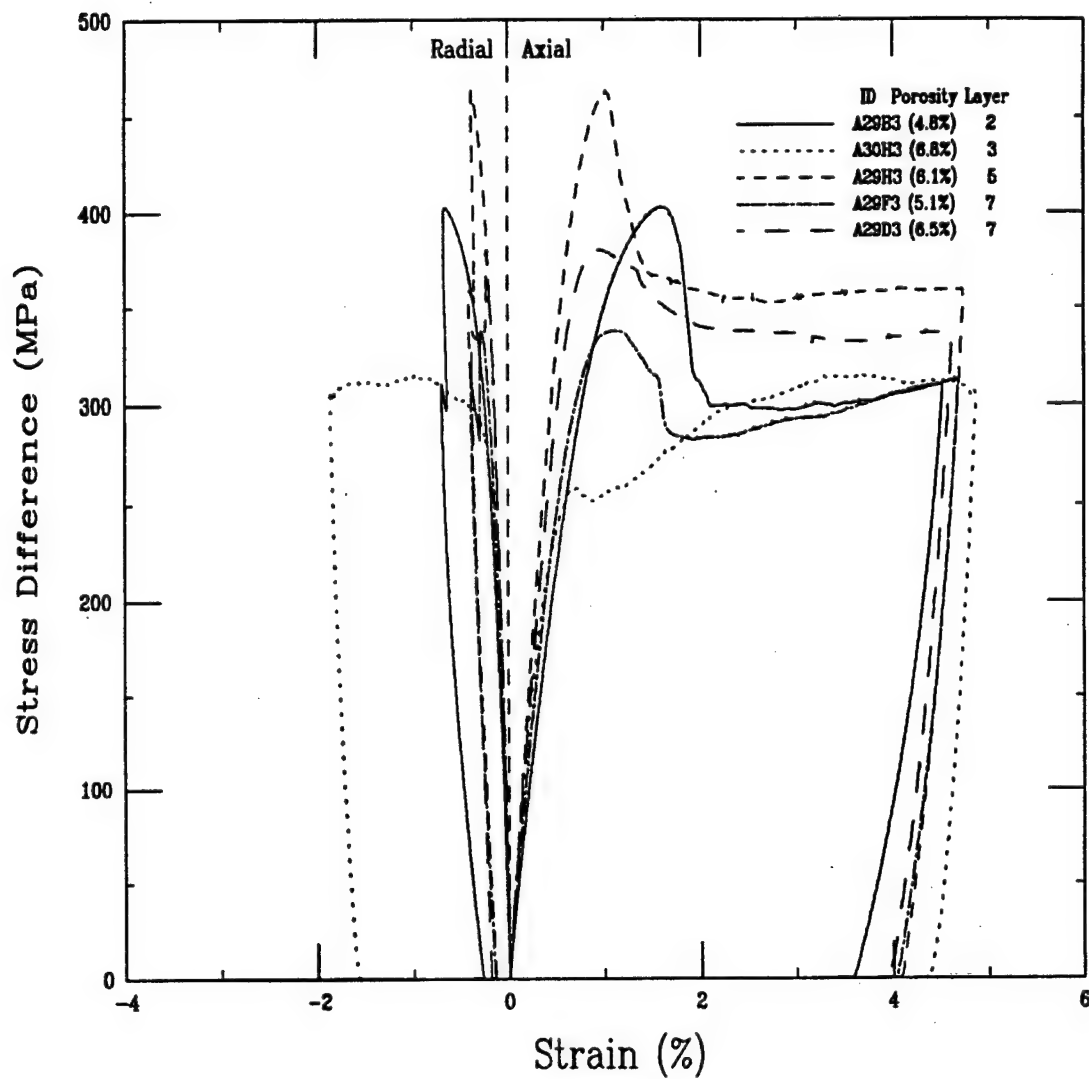


Figure 2-15. Axial and radial strains plotted against stress difference for specimens low-porosity carbonate rocks from core hole CS-4 at Fort Knox tested in triaxial compression with 100 MPa confining pressure.

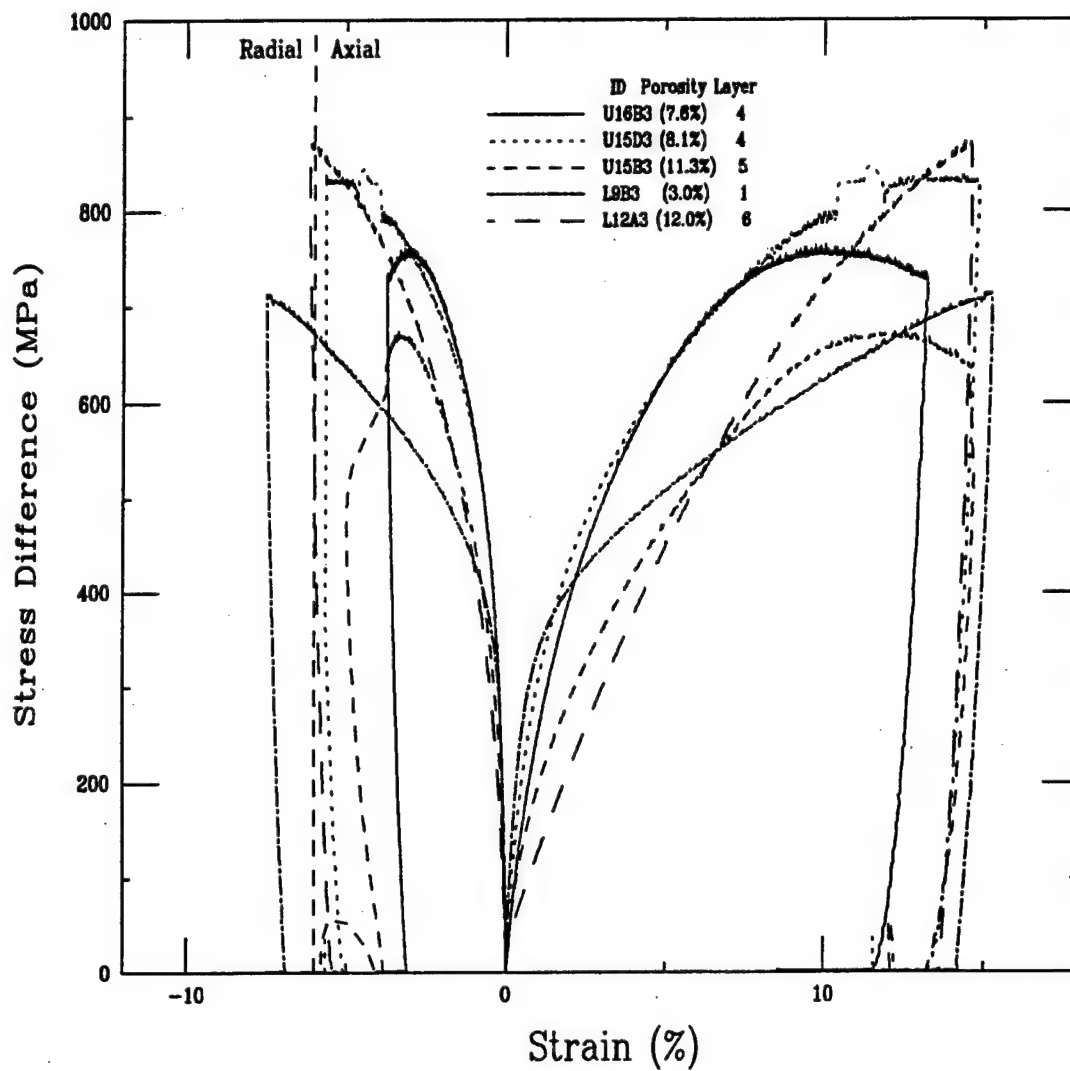


Figure 2-16. Axial and radial strains plotted against stress difference for specimens carbonate rocks from core hole CS-4 at Fort Knox tested in triaxial compression with 400 MPa confining pressure.

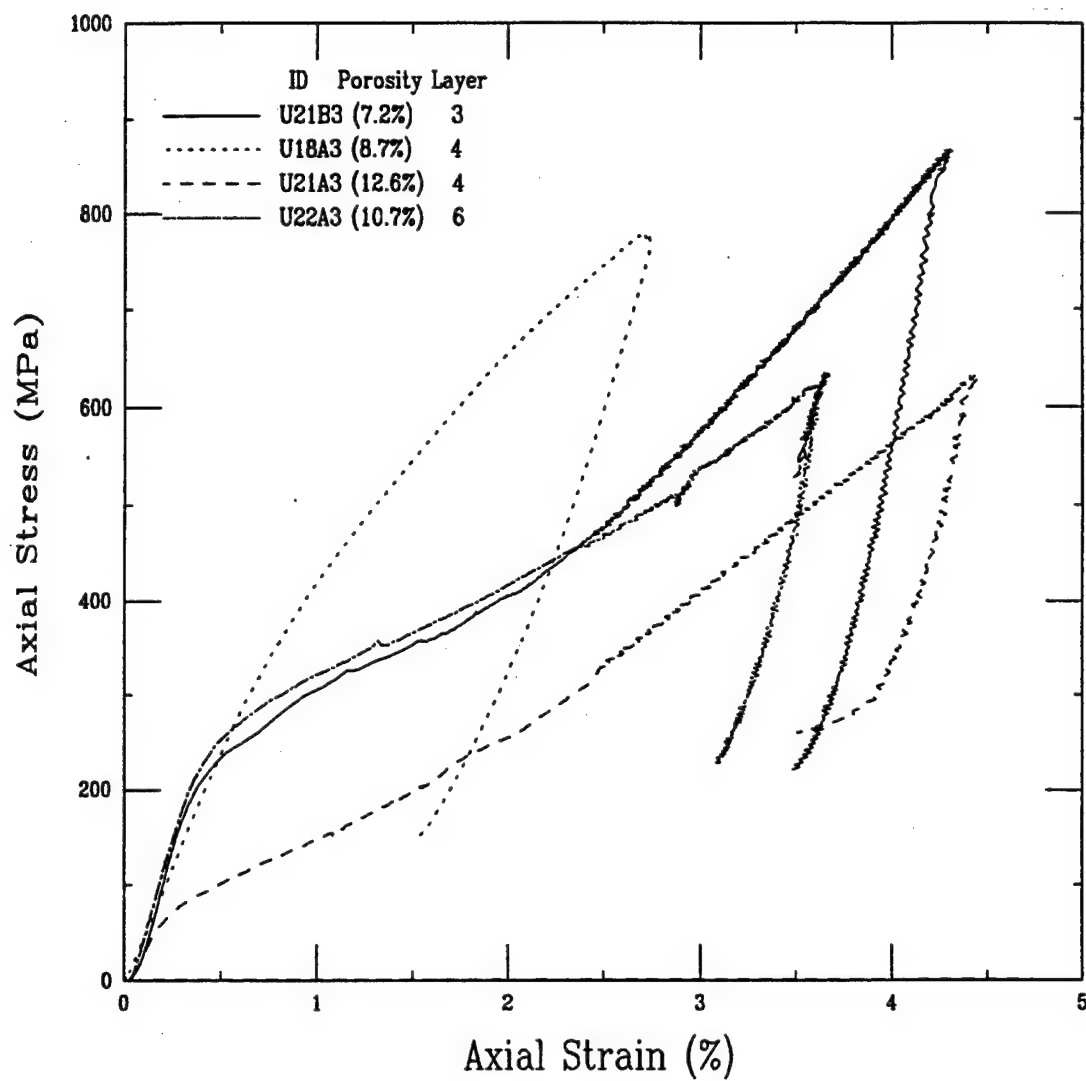


Figure 2-17. Relationships between axial stress and axial strain for specimens of high-porosity carbonate rocks from core hole CS-4 at Fort Knox tested in uniaxial strain.

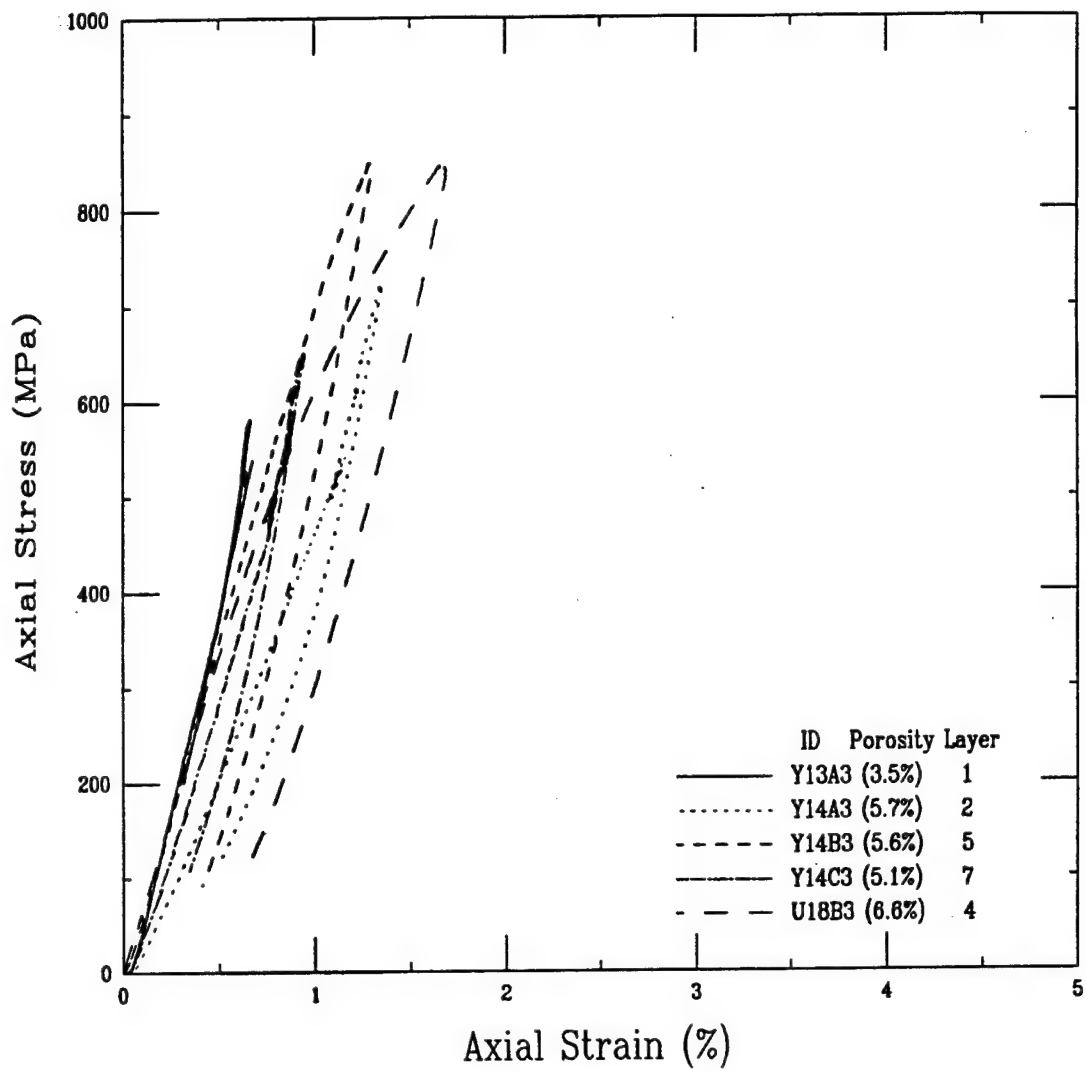


Figure 2-18. Relationships between axial stress and axial strain for specimens of low-porosity carbonate rocks from core hole CS-4 at Fort Knox tested in uniaxial strain.

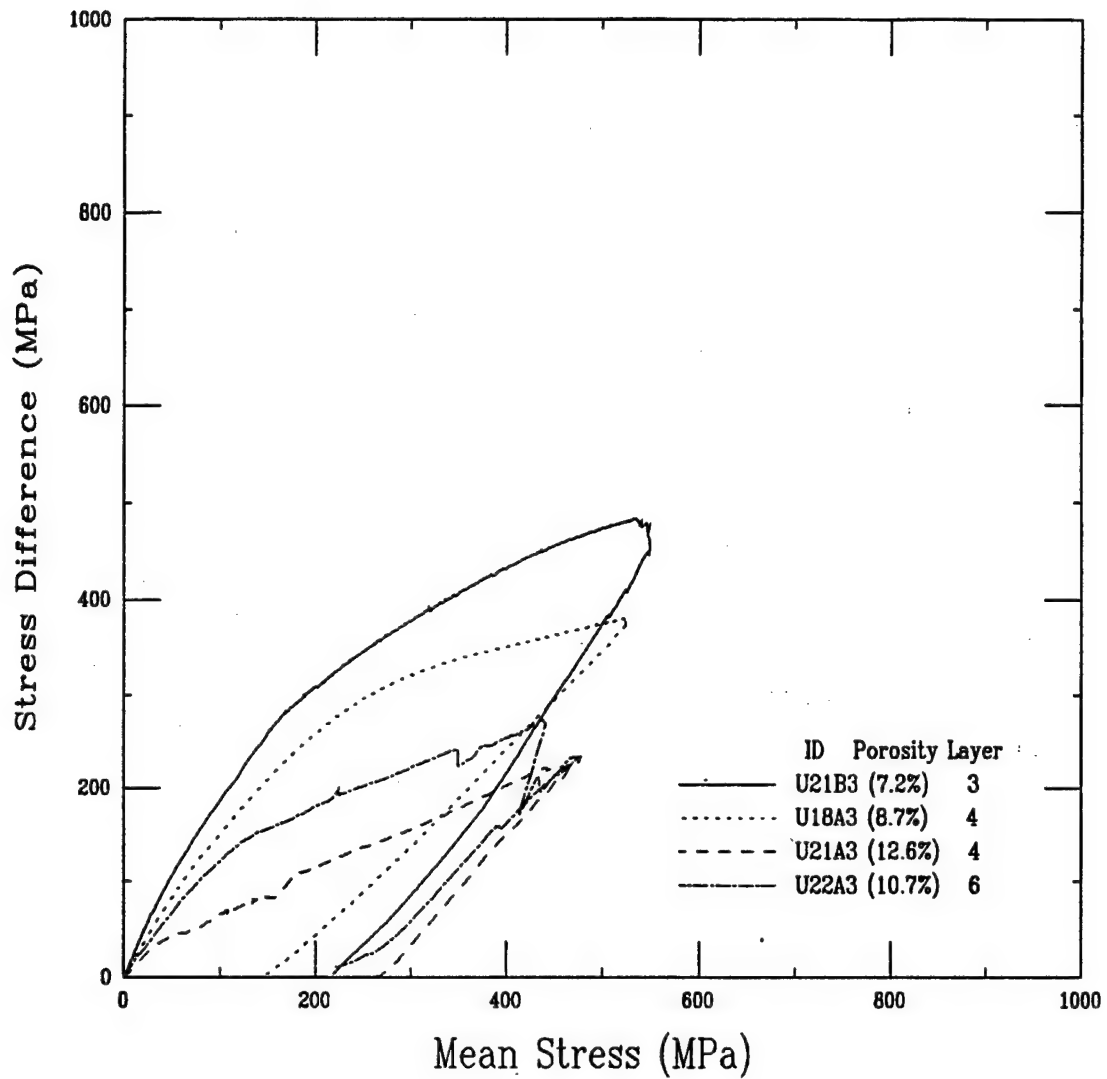


Figure 2-19. Relationships between stress difference and mean stress for specimens of high-porosity carbonate rocks from core hole CS-4 at Fort Knox tested in uniaxial strain.

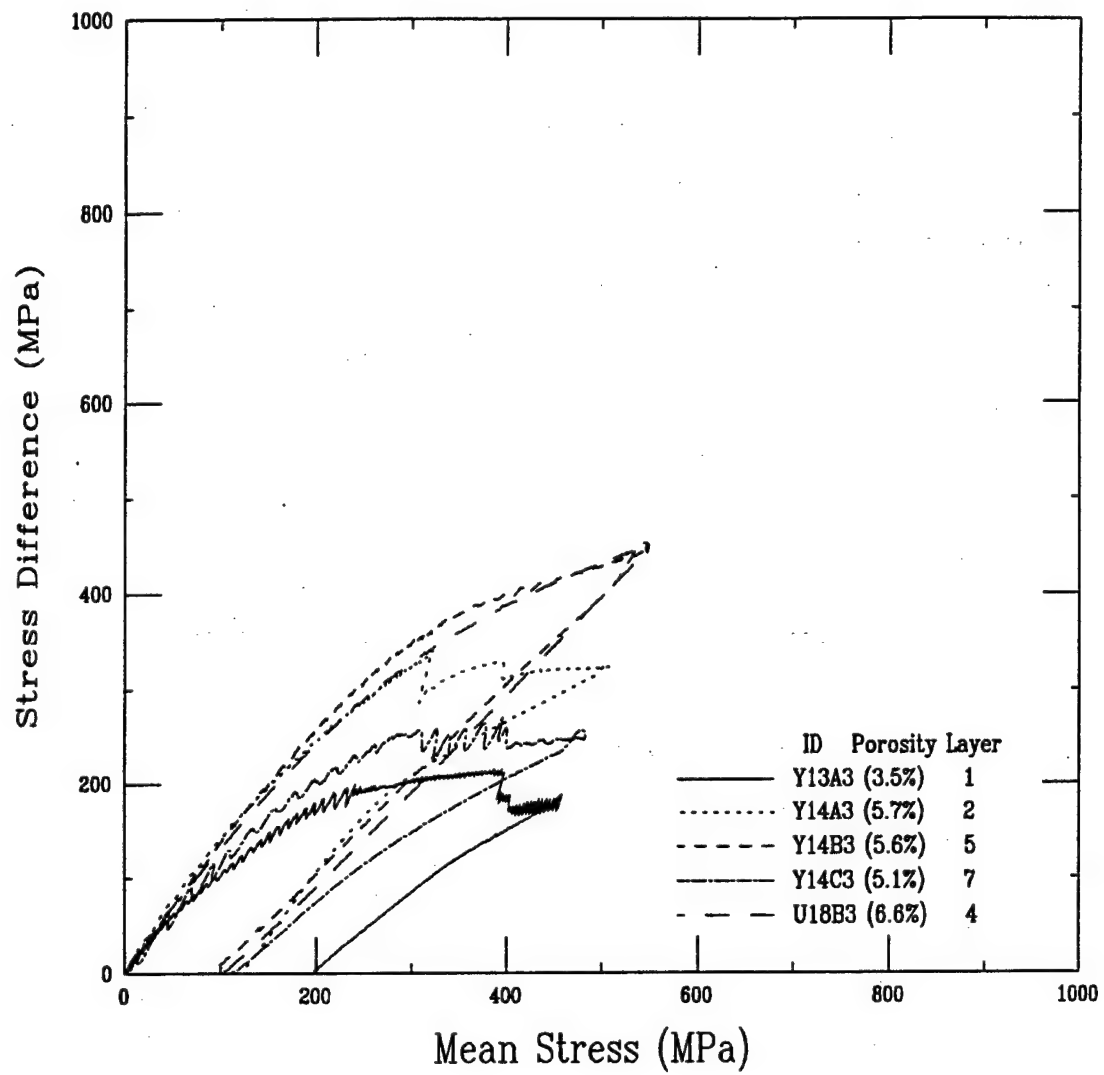


Figure 2-20. Relationships between stress difference and mean stress for specimens of low-porosity carbonate rocks from core hole CS-4 at Fort Knox tested in uniaxial strain.

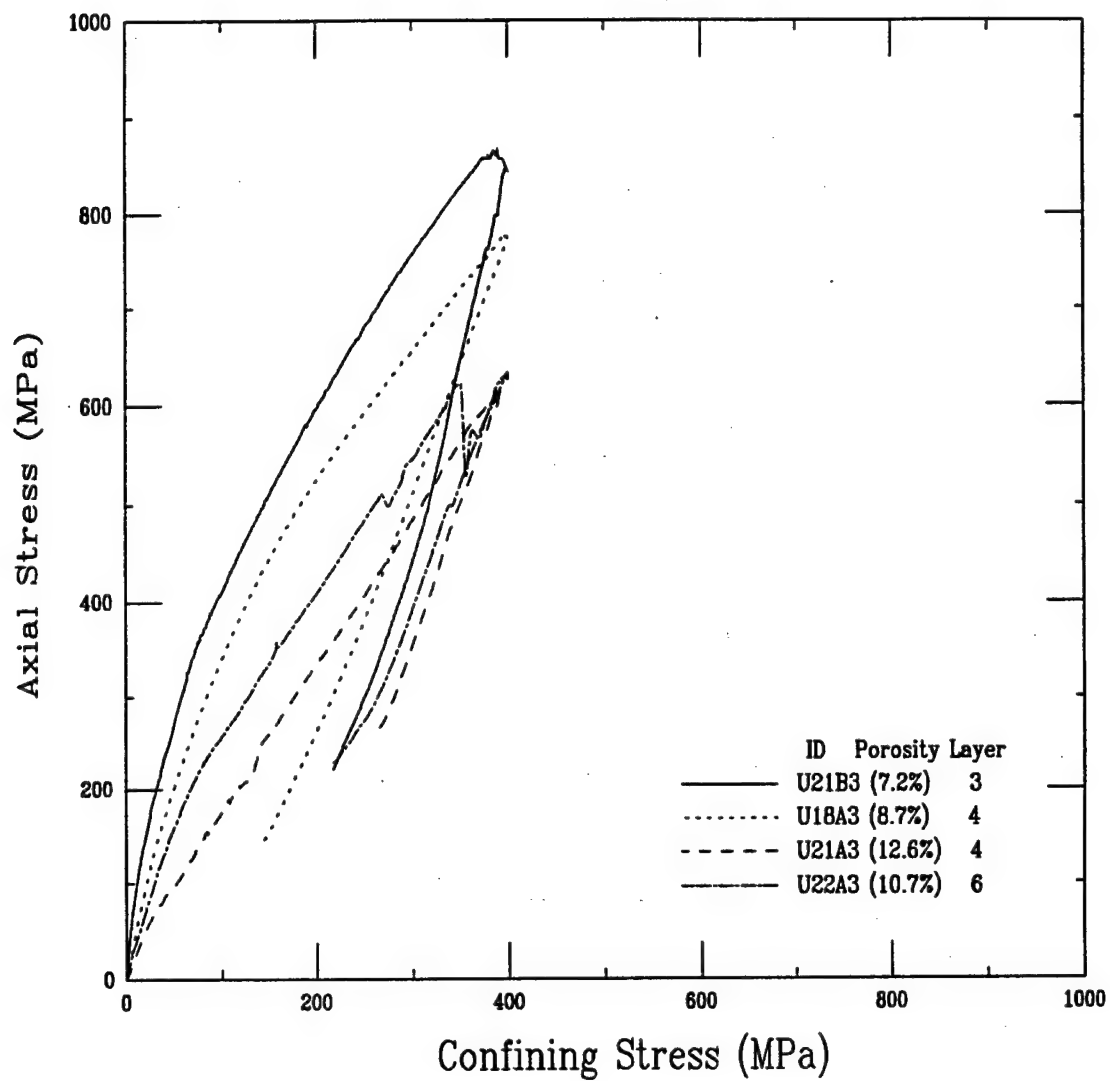


Figure 2-21. Relationships between axial stress and confining pressure for specimens of high-porosity carbonate rocks from core hole CS-4 at Fort Knox tested in uniaxial strain.

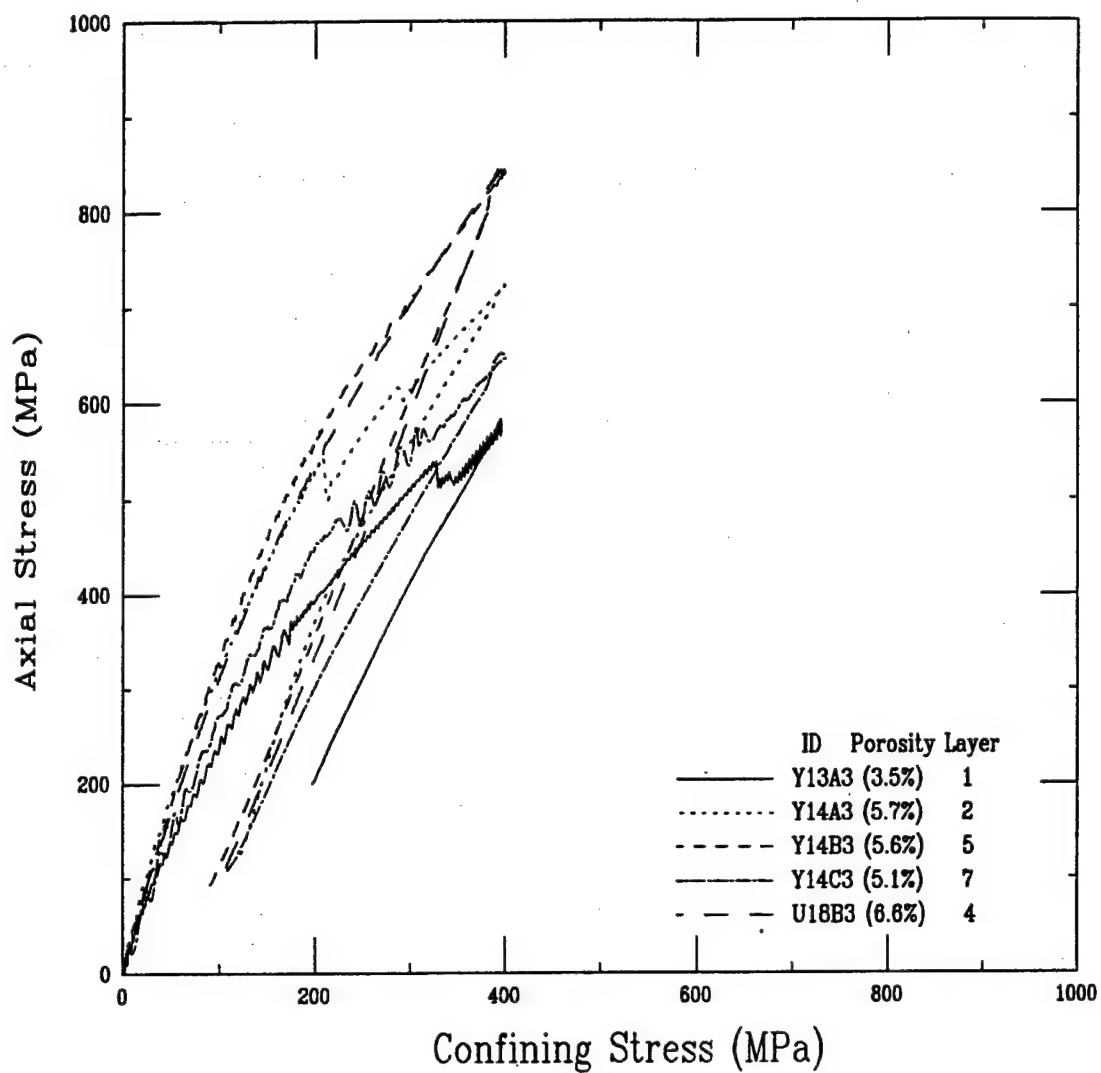


Figure 2-22. Relationships between axial stress and confining pressure for specimens of low-porosity carbonate rocks from core hole CS-4 at Fort Knox tested in uniaxial strain.

SECTION 3

ANALYSIS OF LIMESTONE TEST DATA

From the physical and mechanical property test data presented in Section 2, it is clear that there are significant inhomogenities in the Fort Knox carbonates, even within the materials nominally identified as layers. Thus, for some modeling purposes, it may not be possible to adequately characterize the rocks using a small number of discrete material property sets. An alternative approach, which is developed in this section, is to model the relevant mechanical properties as functions of a relevant physical property, e.g. porosity. Based on *in situ* geophysical logs of the boreholes at a site of interest, it is possible to construct a three-dimensional model of the spatial variation in porosity. Using that three-dimensional representation of porosity variation, along with the correlations between physical and mechanical properties presented in this section, it would be possible to create a site model that captures the spatial variations in material properties over the volume of interest. With sufficient data, it would also be possible to extend this approach to create a probabilistic representation of the relevant material properties. The following subsections present models for both strength and deformation properties of the Fort Knox rocks.

3.1 MODULUS MODELING.

The variations in properties of carbonate rocks can be conceptualized by considering them to be composed of solid calcium carbonate mineral with homogeneously distributed voids. While this is admittedly a gross simplification of nature, it provides a useful basis for formulating a model. It seems intuitively reasonable that a rock composed of solid mineral with no voids should have the highest modulus of any carbonate material, and modulus should decrease in some relation to increasing void fraction, i.e. porosity. In previous work, Blouin and Chitty (1989) presented a model for the constrained modulus of carbonate rocks based on a measure of their void content. Instead of porosity, the model was developed in terms of a quantity called the normalized specific volume. The specific volume is simply the inverse of density, i.e. volume per unit mass. In the formulation of the original model, test data from a wide variety of carbonate materials were included. In order to compensate for the variations in grain density resulting from

variations in mineral content, the specific volume was normalized by the grain density. This normalization also has the advantage of making the resulting quantity unitless. The normalized specific volume, (ψ), is thus given by:

$$\Psi = \frac{\rho_g}{\rho_d} \quad (3.1)$$

where: ρ_g = grain density
 ρ_d = dry bulk density

The normalized specific volume is related to porosity, n , by:

$$\Psi = \frac{1}{1 - n} \quad (3.2)$$

The 1989 model was based on data for carbonate rocks ranging in porosity from near zero to almost 50%. It was also constrained to yield the correct value of calcium carbonate modulus at zero porosity. The relationships are summarized in Table 3-1.

Table 3-1. Engineering model for constrained modulus of carbonate rocks as a function of porosity.

Normalized Specific Volume ψ	Porosity n	Constrained Modulus (GPa)
< 1.16	<0.138	$5.164 \times 10^5 e^{-8.16\psi}$
1.16 to 1.38	0.138 to 0.275	$1.30 \times 10^4 e^{-4.99\psi}$
> 1.38	>0.275	$3.393 \times 10^3 e^{-4.01\psi}$

The constrained modulus values derived from uniaxial strain tests on carbonate rocks from Fort Knox, and compiled in Table 2-9, are plotted against normalized specific volume in Figure 3-1. Also shown in Figure 3-1 is the relevant model equation from Table 3-1. Clearly, the data fall predominantly below the model curve. A downward shift of the model curve by about 20% would produce a much improved fit to this particular data set.

3.2 STRENGTH MODELING.

To completely specify the strength of a rock, it is necessary to define a strength envelope, that is, some measure of shear strength as a function of some measure of the mean normal stress on the

rock. For an individual rock, the strength envelope is typically constructed by plotting the results of conventional (constant confining pressure) triaxial compression tests performed at a range of different confining pressures. Section 2.9.2 presents triaxial compression test results for the Fort Knox carbonates at confining pressures of 0, 50, 100, and 400 MPa. Initially, consider the variation in strength with modulus at each of the four confining pressures. Figure 3-2 presents the results of the unconfined compression tests on rock specimens from borehole CS-4. In Figure 3-2, the unconfined strength is plotted against porosity, and a line representing the least squares fit to the data set is also shown. The peak stress difference, σ_{Δ} , is given in terms of porosity, n , by:

$$\sigma_{\Delta} = 160 \text{ MPa } e^{-7.30n} \quad (3.3)$$

A similar analysis, including data from a variety of limestones from multiple continents, was presented by Blouin and Chitty (1991). That analysis produced a slightly different expression, $\sigma = 177 e^{-8.5n}$, which is also shown in Figure 3-2 for comparison.

Similar data plots, including least squares fits, are presented for the 50- and 100-MPa tests in Figures 3-2 and 3-4, respectively. For 50 MPa confining pressure, the fit is:

$$\sigma_{\Delta} = 410 \text{ MPa } e^{-6.90n} \quad (3.4)$$

And, for 100 MPa confining pressure:

$$\sigma_{\Delta} = 603 \text{ MPa } e^{-7.30n} \quad (3.5)$$

The strengths determined in tests at 400 MPa confining pressure are shown in Figure 3-5. Here, unlike the lower confining pressure tests, there does not appear to be any dependence of strength on porosity. One possible explanation for this phenomenon is that at 400 MPa normal stress, the porosity is so well crushed out that the materials are all essentially the same, regardless of their initial unstressed porosity. A model for strength at 400 MPa is simply the average of the strengths determined in the five tests:

$$\sigma_{\Delta} = 770 \text{ MPa} \quad (3.6)$$

Based on Equations 3.3 through 3.6, strength envelopes were constructed for five porosity values ranging from 0.03 to 0.15, as shown in Figure 3-6. To illustrate how well the constructed strength envelopes compare with the test data, the five strength envelopes are plotted individually in Figures 3-7 through 3-11, and each of the strength test data points is plotted on the figure that most closely matches the actual porosity of the test specimen.

3.3 DISCUSSION.

The carbonate rocks sampled from the boreholes at Fort Knox are not well modeled as layers of uniform material. Even within the regions nominally defined as layers, there are significant variations in physical and mechanical properties. There are also variations in the distribution of porosity, i.e. in some cases, the voids may be approximately uniformly distributed through out the rock matrix while in others the porosity is more vugular, forming voids that are very large in comparison with the grain dimensions.

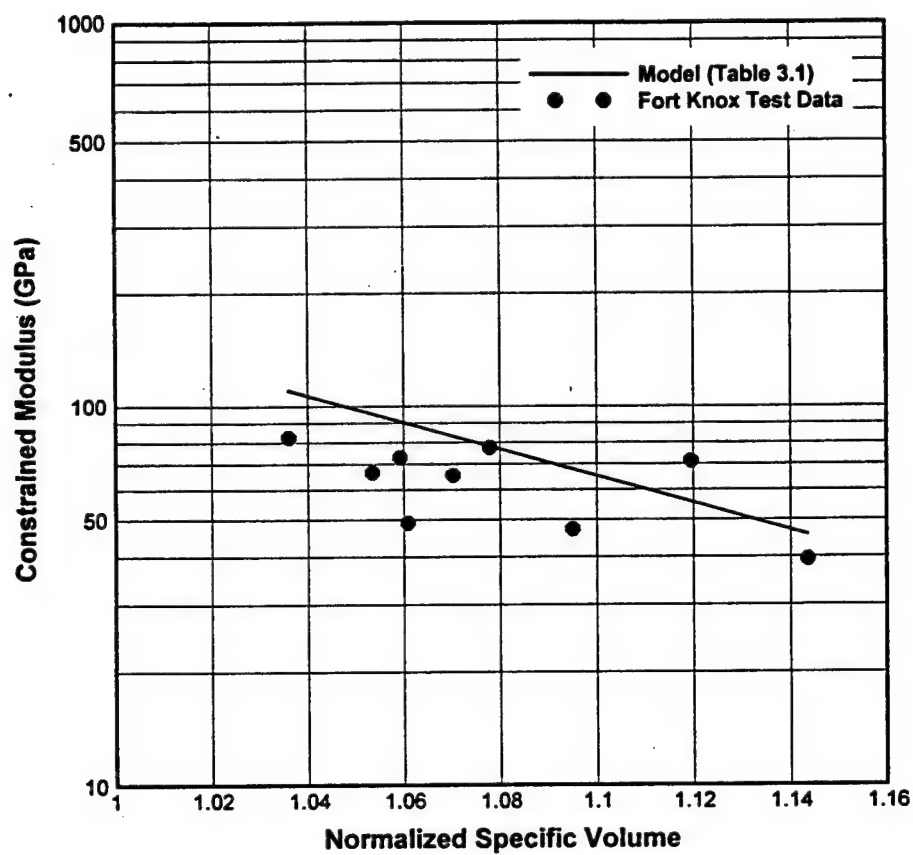


Figure 3-1. The constrained moduli determined from uniaxial strain tests on carbonate rocks from Fort Knox plotted against their unstressed normalized specific volumes. Also shown is a line representing a model that was previously derived for a wide range of carbonate rocks.

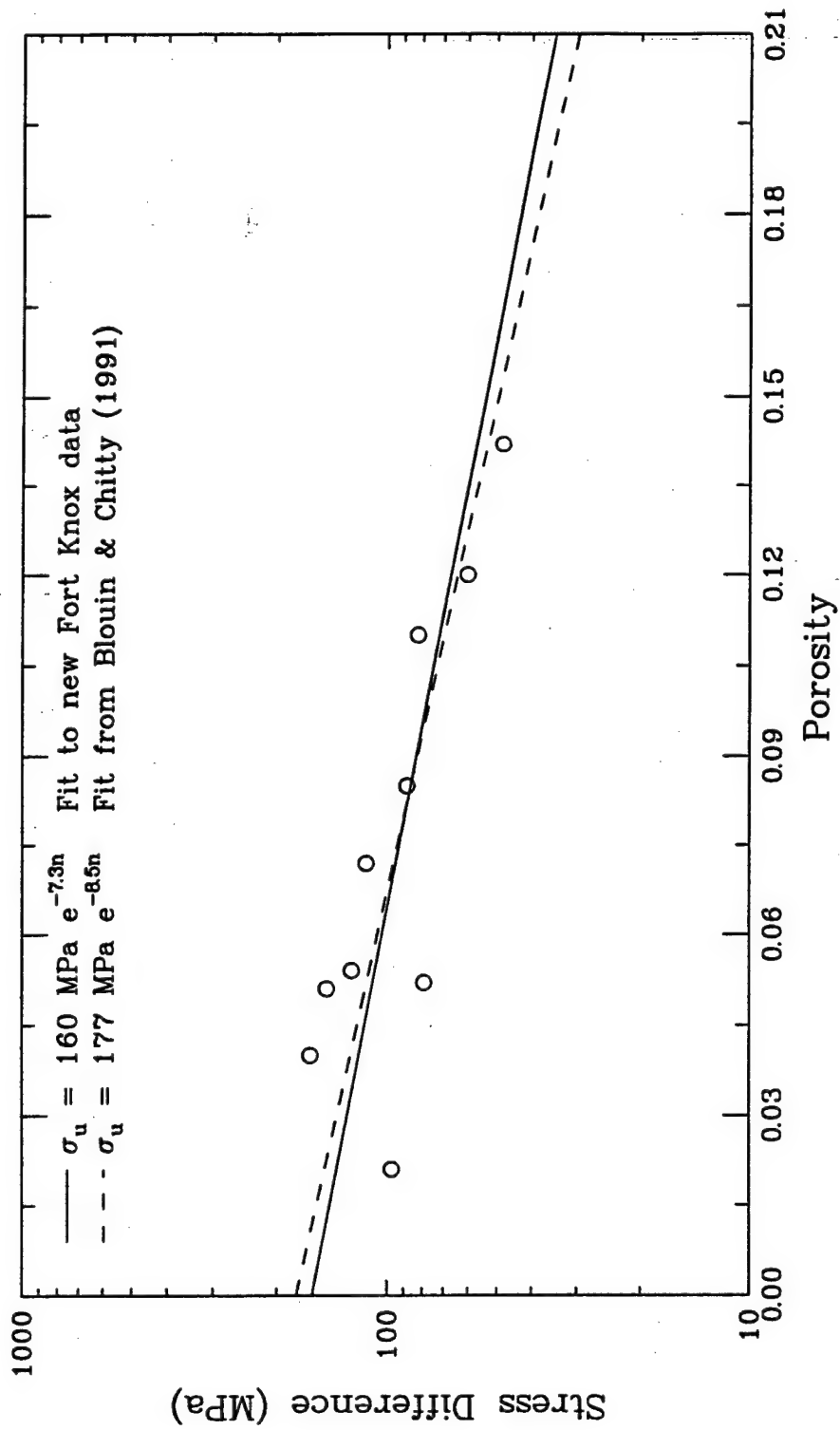


Figure 3-2. Values of peak stress difference determined from unconfined compression tests on specimens of carbonate rocks from Fort Knox plotted against their initial porosity, and a straight line fit to the data points.

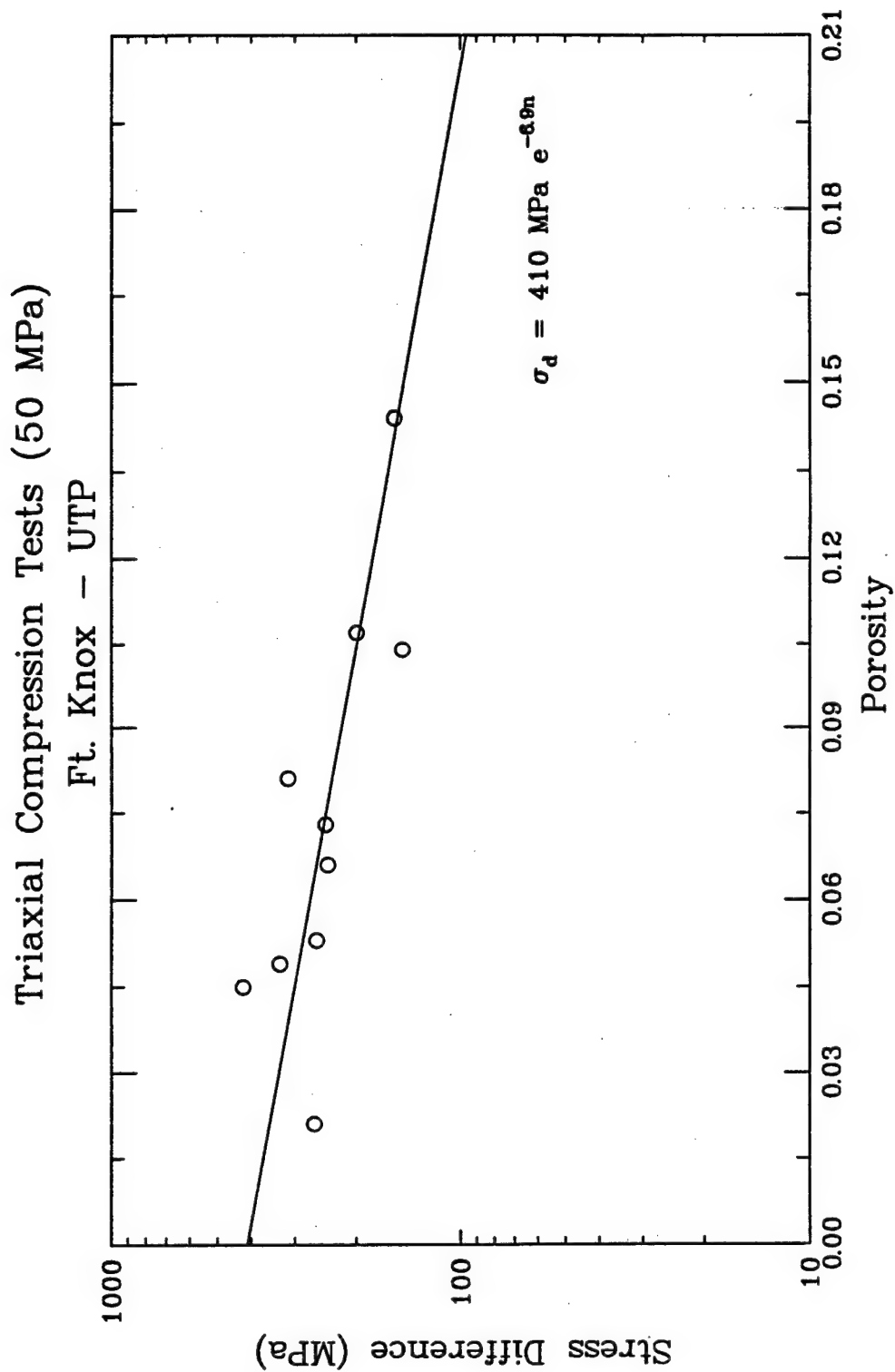


Figure 3-3. Values of peak stress difference determined from 50-MPa triaxial compression tests on specimens of carbonate rocks from Fort Knox plotted against their initial porosity, and a straight line fit to the data points.

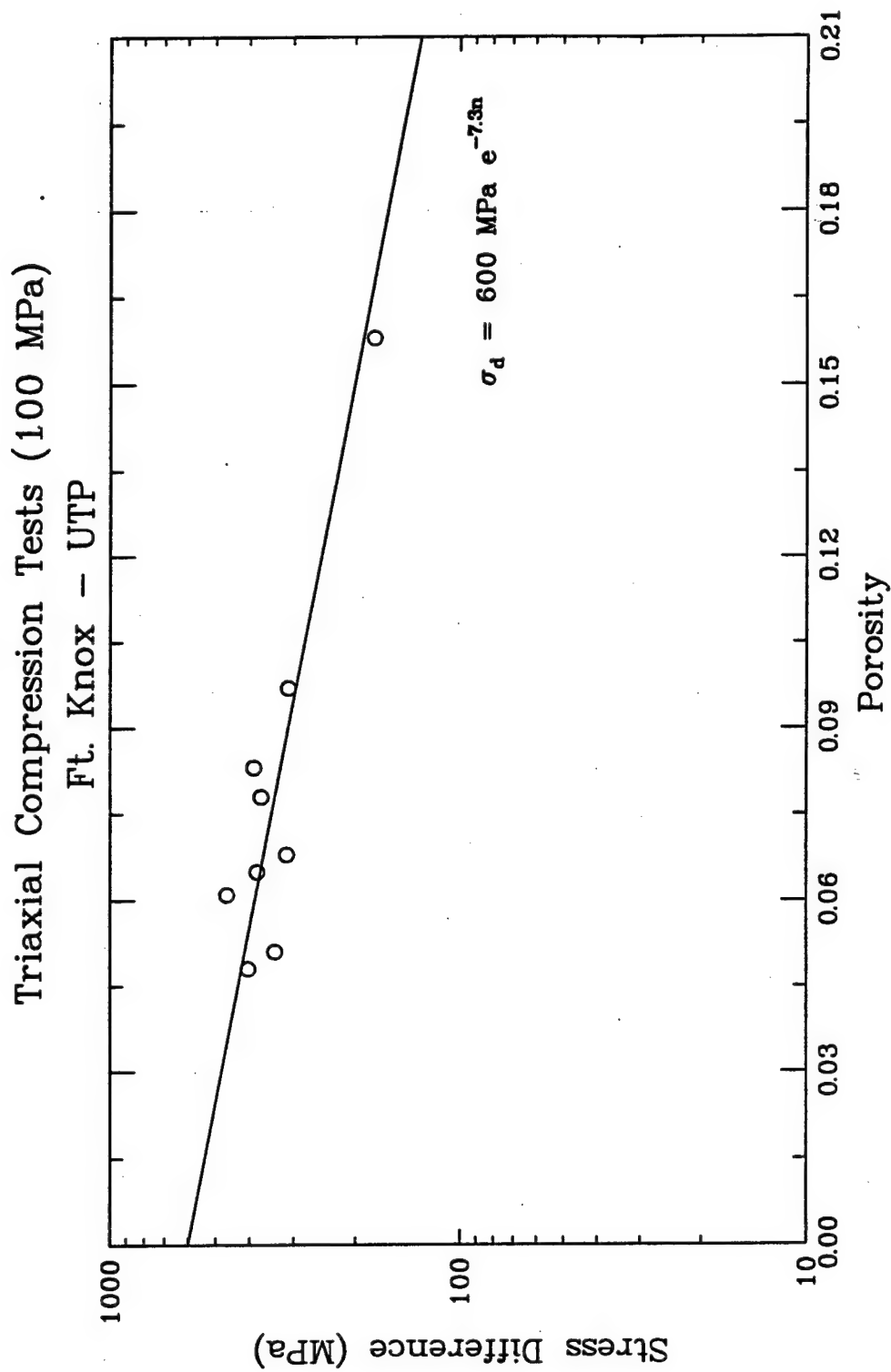


Figure 3-4. Values of peak stress difference determined from 100-MPa triaxial compression tests on specimens of carbonate rocks from Fort Knox plotted against their initial porosity, and a straight line fit to the data points.

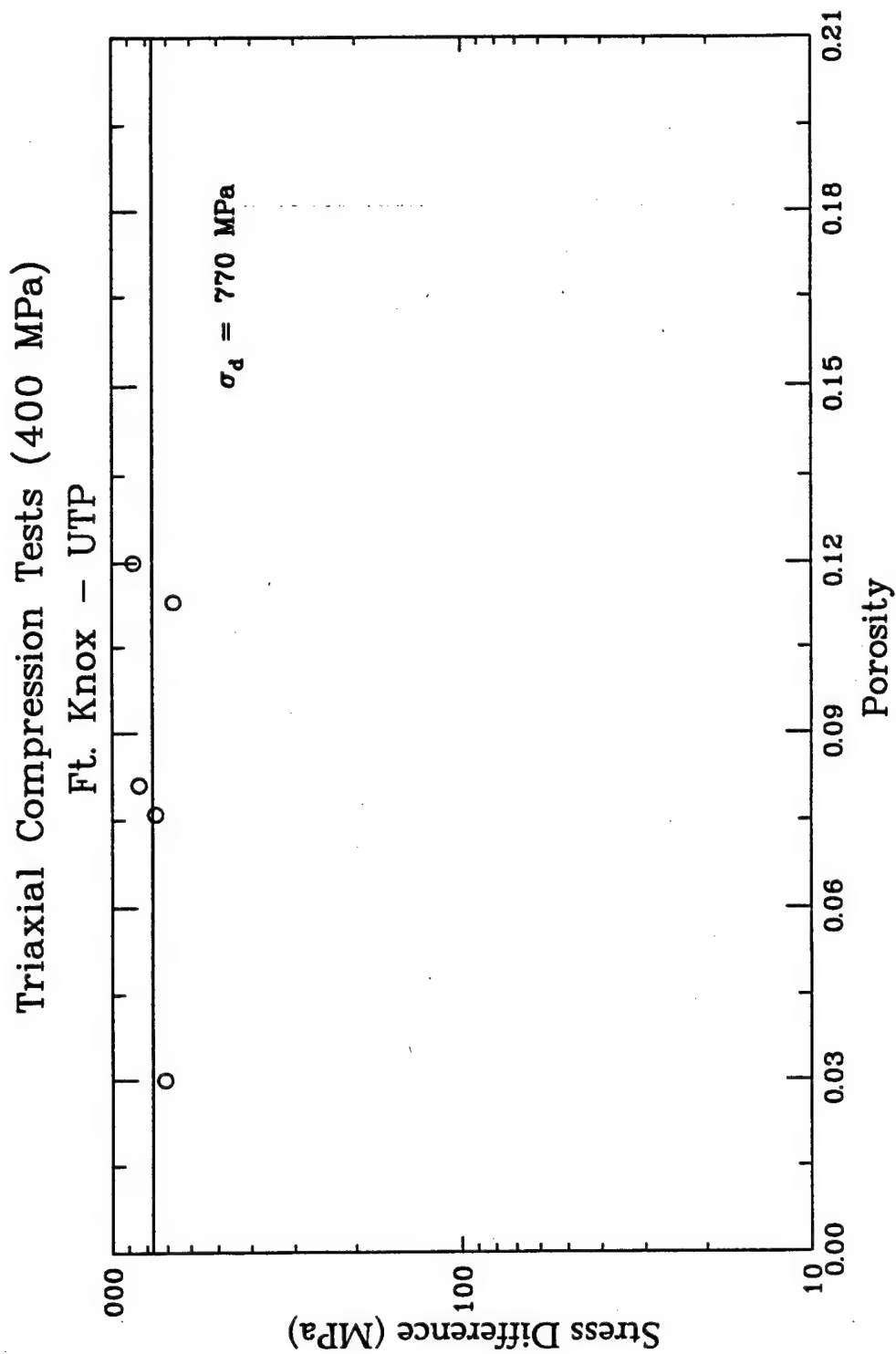


Figure 3-5. Values of peak stress difference determined from 400-MPa triaxial compression tests on specimens of carbonate rocks from Fort Knox plotted against their initial porosity, and a straight line fit to the data points.

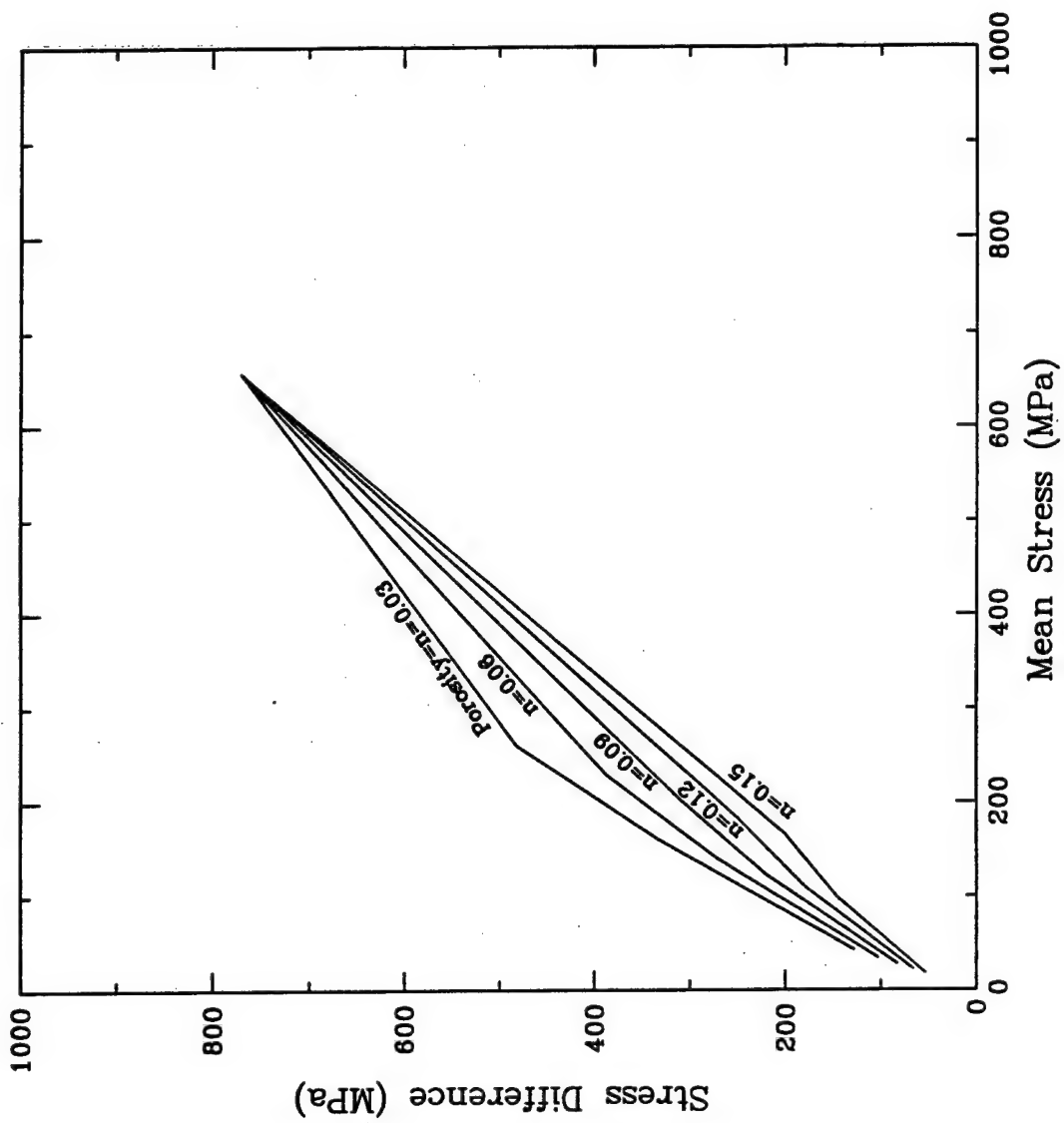


Figure 3-6. Strength envelopes synthesized from the fits shown in Figures 3-2 through 3-5 for carbonate rocks with porosities ranging from 0.03 to 0.15.

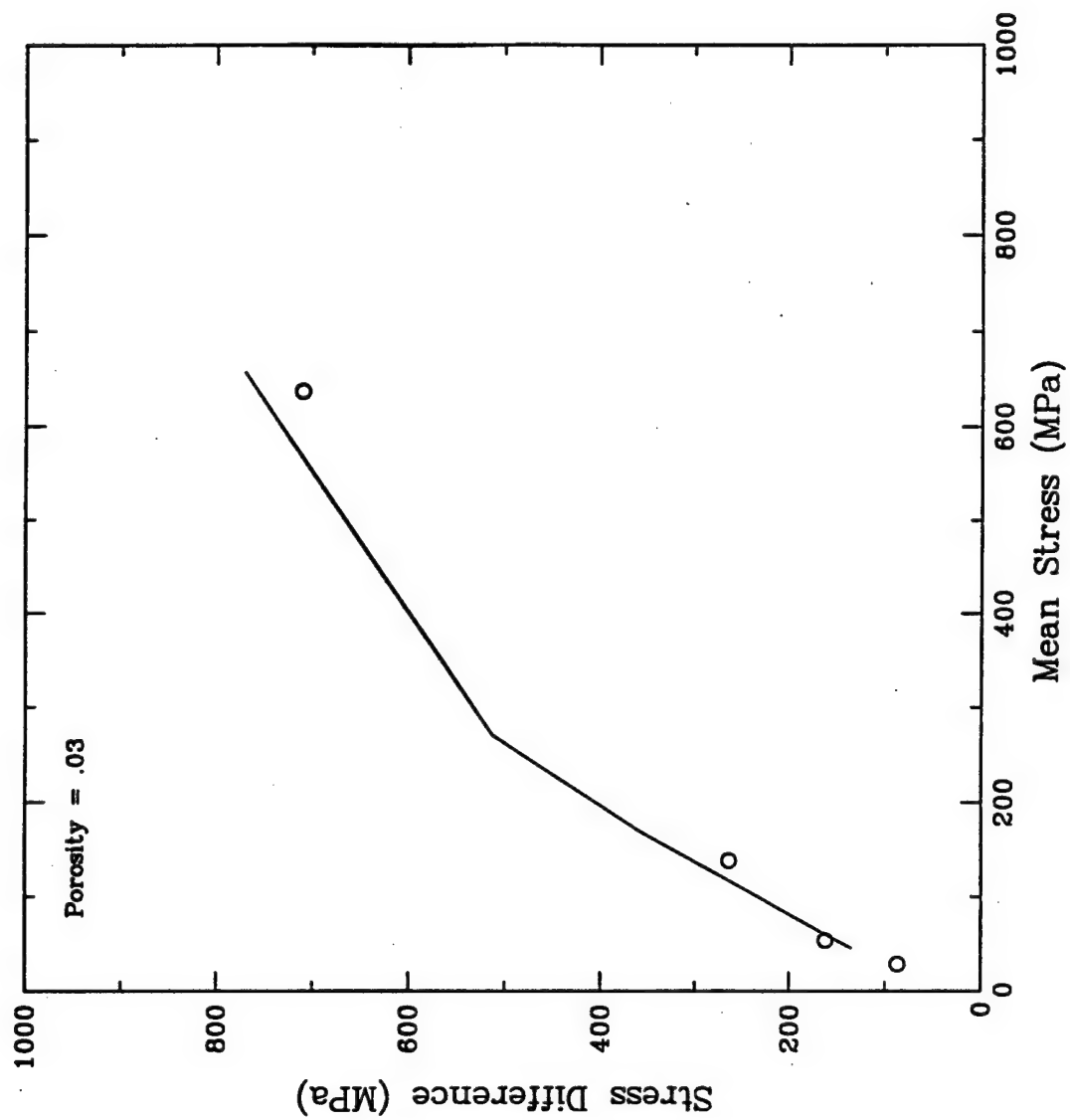


Figure 3-7. Synthesized strength envelope for 0.03 porosity shown along with the strength points from the Fort Knox data set that most closely match that porosity.

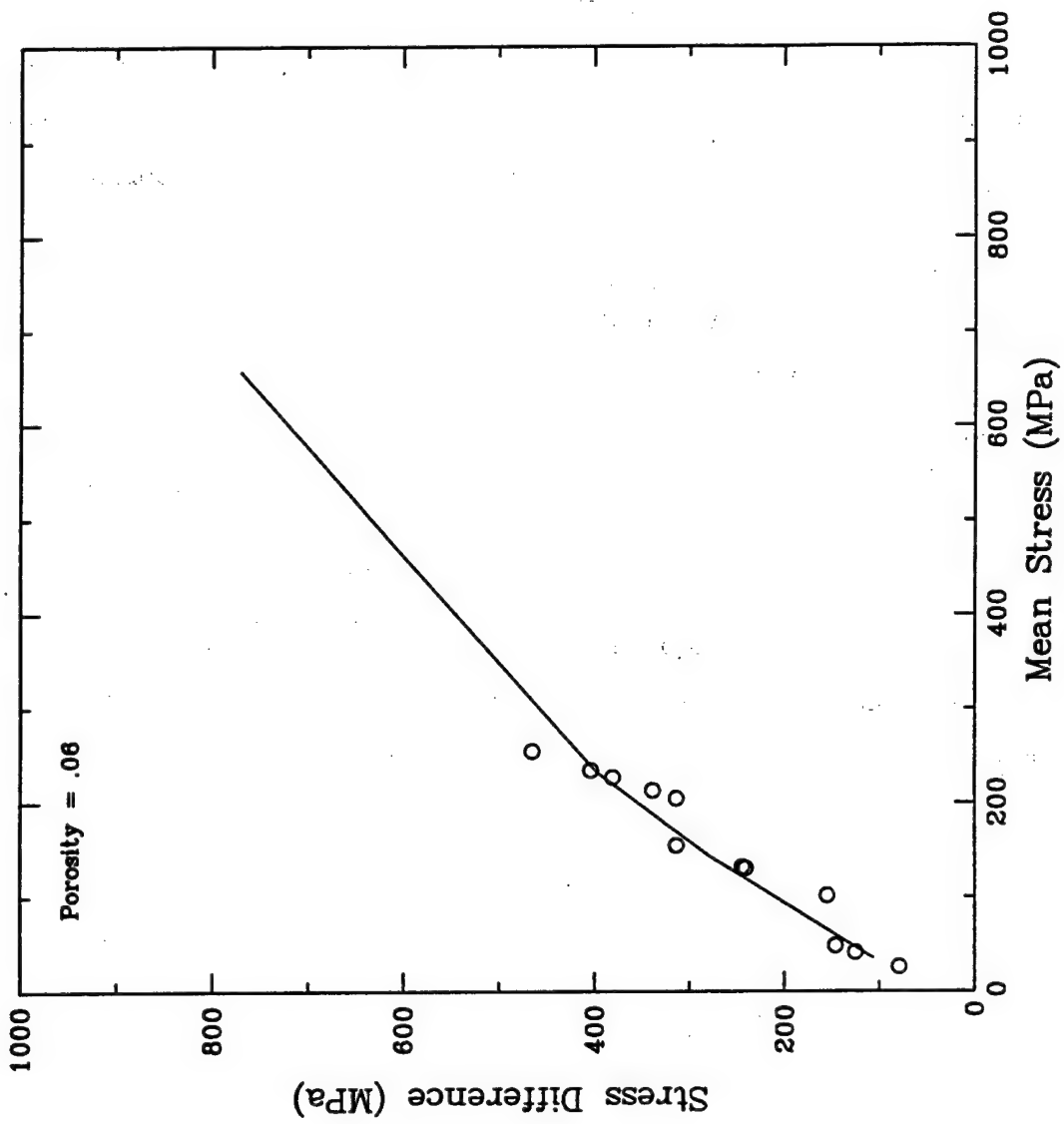


Figure 3-8. Synthesized strength envelope for 0.06 porosity shown along with the strength points from the Fort Knox data set that most closely match that porosity.

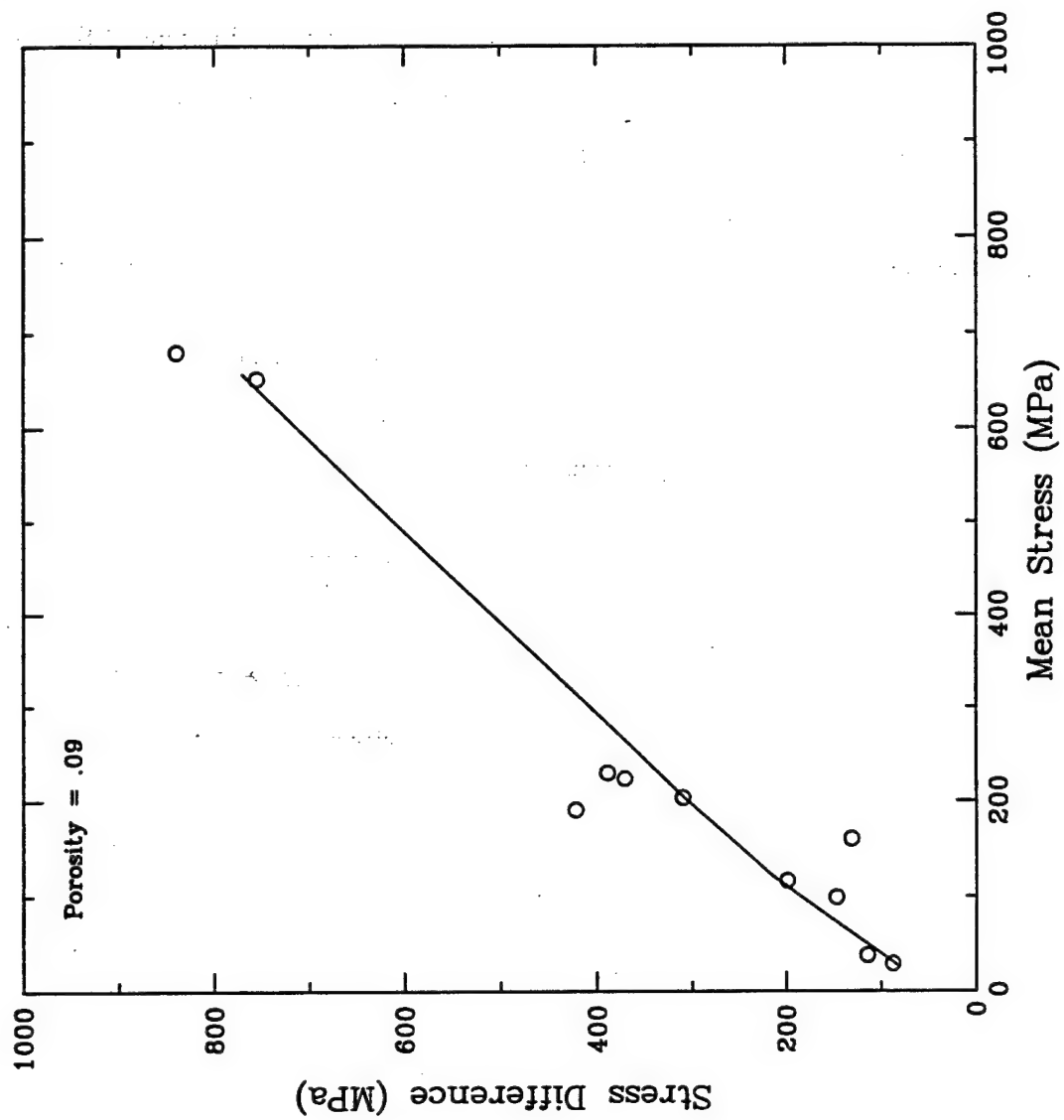


Figure 3-9. Synthesized strength envelope for 0.09 porosity shown along with the strength points from the Fort Knox data set that most closely match that porosity.

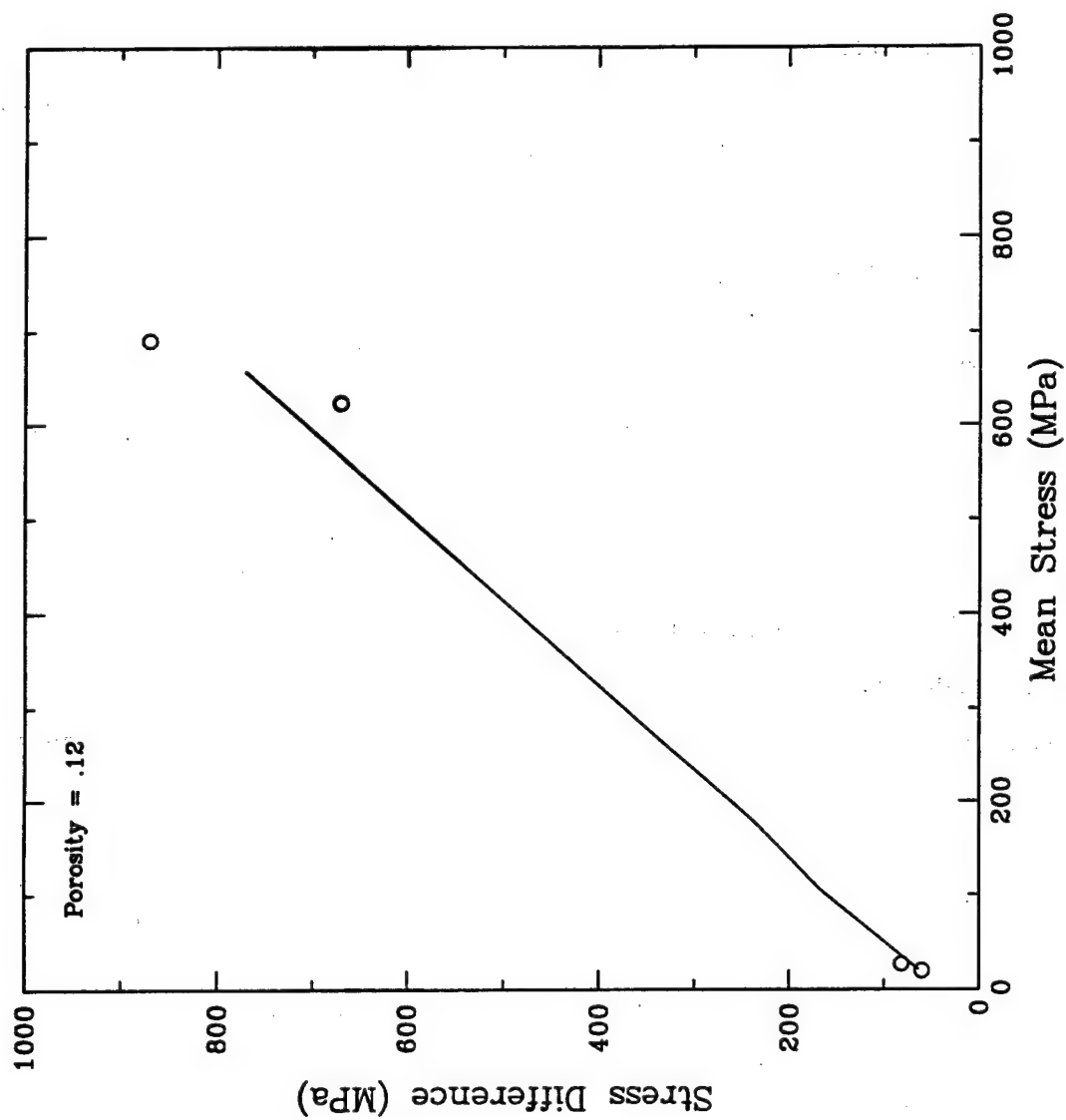


Figure 3-10. Synthesized strength envelope for 0.12 porosity shown along with the strength points from the Fort Knox data set that most closely match that porosity.

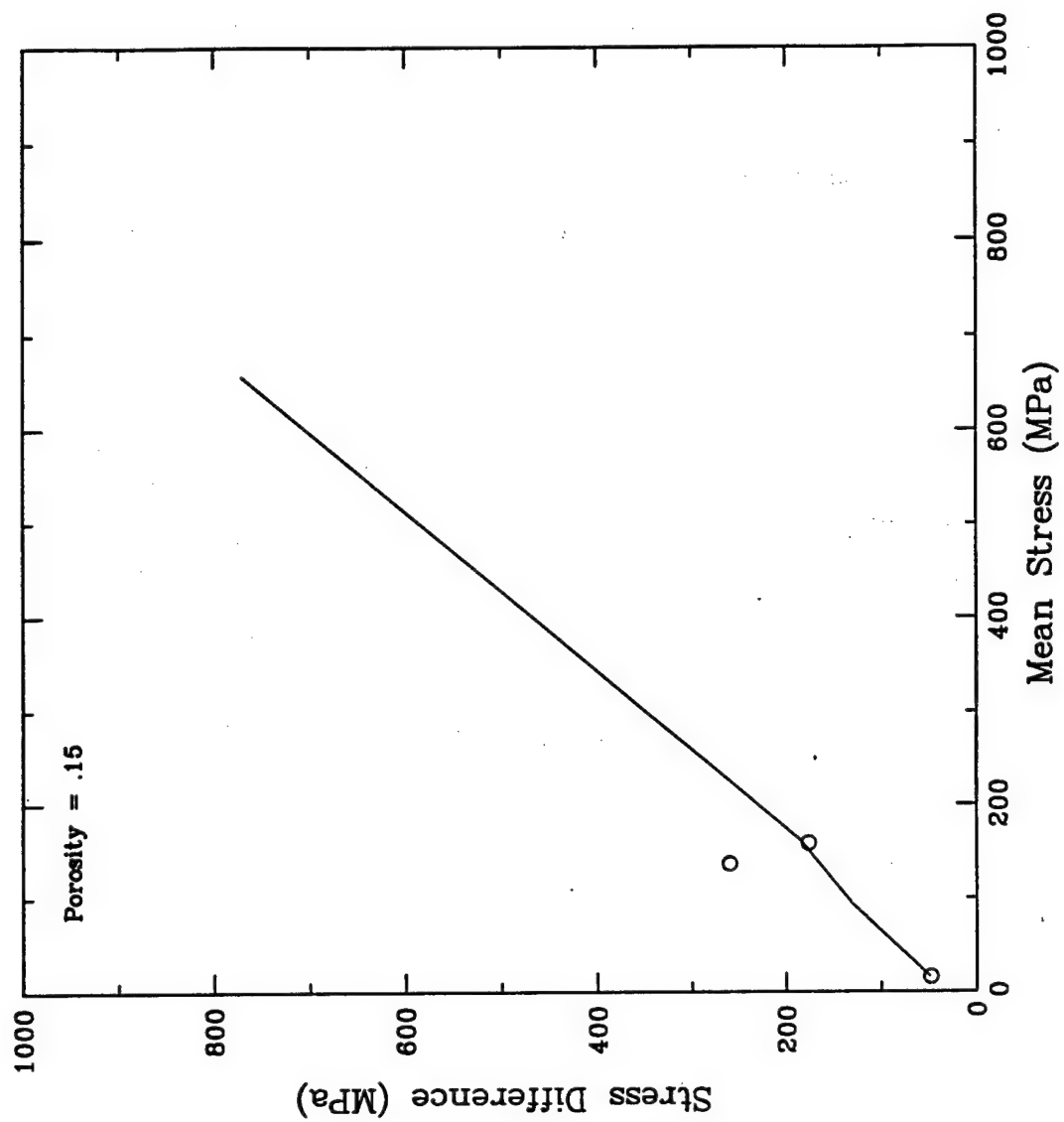


Figure 3-11. Synthesized strength envelope for 0.15 porosity shown along with the strength points from the Fort Knox data set that most closely match that porosity.

SECTION 4

LABORATORY TESTING OF TUFF FROM NEVADA TEST SITE

This section describes a laboratory test series that was conducted to characterize rock from the tunnel in which the Dipole Hole test was performed. The test series was necessarily brief because both the time and material available for testing were severely limited. The porous tuff was believed to be partially saturated *in situ*, and in addition to mechanical property characterization, an objective of the test series was to evaluate the degree of saturation of the material as received. The tests were performed during March and April 1995.

The organization of this section parallels that of Section 2, describing the material origin, its physical properties, and the mechanical property testing and test results. Descriptions of test procedures are only presented in this section in those cases where they were different from those described in Section 2.

4.1 MATERIAL ORIGIN.

The material was supplied to ARA for testing in the form of waxed cores by DNA Field Command, Nevada Operations Office. The origin of the cores is documented in memorandum by Harris-West (1995). The rock samples were cored from two different holes in the U16a tunnel at Nevada Test Site. The core holes, designated GI-1 and GI-2 were made at an elevation corresponding to the stratigraphic position of the two bomb locations closest to the portal, at stations CS 1+70 and CS 2+85, respectively. The shipment included a total of 1.0 m of 50-mm diameter core in five pieces.

It is ARA's understanding that the cores were drilled using water as coolant, and that they were wrapped in aluminum foil and dipped in wax for moisture content preservation immediately after coring.

4.2 SPECIMEN PREPARATION.

To the extent possible, test specimens were prepared from the supplied cores without altering the as-received water content. Immediately prior to conducting a test, a segment of the waxed core

of the appropriate length was cut using a diamond saw with no coolant, and without removing the wax covering. To prepare for a test with confining pressure, it is necessary to place a fluid-tight membrane, or jacket, around the specimen and seal it to endcaps of the same diameter as the specimen on each end. The 50-mm diameter core from NTS was a non-standard size, smaller than NX and larger than NQ-wireline. Thus, endcaps of the correct diameter were not available in the ARA laboratory. Since there was not time to fabricate new test fixtures, the rock that was tested with confining pressure was recored to NQ-wireline size (48 mm). As with the sawing, the recoring was performed without coolant. The unconfined compression tests were performed on specimens the full diameter of the core as received. In all cases, the ends were ground flat, parallel to each other, and perpendicular to the core axis as described in Section 2.3.

Once the necessary machining on each specimen was completed, it was jacketed and test as soon as possible to avoid changes in the water content. Except as described above, the specimen preparation procedures followed those described in Section 2.4.

4.3 INSTRUMENTATION.

The instrumentation used in the tuff tests was essentially the same as that used for testing the carbonates from Fort Knox, as described in Section 2.6. In addition to the stress and deformation measurements described in Section 2.6, a specially designed pore pressure transducer was used to measure the pore fluid pressure in the rock as it was being loaded. As shown in Figure 2-5, the pore pressure transducer was located in the base cap approximately 5 mm from the base of the specimen. This location serves to limit the dead volume of water in the pore pressure measurement system to a small fraction (less than 1%) of the pore volume of the specimen, thereby limiting the influence of the measurements system on the test results. Such a pore pressure measurement system only yields useful results when the permeability of the specimen is such that the any pore pressure gradients that develop in the specimen can quickly (on the time scale of the test) equilibrate so that the pressure measured at the base of the specimen is the same as the pore pressure everywhere else in the specimen. All indications suggest that this condition was satisfied in these tests, and the resulting pore pressure data can be considered representative of the pore pressure in the test specimens.

4.4 PHYSICAL PROPERTIES.

A summary of the physical properties of all of the test specimens is presented in Table 4-1. That table also indicates the precise origin, i.e. core number and depth, and the type of test that was performed on each specimen. The following paragraphs describe how those properties were measured.

4.4.1 Grain Density.

The grain density of a typical sample of the tuff was determined as described in Section 2.2.1.

4.4.2 Bulk Densities and Water Content.

The bulk density as tested was determined by weighing and measuring each prepared test specimen immediately before jacketing and testing. Since the objective of the process was to perform the tests with minimal alteration of the as-received water content, it was not possible to determine the oven dry bulk densities of the test specimens prior to testing. However, the knowledge of the dry bulk density is essential to understanding the mechanical behavior of a partially saturated material. The compromise was to measure the water content of each specimen after testing. Following each test, as much as possible of the specimen was put in a pan, weighted, and oven dried. Because of concerns that oven drying might drive off some water of crystallization, altering the mineral structure of the rock, the tuff was dried at 60 C, instead of the usual 100 C that most other types of rocks are subjected to for drying. Due to this lower temperature, the rocks took several days to reach an equilibrium mass. The dry bulk densities reported in Table 4-1 are based on ten days in the 60 C oven. In computing the dry bulk density from the post-test water content measurements, it was assumed that the water content of the test specimen did not change in the course of the triaxial testing, but that some of the specimen might have been lost between mechanical testing and drying. Thus, the dry bulk density of the specimen before testing was computed from the pre-test volume, and the pre-test mass multiplied by the ratio of the dry mass to the wet mass after testing, i.e.:

$$\rho_d = \frac{m_{1w}}{v} \frac{m_{2d}}{m_{2w}} \quad (4.1)$$

where: ρ_d = dry bulk density
 m_{1w} = wet pre-test mass
 m_{2w} = wet post-test mass
 m_{2d} = mass after post-test drying

The water content, w , defined as the mass of water divided by the mass of dry rock, was computed as:

$$w = \frac{m_{2w} - m_{2d}}{m_{2d}} \quad (4.2)$$

Knowing the dry bulk density and the grain density, the porosity was determined. Porosity, n , is the volume fraction of voids relative to the total (bulk) rock volume, computed by:

$$n = 1 - \frac{\rho_d}{\rho_g} \quad (4.3)$$

where: ρ_g = grain density

The degree of saturation, s , is defined as the fraction of the void space that is filled with water. Based on the laboratory measurements, it was computed for each test specimen using the expression:

$$s = \frac{w\rho_g(1-n)}{n\rho_w} \quad (4.4)$$

where: ρ_w = water density

Finally, the air content, ρ , is the volume fraction of air in the rock. It was computed by:

$$A = n(1 - s) \quad (4.5)$$

4.5 MECHANICAL PROPERTY TESTS.

This subsection presents the mechanical property tests, including procedures and results. The uniaxial strain and hydrostatic compression tests are presented together because they both

address the compressibility of the rock, the air content, and the changes in compressibility as the air voids are crushed out and it begins to behave as a fully saturated material. Following that is a discussion of the strength of the rock based on unconfined compression, triaxial compression, and splitting tensile strength tests.

4.5.1 Compressibility Tests.

When this test series was planned, it was believed that the tuff was highly impermeable. This was based on years of experience with the zeolytized tuffs at NTS. If this were the case, it would be difficult to obtain reliable air content measurements by the simple mass/volume measurements described in Section 4.4.1, and it would not be practical to run a drained test, in which no pore pressure is allowed to develop in the specimen. Since air content is very important to the prediction of ground shock stress attenuation, the plan was to determine it from uniaxial strain tests. If a tuff specimen is porous, having its pore space partially saturated with water and the remainder of its pore space filled with gas (air), then its initial stiffness (apparent constrained modulus) under uniaxial strain loading should be essentially that of an unsaturated specimen. The air has very low compressibility in comparison with the rock skeleton, and thus has negligible effect. However, when the volumetric compaction, as measured by the axial strain in a uniaxial strain test, becomes equal to the volume fraction of air in the specimen, the gas will be completely compressed and forced into solution. Any further loading of the specimen must compress not only the rock skeleton, but also the pore fluid. Since the compressibility of the pore fluid is significant in comparison with the rock skeleton, the specimen will exhibit an increase in apparent stiffness when this point is reached. Thus, a distinct increase in apparent loading modulus at a strain level significantly below porosity of the specimen indicates a transition from unsaturated to saturated response, and the axial (volumetric) strain at which it occurs is a measure of the air content of the specimen.

As it turned out, the permeability of the tuff was much higher than expected, and it was possible to obtain good measurements of the air contents of the specimens based only on mass and volume measurements. However, comparison with those results, as reported in Table 4-1, with the mechanical test measurements is still of interest. Two uniaxial strain tests were performed.

In both cases, specimens were prepared with as little alteration to the as-received water content as possible and tested without allowing drainage of the pore water.

Figure 4-1 presents the results of one uniaxial strain test. The independent variable for all three curves is the axial strain, which is also volumetric strain because the other components of strain are zero. The solid line is the measured total axial stress, and the measured pore pressure is indicated by the dot-dash line. The effective stress, which is computed by subtracting the pore pressure from the total axial stress is shown with a dotted line. At the beginning of the test, the unsaturated tuff responds to the uniaxial strain loading with an initial constrained modulus of 6.37 GPa, as shown in Figure 4-1. At an axial stress of about 40 MPa, the cementation in the rock skeleton begins to crush up, resulting in a decrease in apparent constrained modulus to about 1.2 GPa. When the axial strain reached 6%, the slope of the total stress curve increased significantly, with an even greater increase occurring at 6.5% axial strain. At about the same time (5.5% axial strain) the pore pressure measurement began to move away from zero, and consequently the effective stress curve began to diverge from the total stress. The effective stress curve, representing the response of the rock skeleton continued along approximately the line that was established with the crush-up of the cementation, at a slightly lower, 0.91-GPa slope. From the point where pore pressure first began to register to the end of the test, the axial load increased by 370 MPa. During that same period, the pore pressure increased by 340 MPa and the effective stress increased by only 30 MPa. Thus, over 90% of the load increment was carried by the pore water, not the rock skeleton.

Clearly, this mechanical response tests suggests that there was somewhere between 5.5 and 6.5% air in the specimen at the beginning of the test. This compares very well with the value of 6.2% that was derived from the mass and volume measurements and presented in Table 4-1.

In Figure 4-1, the unloading portions of the curves are truncated at approximately 8.6% axial strain. The test continued beyond that point, but the uniaxial strain condition was not maintained. Because of the test specimen underwent significant permanent plastic axial deformation during loading, it came to a point during unloading where it would have been necessary to stretch it with an axial stress lower (i.e. less compressive) than the confining pressure, a condition called triaxial extension. Since this test was not configured to impose

triaxial extension, the specimen simply unloaded hydrostatically from that point on. The hydrostatic unloading was accompanied by expansion of the specimen in all three directions. To avoid confusion, the hydrostatic unload portion of this test is not presented in this figure.

Figure 4-2 presents the same test as Figure 4-1 (Test M24A5) in term of mean stress and volumetric strain. The essential features of the test are similar in this presentation. Initially there was no pore pressure and the skeleton behaved elastically. At a mean stress of about 15 MPa, the skeleton began to crush up, and at about 6% volumetric strain the pore air was compressed into solution and the pore fluid began to carry the majority of the incremental load. Again, the portion of the test where the uniaxial strain condition was not maintained is not shown.

Figures 4-3 and 4-4 are the same presentations of the data from another uniaxial strain test. In this test (M28A5), the first appearance of pore pressure and the change in slope were much closer together at 2.8% and 2.95%, respectively. The value of air content computed from mass and volume relationships (Table 4-1) agrees well at 3.0%.

Since the rock available for testing was very limited, a cyclic hydrostatic compression test was not performed. Instead, the hydrostatic portion of a 400-MPa triaxial compression test was recorded for purposes of examining the hydrostatic compression response of the material. As in the case of the uniaxial strain tests, the hydrostatic loading was applied without allowing drainage of the pore water. Figure 4-5 presents the results of that test. The hydrostatic compression tests exhibits similar characteristics to the uniaxial strain tests. After initial elastic loading and cementation crush-up, the development of pore pressure occurred at the same time as an abrupt increase in slope of the total stress curve. At the first appearance of pore pressure at 4.5% volumetric strain, there is an initial drop in effective stress. Since both the total stress and pore pressure are increasing, it does not seem reasonable that the effective stress should actually drop. Based on the shapes of the curves, it appears that there may actually have been a small amount of pore pressure at about 3.8% volumetric strain, but that the flow of pore fluid to the pore pressure transducer was somehow blocked until about 5 MPa of pressure developed. It is possible to draw a very smooth transition from the total (and effective) stress curve before the onset of pore pressure to the flat portion of the effective stress curve that developed after the initial blip.

In summary, both the uniaxial strain test and the hydrostatic compression test suggest that the tuff that was tested is sufficiently permeable to perform either undrained tests with pore pressure measurements or drained tests to support development of effective stress models. The measured responses of total stress and pore pressure and the computed effective stresses are completely consistent with an effective stress model of the rock, and also completely consistent with the air content values derived from mass and volume measurements. The apparent high permeability of this material suggests a re-examination of the procedures used to obtain and prepare the test specimens. Due to the significant permeability of this material, the water/air contents of a specimen can change very quickly, either due to taking on water from the coring process or drying upon exposure to the atmosphere. It is recommended that in further studies of this material, it be cored without a coolant and immediately weighed in the field. This is the best opportunity to document the condition of the material as it comes from the ground. Later laboratory studies can provide the additional information necessary to characterize the water/air contents.

4.5.2 Strength Tests.

Five tests were performed to evaluate the strength of the tuff under a range of stress conditions. Two unconfined compression tests were conducted along with one each of undrained and drained triaxial compression tests, and one "Brazilian" splitting tensile test.

Two specimens of significantly different porosity were tested in unconfined compression. The resulting stress-strain curves from both tests are presented in Figure 4-6, and labeled with their respective porosities. The specimen with 0.34 porosity exhibited a strength of 19.5 MPa, and the specimen with porosity of 0.24 had unconfined strength of 23.3 MPa.

One undrained triaxial compression test was performed with 400 MPa confining pressure. The initial hydrostatic compression portion of that test is presented in Figure 4-5. That figure shows that there was approximately 325 MPa of pore fluid pressure and only 75 MPa of effective stress when the shearing phase of the test began. Figure 4-7 presents the resulting axial and radial strains plotted against stress difference. The maximum stress difference developed in this test was 53 MPa.

Figure 4-8 presents axial and radial stress-strain curves from a drained triaxial compression test with 200 MPa confining pressure. The intent of this test was that no pore pressure be allowed to develop. Since the drain was at essentially the same location as the pore pressure transducer, no pore pressure was measured. However, that does not prove for certain that pore pressure did not develop somewhere in the specimen.

With the limited available data, it is not possible to construct a strength envelope for the material with certainty. Figure 4-9 presents the available strength data in terms of effective stress. The two unconfined compression tests are shown as solid dots near the left edge of the plot. In the 400-MPa undrained triaxial compression test, both the stress difference and pore pressure were changing during the shear loading and the highest stress difference recorded in the test is not necessarily indicative of the strength envelope. Thus, the stress path for the entire test is shown in Figure 4-9. The arrows indicate the direction of progress of the test. In an undrained triaxial compression test, it is typical for the stress path to reach the strength envelope and then turn and follow it. Such behavior is illustrated in Figure 4-9, as the stress path for the 400 MPa-test peaks then turns and follows the strength envelope down and left. The projection of this line would fall above the two unconfined compression test data points. Again, this is probably to be expected. The initial compaction of the material in the hydrostatic compression phase of the test crushed out some of the void space, creating an altered material that was probably somewhat stronger than the original. The 200-MPa drained triaxial compression tests plots as a point on the far right of the page.

In addition to the four strength tests, Figure 4-9 shows the stress paths recorded in the two uniaxial strain tests. The stress path of a uniaxial strain test will typically approach the strength envelope from below. However, since dilation is prevented in the uniaxial strain test, its stress path typically does not reach the strength envelope. The dashed line in Figure 4-9 is an estimate of how the strength envelope of the material might look based on the limited available data. The approximate strength envelope is based on a reasonably consistent set of data below about 80 MPa confining pressure. However, the flattening of the envelope at higher pressures is based on a single test data point, and additional testing should be performed before the strength envelope can be established in that region with high confidence.

The tensile strength of the specimen was determined by performing a splitting tensile test. In this test, a short cylinder of the specimen material is loaded in compression along the diametrically opposite sides of the cylinder. This loading creates a stress field that is approximately tensile along the loaded diameter. The load, P_t , required to break the specimen is recorded, and the tensile strength is computed by:

$$\sigma_t = \frac{2P_t}{\pi l_d} \quad (4.6)$$

where: l = length of cylindrical specimen
 d = specimen diameter

The resulting value of tensile strength for the NTS tuff is 3.2 MPa.

4.5.3 Table Summary.

Table 4-2 summarizes the recommended physical and mechanical properties of the tuff that based on a very limited test data set. Summary data plots for NTS rocks are presented in Appendix E.

Table 4-1. Summary of mechanical property tests performed on NTS tuff.

Test ID	Specimen ID	Depth (m)	Specimen Length (mm)	Specimen Diameter (mm)	As-Received Density (Mg/m ³)	Dry Bulk Density (Mg/m ³)	Porosity	Water Content	Degree of Saturation	Air Content	P- wavespeed	Test Description
M24A5	GI-2B	0.30	96.7	47.4	1.826	1.541	0.35	0.19	0.82	0.062	2806.2936	Uniaxial Strain
M28A5	GI-2E	0.98	96.8	47.4	1.853	1.531	0.35	0.21	0.92	0.030	2914.8024	Uniaxial Strain
M29AB5	GI-2D	0.68	102.1	47.4	1.831	1.505	0.36	0.22	0.90	0.038		400-MPa Hydro Triax
M30A5	GI-1B	0.62	95.4	50.0	1.990	1.797	0.24	0.11	0.81	0.046		Unconfined Compression
A3A5	GI-1D	0.84	96.1	50.2	1.837	1.561	0.34	0.18	0.81	0.063		Unconfined Compression
A3E5	GI-1C	0.75	96.0	47.4	1.831	1.614	0.32	0.13	0.89	0.100		200-MPa Triax
A3B5	GI-1E	0.91	35.1	50.0	1.914	1.701	0.28	0.13	0.76	0.067		Splitting Tensile Test

Table 4-2. Summary of NTS tuff properties.

PHYSICAL		MECHANICAL	
Grain Density	2.36 Mg/m ³	Elastic Modulus	5.8 GPa
Dry Bulk Density	1.55 Mg/m ³	Poisson's Ratio	0.18
Porosity	0.34	Bulk Modulus	3.0 GPa
Water Content	0.196	Constrained Modulus	6.3 GPa
Degree of Saturation	0.90	Unconfined Compressive Strength	20 MPa
Air Content	0.035	Tensile Strength	3 MPa
Wet Bulk Density	1.85 Mg/m ³	Ultrasonic Compression Wavespeed	2800 m/s

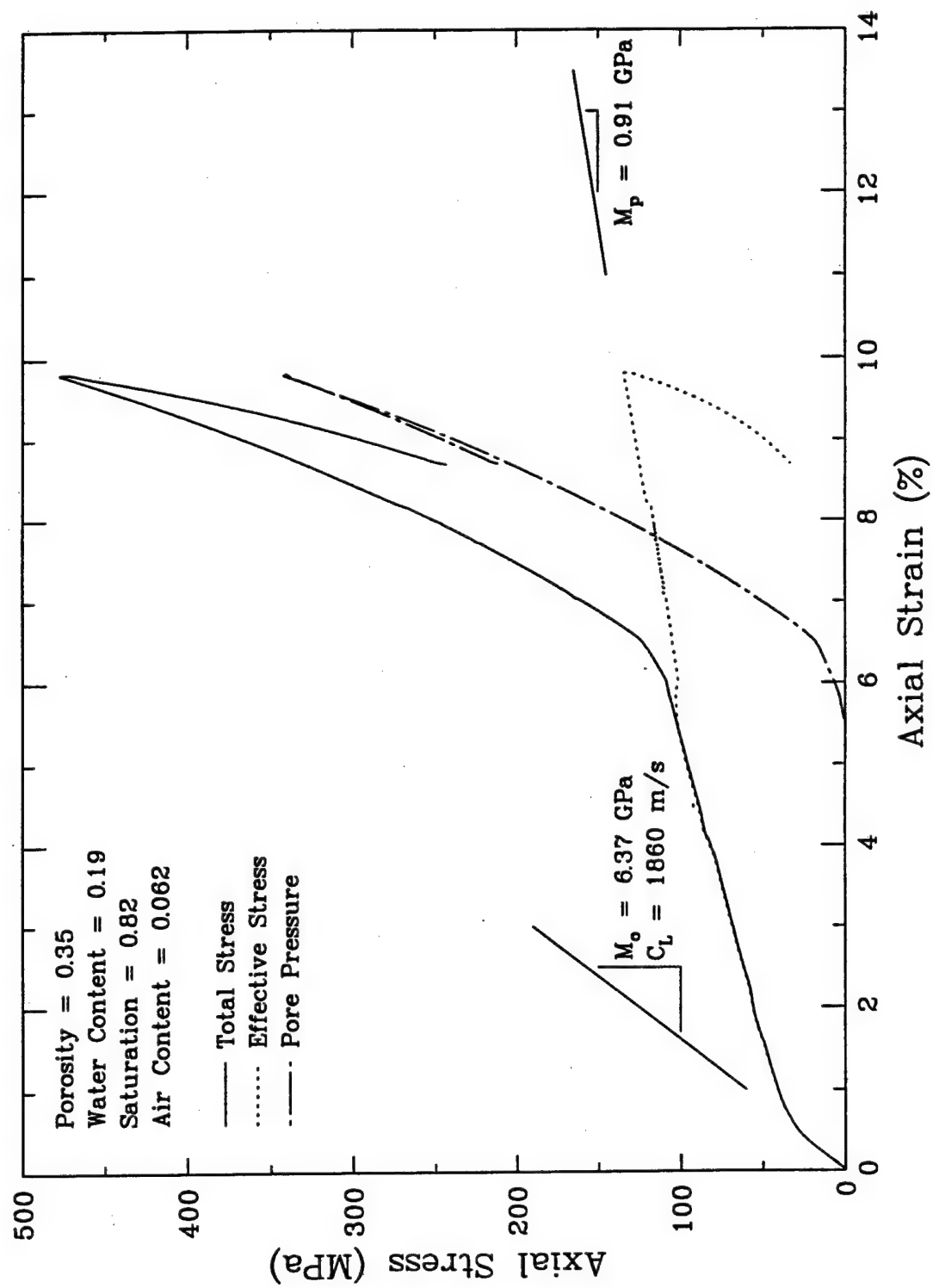


Figure 4-1. Total axial stress, effective axial stress, and pore pressure plotted against axial strain for an undrained uniaxial strain test (M24A5) on a specimen of tuff from Nevada Test Site.

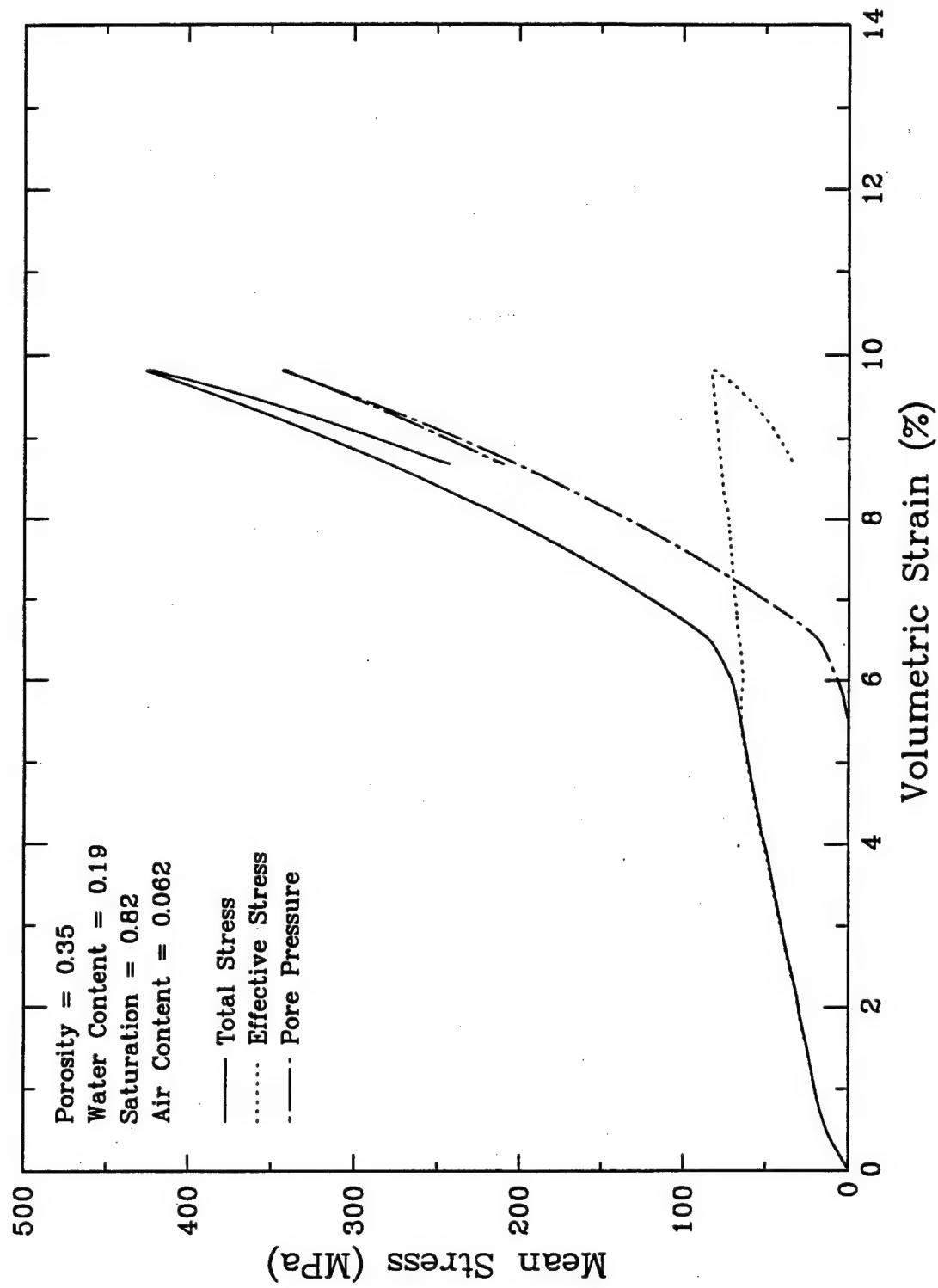


Figure 4-2. Total mean stress, mean effective stress, and pore pressure plotted against volumetric strain for an undrained uniaxial strain test (M24A5) on a specimen of tuff from Nevada Test Site.

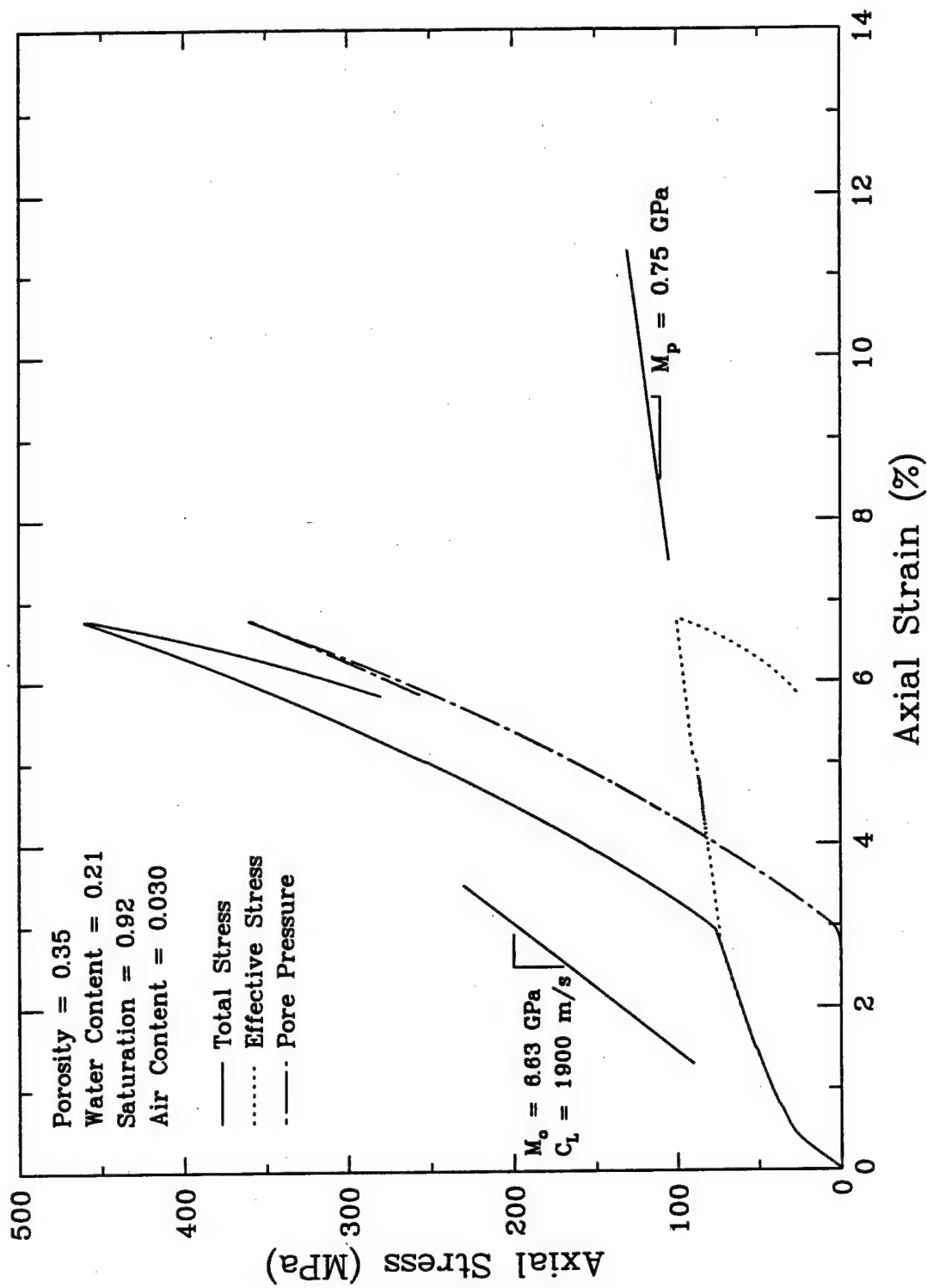


Figure 4-3. Total axial stress, effective axial stress, and pore pressure plotted against axial strain for an undrained uniaxial strain test (M28A5) on a specimen of tuff from Nevada Test Site.

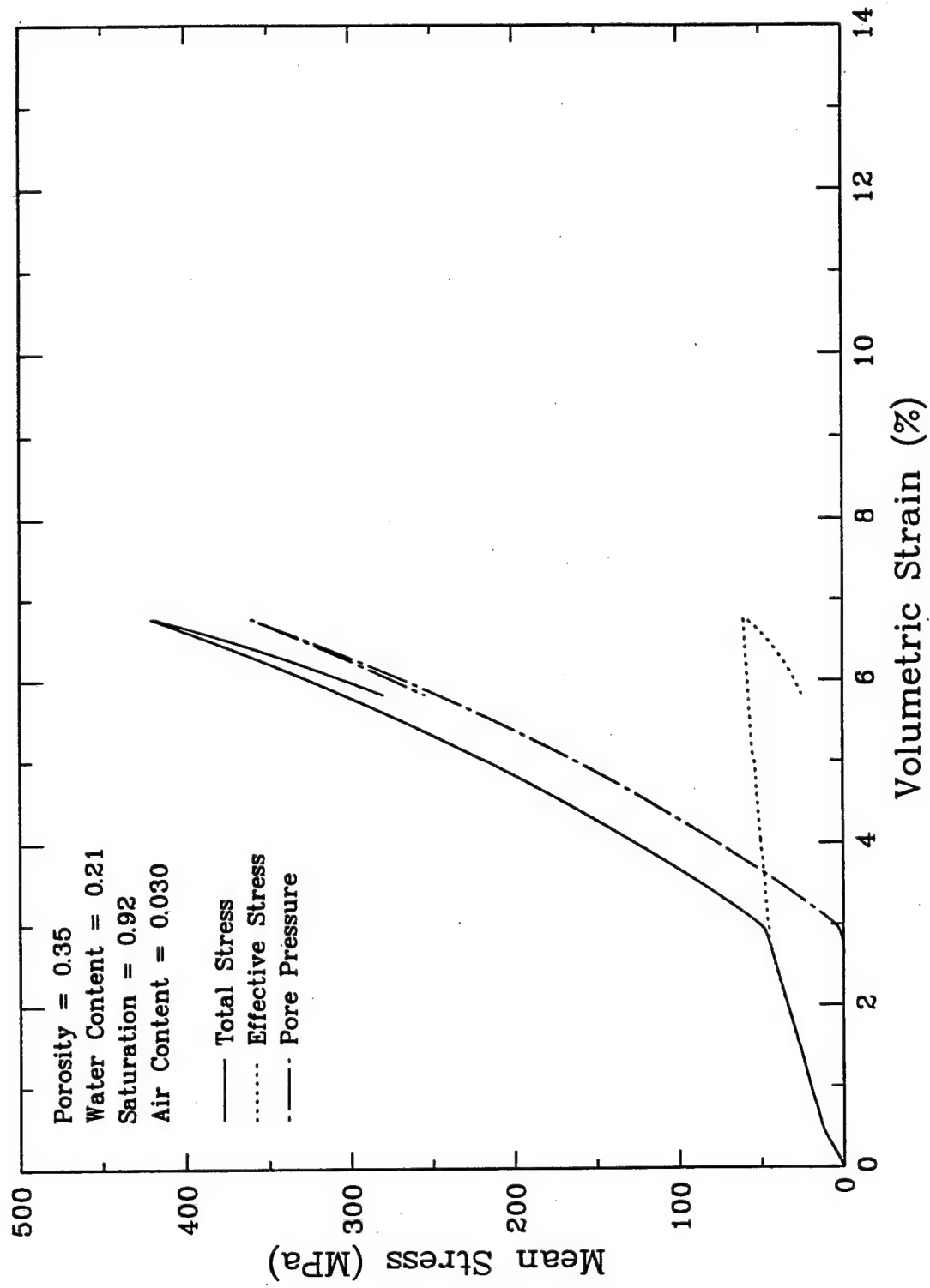


Figure 4-4. Total mean stress, mean effective stress, and pore pressure plotted against volumetric strain for an undrained uniaxial strain test (M28A5) on a specimen of tuff from Nevada Test Site.

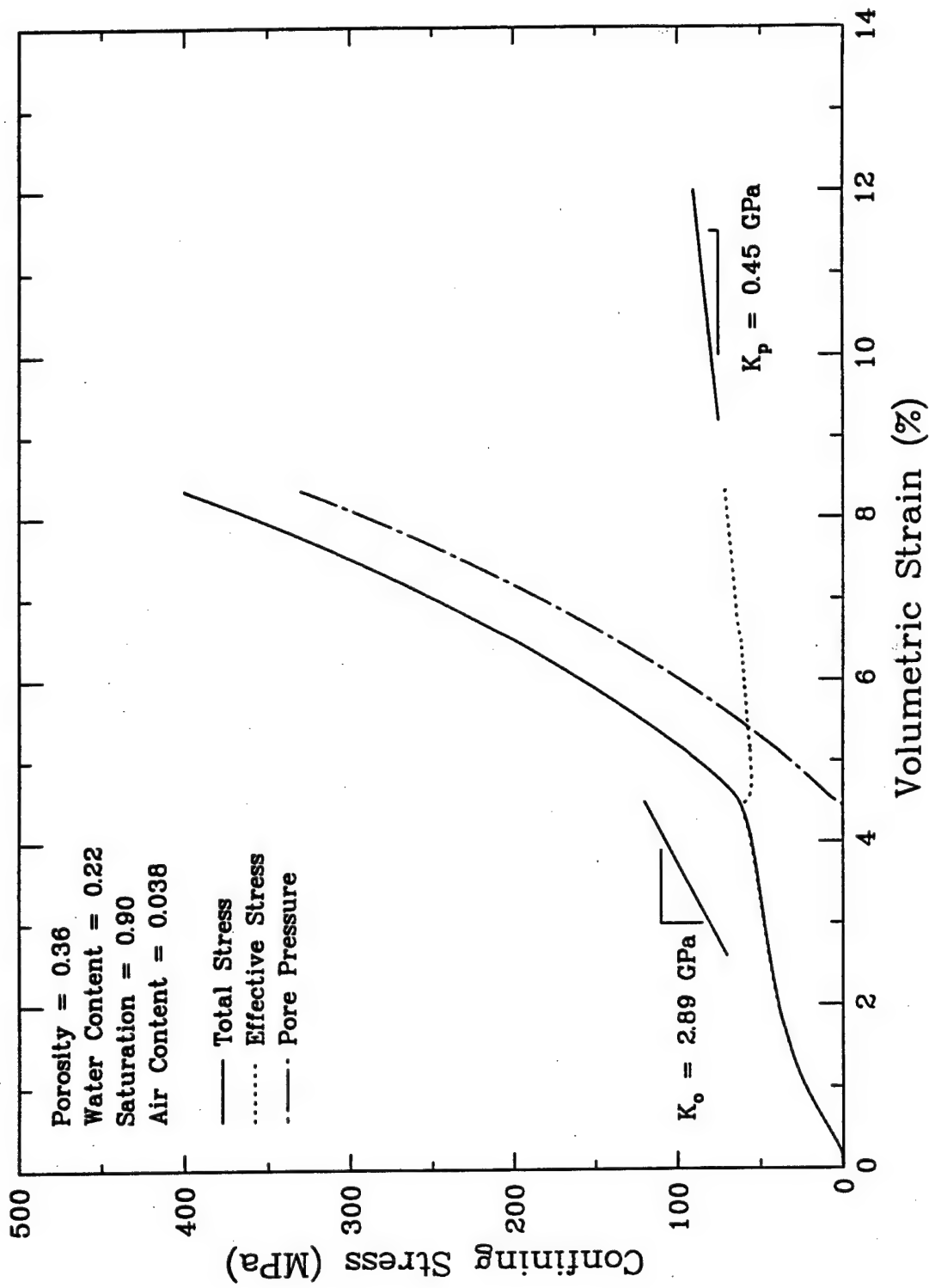


Figure 4-5. Total mean stress, mean effective stress, and pore pressure plotted against volumetric strain for an undrained hydrostatic compression test (M29A5) on a specimen of tuff from Nevada Test Site.

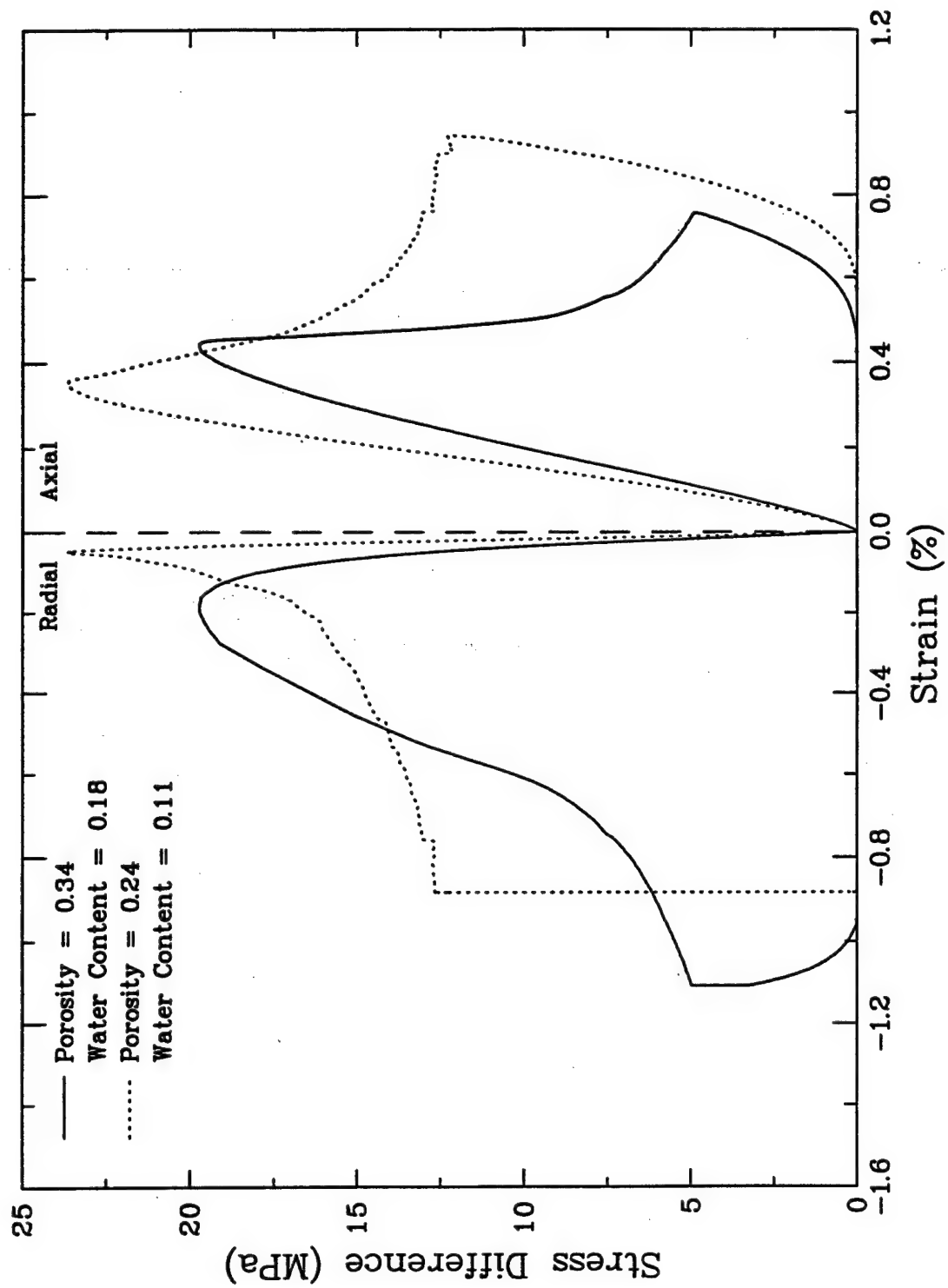


Figure 4-6. Axial and radial strains plotted against stress difference for specimens of tuff from Nevada Test Site tested in unconfined compression.

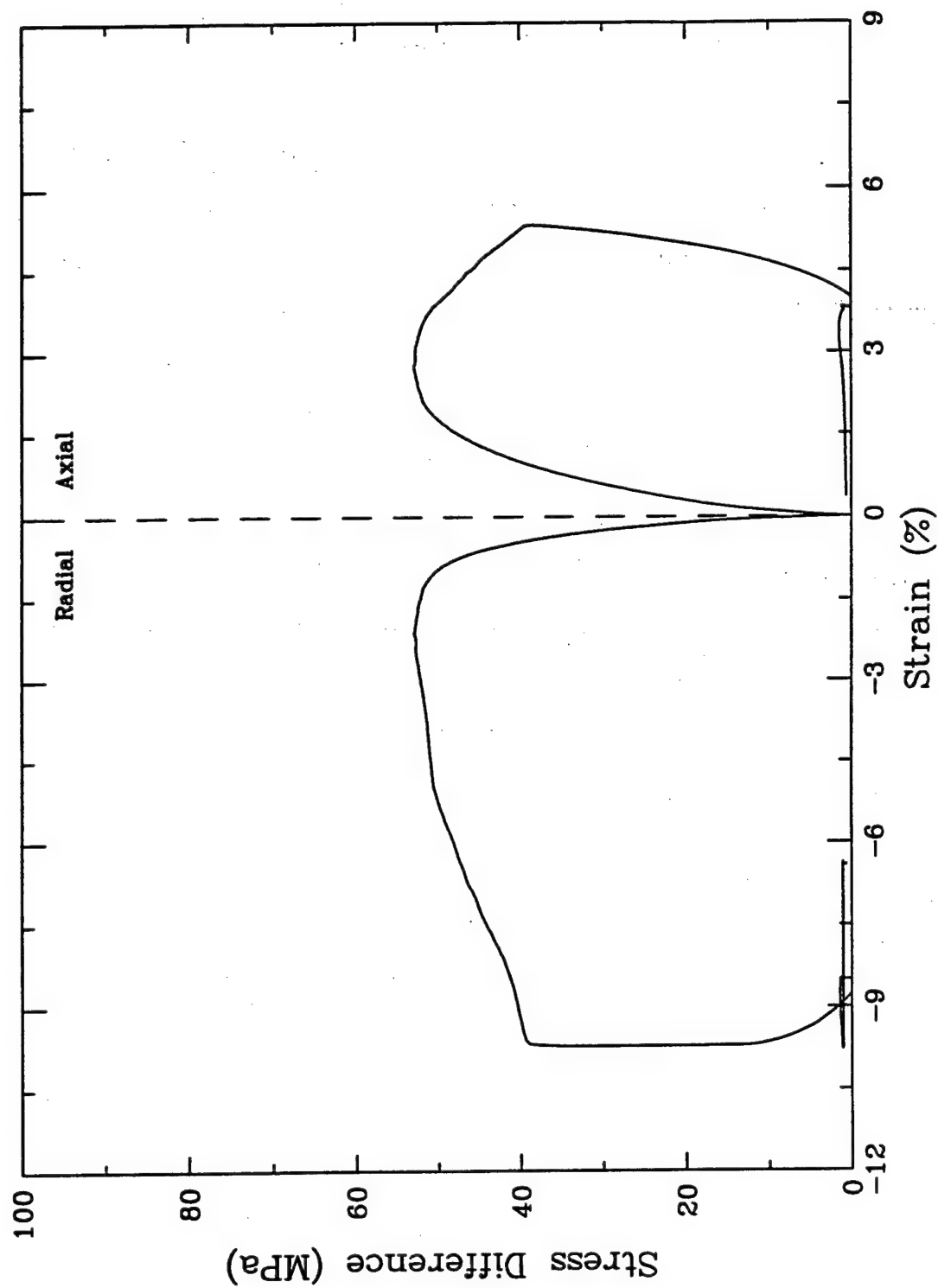


Figure 4-7. Axial and radial strains plotted against stress difference for a specimen of tuff from Nevada Test Site, tested in undrained triaxial compression with 400 MPa confining pressure.

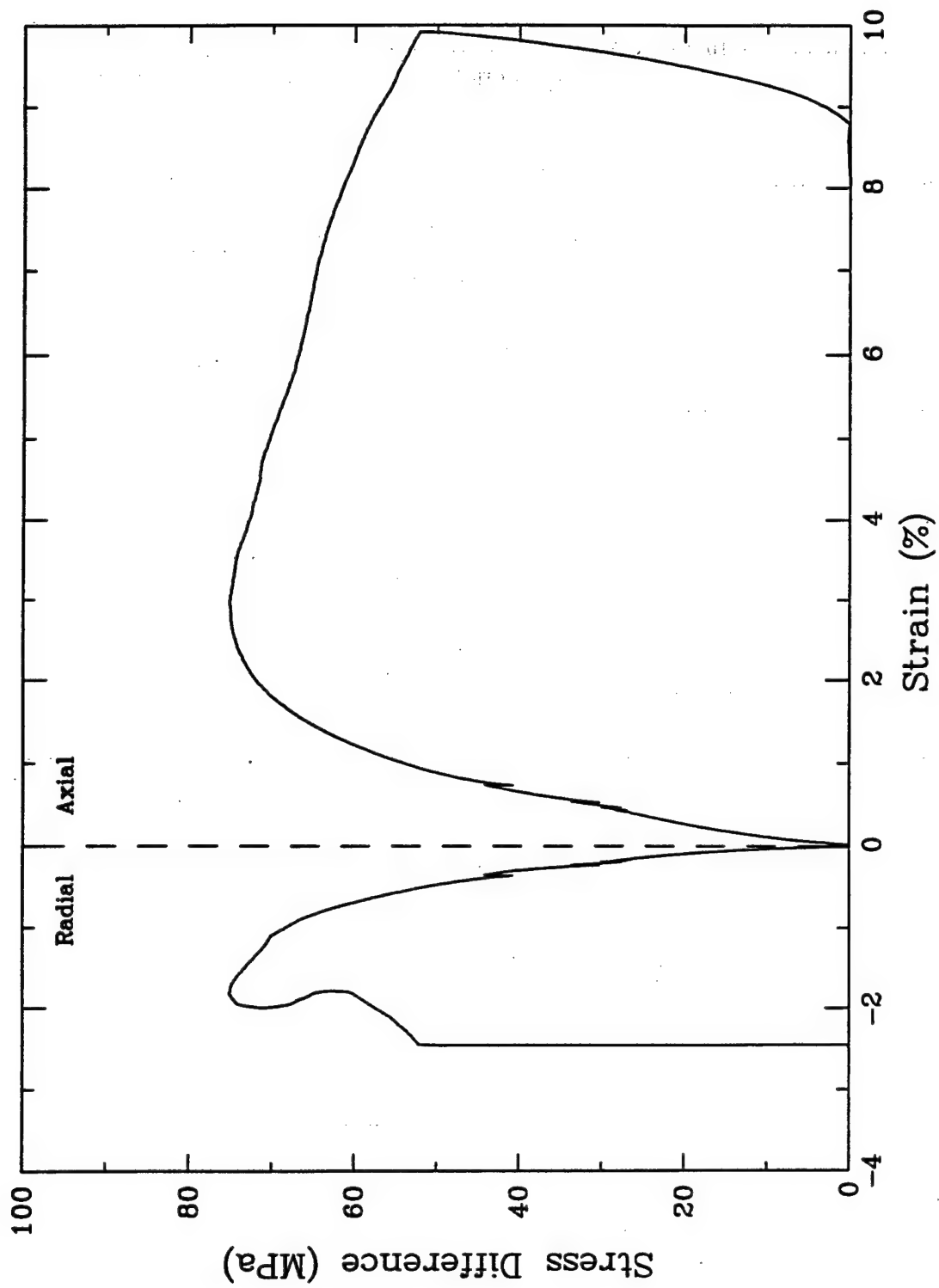


Figure 4-8. Axial and radial strains plotted against stress difference for a specimen of tuff from Nevada Test Site, tested in drained triaxial compression with 200 MPa confining pressure.

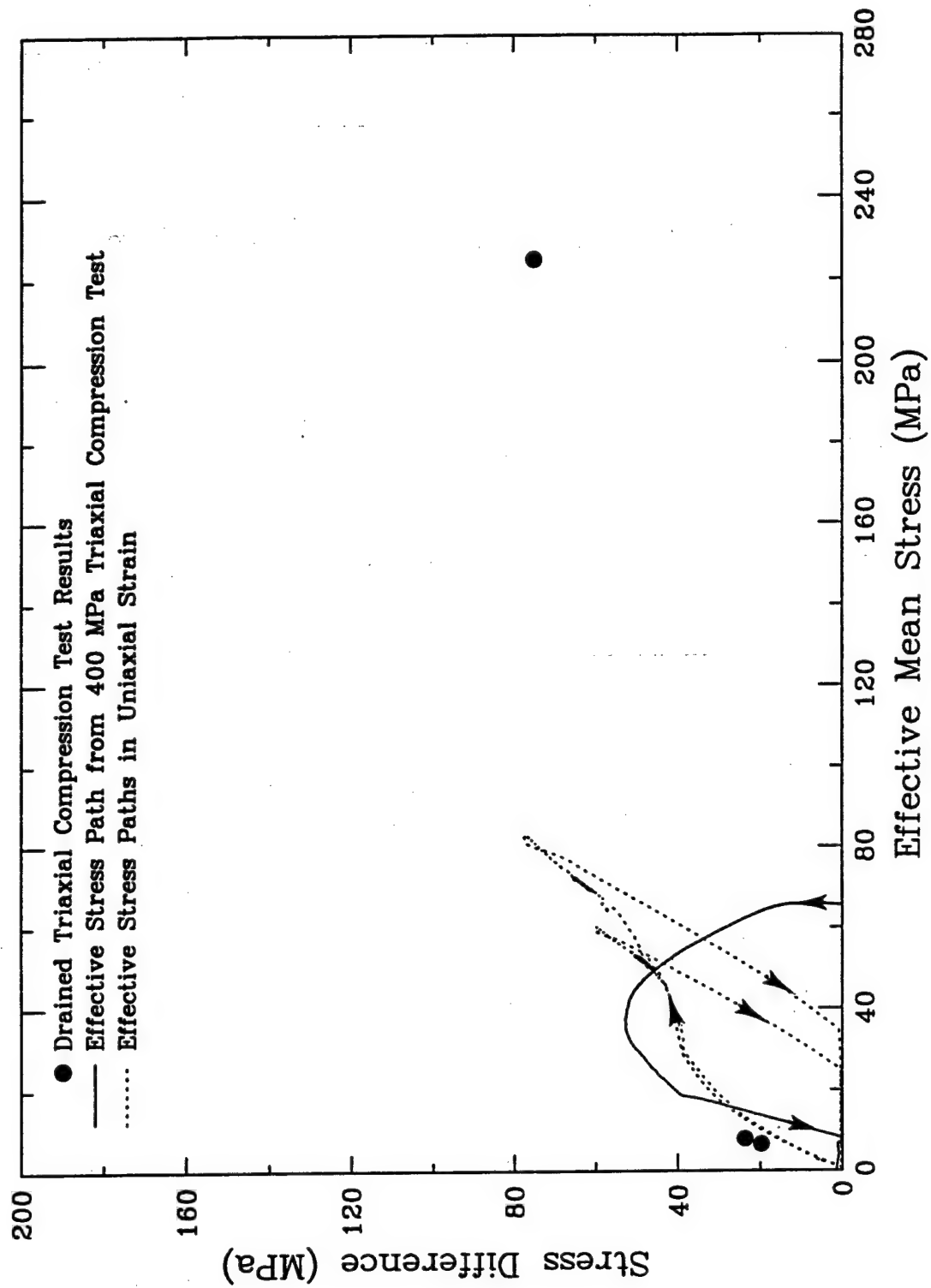


Figure 4-9. Summary of strength data for tuff from Nevada Test Site.

SECTION 5

ISSUES RELATED TO THE HYDROLOGIC PUMPING OF UNDERGROUND OPENINGS

5.1 INTRODUCTION.

A detailed hydrological study of a moderate to high permeability aquifer was performed for the proposed test site in the Louisville formation at Ft. Knox. The study reviewed and integrated all hydrological data from the site and included both analytical and two-dimensional computer modeling calculations. The effort was conducted by the University of Texas of the Permian Basin's Center for Energy and Economic Diversification in Midland, Texas, sponsored by the U.S. Army Corps of Engineers Waterways Experiment Station (WES) Structural Laboratory and documented in a report to WES (Melzer, et al., 1995).

The above study was conducted to better understand and scope the effects of hydrological pumping on the construction of the access and subsequent test adits at the site. In this section, the results of this previous hydrologic work are examined in light of their pertinence to hardness and wave propagation issues in underground openings sited in saturated rock.

One of the primary insights of the hydrological study has been to document the magnitude of expected aquifer drainage (desaturation) in the near vicinity of an underground opening and to examine both natural and man-induced procedures which could mitigate or amplify the desaturated zone around the openings.

A transient or permanent zone of desaturation in the near vicinity of an underground opening has both construction and hardness implications. As mentioned, Melzer, et al. (1995) attempts to closely examine the construction issues as they affect both the feasibility and cost of the proposed test series. This section will deal with the qualitative hardness issues. This study falls short of applying the conceptual findings to actual hardness calculations. Additional work is recommended since saturation effects on the strength and compressibility of rocks and underground openings are both important and widely recognized.

Section 5.2 provides the necessary background for the UTP site while reviewing some of the important analytical results of Melzer et al. (1995). Section 5.3 provides additional hydrological insight to the drainage geometry using results from two separate two-dimensional finite element models. Section 5.4 then offers some extrapolations to the results as they pertain to hardness issues and suggests additional work that should be accomplished to quantify the effects.

5.2 HYDROLOGICAL SUMMARY AND ANALYTICAL MODELING.

5.2.1 Test Site Materials.

The Louisville formation aquifer at the Ft. Knox test site is overlain and confined by two competent shale formations, the New Providence and New Albany of Mississippian and Devonian ages, respectively. The target materials consist of moderately strong limestones and dolomites of the Jeffersonville and Louisville formations (Figure 5-1). Beneath the Louisville lie a mixture of competent shales, siltstones and dolomites/limestones of Silurian age.

The Jeffersonville formation is a very low permeability (Devonian) limestone capping the Silurian Louisville formation and it varies in thickness from four to ten feet in the test area. For the purposes of simplification, the Jeffersonville is often combined with the Louisville formation and referred to as the Louisville formation interval.

The Louisville formation is the predominant aquifer at the site and is a water saturated, very fine grained dolomitic limestone and dolomite averaging 110 feet in thickness in the test area. The permeabilities vary from less than a millidarcy in the Jeffersonville and lower zones within the Louisville to a high of approximately 1 darcy. With the impermeable shales located both above and below, the Louisville formation is a classic example of a confined aquifer.

In the vicinity of the test site all the formations have been shown to dip at less than 2 degrees. In addition, no significant faulting is believed to be present in the test bed area (Melzer et al., 1995).

For the purposes of the analytical hydrological predictions and groundwater flow numerical simulations, an estimation of the effective thickness of the aquifer was performed. Correlation of

the borehole logs and electric logs from the pump test observation wells at the site provided the information needed to zone (layer) the Louisville aquifer. The log derived porosities were calculated for each half-foot of the Louisville formation, and then a series of porosity cutoffs were used in calculating an aquifer thickness for each porosity cutoff. A 7.5 percent porosity was felt to adequately represent that portion of the Louisville formation that yielded water upon borehole penetration. Using the 7.5% porosity cutoff, the aquifer thickness of the Louisville formation calculates to an average of 74 feet in the immediate UTP test area.

Previous studies (Melzer, 1993) performed on the Louisville had provided for vertical zonation (layering) of the Louisville. Although a layered aquifer model may be more appropriate for the Louisville formation, there is currently not enough hydrologic data available to warrant the use or development such a layered model in the simulations. For that reason and for the entire study reported herein, no provision for vertical zoning within the Louisville has been included except for the reduction in total thickness from 110 to an effective thickness of 74 feet.

5.2.2 Analytical Ground Water Modeling.

A pump test was performed at the UTP site and data from the pump test and nearby observation wells were first used to estimate water influx into a twelve foot diameter adit penetrating the Louisville. For this purpose, a horizontal well model was used. The access adit was assumed to have a maximum length of 500 feet in the aquifer. A reasonable size of the aquifer was concluded to be 39,000 feet in radius with a constant thickness of 74 feet (Melzer et al., 1995). The horizontal well representing the adit was positioned in the middle of the aquifer with 31 feet of aquifer above and below the well. Calculations were made assuming no damaged zone (skin) around the face of the adit. In the real case, the skin may either be positive and restricting flow (analogous to formation damage often created during drilling of wells) or negative and increasing flow (analogous to construction-induced fracturing at the adit walls). Two cases were calculated, one for a permeability of 629 md as determined from the pressure buildup data from the pumping well and the other for a permeability of 468 md, the average value determined from analysis of the observation wells. Figure 5-2 shows the estimated water influx in gallons per minute for adit lengths from 0 to 500 feet. Notice the rapid increase in the rate for the first 100 feet and then a much slower increase as the adit lengthens. The maximum influx into the adit for the 629 md

case is estimated to be 270 gpm and 200 gpm for the 468 md case. Although the horizontal well model does not accurately represent the actual adit, it does give a good estimate of the magnitude of the water influx to be expected from an opening of this size. It was also used as a simple check on the more sophisticated numerical model runs.

As determined in the pump test analysis, the volume of the aquifer would be a minimum of 9.4 billion gallons, with a possibility of as much as 317 billion gallons. Using a value for ultimate yield of 50 percent (half the water producible), it would require 30 years to deplete the minimum volume at 300 gpm. This simple analysis thereby indicates the large size of the aquifer and the practical impossibility of its depletion. However regardless of the flow regime, there will be a pressure gradient into the access adit and other adits used for the tests. Since the aquifer pressure will be zero psig inside the adit, it follows that it will not be fully saturated for some distance from the adit walls, and this distance will increase with time. An analytical calculation was performed to estimate the time varying desaturation zone.

A simple model was created using the point source analytical solution and superposition to simulate the access adit. Figure 5-3 is a schematic showing the model configuration. Five withdrawal points were selected along the adit length (at distances of 500, 400, 300, 200, and 100 feet from the observation point).

For this example, it was assumed that the adit was horizontal along the bottom of the Louisville formation. This condition would represent the maximum case and is not the configuration actually planned for the access adit; however, it is a simple method to illustrate the problem. It was further assumed that adit excavation would proceed at the rate of 10 feet per day. Instantaneous withdrawal volumes were obtained from the horizontal well model (Figure 5-2) using the 629 md curve.

Figure 5-4 shows the free-water level at a distance of 100 feet from the terminal end of the access adit with time. In this example, desaturation of the aquifer begins coincidentally with completion of the adit in about 50 days. Pumping must, of course, continue indefinitely as long as operations are occurring in the adit.

The above example demonstrates that water saturation in the aquifer will be something less than 100 percent for some substantial distance from the adit walls. Even allowing for full recharge of the aquifer at some distance from the testing area, the pressure gradient will be such that the region in the near-vicinity of the adits will not be fully saturated. It follows that a saturated condition cannot be maintained near the access adit or subsequent test-bed adits without either sealing the adit walls or reinjecting at least some of the produced water in the test bed vicinity.

In an attempt to model an aquifer that is fully recharged near the underground opening, injection wells were included in the analytical model. One case is shown wherein the potential for reinjection to maintain a saturated condition near the closest point of withdrawal. In this case, the withdrawal point is 100 feet from the observation point, and reinjection occurs a distance of 1000 feet from the observation point (1100 feet from the withdrawal point). Figures 5-5a and 5-5b show the water level vs. distance for this case after six months of withdrawals. In this case, the aquifer remains saturated for all distances greater than 15 feet from the withdrawal point. If saturated conditions are to be maintained at distances even closer to the adits, then the walls must be sealed in some manner coupled with full recharge (or reinjection).

5.3 TWO-DIMENSIONAL MODELING.

The 2-D modeling effort consisted of simulation runs using two separate, commercially available software packages.

The initial problems utilized a numerical groundwater model called ASM (Aquifer Simulation Model). Our applications of ASM for this study called for running one or more first approximation models to the hydrological problem of interest prior to going to the expense of running the more elaborate and complex computer code (MODFLOW). This procedure allowed for previewing of results, efficient problem scoping, and optimization of results presentation. More information regarding each of the computer codes is provided below.

5.3.1 ASM Groundwater Flow Modeling Software.

The numerical groundwater model ASM (Aquifer Simulation Model) was developed in 1991 by W. Kinzelbach and R. Rausch. This software was primarily designed for educational uses; however, it possesses many of the same features as the larger and more complex commercial software packages. The 2-D flow computation is accomplished using a node-centered finite difference approach. A numerical solution is determined using either the iterative alternating direction implicit or the conjugate-gradient methods. Models consisting of a finite difference mesh as large as 60x60 cells are allowed.

ASM can model a variety of situations including both heterogeneous and isotropic media; steady-state and transient flow, and confined, phreatic and leaky-confined aquifers. The user may define both temporally and spatially variable pumping and recharge rates. Infiltration and exfiltration is also allowed from surface waters. A solute transport algorithm is available using a random-walk technique.

ASM is written in QuickBASIC version 4.0 and both the source and executable image code are available from the International Ground Water Modeling Center at the Colorado School of Mines in Golden, Colorado. To use ASM, the user interacts with the software through a fully interactive and menu driven interface. A variety of data output is available through numerical listings and graphical displays, a feature which was critical to this study.

The ASM program was chosen initially for its simplicity and ease of use to evaluate the feasibility of using a 2-D areal model to simulate the access adit and to determine the fluid flow and pressure levels with time and distance from the adit. The model consisted of a 55 x 55 grid representing an aquifer 78,000 feet square. The central area of the model consisted of a 17 x 17 section of grid blocks that were 100 feet square. Cell size increased outwardly until the outermost cell was 8074 feet square. A uniform thickness of 74 feet was assigned to the model. Other pertinent parameters were as follows:

Porosity:	.12
Permeability:	468 md
Compressibility:	5.3×10^{-6}
Net Effective Pay Thickness:	74 ft
Initial water level above bottom of adit:	342 ft

In order to proceed with the model, several assumptions were required. First, it was assumed that adit excavation would proceed at 10 feet per day. Secondly, the adit would penetrate the Louisville on a 10-percent downward grade with an ultimate depth of penetration of 50 feet into the Louisville formation and, at this point, the excavation would cease. Thus, with 100-foot grid blocks, the adit could be represented by five cells. Appropriate elevations were assigned to a drain in each of these cells. After the 50 days to complete the adit, the model was run additionally for a total of five years.

Figure 5-6 shows production (withdrawals from the adit) for a period of two years including the excavation time. Production increased from an initial 140 gpm to 172 gpm at the end of the 50 days when the adit was completed. Because of the 10-day steps used in the model, the sixty-day rate of 159 gpm was used for adit completion and as a starting point for the reinjection phase described below.

With no additional excavation, production declined to less than 100 gpm at the end of two years. An observation well was placed in the model, 100 feet from the terminal end of the access adit. Figure 5-7 shows the water level at this observation point with time. Notice that the water level declined below the top of the aquifer in about 550 days. The water level will continue to decline and the volume of the unsaturated aquifer will continue to increase as withdrawals continue. Figure 5-8a shows the increase in distance of the unsaturated zone for time periods from 60 days to 5 years. Figure 5-8b shows the same data on an enlarged scale. In five years, the unsaturated zone will extend 650 feet from the terminal end of the access adit. The drop in head with time is also proportional to the size of the aquifer. For example, when an aquifer 16,000 feet square was modeled instead of 78,000 feet square, the time required to lower the water level to the top of the aquifer was only 41 days.

In the analytical model previously discussed, it was estimated that the water level would decline below the top of the aquifer in about 50 days. In the analytical model, the adit was horizontal along the bottom of the aquifer; whereas in the ASM model, it was more realistically represented as sloping on a 10-percent grade with a maximum penetration of 50 feet into the aquifer. An additional ASM model was run that more nearly duplicated the analytical model. In this case, the water level at the observation point declined below the top of the aquifer in 59 days, a time similar to the analytical model. It is concluded that the large differences that were observed were caused mostly by the geometry of the adit and the size of the aquifer rather than by the technique used in the analysis.

Figure 5-9 is a profile of water level with distance that is perpendicular to the adit at its center length. At the zero point on Figure 5-9, the adit floor is only 30 feet below the top of the aquifer. Figure 5-10 is similar to Figure 5-9 except it has been adjusted for the slope of the adit. It shows the same data as water level above the adit floor.

In the previous analytical solutions, it was demonstrated that reinjection of some or all of the water produced from the adit would have to be accomplished if saturated conditions were to be maintained near the adit walls. Again, there are an infinite number of injection schemes that would depend on aquifer parameters yet to be determined and the requirements for reliable testing. One reinjection case was run using the ASM model. Three injection wells were located approximately 1000 feet from and parallel to the adit. At the completion of the adit, the model was estimating withdrawals of 159 gpm. This amount was divided equally among the three injection wells and maintained at a constant rate for a total of two years. Figure 5-11 shows the production and injection for this period. With constant injection of 159 gpm, production increased rapidly to 240 gpm and then declined slowly to 220 gpm at the end of two years. Also shown on Figure 5-11 is the net production from the adit. With reinjection, the net declined rapidly from 159 gpm to 80 gpm and then slowly to 50 gpm at the end of two years. Although total production increased 50 percent with reinjection, net production also decreased by 50 percent.

More important than the effect on production from reinjection was the effect on the water level in the test bed area. Figure 5-12 shows the water level with and without reinjection for the same

observation point that was used in Figure 5-7. With reinjection beginning at 60 days, the water level increased rapidly from 98 feet to 128 feet and then slowly declined reflecting continuing excess withdrawals. Note that although the water level continued to decline, it was still substantially above the aquifer top.

This is only one of many possible reinjection schemes. With additional data from the actual adit excavation, pumping and piezometer measurements, the reinjection scheme can be optimized. As stated earlier the purpose of this model was to demonstrate the need for modeling actual operations and to evaluate the viability of multi-cell simulation for operations in the Underground Test Program.

5.3.2 Description of the MODFLOW Groundwater Modeling Software.

As mentioned in the previous section, the ASM groundwater modeling package was used to provide first approximations and previews to the groundwater problems included within the study. Once the ASM runs were complete and determinations had been made to conduct the more complex and time consuming hydrological simulations, another code was required. Thus, for the detailed numerical modeling of the pump test and for the excavation of the access adit with and without re-injection, a readily available and widely used groundwater flow simulation software package called MODFLOW was utilized. MODFLOW was developed by M.G. McDonald and A.W. Harbaugh working at the U.S. Geological Survey and made available for public dissemination in 1988. MODFLOW allows the simulation of two- or three-dimensional applications and uses a block-centered, finite-difference approach. Aquifers can be simulated as confined, unconfined, or a combination of both, along with flow associated with external stresses, such as wells, areal recharge, evapotranspiration, drains, and streams.

5.3.3 Description of MODFLOW Test Site Grid Idealizations.

A 40,000-ft-square grid was used to simulate the adit excavation. The grid for the adit excavation model consisted of 161 rows by 110 columns irregularly spaced with the smallest cell size being 10 by 10 feet. In both directions, the cell size increased from the center of the grid following the general rule of limiting changes to 50 percent of the previous cell size.

A conceptual model (referred to as Model 30) was used to simulate the excavation of the UTP access adit with MODFLOW. In this conceptual model, the access adit entered the top of the pay at a point 250 feet from the center of the model and excavation proceeded northward for 500 feet. Average aquifer data from the pump test as reported by Warriner (1991) was used as follows:

Porosity	0.12
Aquifer thickness*	74 ft
Transmissivity	98 ft ² /day
Storativity	1.52
Top of porosity, msl**	195 ft
Static fluid level, msl	455 ft

* For this model, the aquifer thickness was assumed to be the net pay as used in Warriner (1991).

** Mean sea level

During the first 50 days, the adit was excavated at the rate of 10 ft per day. For the next 10 days, the adit was allowed to continue draining the aquifer with no additional excavation. Since MODFLOW's drain package allows the specification of the drain elevation for each cell selected as a drain, it was possible to create a sloping drain with a 10 percent decline. The Louisville aquifer was modeled as a combination of confined and unconfined (water table) aquifer for the necessary transition between unconfined aquifer in the near vicinity of the adit and confined aquifer that occurs further out. This phenomenon is caused by the lowering of the water level to the floor of the adit as water is pumped to keep the adit free of standing water. The head distributions for the entire grid as well as for the immediate UTP test area are included in Melzer et al. (1995). Cross-sections of the head distributions at various time intervals are also included in that reference. Figures 5-13a and 5-13b illustrate the close-in and long-range water table position at day one after the excavation begins. Figures 5-14a and 5-14b illustrate the close-in and long-range water table at the end of Model 30 simulation (60 days) in which the excavation was completed in 50 days. The ordinate axis is shown in unit of head in feet above sea level. The position of the water table at the adit point is the base of the adit. The three curves shown reflect water profiles normal to the adit azimuthal centerline. As a reminder, Model 30 does not provide for either reinjection or recharge of the aquifer.

The volumetric information from this run (Model 30) is shown in Table 5-1. Note that on the 50th day of the simulation the rate of water influx into the adit peaked at 177 gpm and declined to 150 gallons per minute at the end of 60 days. The cumulative water produced at the end of 60 days was 13.6 million gallons.

The second simulation (Model 31) of the adit consisted in injecting a large portion of the water (150 gallons per minute) being produced from the adit back into the aquifer once the adit had been completed. Three wells, strategically located to maintain the water level in the vicinity of the proposed test bed were used to begin re-injecting water at the constant rate of 50 gallons per minute in each well on the 61st day after the first simulation (Model 30) was completed. The Model 31 simulation was continued for an additional year. The head distributions for the entire grid and the immediate UTP test area, as well as large-scale and small scale cross-sections of the head distributions at various times are included in Melzer et al. (1995). Figure 5-15 illustrates the head distribution of the test bed area at the end of the Model 31 (w/reinjection) simulation; Figure 5-16 provides the water table profiles normal to the adit direction also at the end of the Model 31 simulation.

The volumetric information from Model 31 is shown in Table 5-2. Water production increased from 150 gpm to 197 gpm on the 72nd day and then declined to 156 gpm on the 420th day (end of simulation). The cumulative water produced at the 420th day was 77.9 million gallons. Volumetric data in gallons per minute vs. time for both models (Model 30 and Model 31) has been plotted together in Figure 5-17.

5.4 HARDNESS ISSUES.

The calculations of the UTP adit convincingly show that, even with efficient aquifer recharge (or nearby reinjection of pumped water), desaturation zones around underground openings in materials of moderate permeabilities will extend several tens of feet laterally away from the opening. This "inverted cone" of desaturated material will be larger for material with greater permeability and smaller for saturated materials with permeabilities lower than that of the UTP site.

For most attack scenarios where the weapon is above the underground opening, the shock propagation through the desaturated materials will be more attenuative and will lead to lower incident shock pressures, longer rise times, and greater hardness of the opening. However, it will be necessary to include the effects of introduced gas (air) to the materials in the arch of the opening. The introduction of gas (air) in the pore space of the rock tends to reduce the pore pressure generated by an explosive stress wake. The reduction in pore pressure will result in an increase in effective normal stress in the rock and thus an increase in shear strength. This is likely to lead to greater resistance to the underground opening to explosive attack.

5.5 CONCLUSIONS AND RECOMMENDATIONS.

With the studies reported by Melzer et al. (1995) as a base, considerable insight into the spatial distribution of water saturated rocks in the vicinity of tunnels in moderate to high permeability rocks has been developed. Due to the high dependence on water saturation of the mechanical properties of rock, the knowledge gained should assist with future development of mechanical property profiles and hardness issues related to underground openings sited in rock.

5.5.1 Conclusions.

For the UTP conditions, the water influx into the adit has been estimated to peak at 170-180 gpm assuming no reinjection (or efficient recharge).

- The UTP pump test was only conducted for a period of 25 hours. From that test, a relatively firm minimum of nine billion gallons of reservoir capacity was calculated, and a possible size of as much as 317 billion gallons was indicated. An aquifer thickness of 74 feet based on well-log data was used in the volumetric calculations. With these parameters for the aquifer, it would require over 100 years to completely deplete the minimum size aquifer.
- Without reinjection or sealing of the underground opening (adit) walls, the water level in the test area will decline below the top of the Louisville formation, resulting in an unsaturated condition in the shape of an inverted cone in the materials above and

lateral to the opening. This unsaturated zone is estimated to extend a lateral distance of 650 feet from the opening within five years.

- Without efficient recharge capacity of an aquifer like that surrounding the UTP adit, reinjection of produced water or sealing of the adit walls would be required to maintain a saturated condition in the vicinity of the adit. Only sealing can maintain a saturation condition very near an adit.
- The profile of the desaturated zone results in unsaturated material above the underground opening. For hardness calculations, the shock wave attenuation from bursts above the opening will be affected by the change in material properties as a result of the desaturated zone.
- Analysis of the pump test data at the UTP site indicates skin or wellbore damage in the pumping well at the site. Data from the injectivity tests at the site indicated possible, but not conclusive, damage in those wells also. This induced skin complicates conclusions related to water influx and formation of the desaturated zone. Depending on the type of excavation, the walls of an underground opening may be damaged in a fashion similar to the UTP pumping well, or, alternatively, they may be stimulated because of procedures such as blasting during excavation. Stimulation would lead to enhanced water flow and resulting in an enlargement of the desaturated zone above and lateral to the opening.
- With other conditions being equal, the inverted cone of desaturation above an underground opening will be larger for materials of high permeability than for materials of low porosity/permeability such as shales and siltstones. The range of permeabilities of the UTP carbonates falls within the expected range of fine to medium grained sandstones, below that of coarse grained sandstones and most soils, and above that of siltstones and shales.
- Even rocks of low permeability are often fractured and saturated with water. The same hydrological effects observed around the UTP adit can be postulated to occur in igneous or metamorphic materials of low intact porosity and permeability.

- Linings in shallow underground openings are often designed to mitigate required pumping. In those cases where sealing is effective and pumping requirements are minimal, the above concerns about the zone of desaturation are overstated. However, it is reasonable to expect that a cone of water table depression will exist above the opening. Depending on the level of aquifer recharge, the desaturation zone may be permanent in spite of the sealing effectiveness. Even in the case of minimal pumping, calculations should be performed to assess whether the water table has been permanently lowered by the pumping during construction.

5.5.2 Recommendations.

- A study should be undertaken to document zones of desaturation around underground openings. When the UTP Test Program resumes, it would be valuable to carefully document the time varying position of the water table as the adit construction proceeds. In addition, it would be helpful to initiate a study wherein several sites with deep to moderately deep underground openings were constructed below the water table and examine the present and past (if possible) water table profiles in the immediate vicinity of the opening.
- Prior to conducting hardness studies for underground openings in rock or soil sites below the water table, one should attempt to reconstruct profiles of desaturation in the vicinity of the openings.
- One and two-phase (effective stress model) hardness calculations of both lined and unlined structures in saturated rocks should be attempted using properties of various real materials with varying saturation percentages. Inverted cones of desaturation above the structures should be included as special cases to assess the effects. Effects from both the wave propagation and structure media interaction should be examined.
- Field testing such as that envisioned at UTP should be planned and executed to examine the effects of desaturation zones. The test results should be used to verify modeling efforts.

Table 5-1. Volumetric information from 2-D areal MODFLOW calculation of access adit excavation without reinjection.

MODEL 30 VOLUMETRICS					MODEL 30 VOLUMETRICS				
500 FEET DRAIN EXCAVATED AT 10 FEET PER DAY					500 FEET DRAIN EXCAVATED AT 10 FEET PER DAY				
SIMULATION TIME IS 60 DAYS					SIMULATION TIME IS 60 DAYS				
D	CUMULATIVE	WATER	WATER	WATER	D	CUMULATIVE	WATER	WATER	WATER
A	WATER	PRODUCTION	PRODUCTION	PRODUCTION	A	WATER	PRODUCTION	PRODUCTION	PRODUCTION
Y	PRODUCED	PER HOUR	PER DAY	PER MINUTE	Y	PRODUCED	PER HOUR	PER DAY	PER MINUTE
	(GALLONS)	(GALLONS)	(GALLONS)	(GALLONS)		(GALLONS)	(GALLONS)	(GALLONS)	(GALLONS)
1	170701.08	160042.08	6668.42	111.14	31	6549787.20	229045.08	9543.55	159.06
2	345882.68	170693.60	7112.23	118.54	32	6788997.60	230084.80	9586.87	159.78
3	526659.32	177425.60	7392.73	123.21	33	7029479.60	231304.04	9637.67	160.63
4	711923.96	182437.20	7601.55	126.69	34	7271457.60	232807.52	9700.31	161.67
5	900891.20	186439.00	7768.29	129.47	35	7515156.00	234258.64	9760.78	162.68
6	1093127.20	189857.36	7910.72	131.85	36	7760500.00	235567.64	9815.32	163.59
7	1288280.40	192841.88	8035.08	133.92	37	8006592.00	236854.20	9868.93	164.48
8	1485976.80	195489.80	8145.41	135.76	38	8254928.00	238163.20	9923.47	165.39
9	1686066.80	197920.80	8246.70	137.45	39	8504012.00	239502.12	9979.26	166.32
10	1888400.80	200179.76	8340.82	139.01	40	8754592.00	241028.04	10042.84	167.38
11	2092754.40	202221.80	8425.91	140.43	41	9006668.00	242479.16	10103.30	168.39
12	2299127.60	204121.72	8505.07	141.75	42	9260988.00	243795.64	10158.15	169.30
13	2507221.20	205909.44	8579.56	142.99	43	9516056.00	245067.24	10211.14	170.19
14	2717633.60	207607.40	8650.31	144.17	44	9771872.00	246398.68	10266.61	171.11
15	2929990.80	209178.20	8715.76	145.26	45	10029932.00	247760.04	10323.34	172.06
16	3144218.00	210666.72	8777.78	146.30	46	10289488.00	249173.76	10382.24	173.04
17	3360090.80	212058.00	8835.75	147.26	47	10549792.00	250565.04	10440.21	174.00
18	3577459.60	213367.00	8890.29	148.17	48	10811592.00	251874.04	10494.75	174.91
19	3796399.20	214571.28	8940.47	149.01	49	11074888.00	253235.40	10551.48	175.86
20	4017283.60	215932.64	8997.19	149.95	50	11339680.00	254507.00	10604.46	176.74
21	4239963.20	217151.88	9048.00	150.80	51	11598764.00	255097.16	10212.38	170.21
22	4464064.00	218221.52	9092.56	151.54	52	11830368.00	238776.56	9949.02	165.82
23	4689660.80	219283.68	9136.82	152.28	53	12065988.00	234034.24	9751.43	162.52
24	4916678.80	220390.72	9182.95	153.05	54	12297868.00	230211.96	9592.17	159.87
25	5145417.20	221722.16	9238.42	153.97	55	12526756.00	227047.92	9460.33	157.67
26	5375801.20	222911.48	9287.98	154.80	56	12752852.00	224400.00	9350.00	155.83
27	5607606.40	224011.04	9333.79	155.56	57	12975556.00	222066.24	9252.76	154.21
28	5840832.80	225095.64	9378.99	156.32	58	13196216.00	219964.36	9165.18	152.75
29	6075555.20	226501.88	9437.58	157.29	59	13415380.00	218056.96	9085.71	151.43
30	6311923.20	227855.76	9493.99	158.23	60	13632300.00	216306.64	9012.78	150.21

Table 5-2. Volumetric information from 2-D areal MODFLOW calculation of access adit excavation with reinjection.

MODEL 31 VOLUMETRICS						
500 FEET DRAIN WITH REINJECTION IN THREE WELLS						
INJECTION RATE IS 50.12 GALLONS PER MINUTE PER WELL						
SIMULATION TIME IS 360 DAYS						
D	CUMULATIVE	CUMULATIVE	NET	WATER	WATER	WATER
A	WATER	WATER	WATER	PRODUCTION	PRODUCTION	PRODUCTION
Y	INJECTED	PRODUCED	PRODUCED	PER DAY	PER HOUR	PER MINUTE
	(GALLONS)	(GALLONS)	(GALLONS)	(GALLONS)	(GALLONS)	(GALLONS)
61	216501.12	13873275.68	24474.56	255187.68	10632.82	177.21
62	433002.24	14136384.68	71082.44	267365.12	11140.21	185.67
63	649503.36	14407527.20	125723.84	273281.80	11386.74	189.78
64	866004.48	14683015.60	184711.12	276677.72	11528.24	192.14
65	1082505.60	14961196.80	246391.20	278906.76	11621.12	193.69
66	1299006.72	15241098.40	309791.68	280350.40	11681.27	194.69
67	1515507.84	15522122.00	374314.16	281345.24	11722.72	195.38
68	1732008.96	15804043.20	439734.24	281951.12	11747.96	195.30
69	1948510.08	16086413.20	505603.12	282414.88	11767.29	196.12
70	2165011.20	16369082.40	571771.20	282594.40	11774.77	196.25
72	2598013.44	16934794.80	704481.36	283245.16	11801.88	196.70
74	3031015.68	17500432.40	837116.72	283043.20	11793.47	196.56
76	3464017.92	18065322.00	969004.08	282631.80	11776.33	196.27
78	3897020.16	18629239.20	1099919.04	282033.40	11751.39	195.86
80	4330022.40	19191884.80	1229562.40	281360.20	11723.34	195.39
82	4763024.64	19753109.20	1357784.56	280664.56	11694.36	194.91
84	5196026.88	20312837.60	1484510.72	279909.08	11662.88	194.38
86	5629029.12	20871144.80	1609815.68	279161.08	11631.71	193.86
88	6062031.36	21427956.00	1733624.64	278405.60	11600.23	193.34
90	6495033.60	21982972.00	1855638.40	277620.20	11567.51	192.79
95	7577539.20	23364528.00	2154688.80	275451.00	11477.13	191.29
100	8660044.80	24736360.00	2444015.20	273573.52	11398.90	189.98
105	9742550.40	26099216.00	2724365.60	271815.72	11325.66	188.76
110	10825056.00	27453844.00	2996488.00	270080.36	11253.35	187.56
115	11907561.60	28799496.00	3259634.40	268404.84	11183.54	186.39
120	12990067.20	30136920.00	3514552.80	266759.24	11114.97	185.25
125	14072572.80	31466116.00	3761243.20	265158.52	11048.27	184.14
130	15155078.40	32787832.00	4000453.60	263647.56	10985.32	183.09
135	16237584.00	34102068.00	4232184.00	262159.04	10923.29	182.05
140	17320089.60	35409572.00	4457182.40	260752.80	10864.70	181.08
145	18402595.20	36709596.00	4674700.80	259391.44	10807.98	180.13
150	19485100.80	38002888.00	4885487.20	258045.04	10751.88	179.20
180	25980134.40	45620520.00	6008085.60	250916.60	10454.86	174.25
210	32475168.00	53046664.00	6939196.00	245067.24	10211.14	170.19
240	38970201.60	60313484.00	7710982.40	240175.32	10007.31	166.79
270	45465235.20	67448656.00	8351120.80	236173.52	9840.56	164.01
300	51960268.80	74476116.00	8883547.20	232807.52	9700.31	161.67
330	58455302.40	81413068.00	9325465.60	230077.32	9586.56	159.78
360	64950336.00	88275968.00	9693332.00	227803.40	9491.81	158.20
390	71445369.60	95074540.00	9996870.40	225963.32	9415.14	156.92
420	77940403.20	101828980.00	10256276.80	224347.64	9347.82	155.80

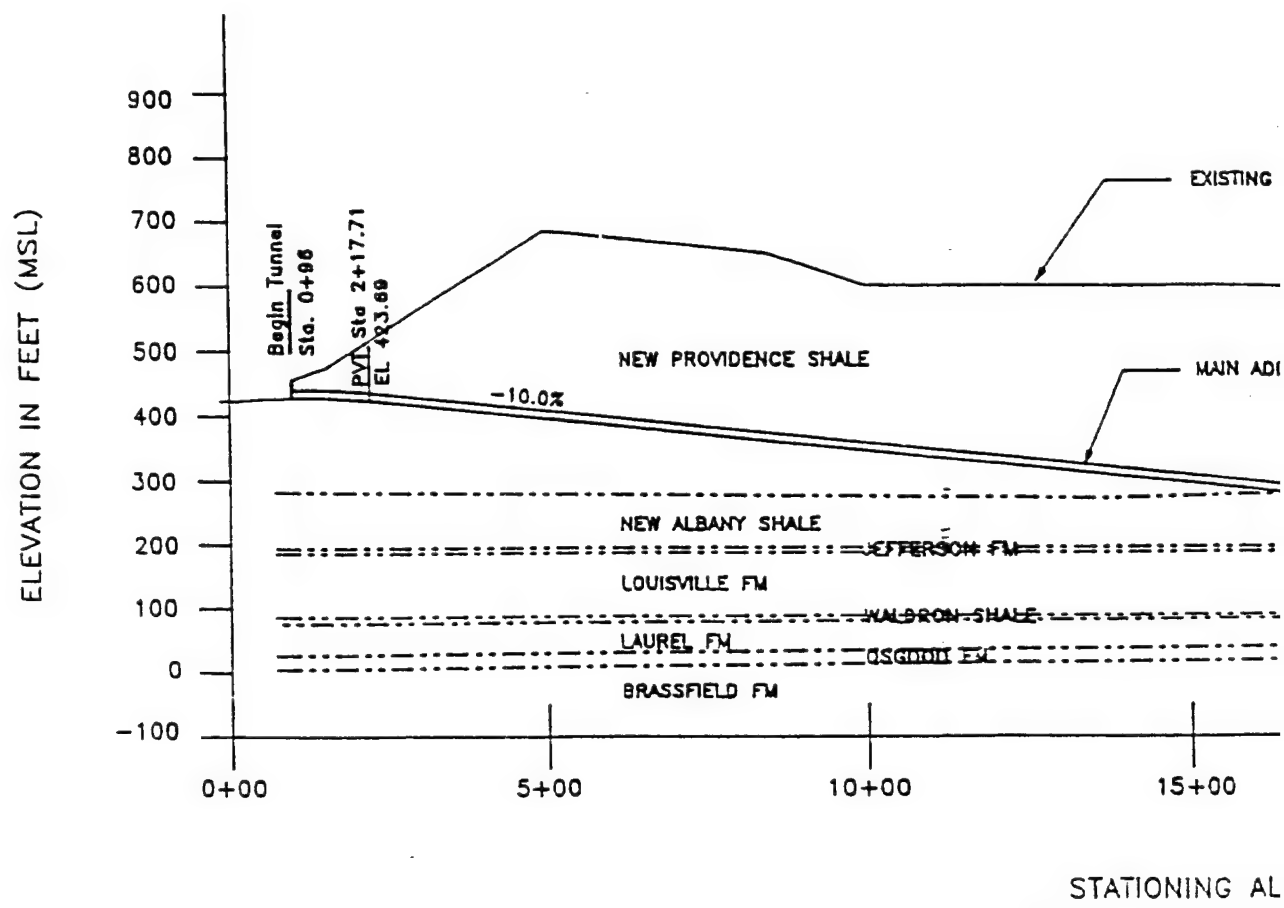
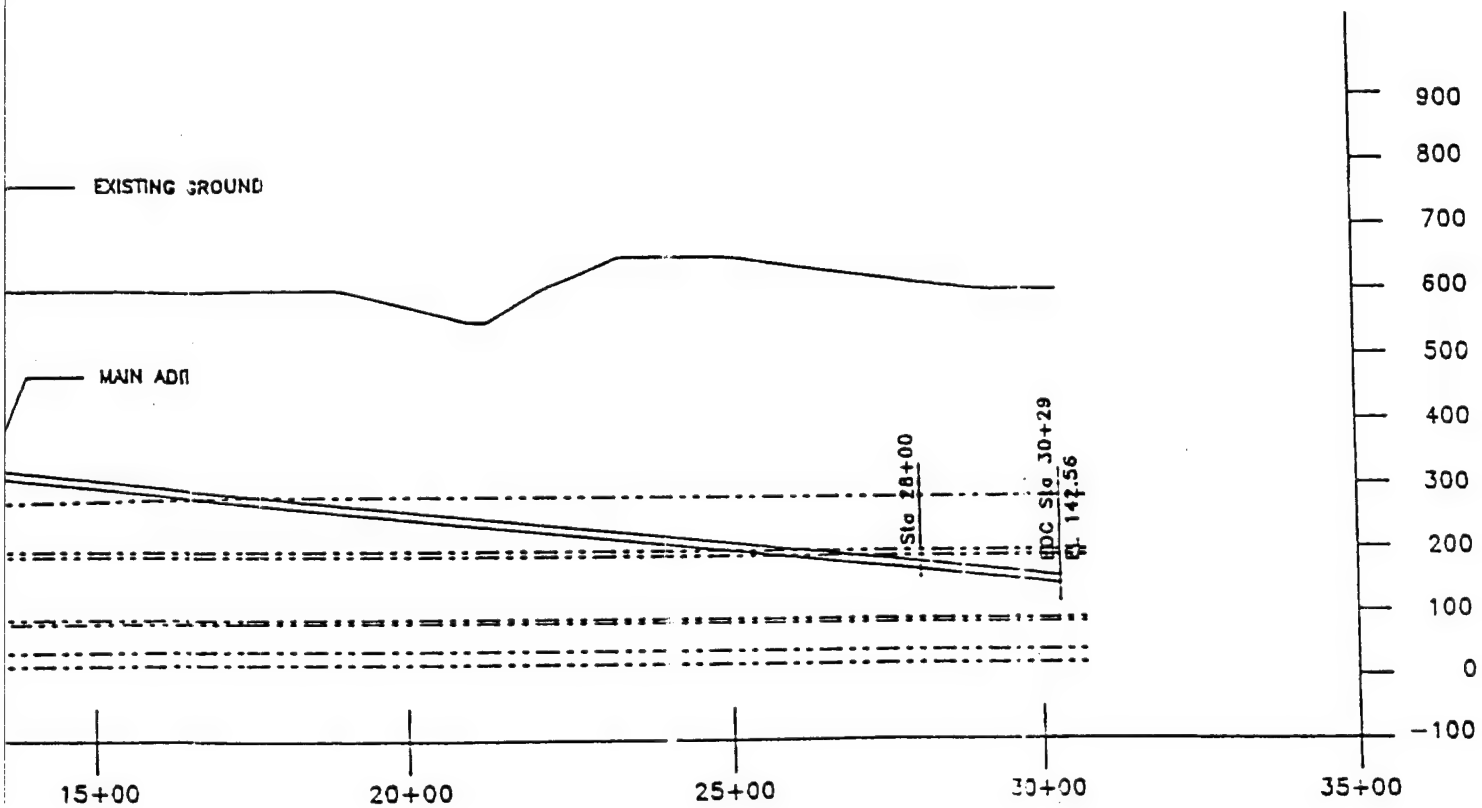


Figure 5-1. Geologic profile along adit centerline.



ATIONING ALONG ADIT CENTERLINE

2

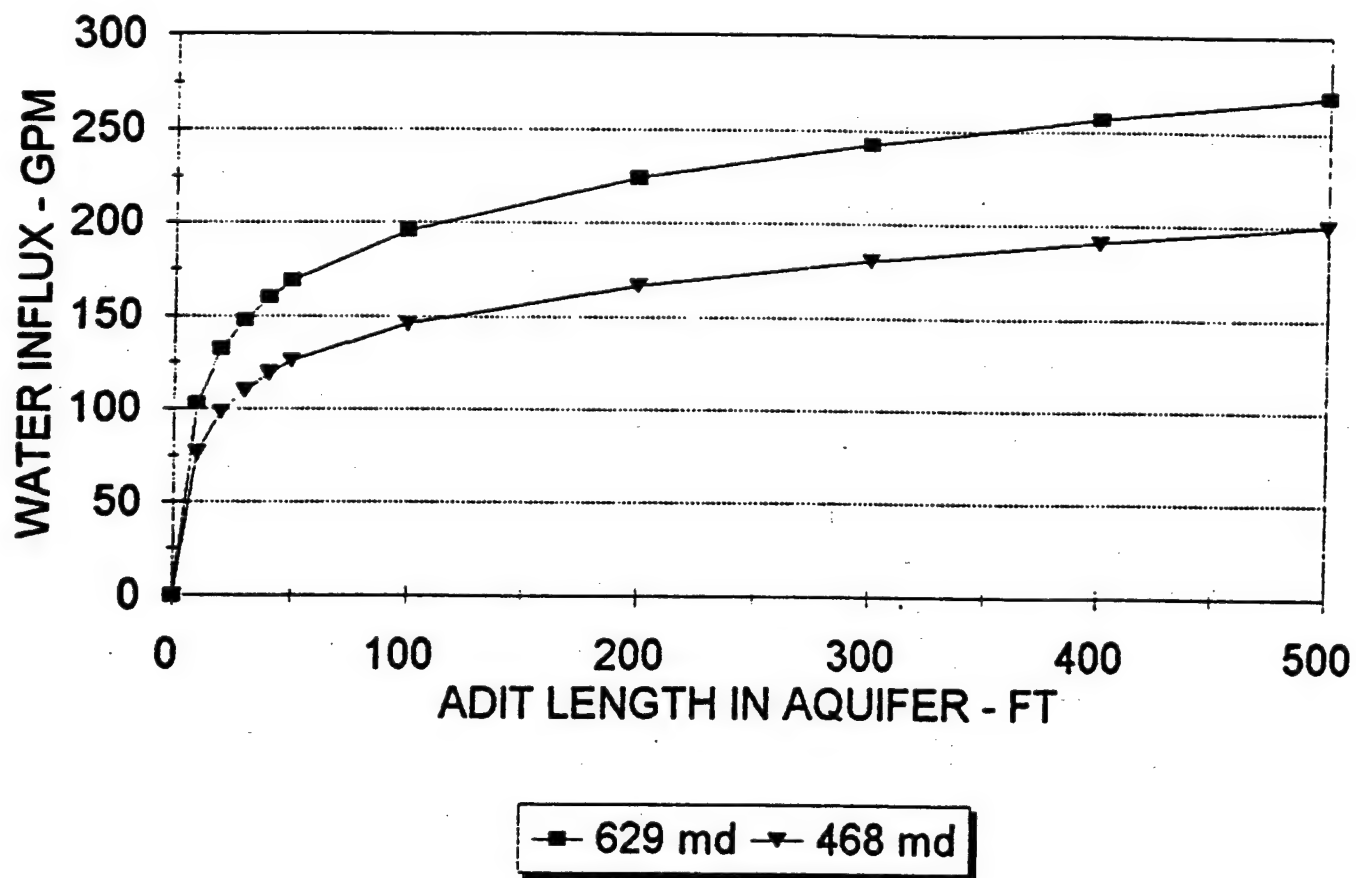


Figure 5-2. Estimated water influx as a function of adit length computed using an analytical model of a horizontal well assuming two different values of aquifer permeability.

ADIT SCHEMATIC

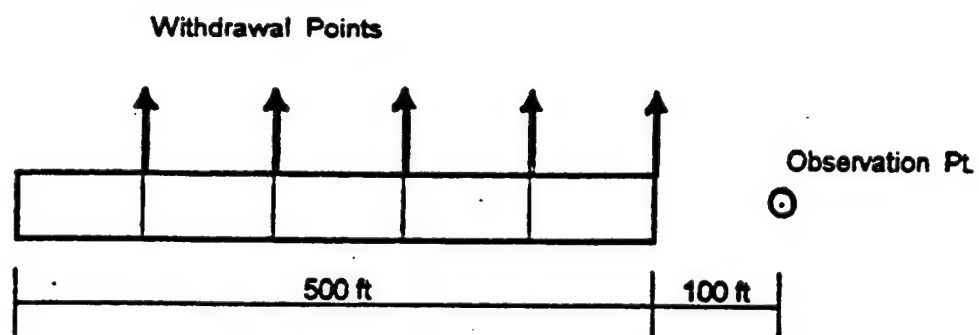


Figure 5-3. Schematic of the adit model used to estimate the desaturation zone.

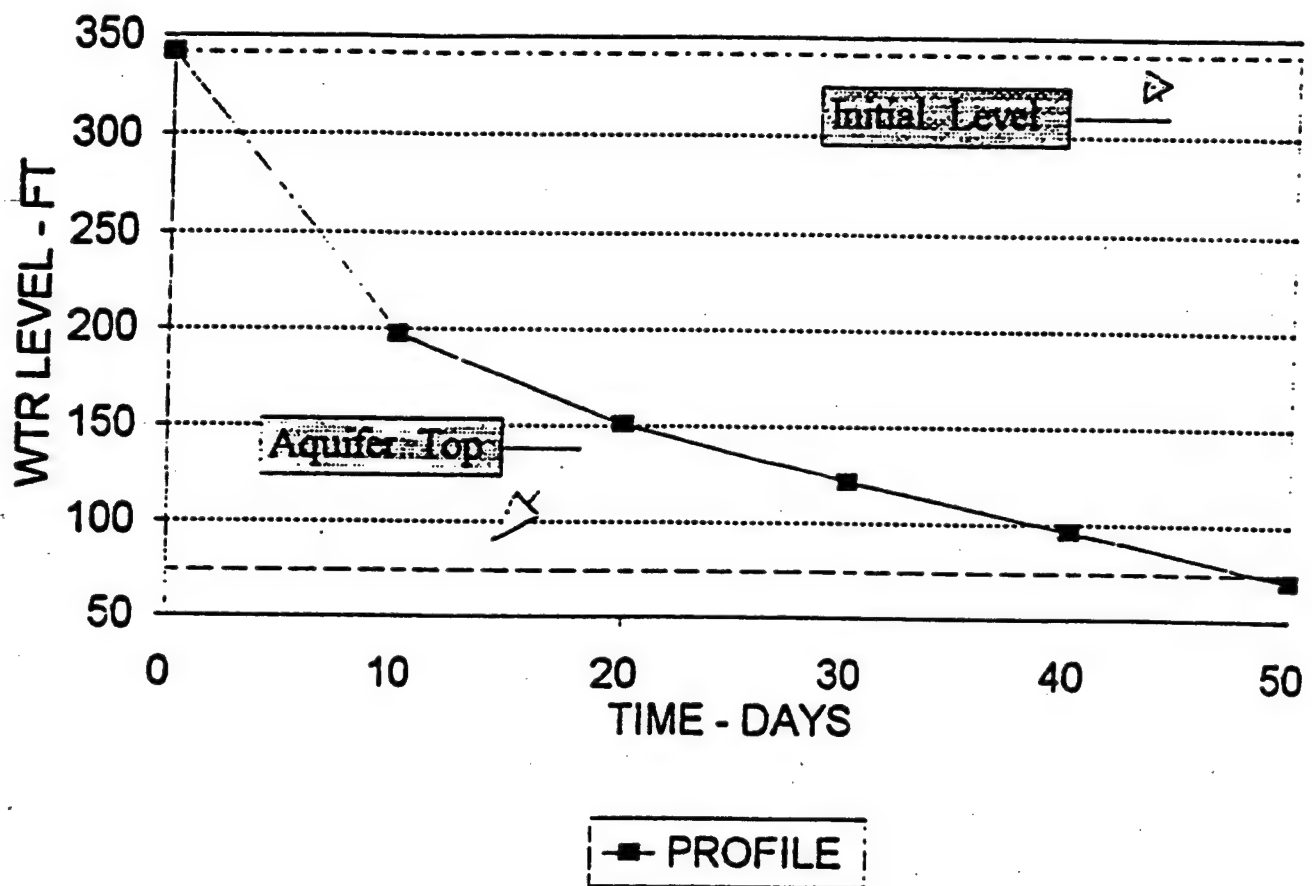
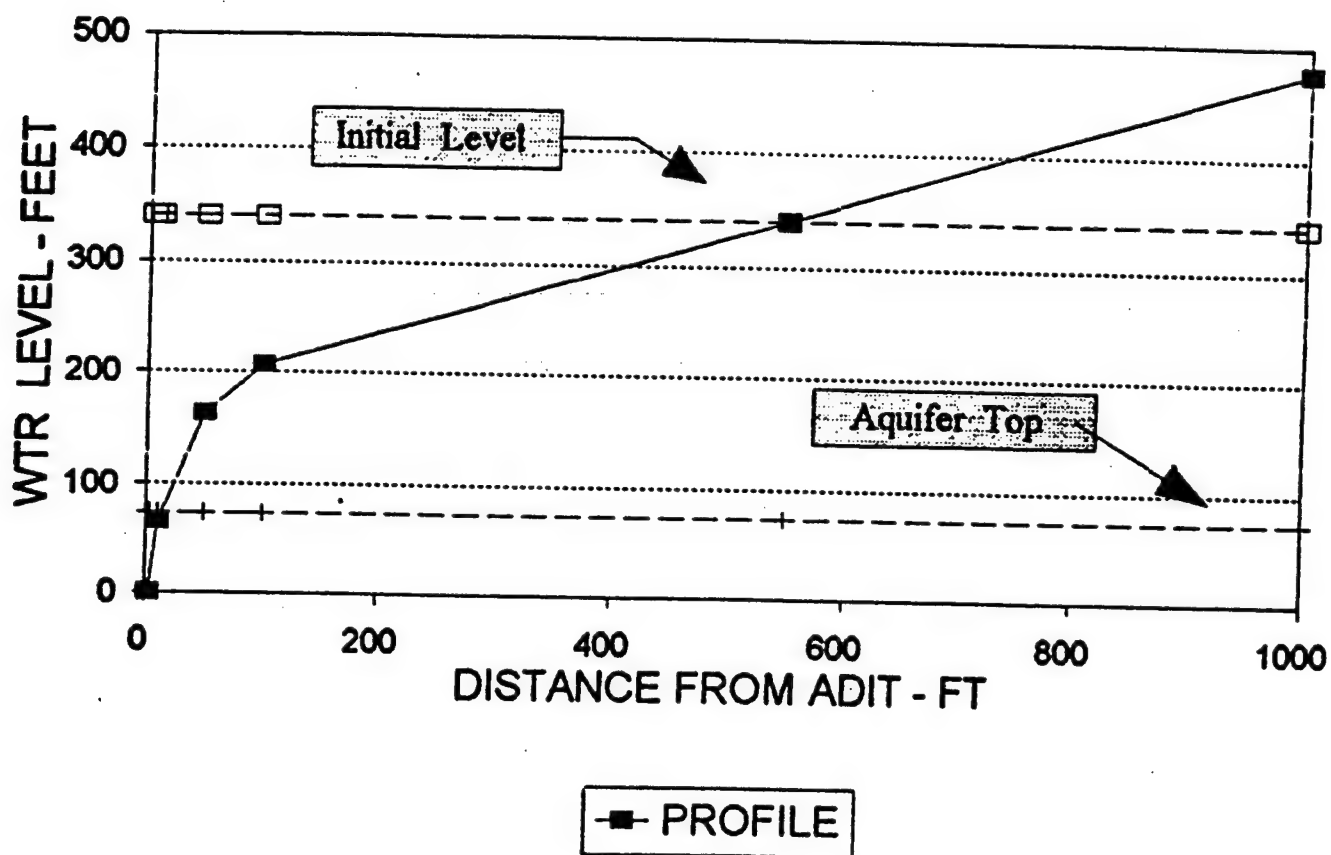
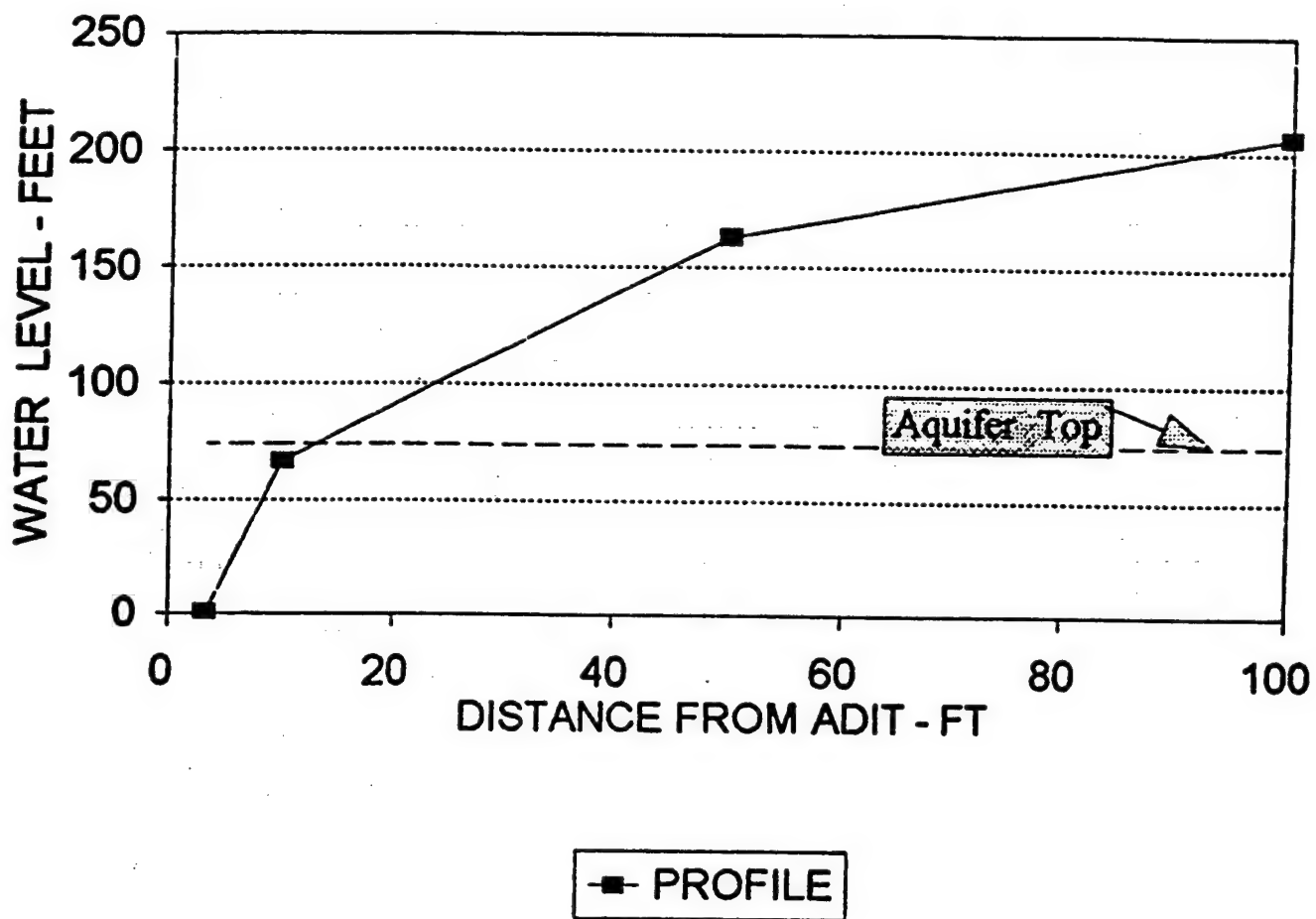


Figure 5-4. Computed variation with time in the water level 100 ft from the terminal end of the access adit.



a) entire model

Figure 5-5. Computed water level as a function of distance from the adit with reinjection.



b) detail of first 100 ft

Figure 5-5. Computed water level as a function of distance from the adit with reinjection (Continued).

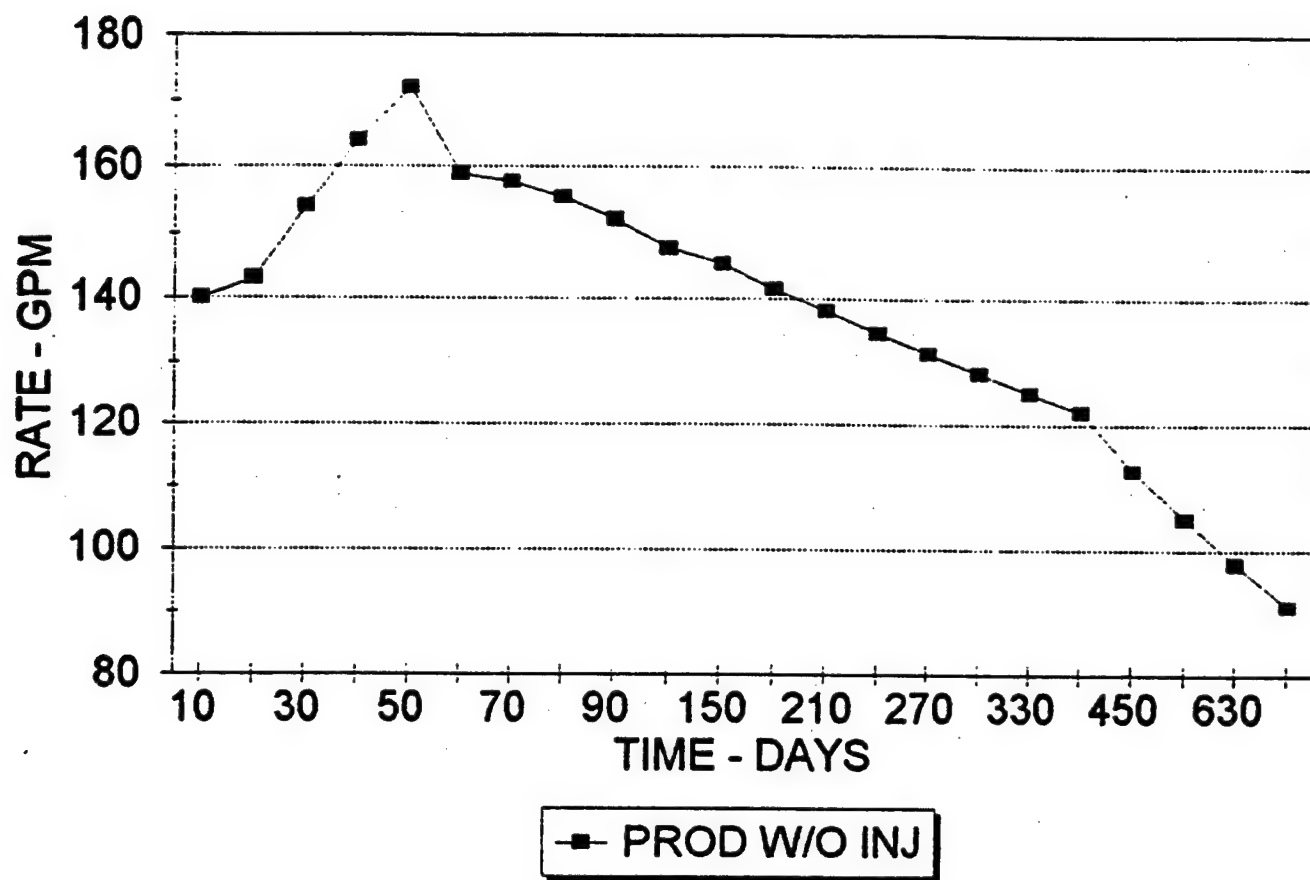


Figure 5-6. Adit production over two years computed by the ASM model.

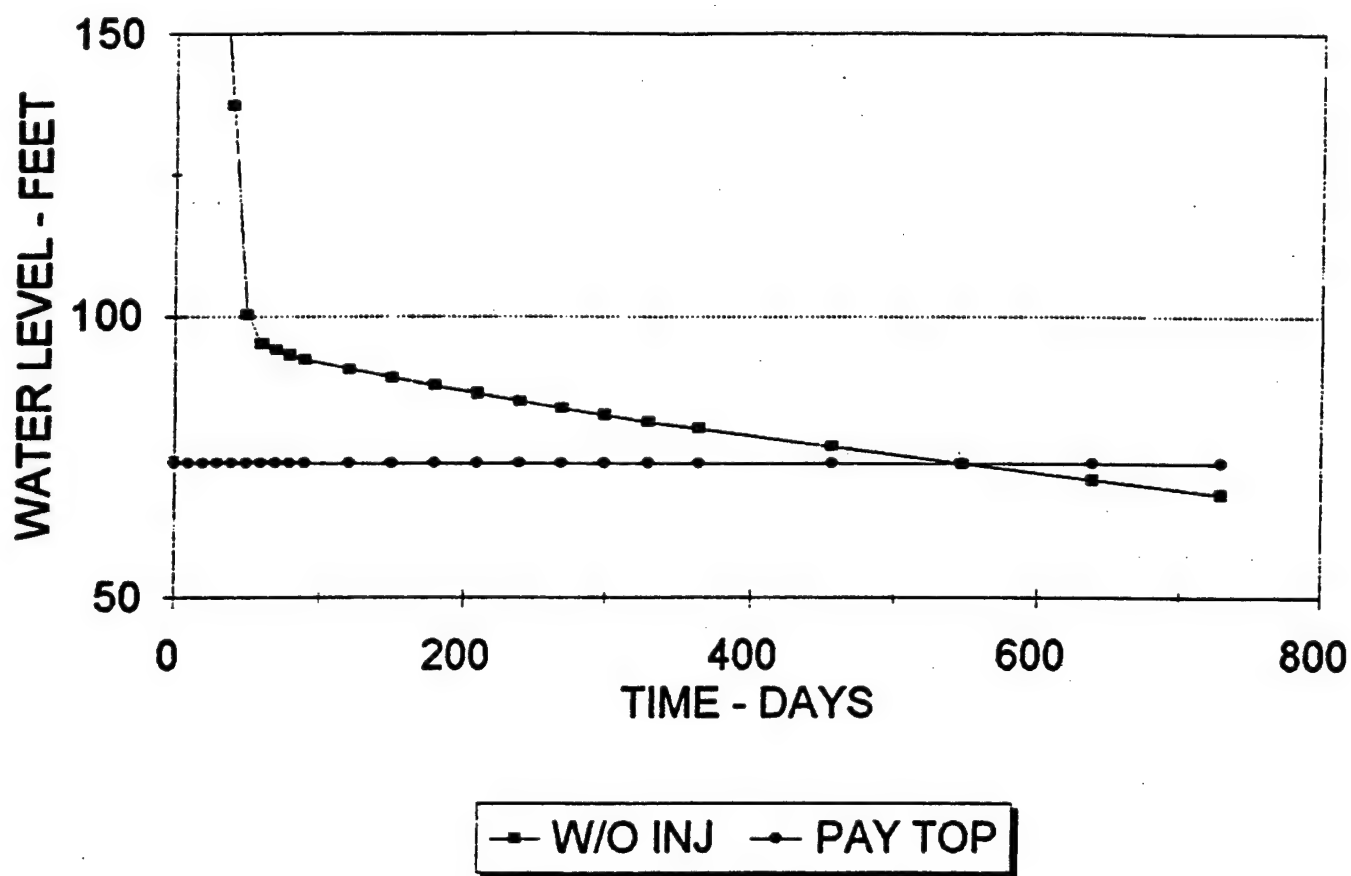
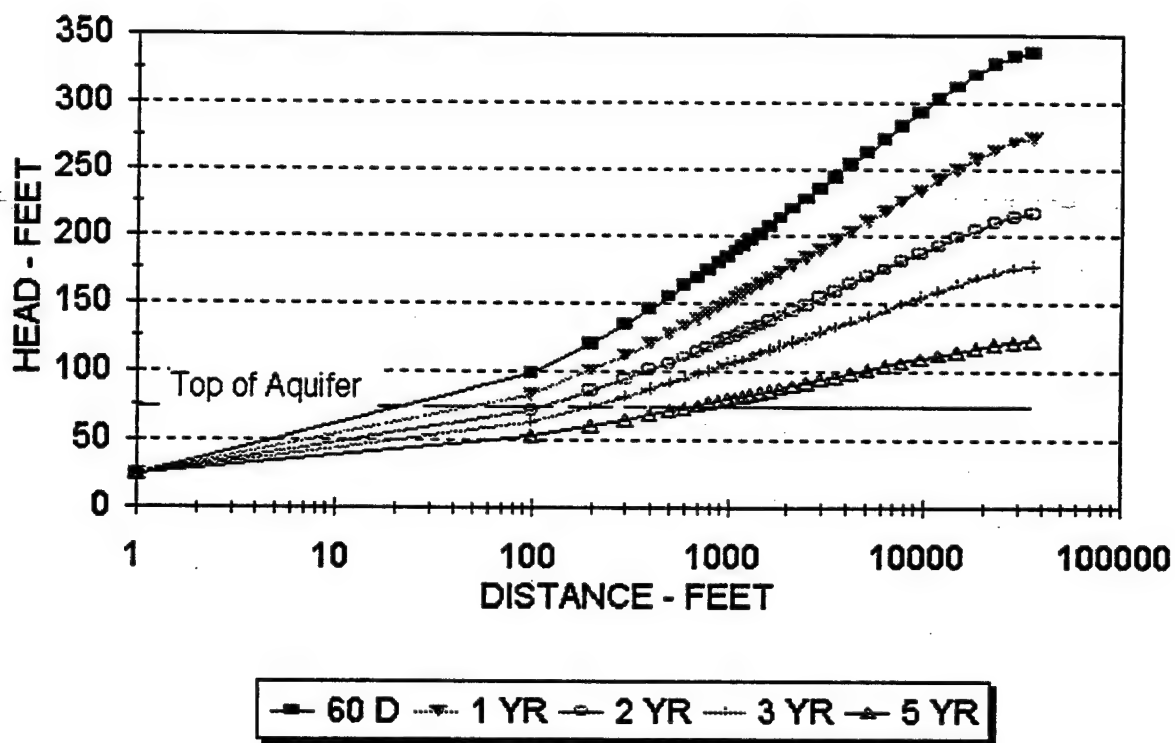
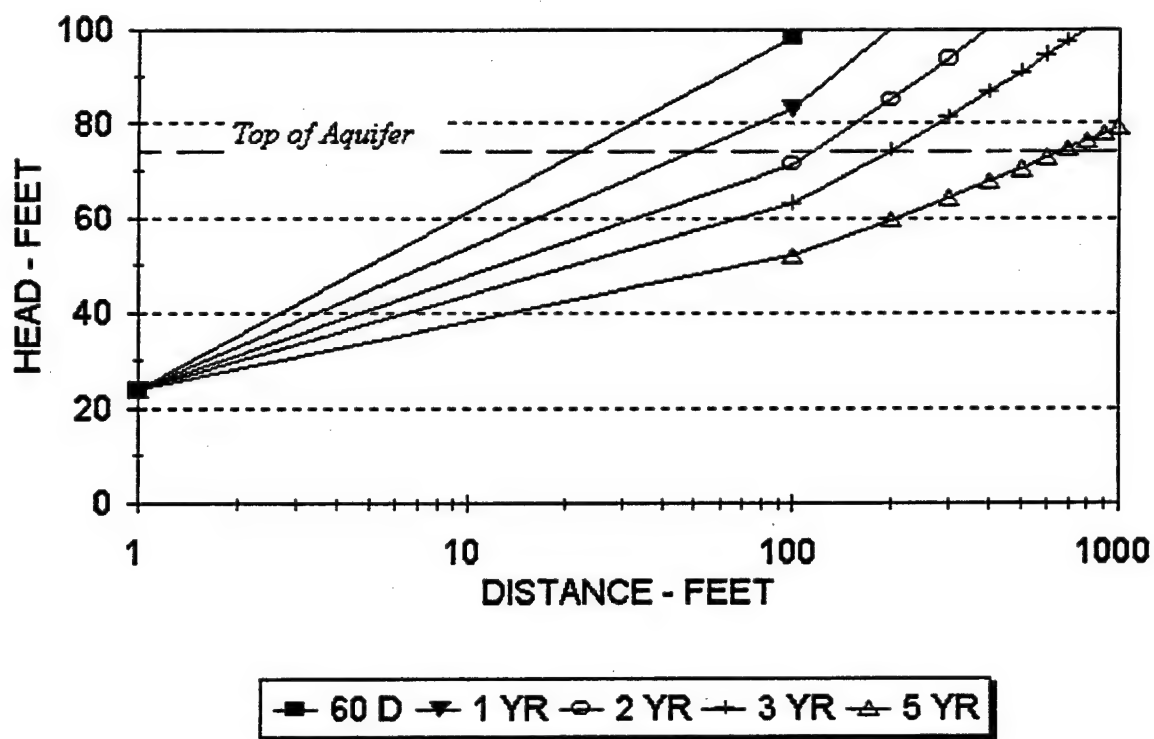


Figure 5-7. Variation in the water level with time 100 ft from the terminal end of the adit computed by the ASM model without reinjection.



a) entire model

Figure 5-8. Distance to the unsaturated zone for time periods from 60 days to five years.



b) details of the first 1000 ft

Figure 5-8. Distance to the unsaturated zone for time periods from 60 days to five years (Continued).

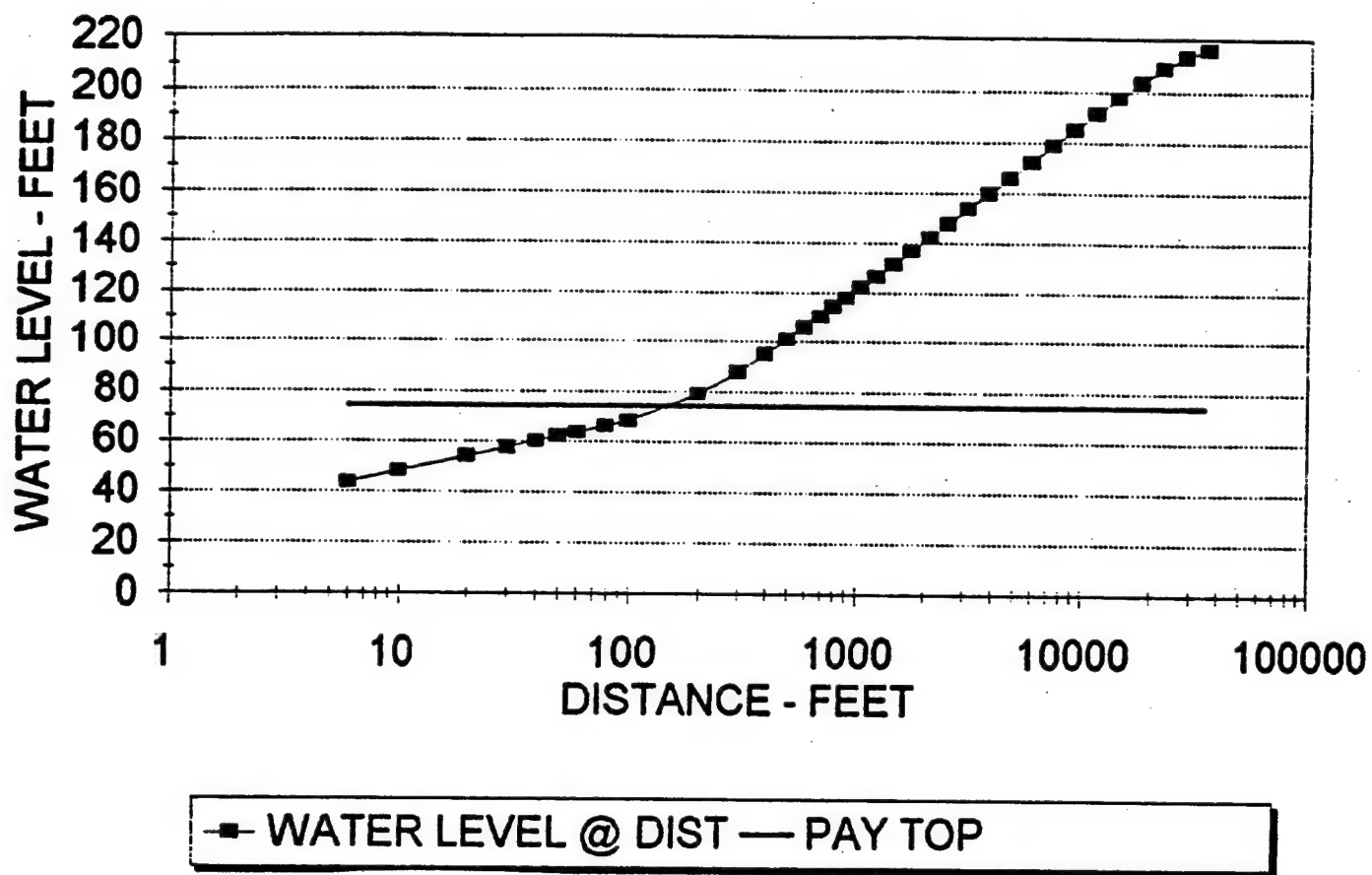


Figure 5-9. Variation in water level with distance at two years as predicted by the ASM model without reinjection.

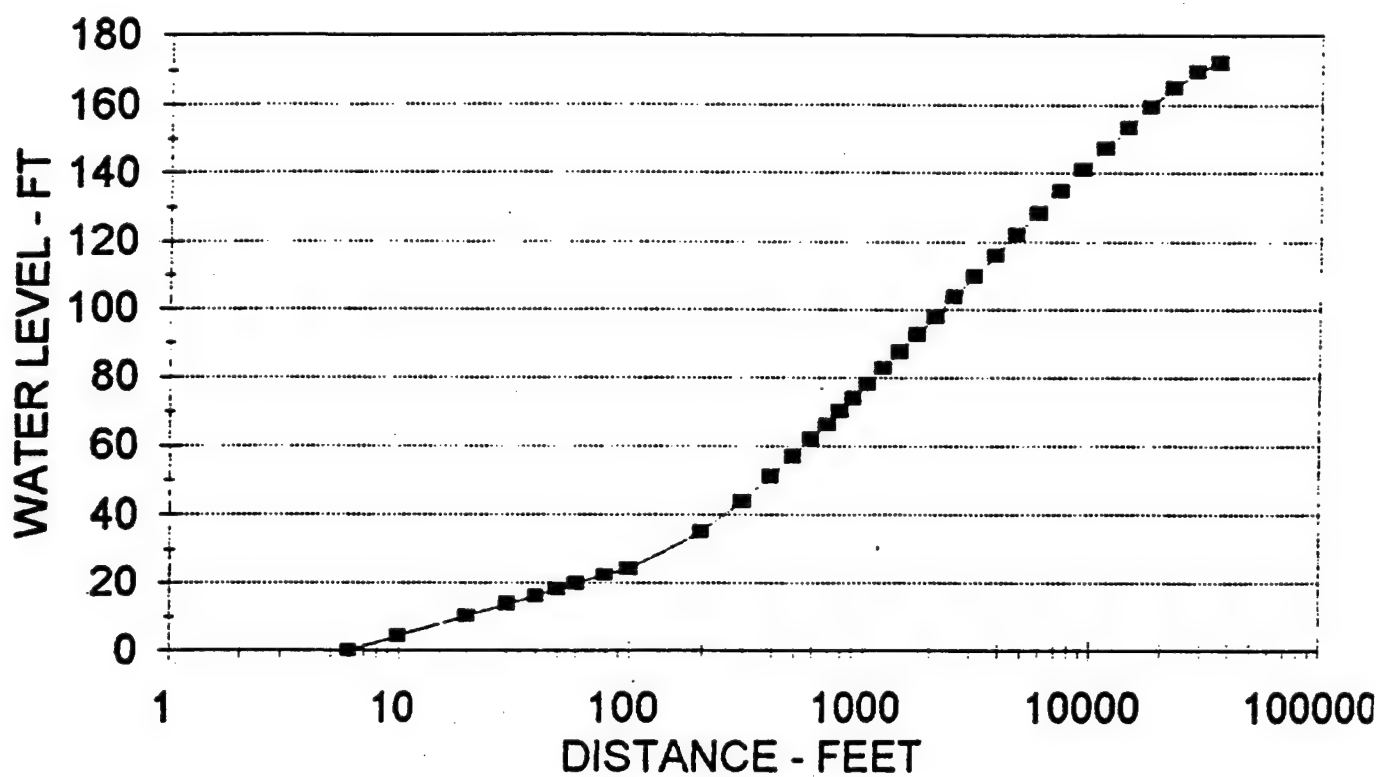


Figure 5-10. Water level above the adit floor at two years as predicted by the ASM model without reinjection.

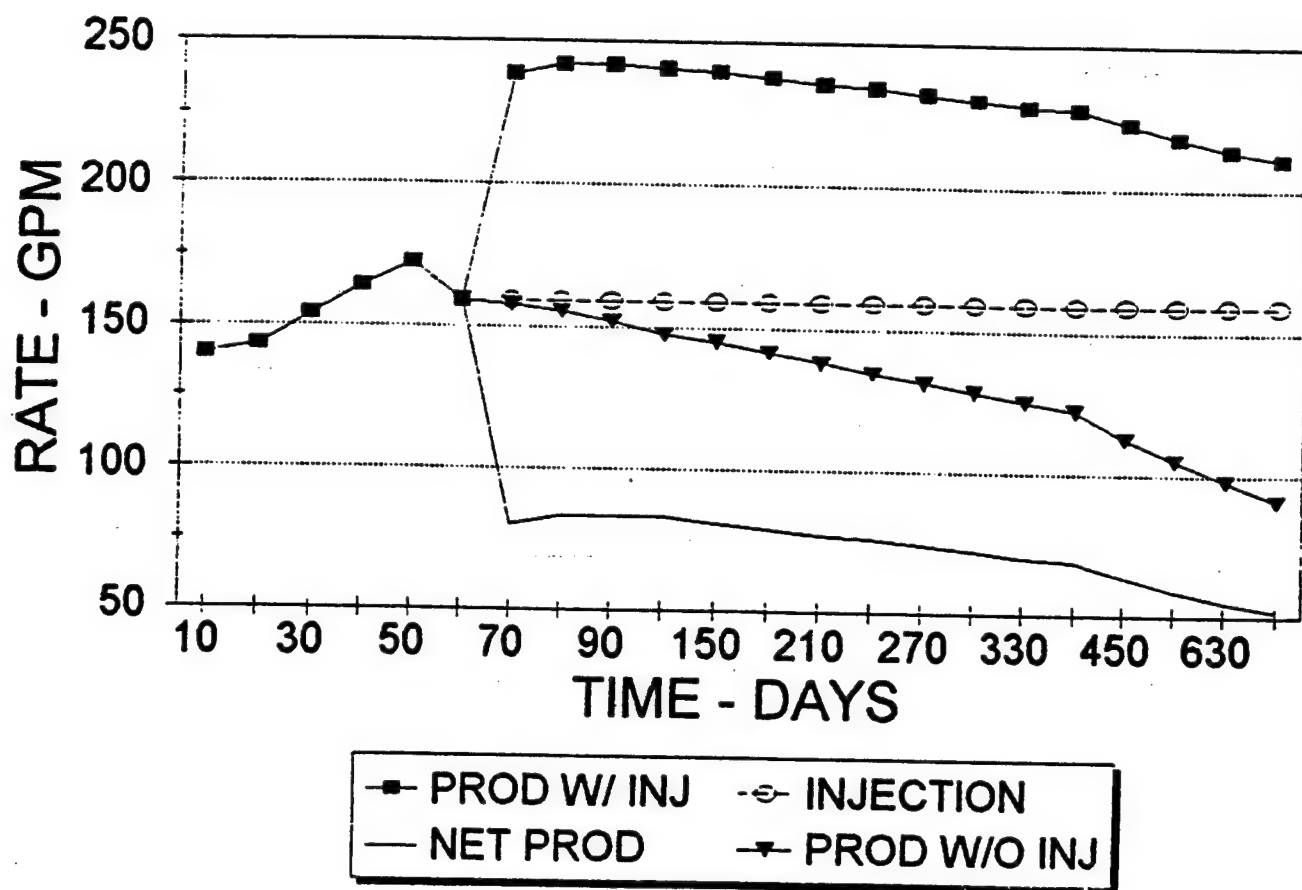


Figure 5-11. Comparison of adit production over time with and without reinjection as predicted by the ASM model.

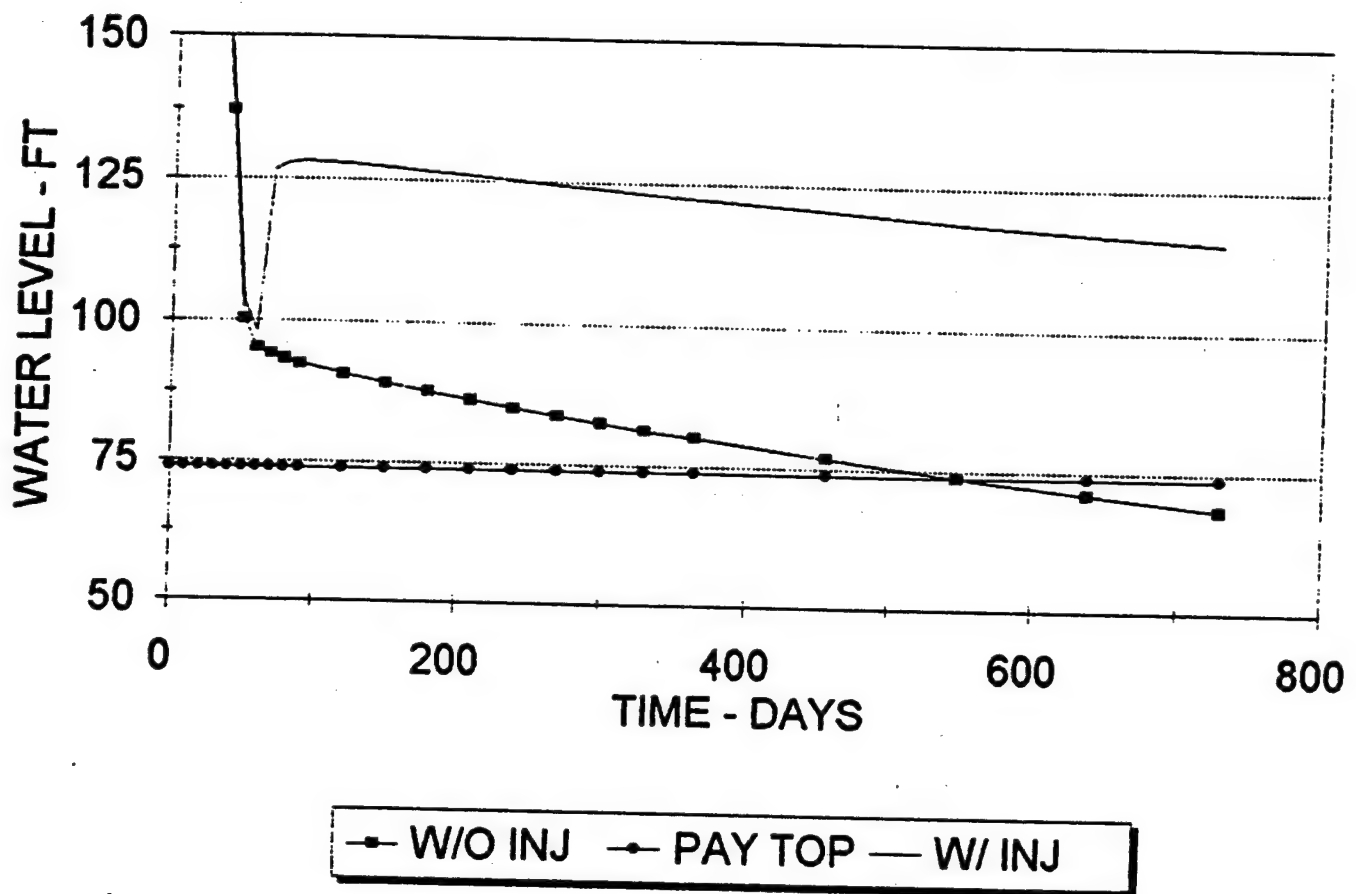
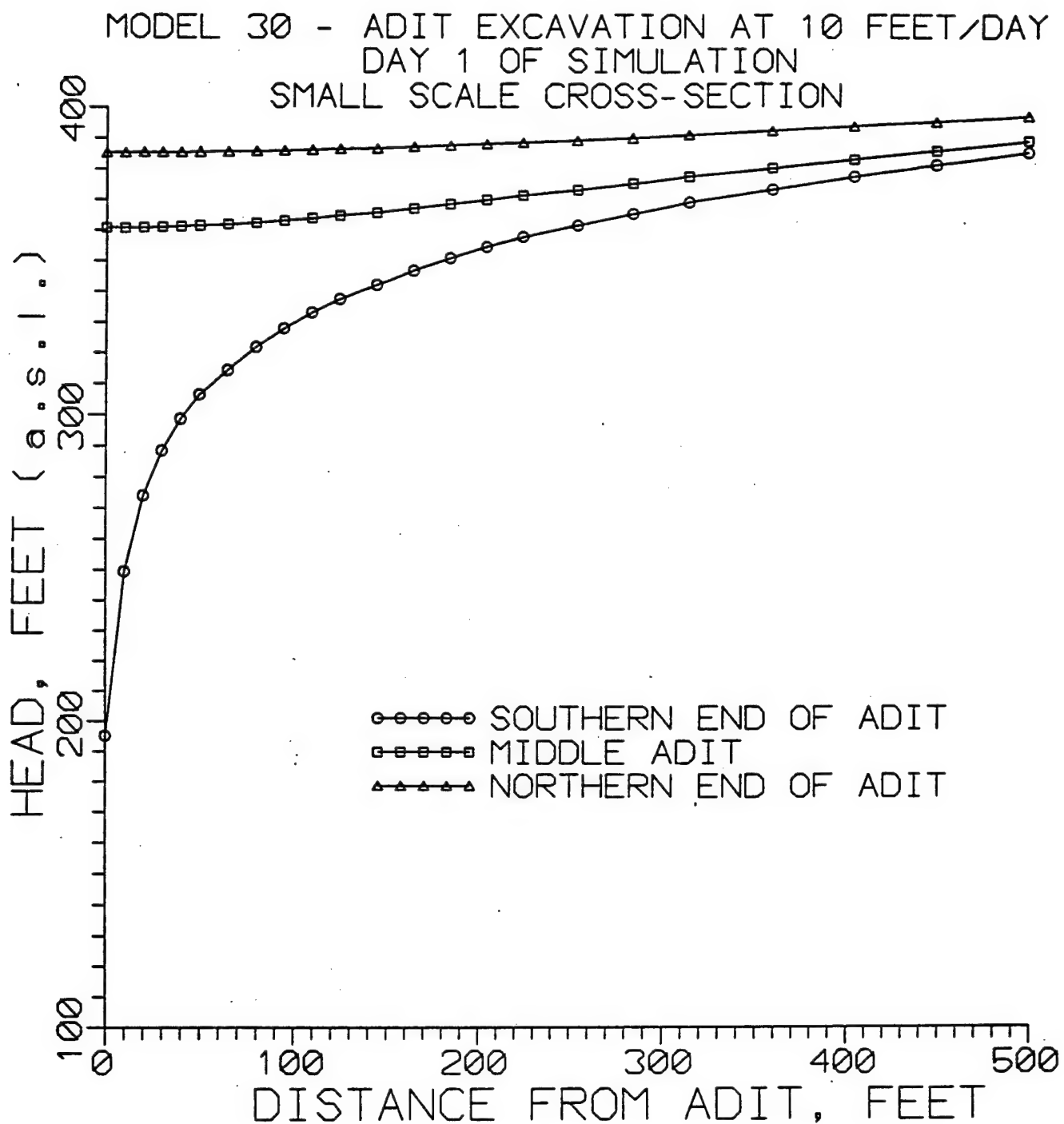


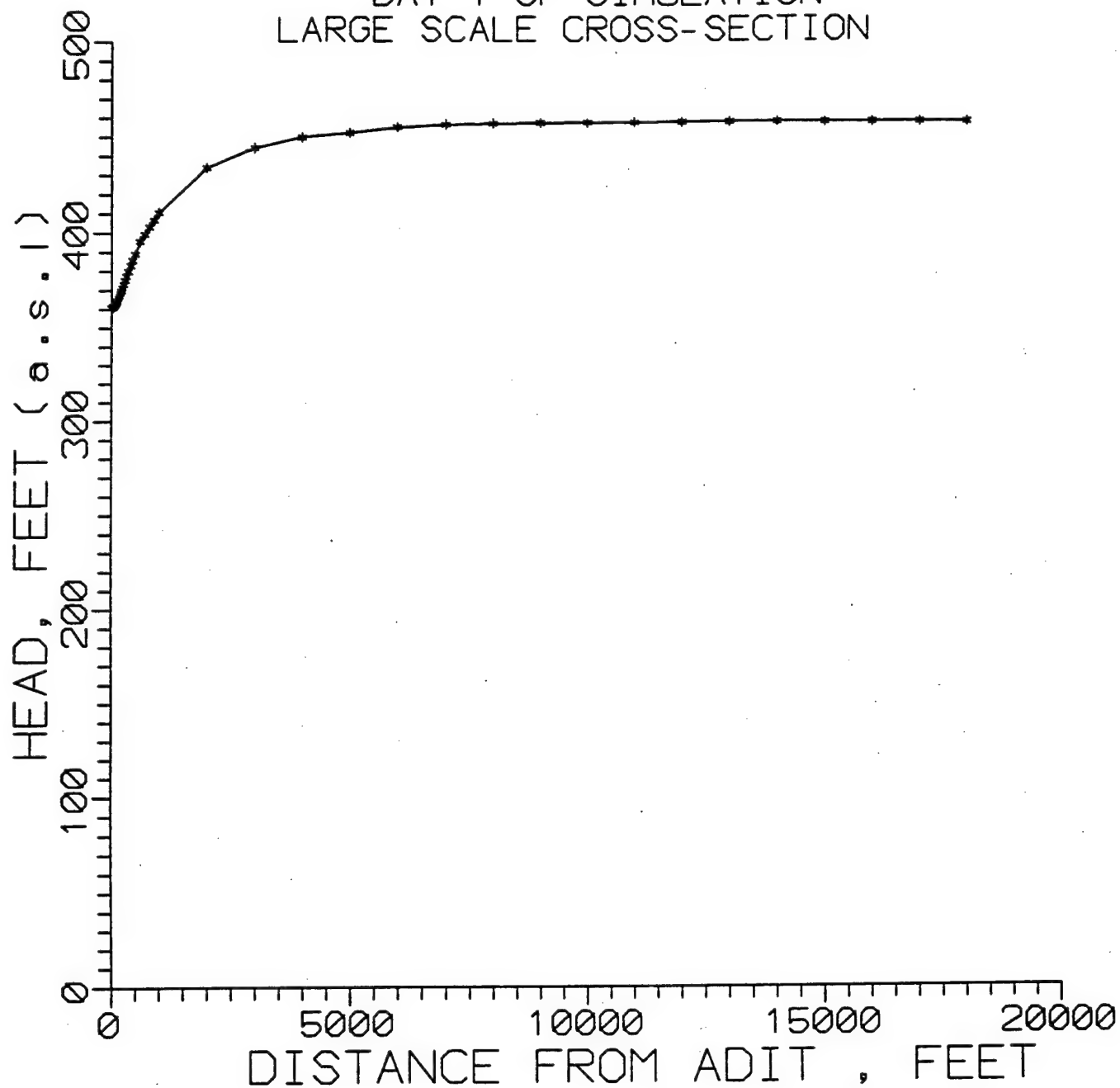
Figure 5-12. Comparison of the variations in the water level with time 100 ft from the terminal end of the adit computed by the ASM model with and without reinjection.



a) first 500 ft

Figure 5-13. Water table position one day after beginning the excavation.

MODEL 30 - ADIT EXCAVATION AT 10 FEET/DAY
DAY 1 OF SIMULATION
LARGE SCALE CROSS-SECTION



b) long-range

Figure 5-13. Water table position one day after beginning the excavation (Continued).

MODEL 30 - ADIT EXCAVATION AT 10 FEET/DAY
 DAY 60 OF SIMULATION
 SMALL SCALE CROSS-SECTION

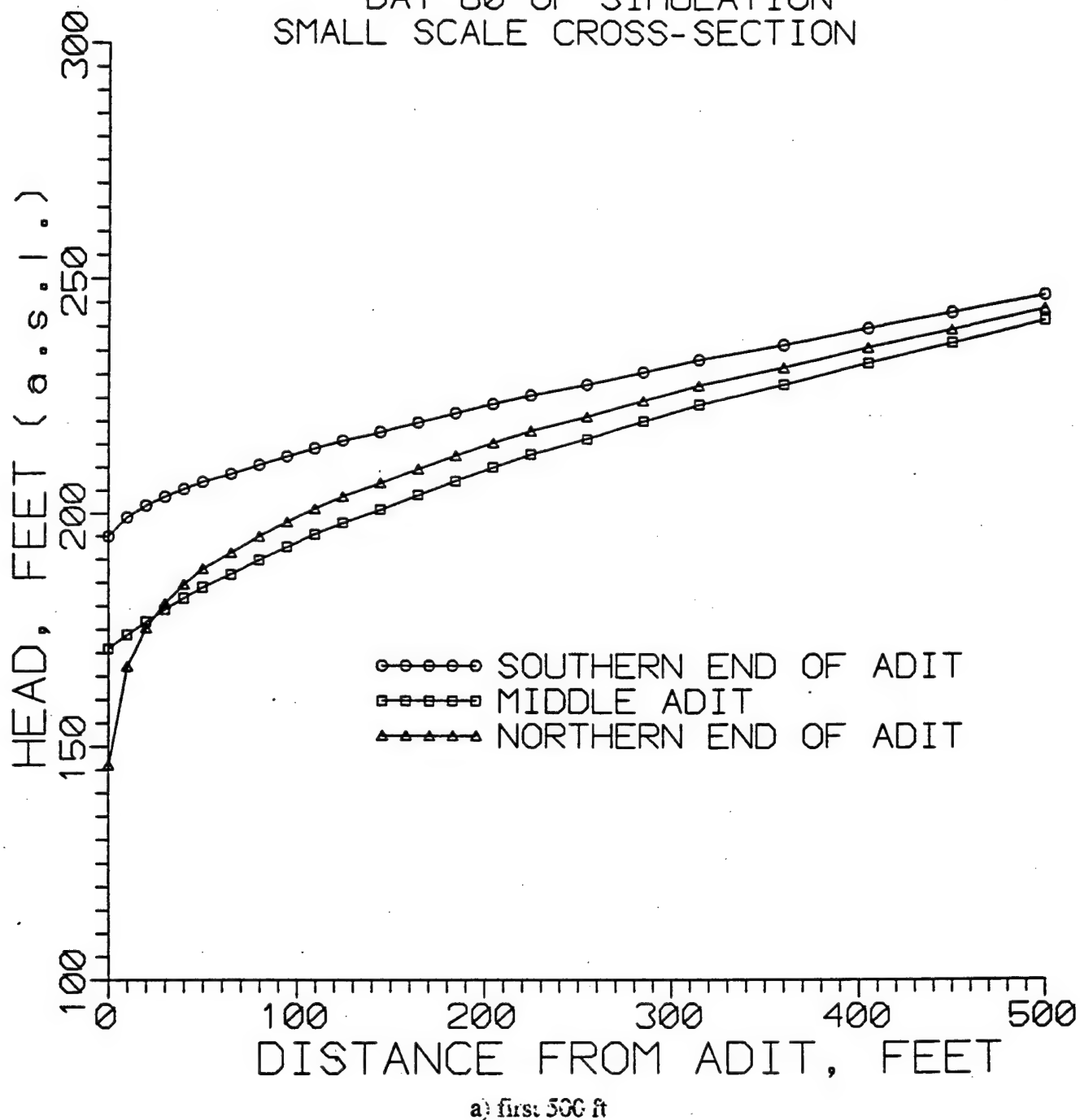
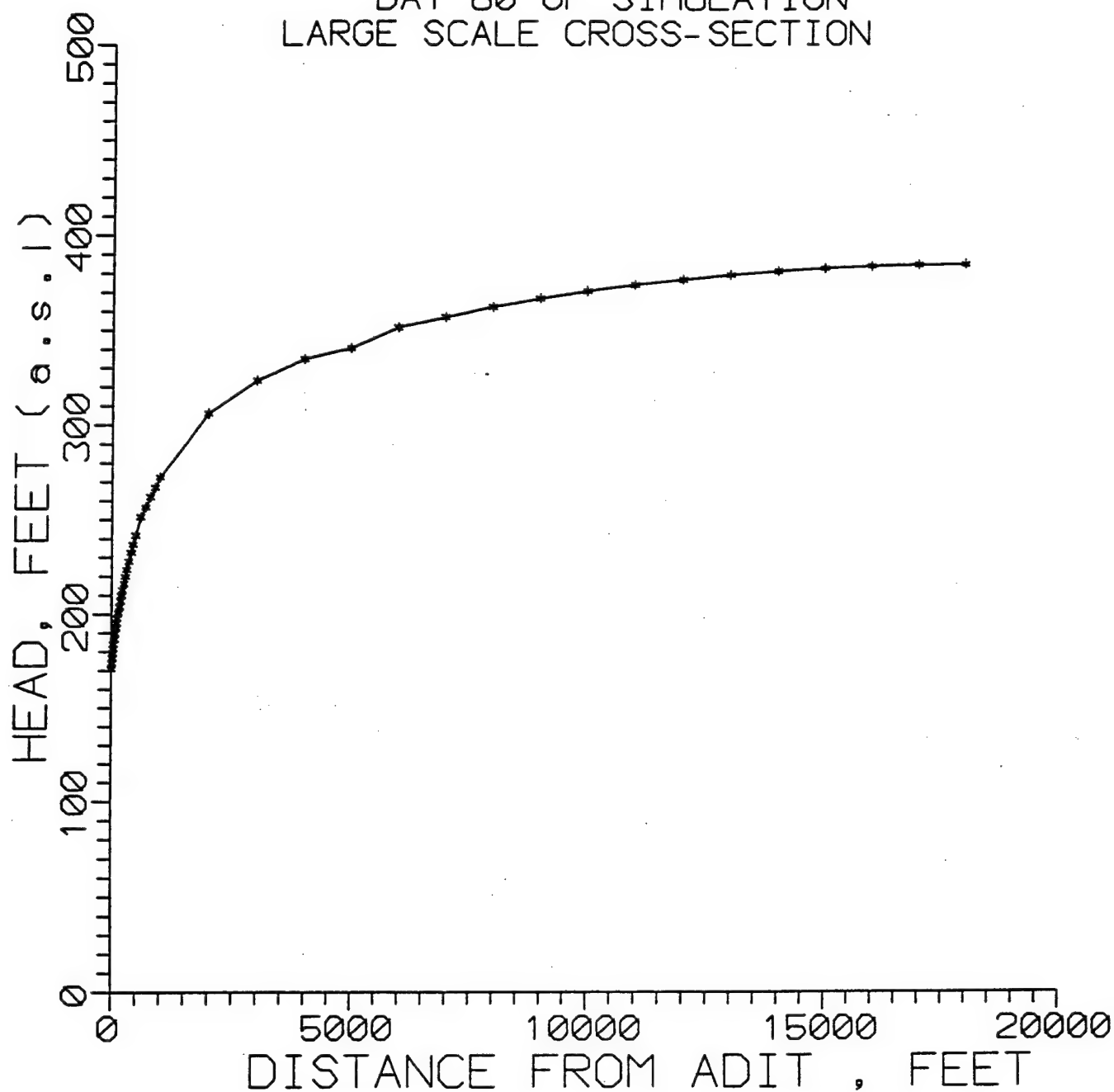


Figure 5-14. Water table position at the end of a 60-day simulation in which the tunnel was completed in 50 days.

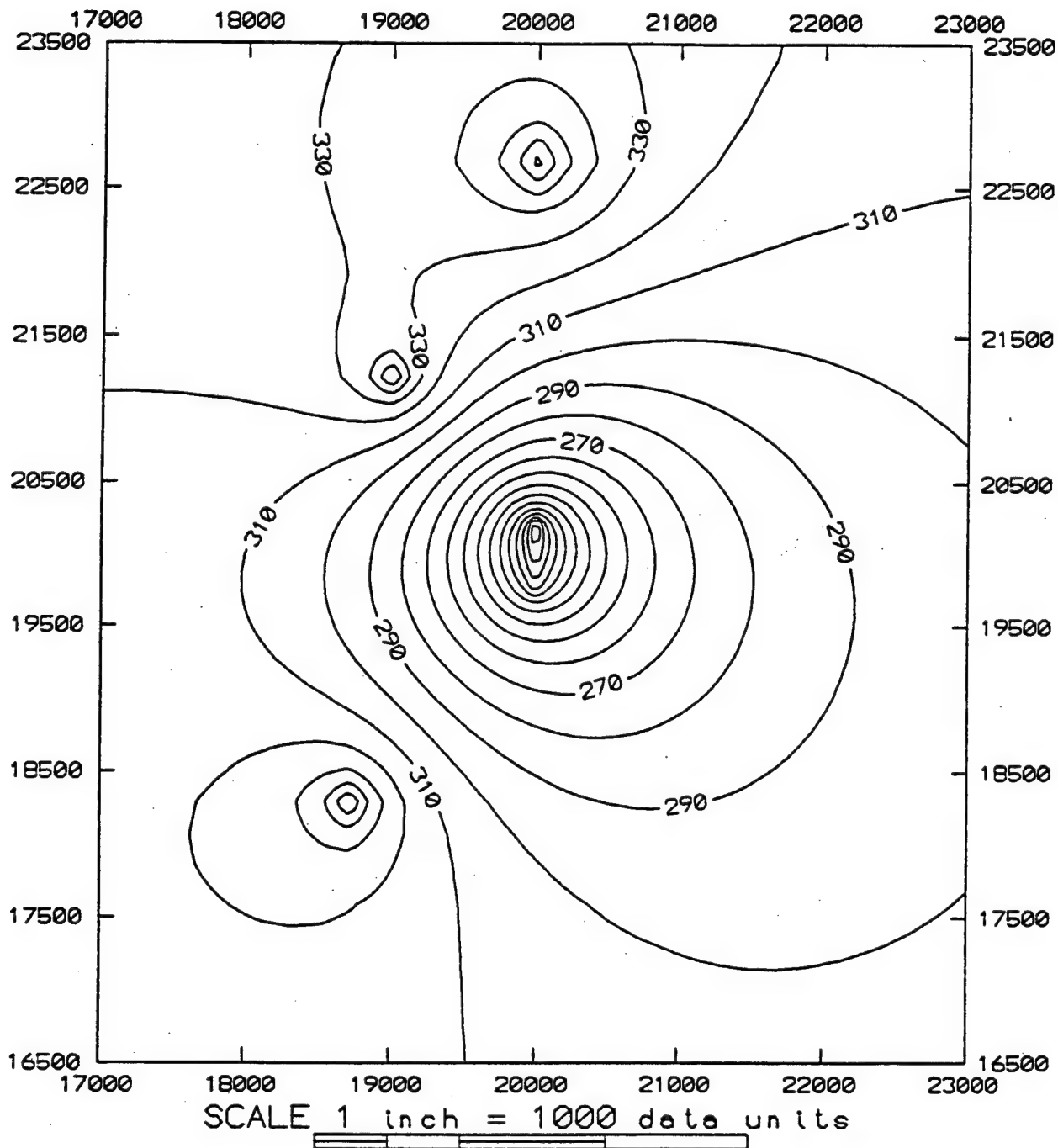
MODEL 30 - ADIT EXCAVATION AT 10 FEET/DAY
DAY 60 OF SIMULATION
LARGE SCALE CROSS-SECTION



b) long-range

Figure 5-14. Water table position at the end of a 60-day simulation in which the tunnel was completed in 50 days (Continued).

MODEL 31
TEST AREA SCALE
DAY 420 - HEAD DISTRIBUTION



CONTOUR INTERVAL : 10 FEET

Figure 5-15. Head distribution in the test area after 360 days of reinjection commencing 10 days after completion of the adit.

MODEL 31 - ADIT WITH RE-INJECTION
 DAY 420 OF SIMULATION
 SMALL SCALE CROSS-SECTION

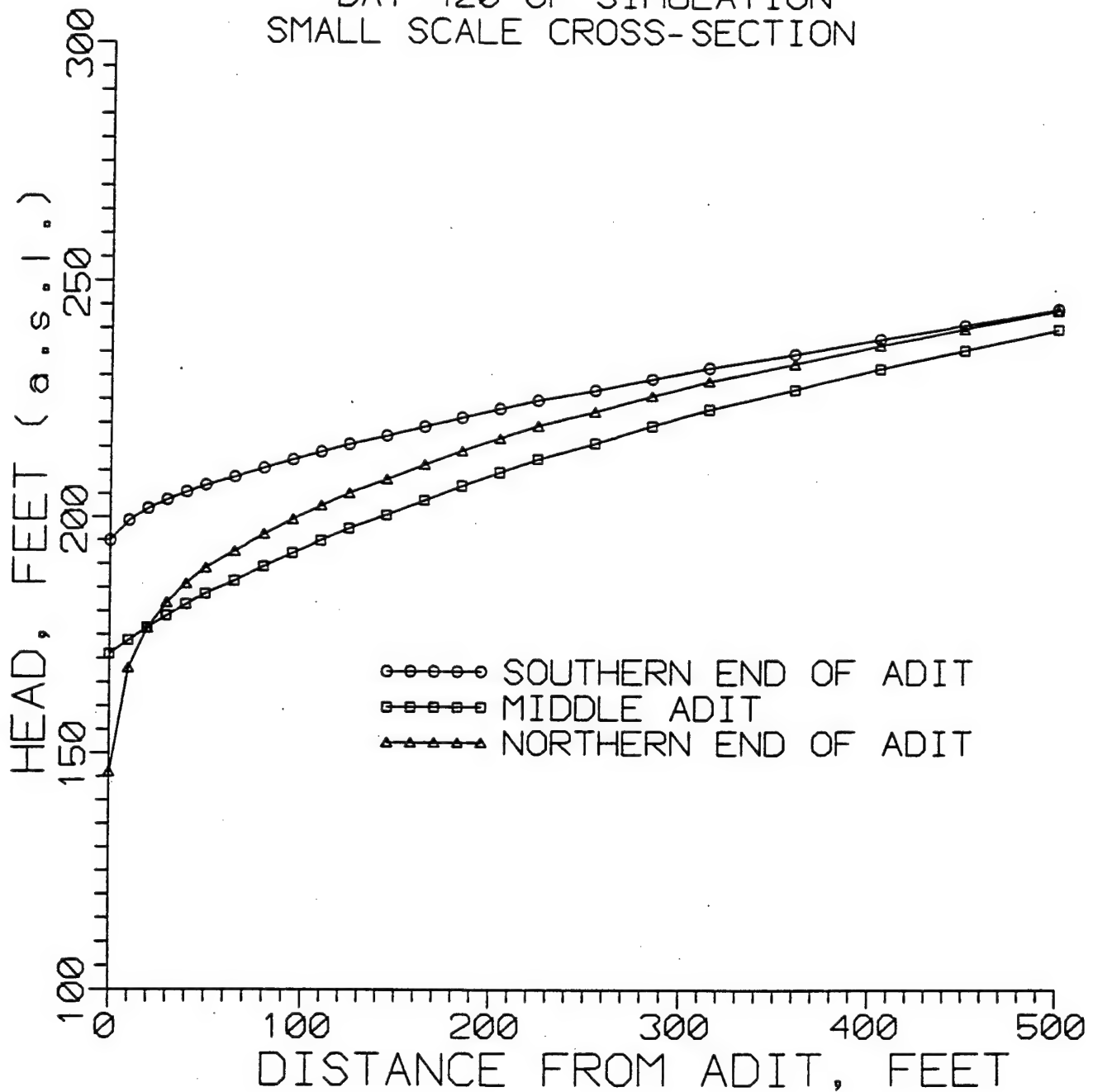


Figure 5-16. Variation in head with distance from the adit at three different locations after 360 days of reinjection commencing 10 days after completion of the adit.

MODEL 30 - MODEL 31 VOLUMETRICS

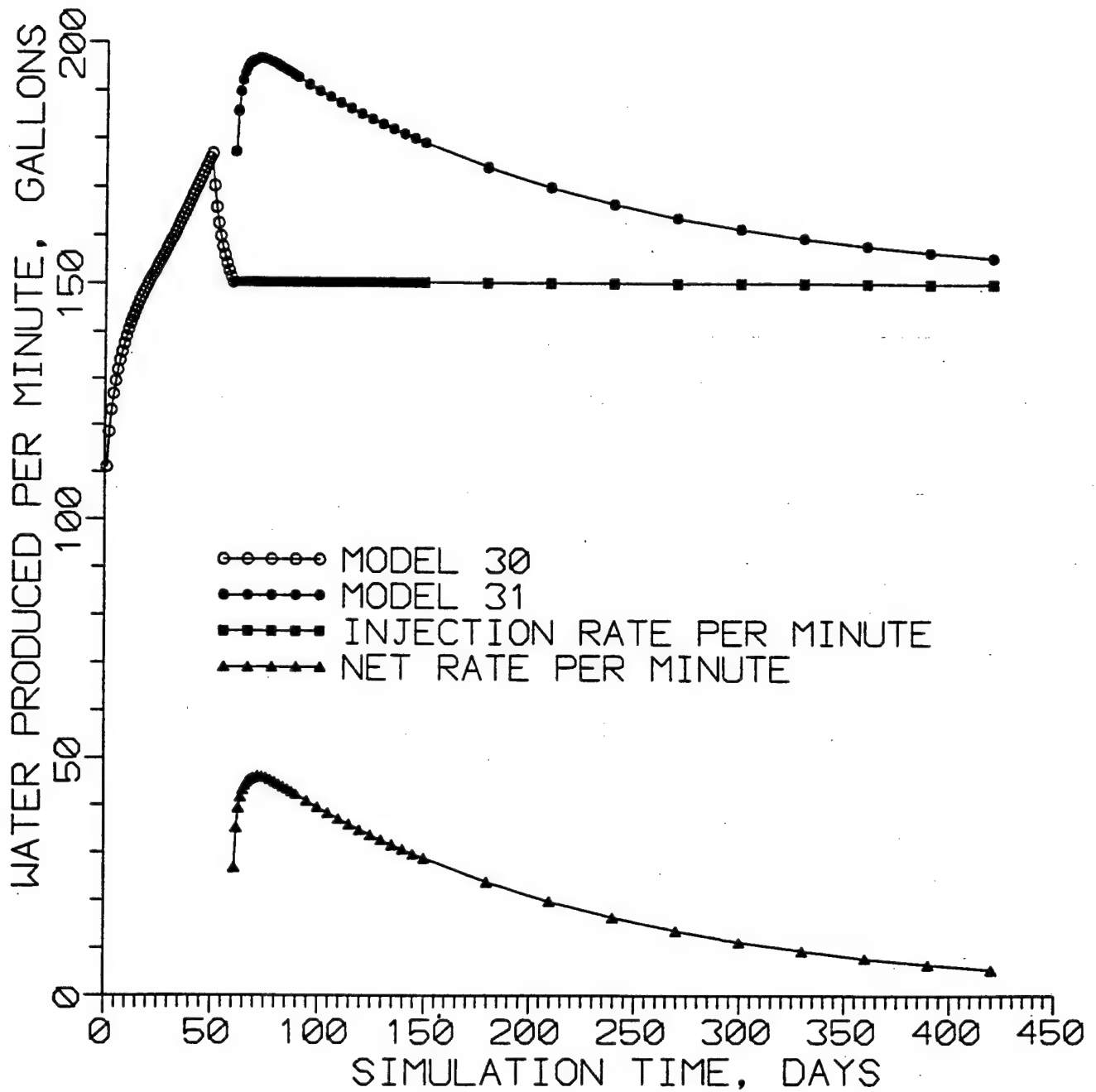


Figure 5-17. Volumetric data from Models 30 and 31 for 50 days of excavation without reinjection and then 350 days of reinjection.

SECTION 6

REFERENCES

Blouin, S.E., and D.E. Chitty (1991), "Characterization of Major Layers at Fort Knox UTP Site and Suggested Method for Selecting Representative Laboratory Test Specimens" (U), Presentation to Waterways Experiment Station, Vicksburg, MS, 6 November 1991. (UNCLASSIFIED)

Green, M.L. (1993), "Ultrasonic Velocity Logs and Stratigraphic Layering for UTP Core Borings CS-1, 2, 3, and 4" (U), US Army Waterways Experiment Station, Vicksburg, MS, 23 February 1993. (UNCLASSIFIED)

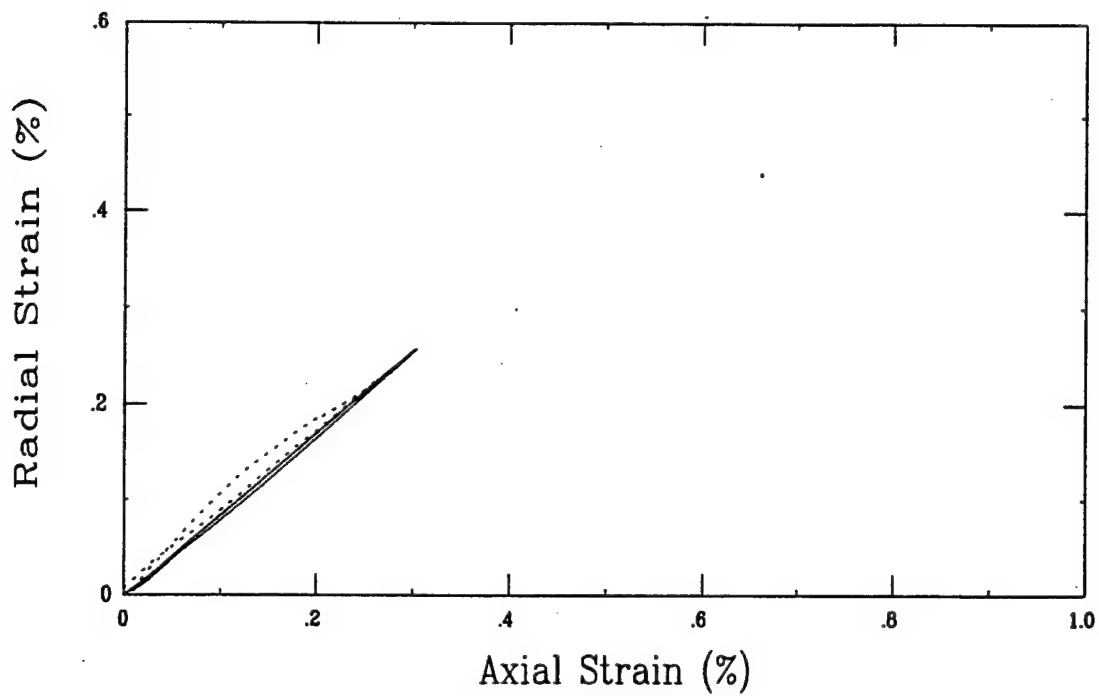
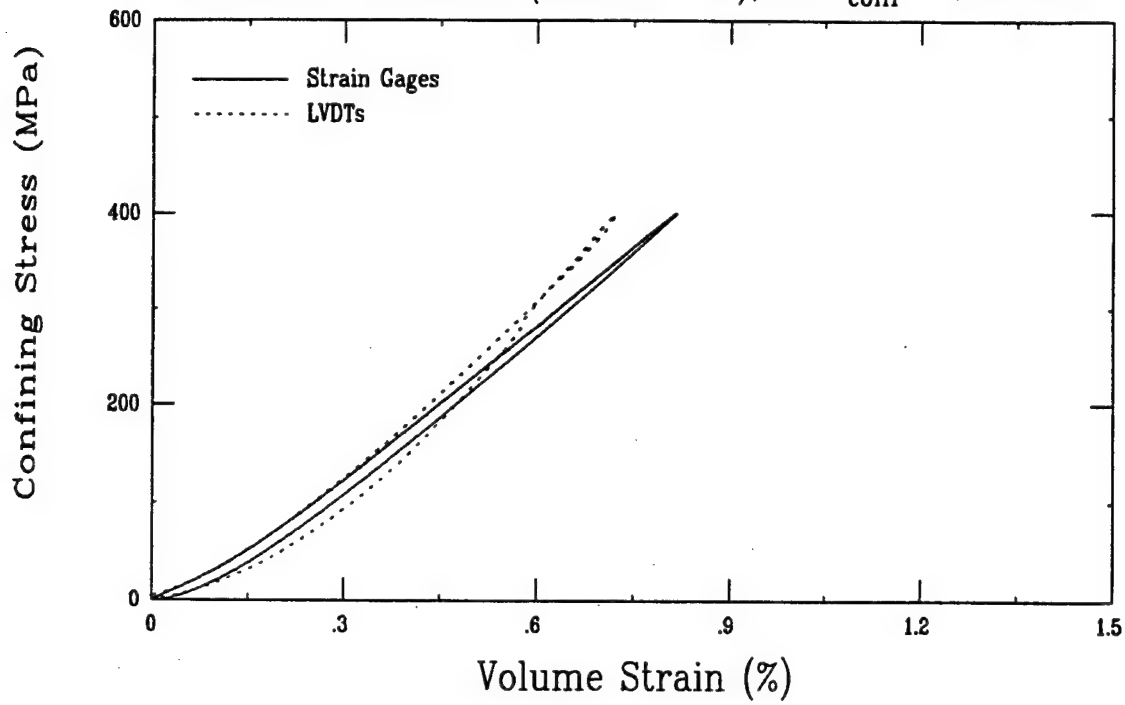
Melzer, L.S. (1993), "Test Design Geotechnical Report, Volume 1 - Technical Report, Underground Technology Program, Roger's Hollow, Ft. Knox, KY" (U), Defense Nuclear Agency Technical Report 92-142, Jan '92. (UNCLASSIFIED)

Melzer, L. S, Stiles, L.H., Covarubbias, O.M., and Reeves, James R.(1995), "Effects of Hydrological Pumping of the Underground Technology Program Access Adit" (U), Report by the Center for Energy and Economic Diversification, Midland, TX to the US Army Corps of Engineers, Waterway Experiment Station, Contract DACA39-93-C-0129, Final Report, March 1995. (UNCLASSIFIED)

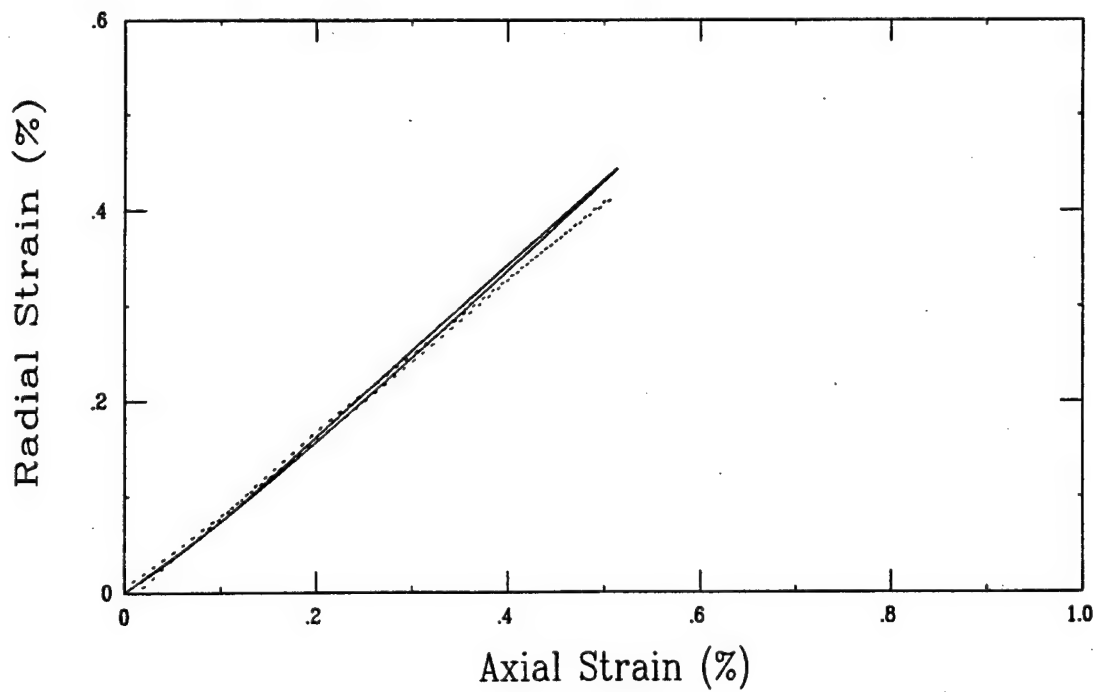
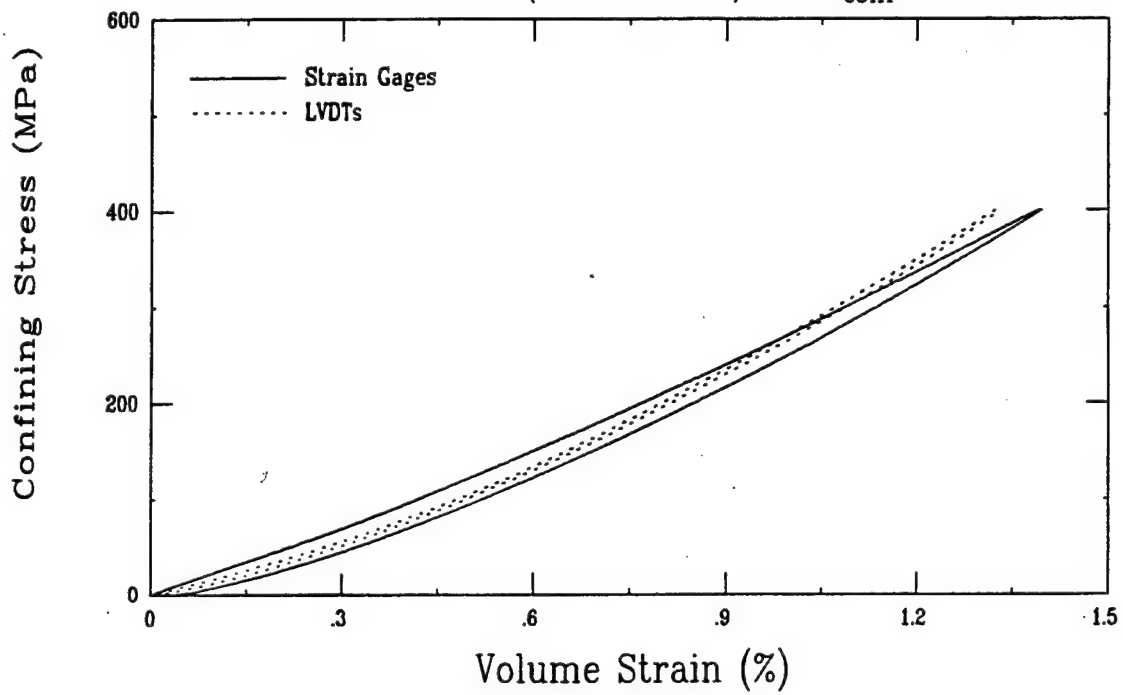
Warriner, J. (1991), "Geohydrological Testing - Pump Test, Ft. Knox, UTP" (U), Waterways Experiment Station Letter Report, September 1991 (Draft). (UNCLASSIFIED)

APPENDIX A
HYDROSTATIC COMPRESSION TESTS ON
CARBONATE ROCKS FROM FORT KNOX

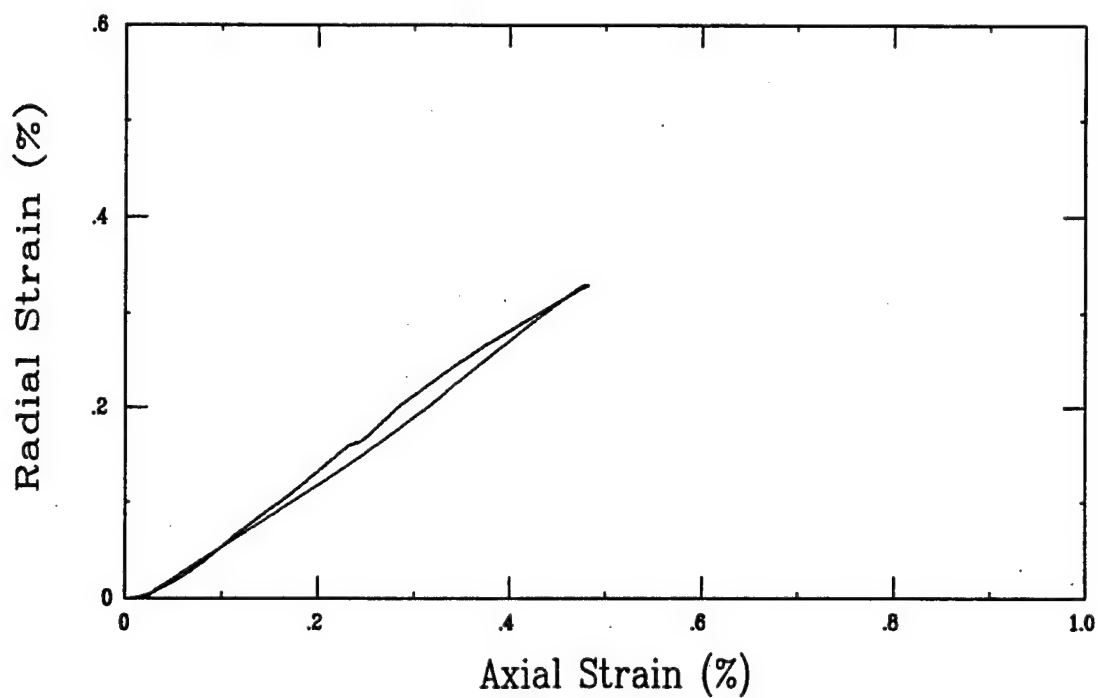
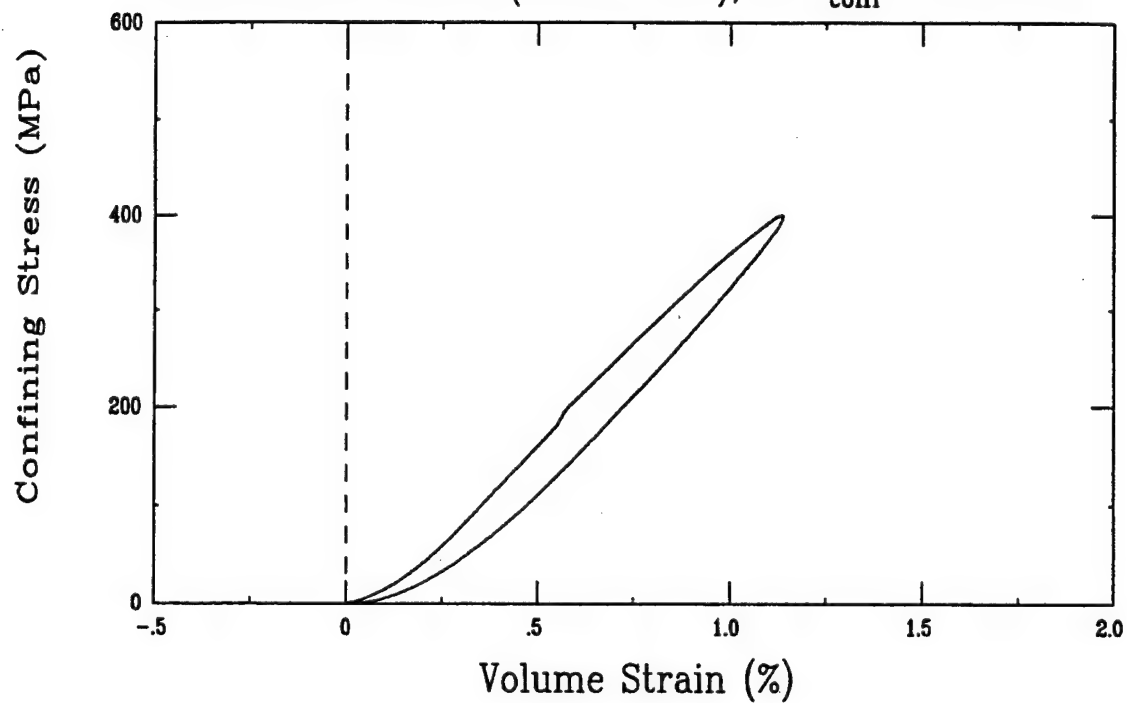
Hydrostatic Compression Test (Y20A3)
Ft. Knox Limestone (FK10-1-05), to $\sigma_{\text{conf}} = 400$ MPa



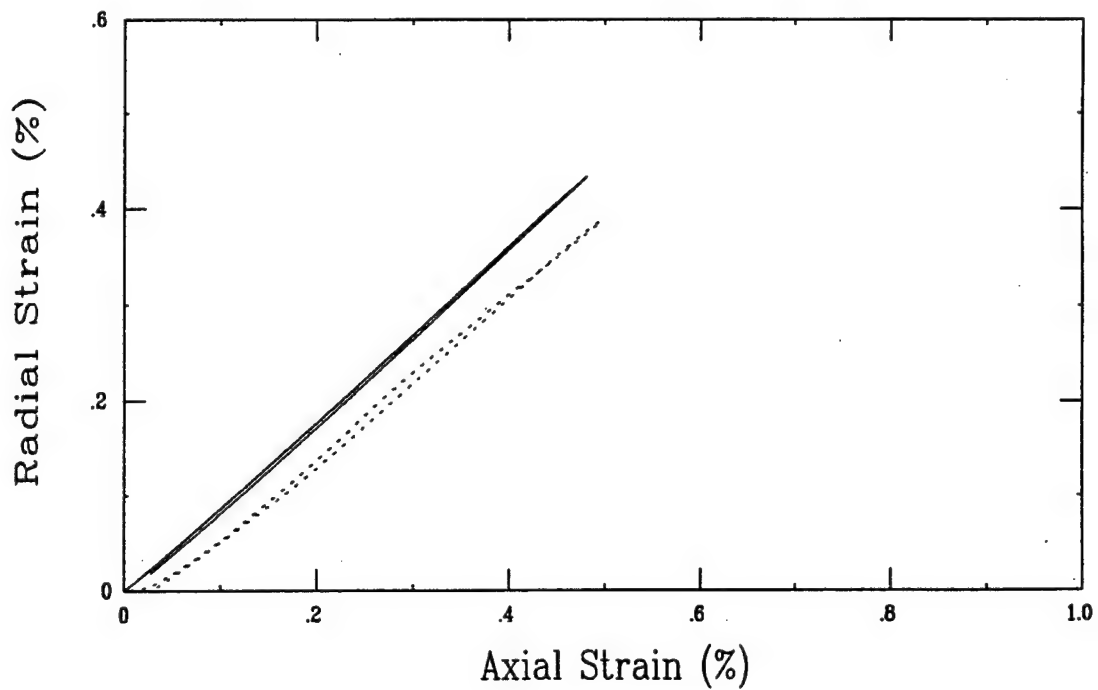
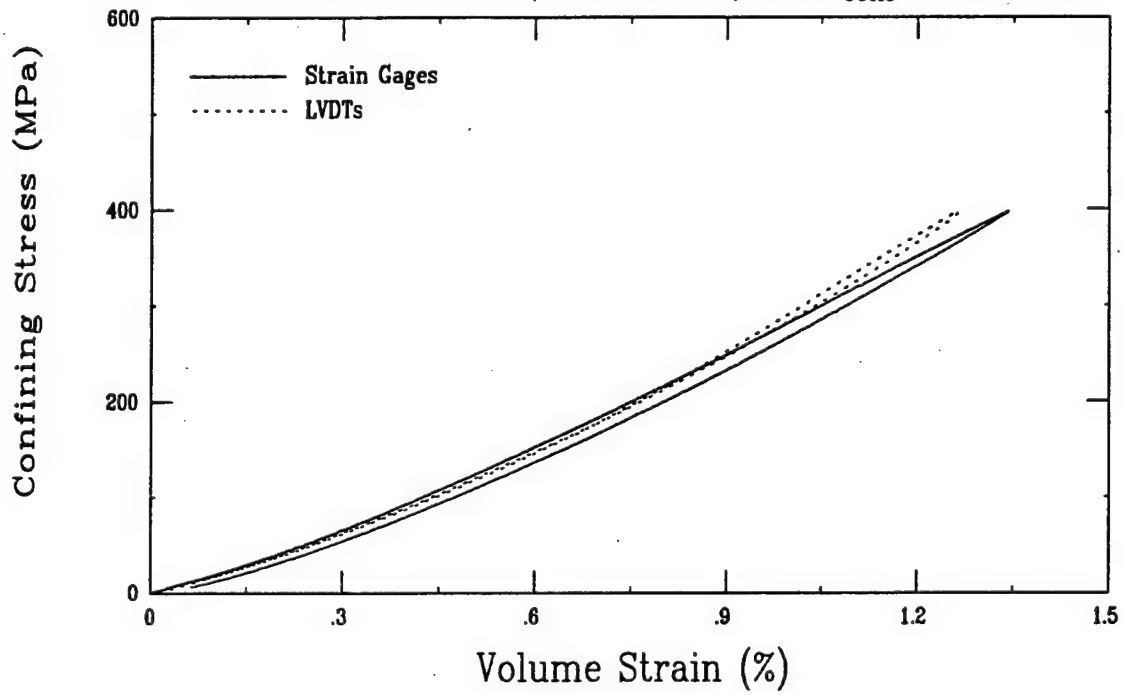
Hydrostatic Compression Test (Y20B3)
Ft. Knox Limestone (FK10-2-06), to $\sigma_{\text{conf}} = 400$ MPa



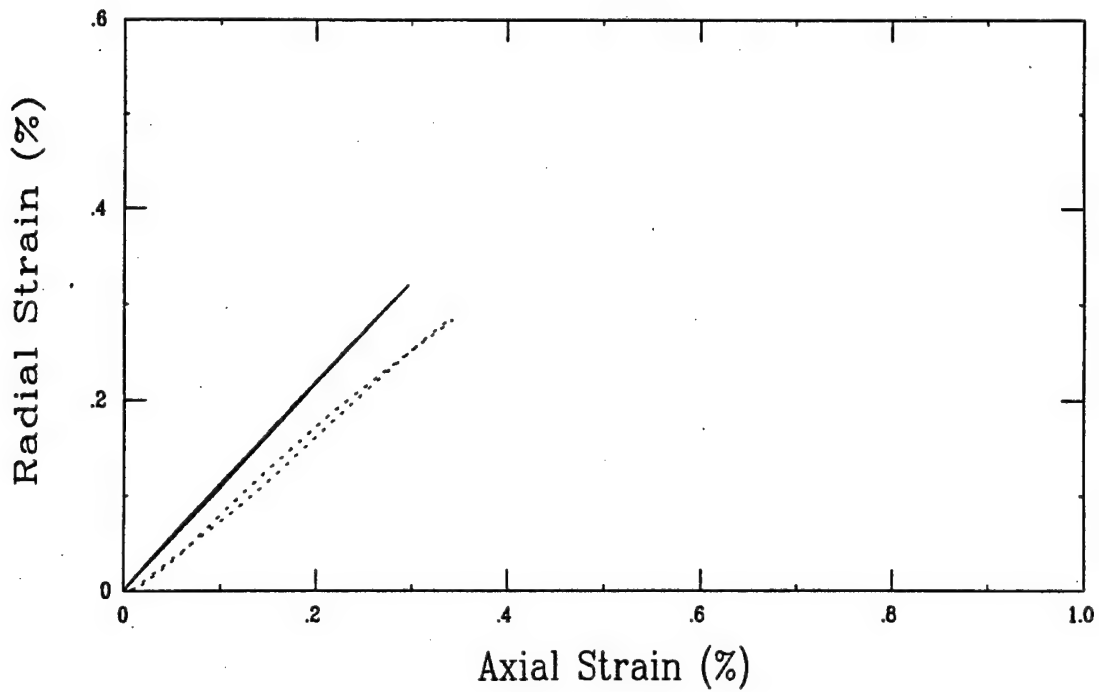
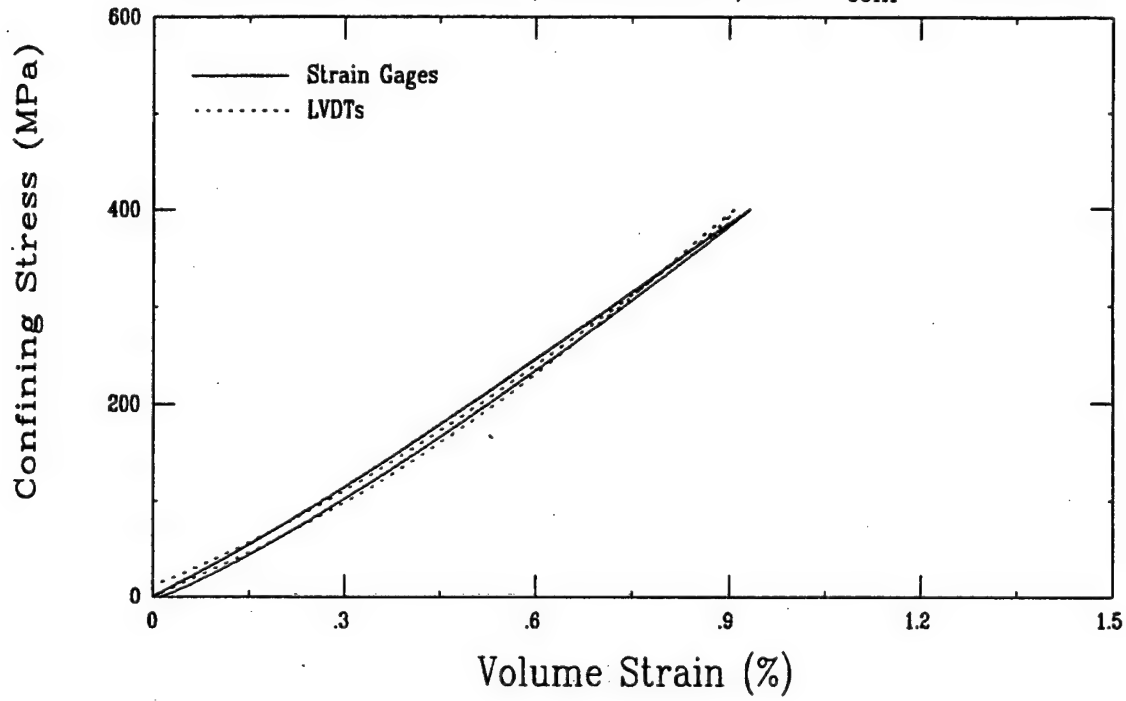
Hydrostatic Compression Test (A20B3)
Ft. Knox Limestone (FK10-3-02), to $\sigma_{\text{conf}} = 400$ MPa



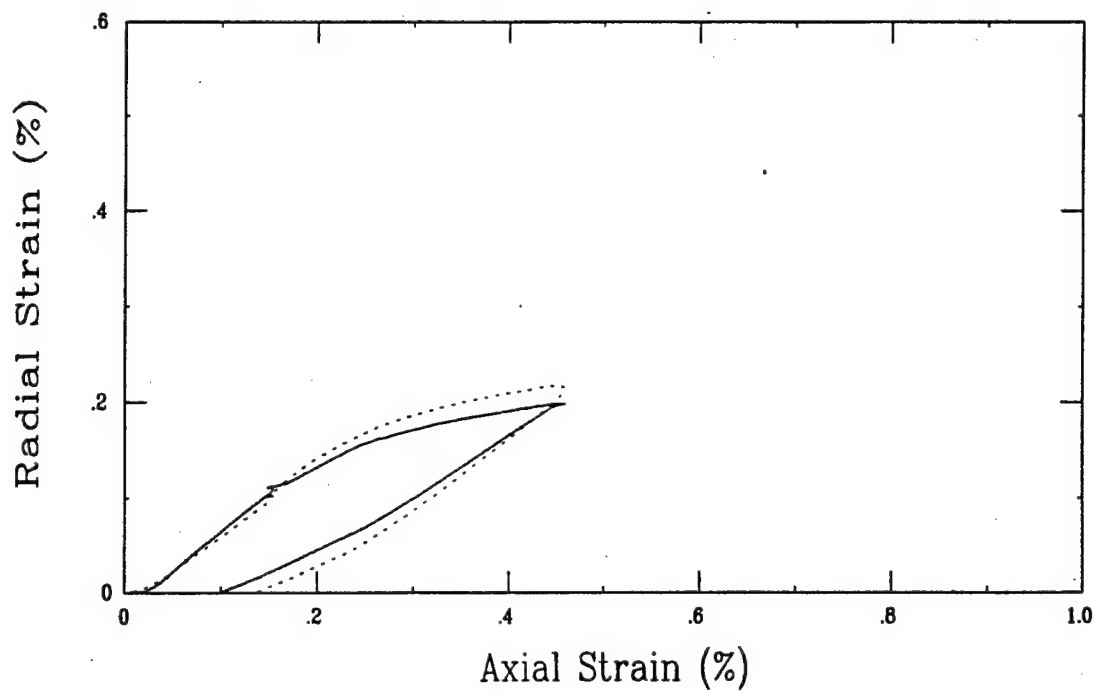
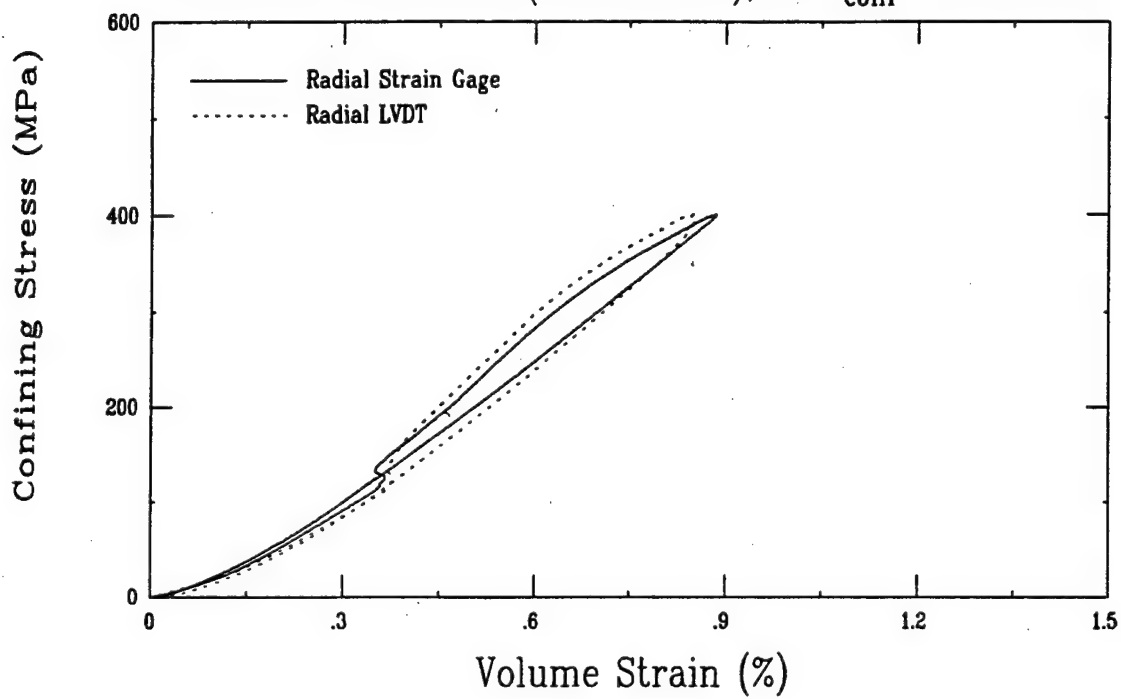
Hydrostatic Compression Test (Y21A3)
Ft. Knox Limestone (FK10-4-04), to $\sigma_{\text{conf}} = 400$ MPa



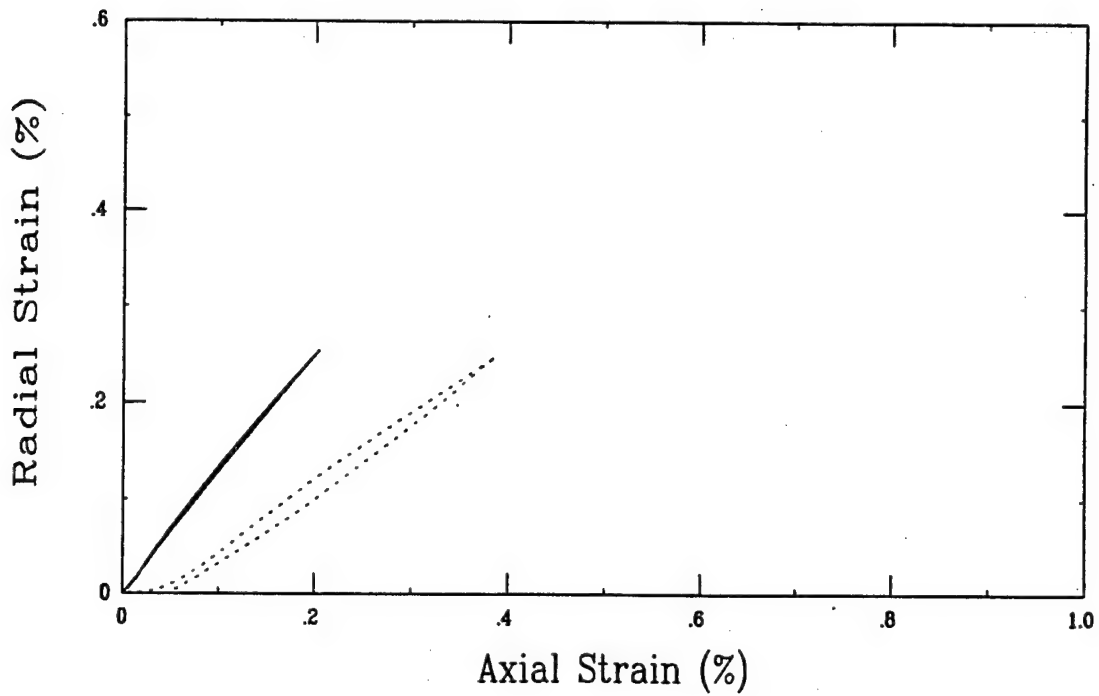
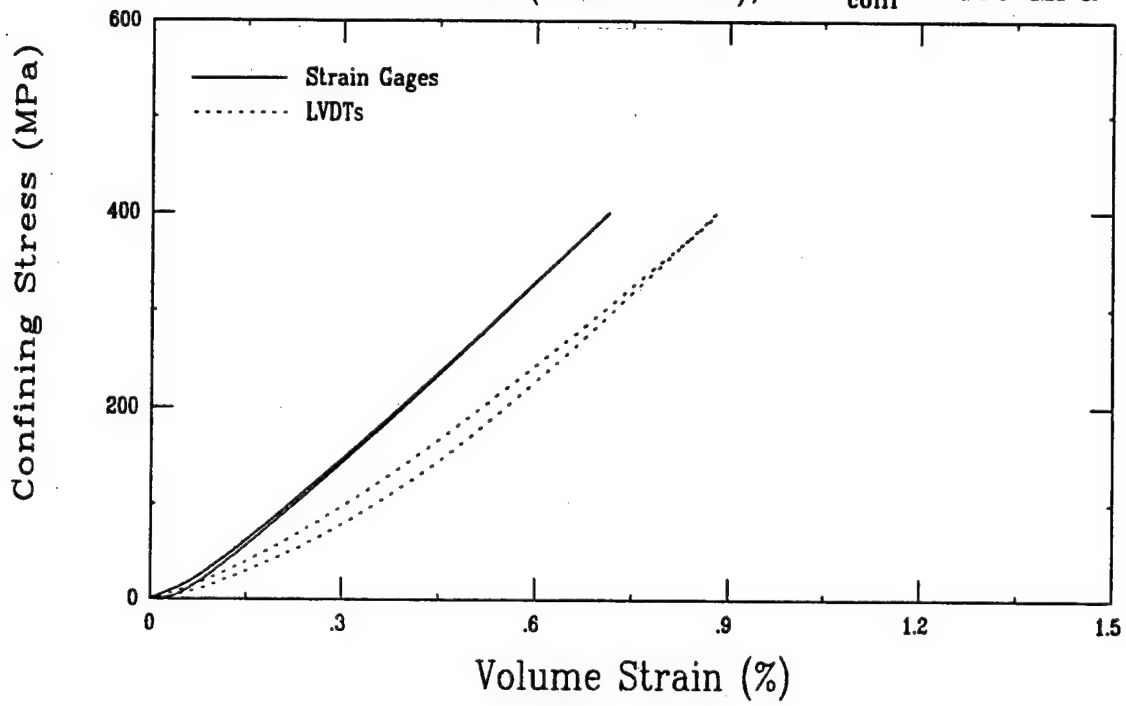
Hydrostatic Compression Test (Y21B3)
Ft. Knox Limestone (FK10-5-05), to $\sigma_{\text{conf}} = 400$ MPa



Hydrostatic Compression Test (U7A3)
Ft. Knox Limestone (FK10-6-06), to $\sigma_{\text{conf}} = 400$ MPa

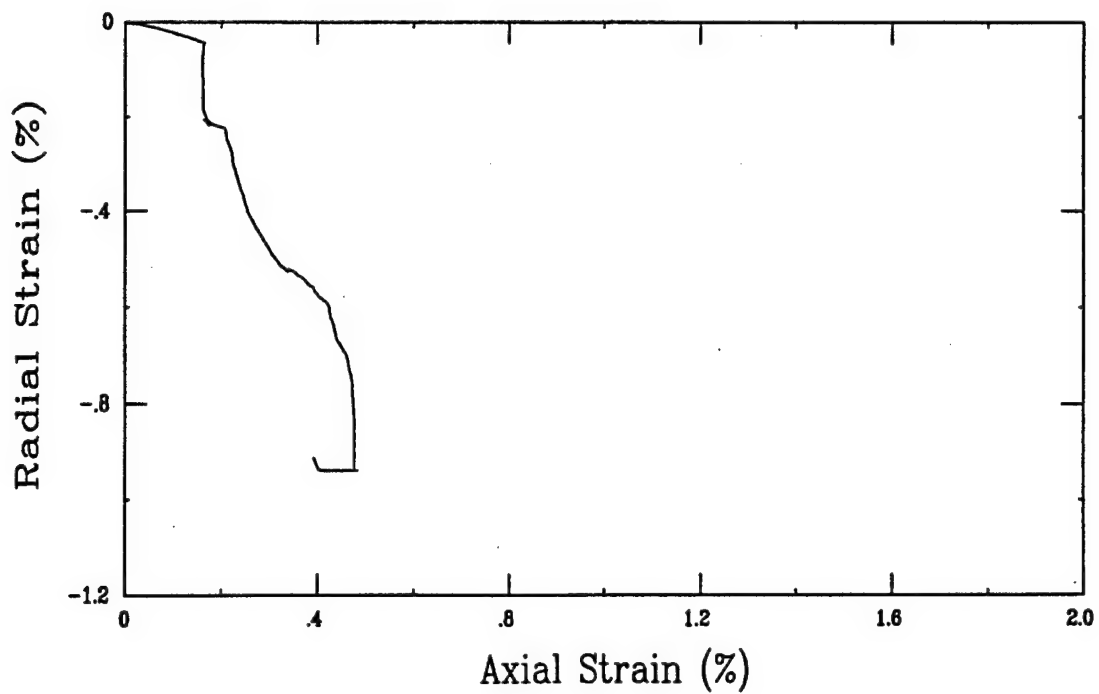
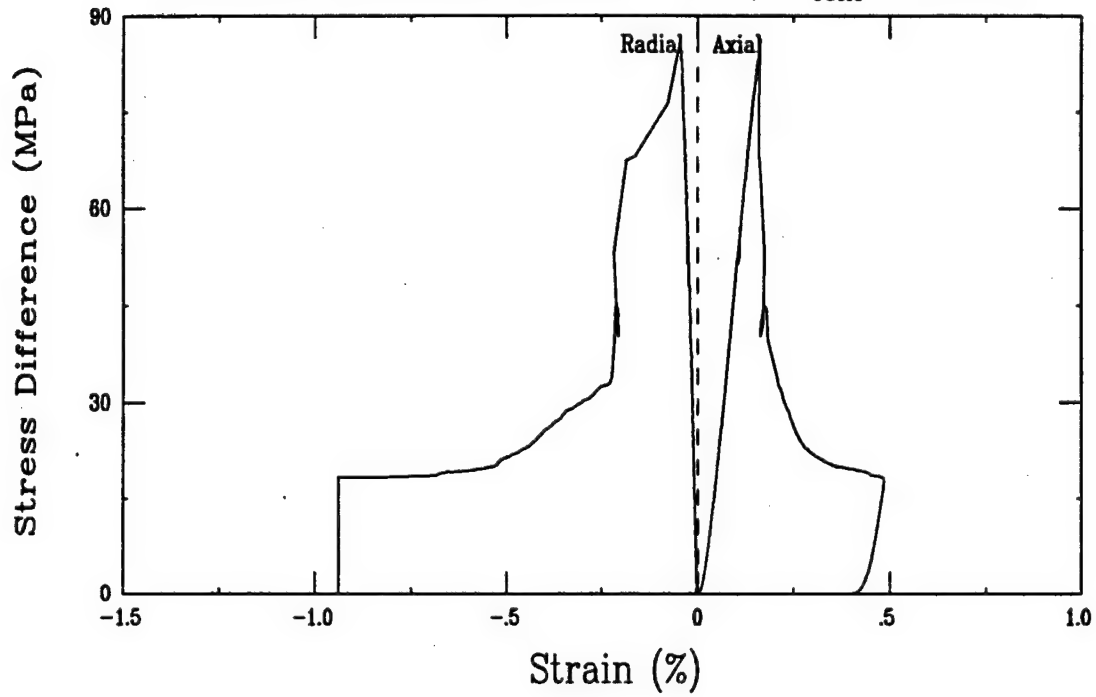


Hydrostatic Compression Test (Y21C3)
Ft. Knox Limestone (FK10-7-04), to $\sigma_{\text{conf}} = 400$ MPa

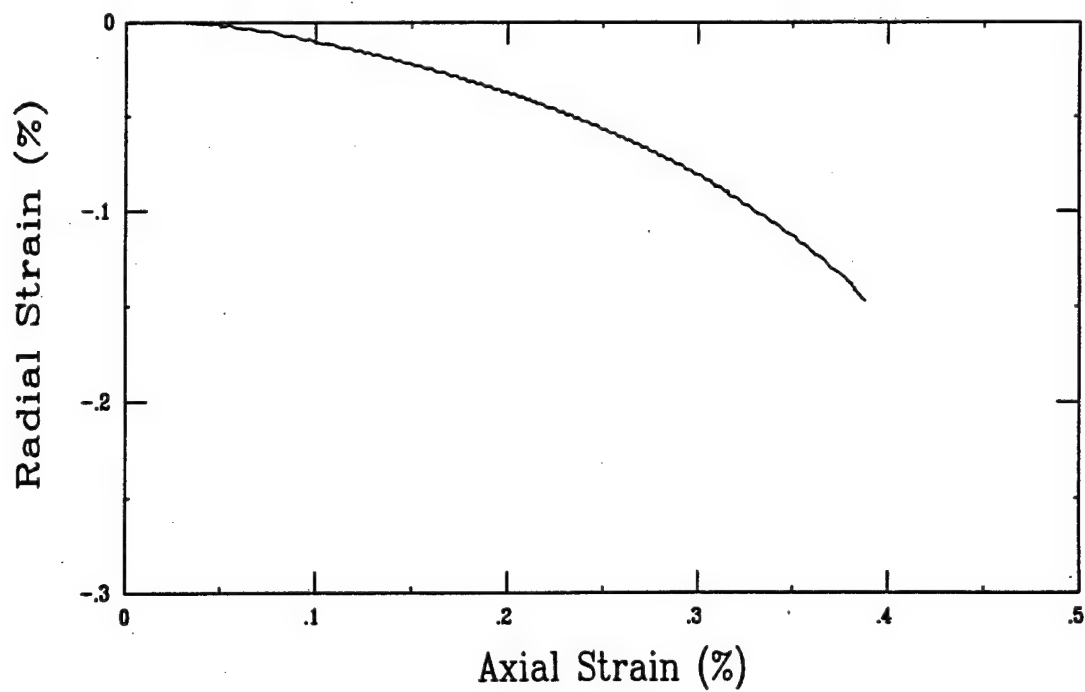
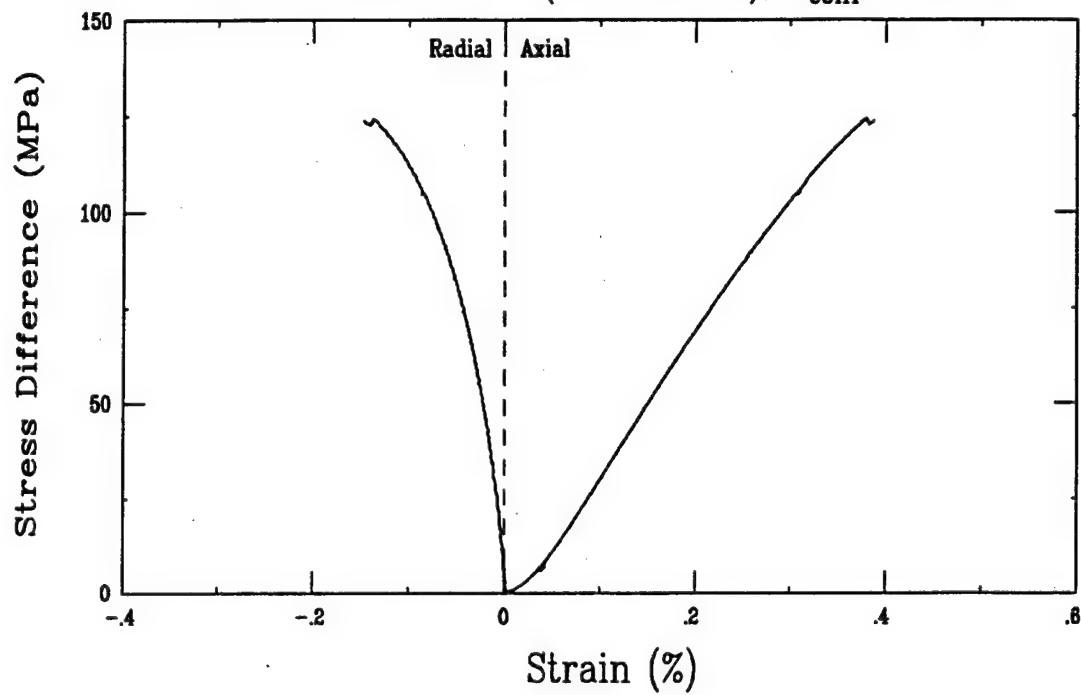


APPENDIX B
UNCONFINED COMPRESSION TESTS ON
CARBONATE ROCKS FROM FORT KNOX

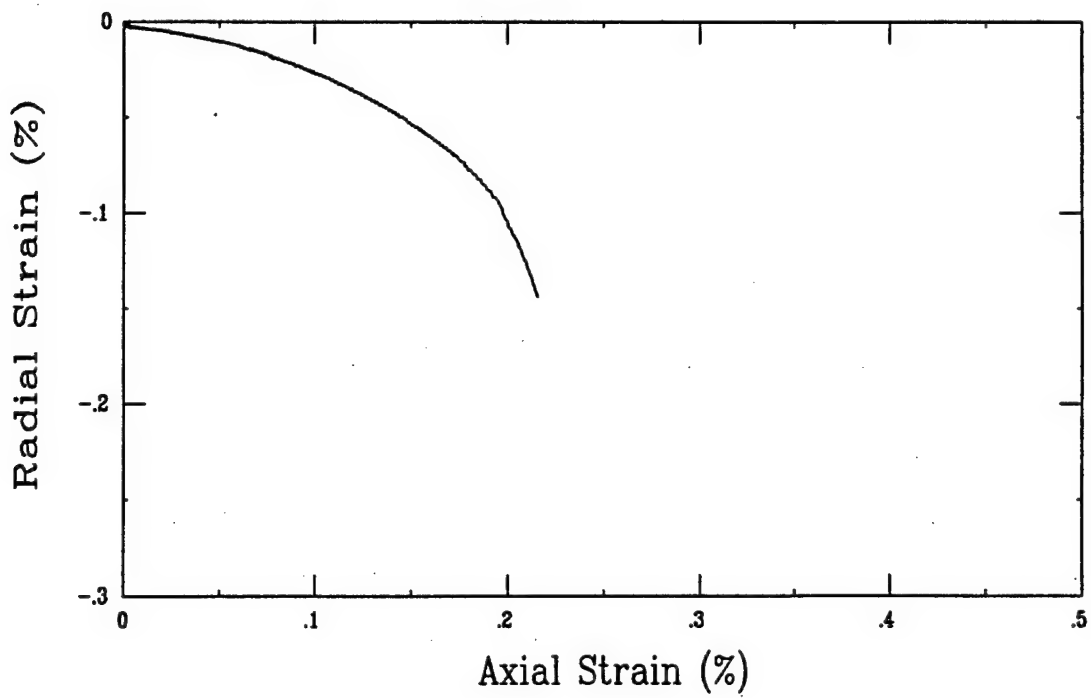
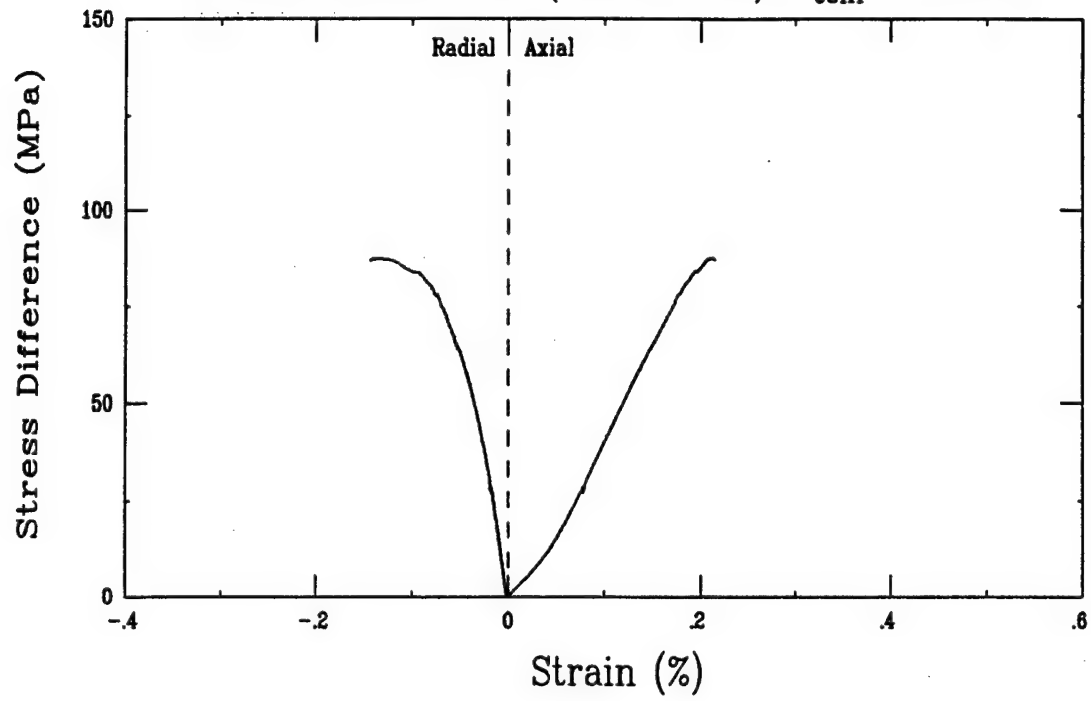
Triaxial Compression Test (A15E3)
Ft. Knox Limestone (FK10-1-02), $\sigma_{\text{conf}} = 0$ MPa



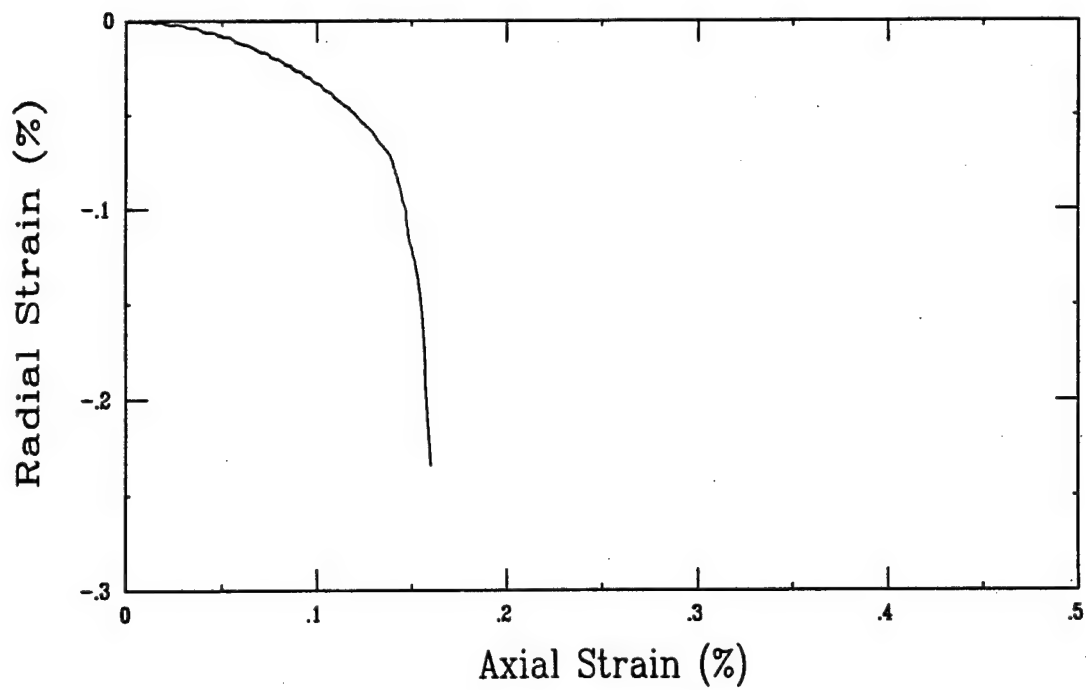
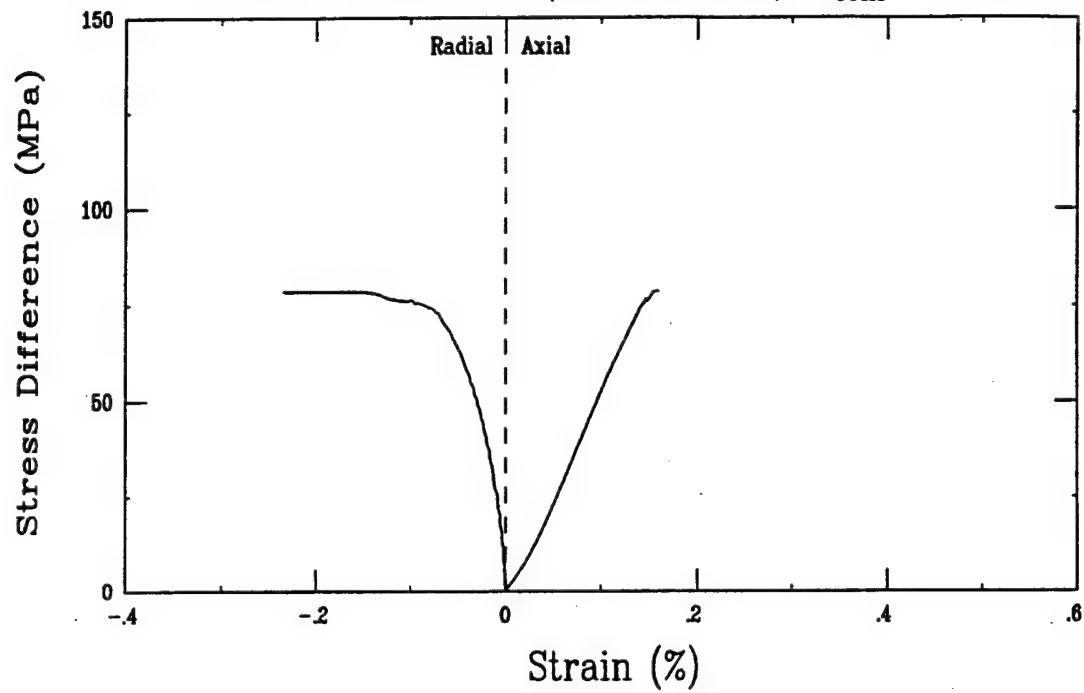
Triaxial Compression Test (A15B3)
Ft. Knox Limestone (FK10-2-03), $\sigma_{\text{conf}} = 0$ MPa



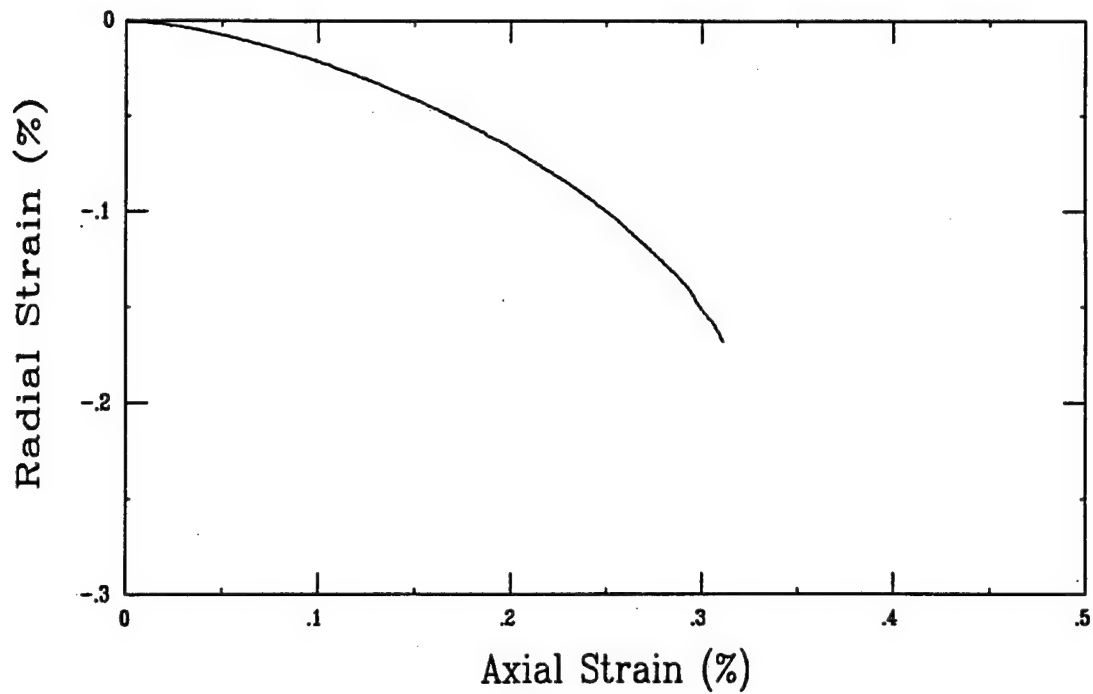
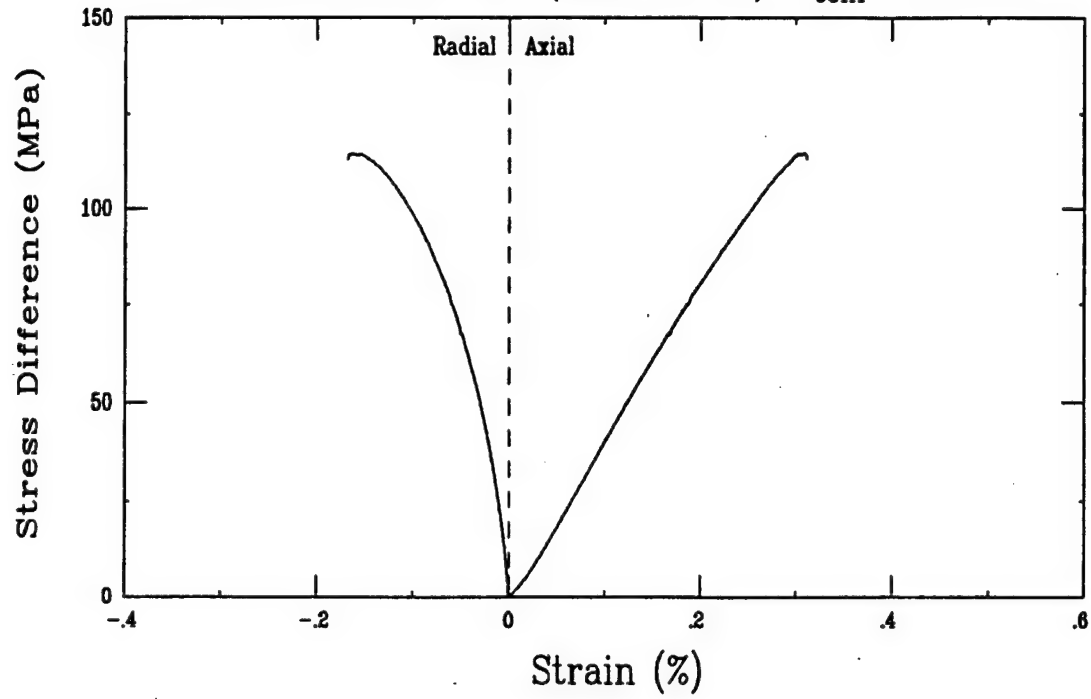
Triaxial Compression Test (A14C3)
Ft. Knox Limestone (FK10-6-01), $\sigma_{\text{conf}} = 0$ MPa



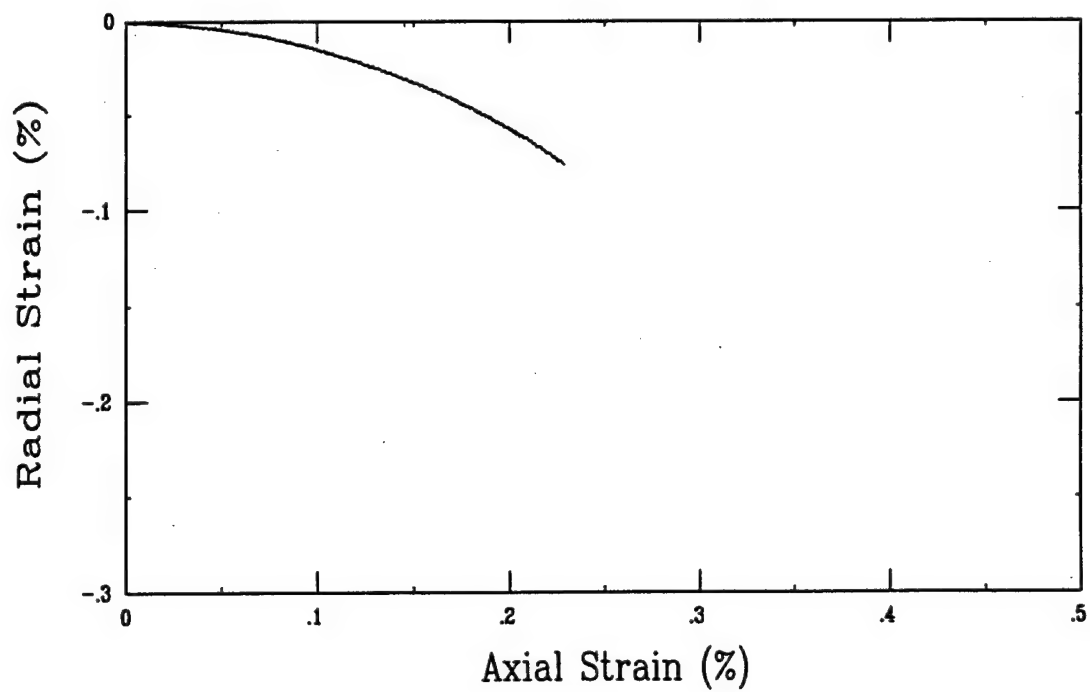
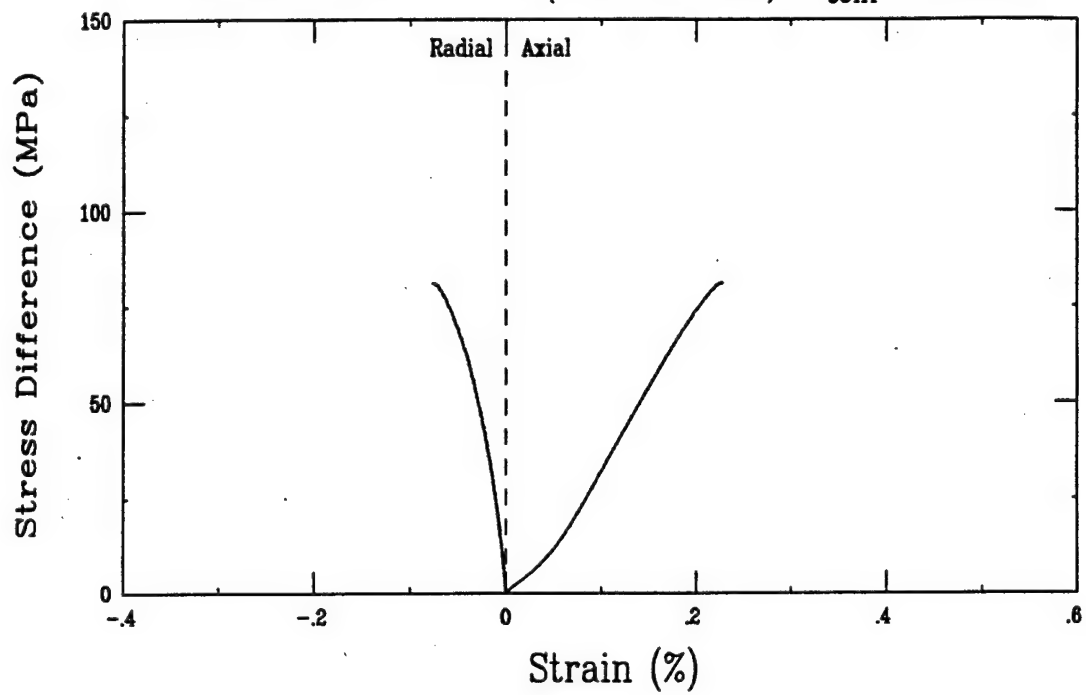
Triaxial Compression Test (A15D3)
Ft. Knox Limestone (FK10-4-01H), $\sigma_{\text{conf}} = 0$ MPa



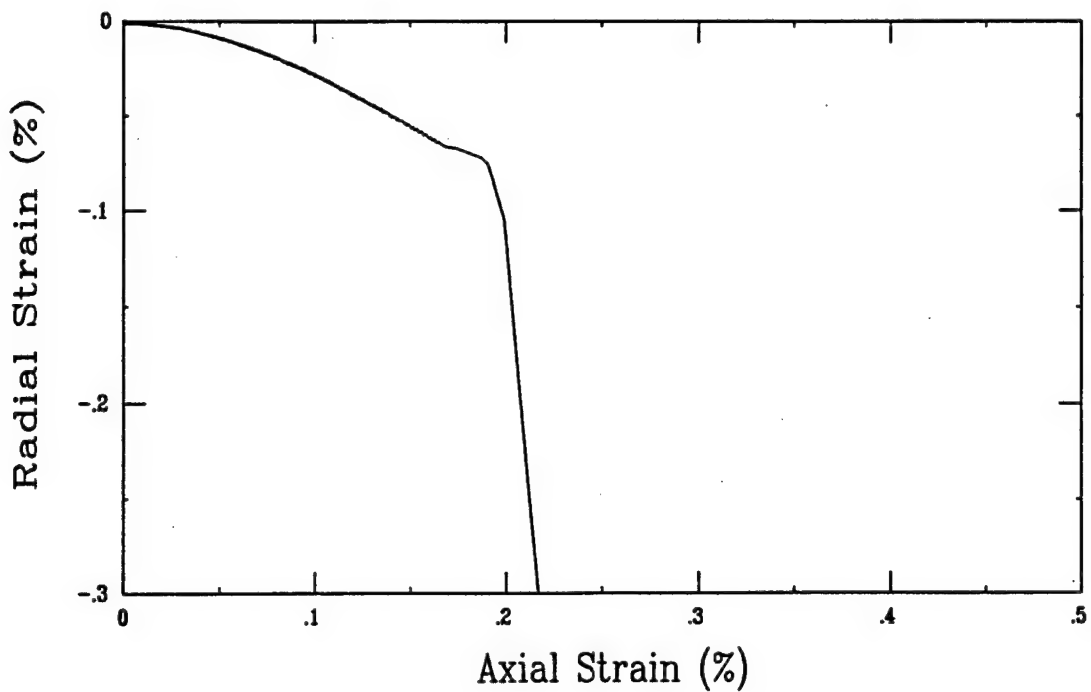
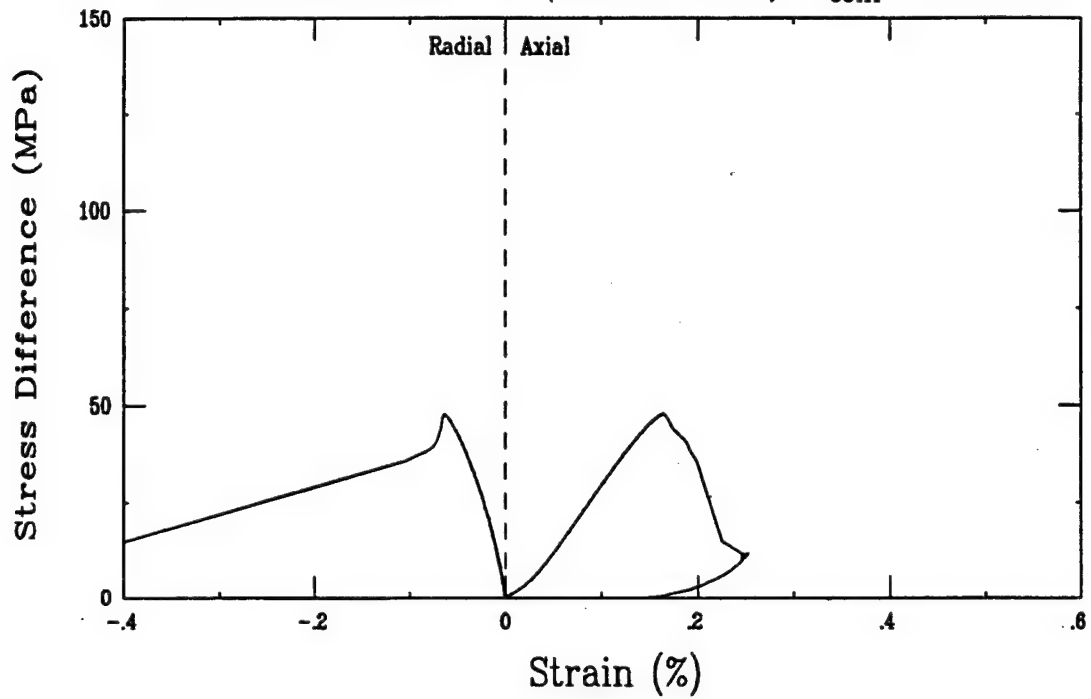
Triaxial Compression Test (A16A3)
Ft. Knox Limestone (FK10-4-03), $\sigma_{\text{conf}} = 0$ MPa



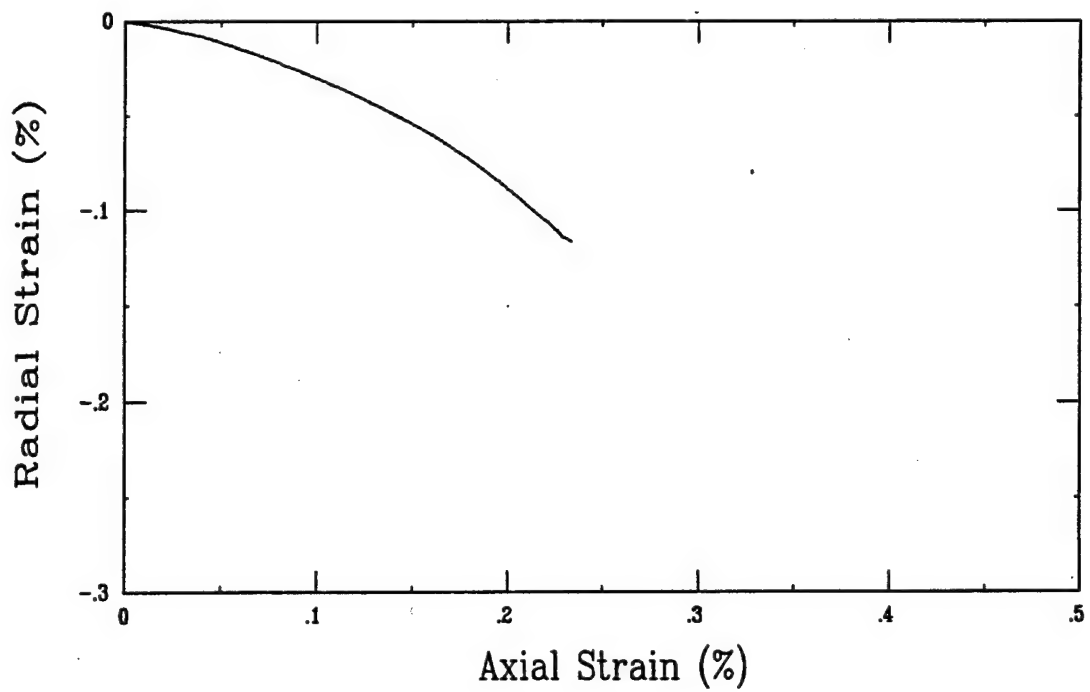
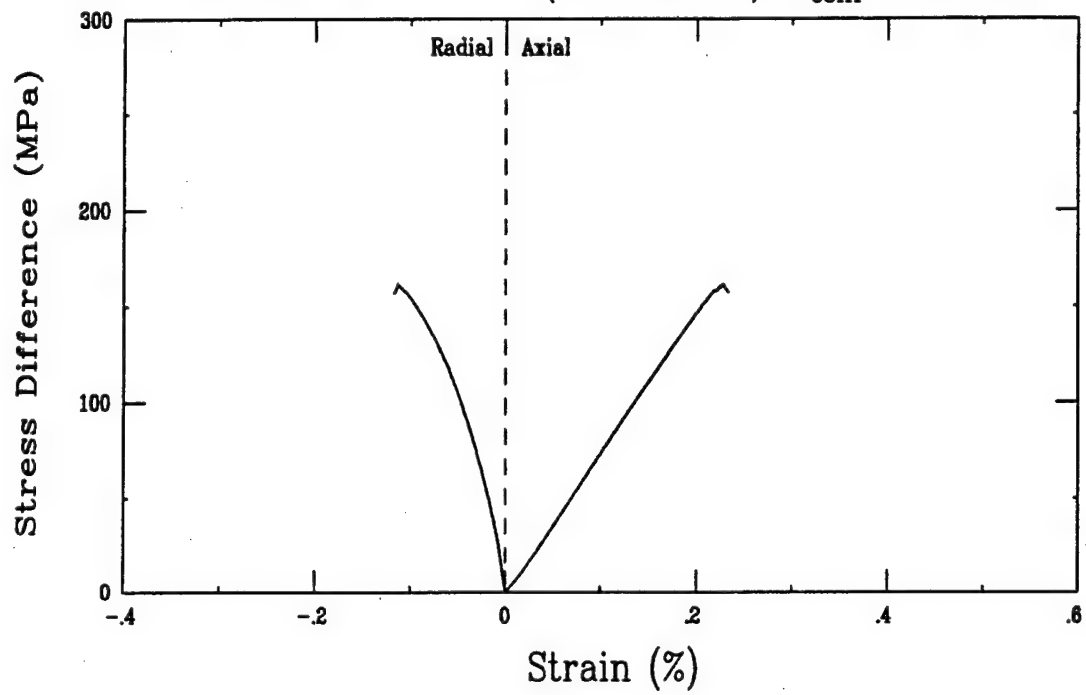
Triaxial Compression Test (A14B3)
Ft. Knox Limestone (FK10-4-06L), $\sigma_{\text{conf}} = 0$ MPa



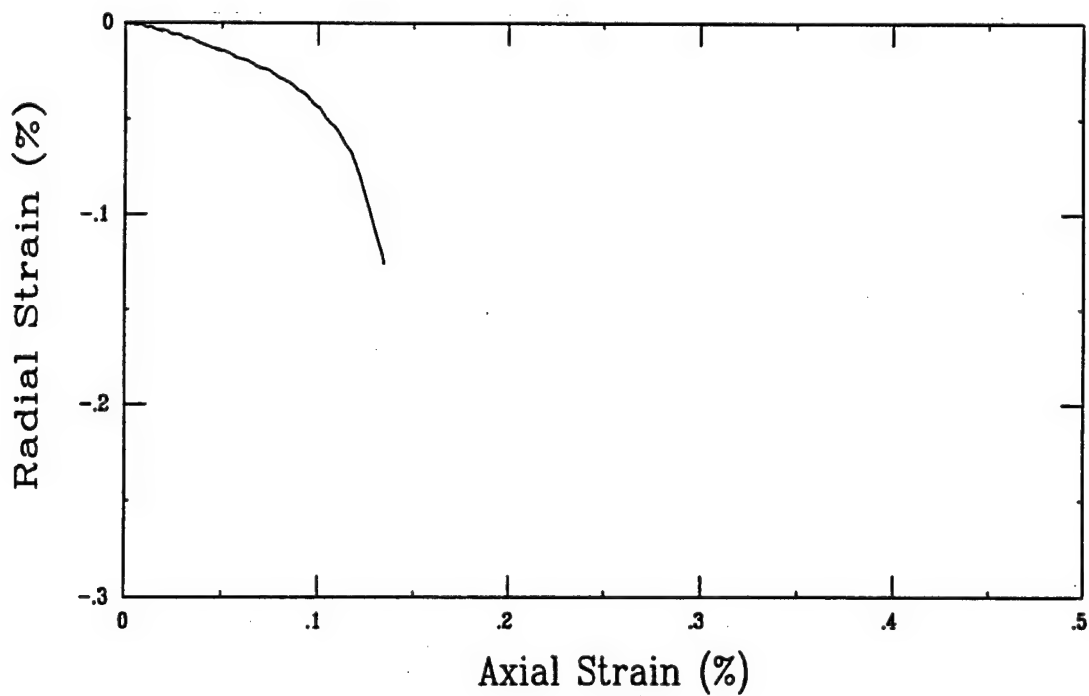
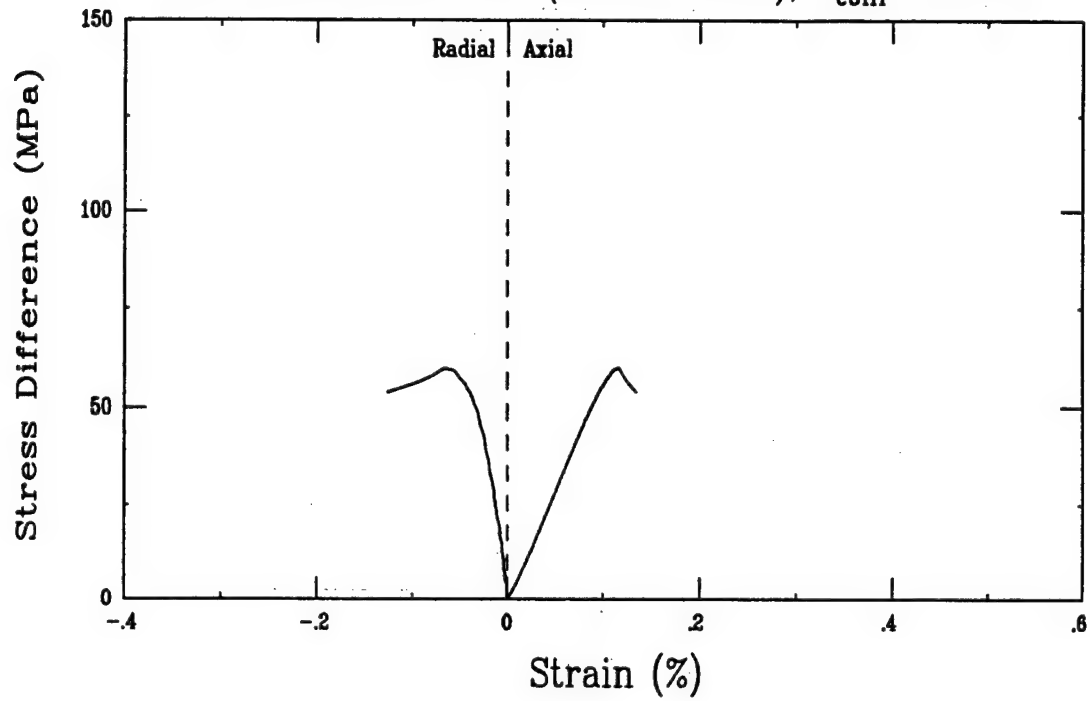
Triaxial Compression Test (A14A3)
Ft. Knox Limestone (FK10-4-07L), $\sigma_{\text{conf}} = 0$ MPa



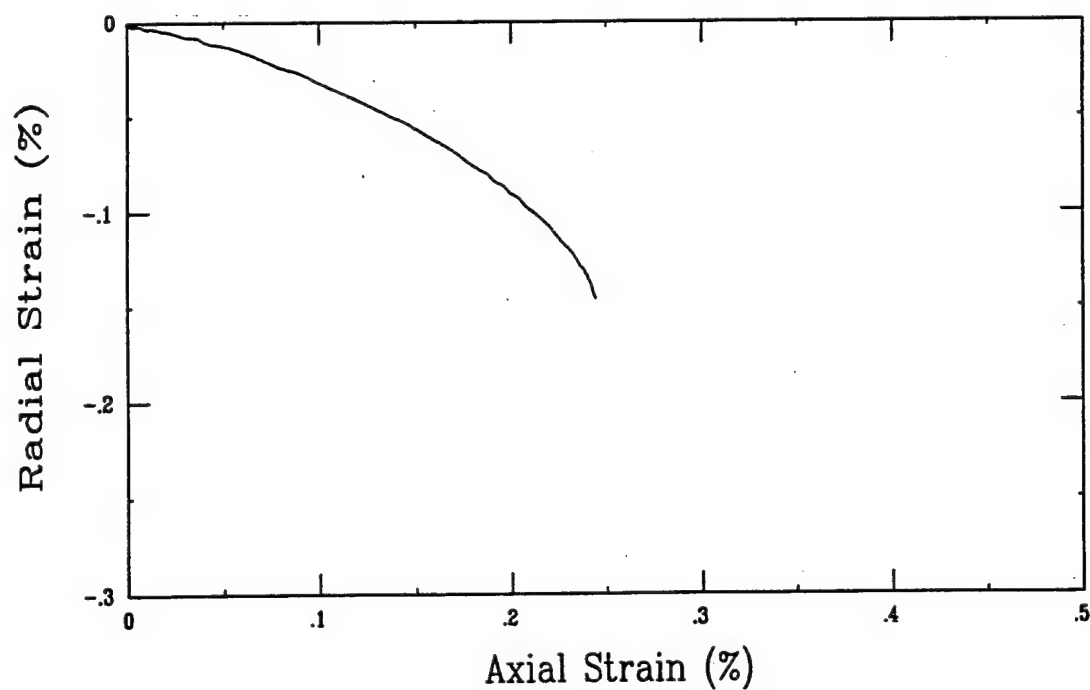
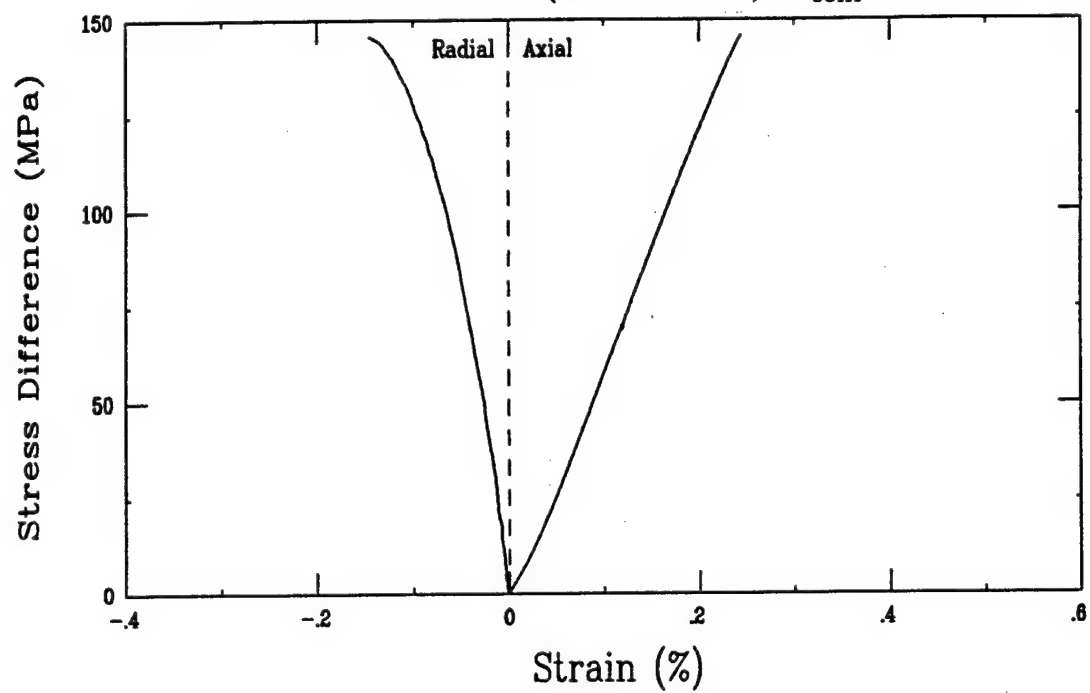
Triaxial Compression Test (A16B3)
Ft. Knox Limestone (FK10-5-04), $\sigma_{conf} = 0$ MPa



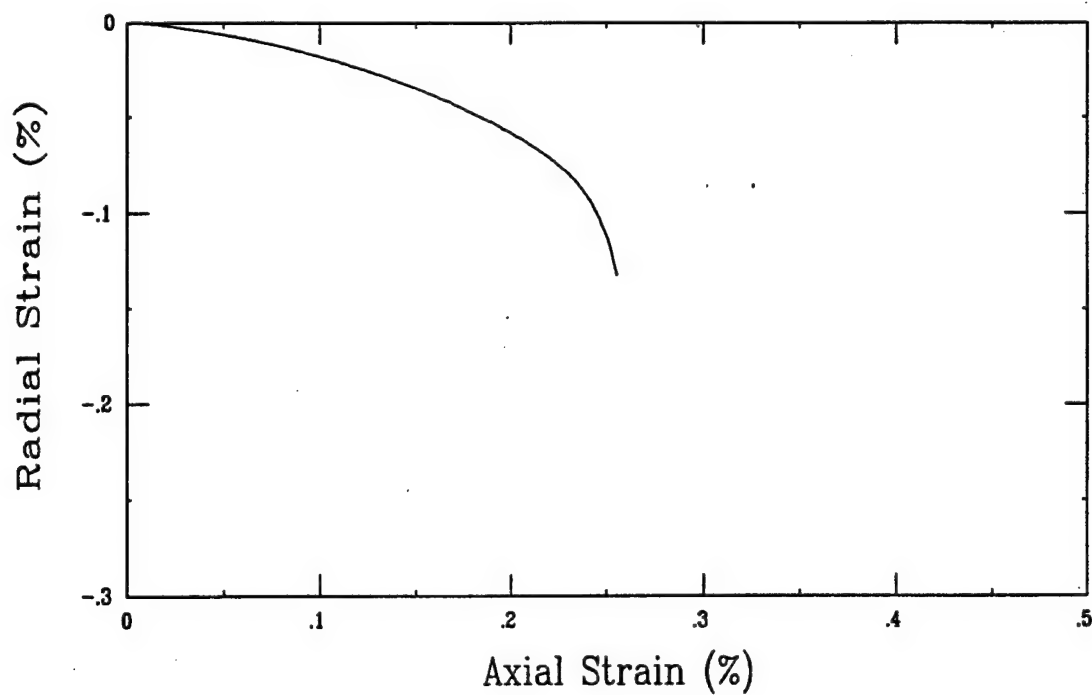
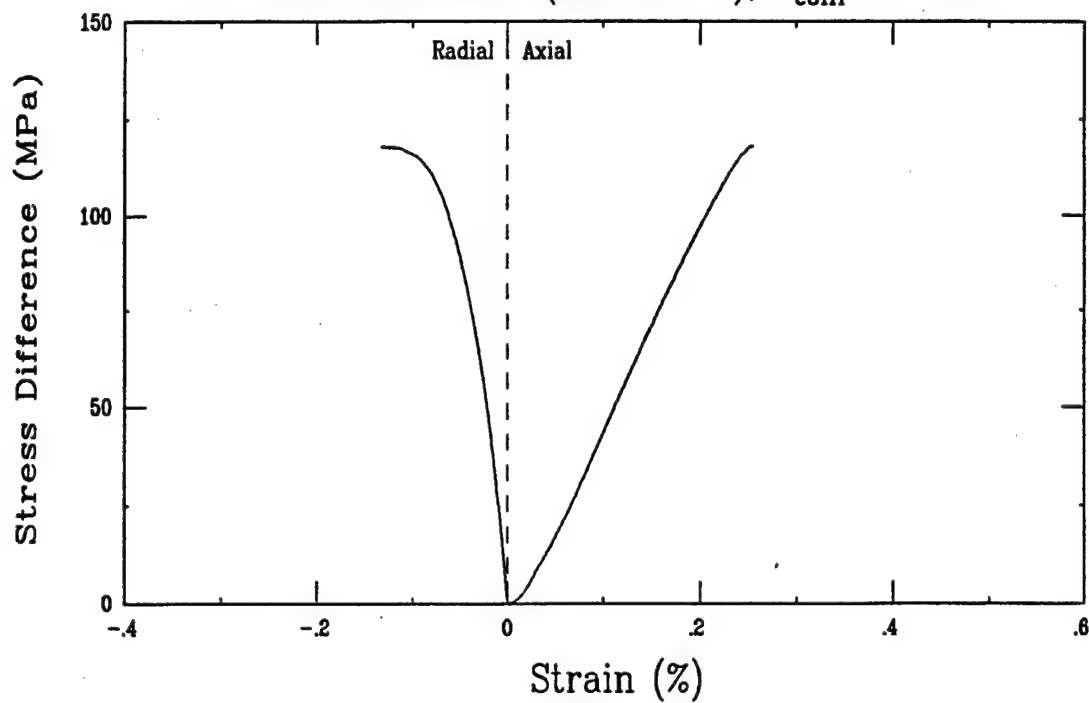
Triaxial Compression Test (A15A3)
Ft. Knox Limestone (FK10-6-010), $\sigma_{conf} = 0$ MPa



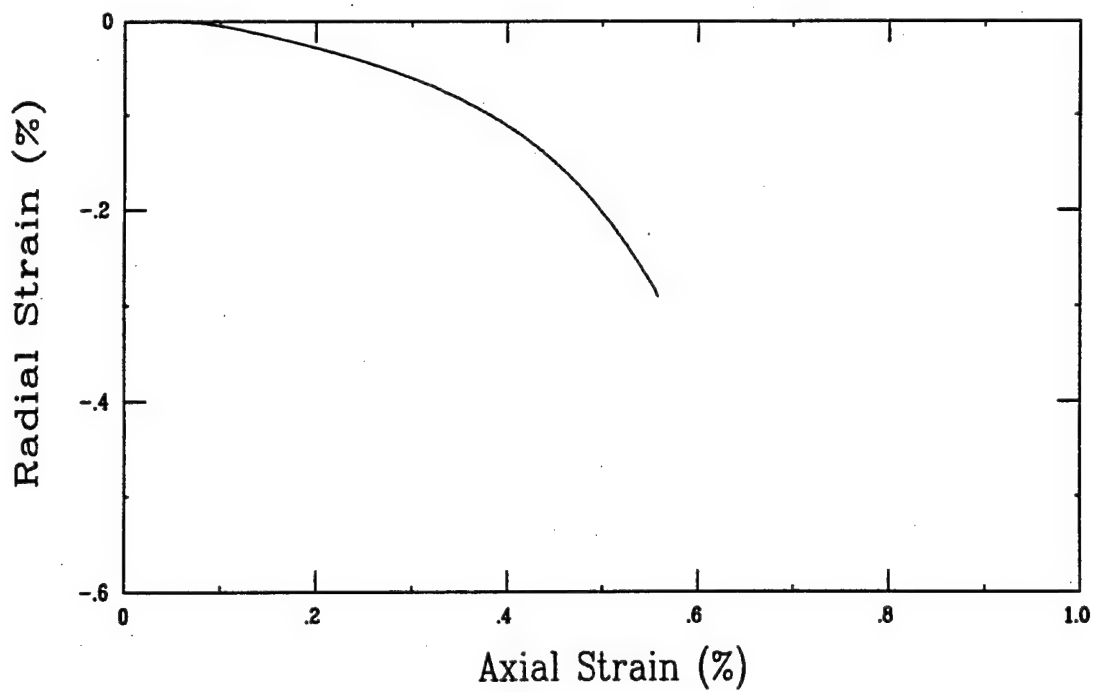
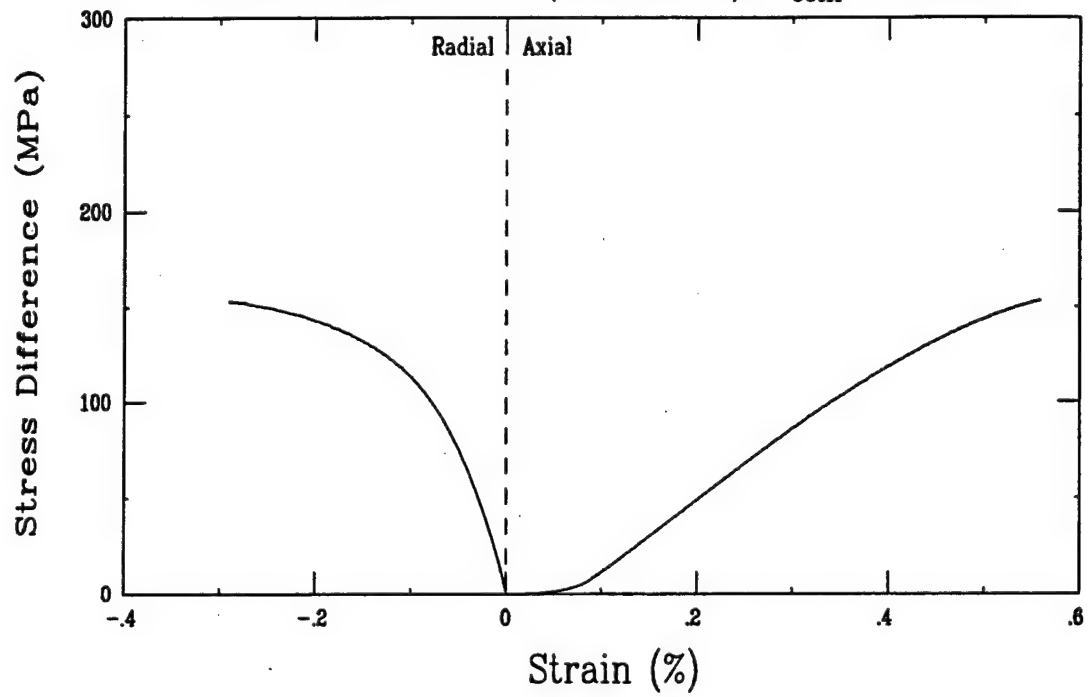
Triaxial Compression Test (A15C3)
Ft. Knox Limestone (FK10-7-02), $\sigma_{\text{conf}} = 0$ MPa



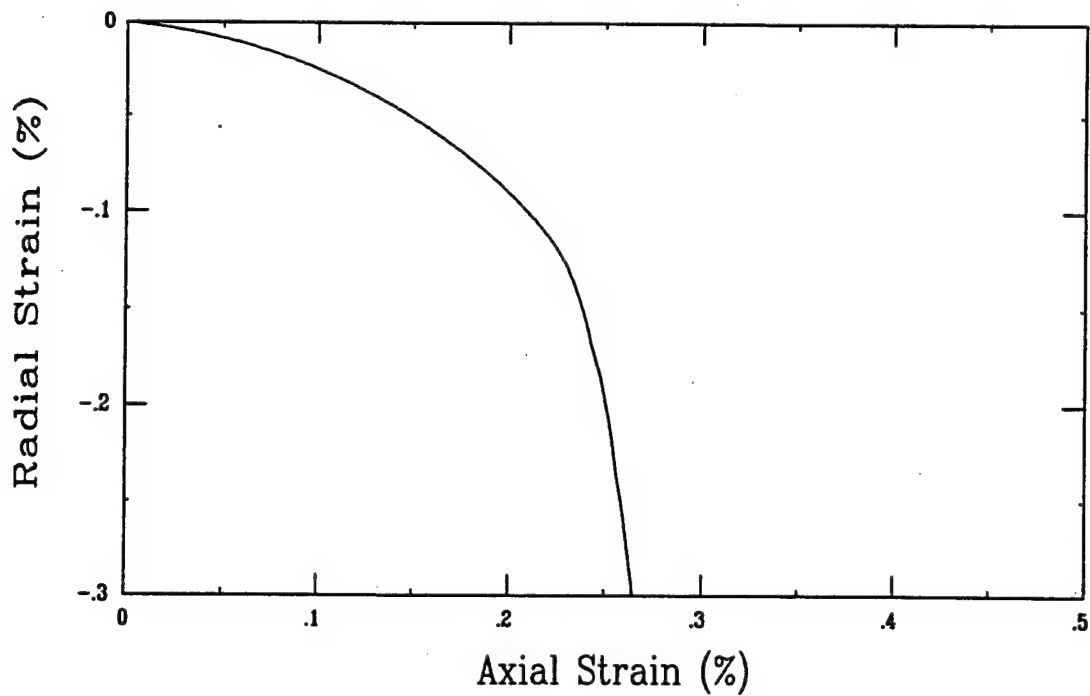
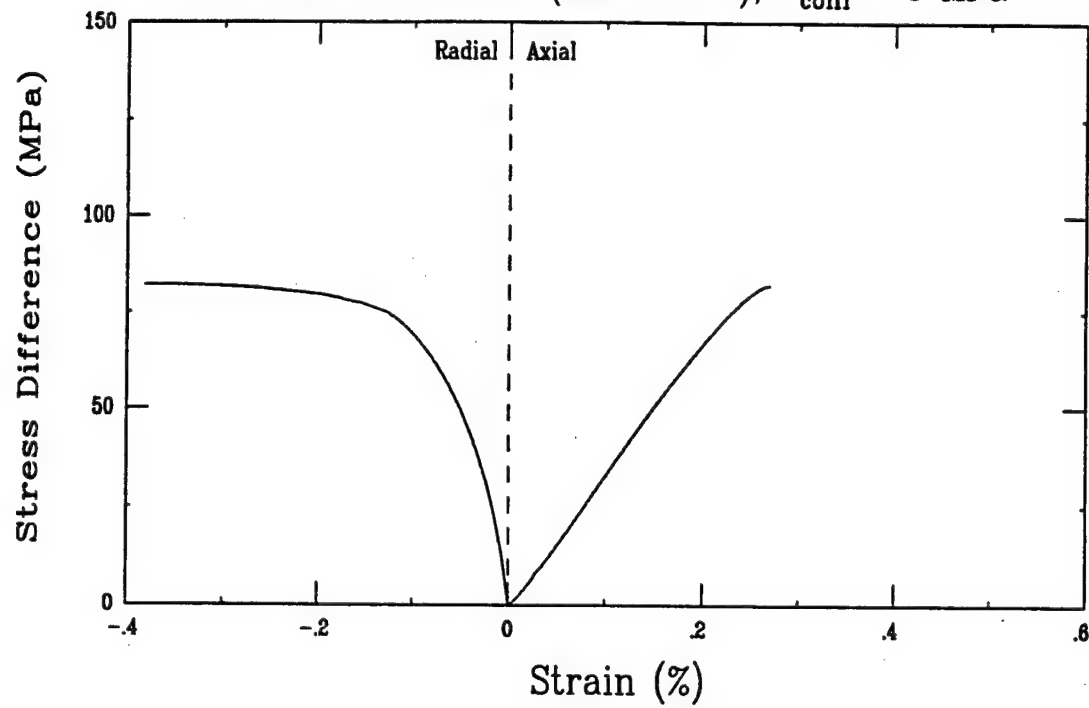
Triaxial Compression Test (S8A3)
Ft. Knox Limestone (FK2-01-3), $\sigma_{\text{conf}} = 0$ MPa



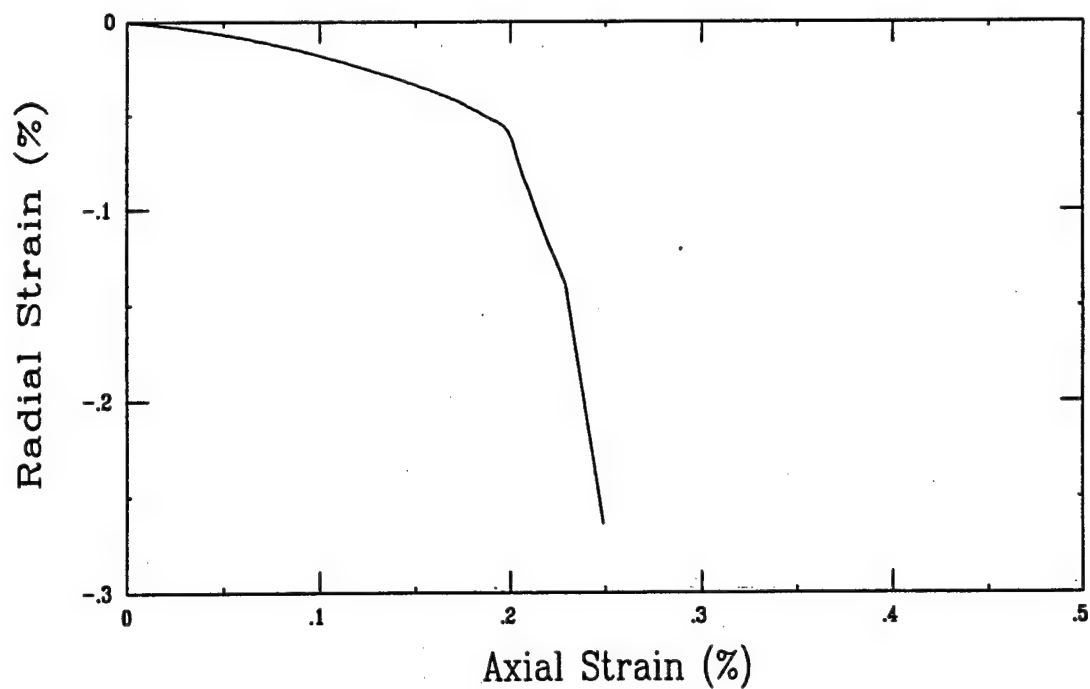
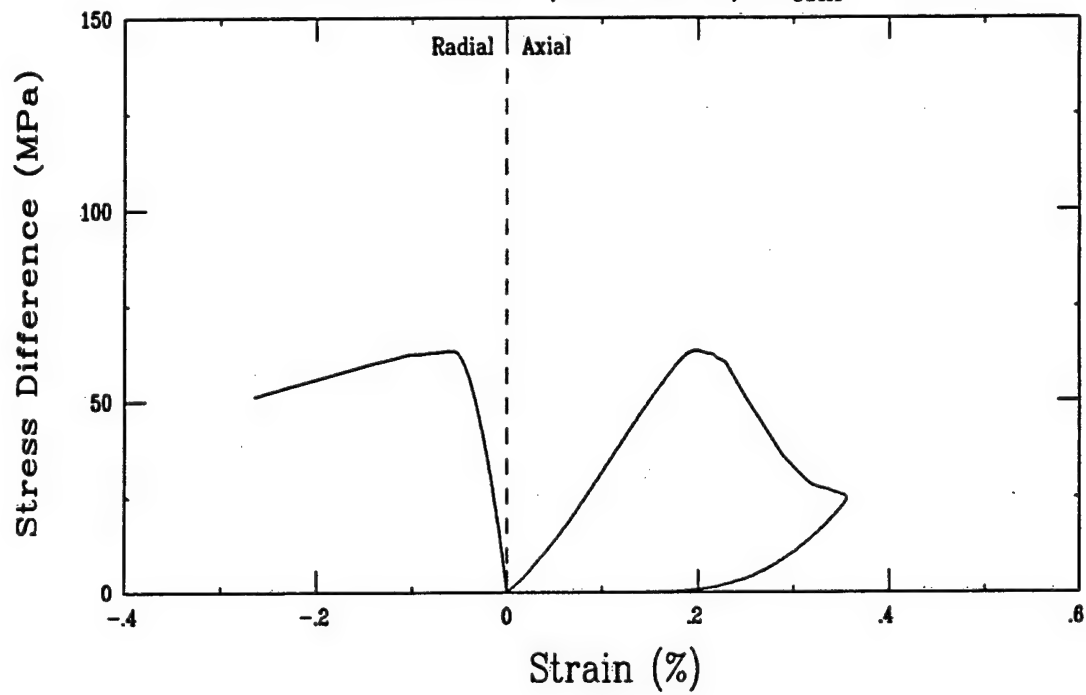
Triaxial Compression Test (S8B3)
Ft. Knox Limestone (FK2-02-1), $\sigma_{\text{conf}} = 0$ MPa



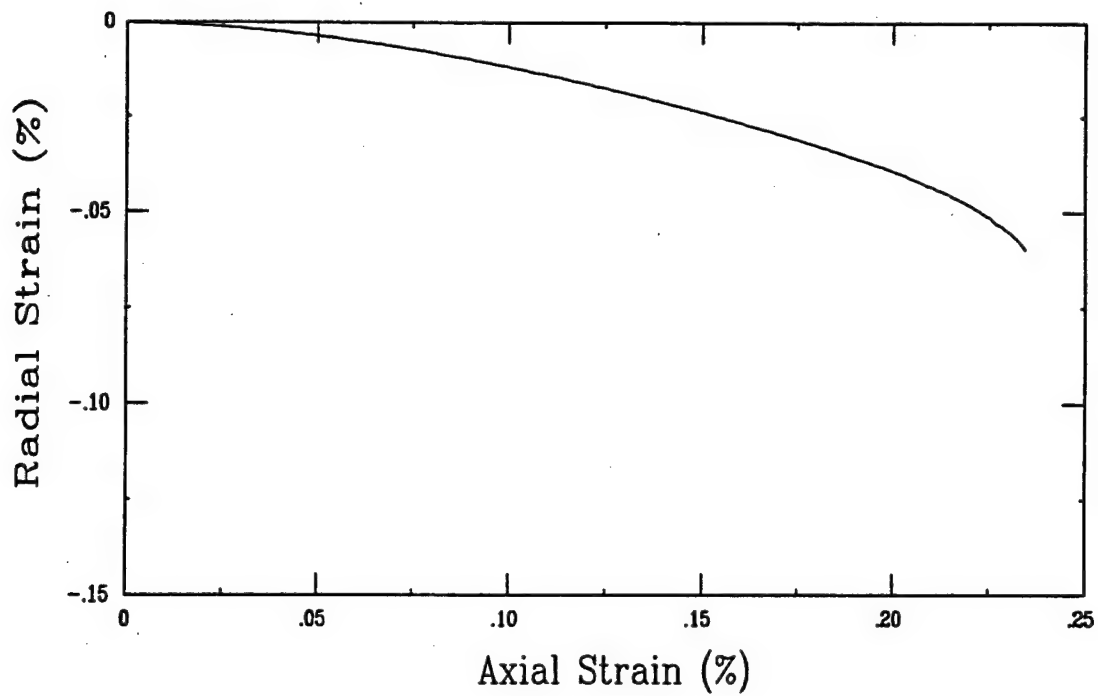
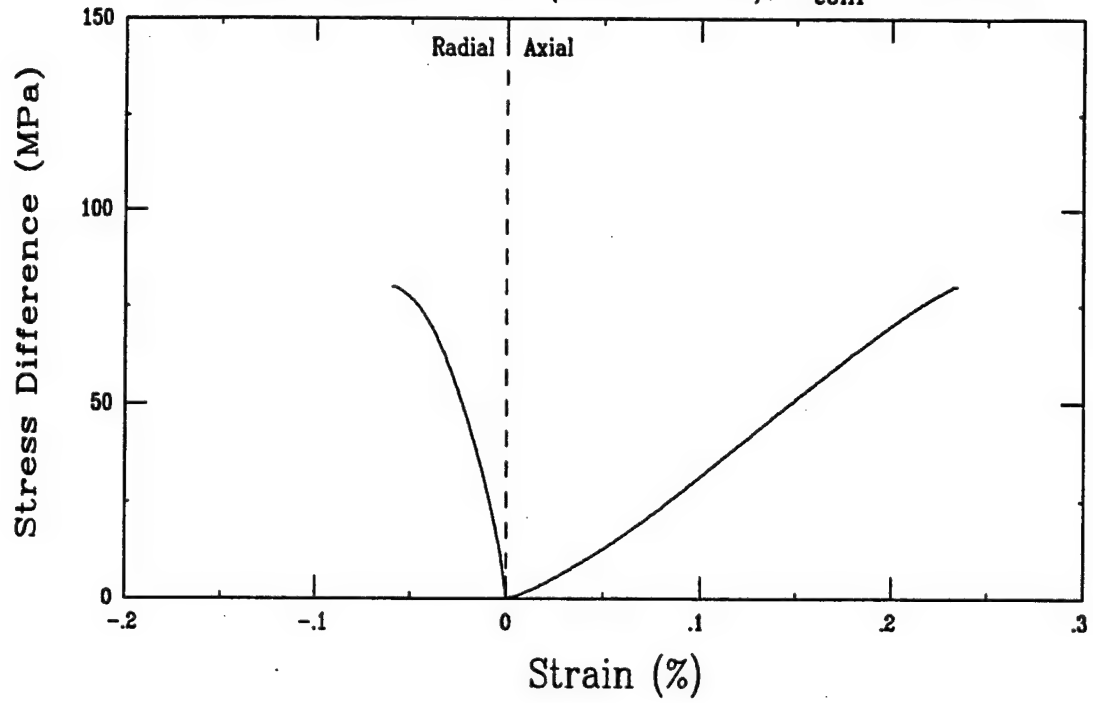
Triaxial Compression Test (S9A3)
Ft. Knox Limestone (FK2-03-1), $\sigma_{\text{conf}} = 0$ MPa



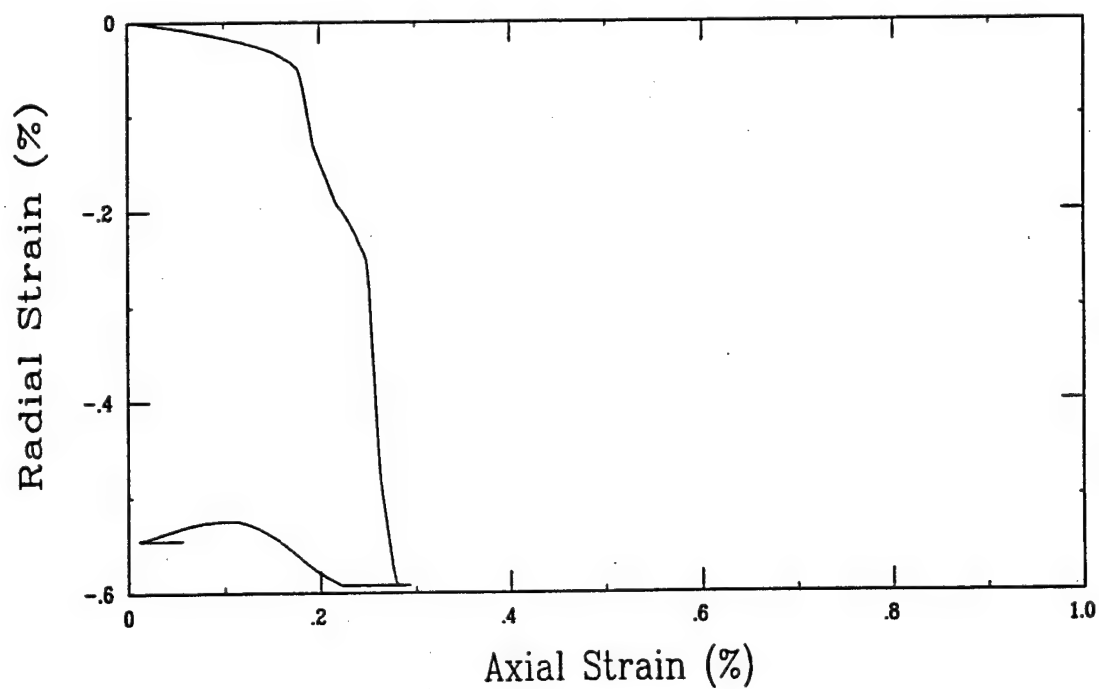
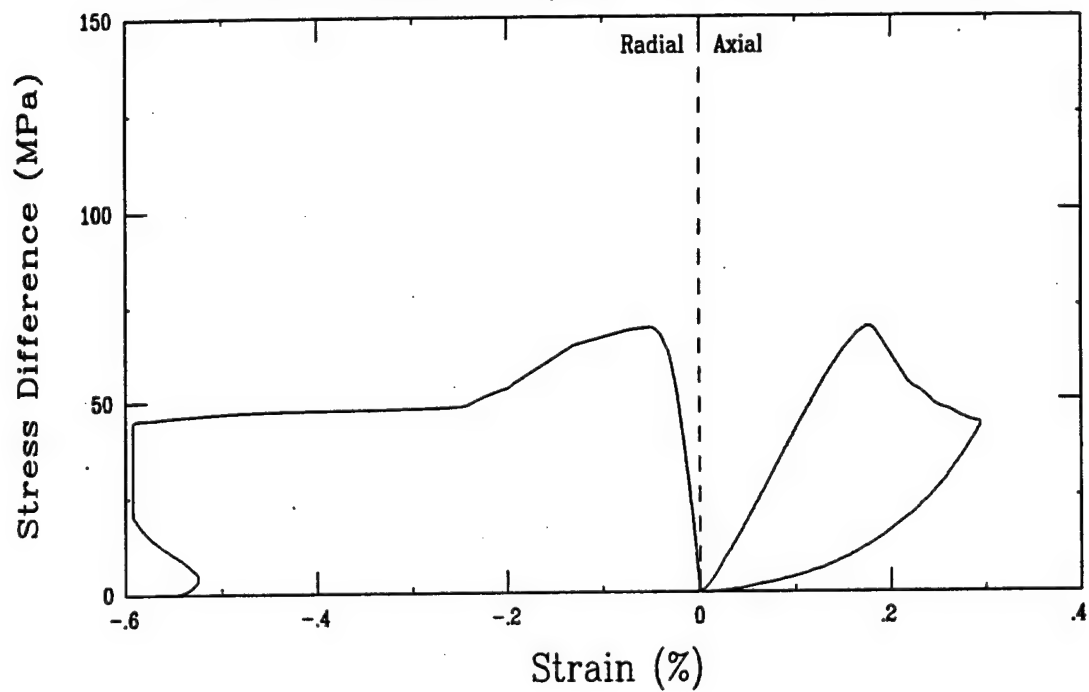
Triaxial Compression Test (S9B3)
Ft. Knox Limestone (FK2-04-2), $\sigma_{\text{conf}} = 0$ MPa



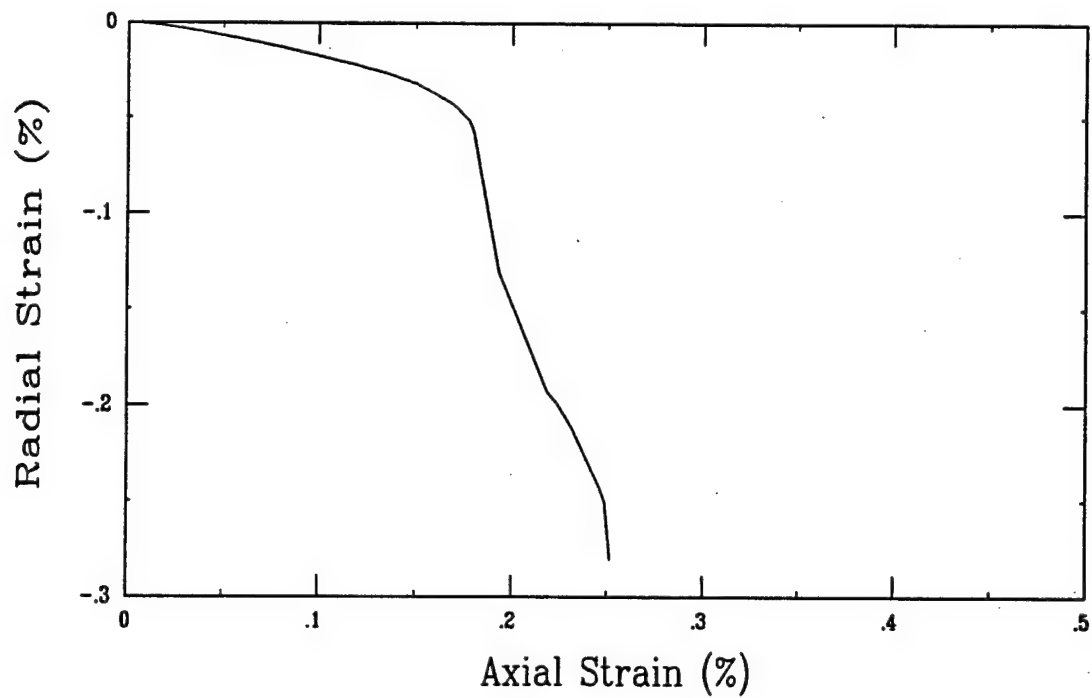
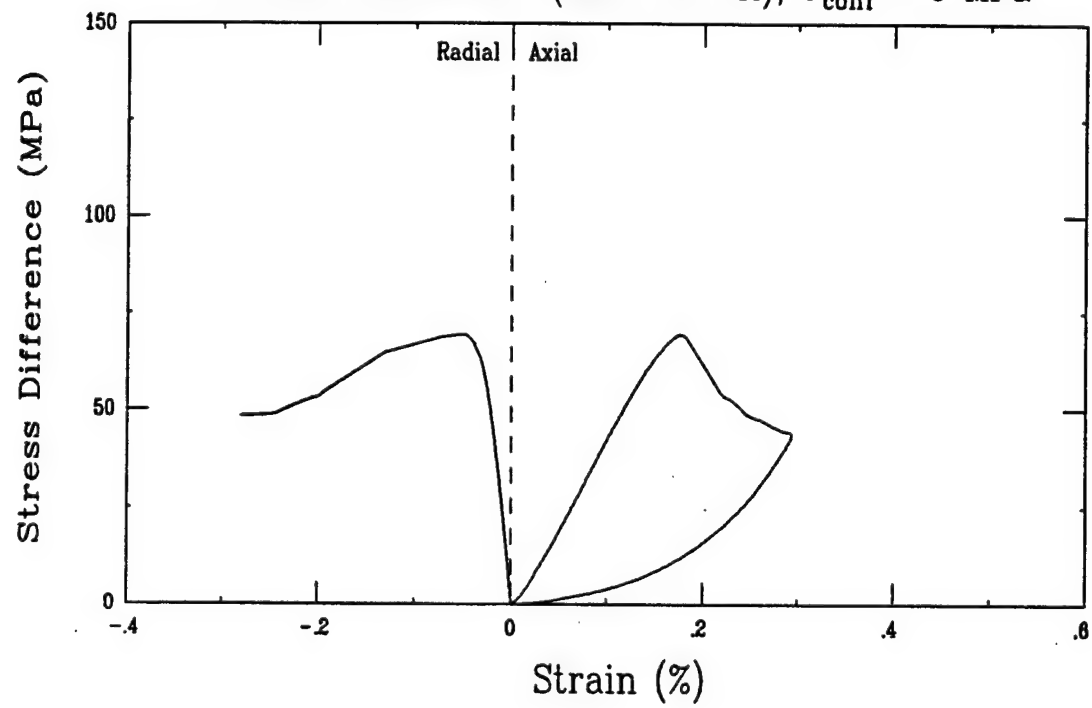
Triaxial Compression Test (S9C3)
Ft. Knox Limestone (FK2-04-7L), $\sigma_{\text{conf}} = 0$ MPa



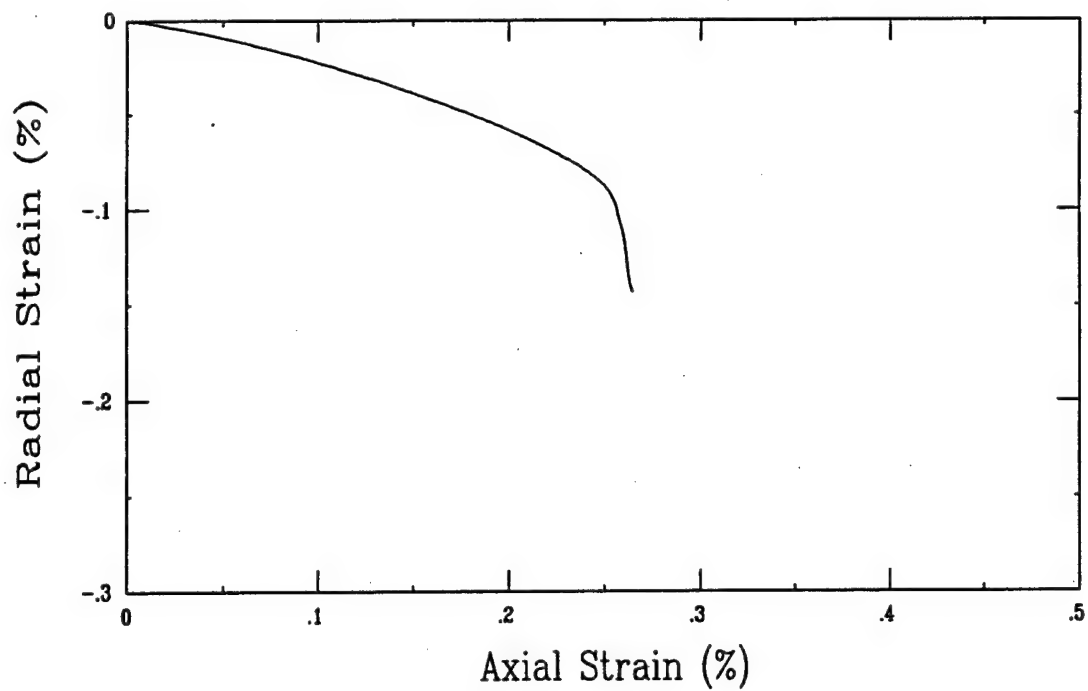
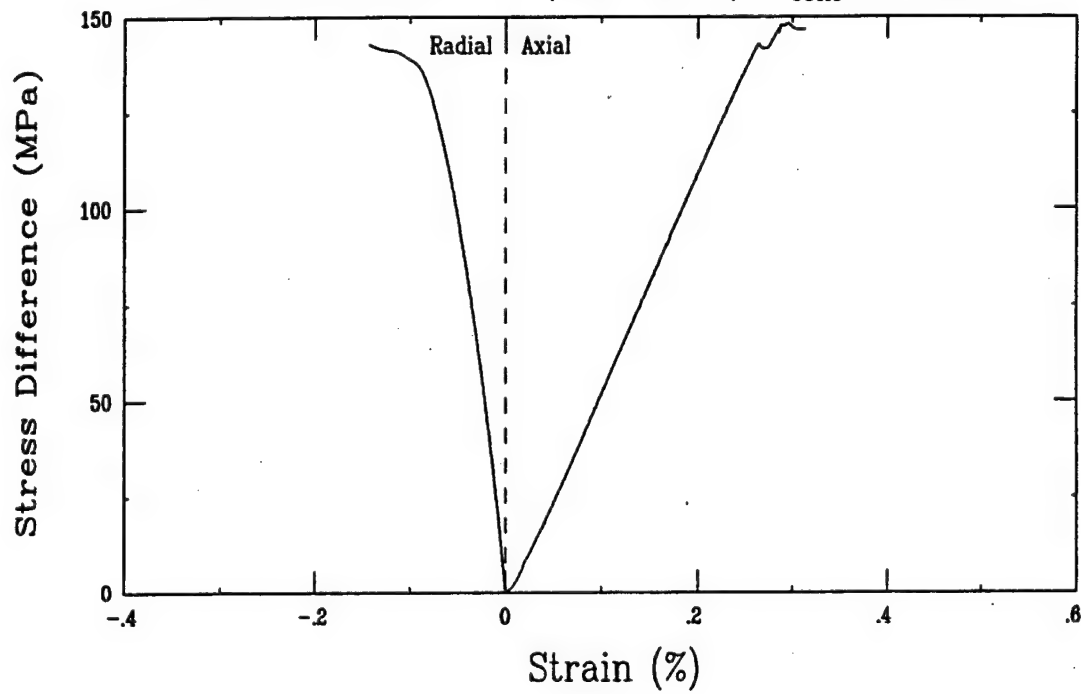
Triaxial Compression Test (S9D3)
Ft. Knox Limestone (FK2-04-7H), $\sigma_{\text{conf}} = 0$ MPa



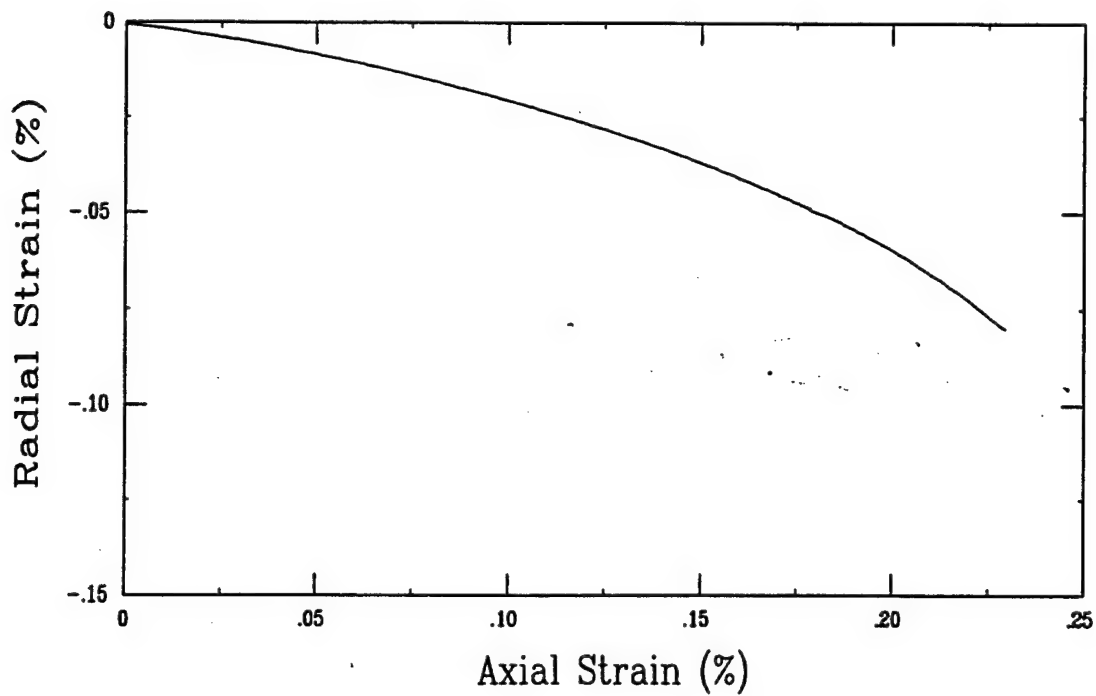
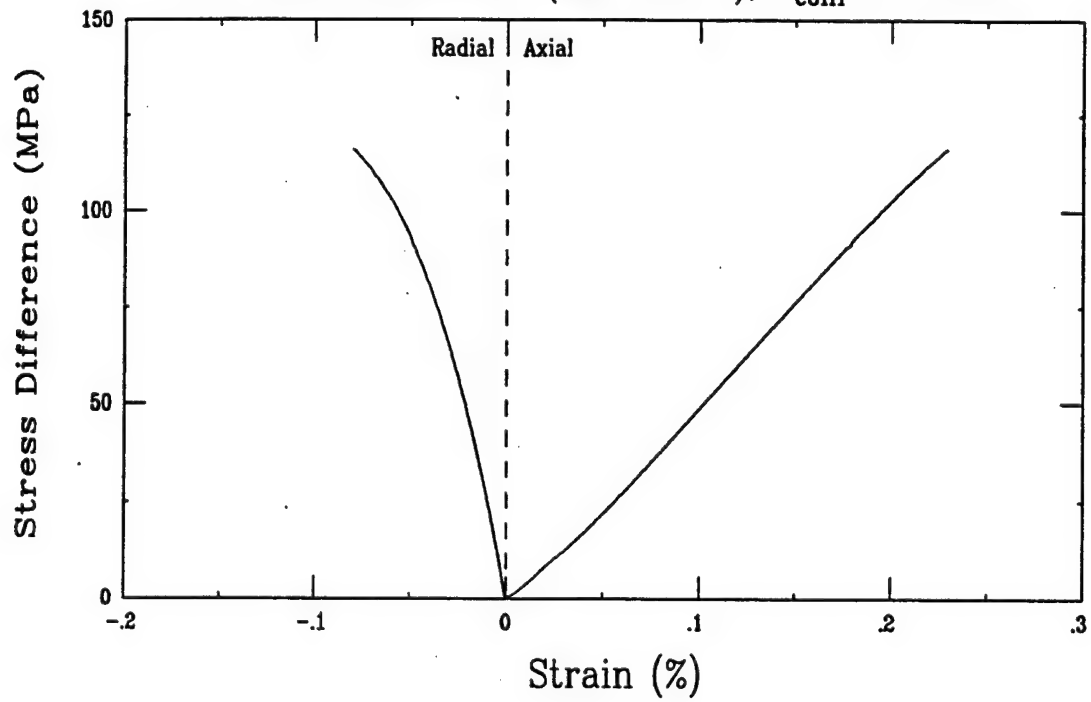
Triaxial Compression Test (S9D3)
Ft. Knox Limestone (FK2-04-7H), $\sigma_{\text{conf}} = 0$ MPa



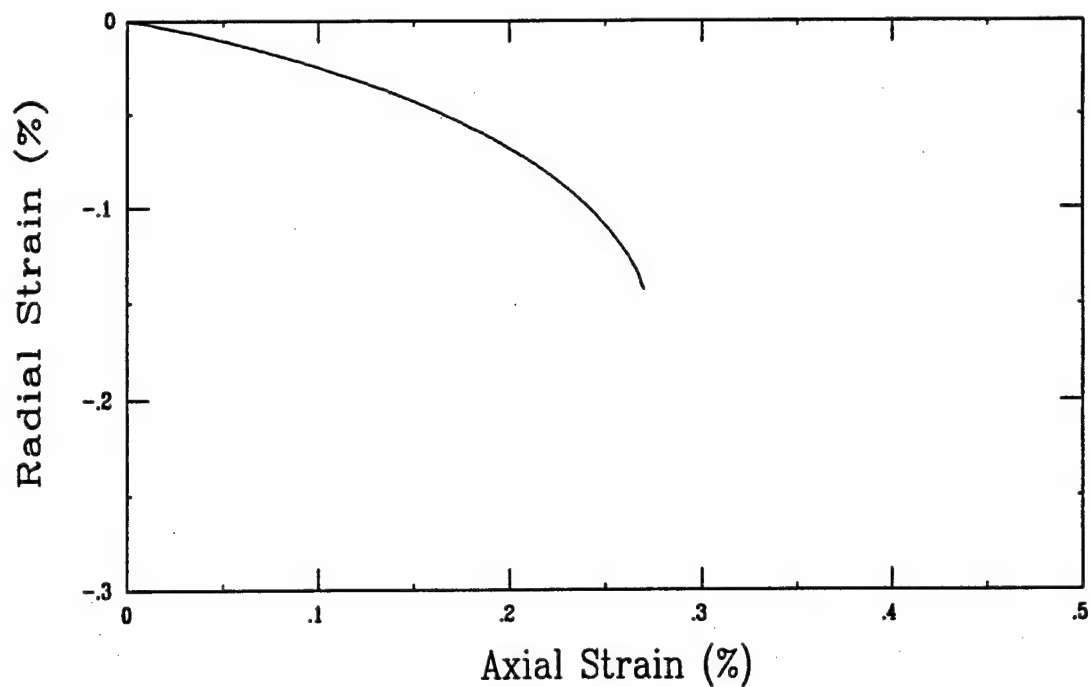
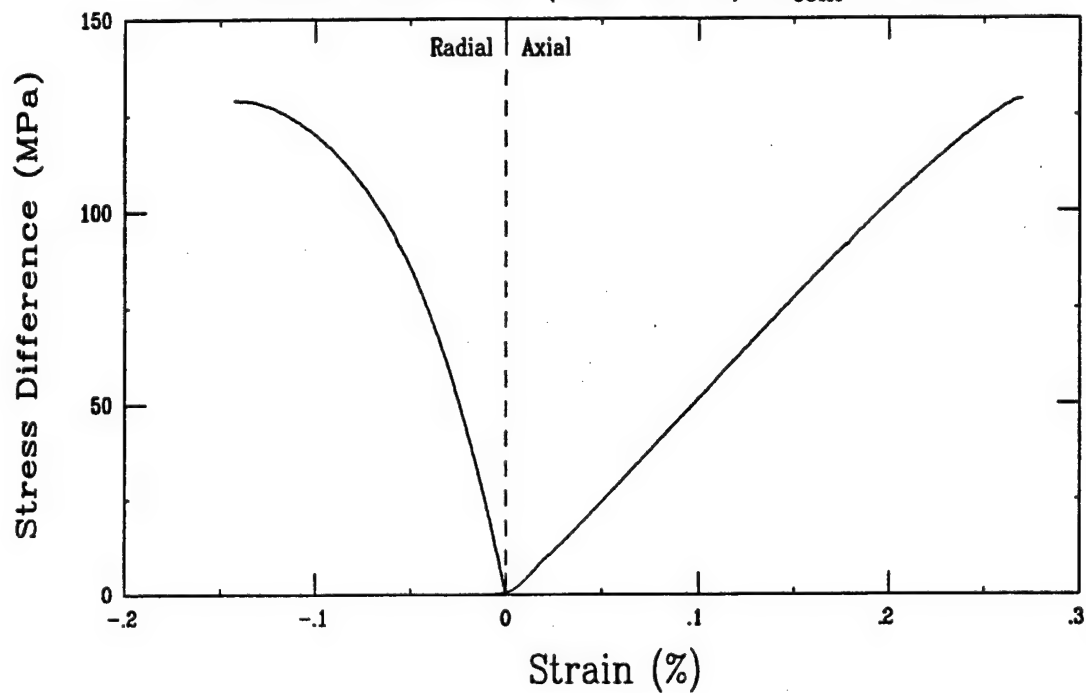
Triaxial Compression Test (S9E3)
Ft. Knox Limestone (FK2-05-1), $\sigma_{\text{conf}} = 0$ MPa



Triaxial Compression Test (S9F3)
Ft. Knox Limestone (FK2-06-3), $\sigma_{\text{conf}} = 0$ MPa

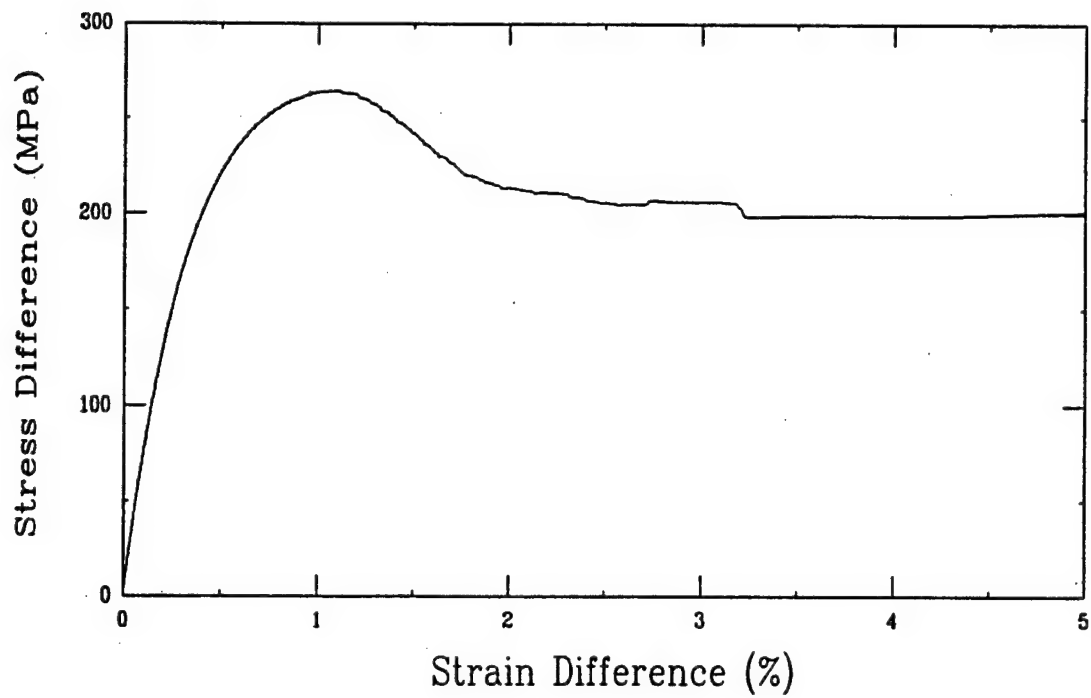
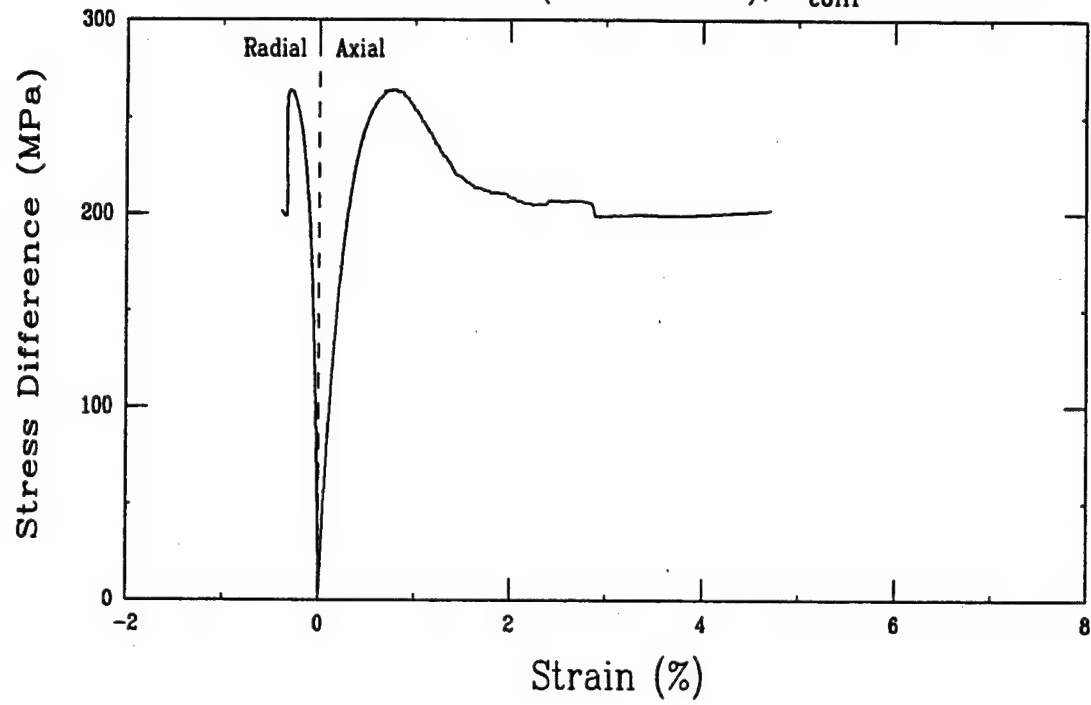


Triaxial Compression Test (S9G3)
Ft. Knox Limestone (FK2-07-1), $\sigma_{\text{conf}} = 0$ MPa

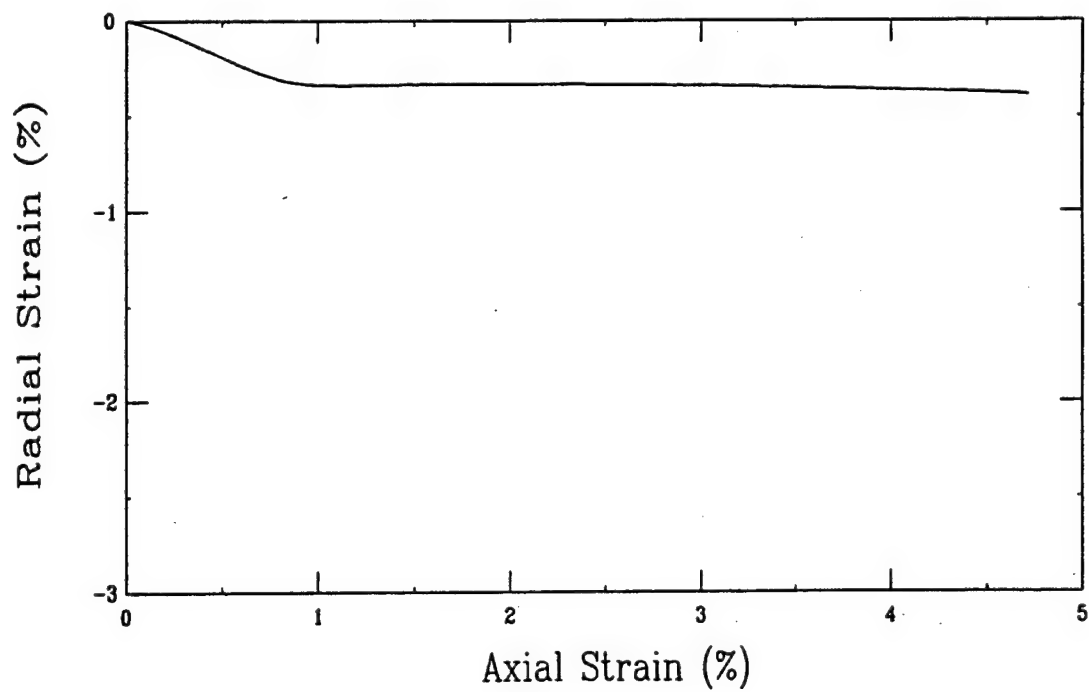
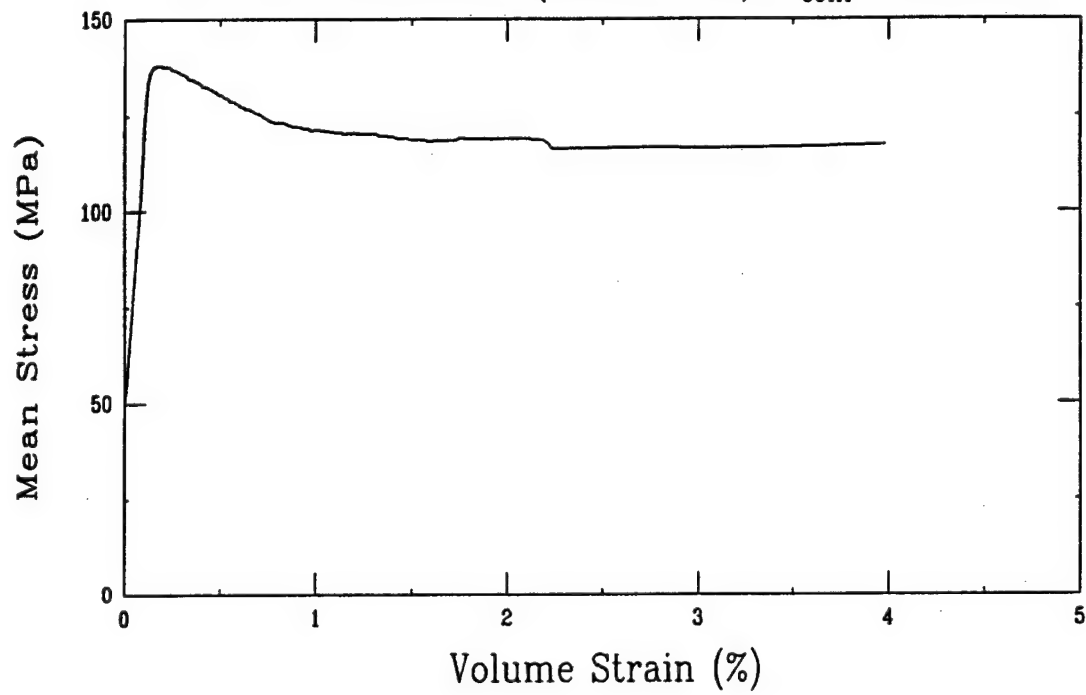


APPENDIX C
TRIAXIAL COMPRESSION TESTS ON
CARBONATE ROCKS FROM FORT KNOX

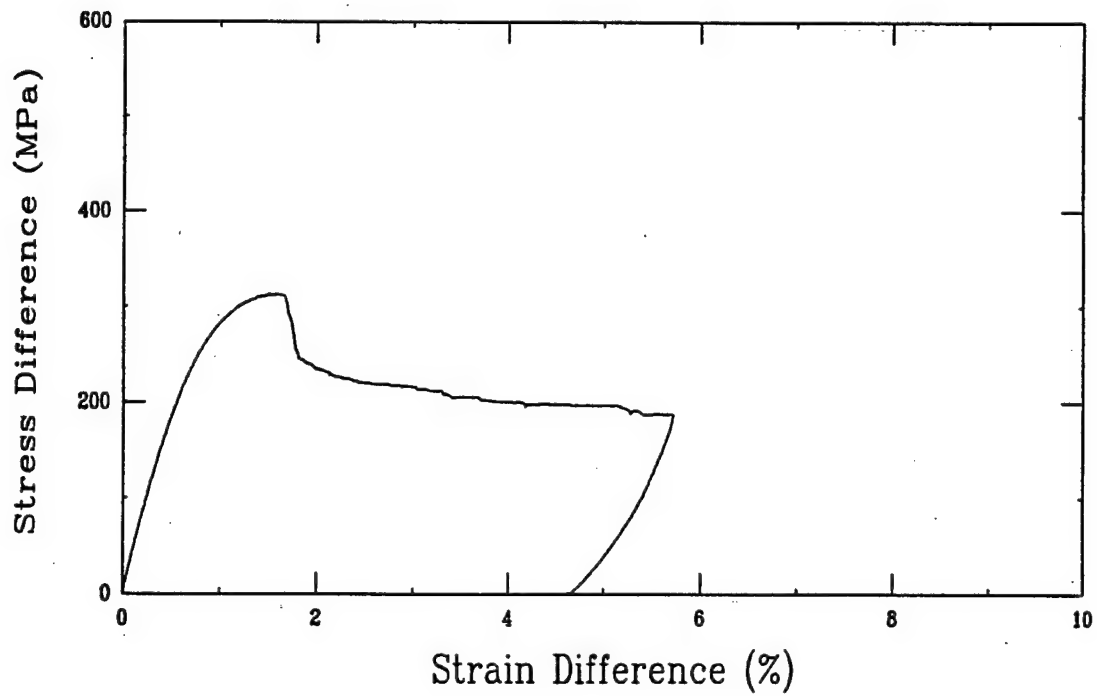
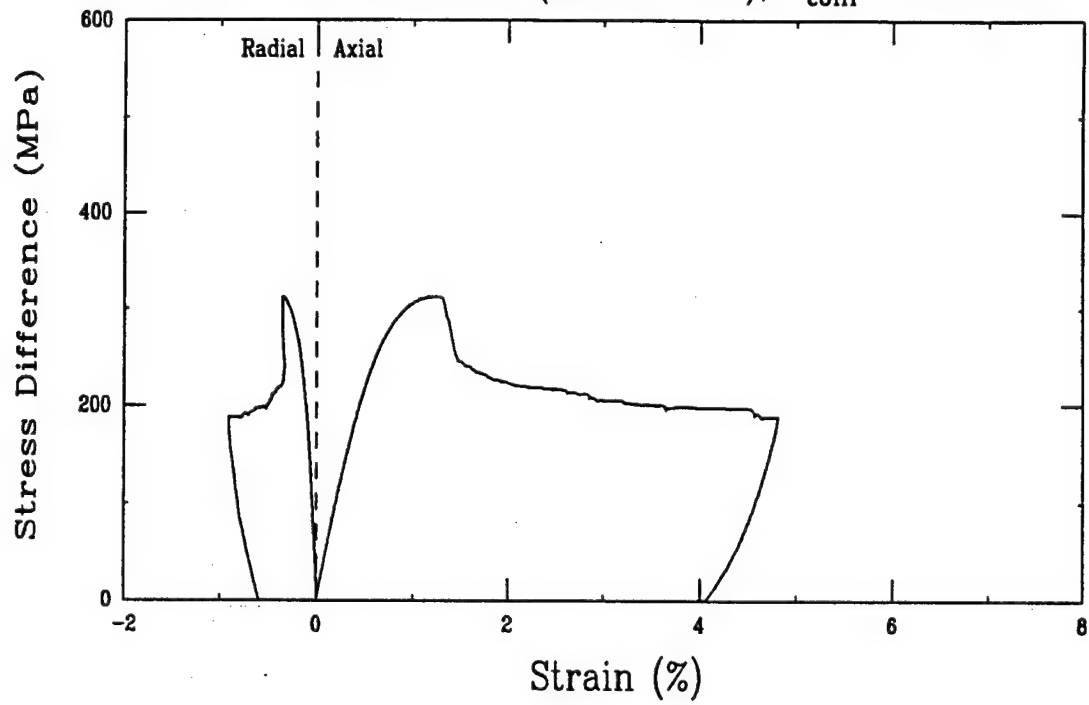
Triaxial Compression Test (A23B3)
Ft. Knox Limestone (FK10-1-03), $\sigma_{\text{conf}} = 50$ MPa



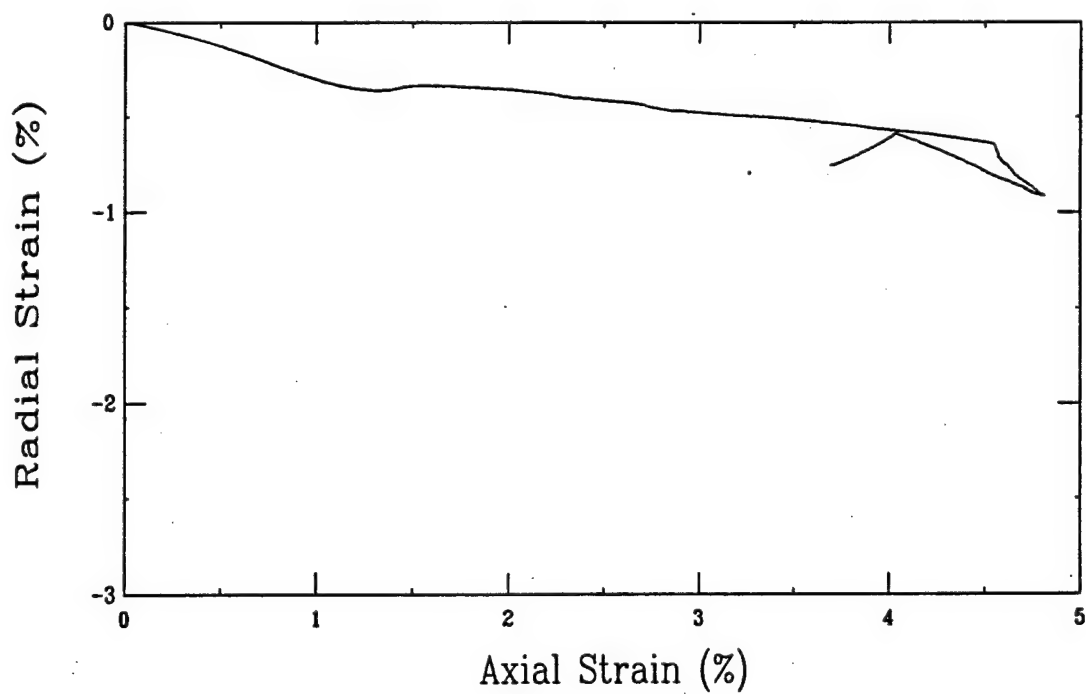
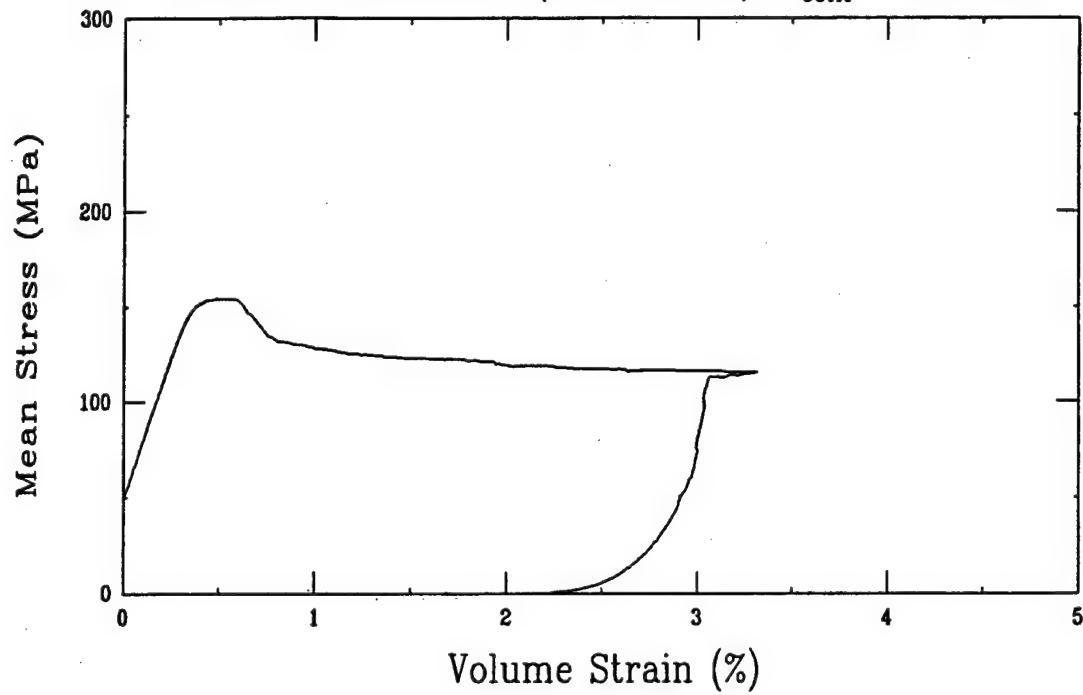
Triaxial Compression Test (A23B3)
Ft. Knox Limestone (FK10-1-03), $\sigma_{\text{conf}} = 50 \text{ MPa}$



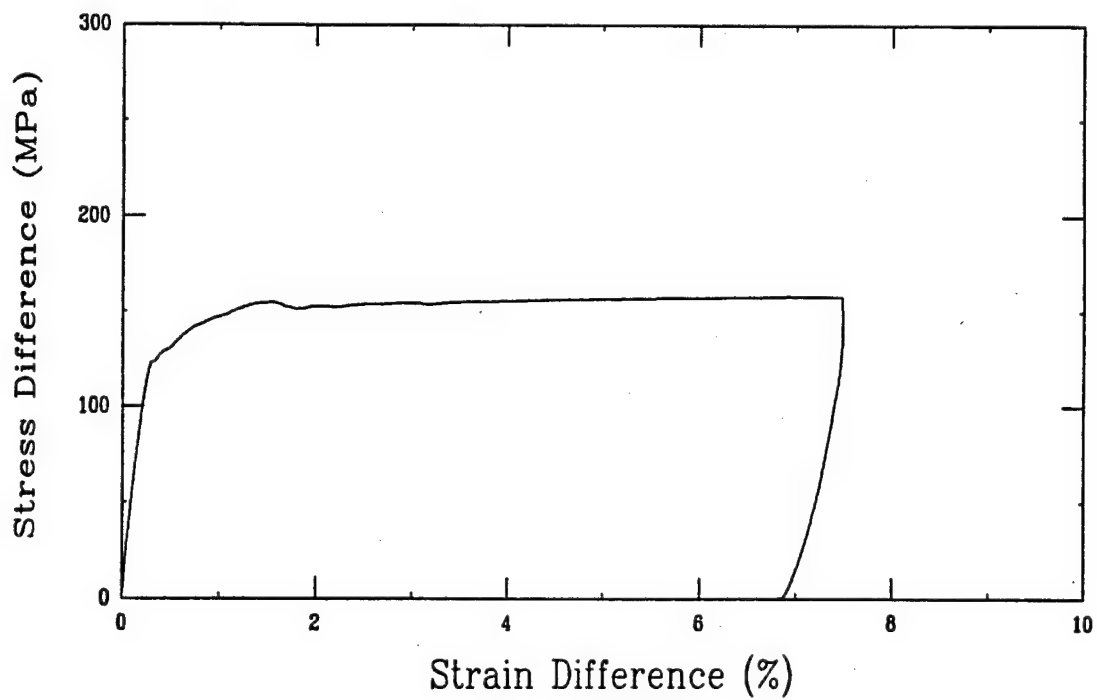
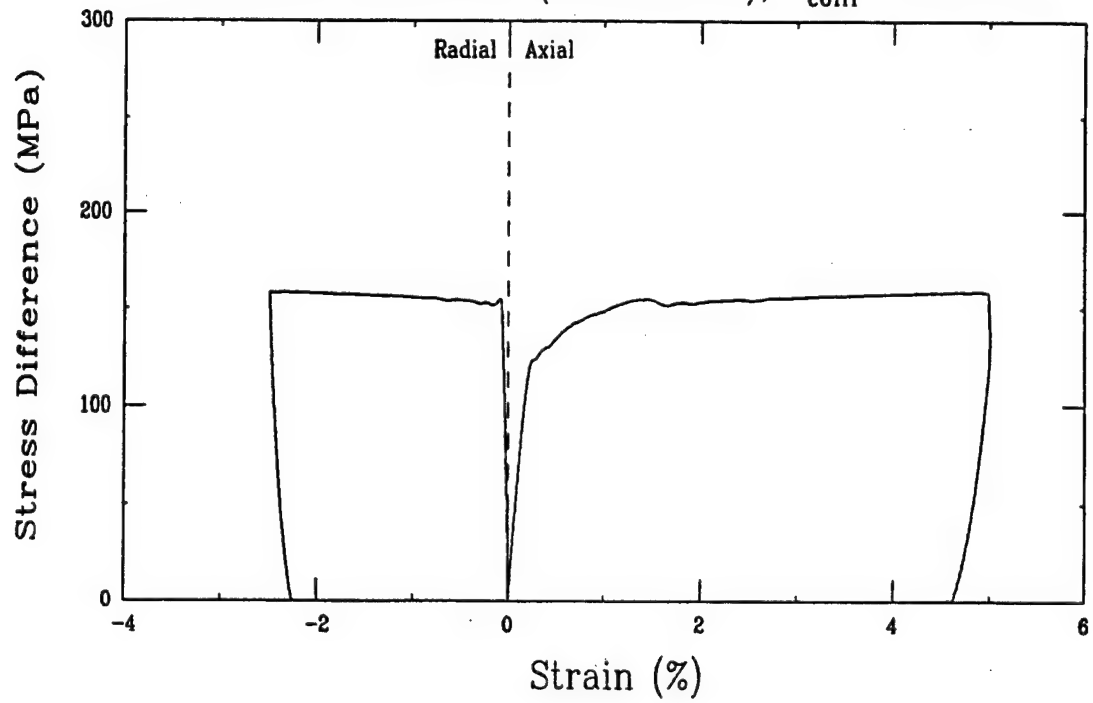
Triaxial Compression Test (A23D3)
Ft. Knox Limestone (FK10-2-01), $\sigma_{\text{conf}} = 50 \text{ MPa}$



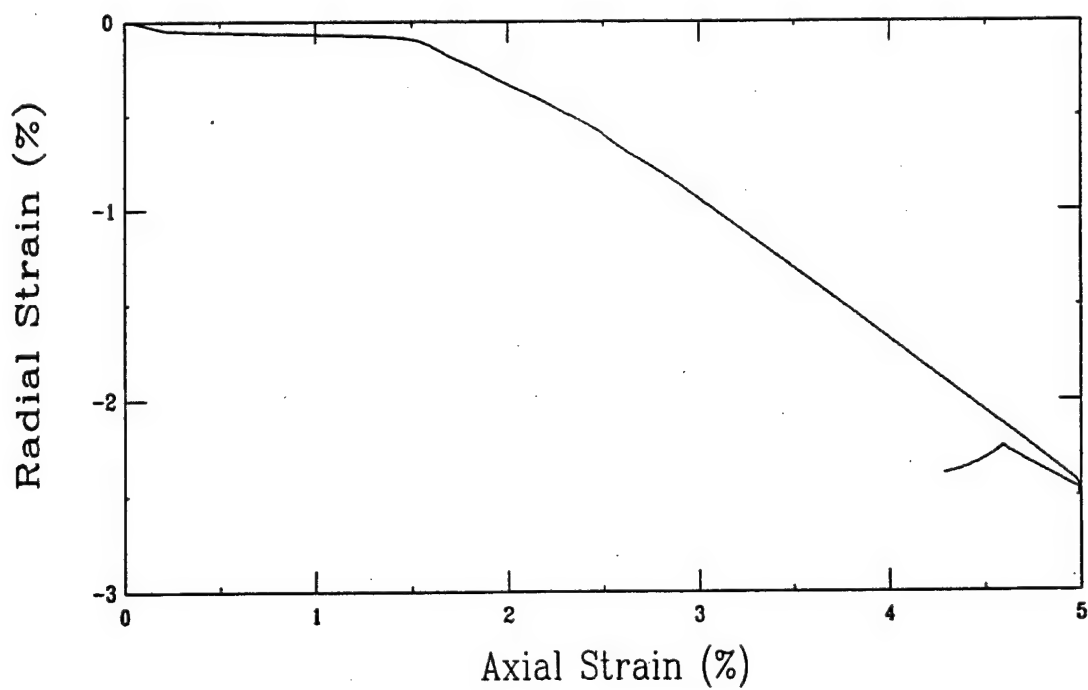
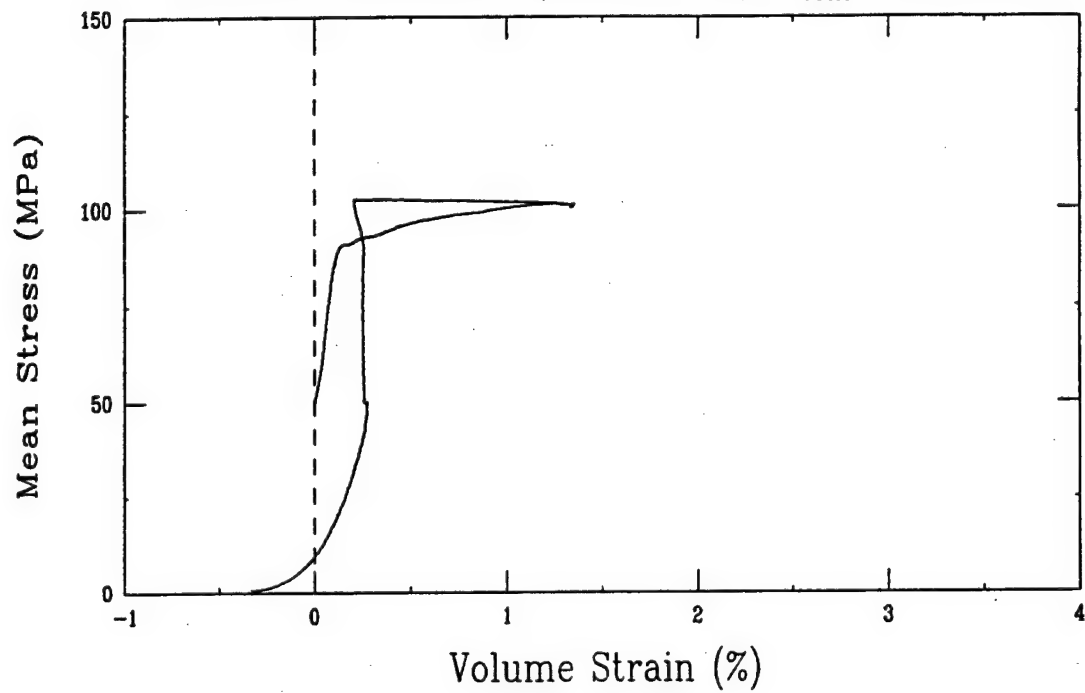
Triaxial Compression Test (A23D3)
Ft. Knox Limestone (FK10-2-01), $\sigma_{\text{conf}} = 50 \text{ MPa}$



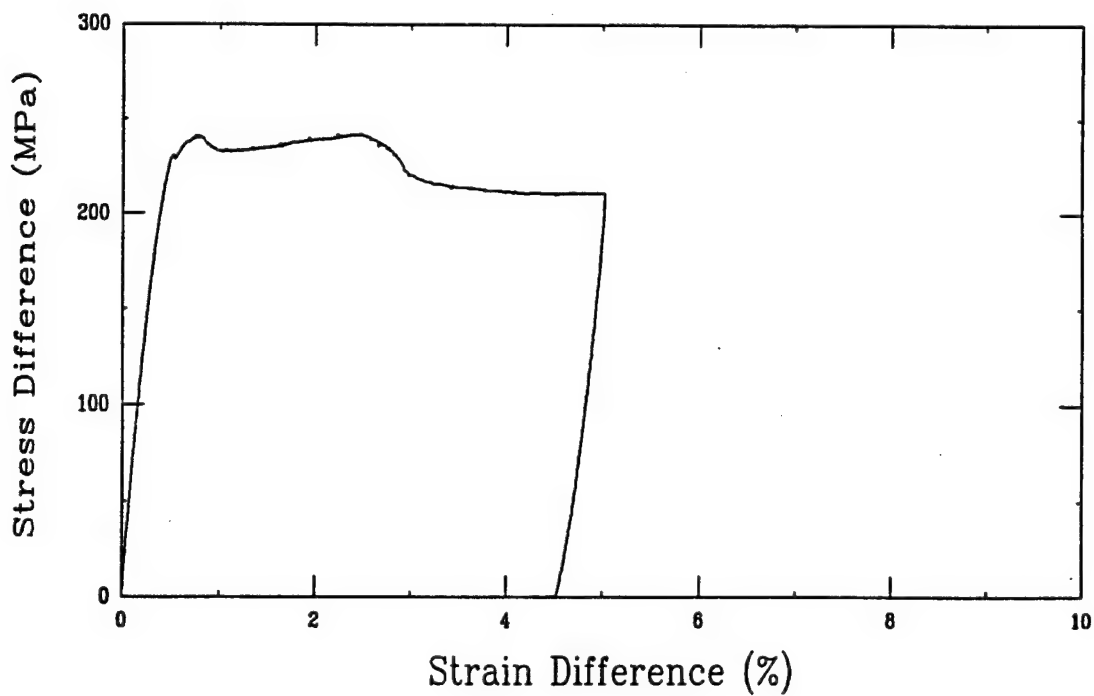
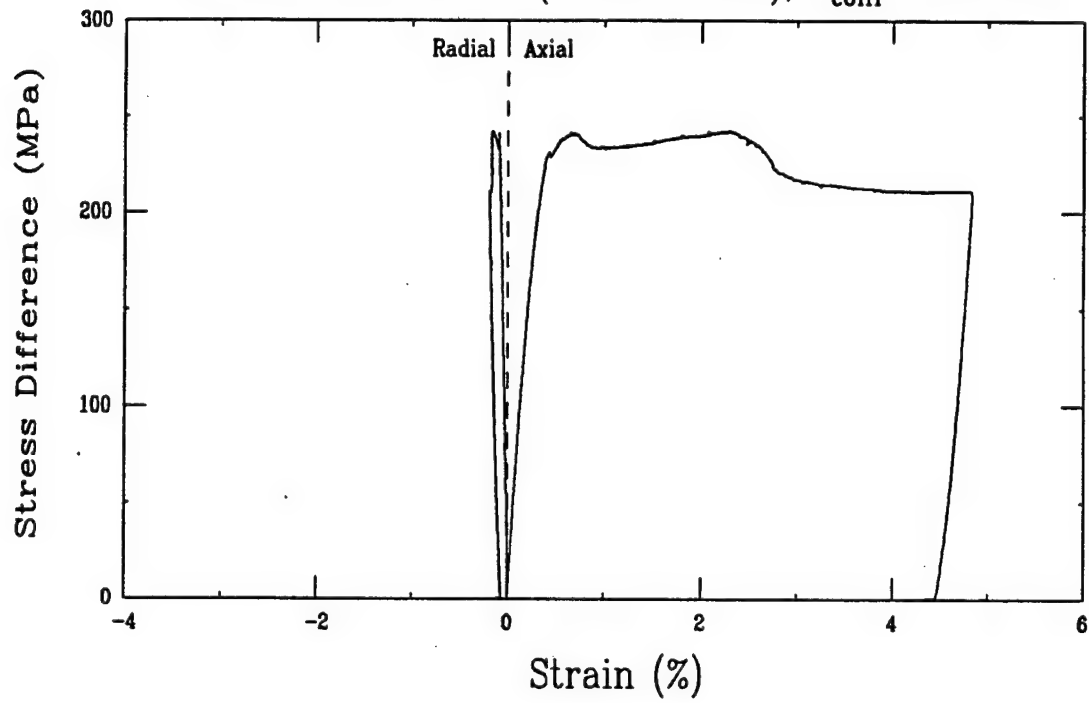
Triaxial Compression Test (A28F3)
Ft. Knox Limestone (FK10-3-06), $\sigma_{\text{conf}} = 50 \text{ MPa}$



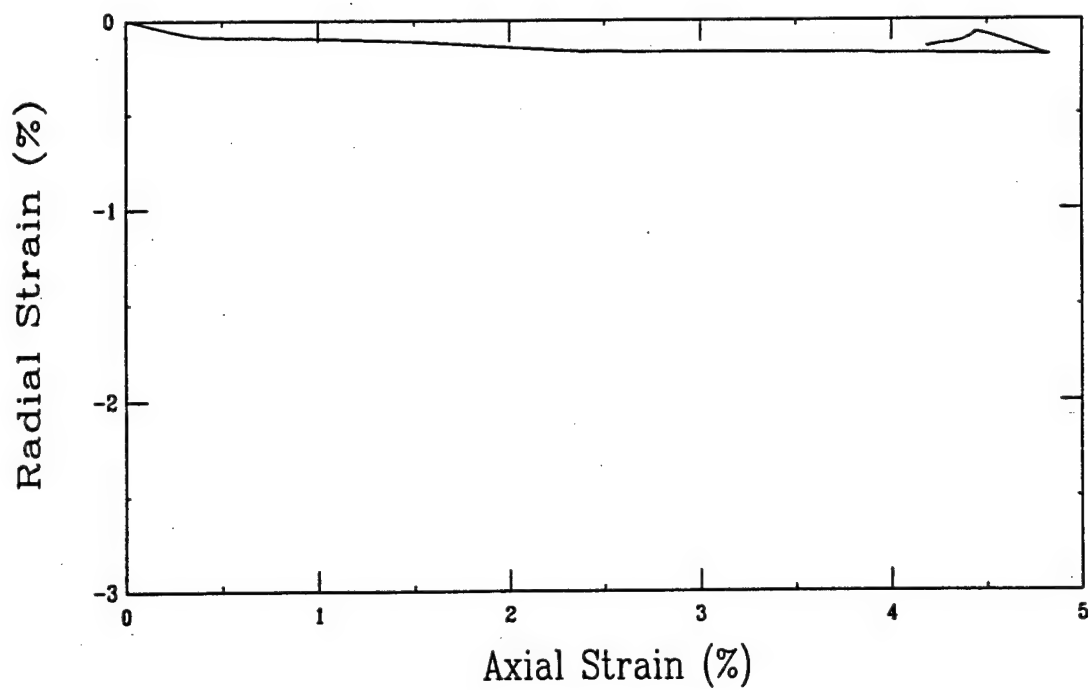
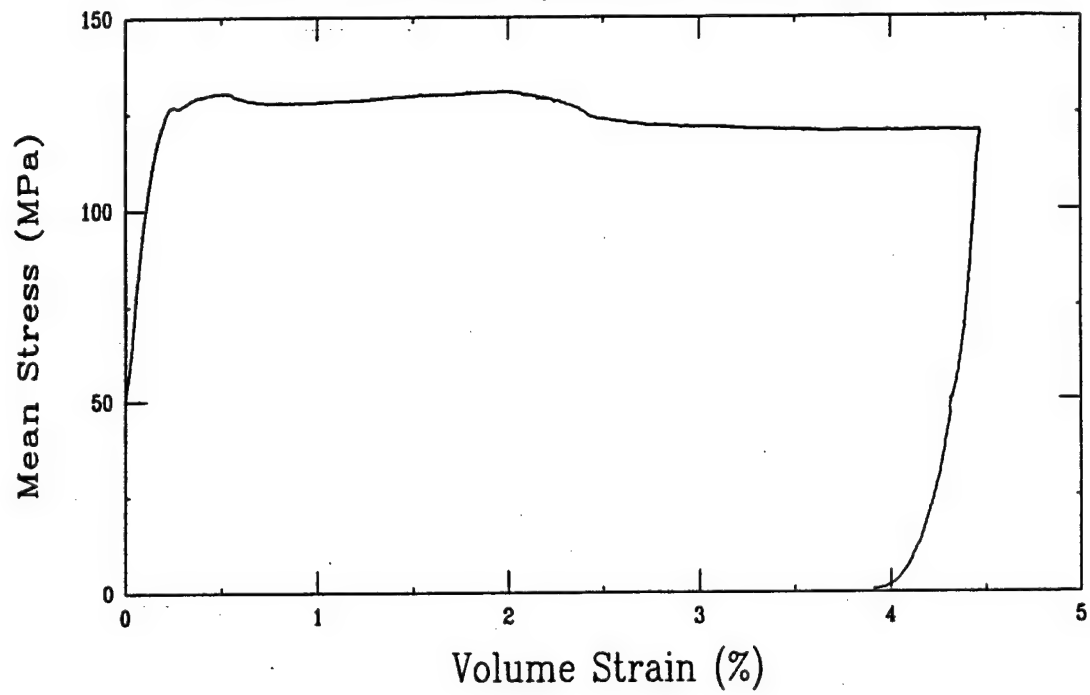
Triaxial Compression Test (A28F3)
Ft. Knox Limestone (FK10-1-03), $\sigma_{\text{conf}} = 50 \text{ MPa}$



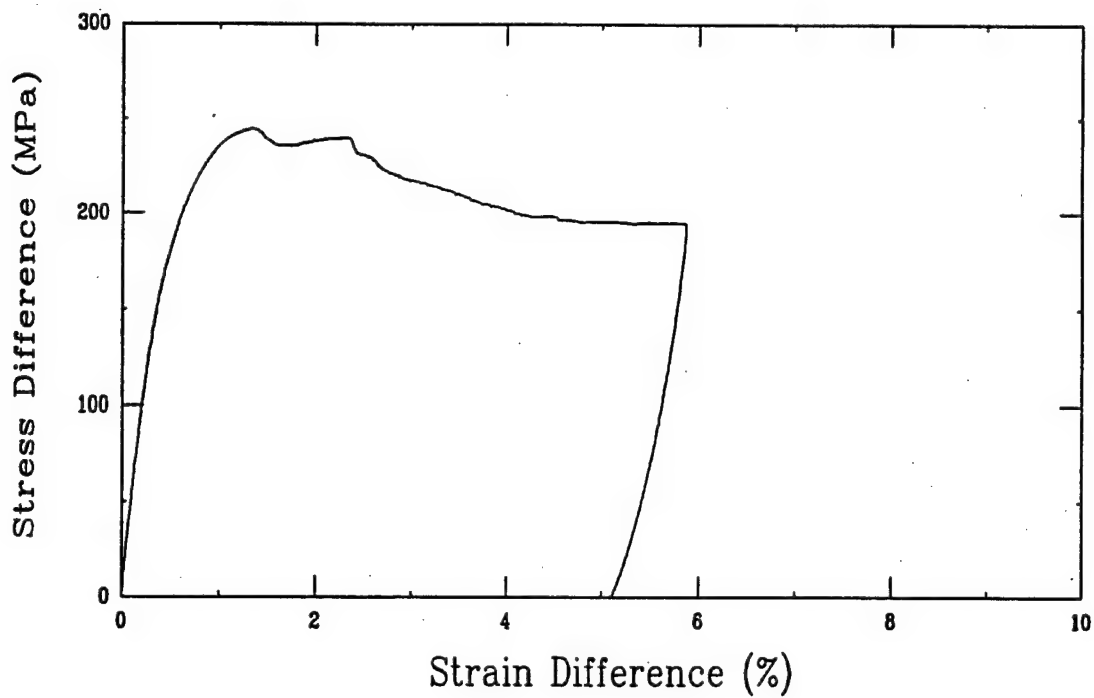
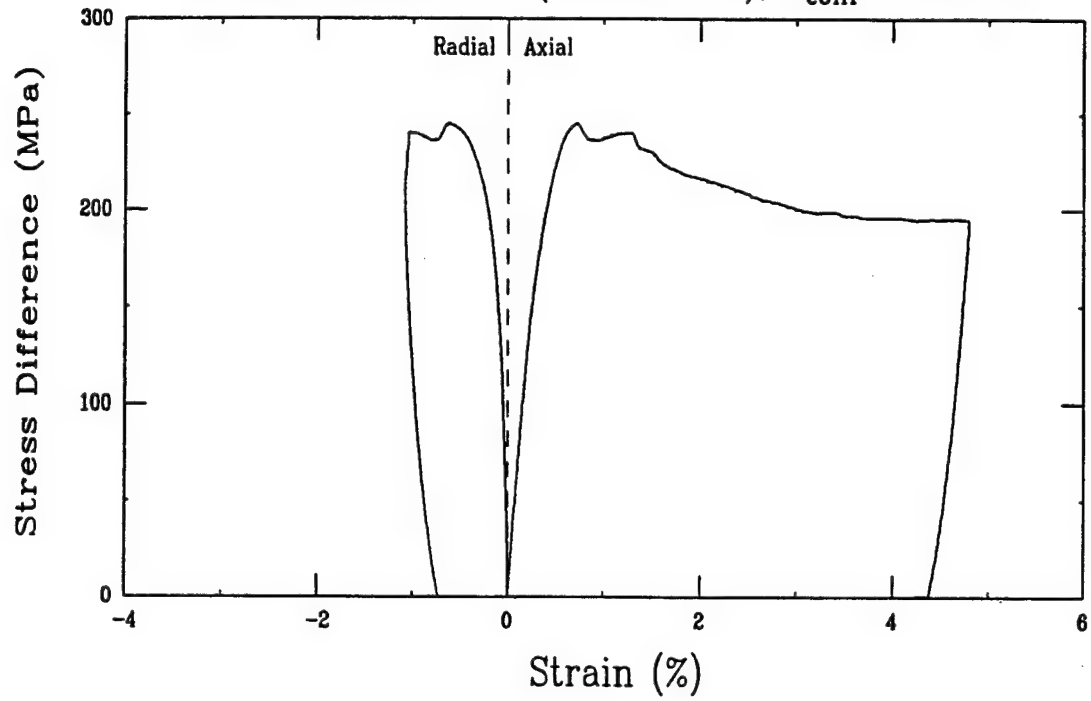
Triaxial Compression Test (A27H3)
Ft. Knox Limestone (FK10-4-05H), $\sigma_{\text{conf}} = 50 \text{ MPa}$



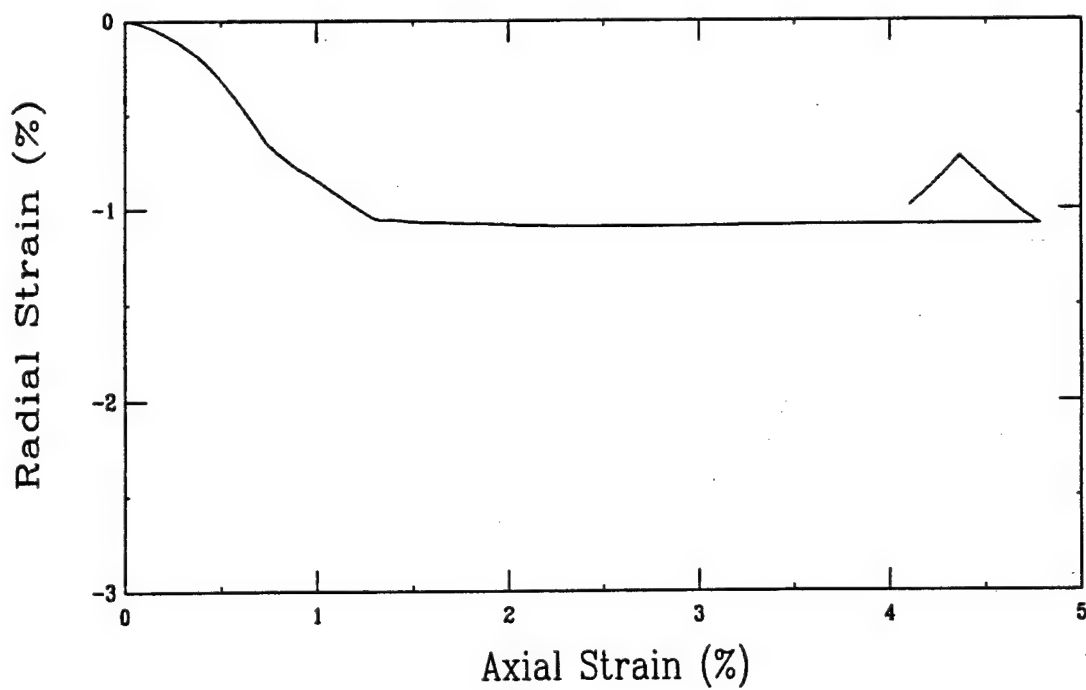
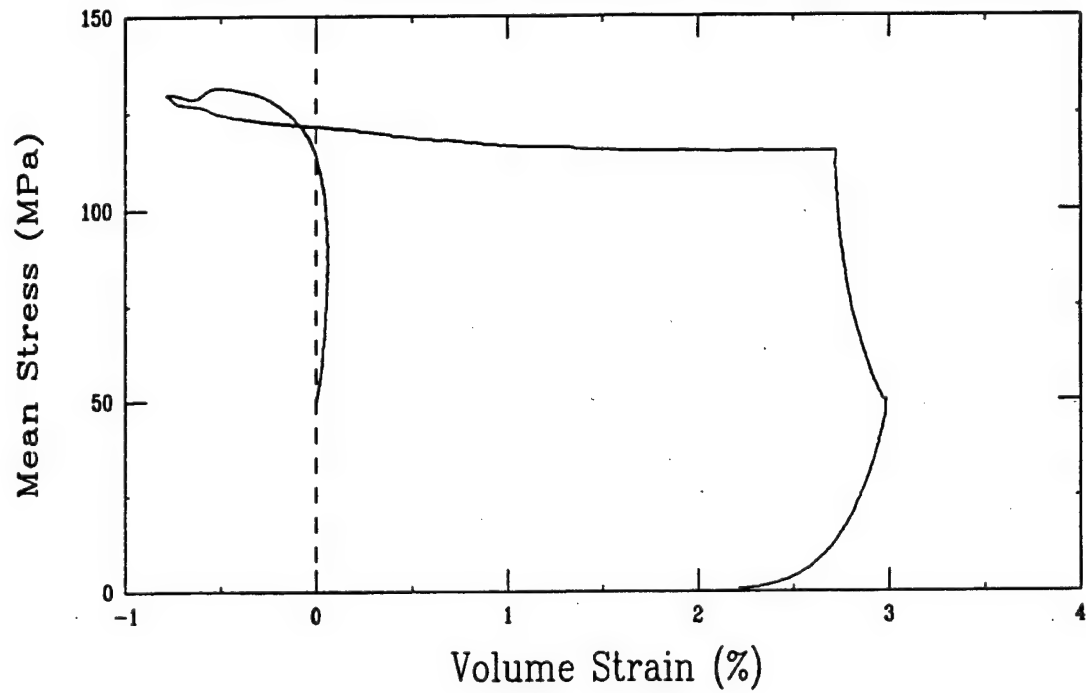
Triaxial Compression Test (A27H3)
Ft. Knox Limestone (FK10-4-05H), $\sigma_{\text{conf}} = 50 \text{ MPa}$



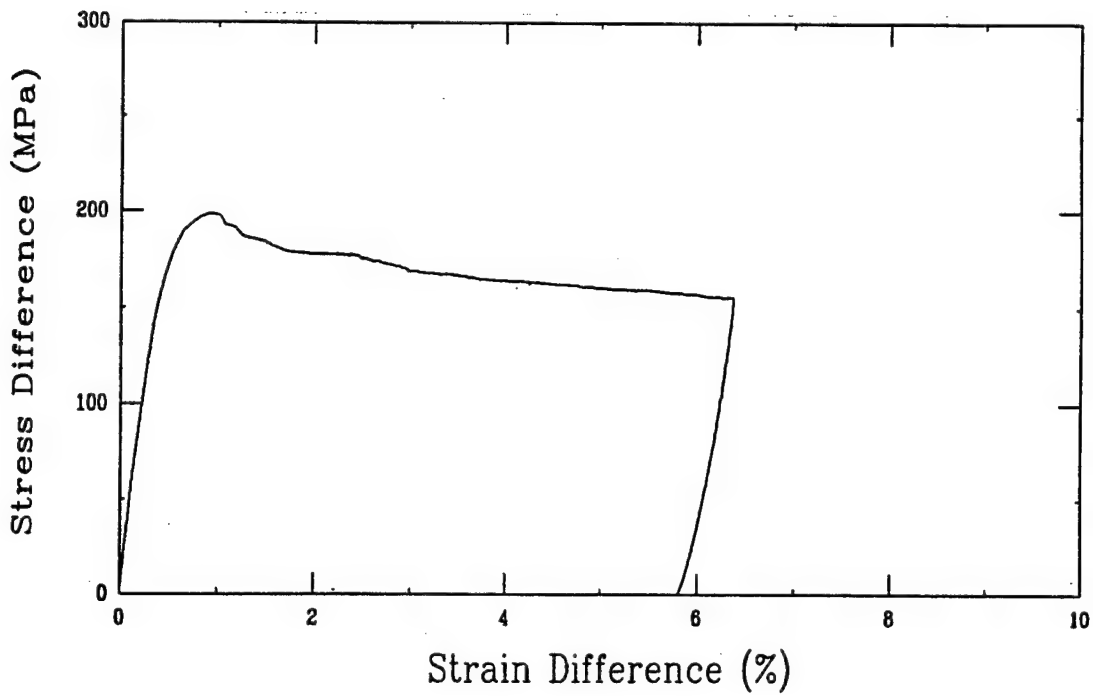
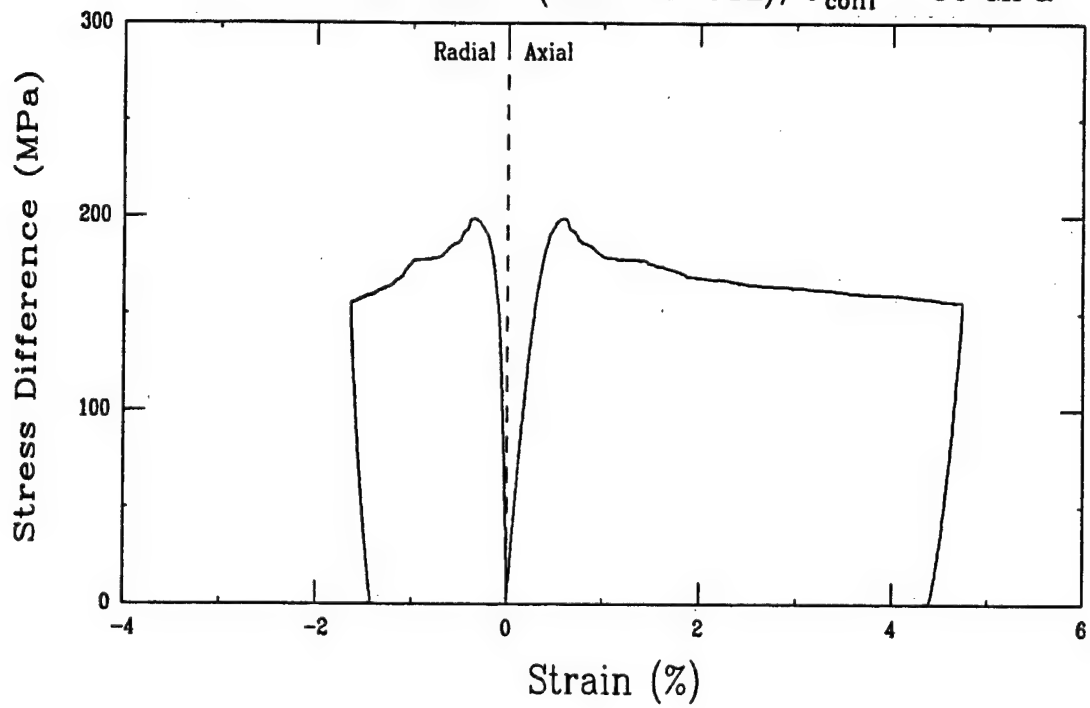
Triaxial Compression Test (A28B3)
Ft. Knox Limestone (FK10-4-07), $\sigma_{\text{conf}} = 50$ MPa



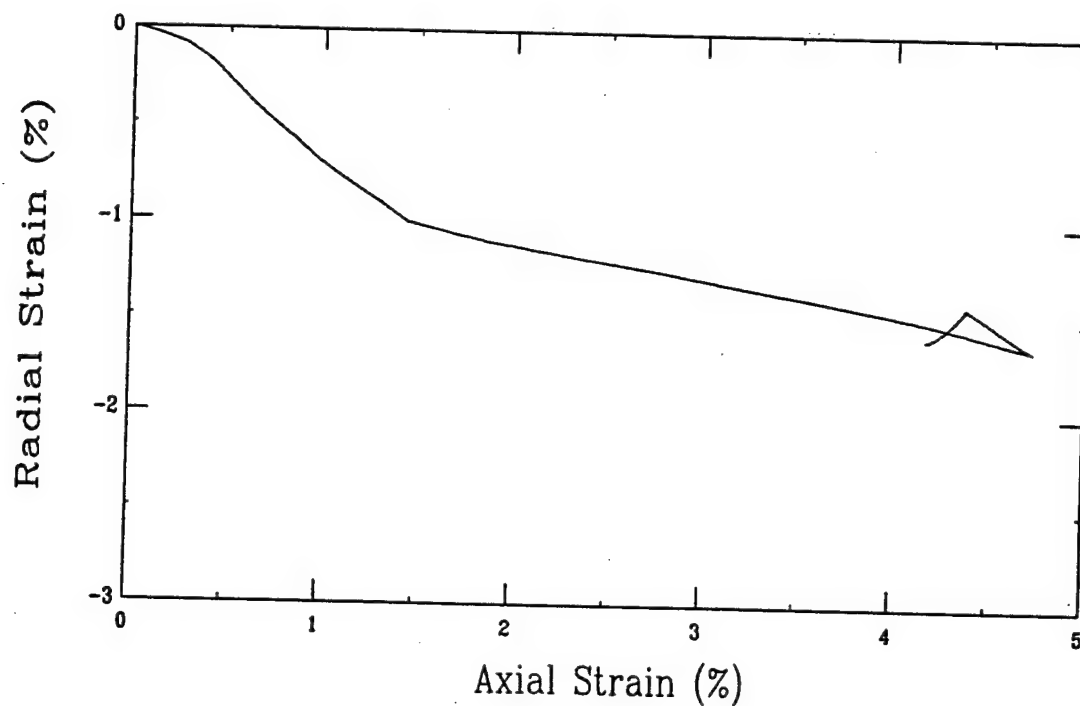
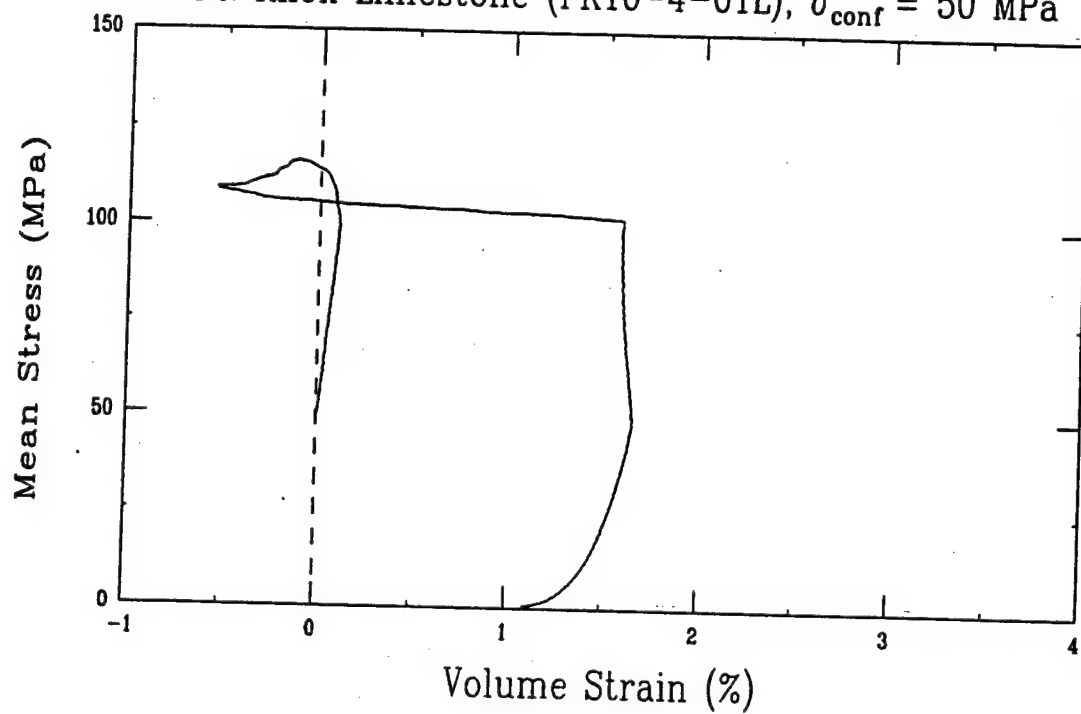
Triaxial Compression Test (A28B3)
Ft. Knox Limestone (FK10-4-07), $\sigma_{\text{conf}} = 50 \text{ MPa}$



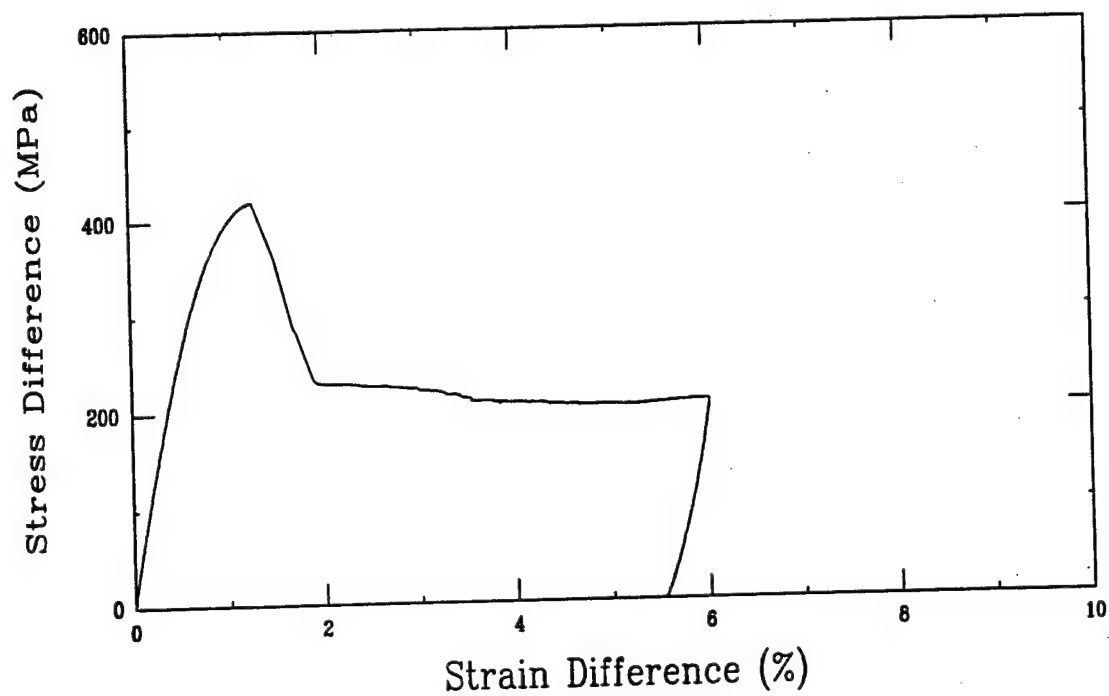
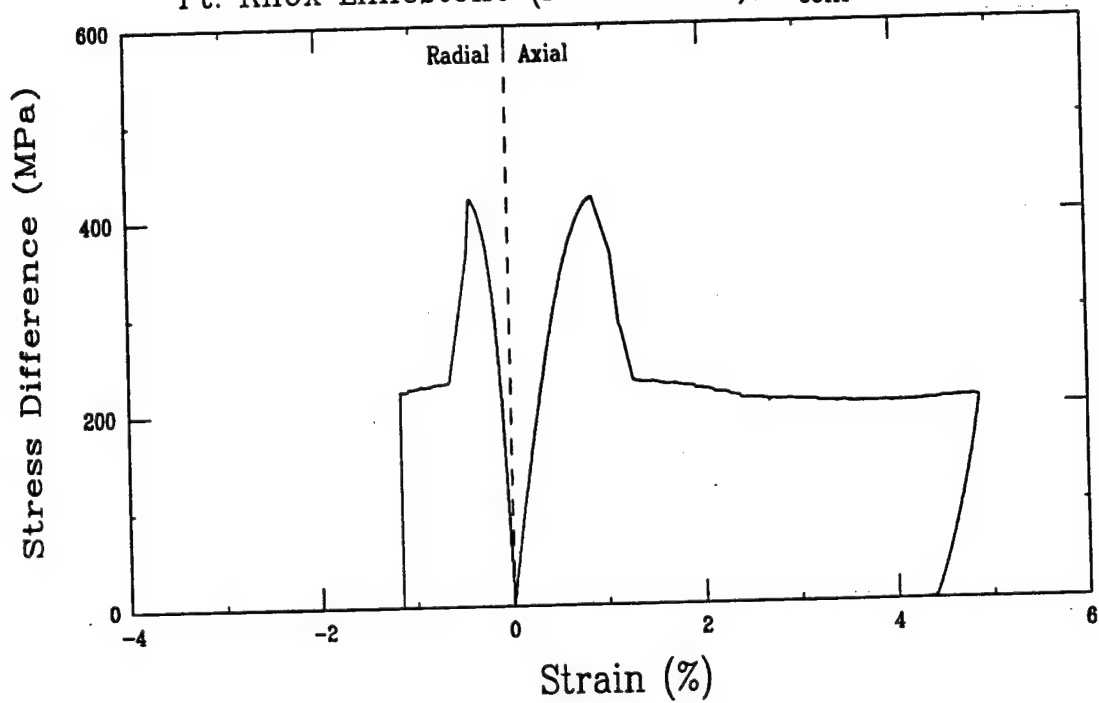
Triaxial Compression Test (A28D3)
Ft. Knox Limestone (FK10-4-01L), $\sigma_{\text{conf}} = 50 \text{ MPa}$



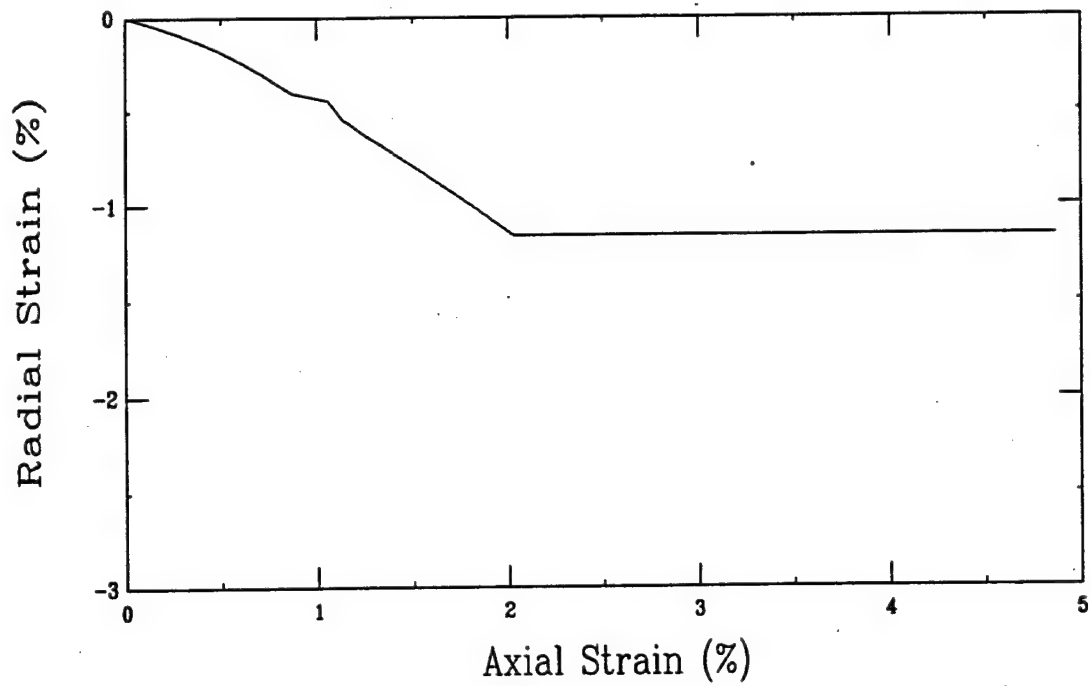
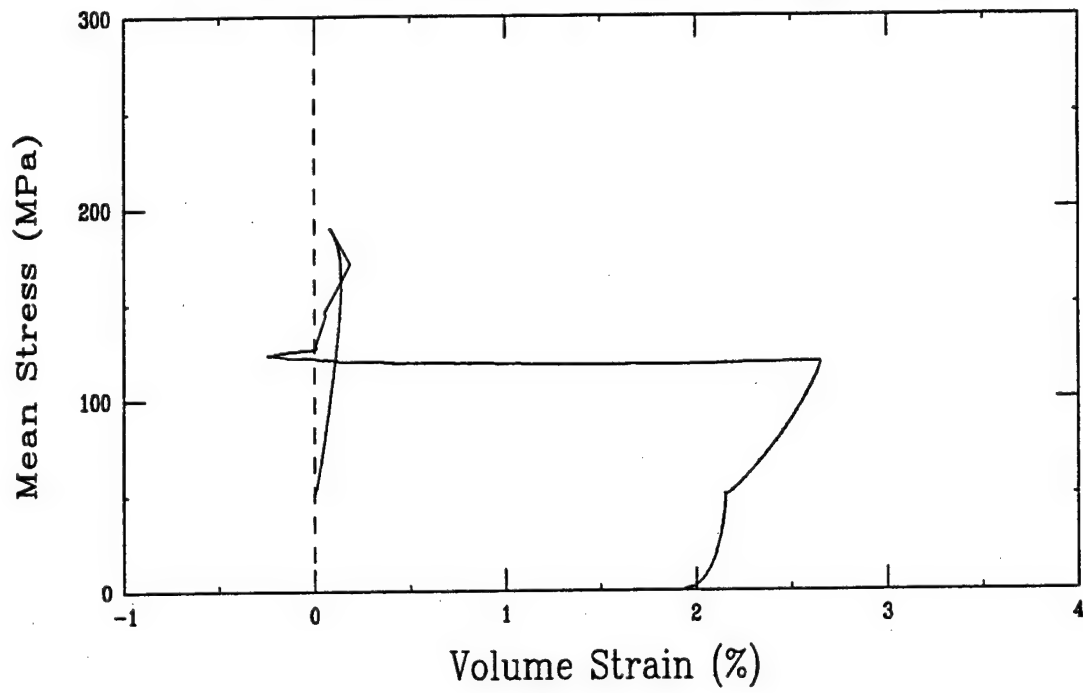
Triaxial Compression Test (A28D3)
Ft. Knox Limestone (FK10-4-01L), $\sigma_{\text{conf}} = 50 \text{ MPa}$



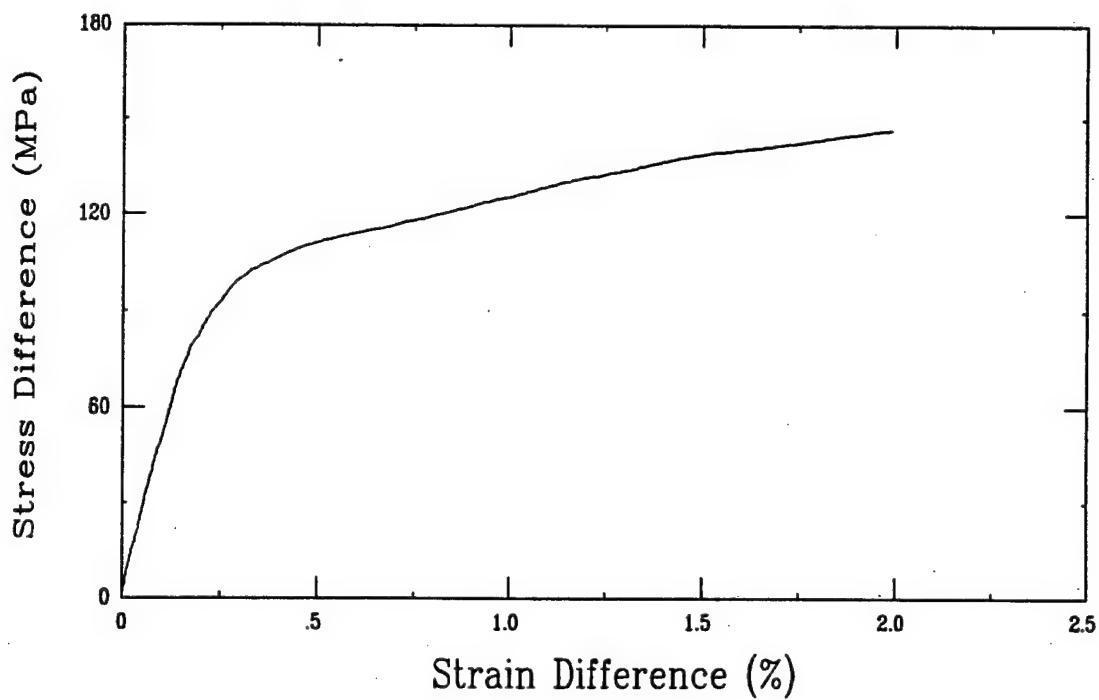
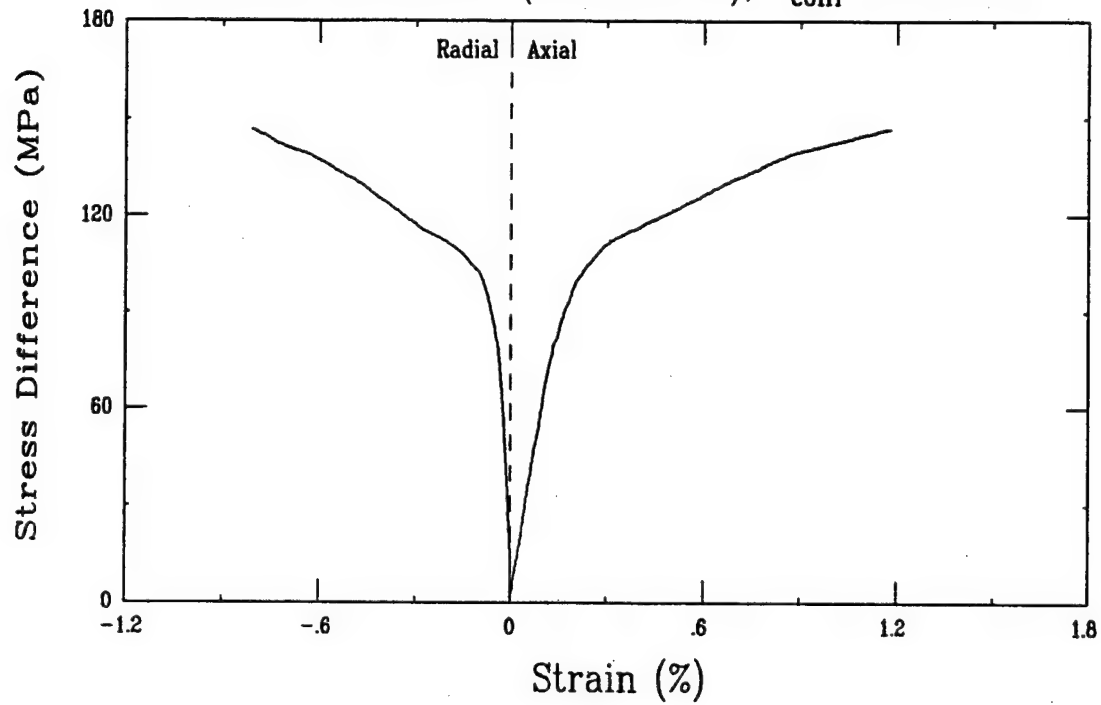
Triaxial Compression Test (A27B3)
Ft. Knox Limestone (FK10-5-03), $\sigma_{\text{conf}} = 50$ MPa



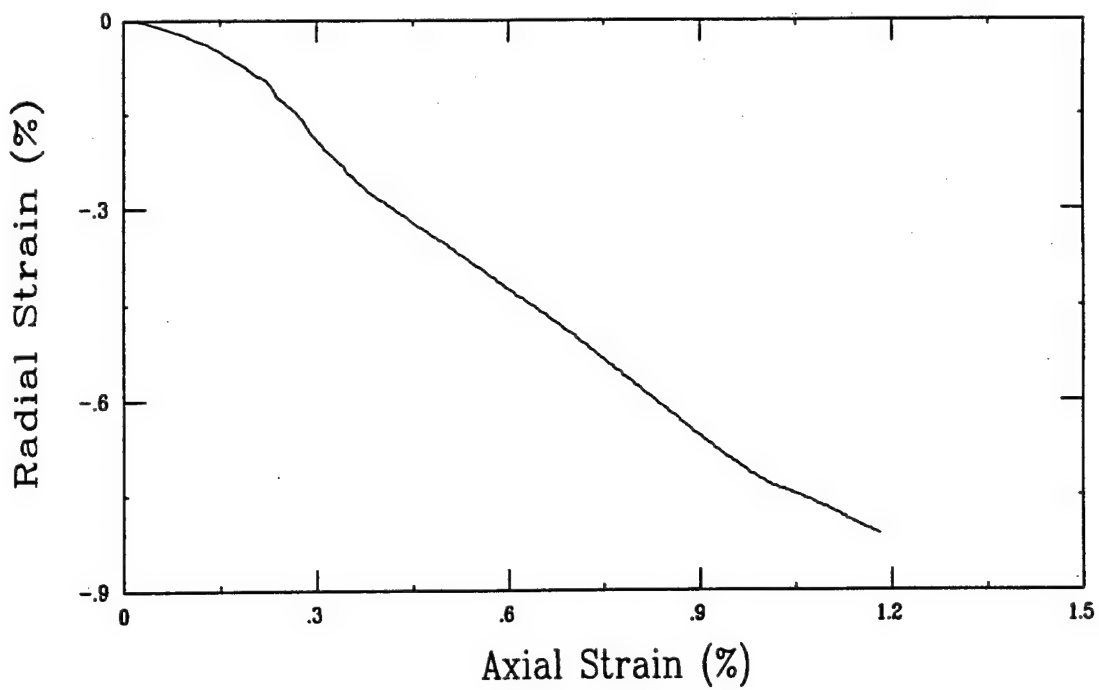
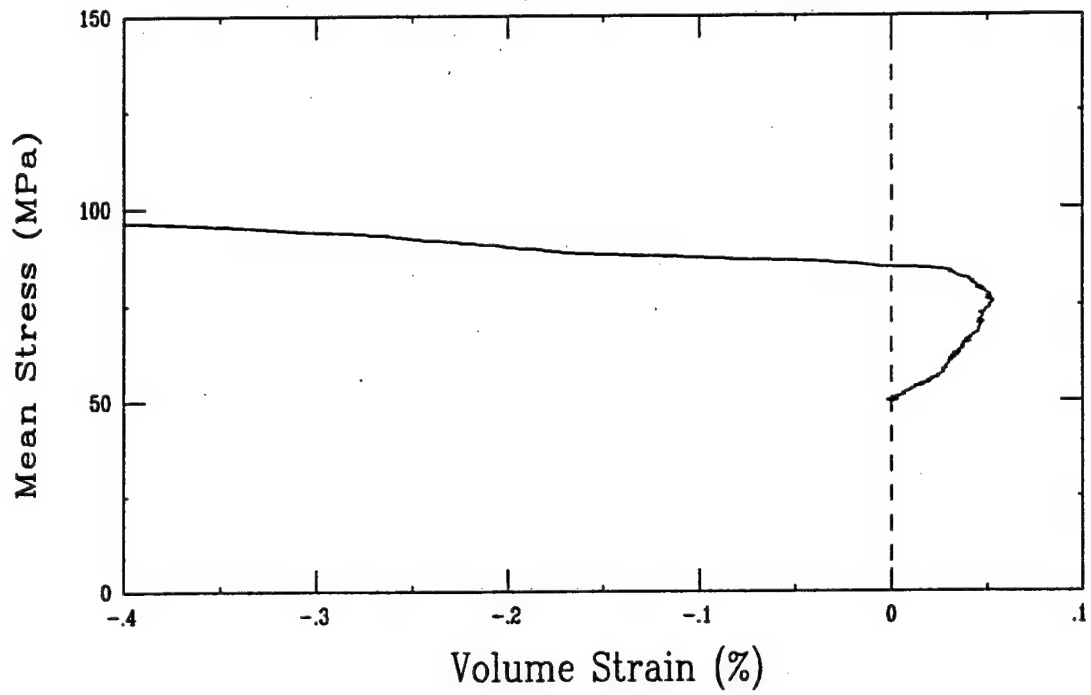
Triaxial Compression Test (A27B3)
Ft. Knox Limestone (FK10-5-03), $\sigma_{\text{conf}} = 50 \text{ MPa}$



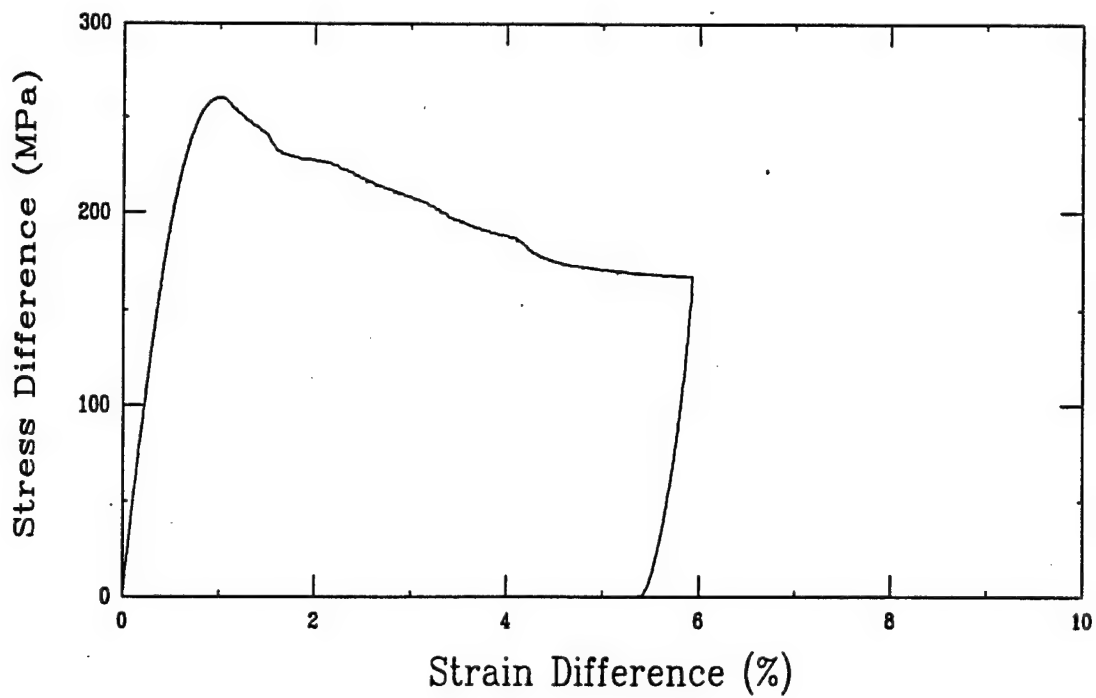
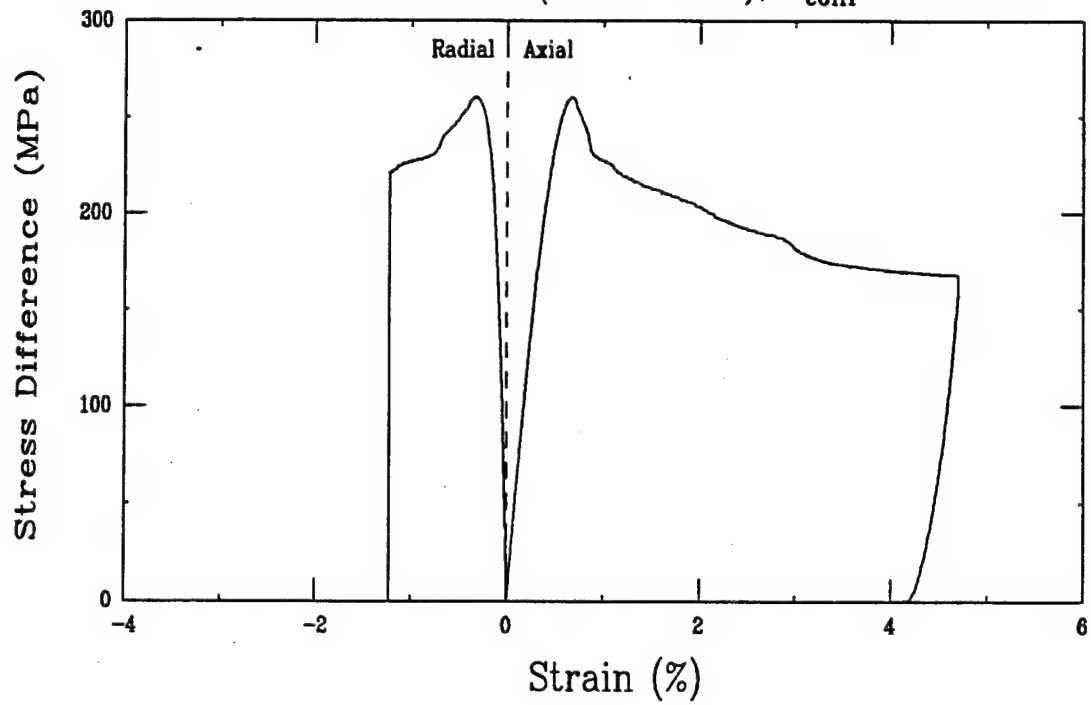
Triaxial Compression Test (A28H3)
Ft. Knox Limestone (FK10-6-03), $\sigma_{\text{conf}} = 50$ MPa



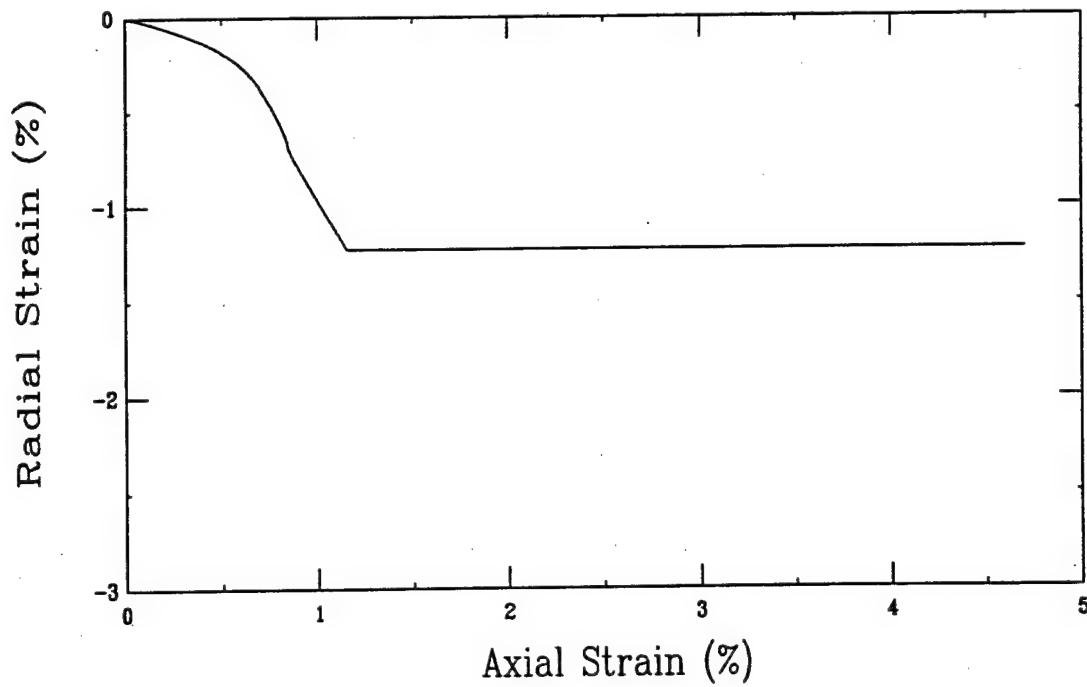
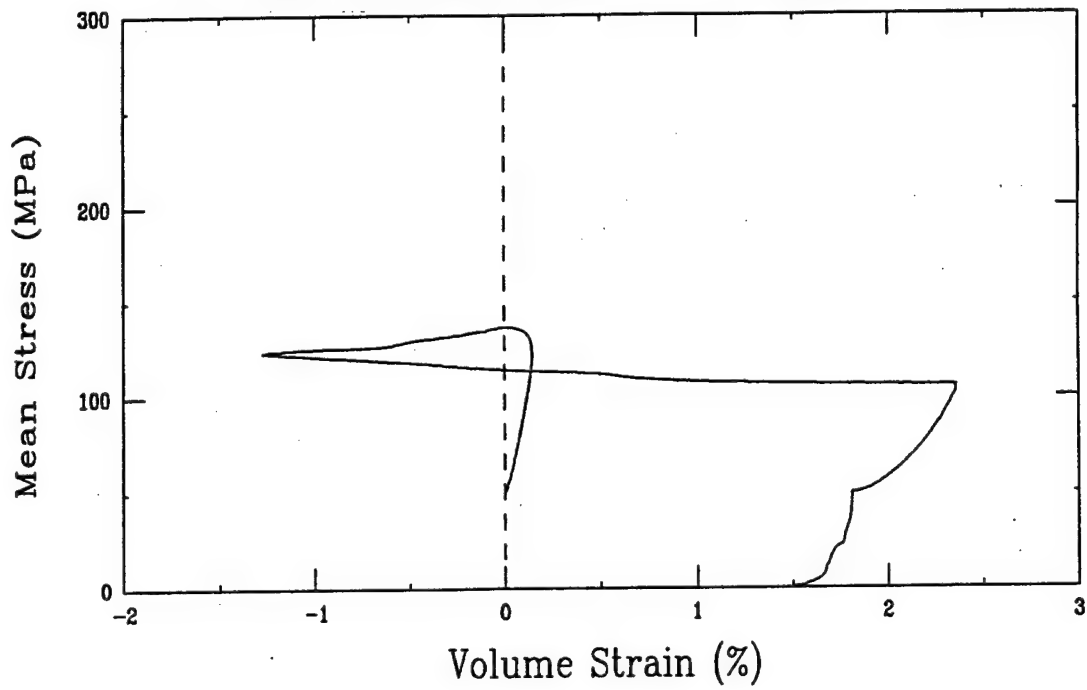
Triaxial Compression Test (A28H3)
Ft. Knox Limestone (FK10-6-03), $\sigma_{conf} = 50$ MPa



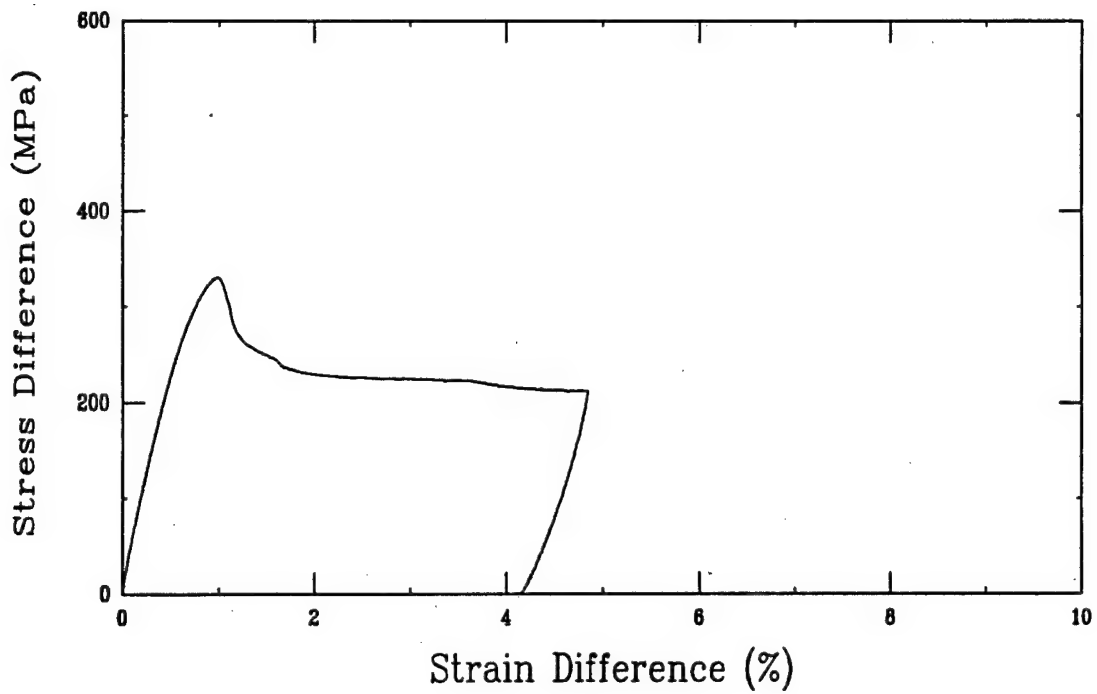
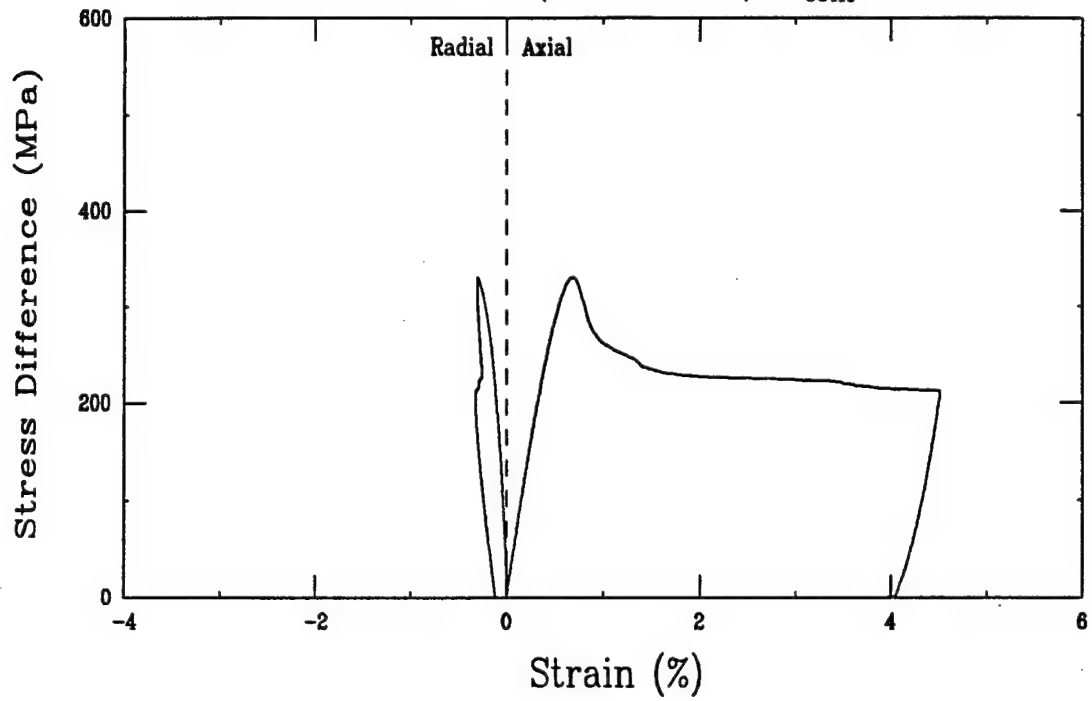
Triaxial Compression Test (A27F3)
Ft. Knox Limestone (FK10-7-01), $\sigma_{\text{conf}} = 50 \text{ MPa}$



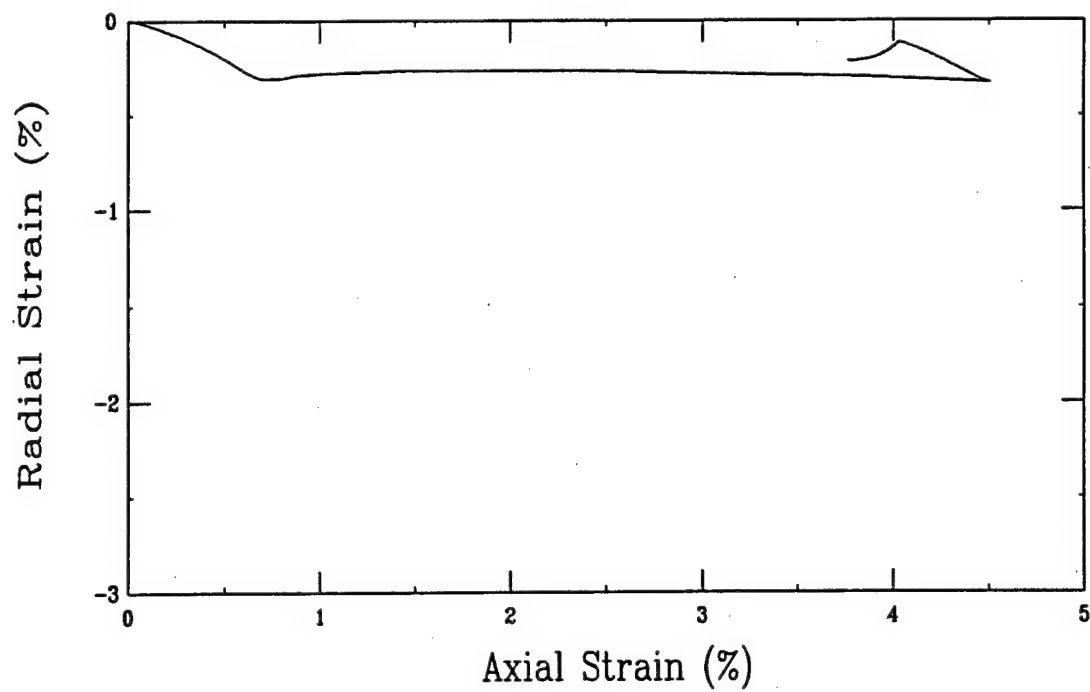
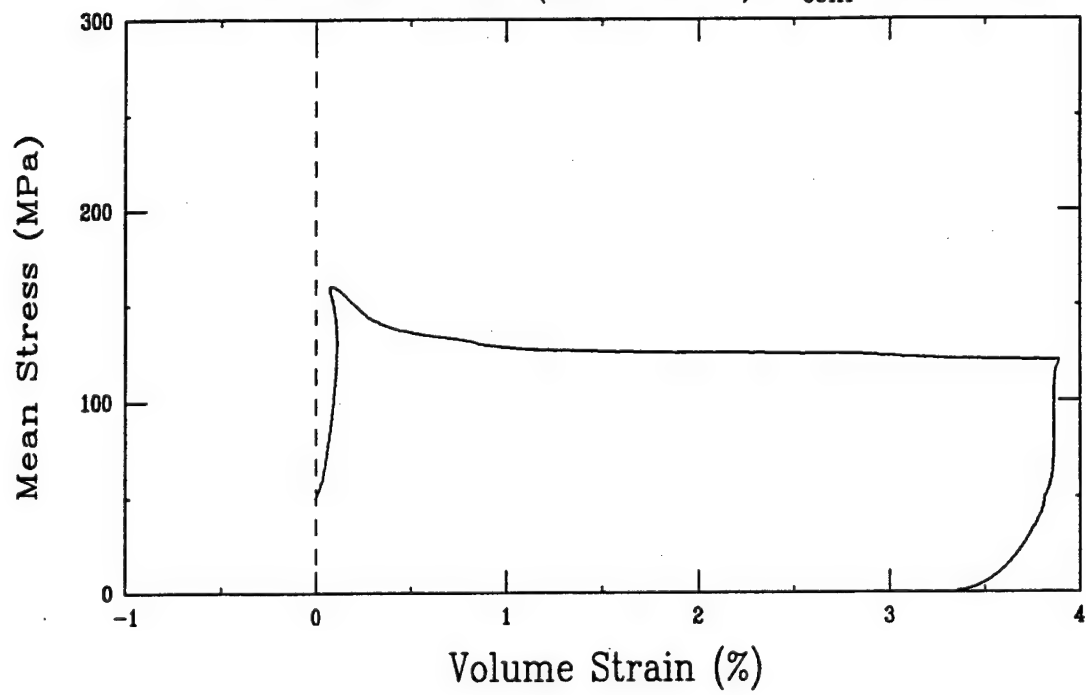
Triaxial Compression Test (A27F3)
Ft. Knox Limestone (FK10-7-01), $\sigma_{\text{conf}} = 50 \text{ MPa}$



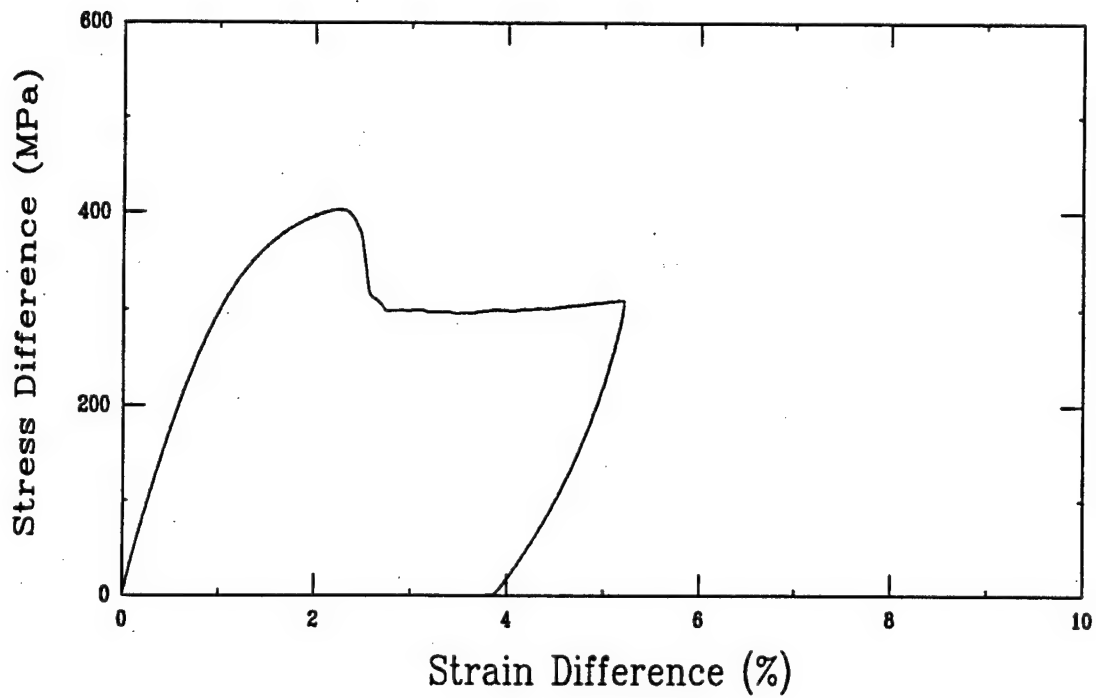
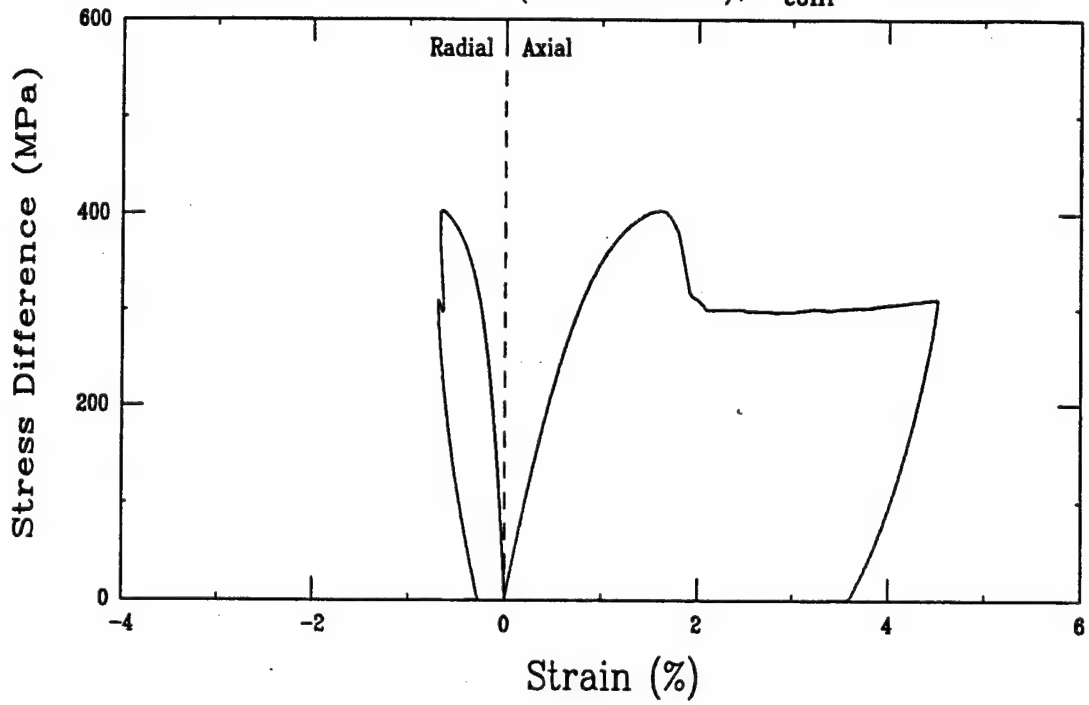
Triaxial Compression Test (A27D3)
Ft. Knox Limestone (FK10-7-03), $\sigma_{\text{conf}} = 50$ MPa



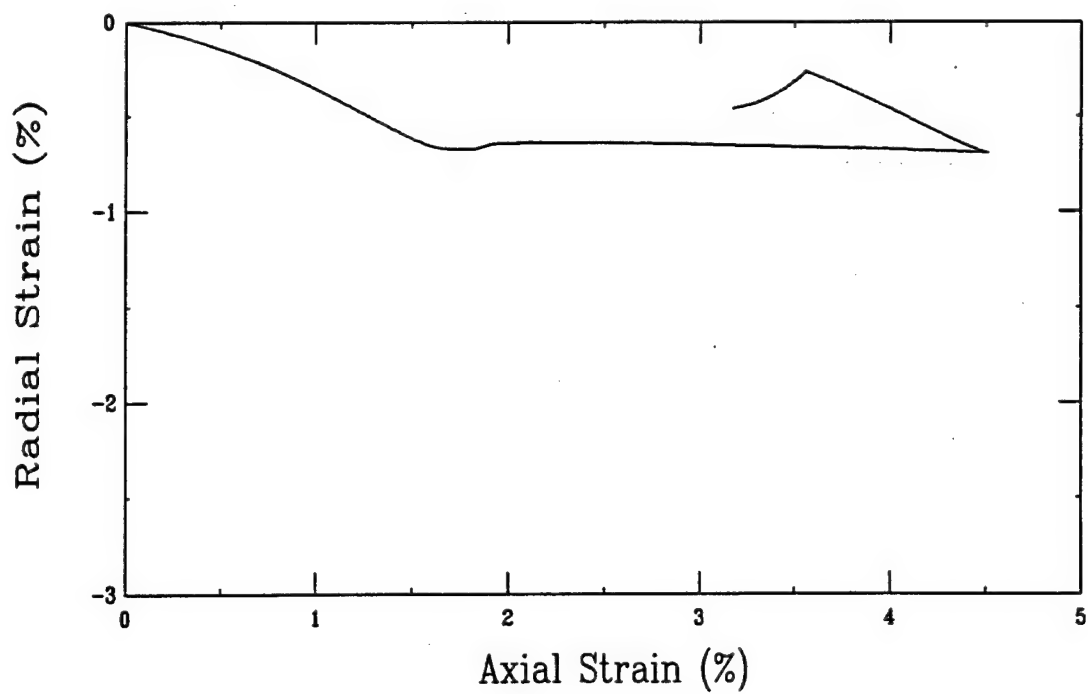
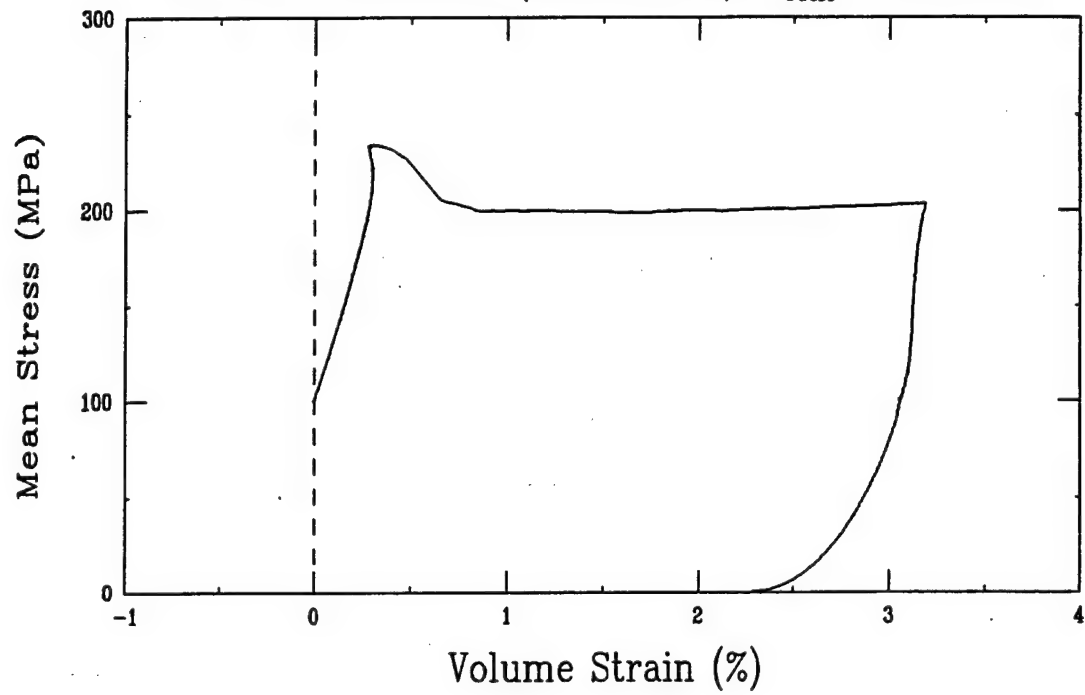
Triaxial Compression Test (A27D3)
Ft. Knox Limestone (FK10-7-03), $\sigma_{\text{conf}} = 50 \text{ MPa}$



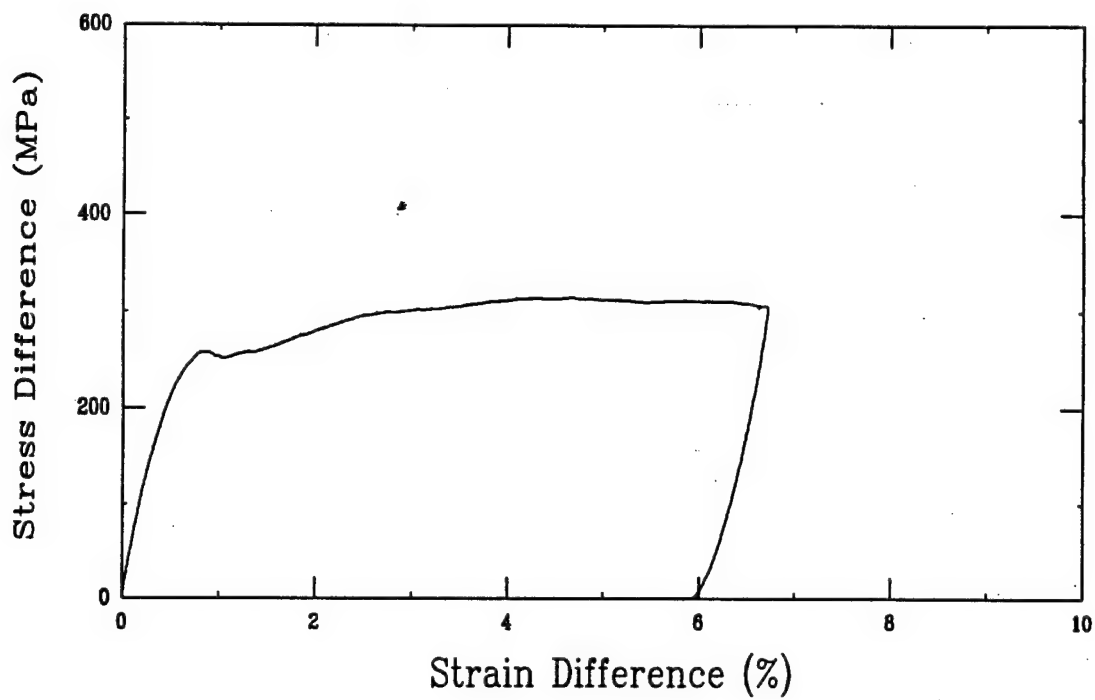
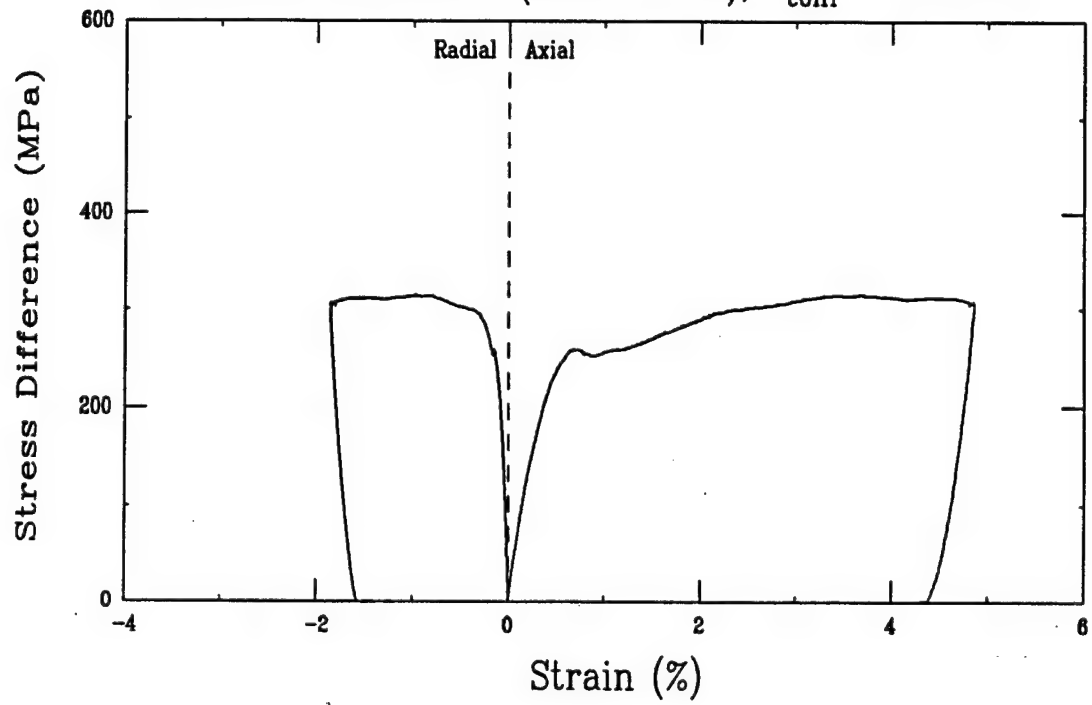
Triaxial Compression Test (A29B3)
Ft. Knox Limestone (FK10-2-04), $\sigma_{\text{conf}} = 100 \text{ MPa}$



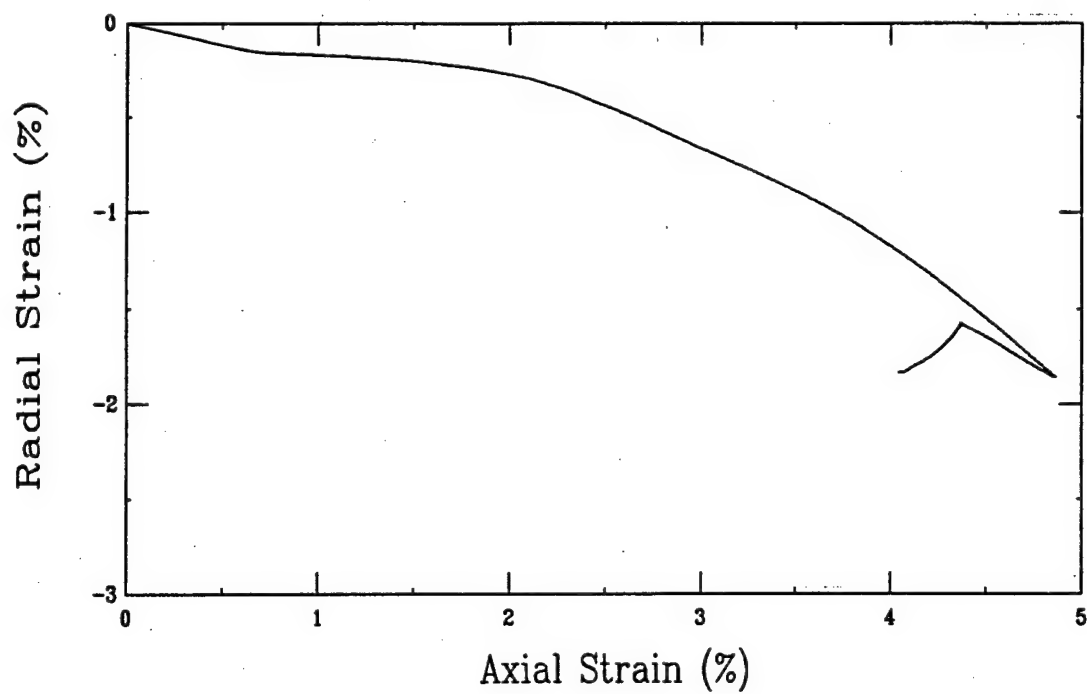
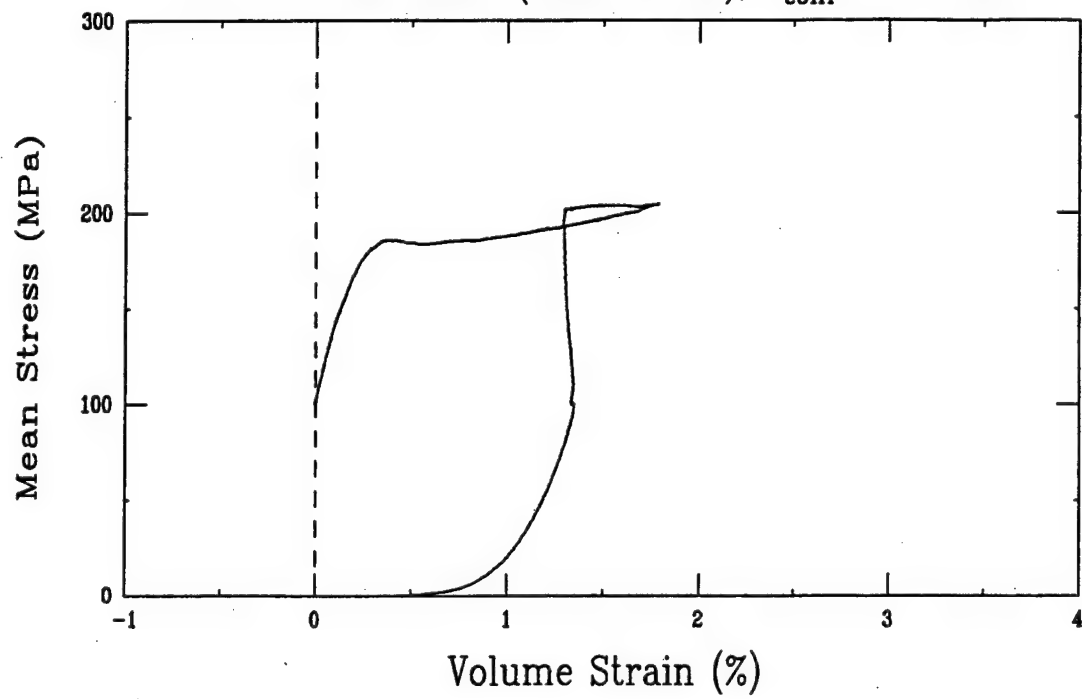
Triaxial Compression Test (A29B3)
Ft. Knox Limestone (FK10-2-04), $\sigma_{\text{conf}} = 100 \text{ MPa}$



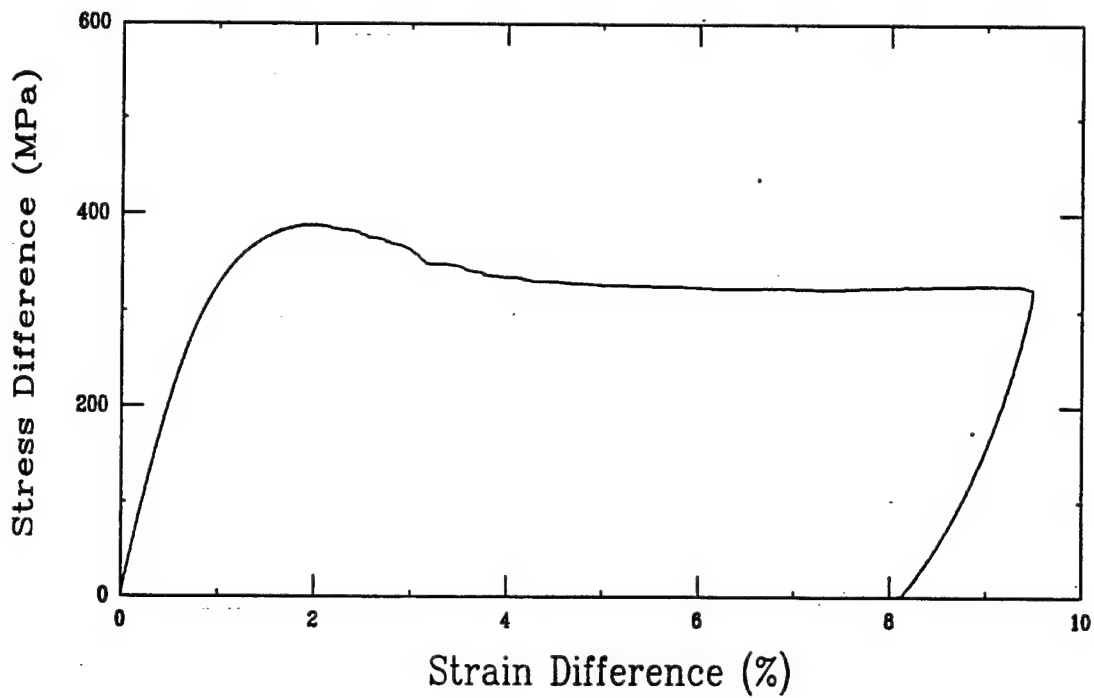
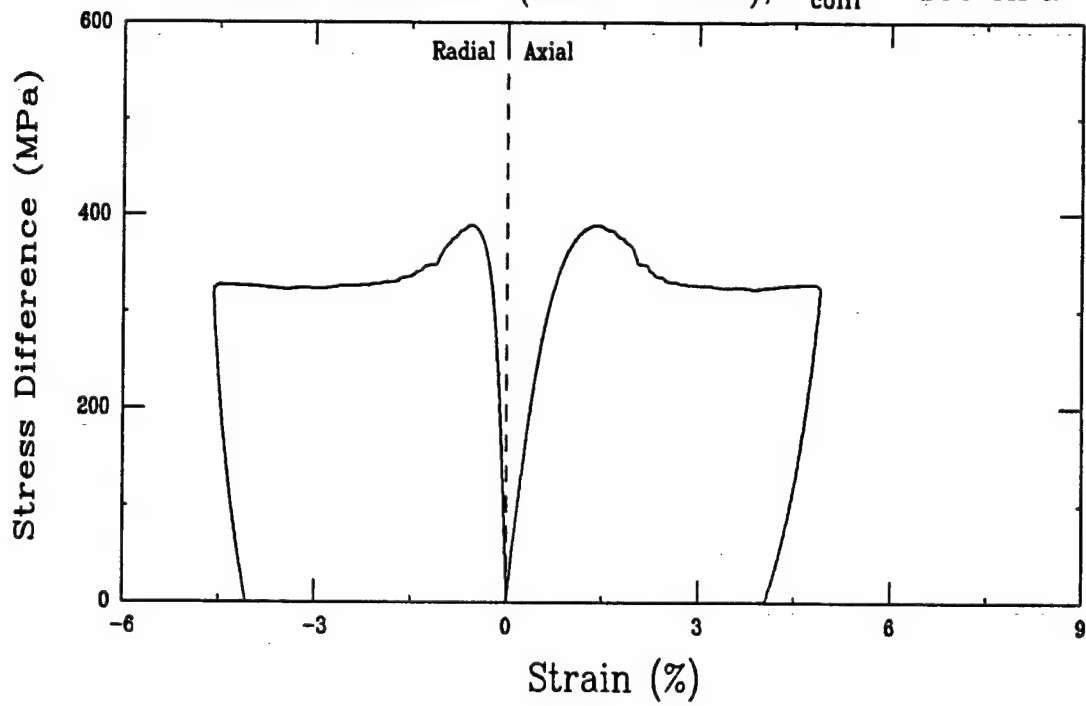
Triaxial Compression Test (A30H3)
Ft. Knox Limestone (FK10-3-05), $\sigma_{\text{conf}} = 100$ MPa



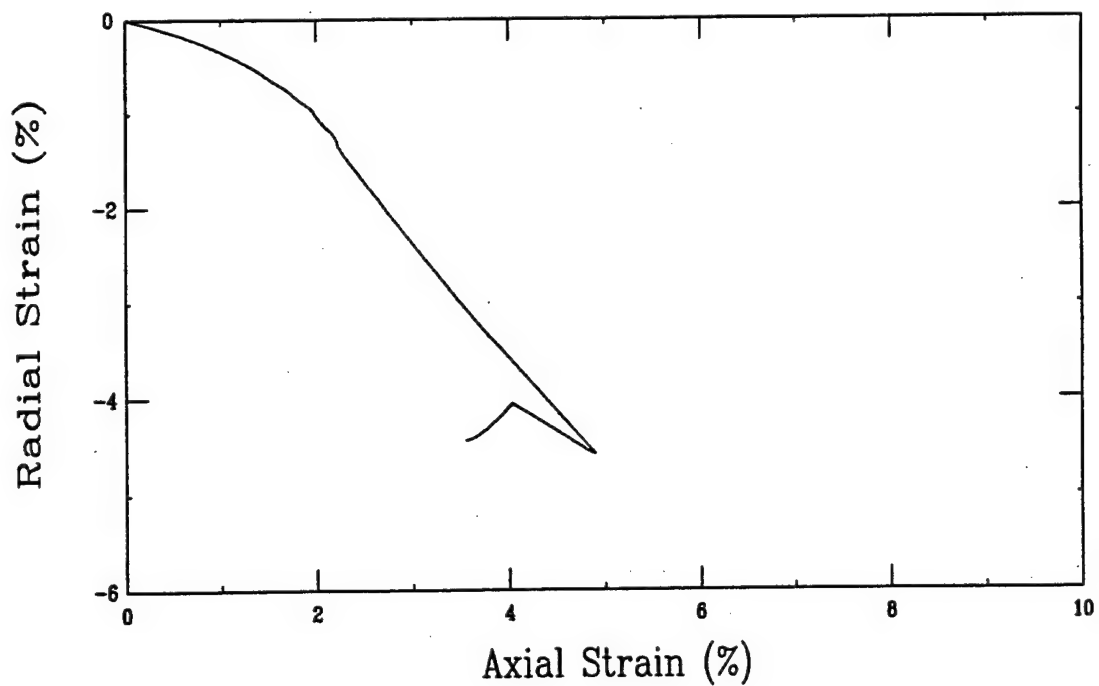
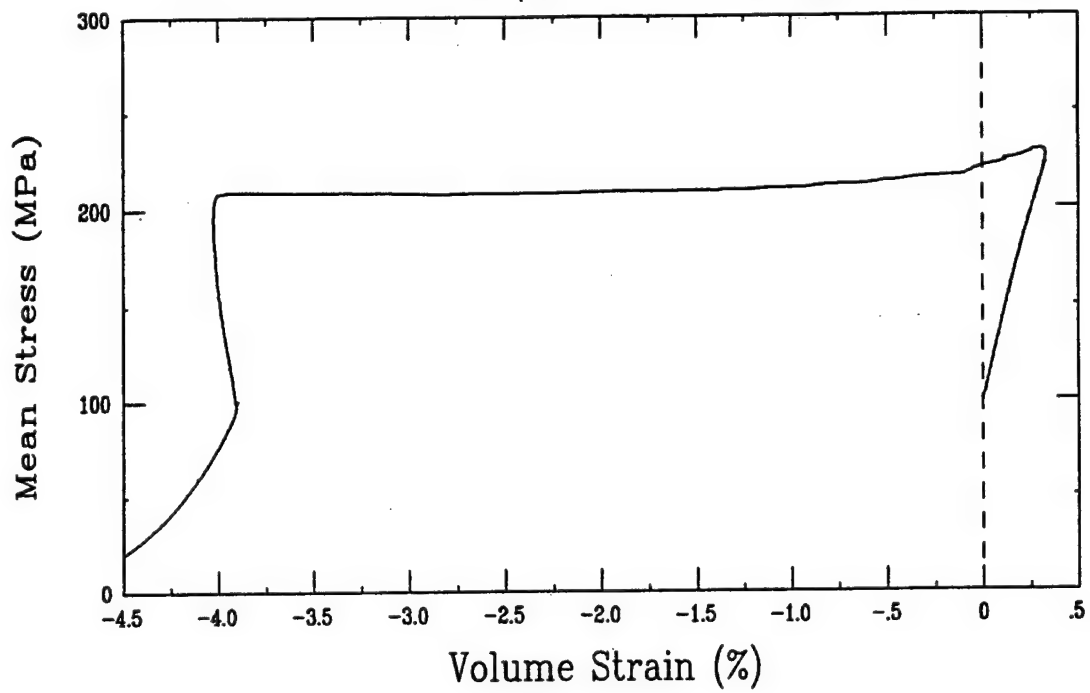
Triaxial Compression Test (A30H3)
Ft. Knox Limestone (FK10-3-05), $\sigma_{\text{conf}} = 100 \text{ MPa}$



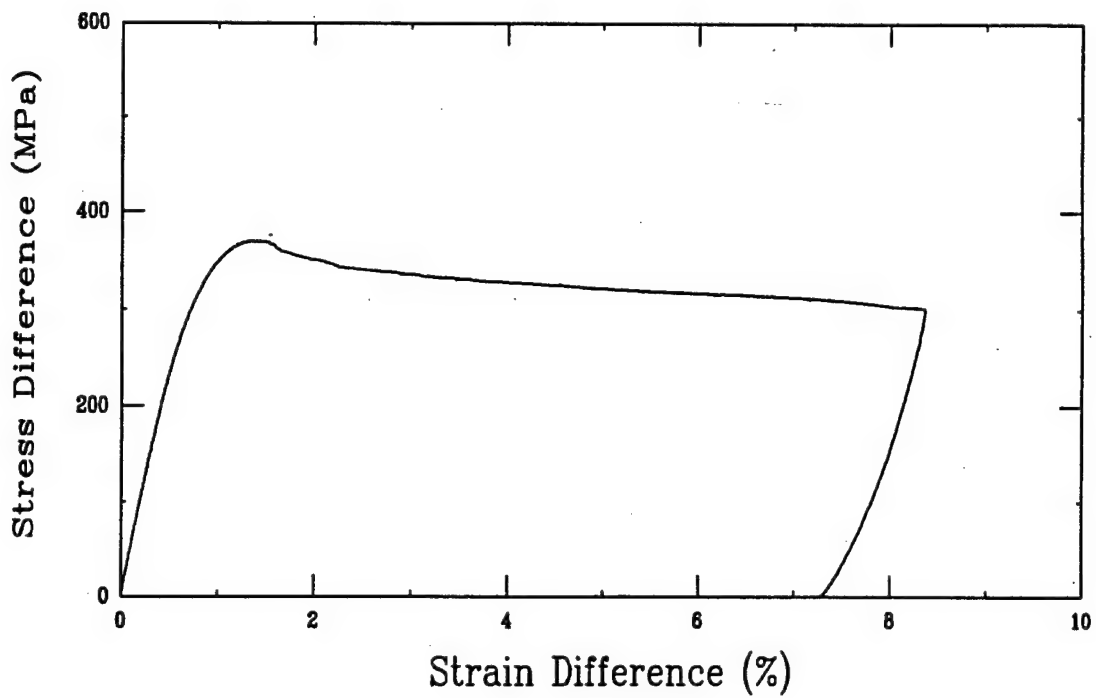
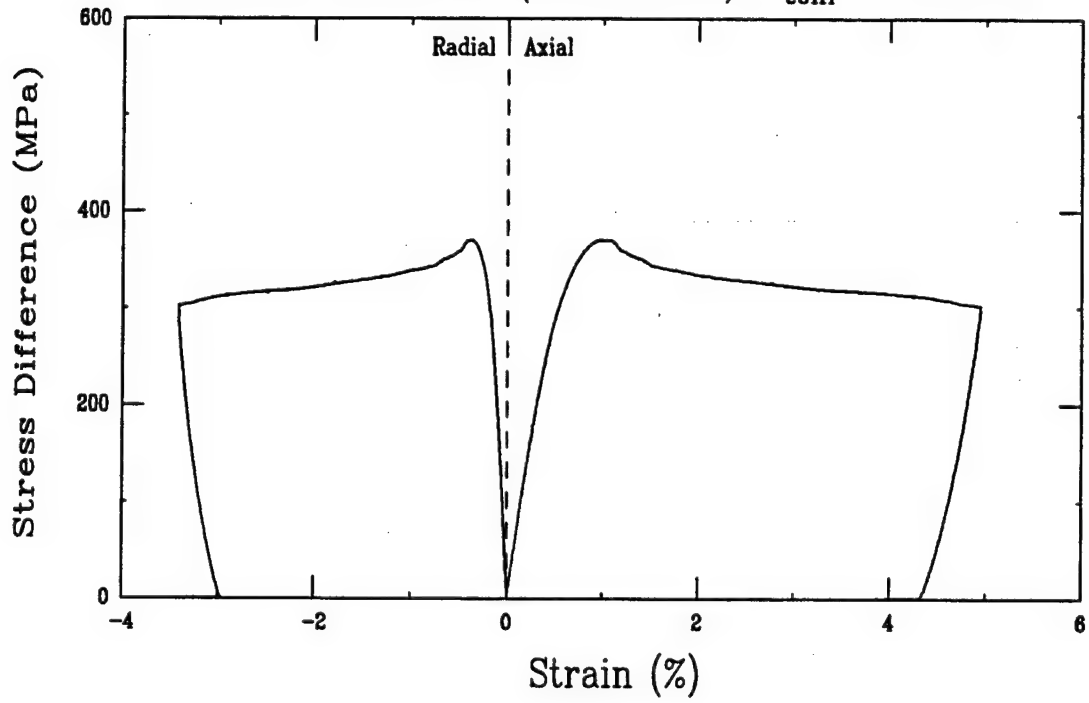
Triaxial Compression Test (A30J3)
Ft. Knox Limestone (FK10-4-03H), $\sigma_{\text{conf}} = 100 \text{ MPa}$



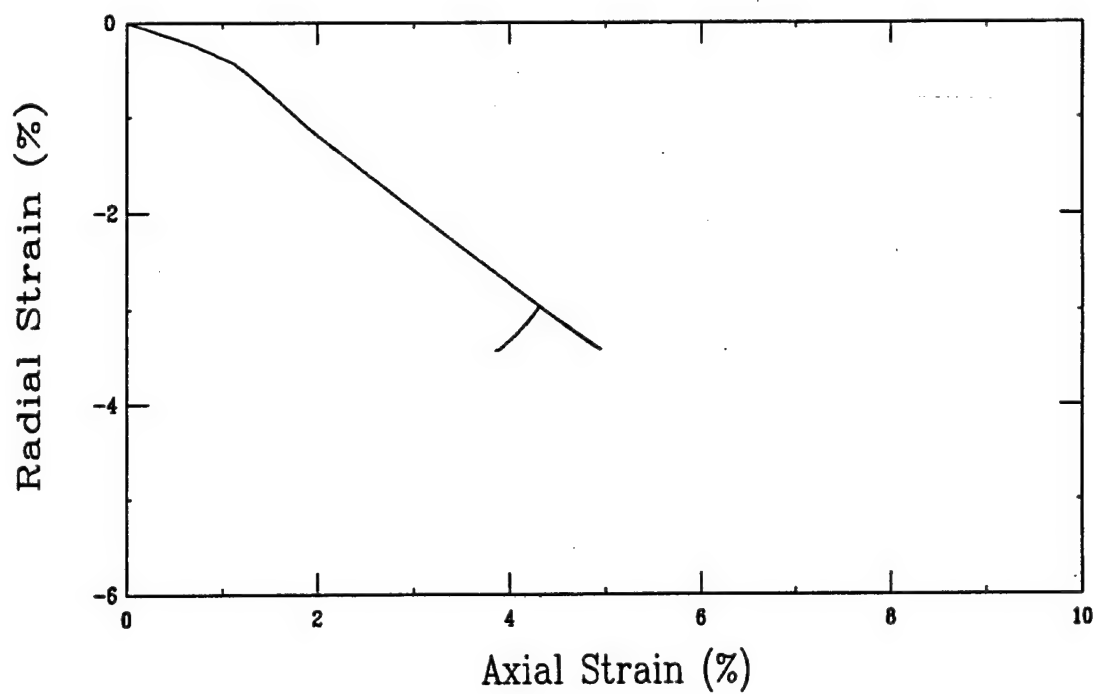
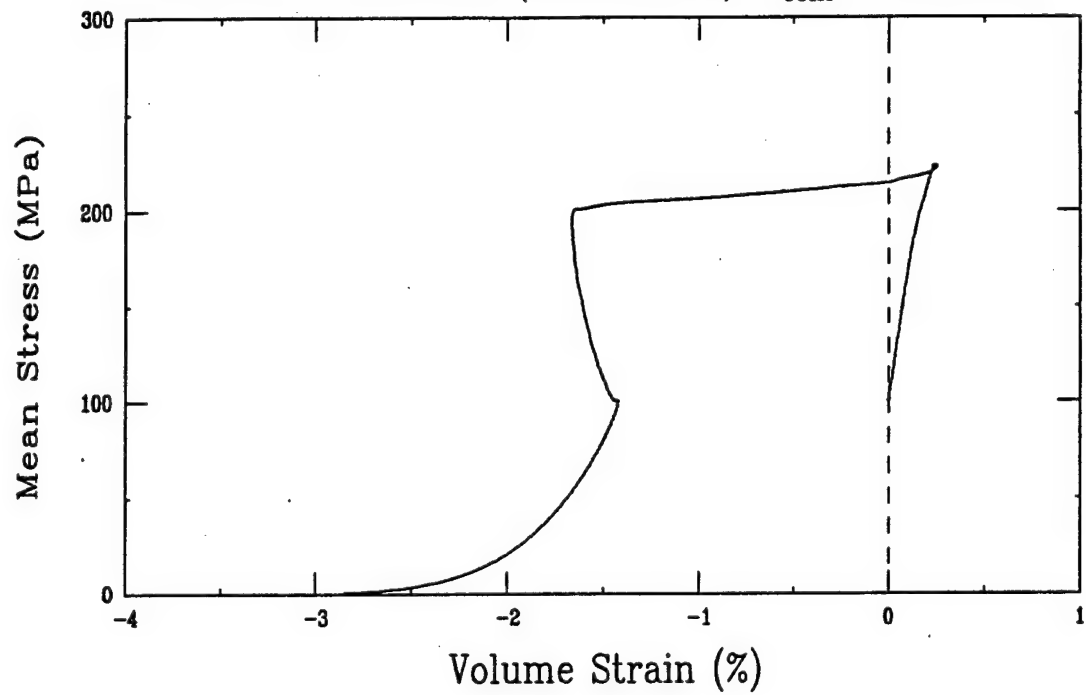
Triaxial Compression Test (A30J3)
Ft. Knox Limestone (FK10-4-03H), $\sigma_{conf} = 100$ MPa



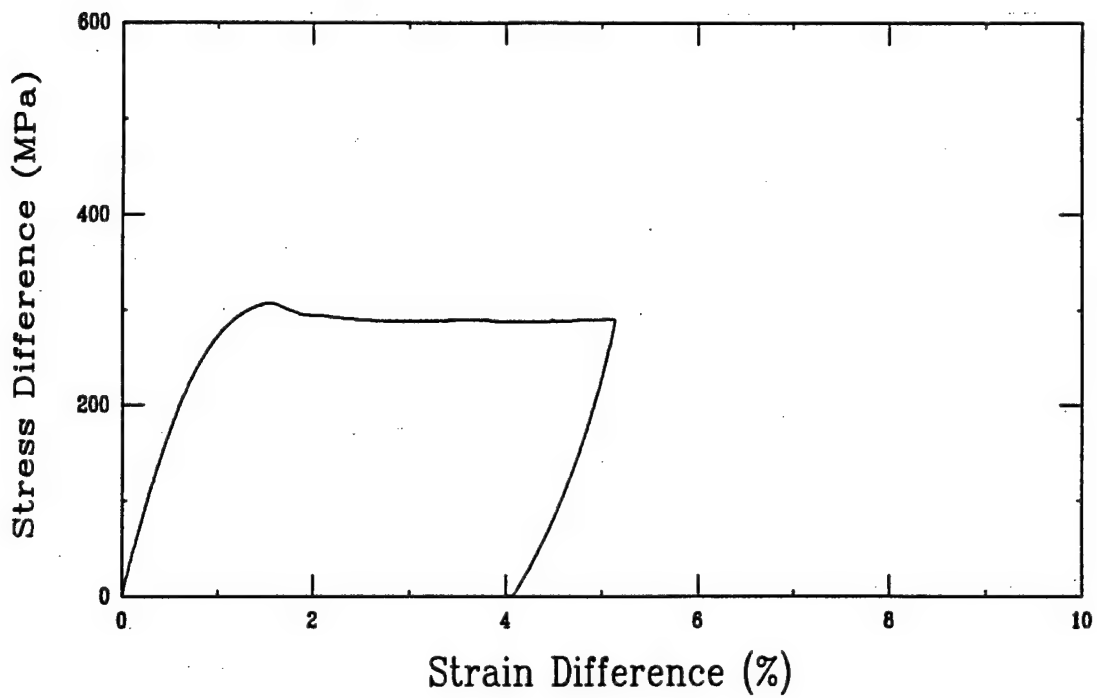
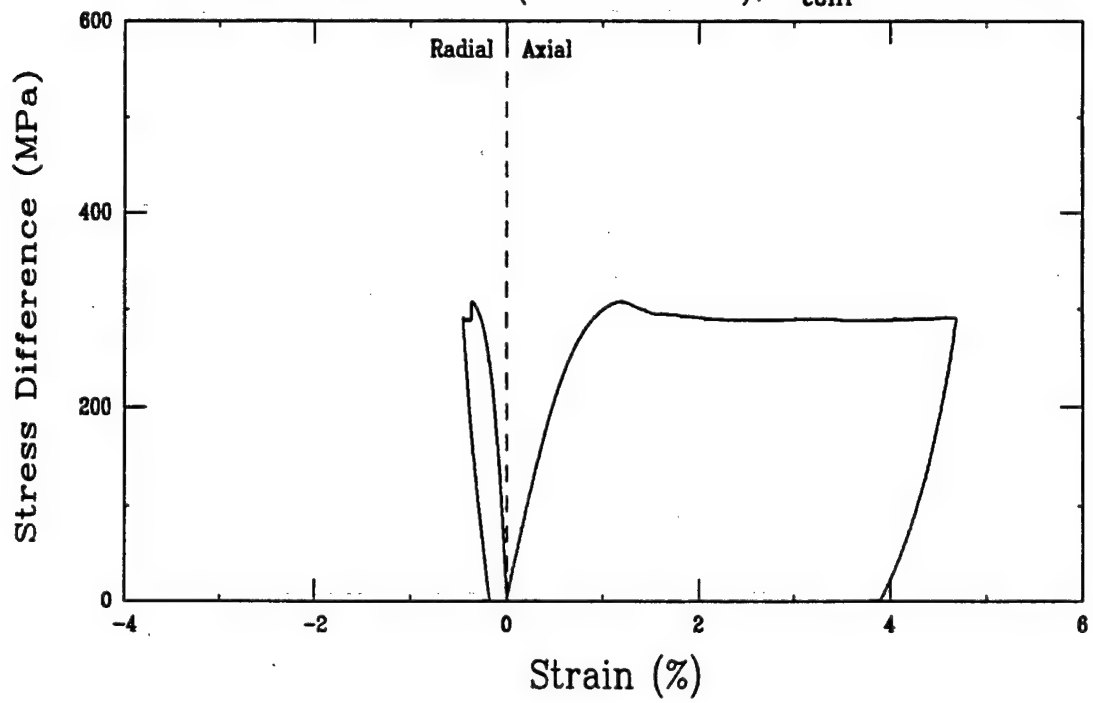
Triaxial Compression Test (A30B3)
Ft. Knox Limestone (FK10-4-01), $\sigma_{\text{conf}} = 100$ MPa



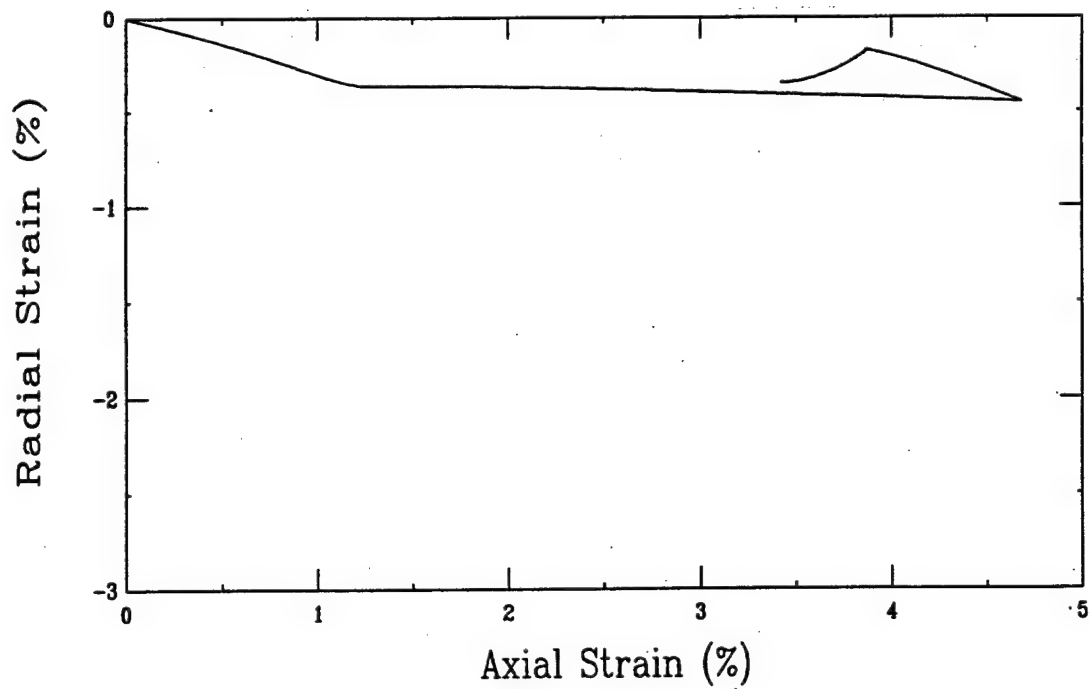
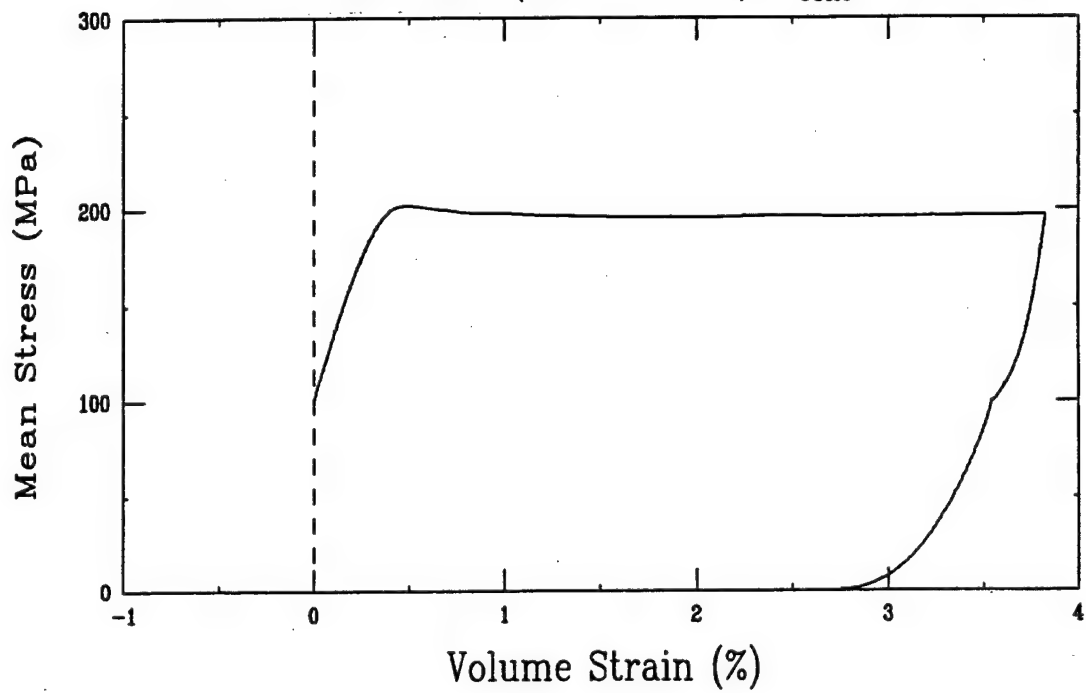
Triaxial Compression Test (A30B3)
Ft. Knox Limestone (FK10-4-01), $\sigma_{\text{conf}} = 100 \text{ MPa}$



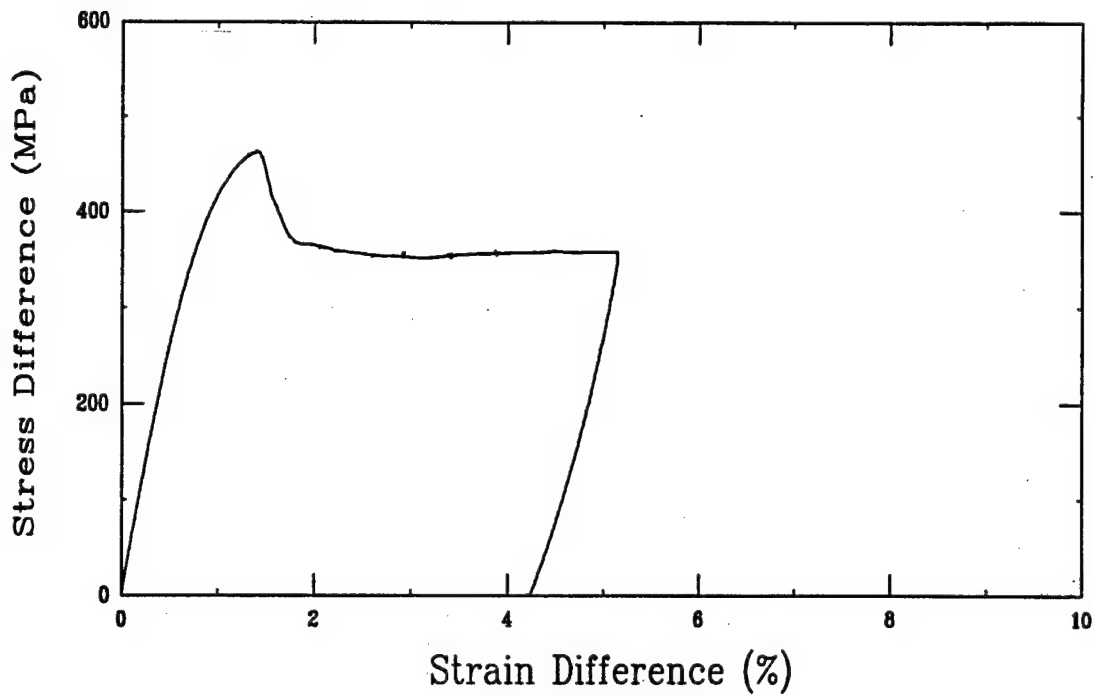
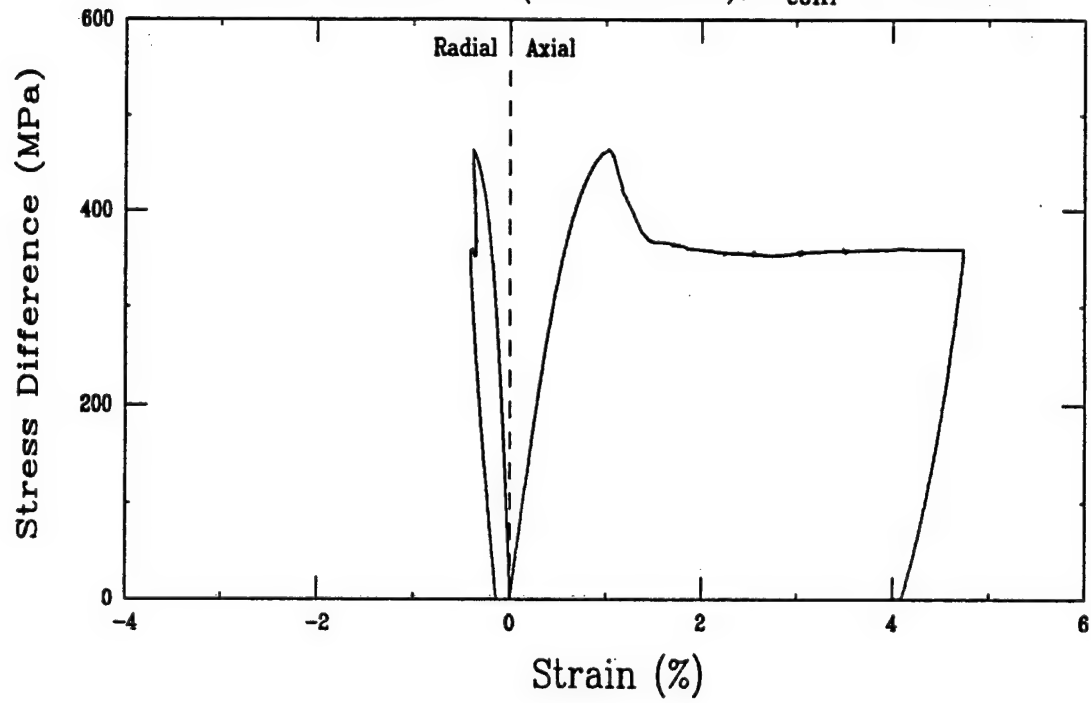
Triaxial Compression Test (A30D3)
Ft. Knox Limestone (FK10-4-04L), $\sigma_{\text{conf}} = 100 \text{ MPa}$



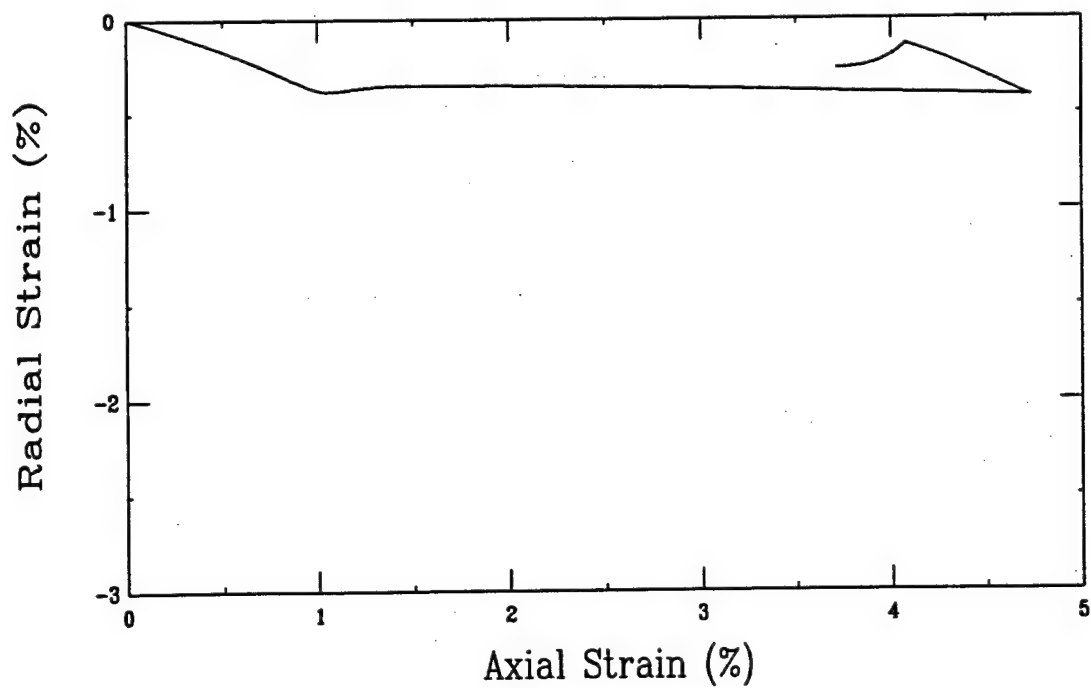
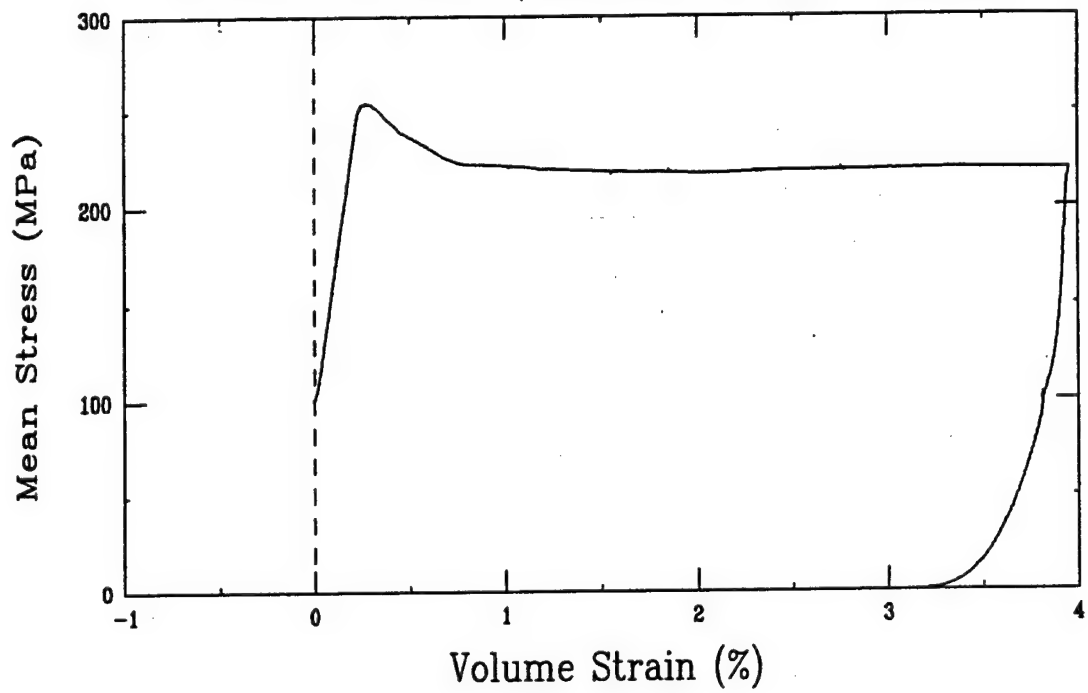
Triaxial Compression Test (A30D3)
Ft. Knox Limestone (FK10-4-04L), $\sigma_{\text{conf}} = 100 \text{ MPa}$



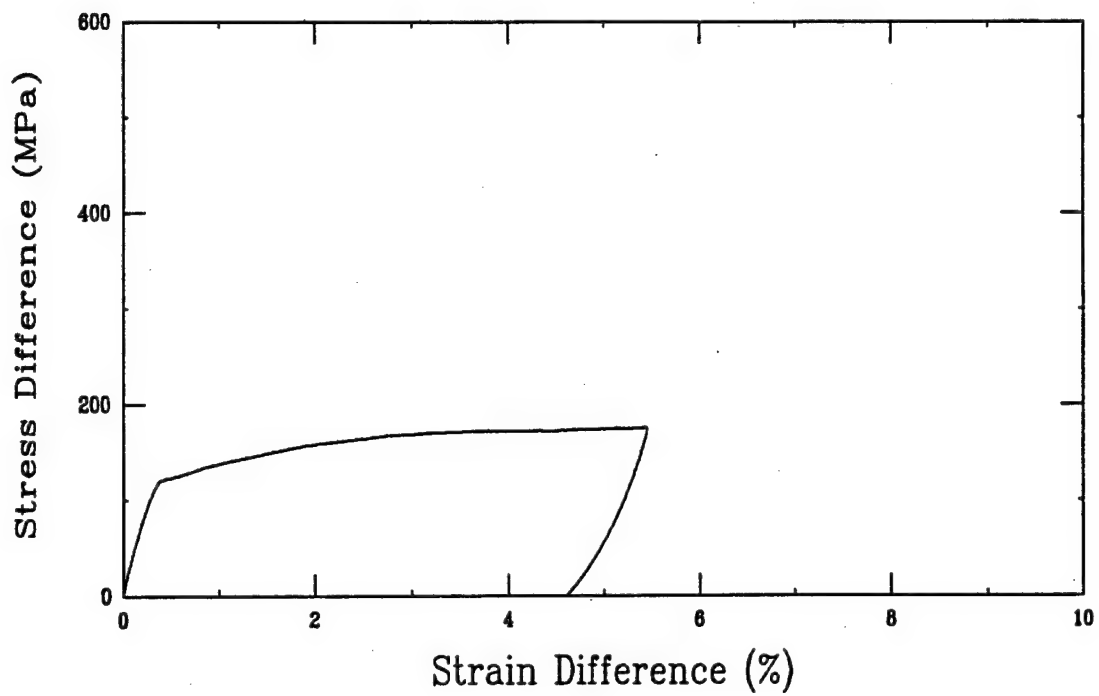
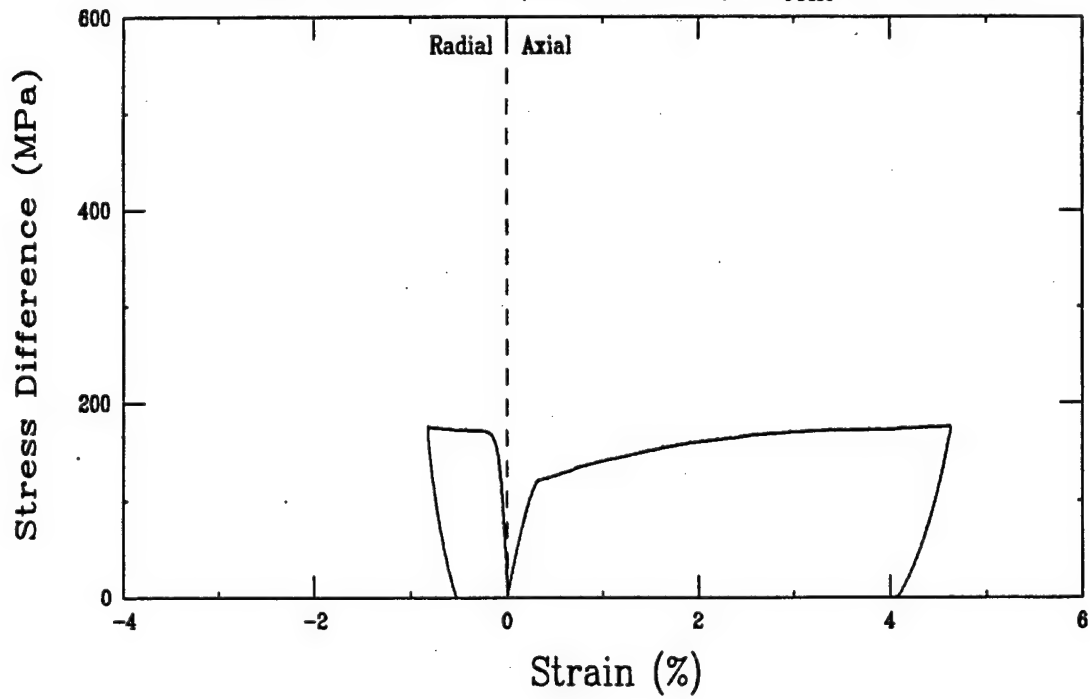
Triaxial Compression Test (A29H3)
Ft. Knox Limestone (FK10-5-01), $\sigma_{\text{conf}} = 100 \text{ MPa}$



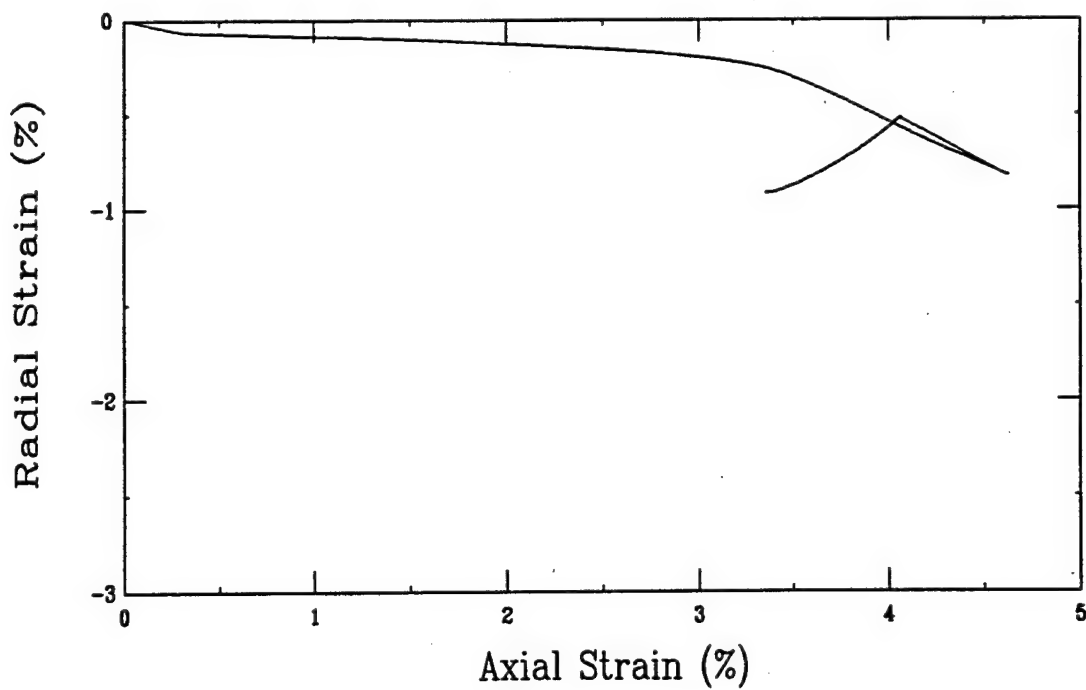
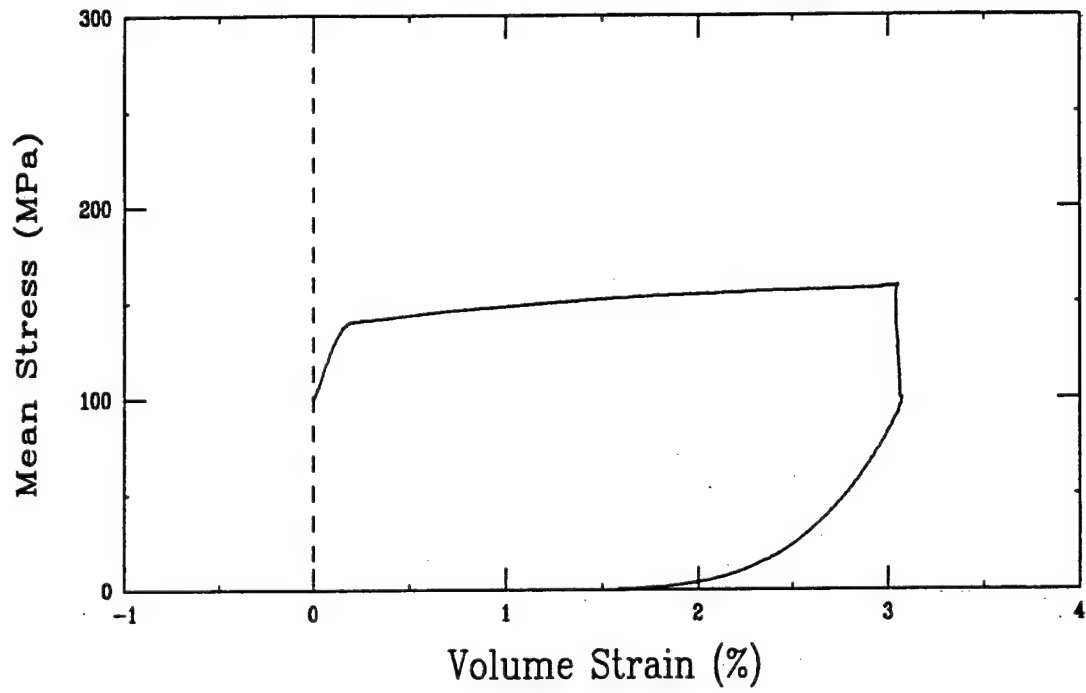
Triaxial Compression Test (A29H3)
Ft. Knox Limestone (FK10-5-01), $\sigma_{\text{conf}} = 100 \text{ MPa}$



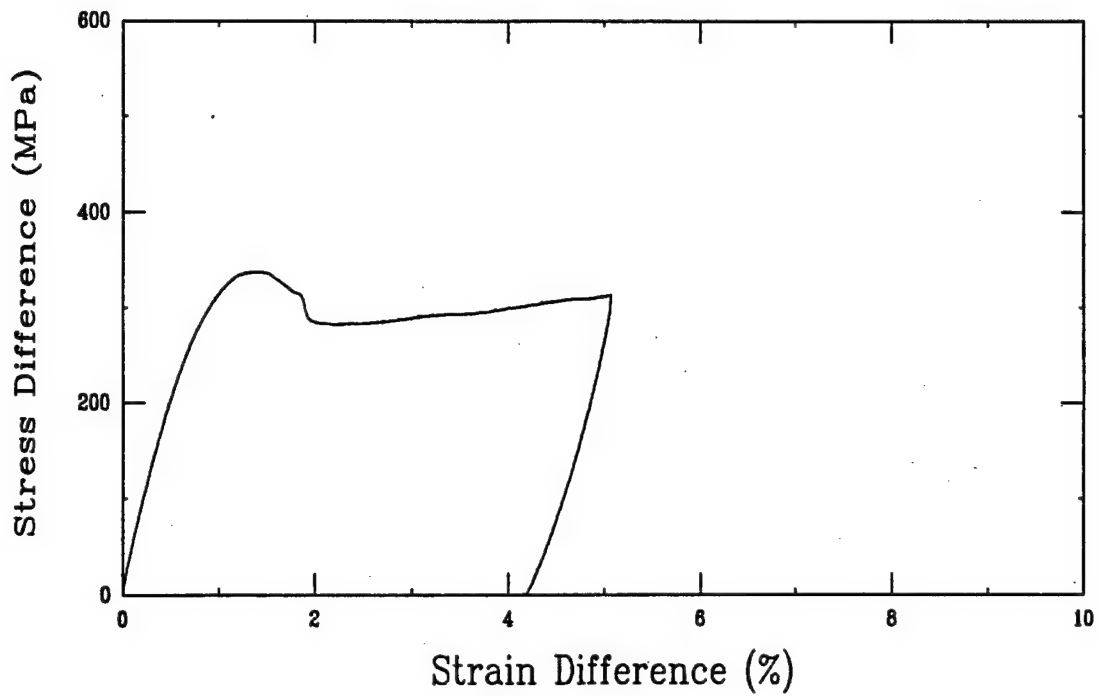
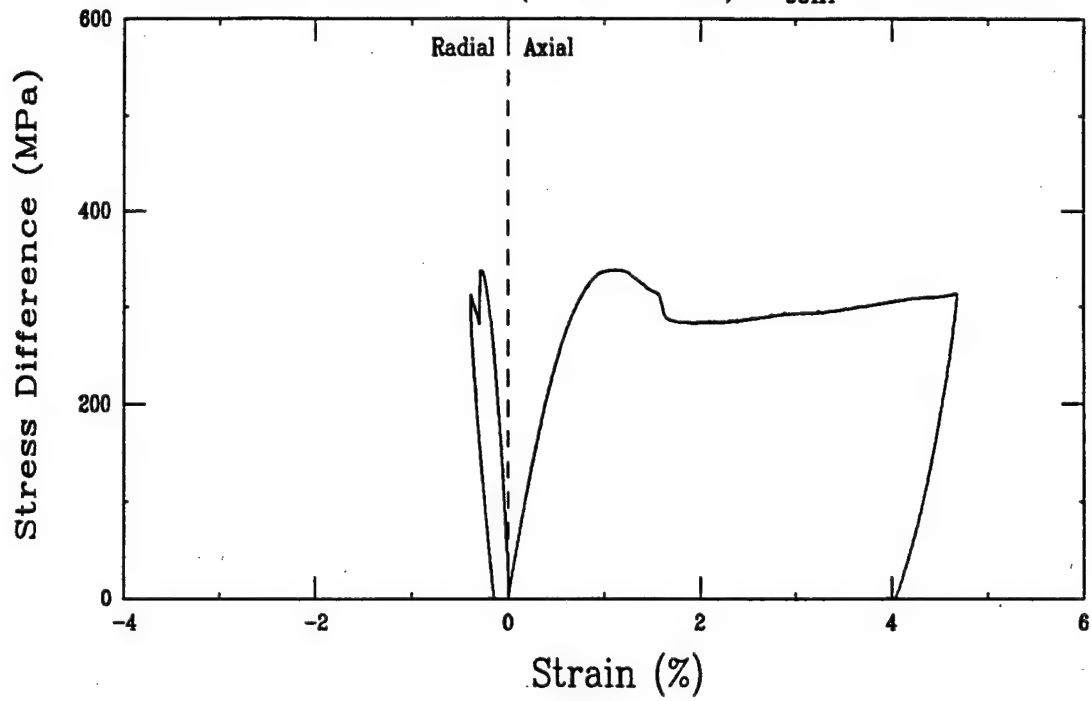
Triaxial Compression Test (A30F3)
Ft. Knox Limestone (FK10-6-05), $\sigma_{\text{conf}} = 100$ MPa



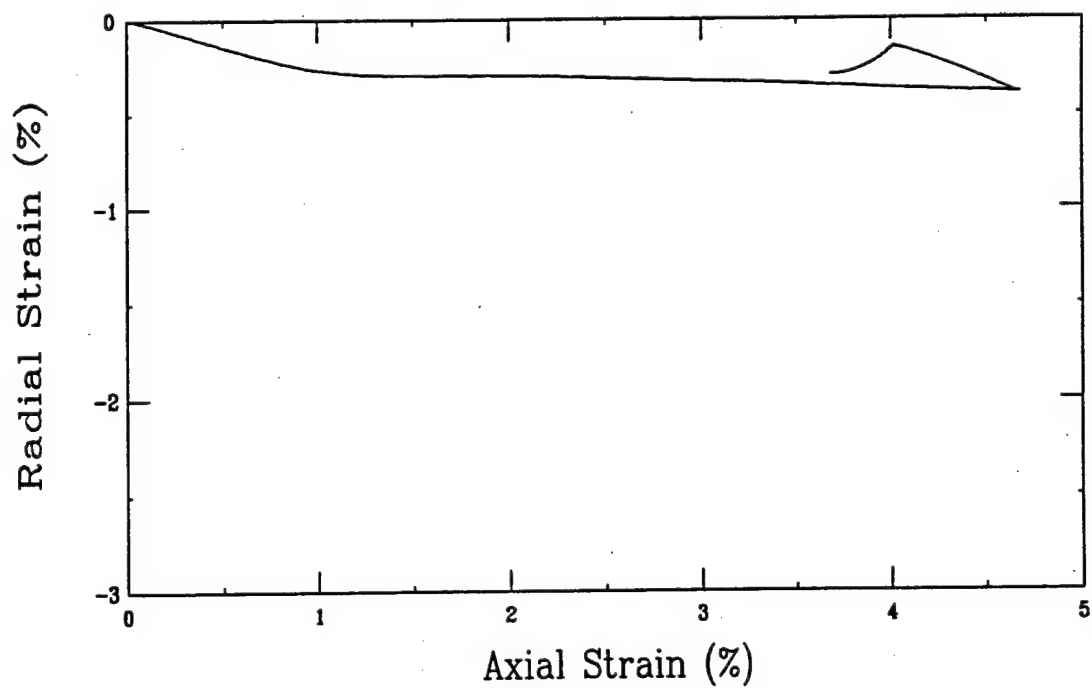
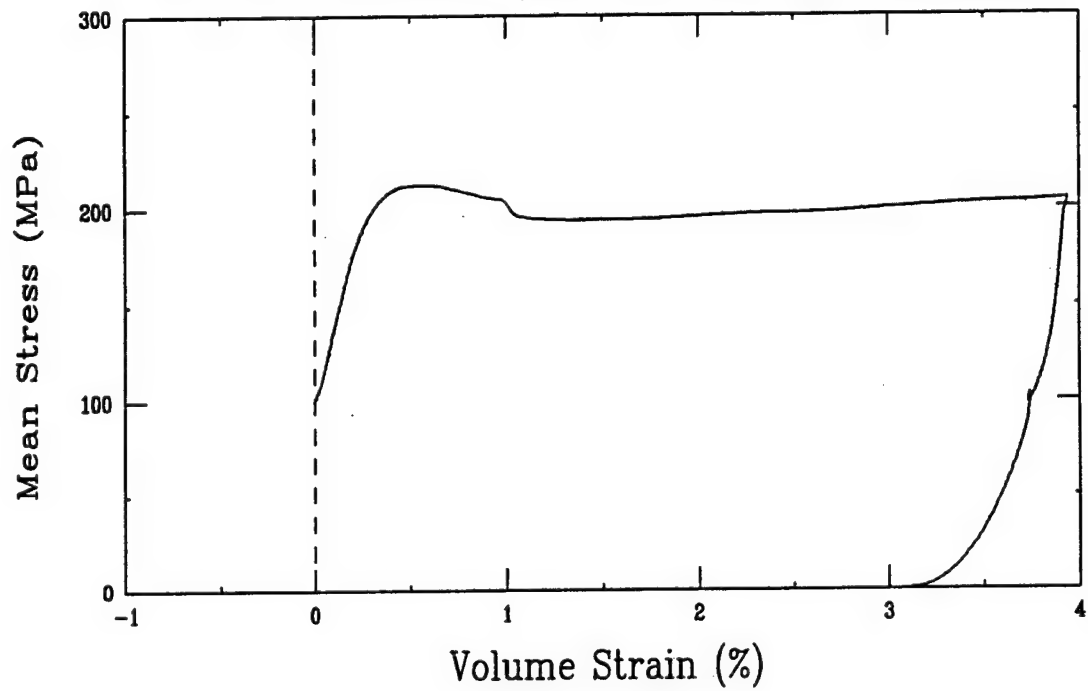
Triaxial Compression Test (A30F3)
Ft. Knox Limestone (FK10-6-05), $\sigma_{\text{conf}} = 100 \text{ MPa}$



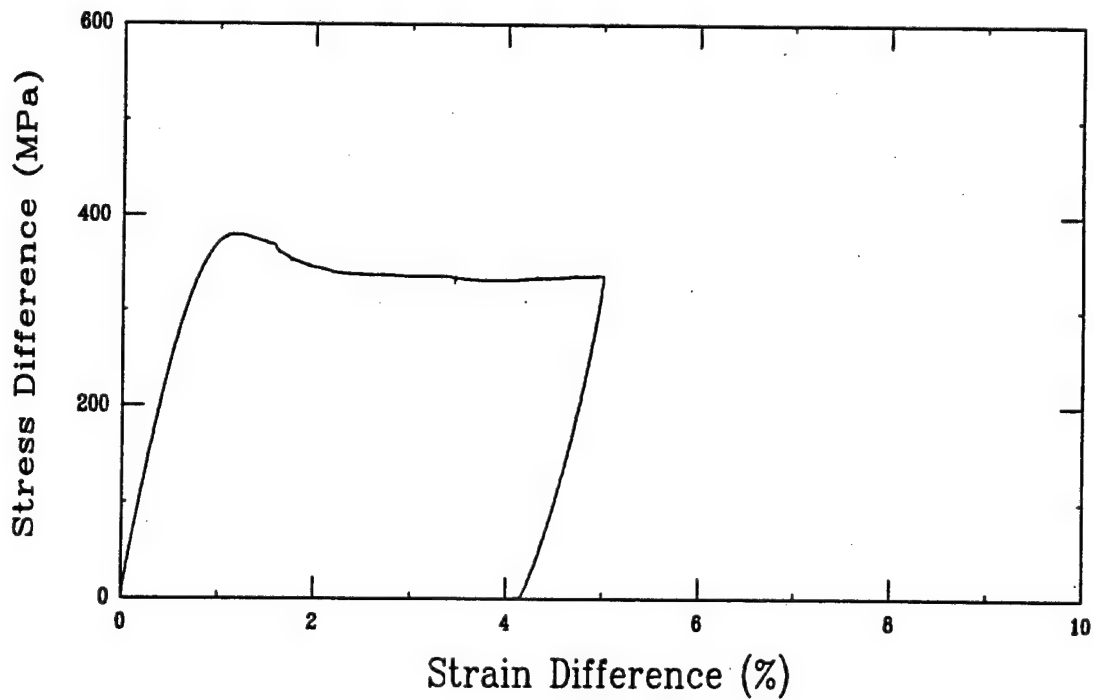
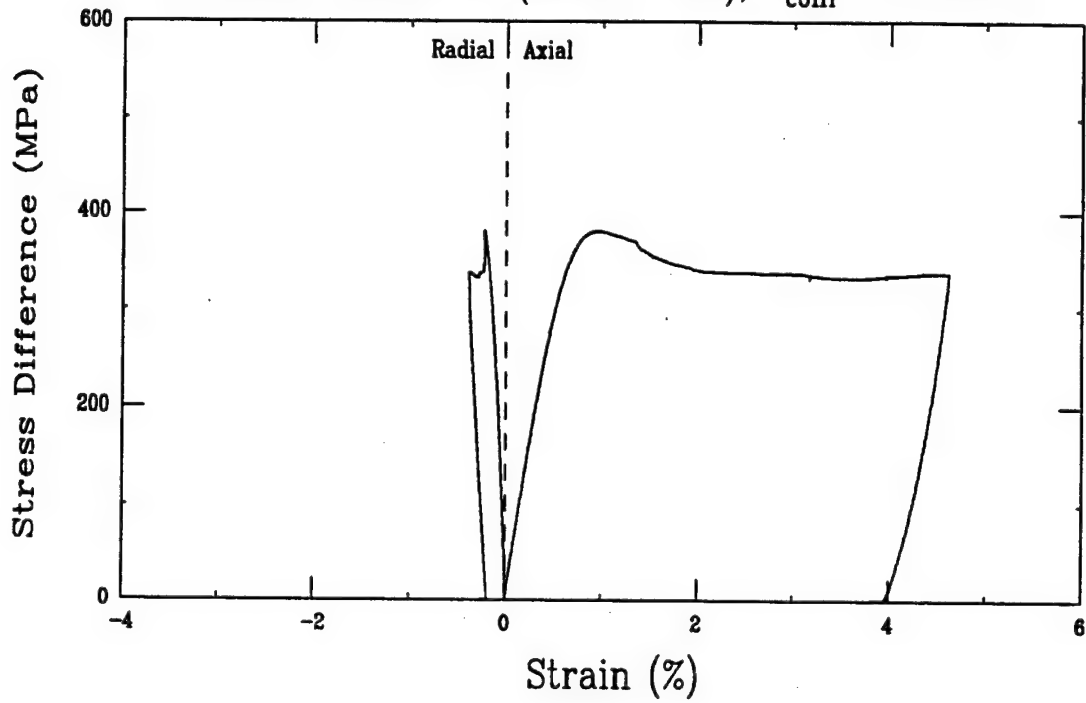
Triaxial Compression Test (A29F3)
Ft. Knox Limestone (FK10-7-06), $\sigma_{\text{conf}} = 100 \text{ MPa}$



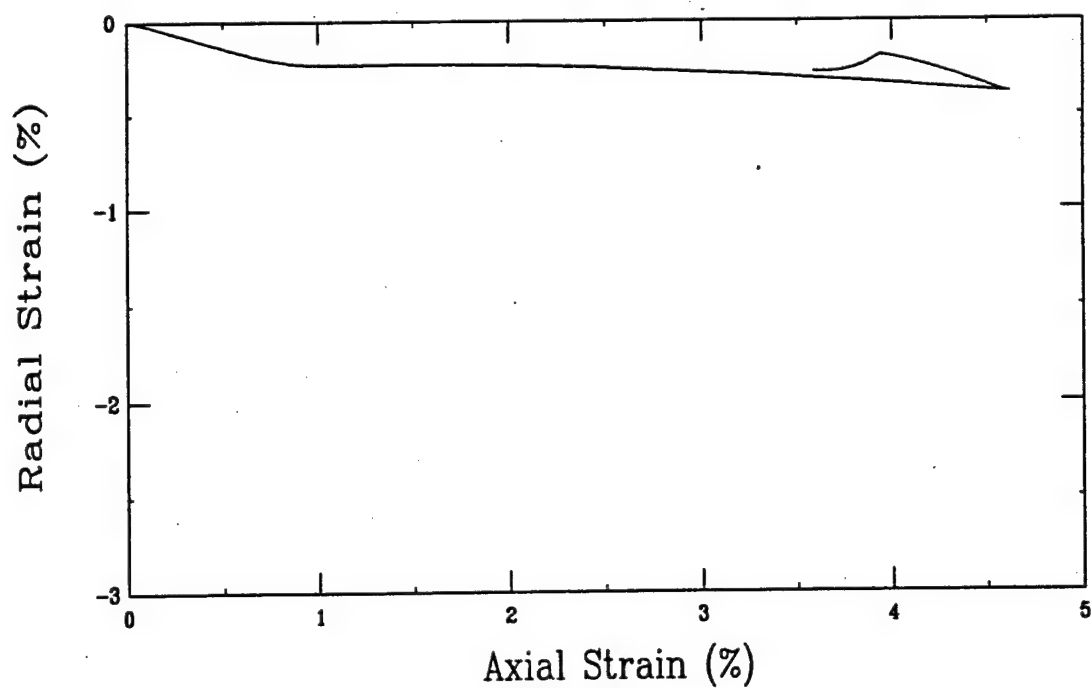
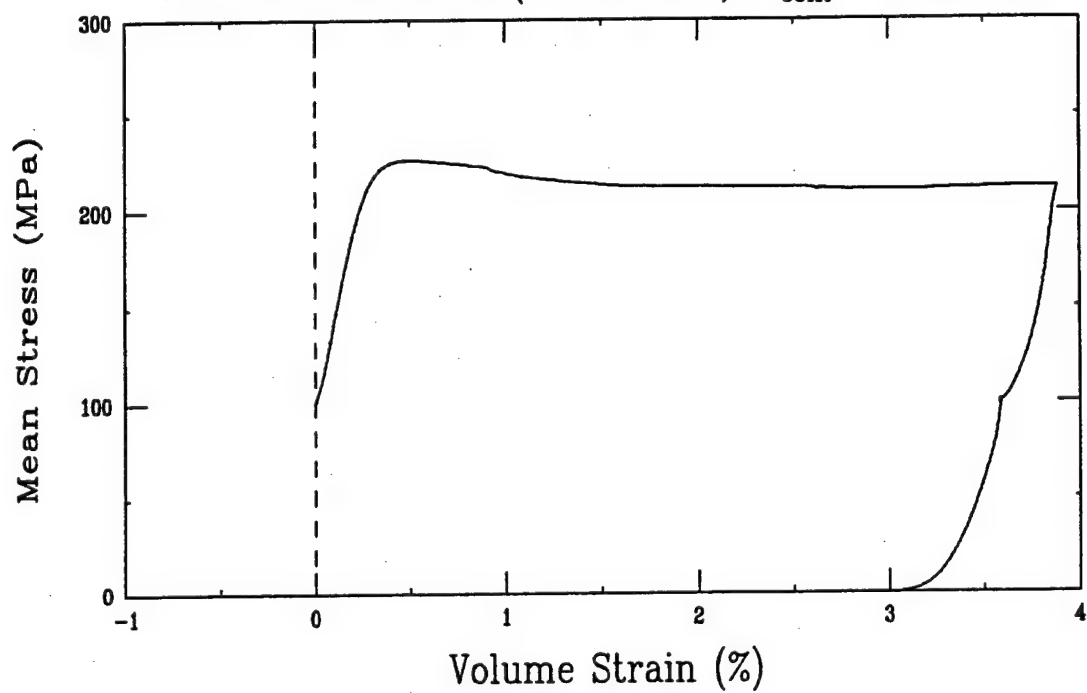
Triaxial Compression Test (A29F3)
Ft. Knox Limestone (FK10-7-06), $\sigma_{\text{conf}} = 100 \text{ MPa}$



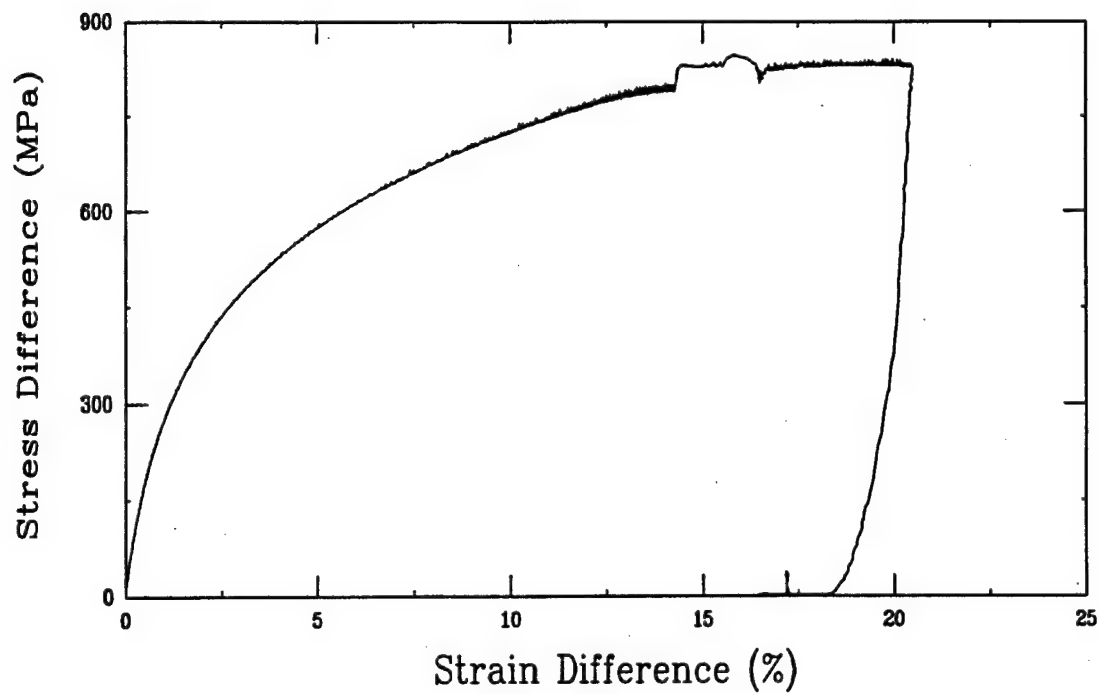
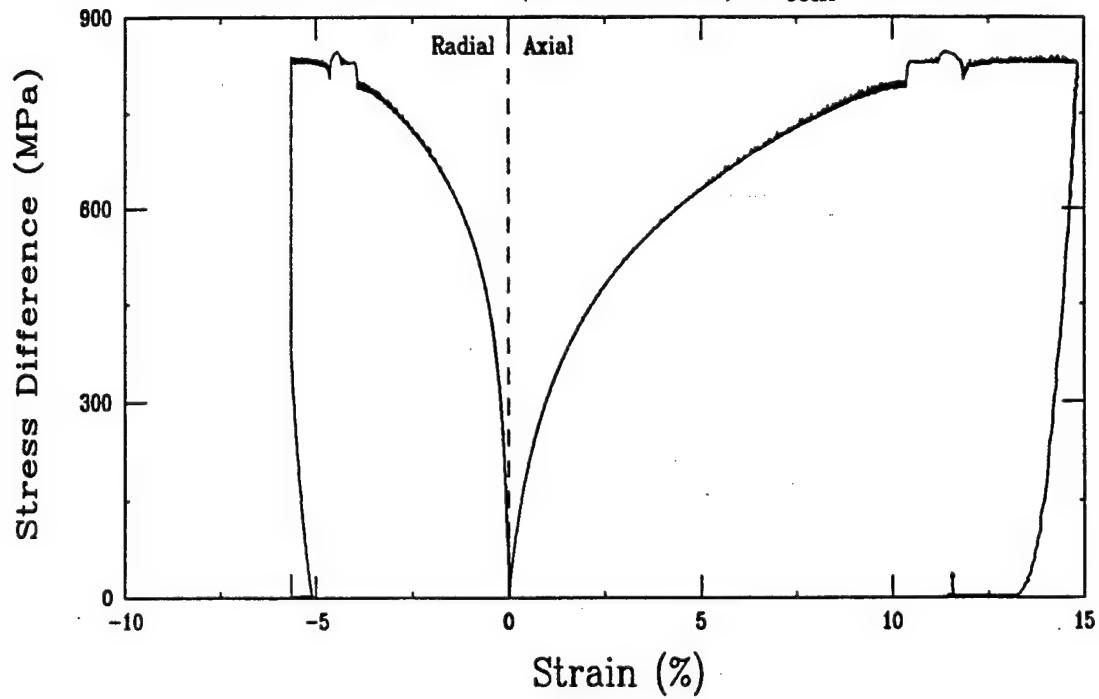
Triaxial Compression Test (A29D3)
Ft. Knox Limestone (FK10-7-07), $\sigma_{\text{conf}} = 100 \text{ MPa}$



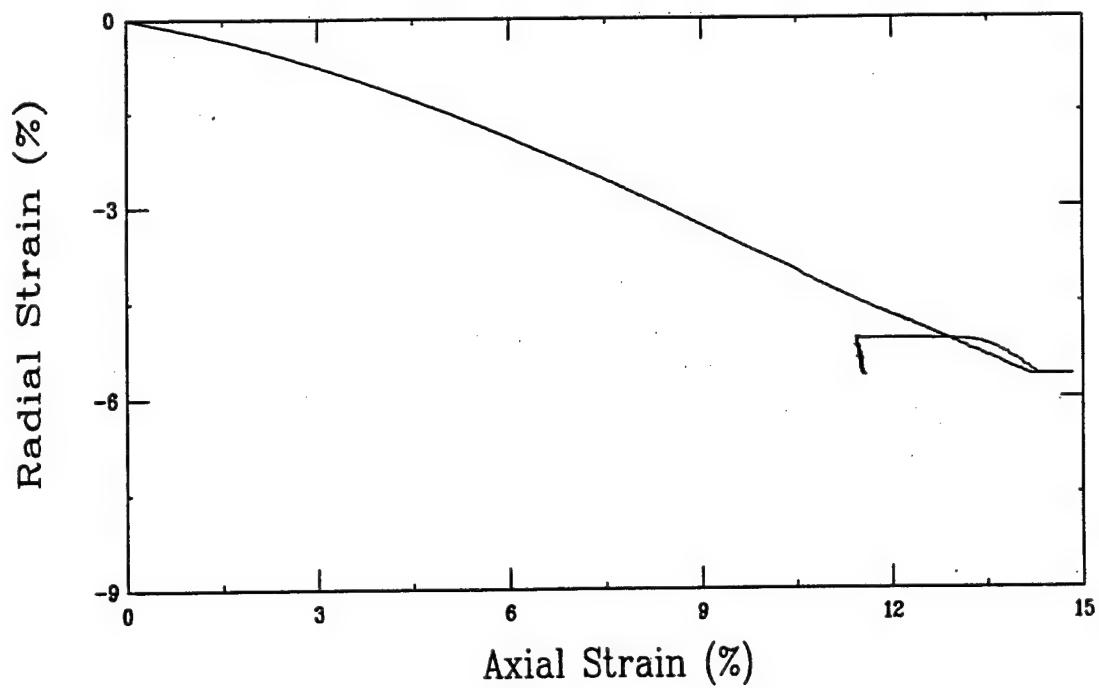
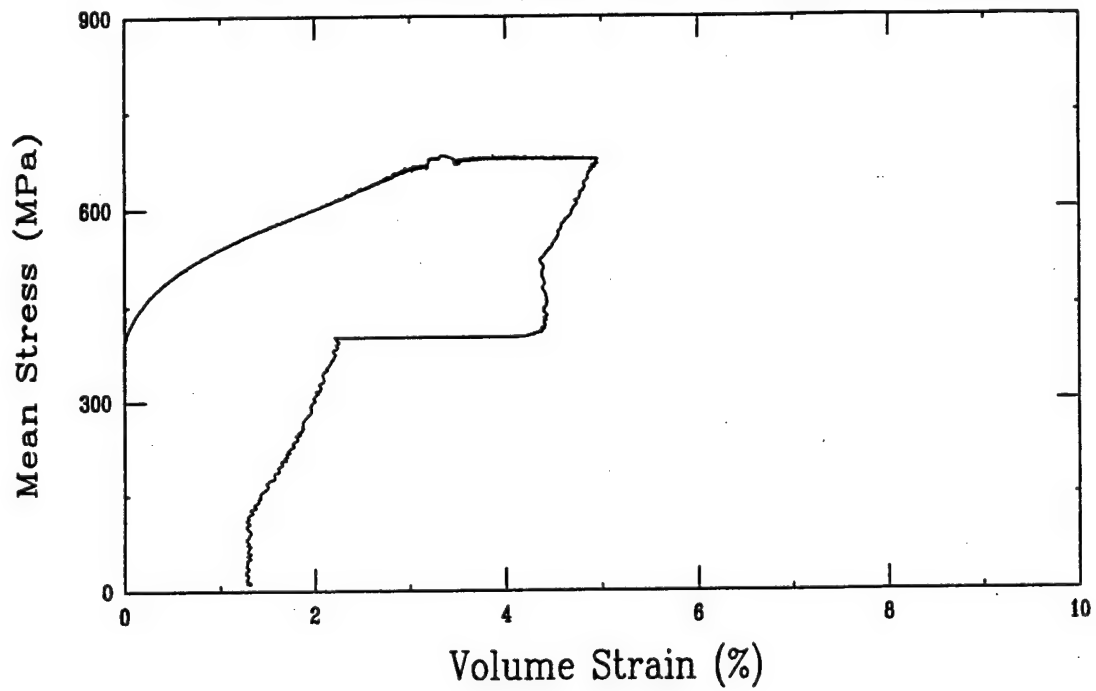
Triaxial Compression Test (A29D3)
Ft. Knox Limestone (FK10-7-07), $\sigma_{\text{conf}} = 100 \text{ MPa}$



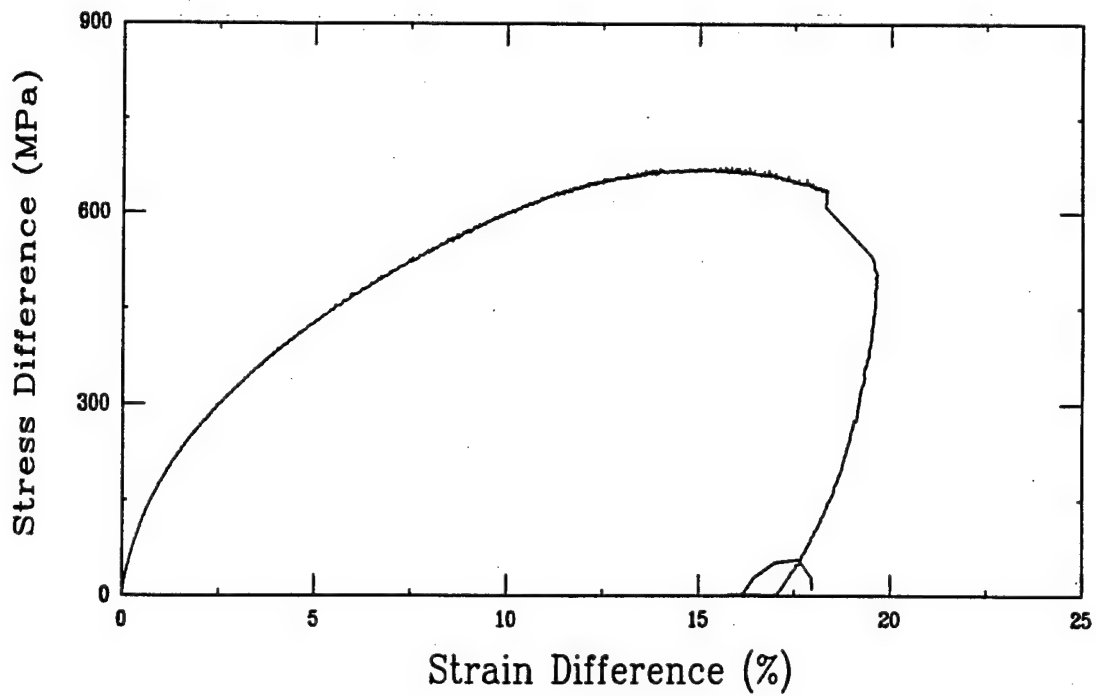
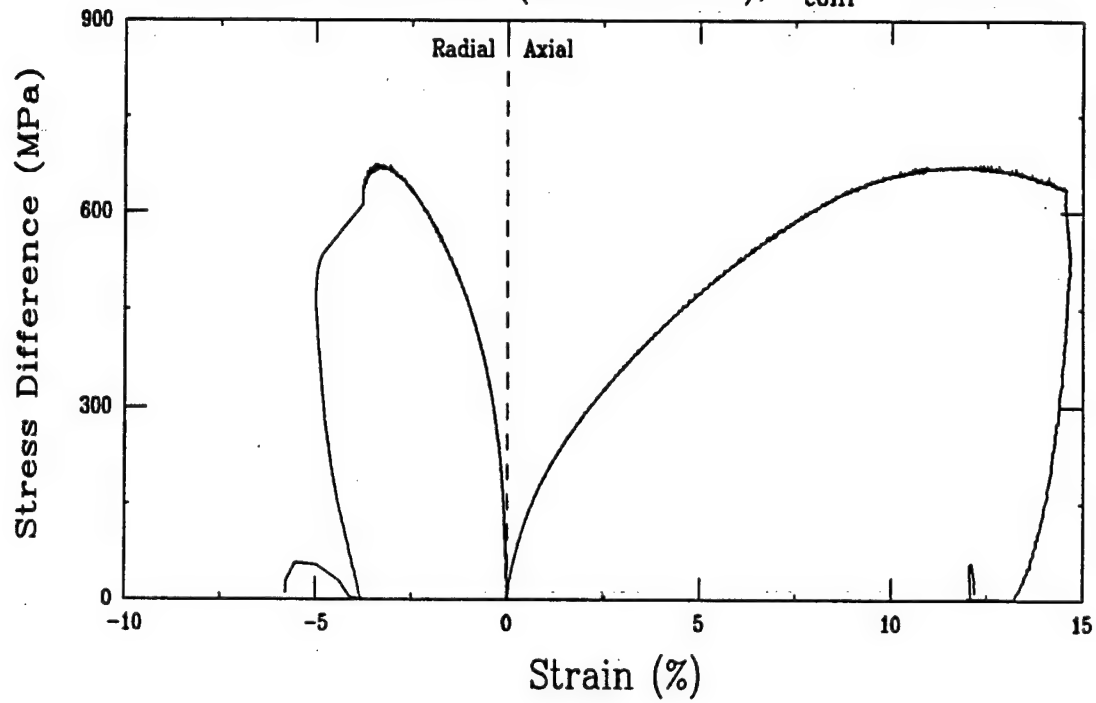
Triaxial Compression Test (U15D3)
Ft. Knox Limestone (FK10-4-08), $\sigma_{\text{conf}} = 400$ MPa



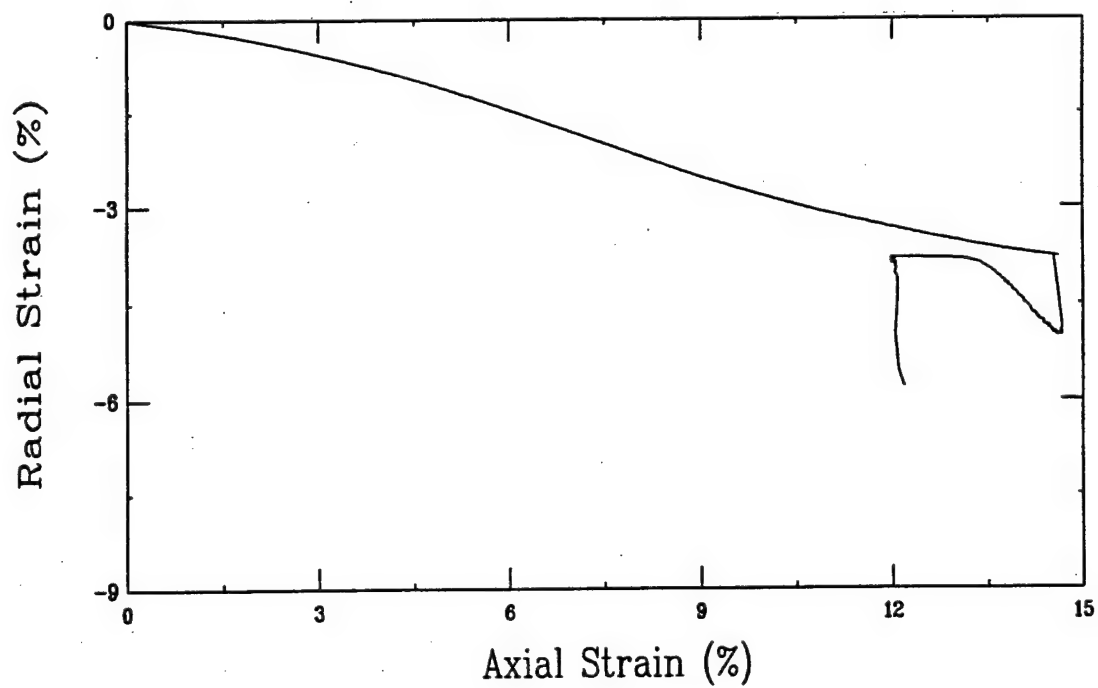
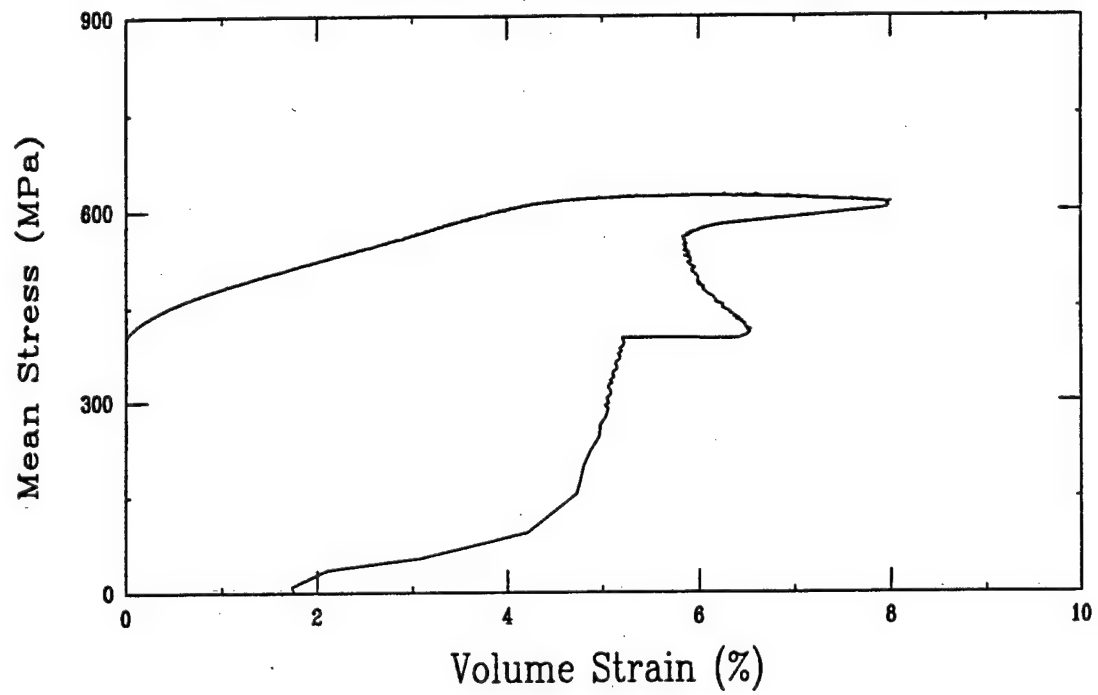
Triaxial Compression Test (U15D3)
Ft. Knox Limestone (FK10-4-08), $\sigma_{\text{conf}} = 400 \text{ MPa}$



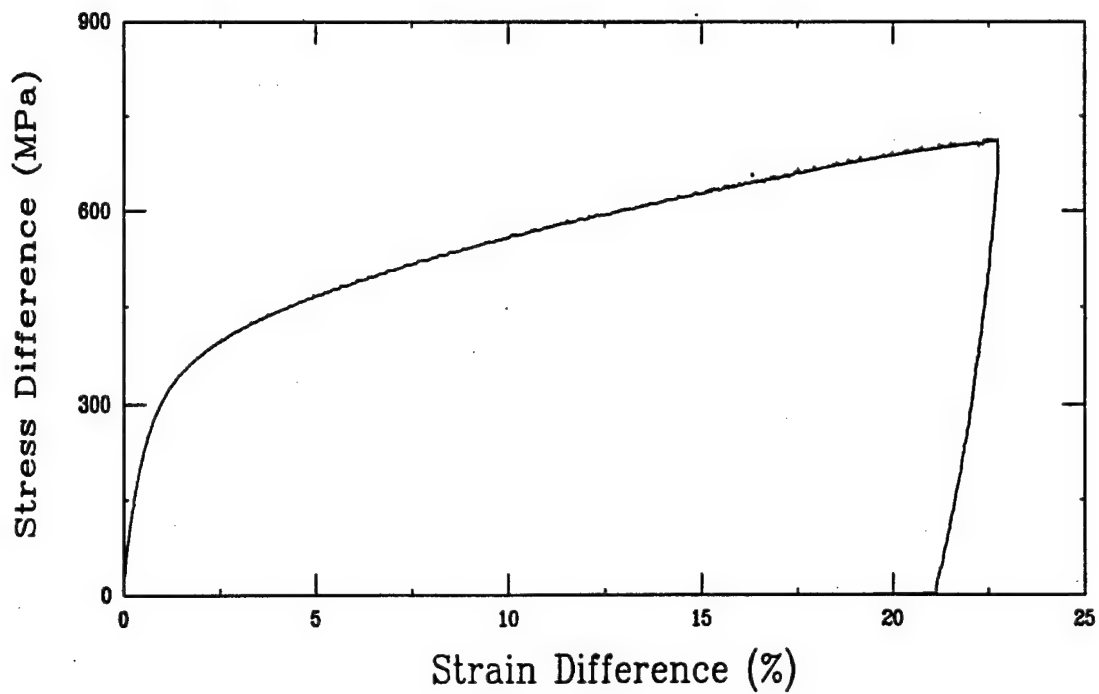
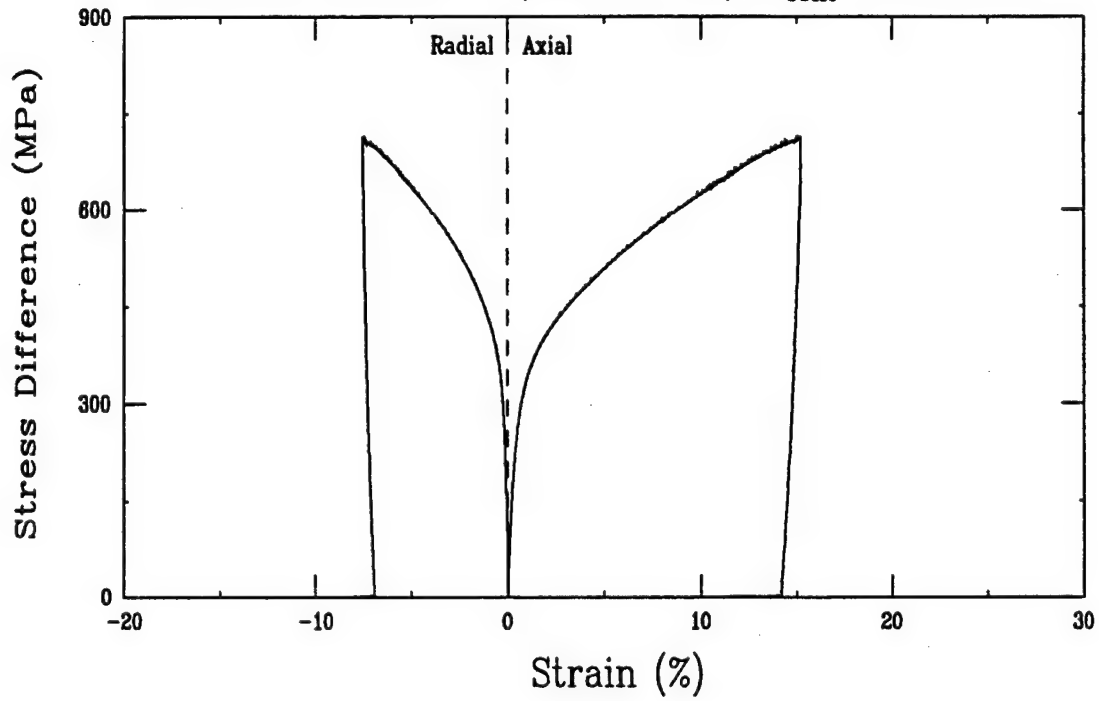
Triaxial Compression Test (U15B3)
Ft. Knox Limestone (FK10-4-05L), $\sigma_{\text{conf}} = 400 \text{ MPa}$



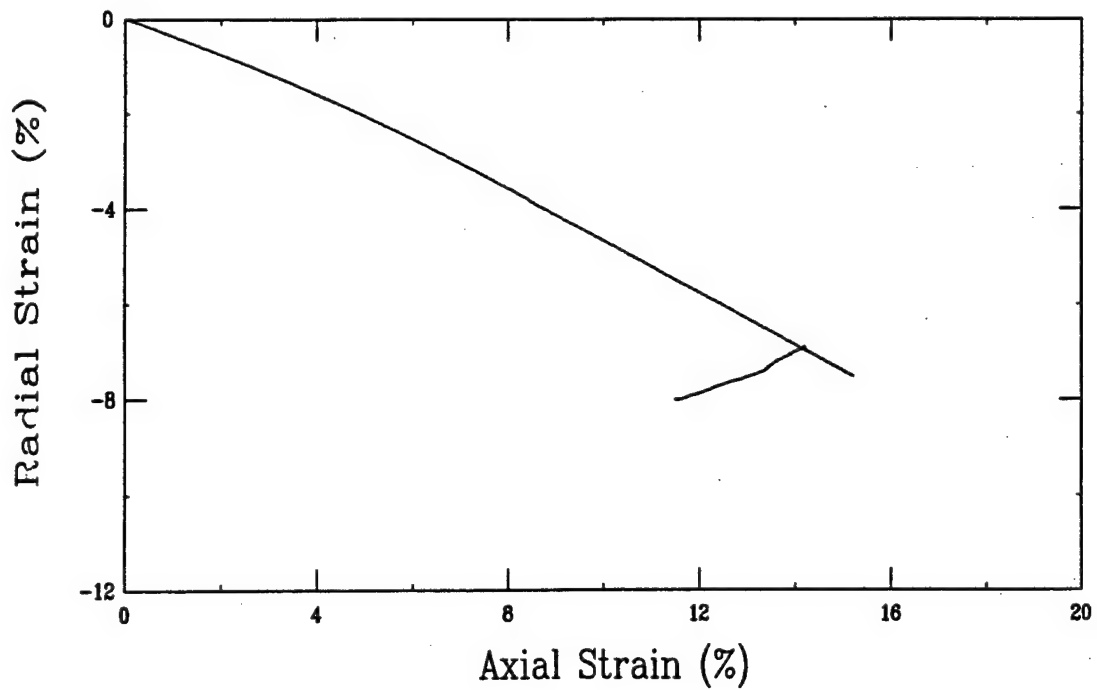
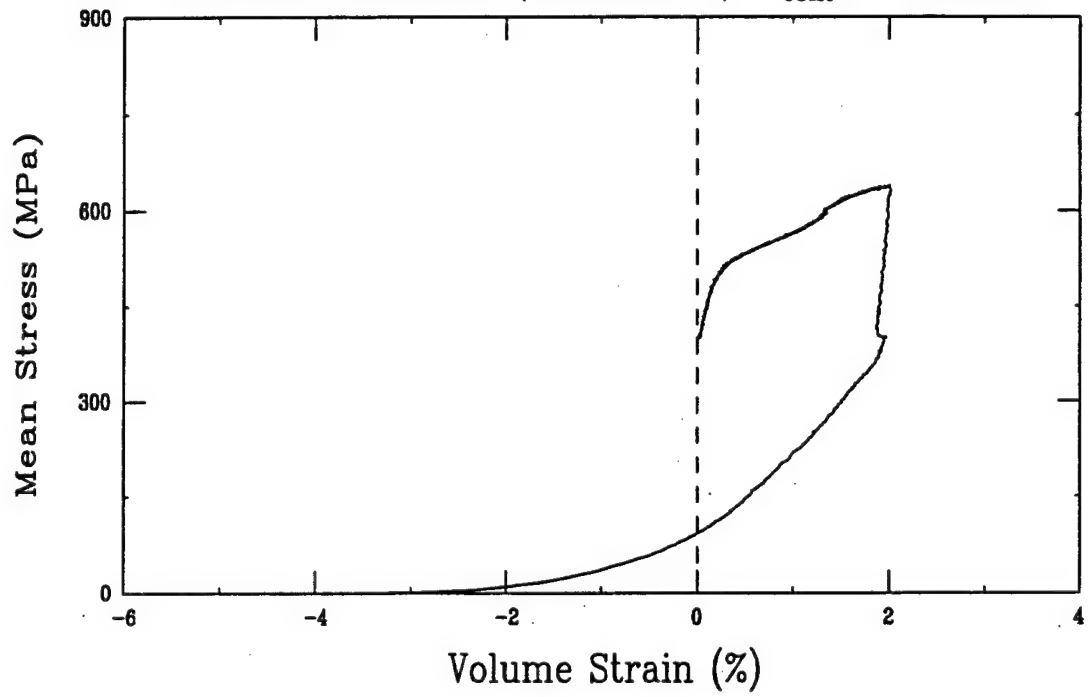
Triaxial Compression Test (U15B3)
Ft. Knox Limestone (FK10-4-05L), $\sigma_{\text{conf}} = 400$ MPa



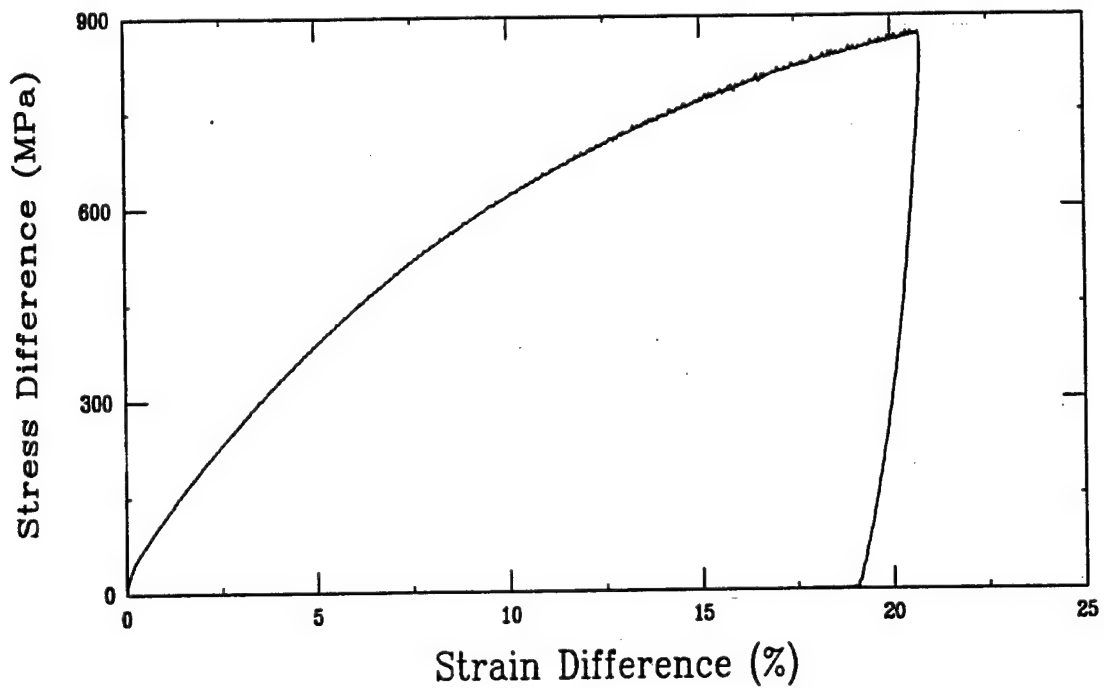
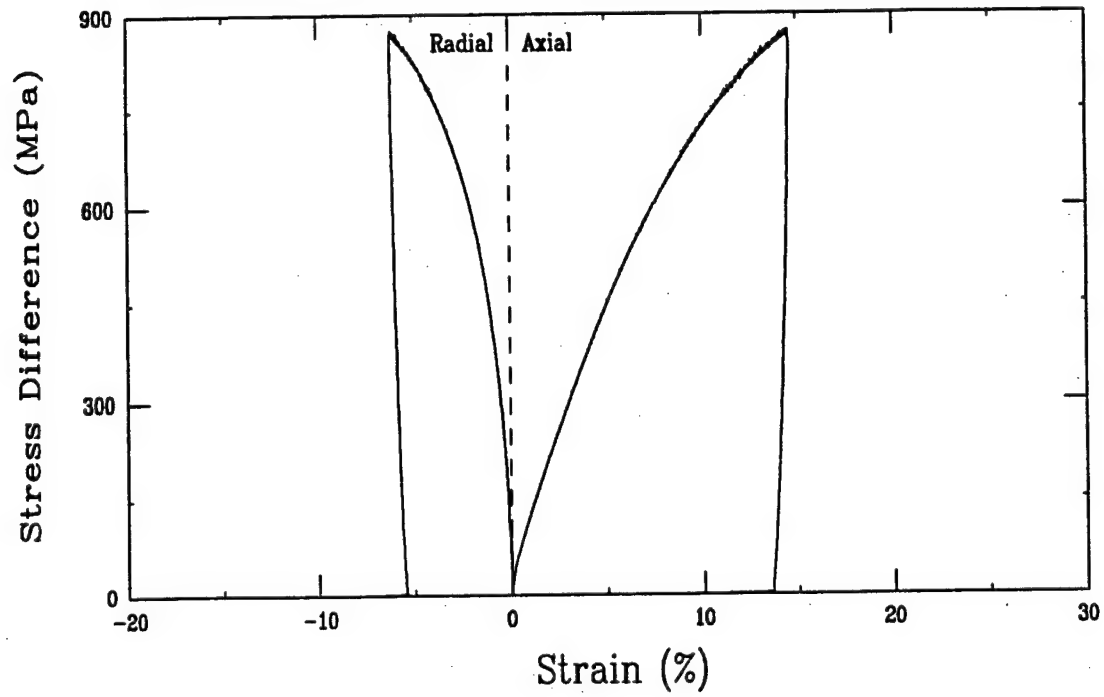
Triaxial Compression Test (L9B3)
Ft. Knox Limestone (FK10-1-05), $\sigma_{\text{conf}} = 400 \text{ MPa}$



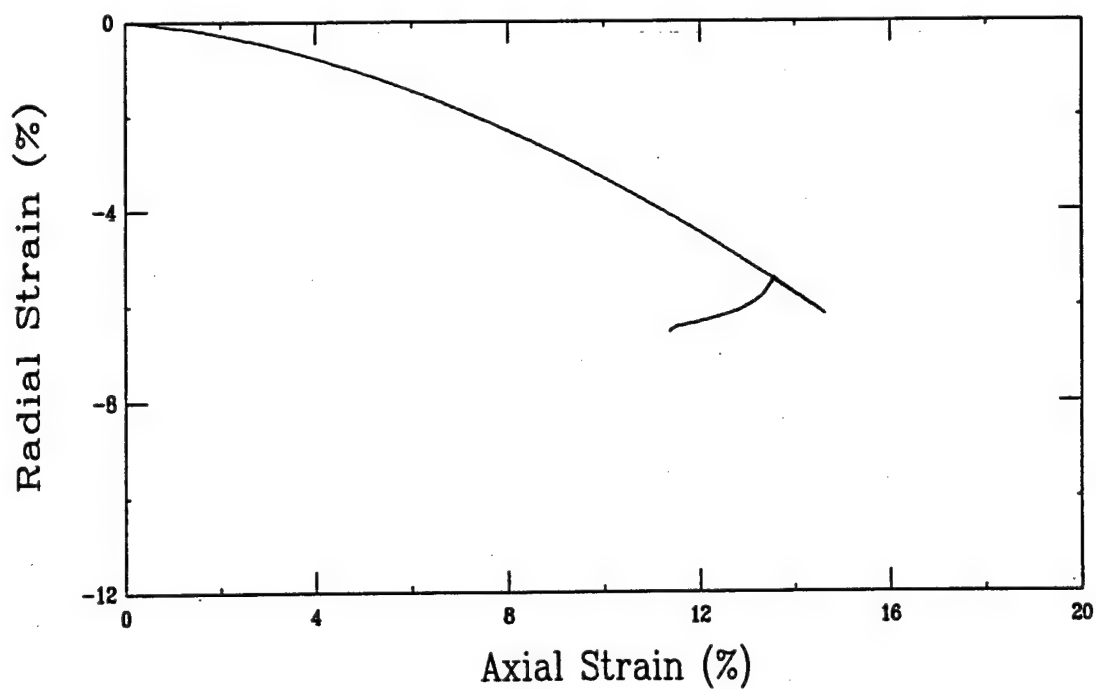
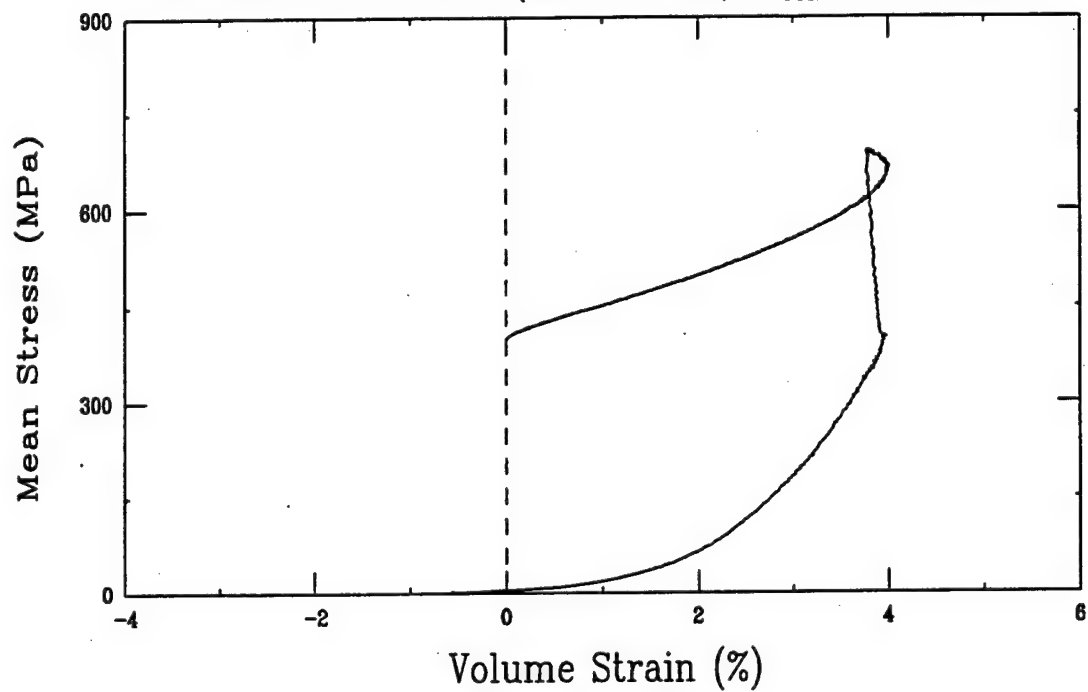
Triaxial Compression Test (L9B3)
Ft. Knox Limestone (FK10-1-05), $\sigma_{\text{conf}} = 400 \text{ MPa}$



Triaxial Compression Test (L12A3)
Ft. Knox Limestone (FK10-6-08), $\sigma_{\text{conf}} = 400$ MPa

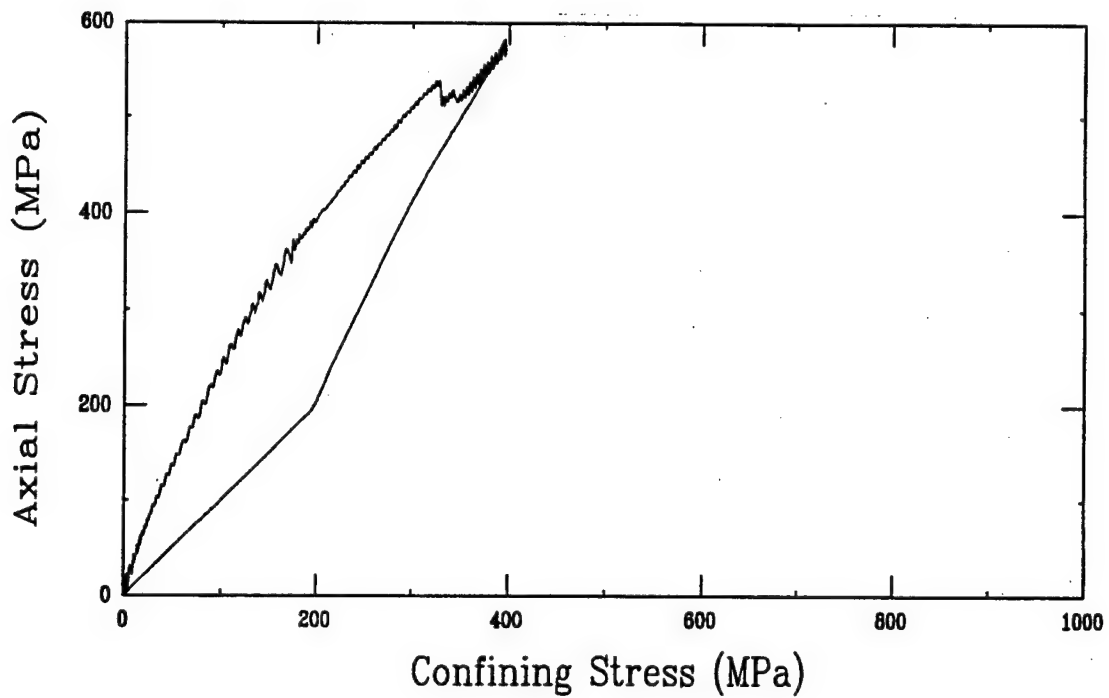
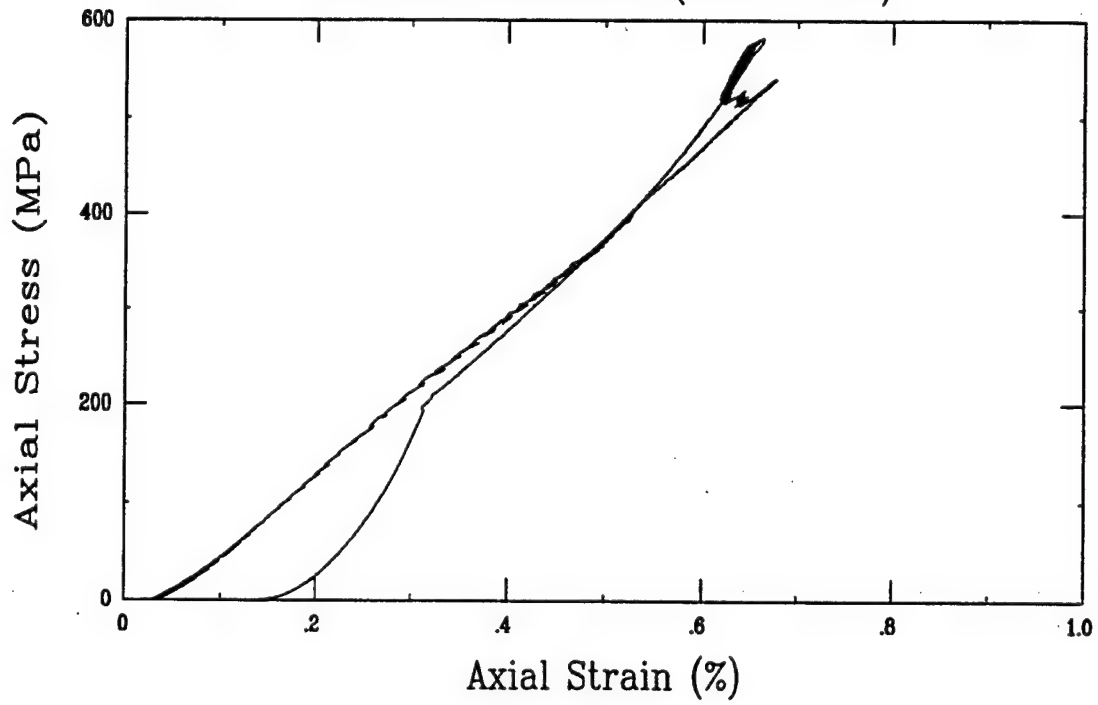


Triaxial Compression Test (L12A3)
Ft. Knox Limestone (FK10-6-08), $\sigma_{\text{conf}} = 400 \text{ MPa}$

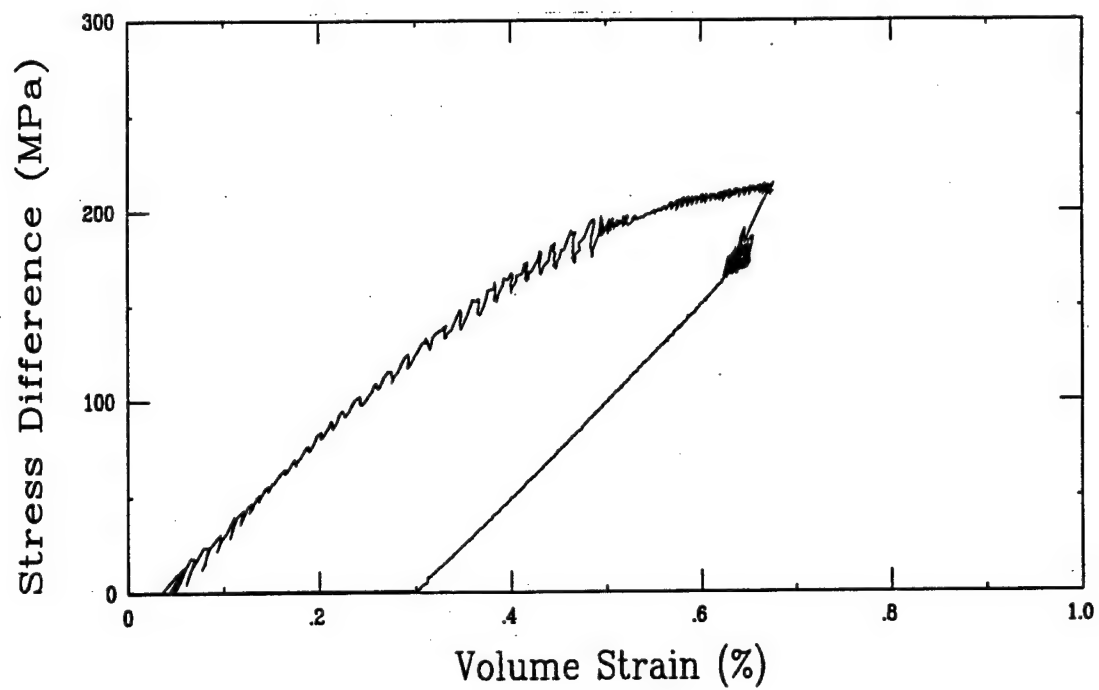
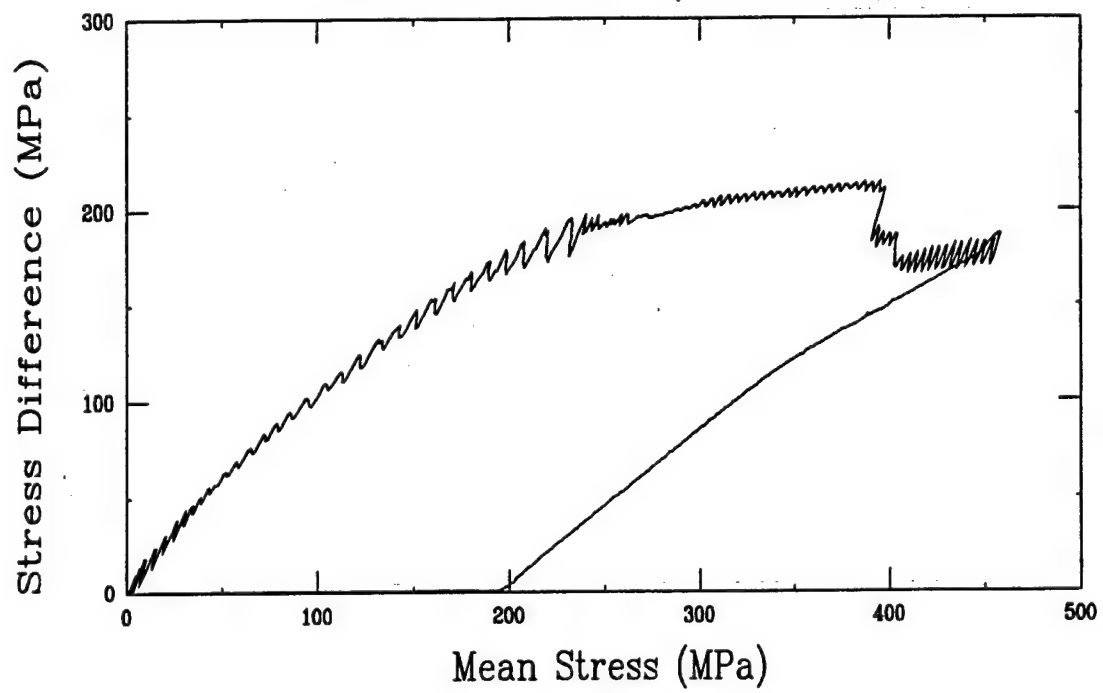


APPENDIX D
UNIAXIAL STRAIN TESTS ON
CARBONATE ROCKS FROM FORT KNOX

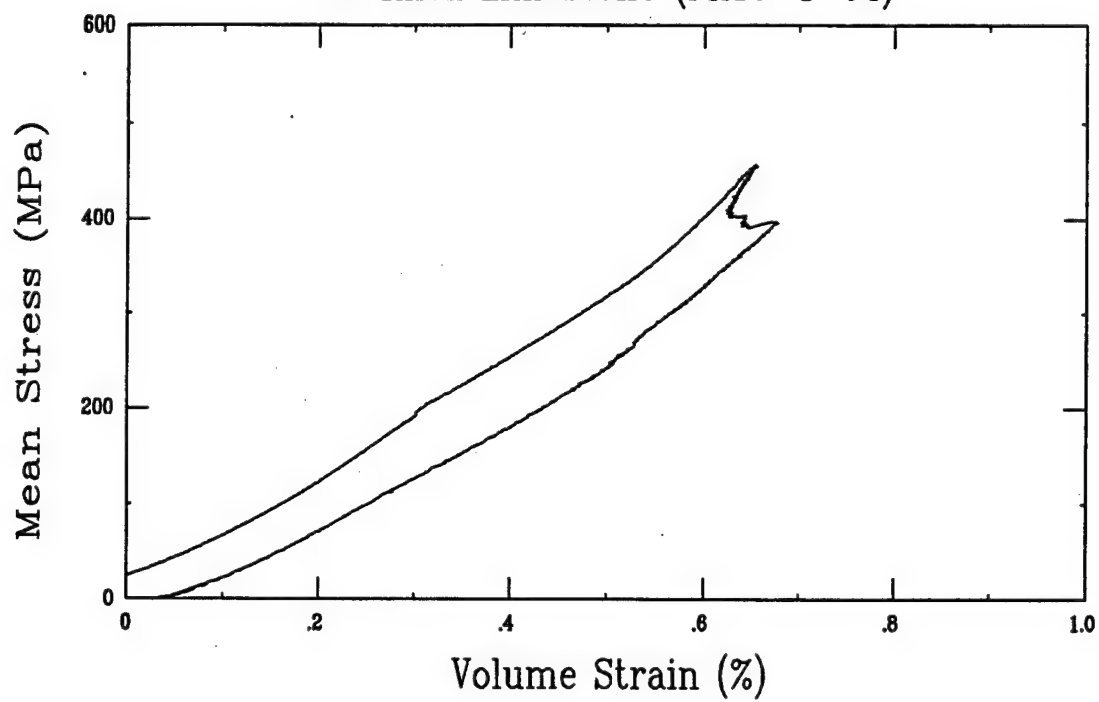
Uniaxial Strain Test (Y13A3)
Ft. Knox Limestone (FK10-1-04)



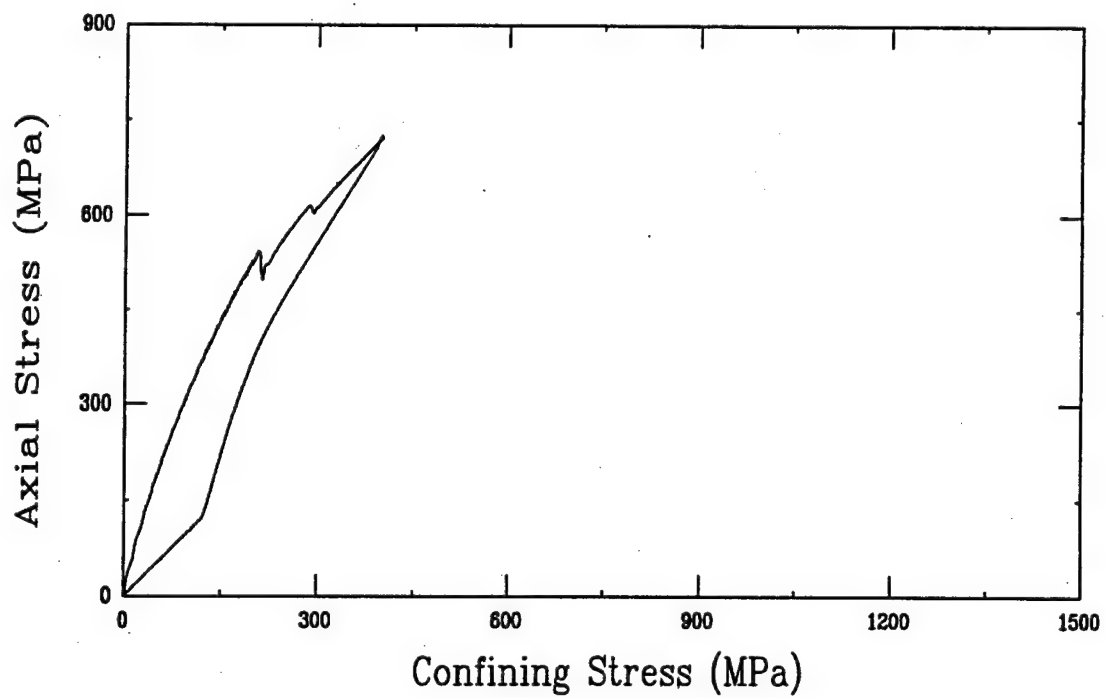
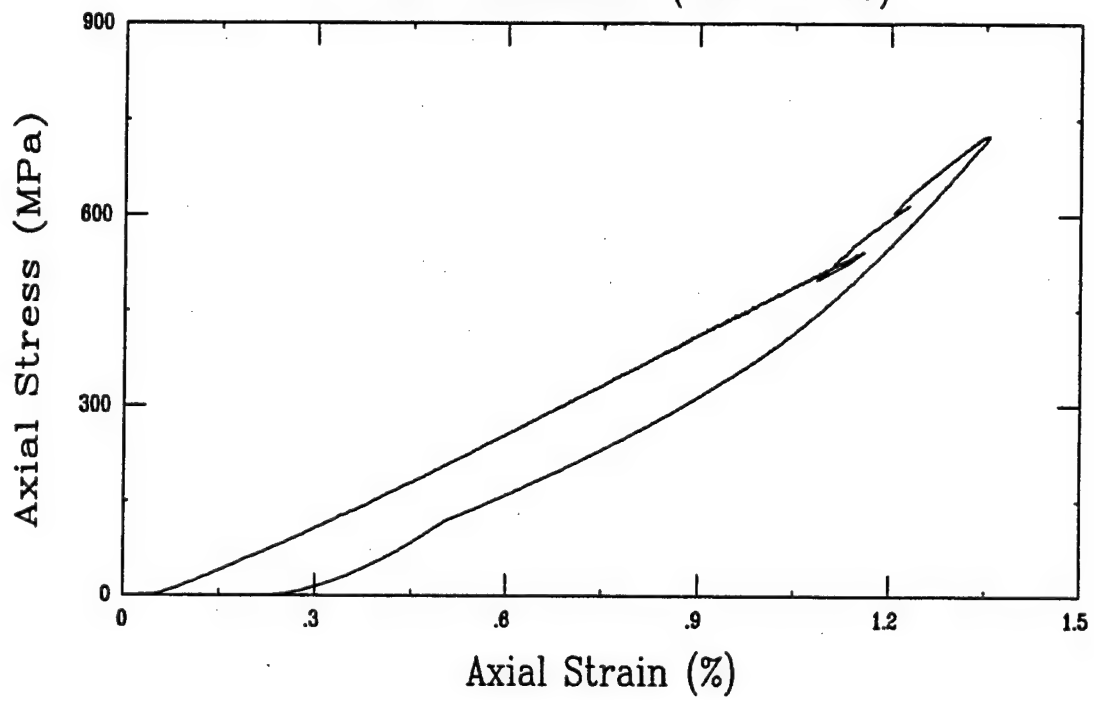
Uniaxial Strain Test (Y13A3)
Ft. Knox Limestone (FK10-1-04)



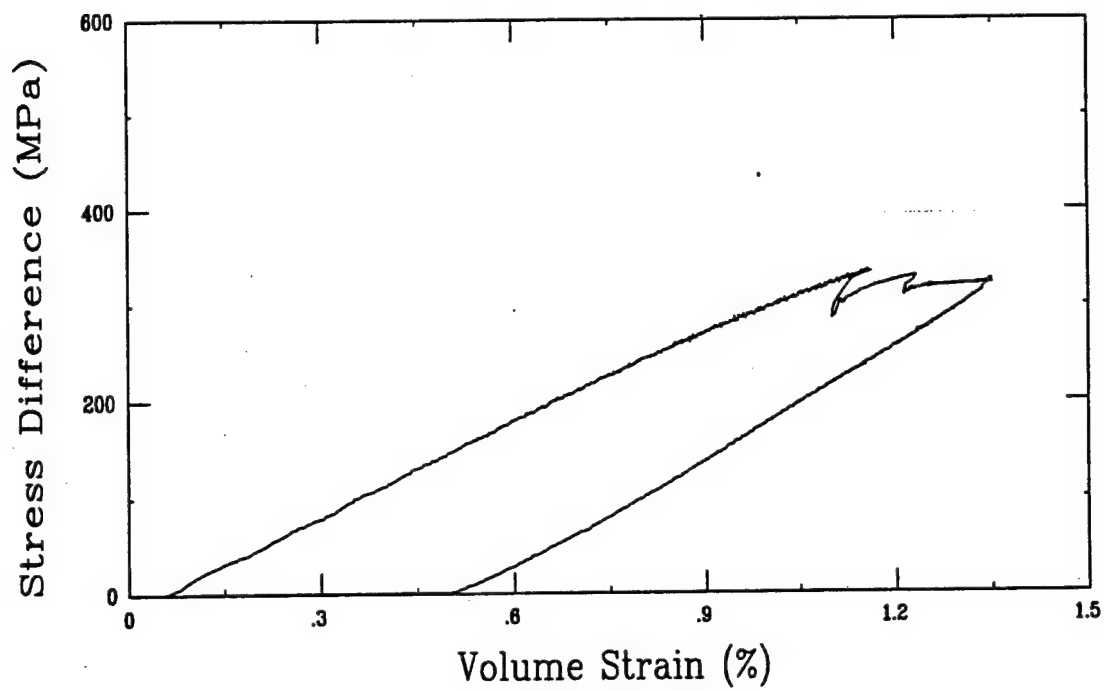
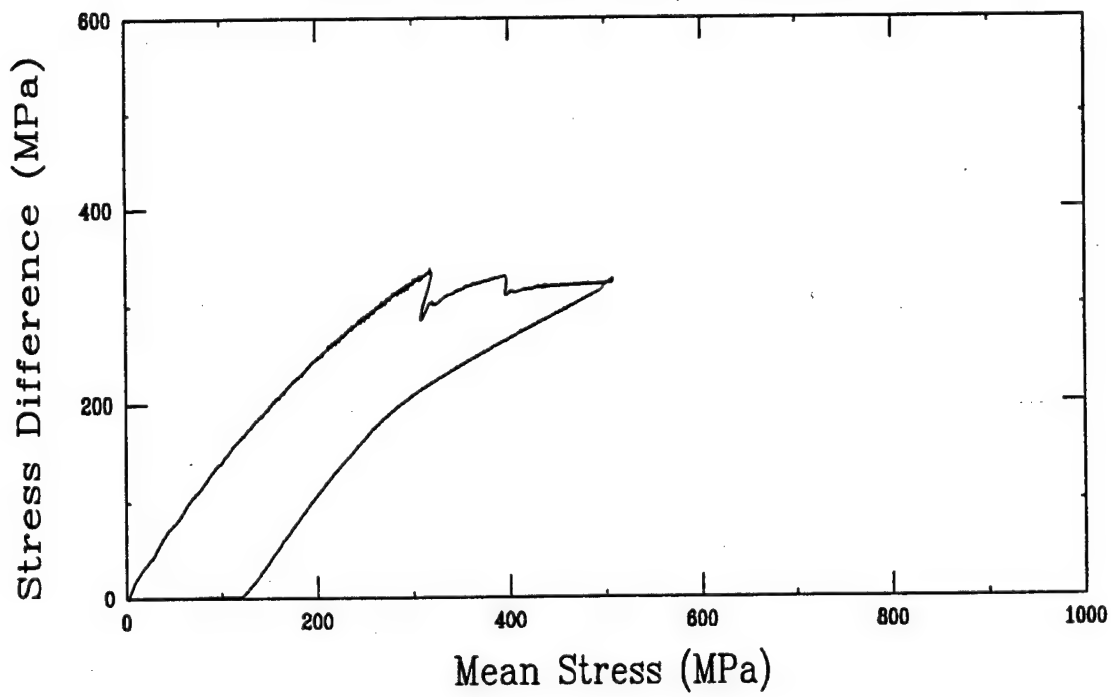
Uniaxial Strain Test (Y13A3)
Ft. Knox Limestone (FK10-1-04)



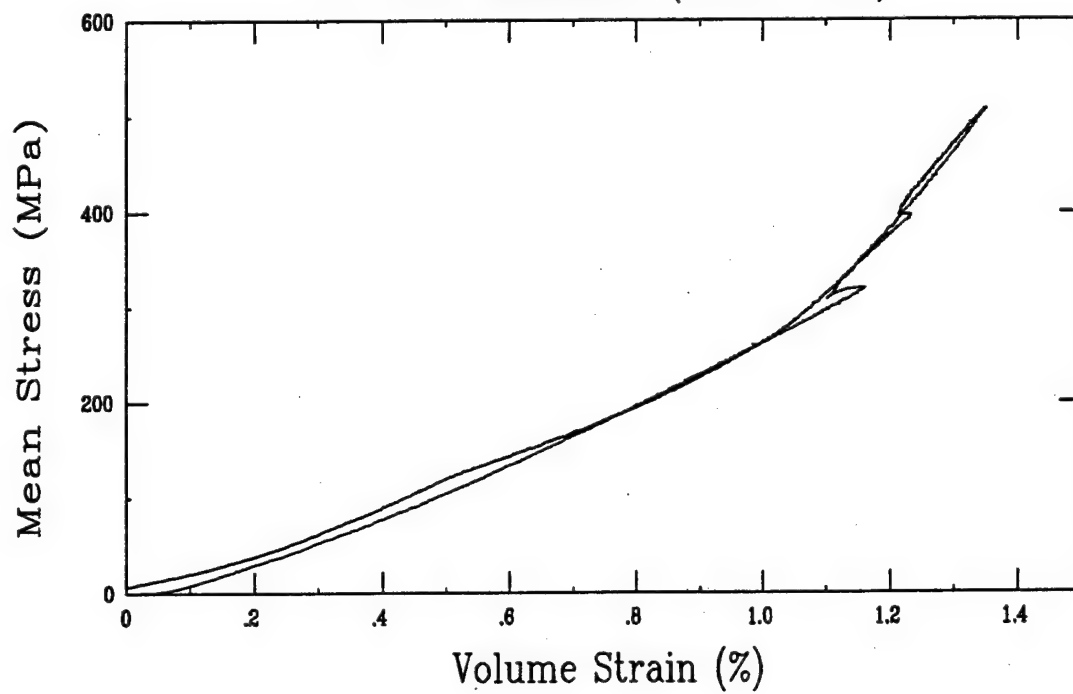
Uniaxial Strain Test (Y14A3)
Ft. Knox Limestone (FK10-2-05)



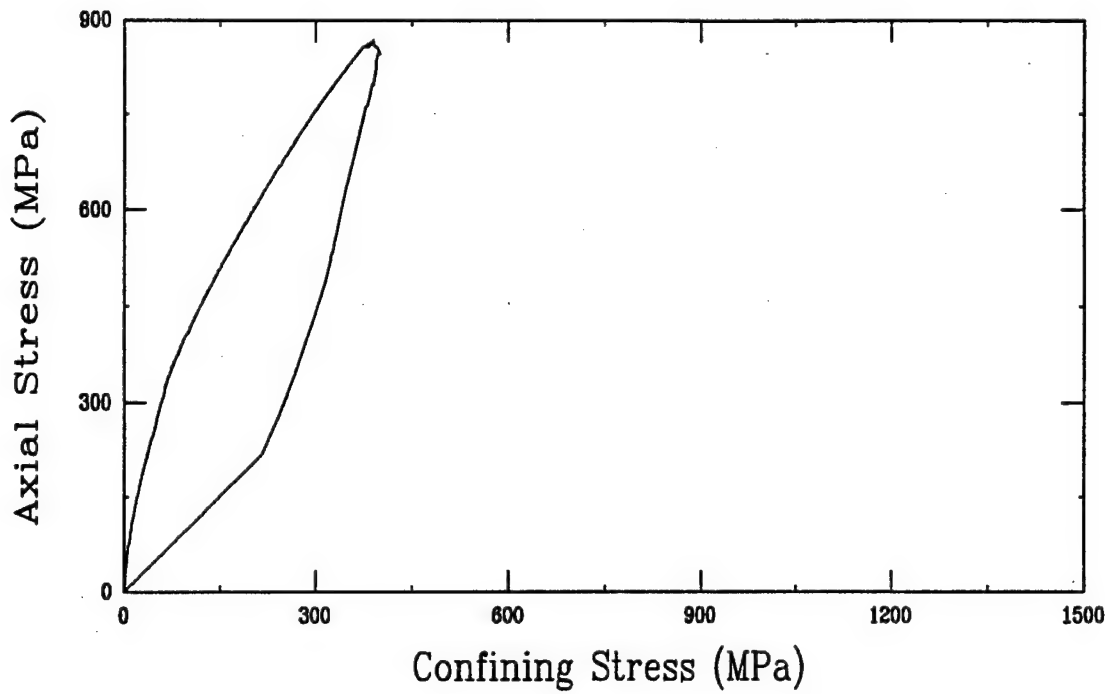
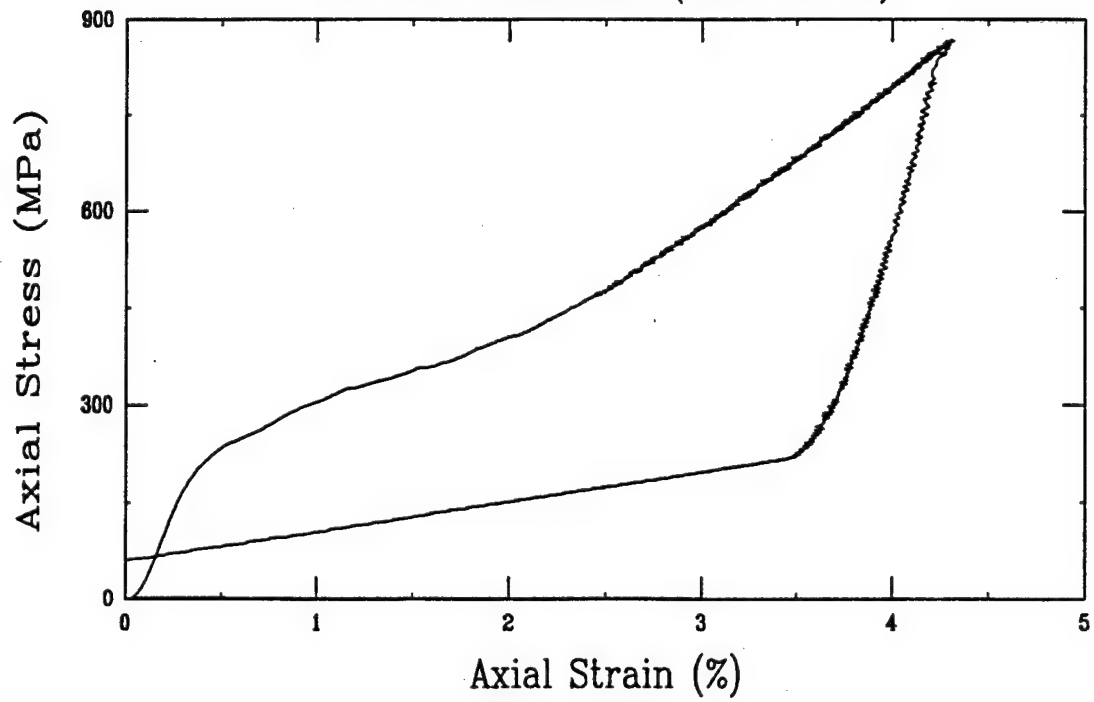
Uniaxial Strain Test (Y14A3)
Ft. Knox Limestone (FK10-2-05)



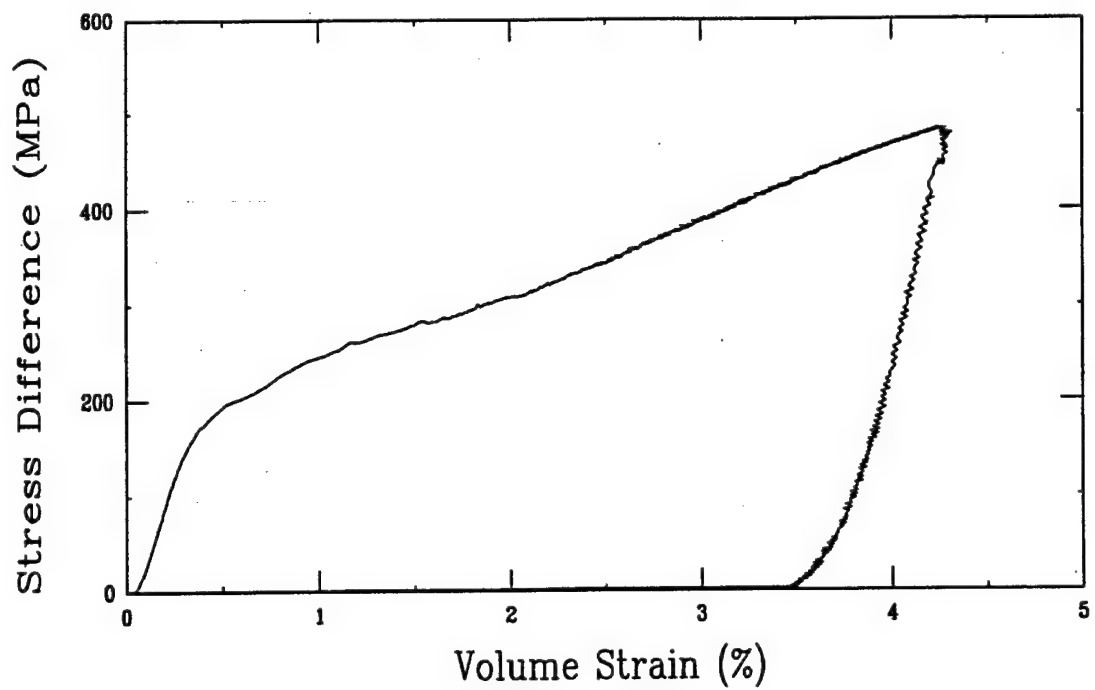
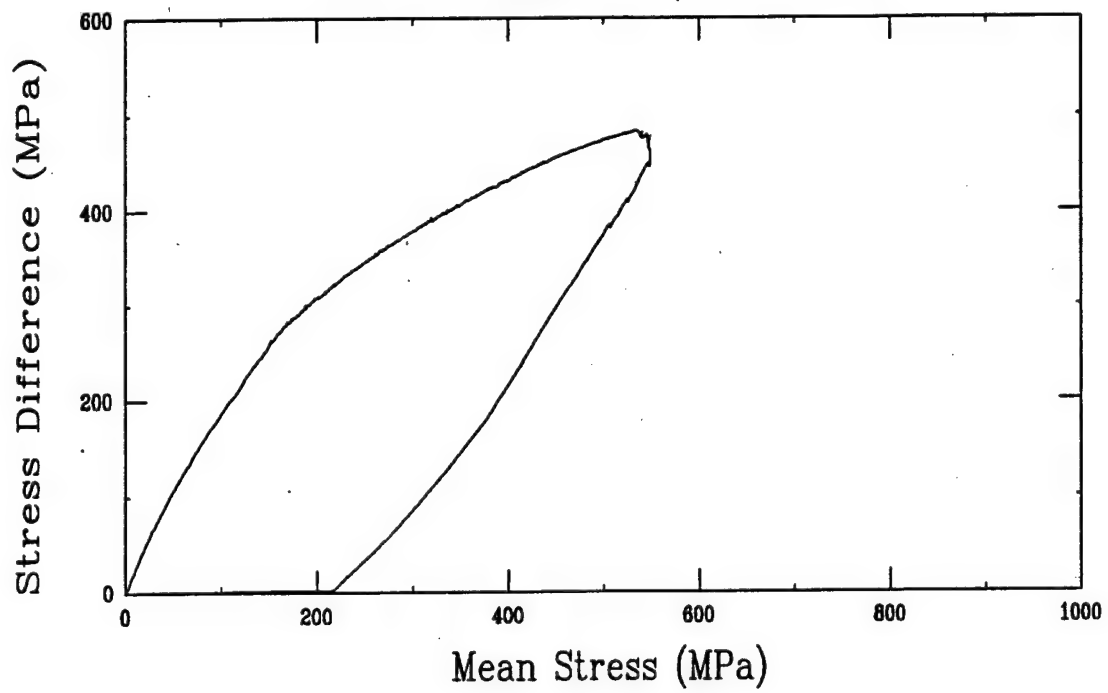
Uniaxial Strain Test (Y14A3)
Ft. Knox Limestone (FK10-2-05)



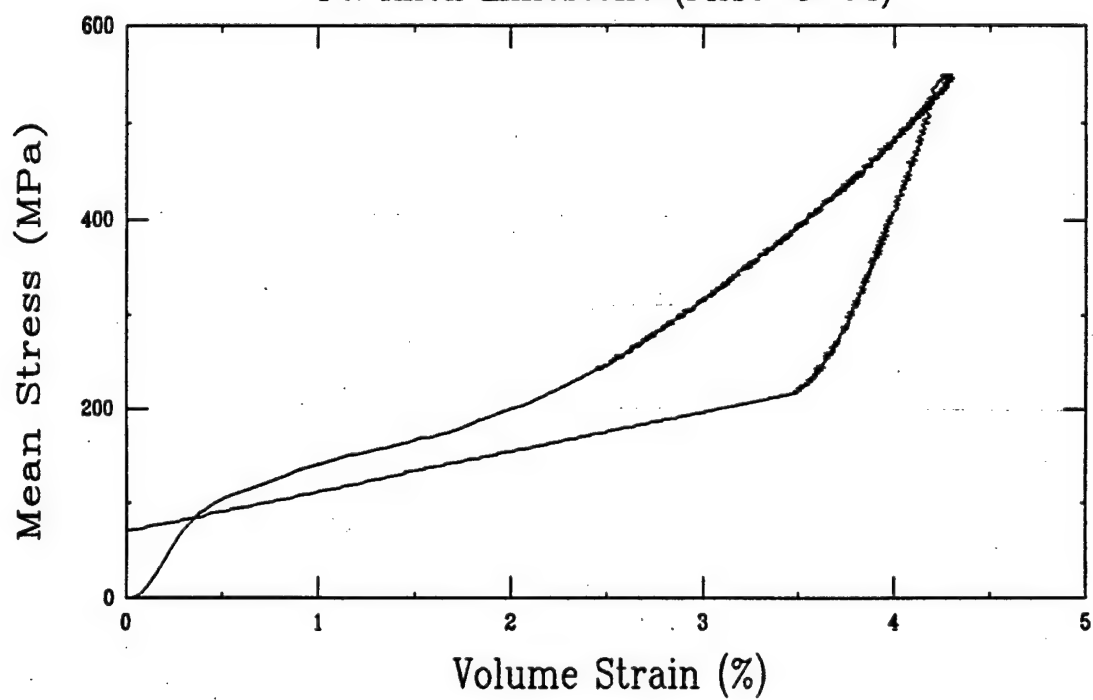
Uniaxial Strain Test (U21B3)
Ft. Knox Limestone (FK10-3-04)



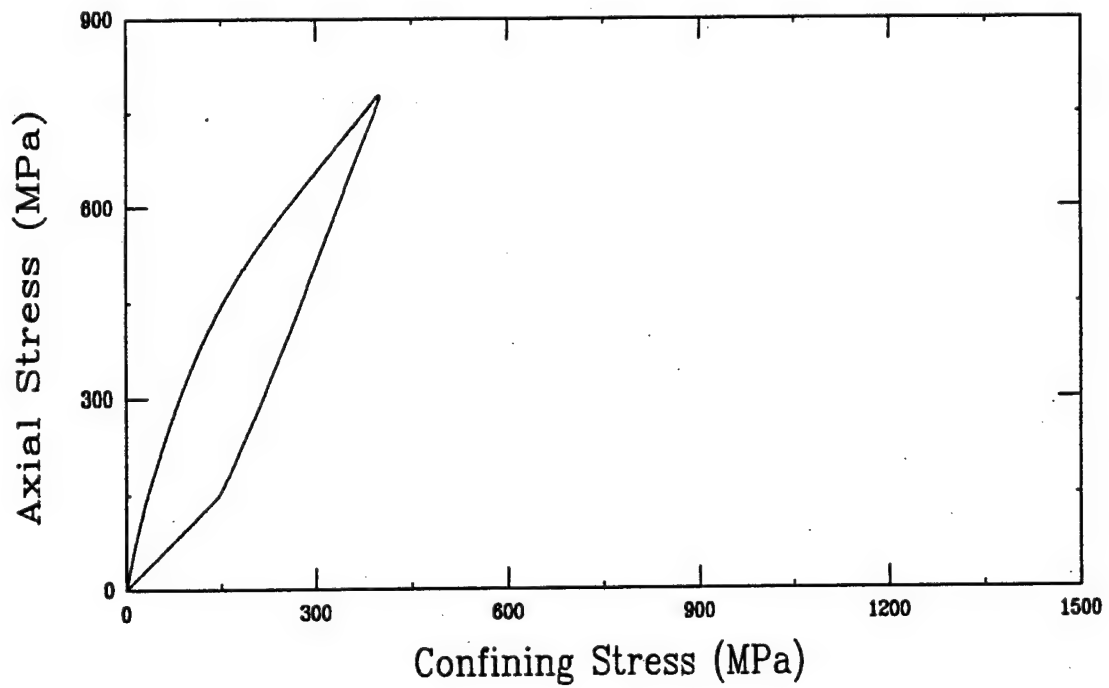
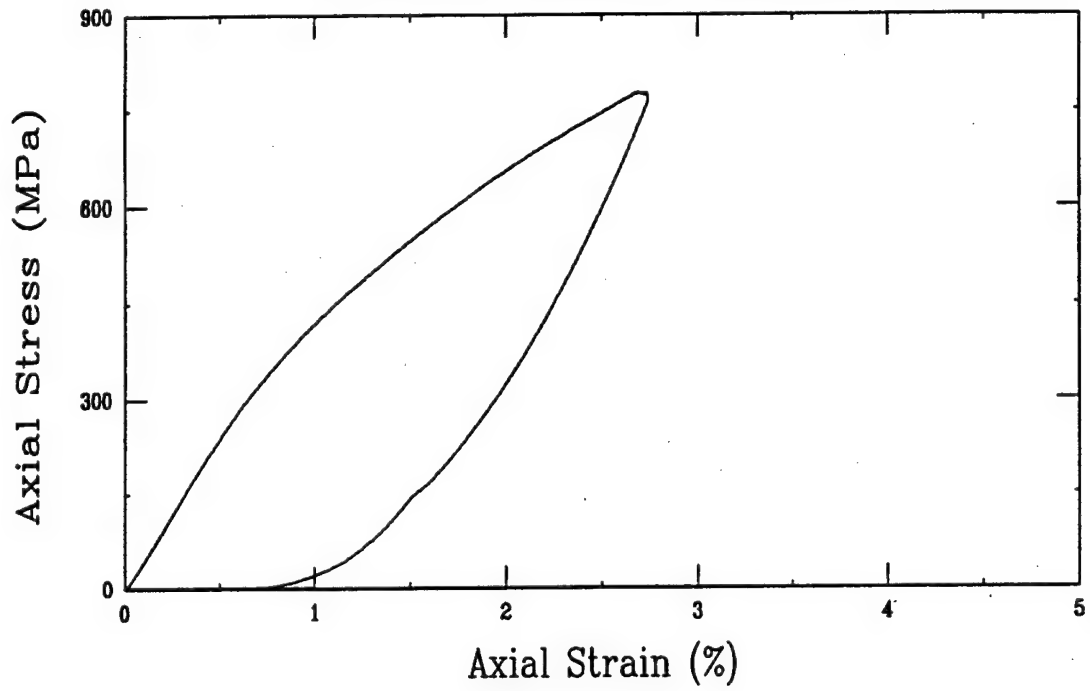
Uniaxial Strain Test (U21B3)
Ft. Knox Limestone (FK10-3-04)



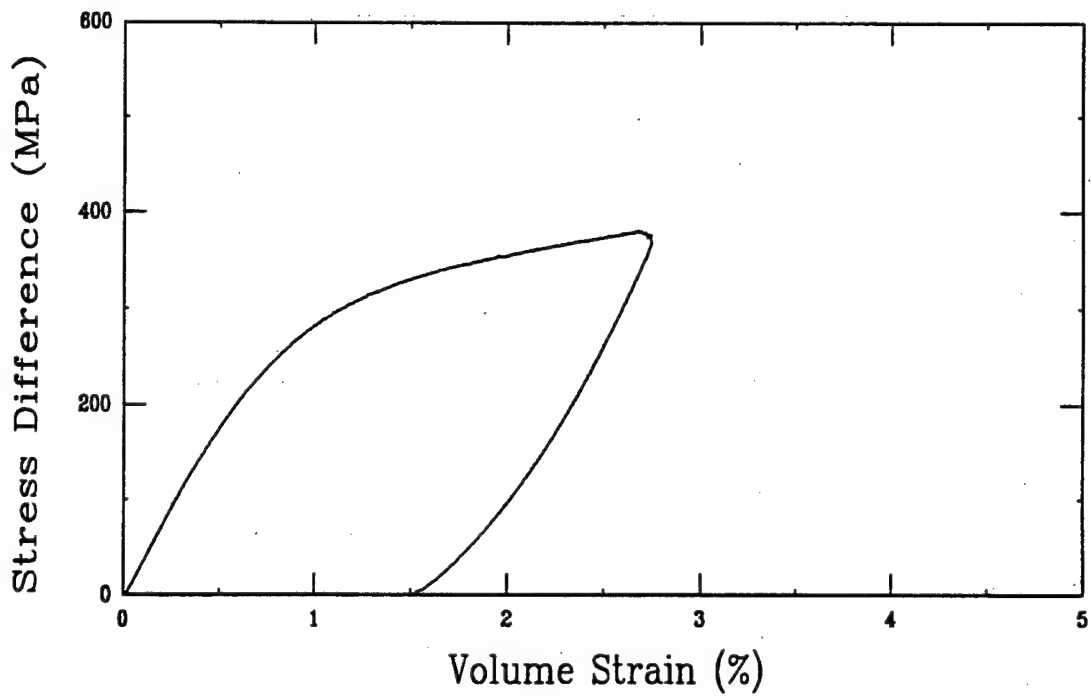
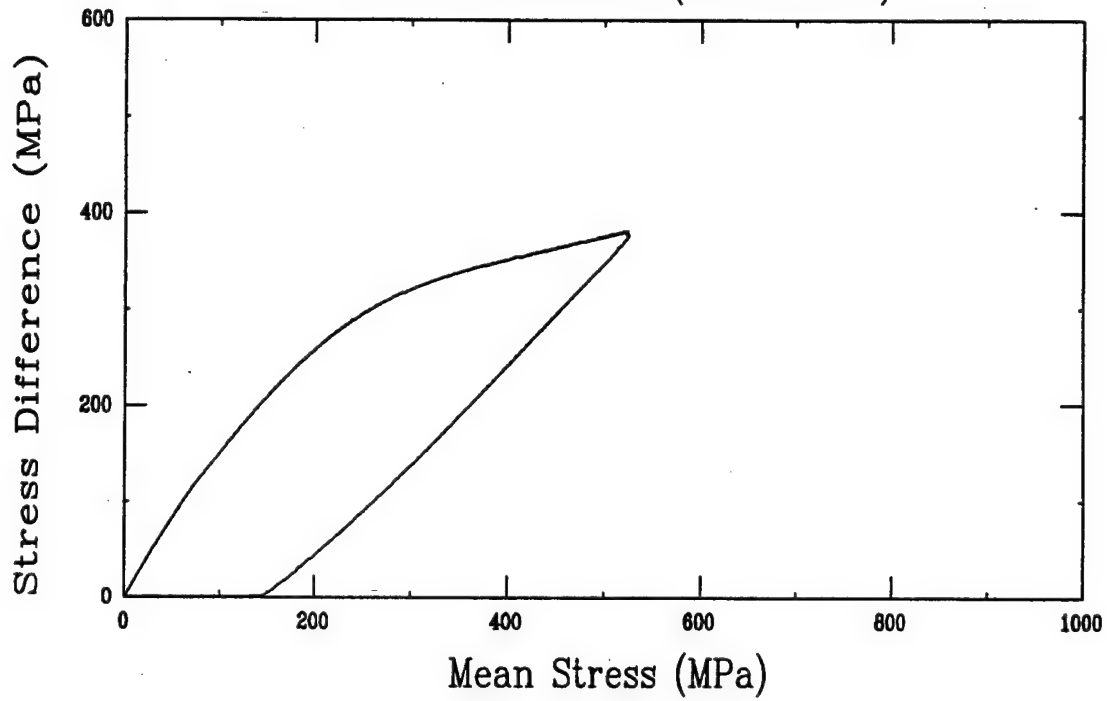
Uniaxial Strain Test (U21B3)
Ft. Knox Limestone (FK10-3-04)



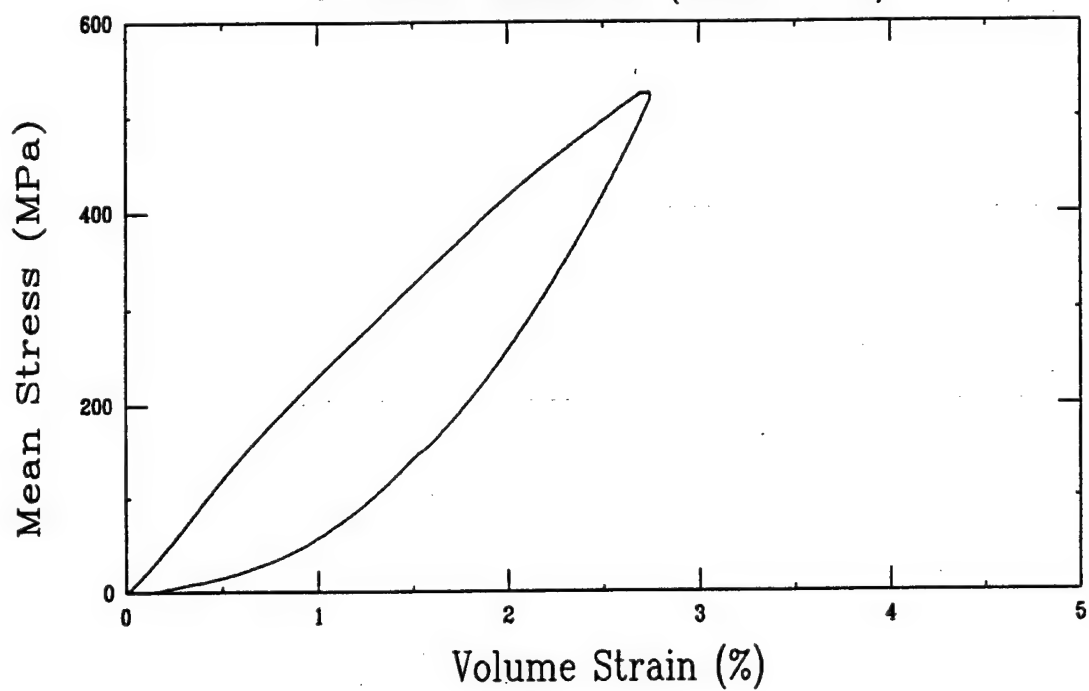
Uniaxial Strain Test (U18A3)
Ft. Knox Limestone (FK10-4-02)



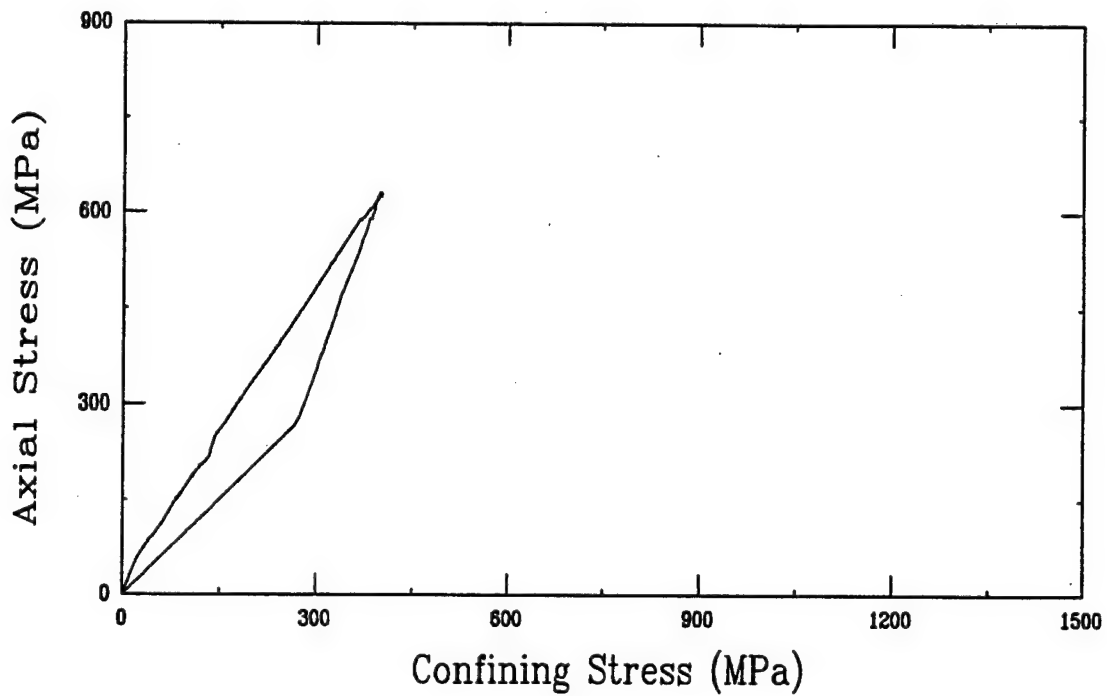
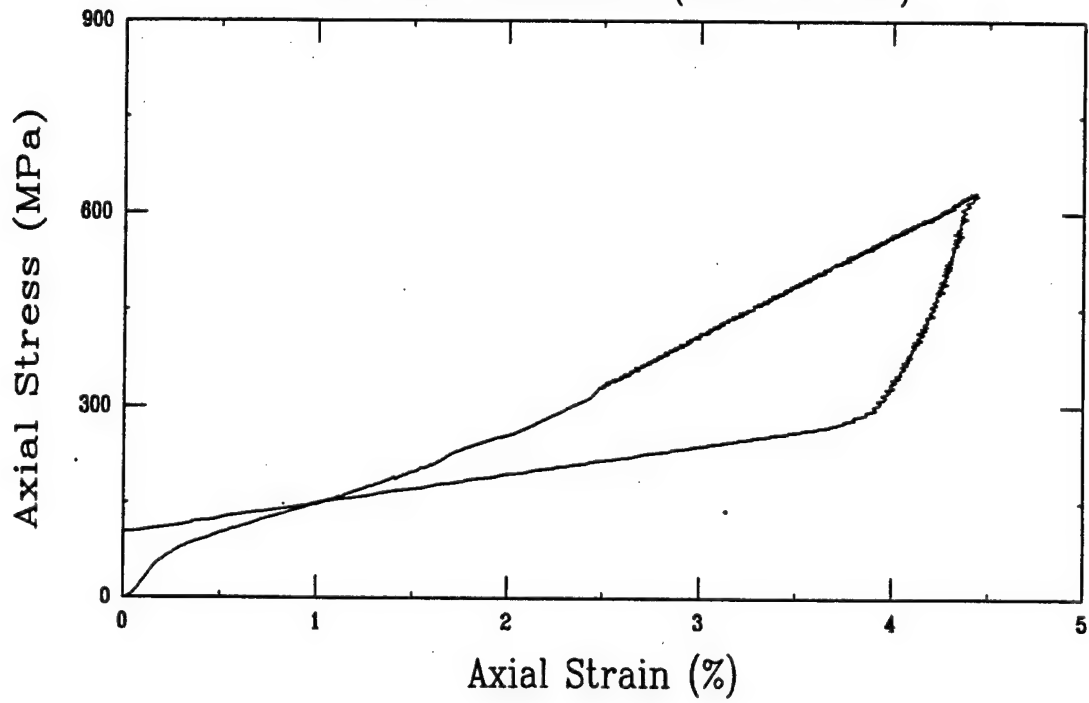
Uniaxial Strain Test (U18A3)
Ft. Knox Limestone (FK10-4-02)



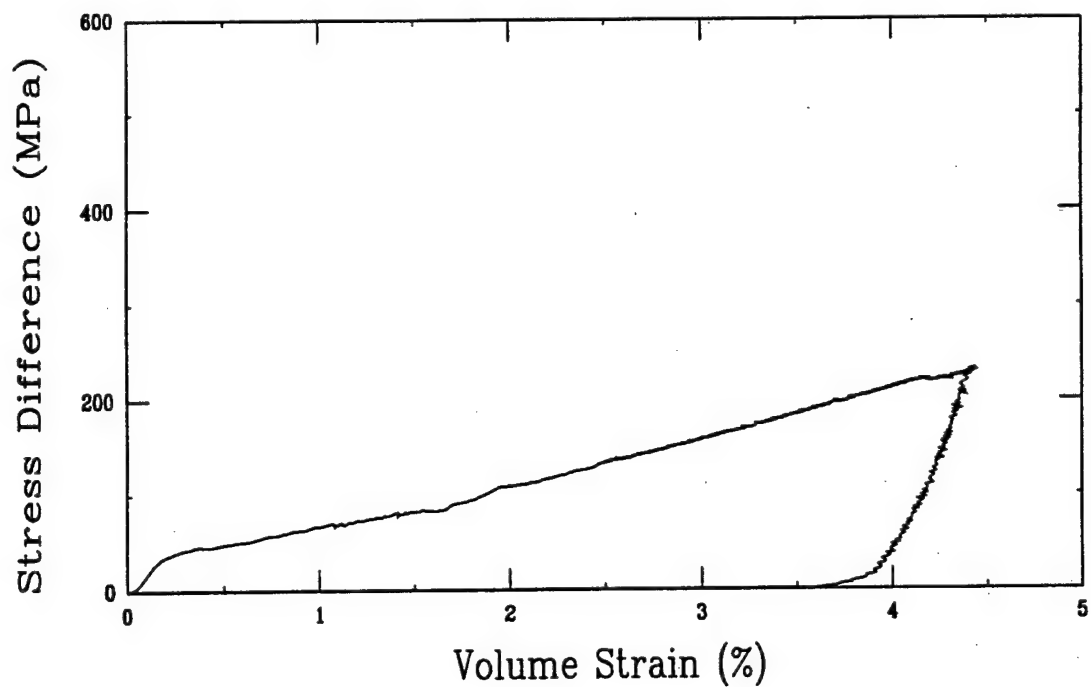
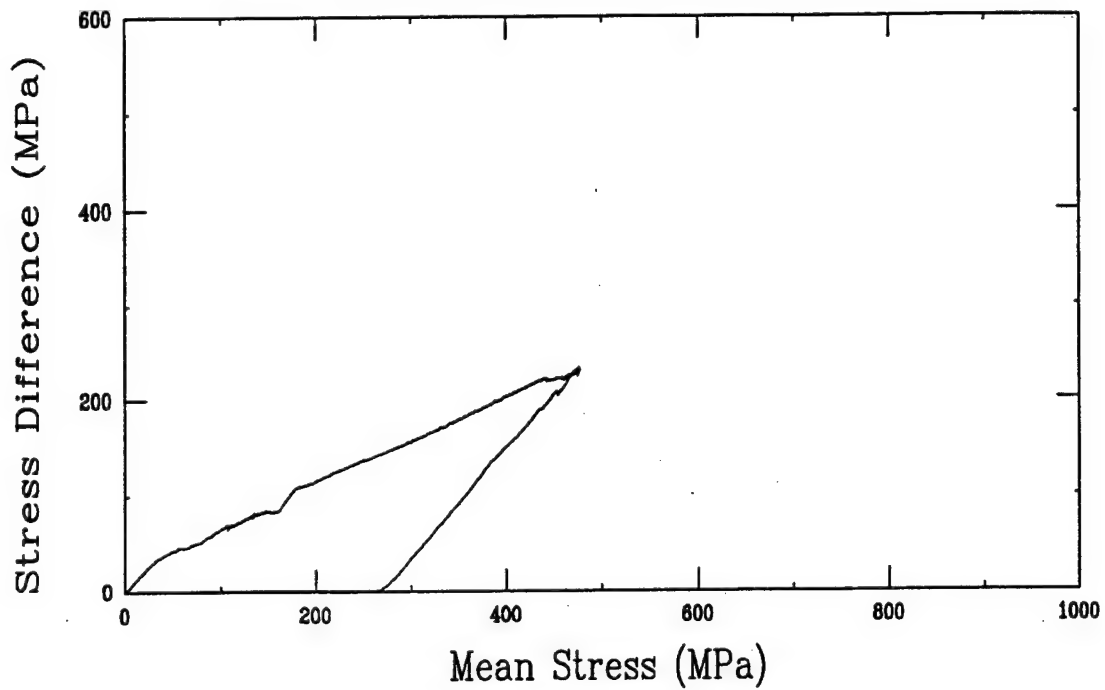
Uniaxial Strain Test (U18A3)
Ft. Knox Limestone (FK10-4-02)



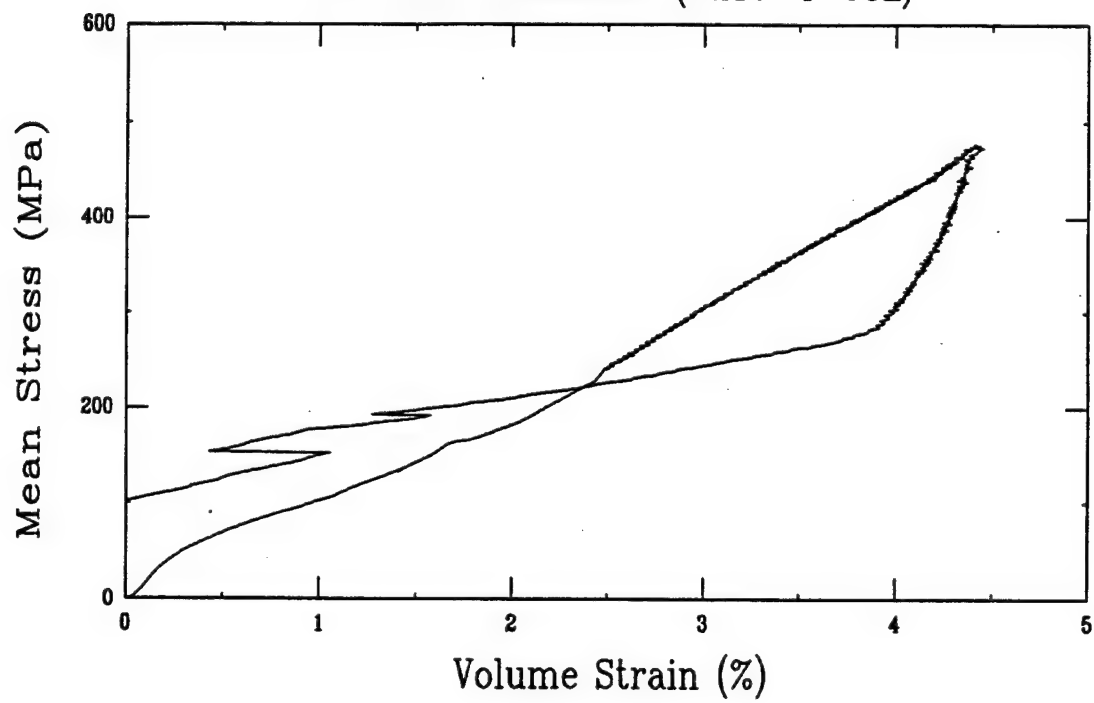
Uniaxial Strain Test (U21A3)
Ft. Knox Limestone (FK10-4-03L)



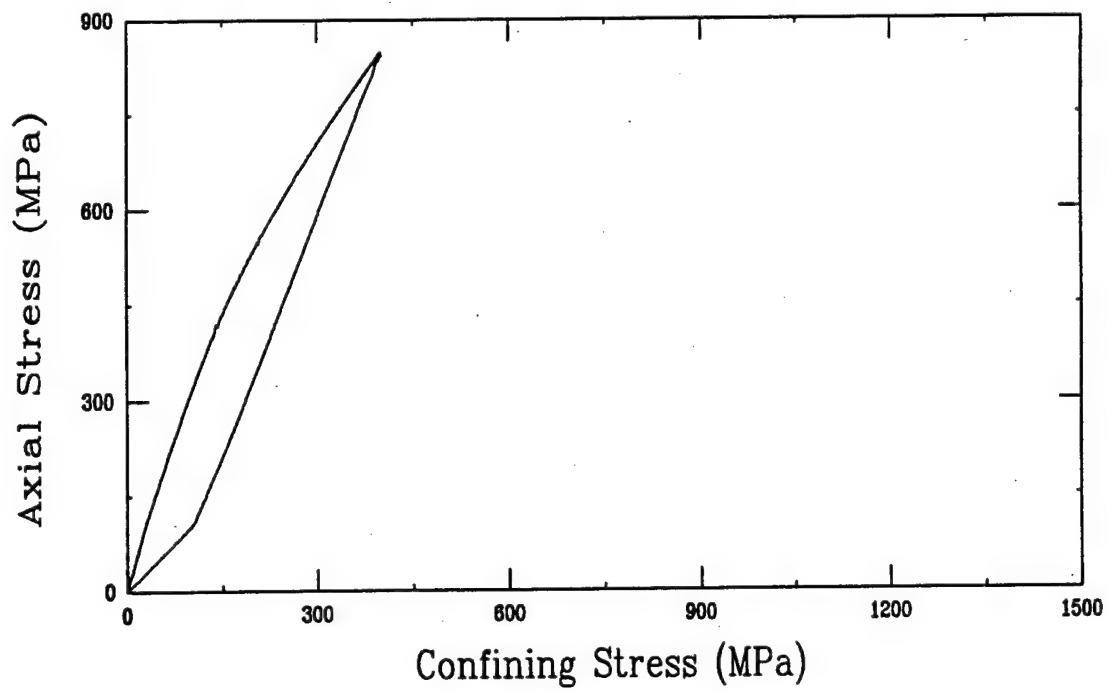
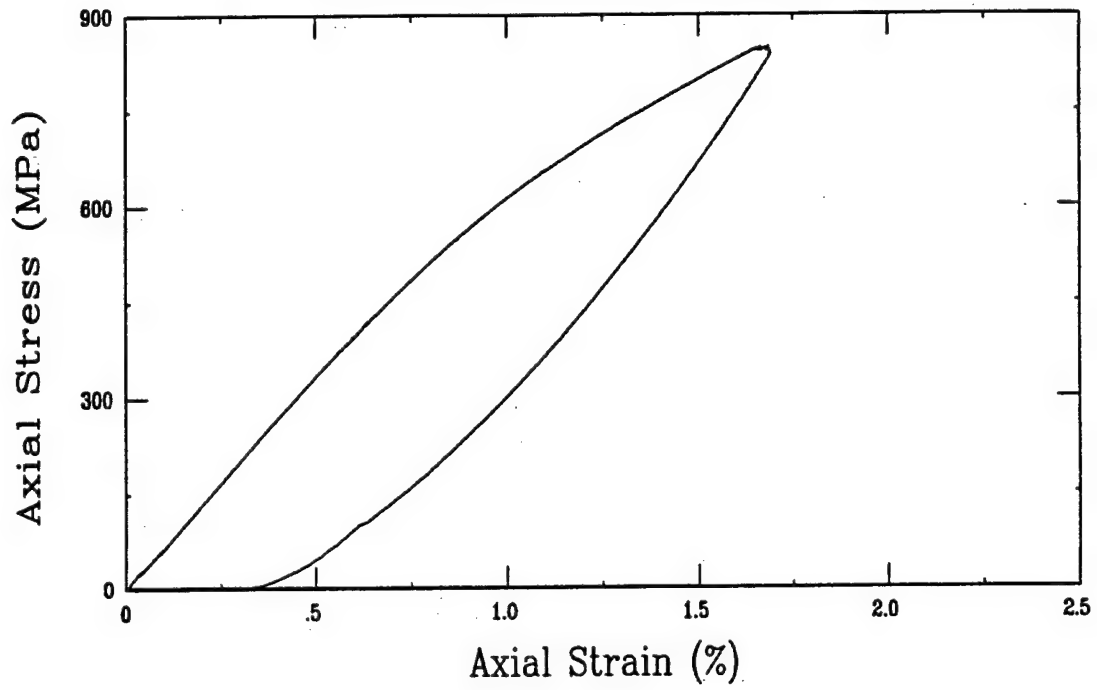
Uniaxial Strain Test (U21A3)
Ft. Knox Limestone (FK10-4-03L)



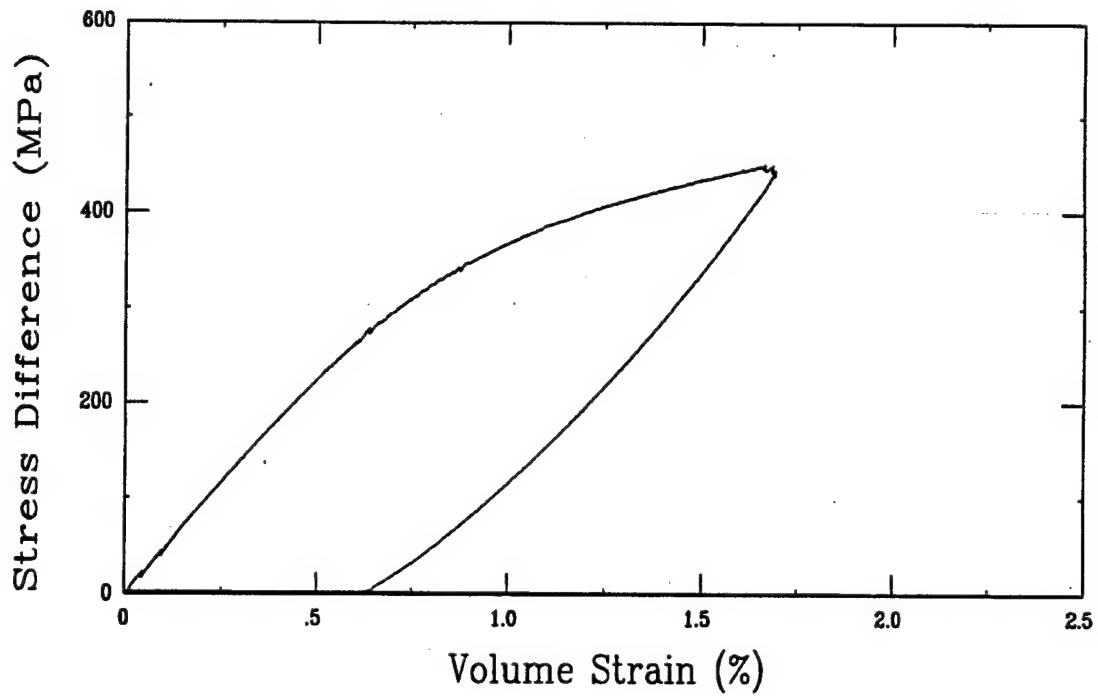
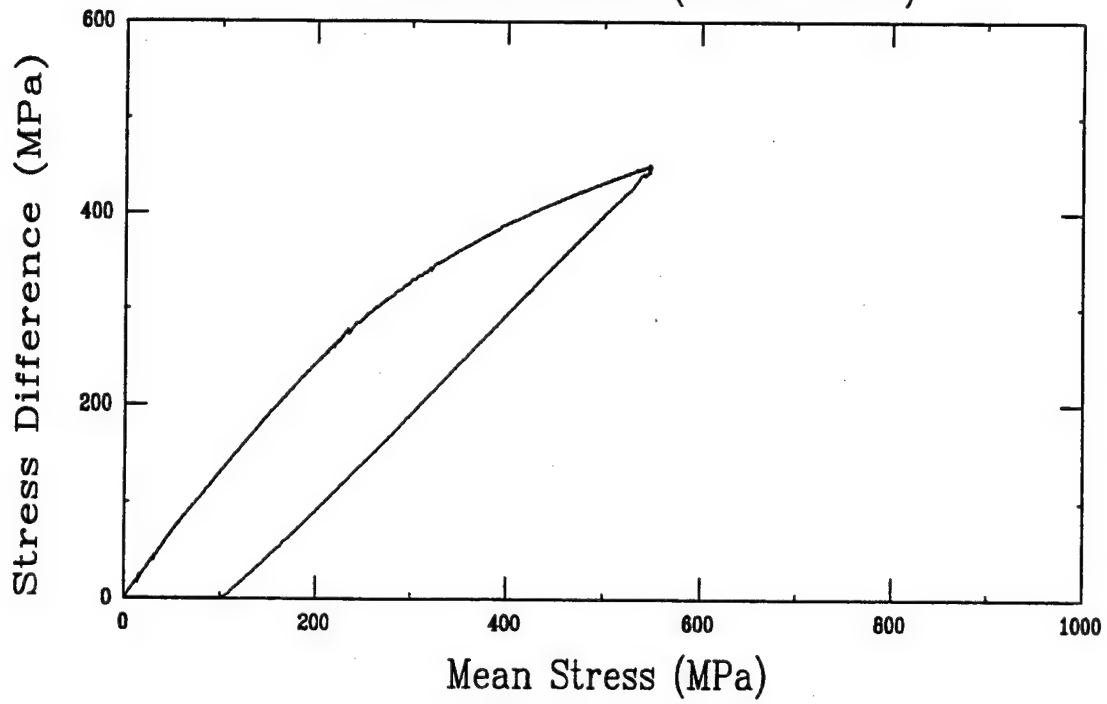
Uniaxial Strain Test (U21A3)
Ft. Knox Limestone (FK10-4-03L)



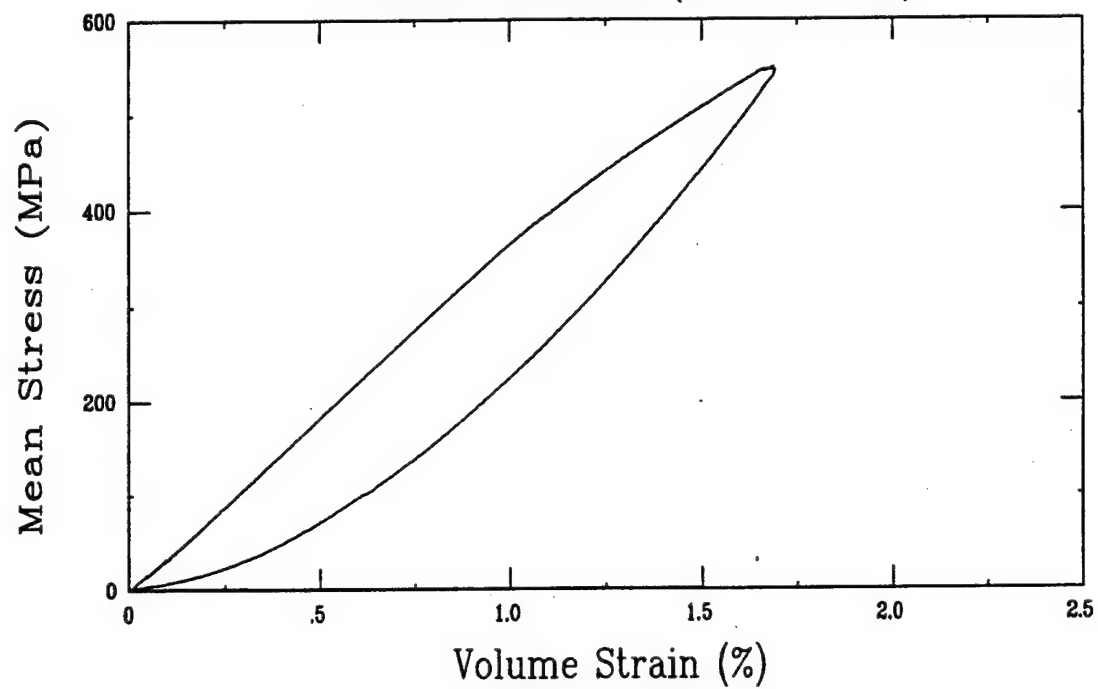
Uniaxial Strain Test (U18B3)
Ft. Knox Limestone (FK10-4-04H)



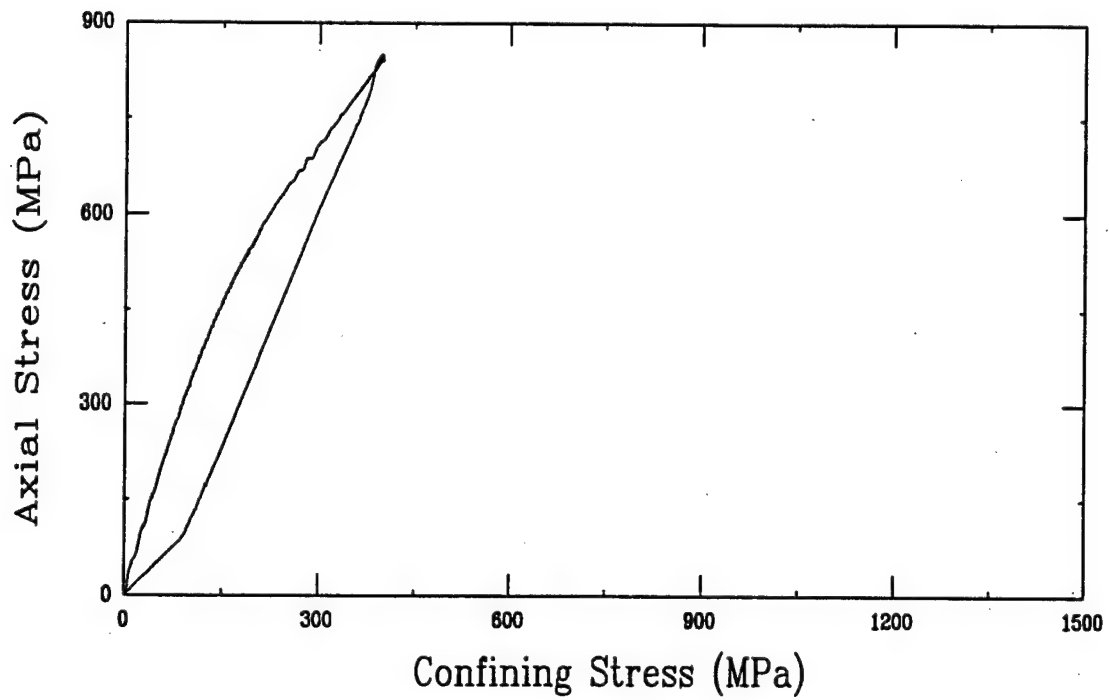
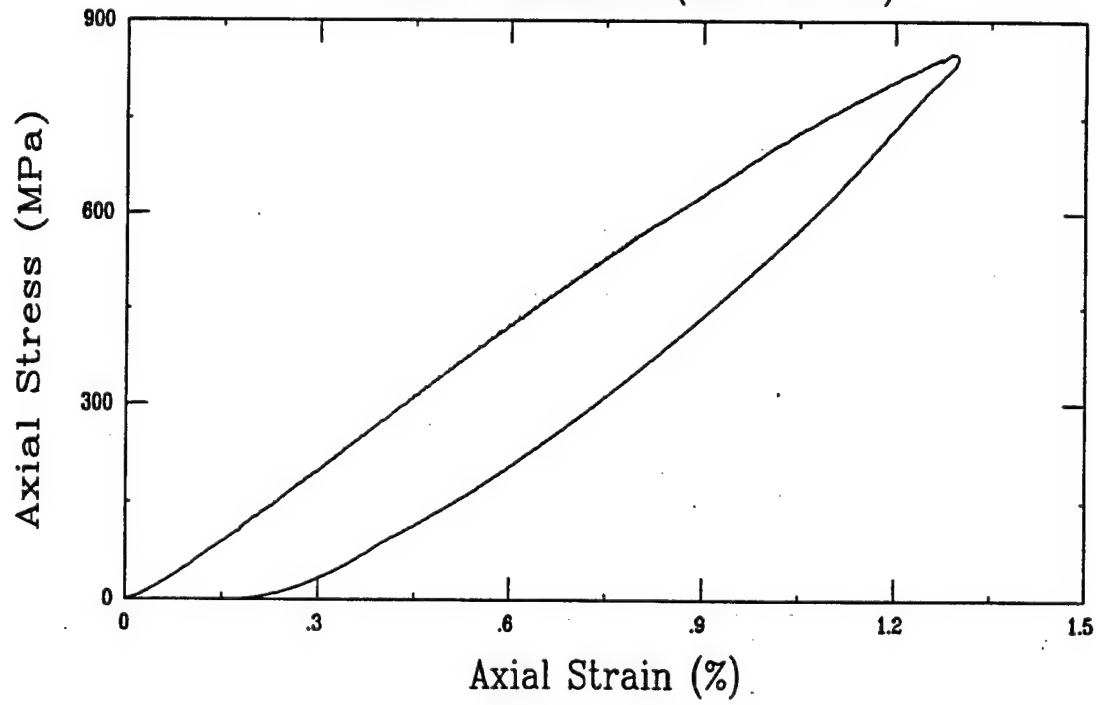
Uniaxial Strain Test (U18B3)
Ft. Knox Limestone (FK10-4-04H)



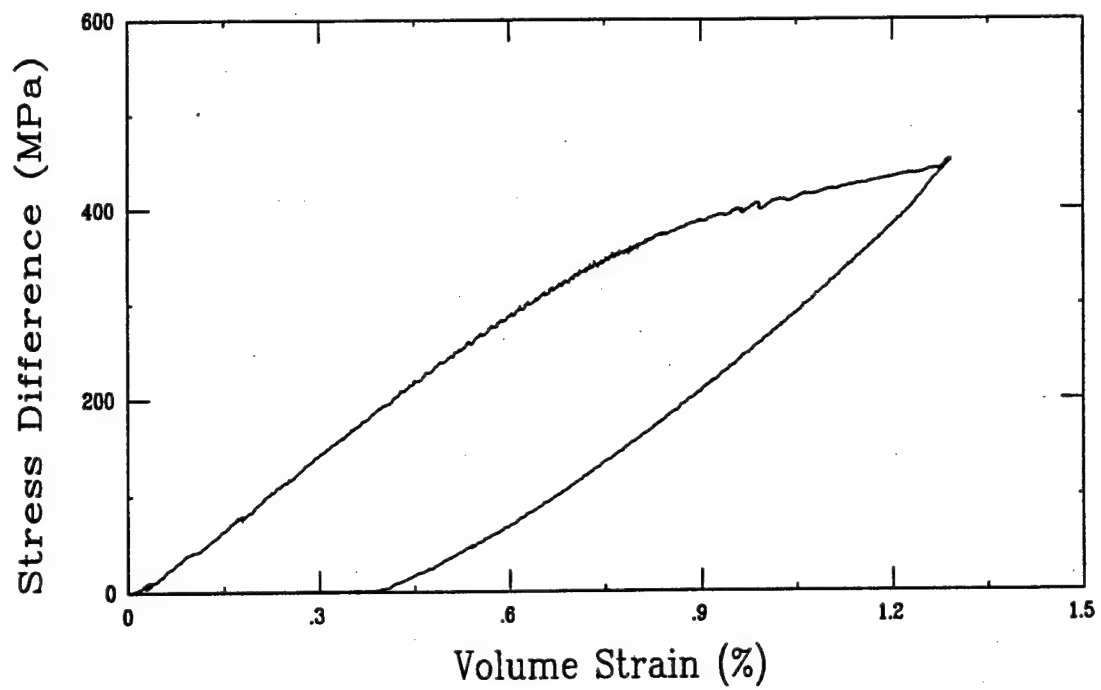
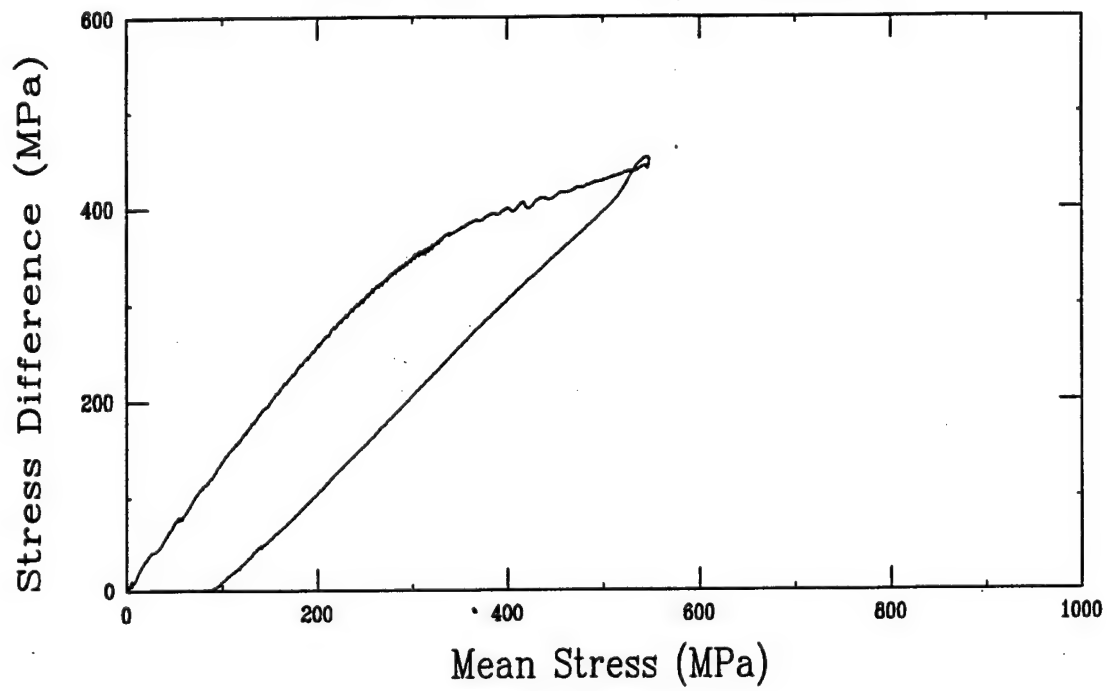
Uniaxial Strain Test (U18B3)
Ft. Knox Limestone (FK10-4-04H)



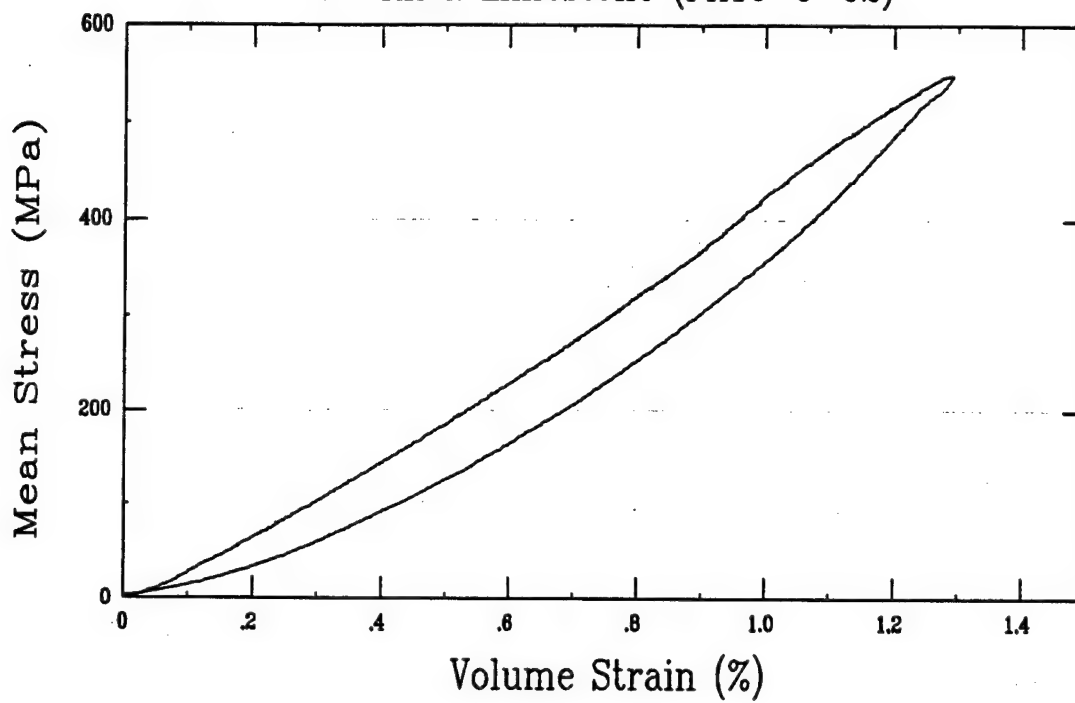
Uniaxial Strain Test (Y14B3)
Ft. Knox Limestone (FK10-5-02)



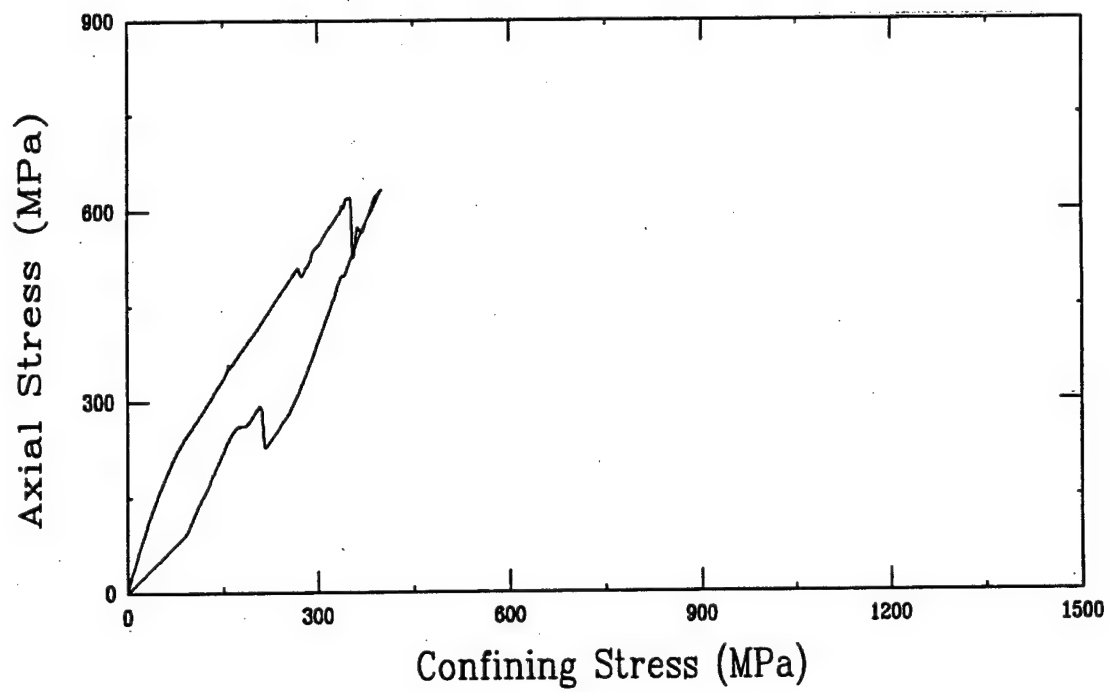
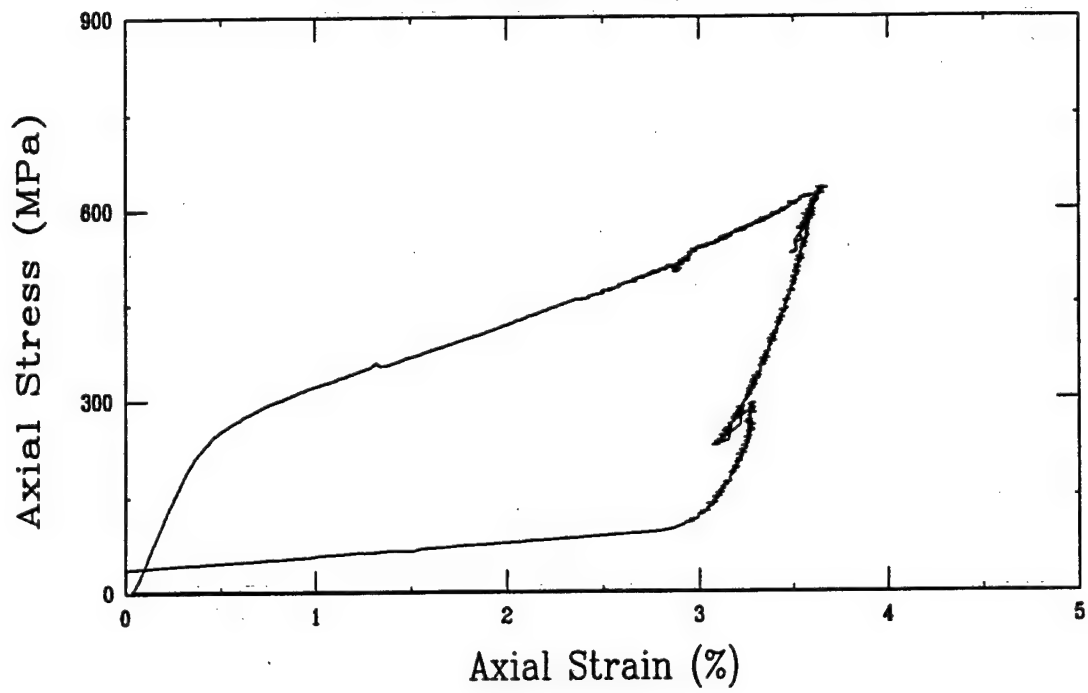
Uniaxial Strain Test (Y14B3)
Ft. Knox Limestone (FK10-5-02)



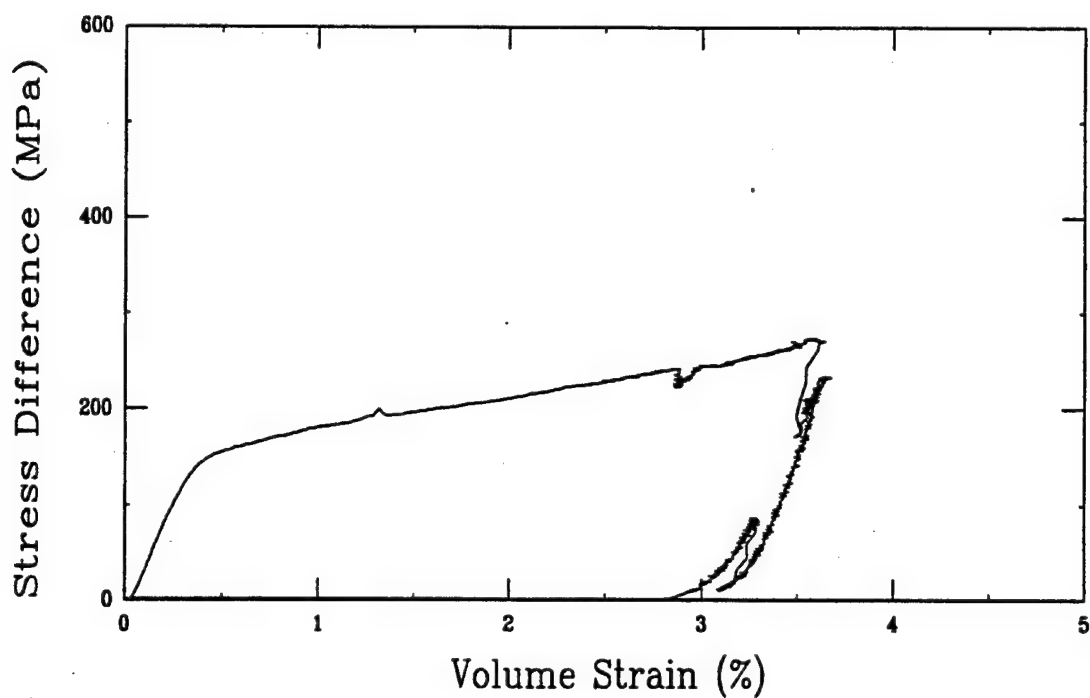
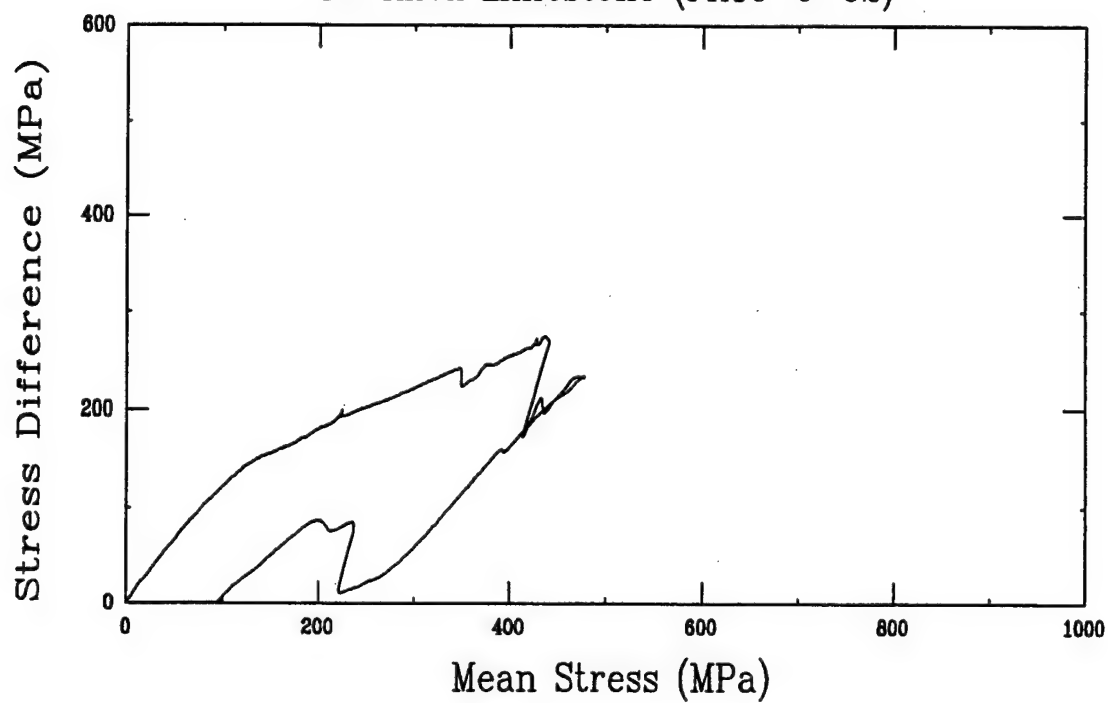
Uniaxial Strain Test (Y14B3)
Ft. Knox Limestone (FK10-5-02)



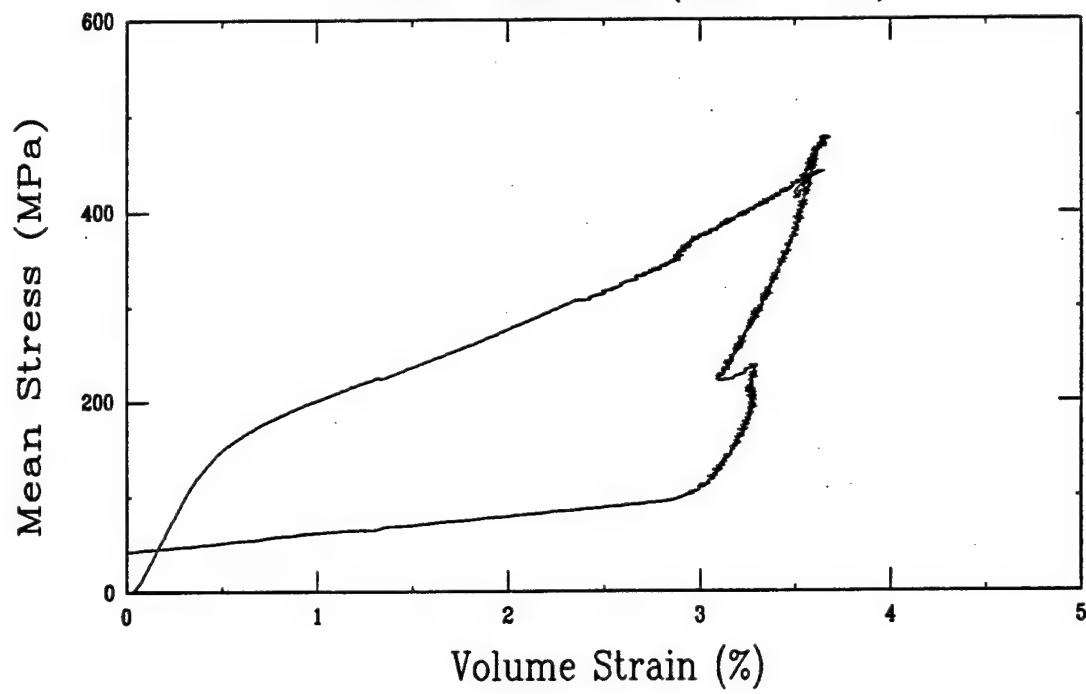
Uniaxial Strain Test (U22A3)
Ft. Knox Limestone (FK10-6-02)



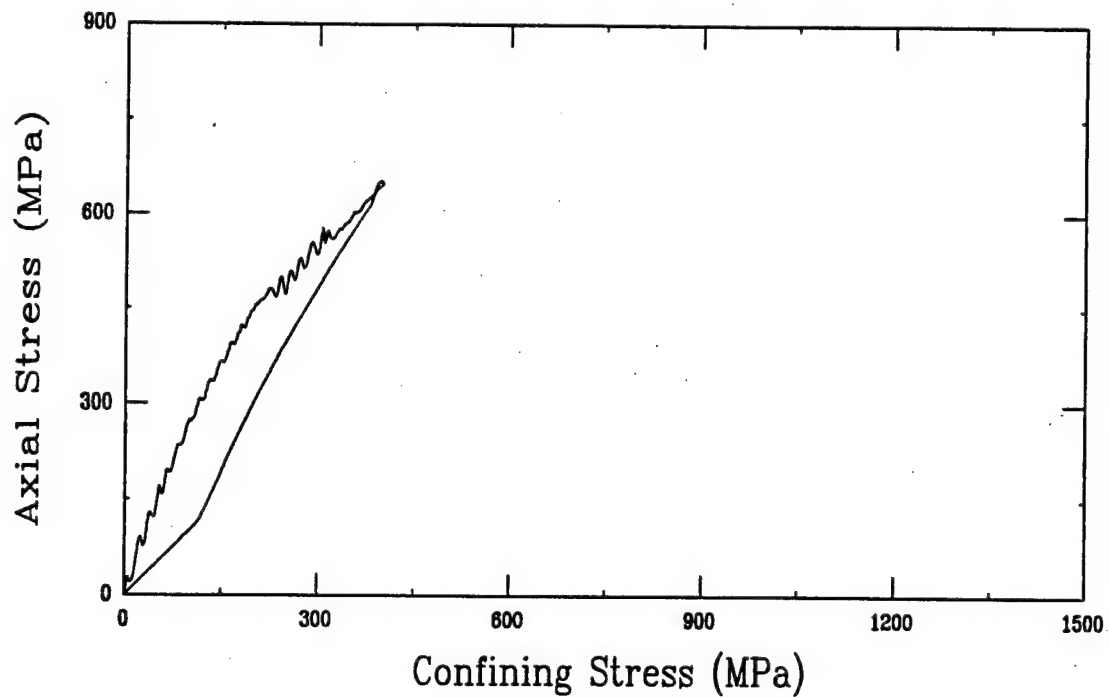
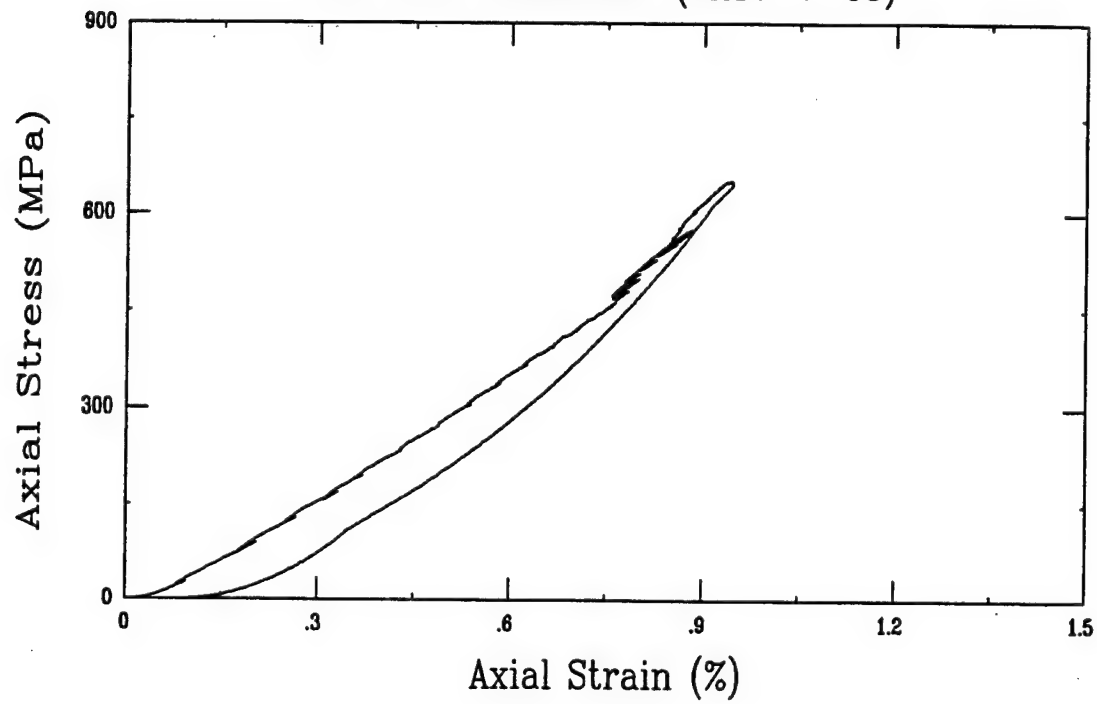
Uniaxial Strain Test (U22A3)
Ft. Knox Limestone (FK10-6-02)



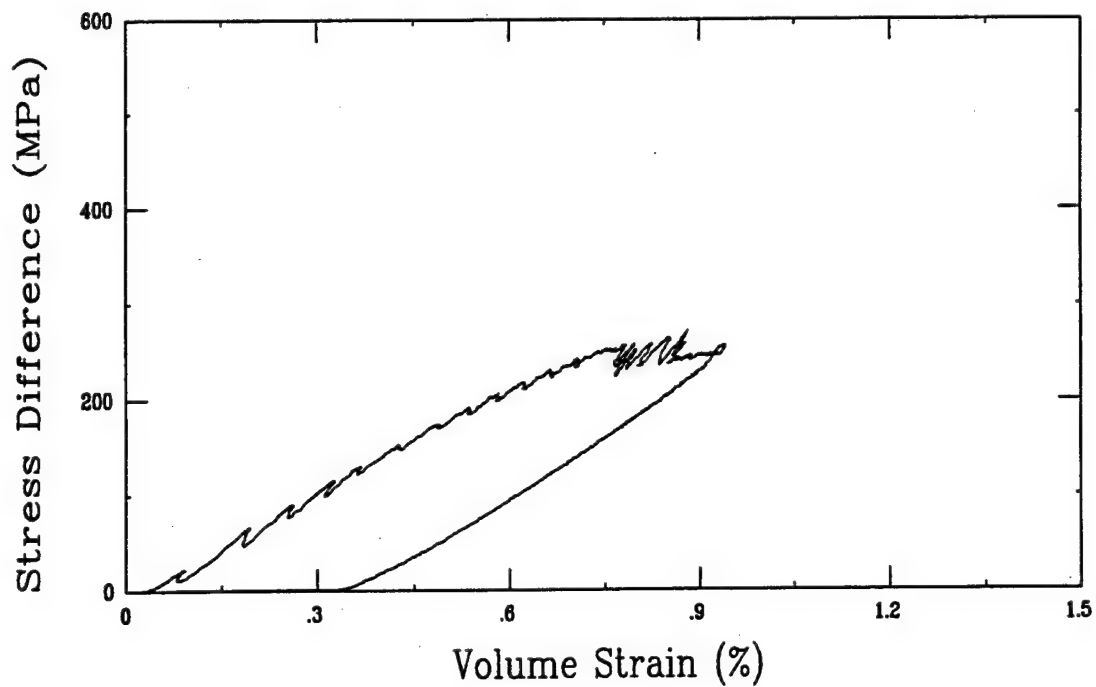
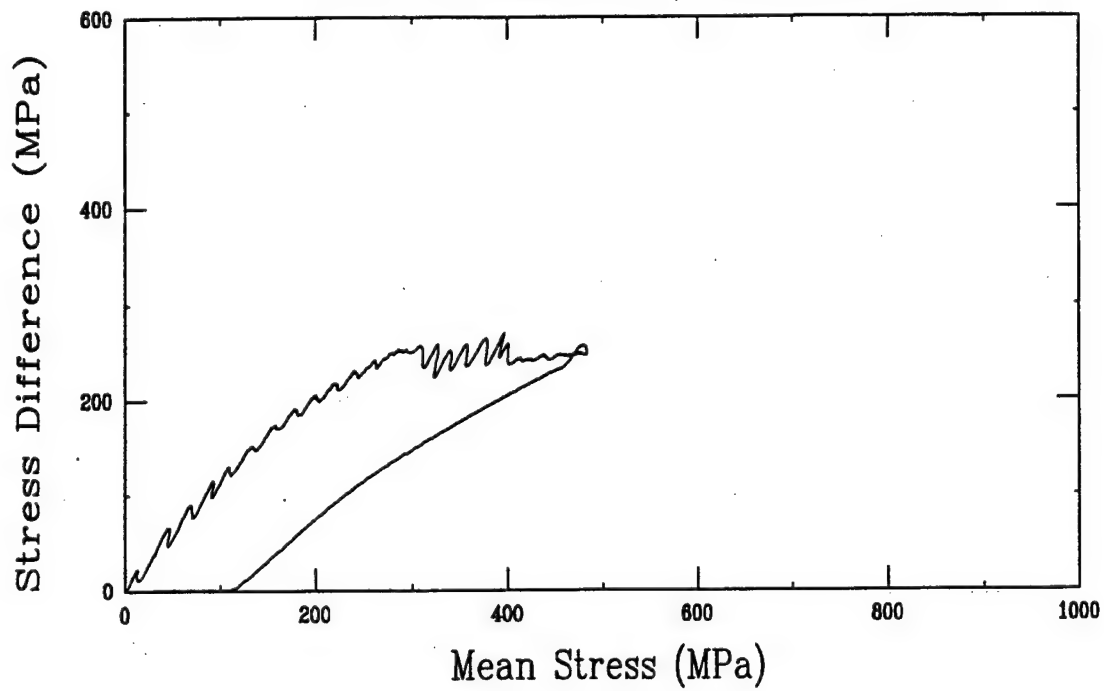
Uniaxial Strain Test (U22A3)
Ft. Knox Limestone (FK10-6-02)



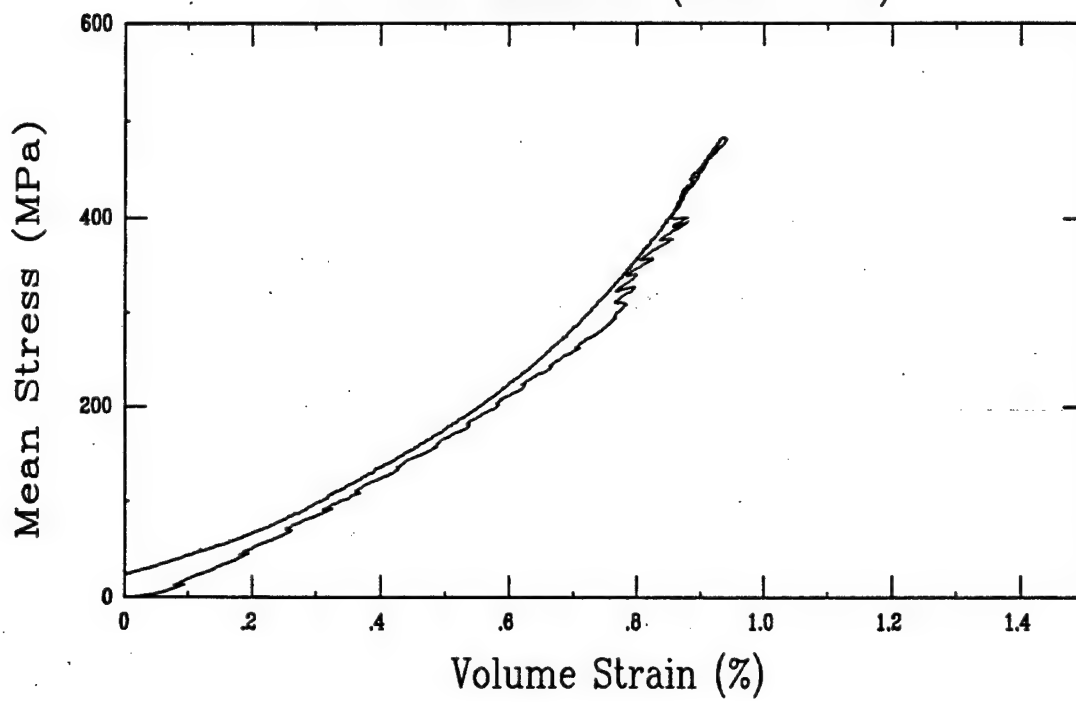
Uniaxial Strain Test (Y14C3)
Ft. Knox Limestone (FK10-7-05)



Uniaxial Strain Test (Y14C3)
Ft. Knox Limestone (FK10-7-05)

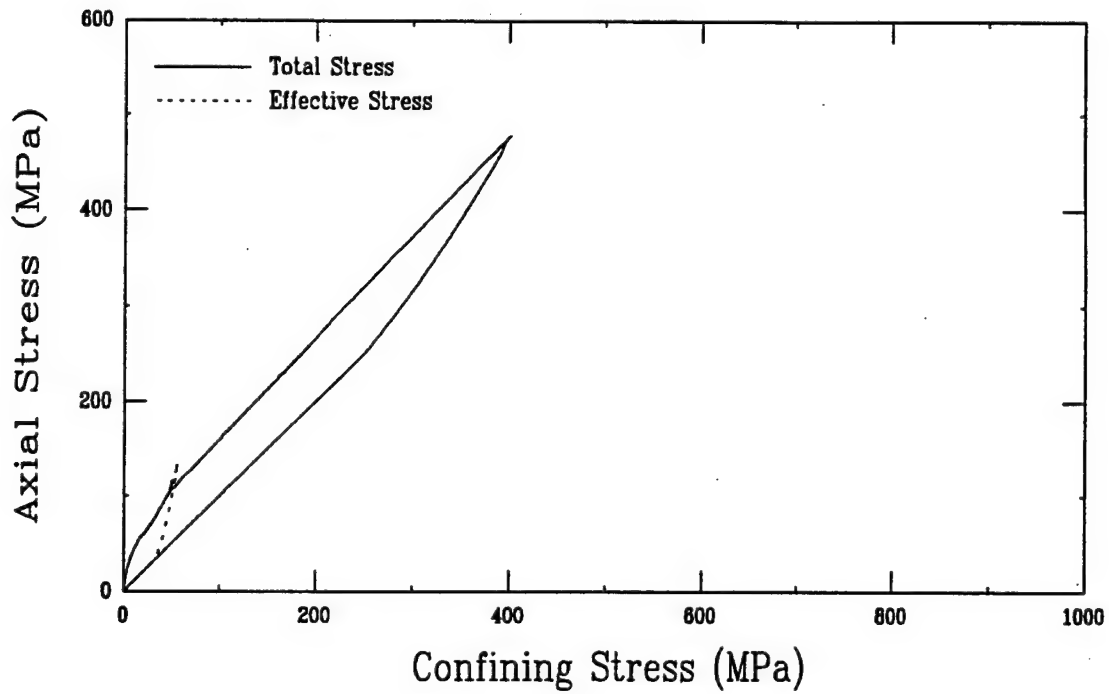
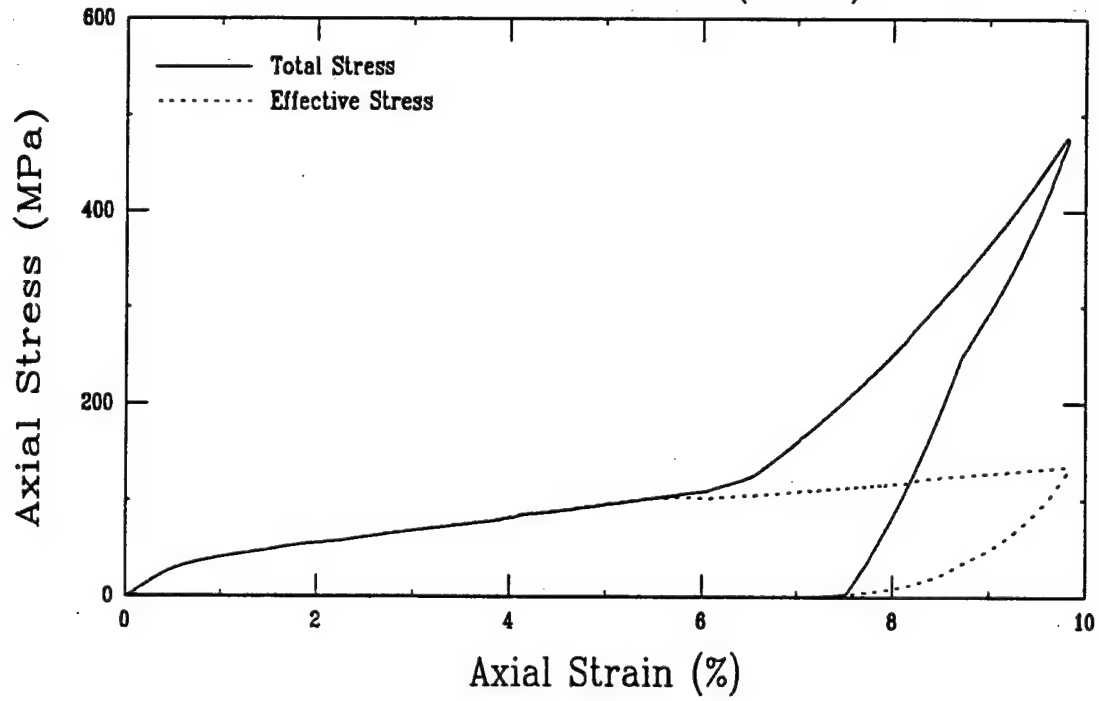


Uniaxial Strain Test (Y14C3)
Ft. Knox Limestone (FK10-7-05)

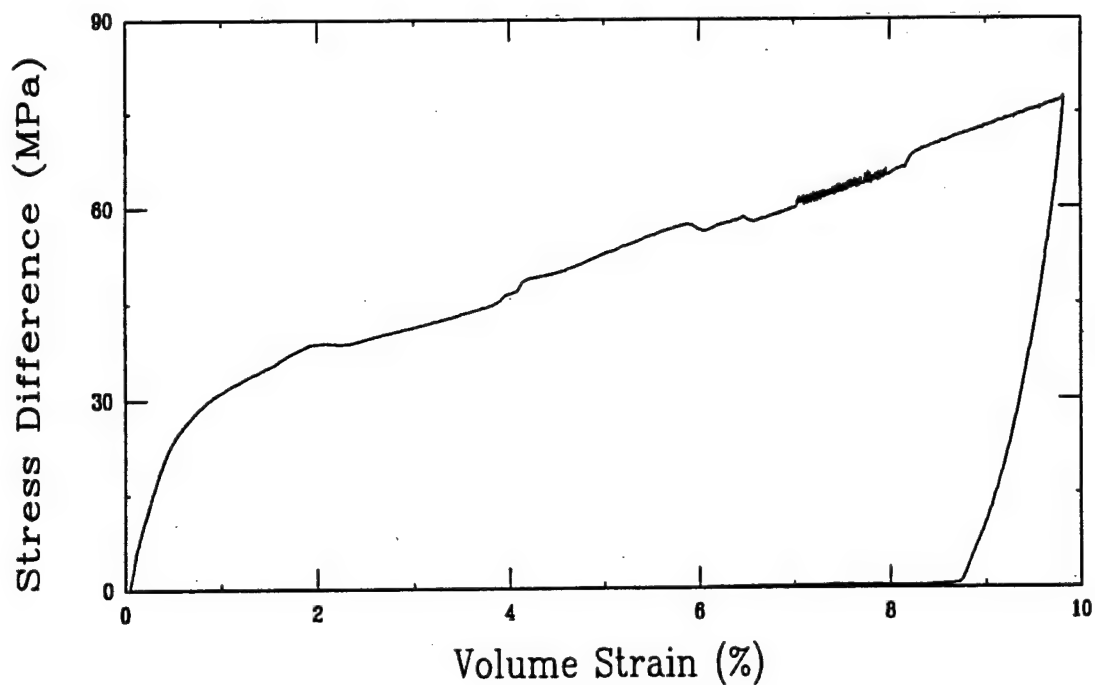
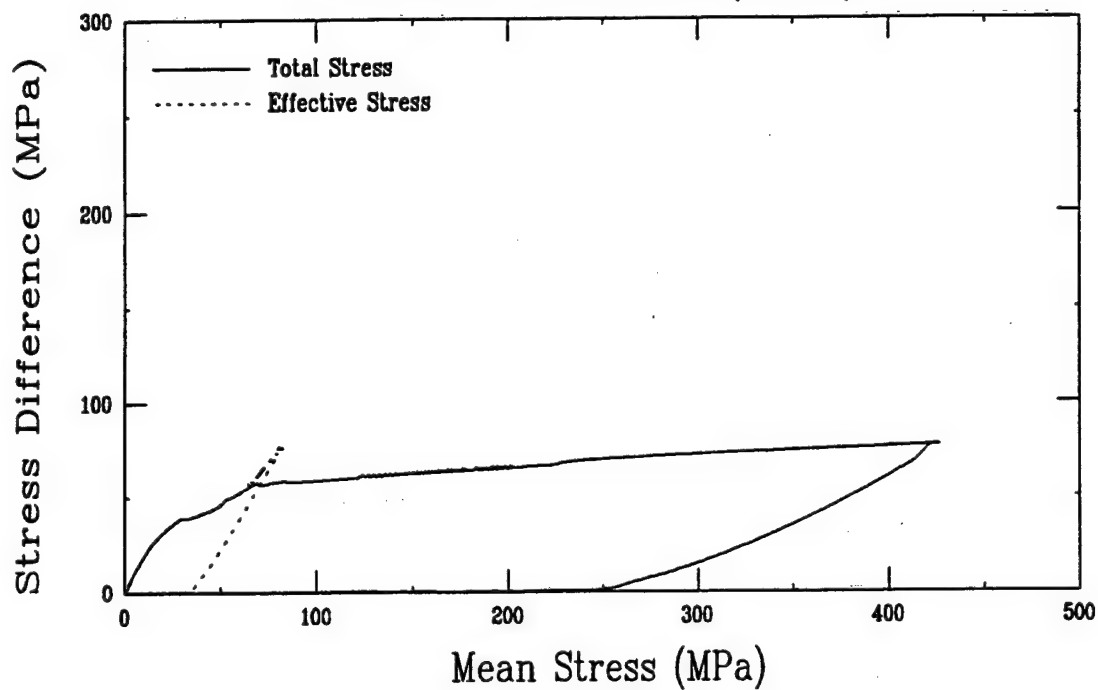


APPENDIX E
TEST DATA FOR
TUFF FROM NEVADA TEST SITE

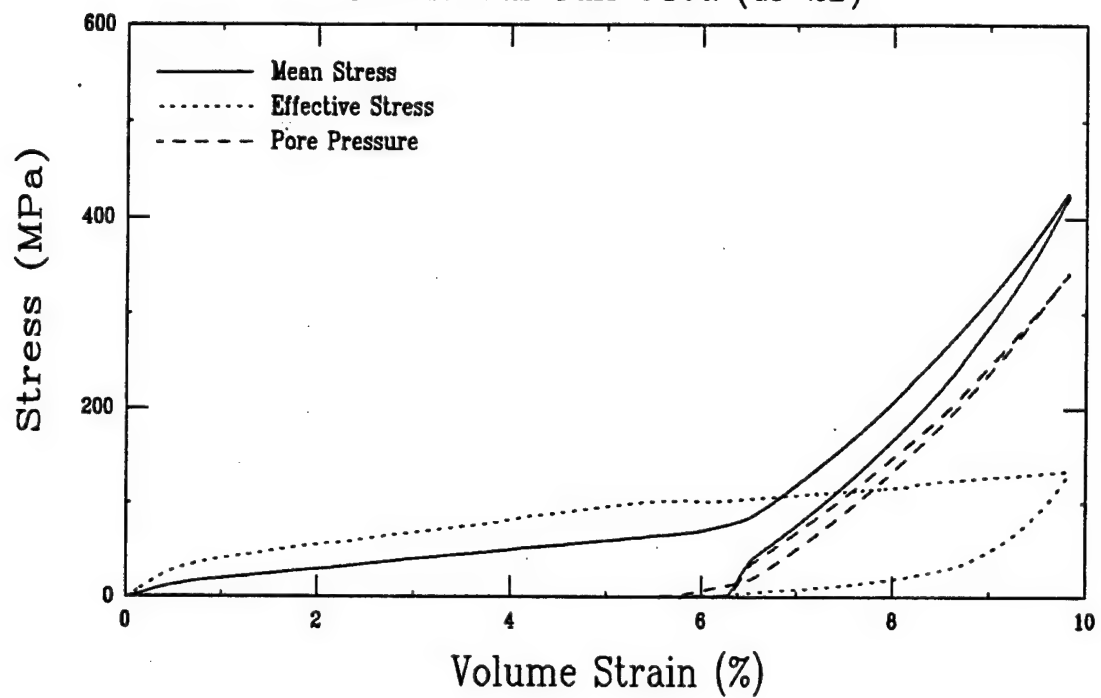
Undrained Uniaxial Strain Test (M24A5)
Pumiceous Tuff U16a (GI-2B)



Undrained Uniaxial Strain Test (M24A5) Pumiceous Tuff U16a (GI-2B)

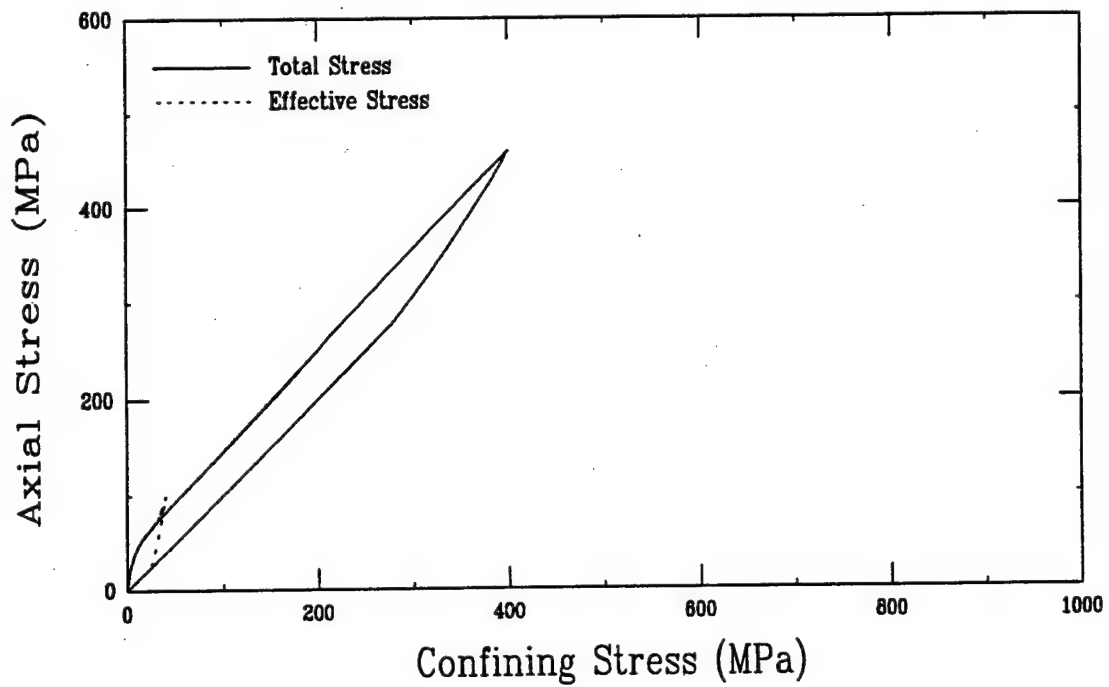
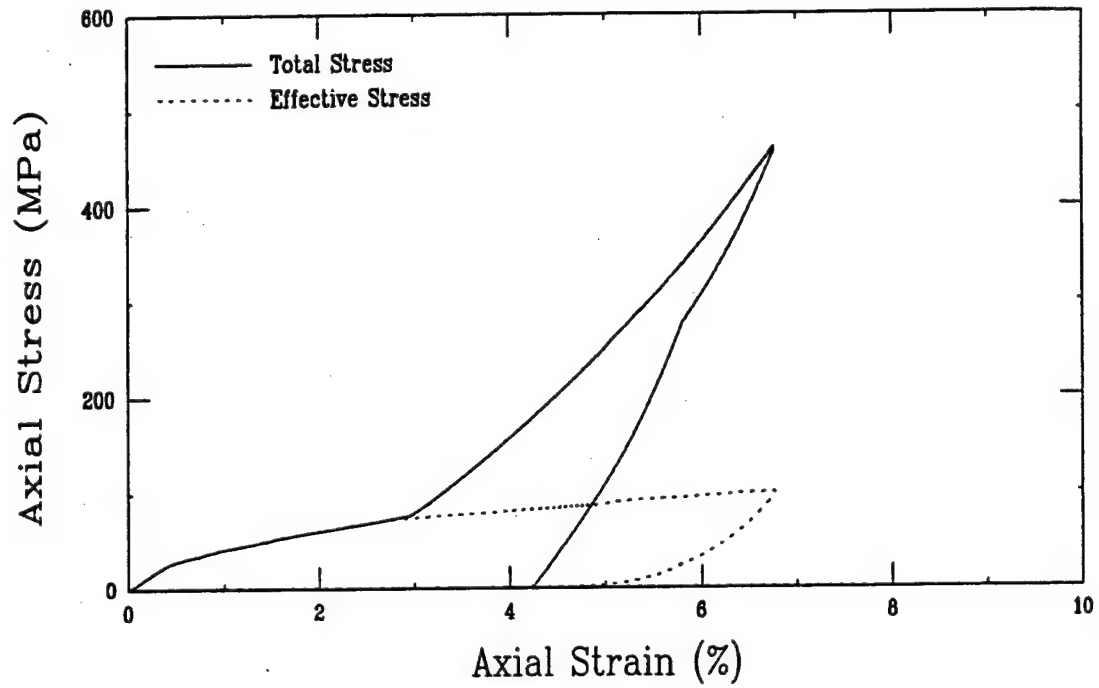


Undrained Uniaxial Strain Test (M24A5)
Pumiceous Tuff U16a (GI-2B)

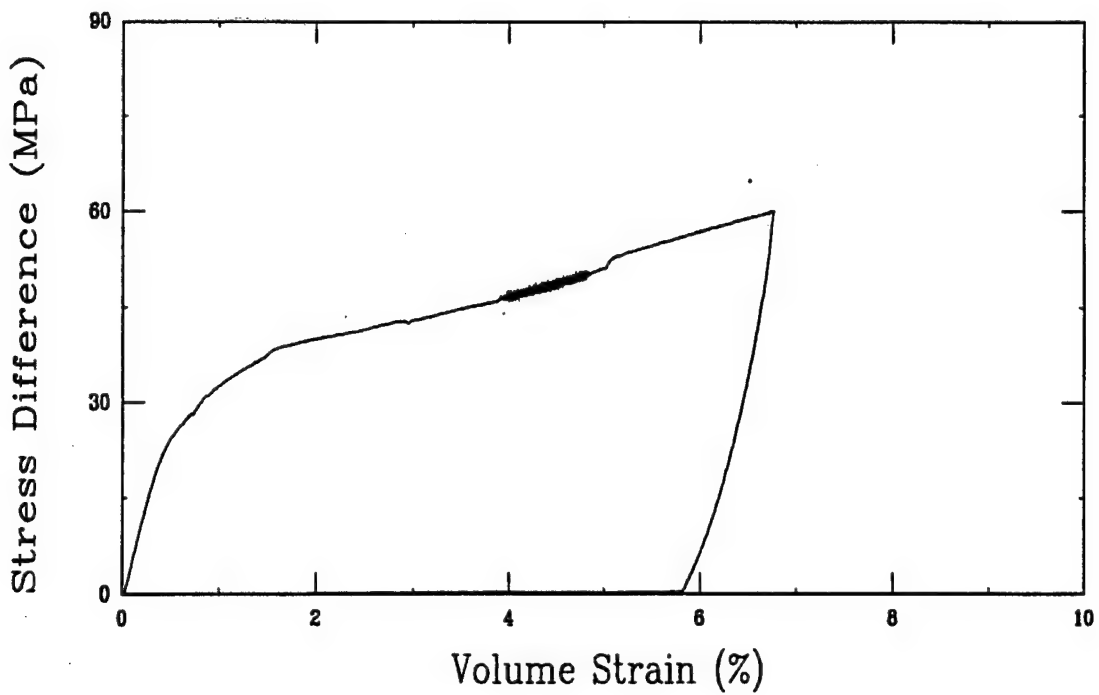
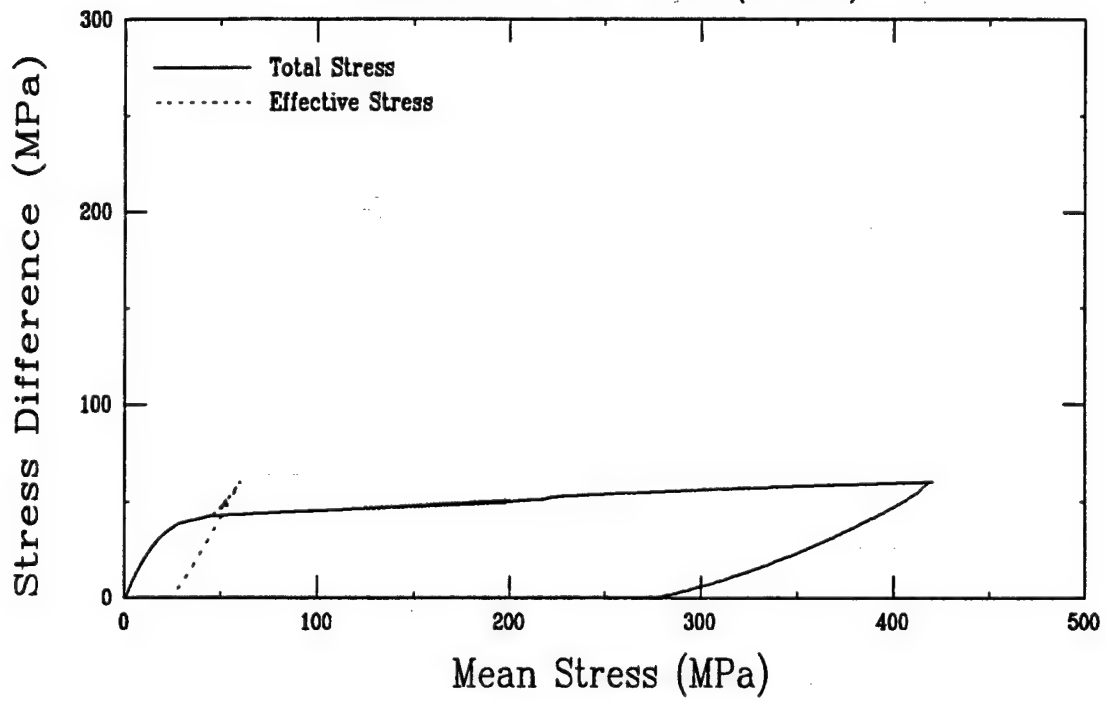


Uniaxial Strain Test (M28A5)

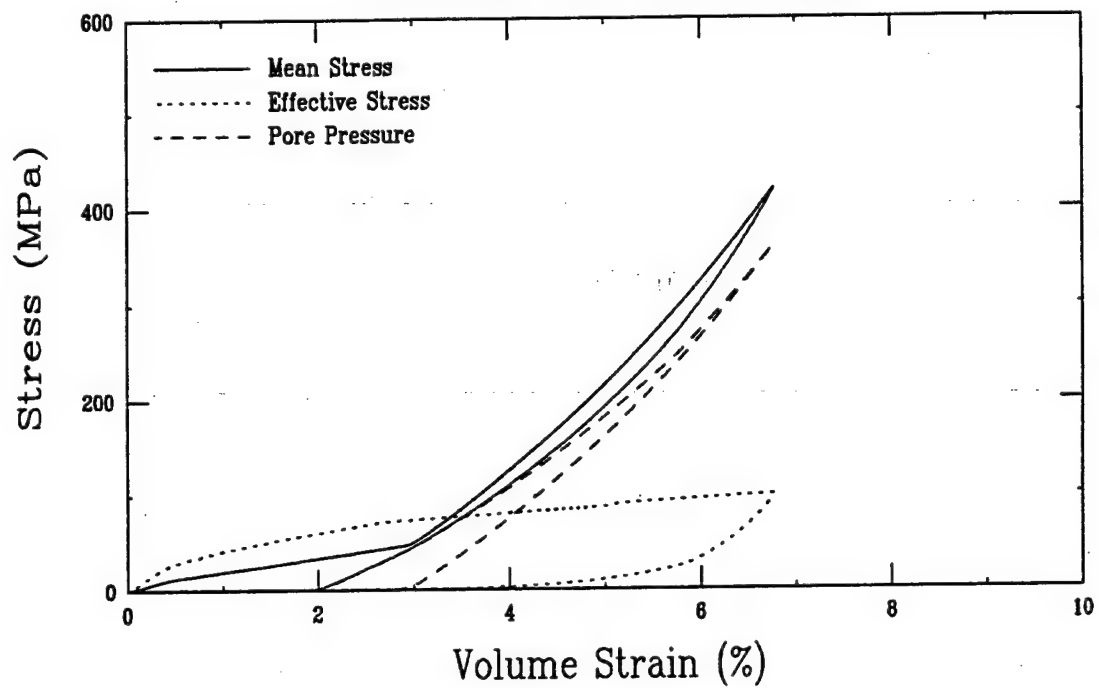
Pumiceous Tuff U16a (GI-2E)



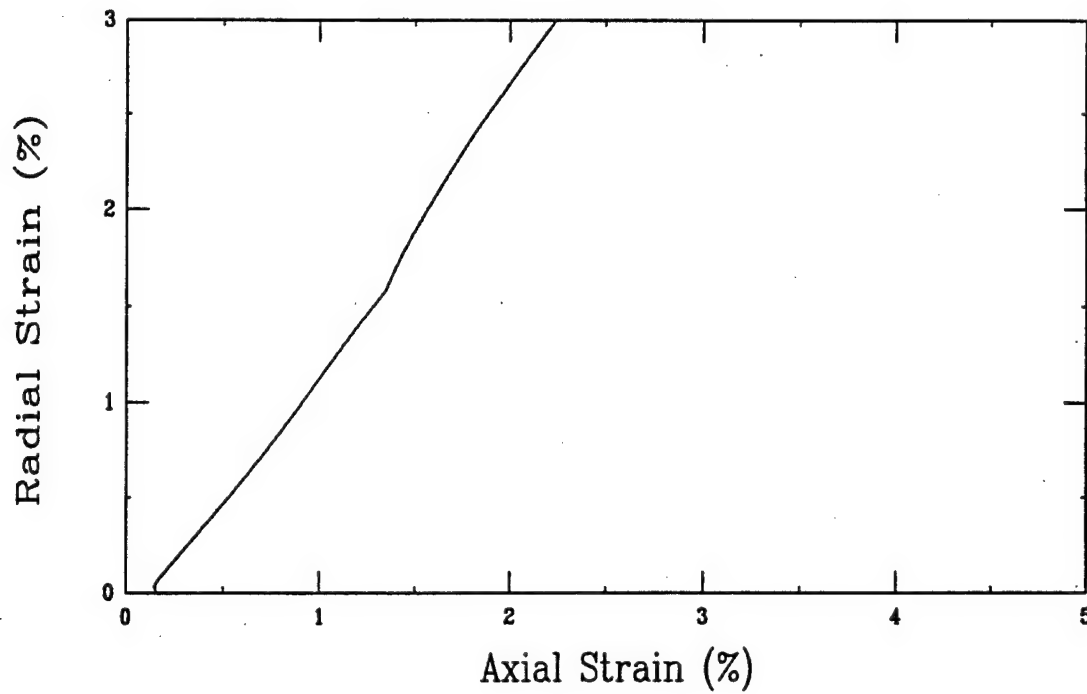
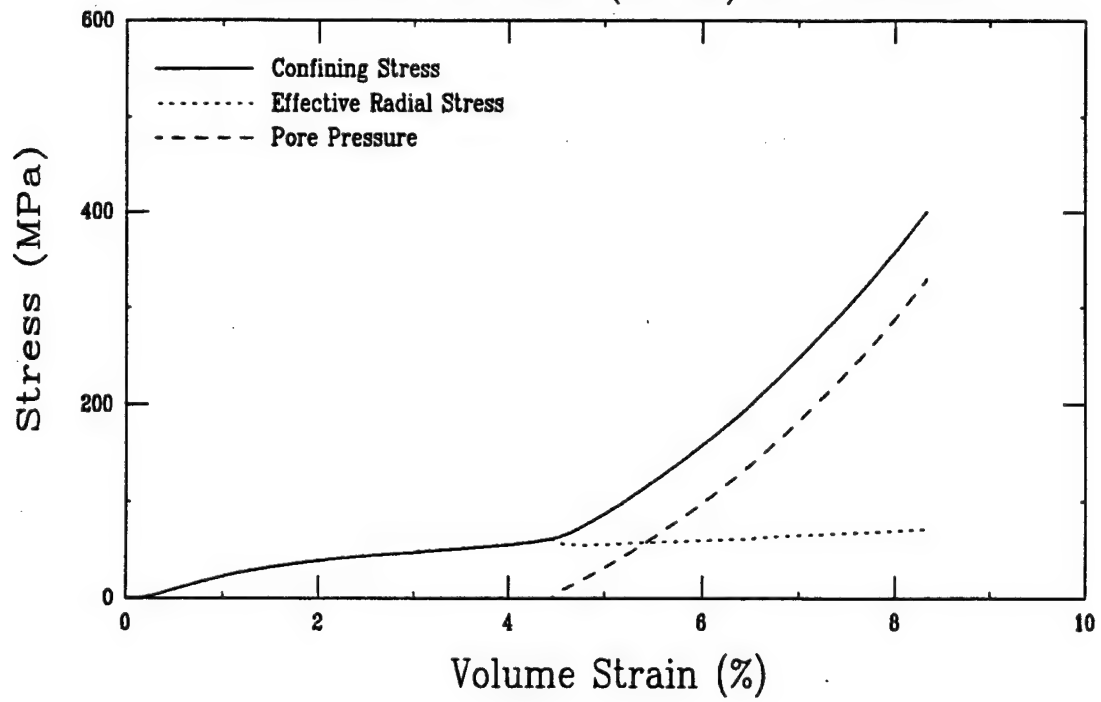
Uniaxial Strain Test (M28A5)
Pumiceous Tuff U16a (GI-2E)



Uniaxial Strain Test (M28A5)
Pumiceous Tuff U16a (GI-2E)

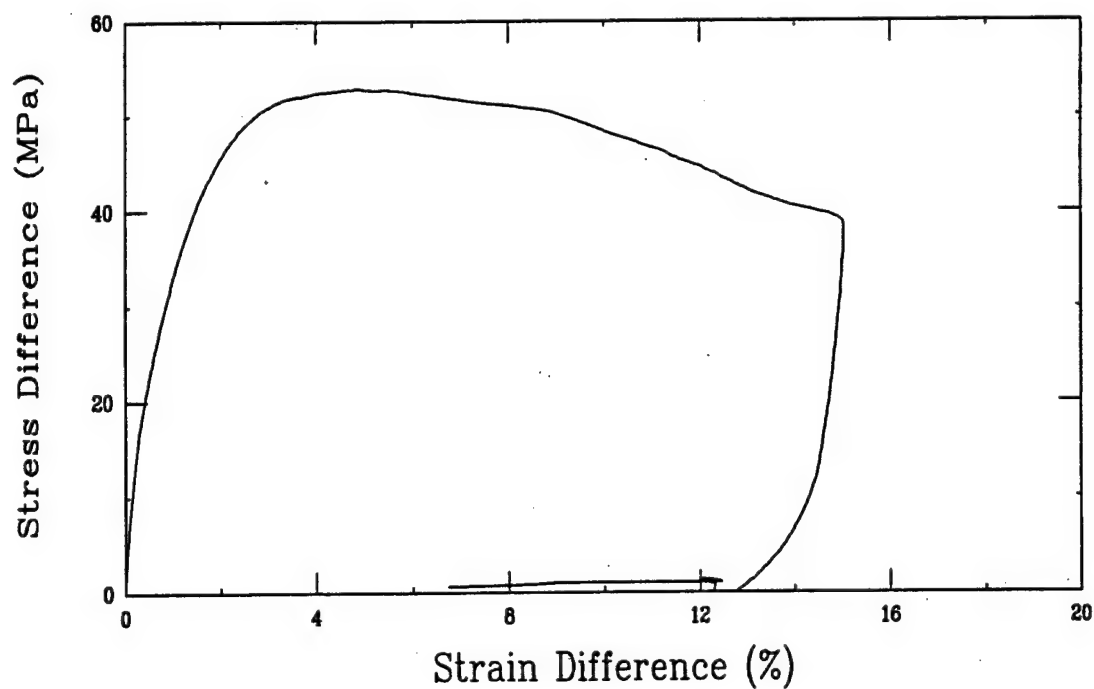
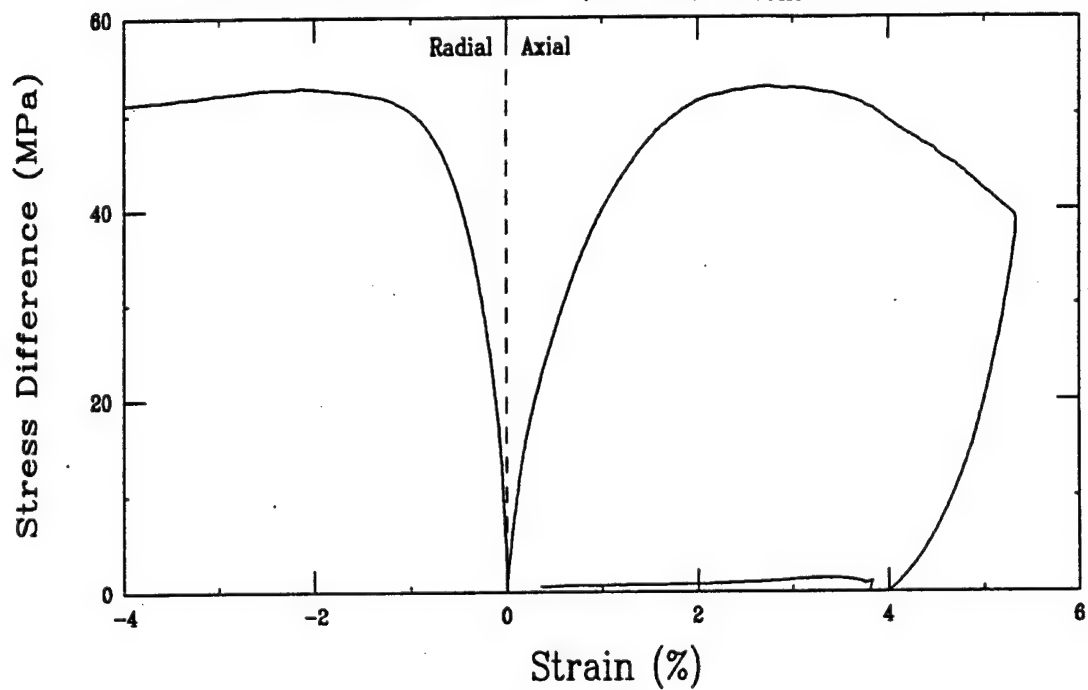


Uniaxial Strain Test (M29A5)
Pumiceous Tuff U16a (GI-2B) to = 400 MPa



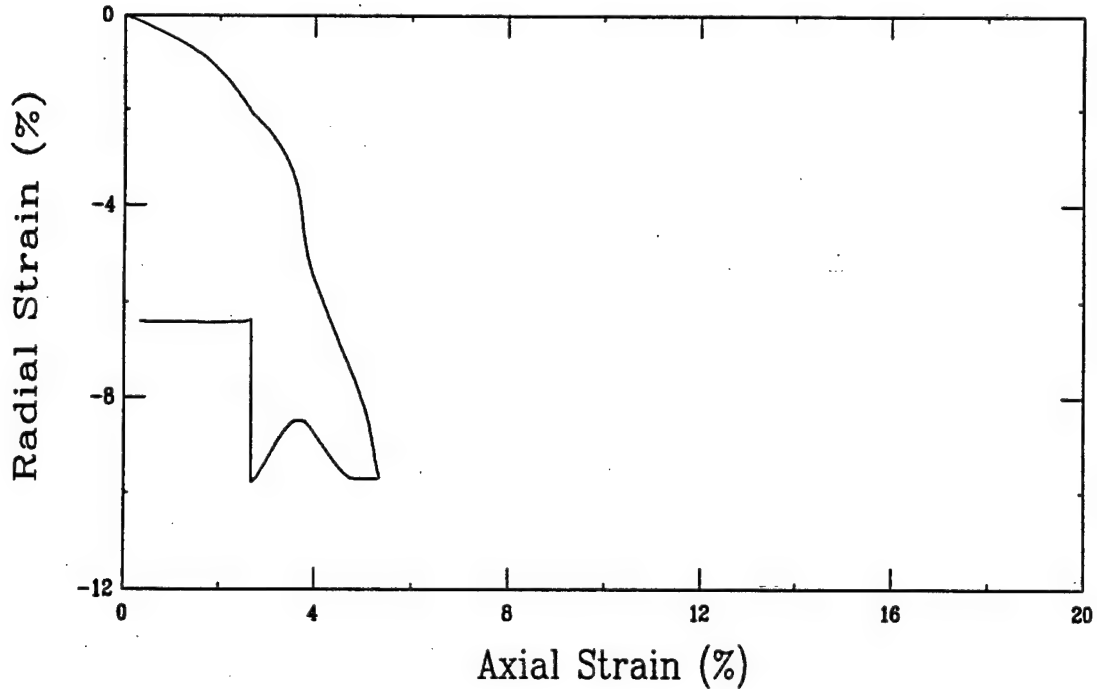
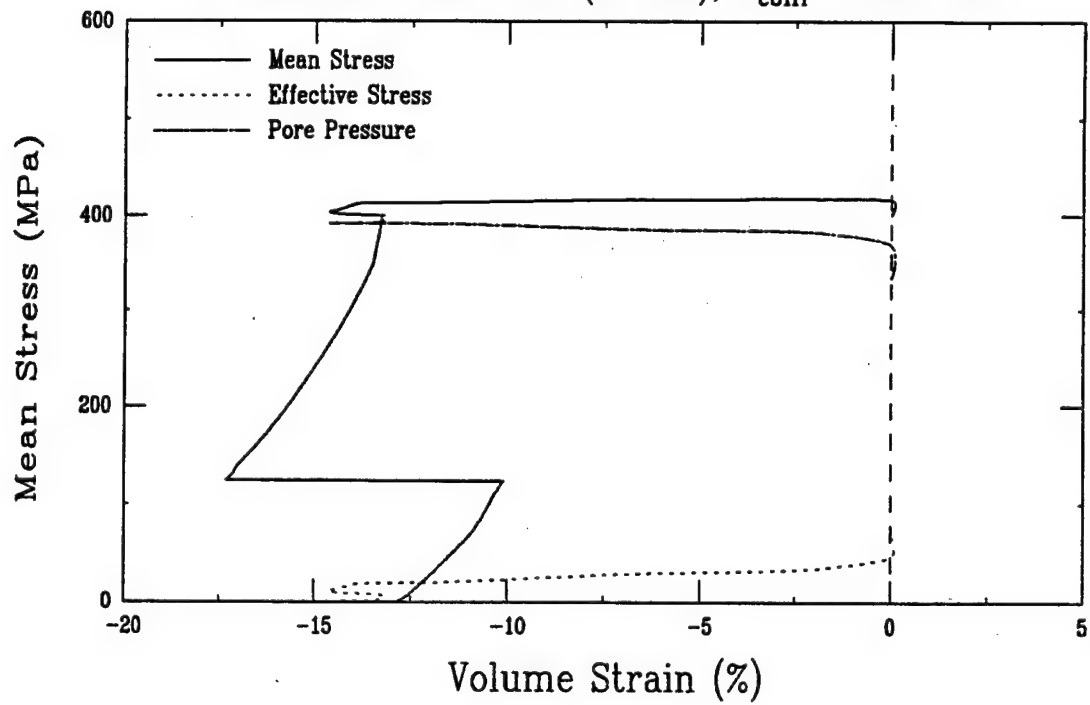
Undrained Triaxial Compression Test (M29B5)

Pumiceous Tuff U16b (GI-2D), $\sigma_{\text{conf}} = 400$ MPa

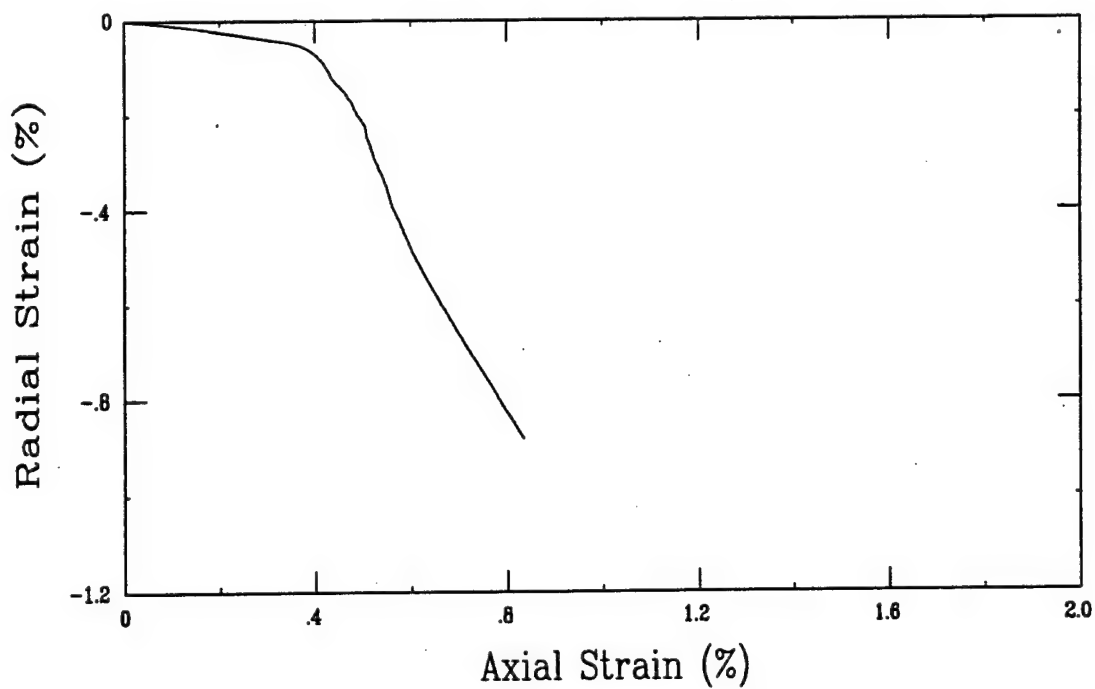
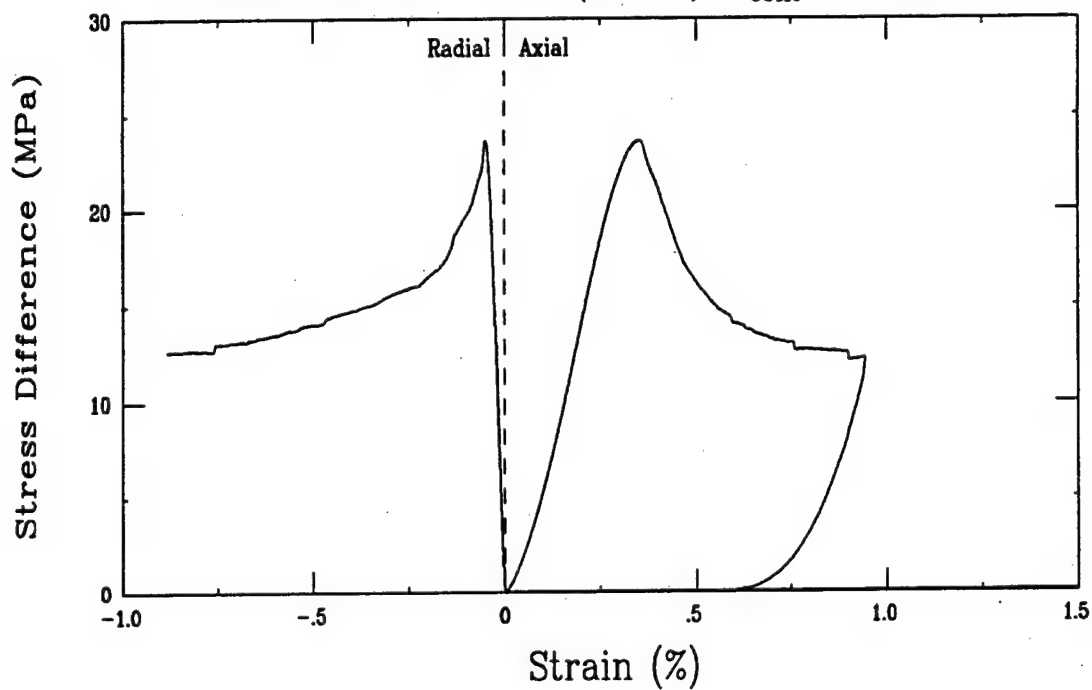


Undrained Triaxial Compression Test (M29B5)

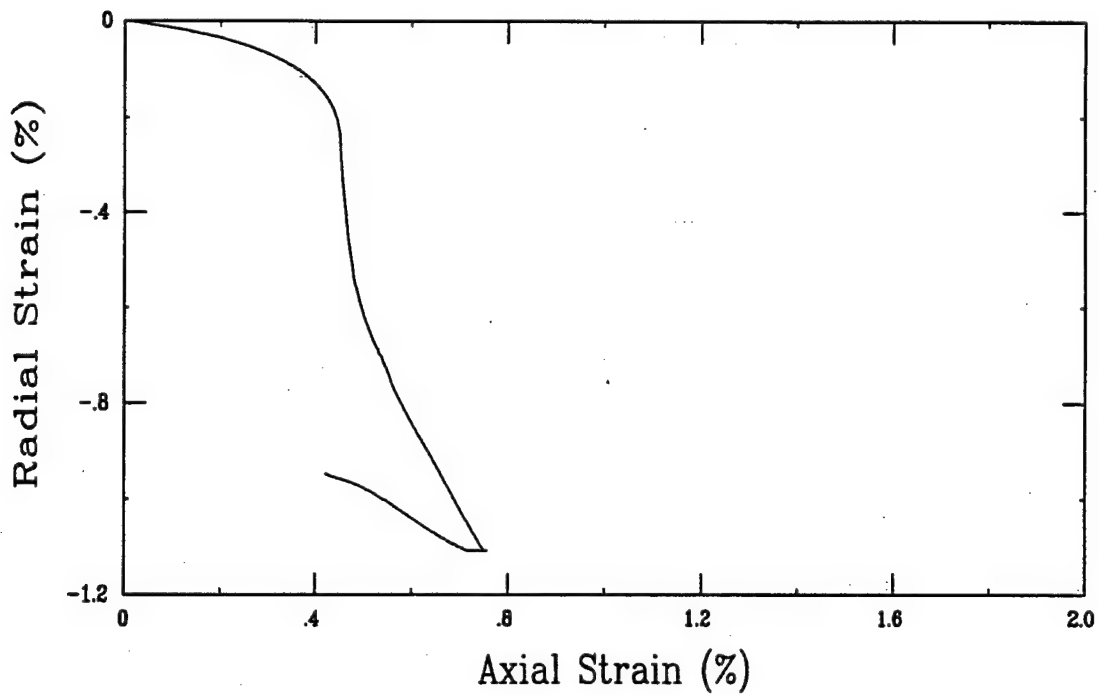
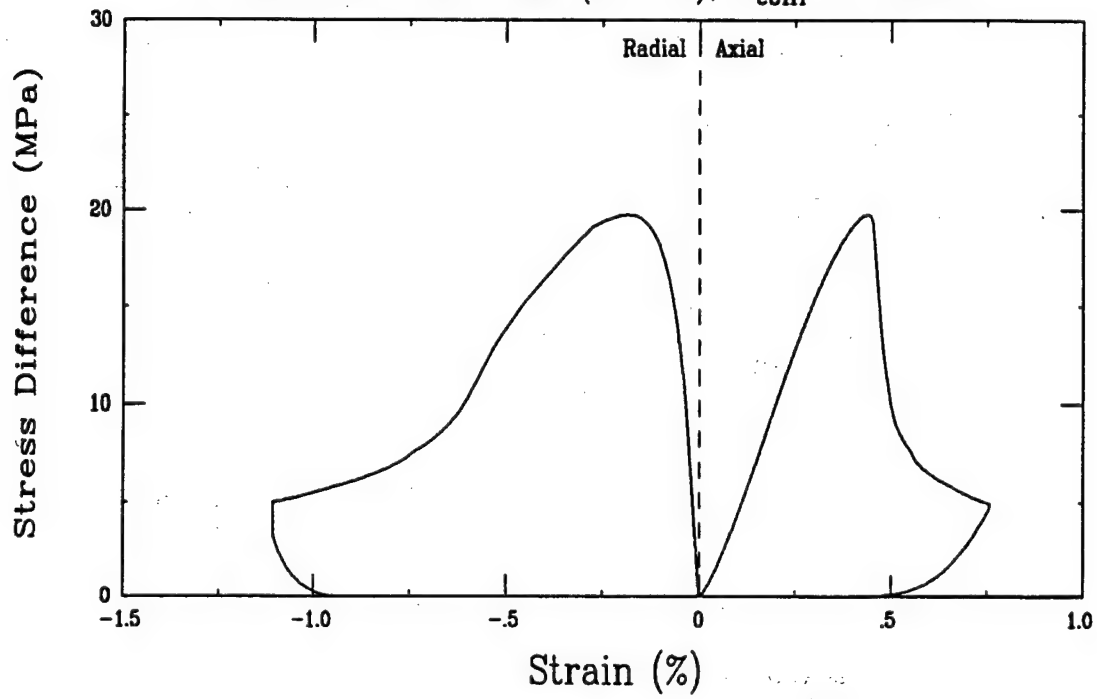
Pumiceous Tuff U16b (GI-2D), $\sigma_{\text{conf}} = 400 \text{ MPa}$



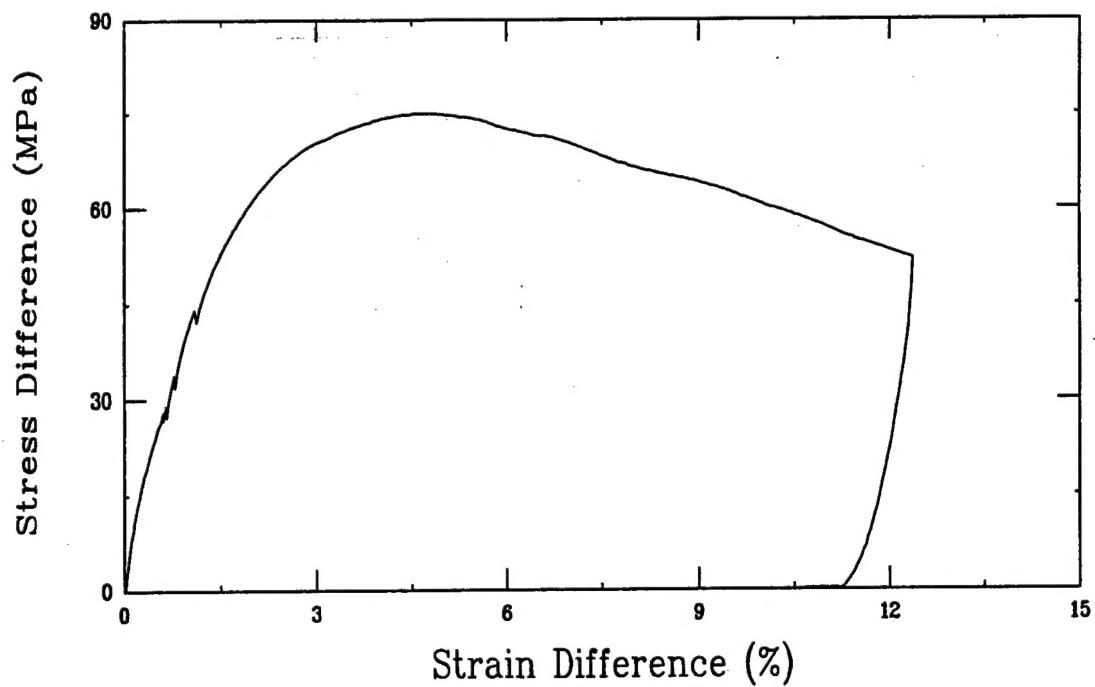
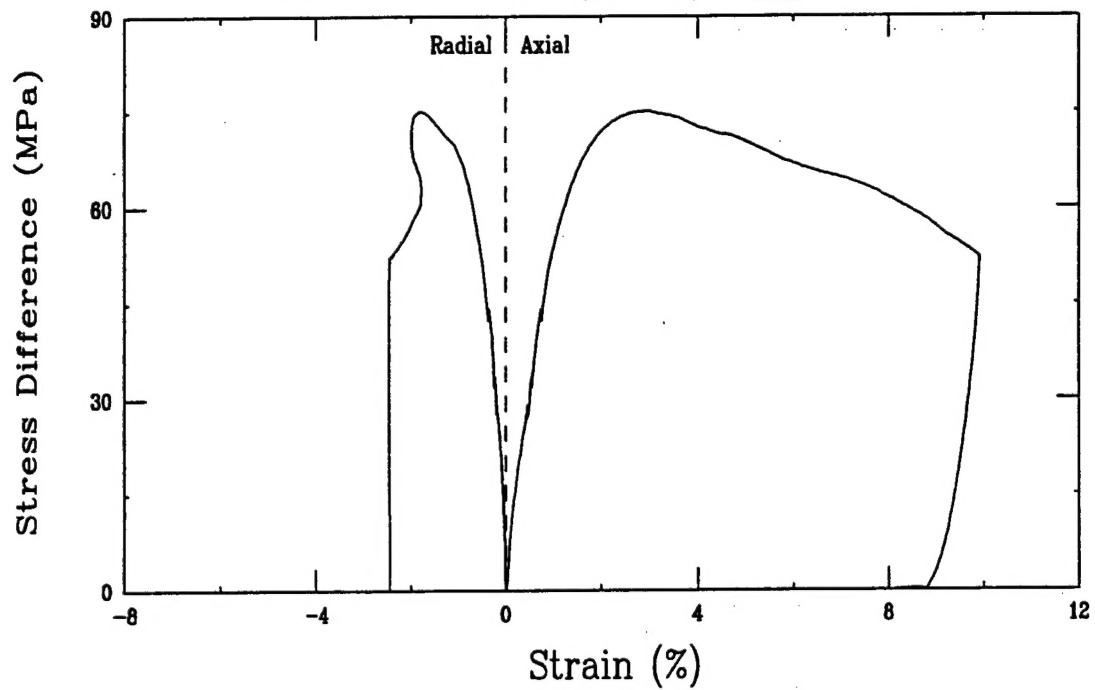
Triaxial Compression Test (M30A5)
Pumiceous Tuff U16b (GI-1B), $\sigma_{\text{conf}} = 0$ MPa



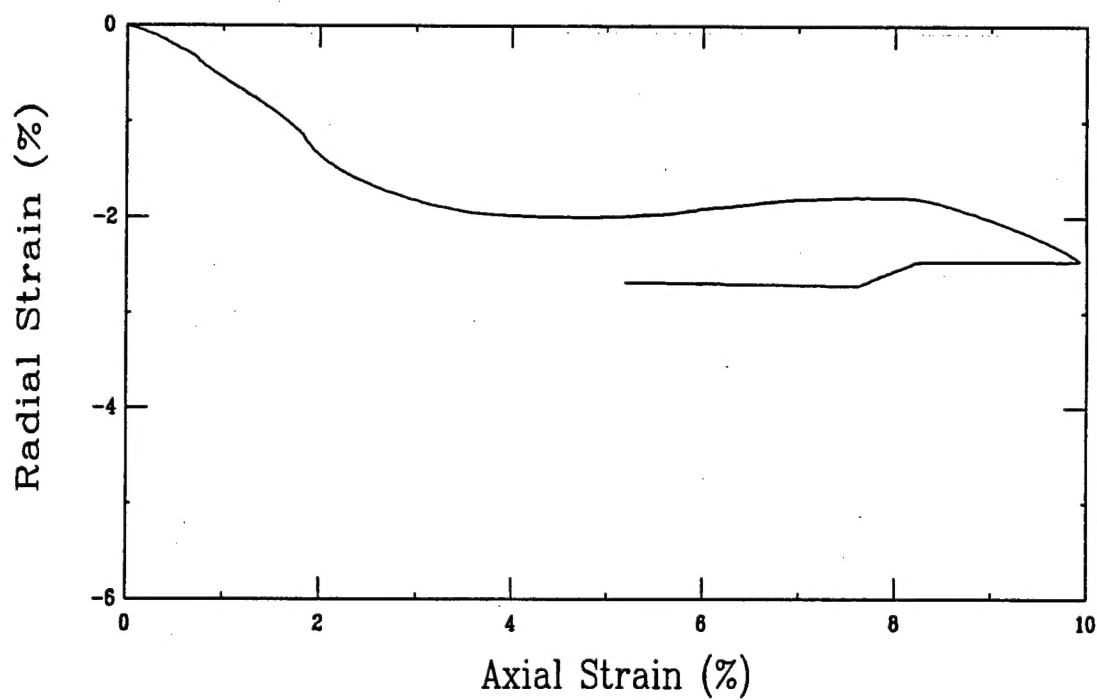
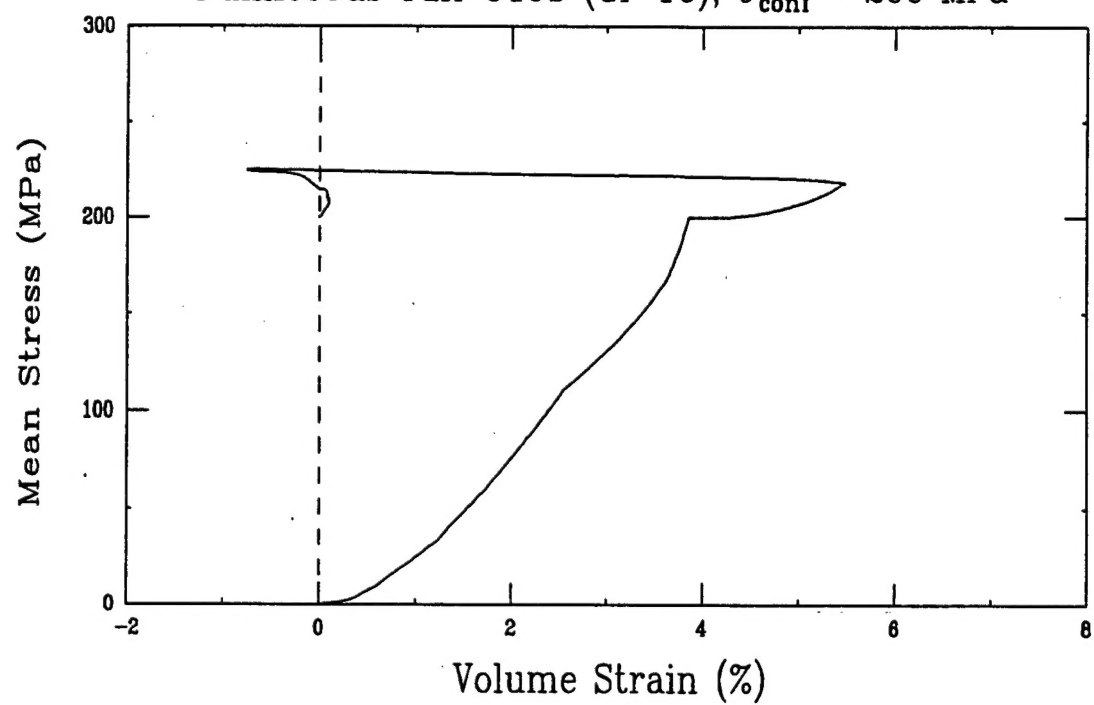
Triaxial Compression Test (A3A5)
Pumiceous Tuff U16b (GI-1D), $\sigma_{conf} = 0$ MPa



Triaxial Compression Test (A3E5)
Pumiceous Tuff U16b (GI-1C), $\sigma_{\text{conf}} = 200$ MPa



Triaxial Compression Test (A3E5)
Pumiceous Tuff U16b (G1-1C), $\sigma_{conf} = 200$ MPa



**DISTRIBUTION LIST
DNA TR-96-10**

DEPARTMENT OF DEFENSE

DEFENSE INTELLIGENCE AGENCY
ATTN: TWJ

DEFENSE SPECIAL WEAPONS AGENCY
ATTN: OPS
ATTN: PMT, K GOERING
ATTN: PMT, MR D BRUDER
2 CY ATTN: TRC
ATTN: WEP, W ULLRICH

DEFENSE TECHNICAL INFO CTR
2 CY ATTN: DTIC/OCF

FC DEFENSE SPECIAL WEAPONS AGENCY
ATTN: FCT-S, G BALADI
ATTN: FCTO
ATTN: FCTOS
ATTN: FCTTS, E TREMBA

DEPARTMENT OF THE ARMY

ADVANCED RESEARCH PROJECT AGENCY
ATTN: DEFENSE SCIENCES OFFICE

U S ARMY CORPS OF ENGINEERS
ATTN: CERD-L

U S A RMY ENGINEER DIST OMAHA
ATTN: MROED-S, H GAUBE

U S ARMY ENGR WATERWAYS EXPER STATION
ATTN: C D NORMAN
ATTN: CEWES-SD
ATTN: CEWES-SE, MR L K DAVIS
ATTN: CEWES-GS, DR D BANKS
ATTN: WESGR-M, J WARRINER
ATTN: TECHNICAL LIBRARY
ATTN: W MCMAHON
ATTN: W MILLER

DEPARTMENT OF THE AIR FORCE

AIR FORCE CTR FOR STUDIES & ANALYSIS
ATTN: AFSAA/SAI, RM 1D363 THE PENTAGON

AIR UNIVERSITY LIBRARY
ATTN: AUL-LSE

DEPARTMENT OF ENERGY

LOS ALAMOS NATIONAL LABORATORY
ATTN: REPORT LIBRARY

SANDIA NATIONAL LABORATORIES
ATTN: A F FOSSUM
ATTN: J D ROGERS
ATTN: R ZIMMERMAN
ATTN: T BERGSTRESSER
ATTN: TECH LIB

DEPARTMENT OF DEFENSE CONTRACTORS

ANALYTIC SERVICES, INC. (ANSER)
ATTN: K BAKER

APPLIED RESEARCH ASSOCIATES, INC.
ATTN: C J HIGGINS

APPLIED RESEARCH ASSOCIATES, INC.
2 CY ATTN: DANIEL E CHITTY
2 CY ATTN: S BLOUIN

APPLIED RESEARCH ASSOCIATES, INC.
ATTN: R FRANK

APPLIED THEORY, INC.
2 CY ATTN: JOHN G TRULIO

APTEK, INC.
ATTN: B LEWIS
ATTN: Y MURRY

BDM INTERNATIONAL INC
2 CY ATTN: DANNY N BURGESS
2 CY ATTN: DAVID M KENDALL
2 CY ATTN: GARY L WINTERGERST

BOEING TECHNICAL & MANAGEMENT SVCS. INC.
ATTN: W M LEAVENS
ATTN: A W SPENCER
ATTN: R BRYAN CAIRNS

UNIVERSITY OF TEXAS THE PERMEAN BASIN
2 CY ATTN: L STEPHEN MELZER

ITT RESEARCH INSTITUTE
ATTN: DOCUMENTS LIBRARY
ATTN: M JOHNSON

DNA-TR-96-10 (DL CONTINUED)

ITT SYSTEMS & SCIENCE CORP

ATTN: DASIAC

ATTN: DASIAC/DARE

ITT SYSTEMS & SCIENCES CORP

ATTN: RICHARD KEEFFE

JAYCOR

ATTN: CYRUS P KNOWLES

LACHEL AND ASSOCIATES, INC

ATTN: C LINAMEN

ATTN: J BECK

LOGICON RDA

ATTN: DR THOMAS A PUCIK

ATTN: LIBRARY

LOGICON RDA

ATTN: ED HUMPHREYS

MAXWELL FEDERAL DIVISION INC.

ATTN: K D PYATT, JR

NTS ENGINEERING

ATTN: S SHORT

PACIFIC-SIERRA RESEARCH CORP.

ATTN: H BRODE

PACIFIC-SIERRA RESEARCH CORP.

ATTN: D GORMLEY

SCIENCE APPLICATIONS INTL CORP

ATTN: H PRATT

ATTN: TECHNICAL REPORT SYSTEM

SCIENCE APPLICATION INTL CORP

ATTN: W LAYSON

SOUTHWEST RESEARCH INSTITUTE

ATTN: B THACKER

SRI INTERNATIONAL

ATTN: DR JIM GRAN

THE AEROSPACE CORP

ATTN: LIBRARY ACQUISITION

THE TITAN CORPORATION

ATTN: J THOMSEN

TITAN CORPORATION

ATTN: LIBRARY

ATTN: S SCHUSTER

ATTN: Y M ITO

TRW SPACE & DEFENSE SECTOR

ATTN: OUT6/W WAMPLER

UTD, INC.

ATTN: E FOSTER

WEIDLINGER ASSOC, INC.

ATTN: E WONG

ATTN: H LEVINE

WEDLINGER ASSOCIATES, INC.

ATTN: I SANDLER